



Universitat Autònoma de Barcelona

ADVERTIMENT. L'accés als continguts d'aquesta tesi queda condicionat a l'acceptació de les condicions d'ús establertes per la següent llicència Creative Commons:  http://cat.creativecommons.org/?page_id=184

ADVERTENCIA. El acceso a los contenidos de esta tesis queda condicionado a la aceptación de las condiciones de uso establecidas por la siguiente licencia Creative Commons:  <http://es.creativecommons.org/blog/licencias/>

WARNING. The access to the contents of this doctoral thesis it is limited to the acceptance of the use conditions set by the following Creative Commons license:  <https://creativecommons.org/licenses/?lang=en>



DOCTORAL THESIS

**Analysis of the single π^+ production in neutrino
neutral current interactions and
instrumentation developments for the future
understanding of neutrino physics using the
ND280 detector of the T2K experiment**

Author:

César JESÚS VALLS

Supervisors:

Dr. Thorsten LUX

IFAE

Prof. Federico SÁNCHEZ

Université de Genève

Academic tutor:

Dr. Maria del Pilar CASADO LECHUGA

IFAE

UAB

UNIVERSITAT AUTÒNOMA DE BARCELONA

Bellaterra (Barcelona), June 13, 2022

*Measure what can be measured,
and make measurable what cannot be measured.*

– GALILEO GALILEI

Abstract

English

Nowadays, one of the most active research fields within the domain of high energy physics is the study of neutrinos. In the mainstream theory, encompassed in the Standard Model (SM) of particle physics, the phenomenology of neutrino physics is determined by seven degrees of freedom, consisting of three masses (m_1, m_2, m_3), three mixing angles ($\theta_{12}, \theta_{13}, \theta_{23}$) and a CP-violating phase (δ_{CP}). Currently, the most prominent experimental challenge in neutrino physics is to determine precisely the values of these parameters in order to better understand the fundamental behavior of nature and to explore the validity of the SM.

The Tokai-To-Kamioka (T2K) experiment is one of the main references in the field. In T2K an accelerator-based neutrino or antineutrino beam is produced and measured at two sites: At 280 m from the production point using the ND280 detector and 295 km away in the Super-Kamiokande detector. ND280 is used to characterize the properties of the neutrino beam before any significant oscillation effects take place and to study how neutrinos scatter in matter at energies relevant to T2K. With this knowledge, an event rate prediction is calculated for Super-Kamiokande that in combination with data is used to measure neutrino properties, in particular θ_{13} , θ_{23} , $\Delta m_{23}^2 \equiv m_2^2 - m_3^2$ and δ_{CP} .

Two factors limit more accurate measurements in T2K. On one hand, the limited number of collected neutrino events determines the amount of statistical error. On the other hand, event rate predictions are affected by systematic uncertainties regarding the detector, beam, and neutrino interaction models. While the statistical error will decrease in the coming years as T2K continues to collect data, active work is needed to reduce systematic uncertainties. In this thesis two ways to achieve it are studied consisting of analysis and instrumentation developments.

In T2K's oscillation analysis (OA) one of the main sources of systematic uncertainty is that of neutrino neutral current interactions that produce a single π^+ in the final state (NC1 π^+). Current knowledge about this process is limited due to the fact that the only reported measurement consists of less than hundred interactions recorded in 1978 by the Gargamelle bubble chamber experiment. In this thesis, the first study of this type of interactions in a modern neutrino experiment is presented using T2K data collected by the ND280 detector. With this purpose, a new selection algorithm for ND280 data has been developed. The preliminary analysis of the output selected samples constitutes the most detailed description of the nature of this process. In addition, the extracted cross section uncertainty is less than half of that currently used in T2K OA and thus has the potential to significantly benefit future T2K oscillation measurements.

Improving existing instruments is an essential task to reduce systematic uncertainties. To this end, the ND280 detector is being significantly upgraded with the addition of three new detection technologies: two new High-Angle TimeProjection-Chambers (HATPCs), a novel fully Super-Fine-Grain-Detector (SuperFGD) and six Time-Of-Flight (ToF). In this thesis, relevant contributions to the development of these technologies are presented, including: simulation-based sensitivity studies, validation tests of the novel ERAM-based readout of the HATPCs, measurements of the response and the PID potential of SuperFGD using prototype data and the development of new deep learning reconstruction methods for SuperFGD and the ToF panels.

Spanish

Hoy en día, uno de los campos de investigación más activos dentro del dominio de la física de altas energías es el estudio de los neutrinos. En la teoría dominante, contenida en el llamado Modelo Estándar (ME) de la física de partículas, la fenomenología de la física de neutrinos está determinada por siete grados de libertad, que consisten en tres masas (m_1, m_2, m_3), tres ángulos de mezcla ($\theta_{12}, \theta_{13}, \theta_{23}$) y una fase que viola la simetría CP (δ_{CP}). Actualmente, el desafío experimental más destacado en la física de neutrinos es determinar con precisión los valores de estos parámetros para ahondar en el comportamiento fundamental de la naturaleza y explorar la validez del Modelo Estándar.

El experimento Tokai-To-Kamioka (T2K) es una de las principales referencias en el campo. En T2K se produce mediante un acelerador un haz de neutrinos o antineutrinos que es medido en dos ubicaciones: a 280 m del punto de producción mediante el detector ND280 y a 295 km de distancia con el detector Super-Kamiokande. ND280 se utiliza con el fin de caracterizar las propiedades del haz de neutrinos antes de que se produzcan efectos de oscilación significativos y para estudiar cómo interactúan los neutrinos en las energías relevantes para T2K. Con este conocimiento, se calcula una predicción de la tasa de eventos para Super-Kamiokande que, en combinación con los datos, se usa para medir las propiedades de los neutrinos, en particular θ_{13} , θ_{23} , $\Delta m_{23}^2 \equiv m_2^2 - m_3^2$ y δ_{CP} .

Dos factores limitan mediciones más precisas en T2K. Por un lado, el número limitado de eventos recopilados determina la cantidad de error estadístico. Por otro lado, las predicciones de la tasa de eventos se ven afectadas por incertidumbres sistemáticas relativas a los modelos que describen las interacción, el detector y el haz. Si bien el error estadístico disminuirá en los próximos años a medida que T2K continúe acumulando datos, se necesita trabajar activamente para reducir las incertidumbres sistemáticas. En esta tesis se estudian dos formas de conseguirlo mediante el desarrollo de un nuevo análisis y avances en instrumentación.

En el análisis de oscilación (AO) de T2K, una de las principales fuentes de incertidumbre sistemática es la de las interacciones de neutrinos mediadas por corrientes neutras que generan un único π^+ en el estado final (NC1 π^+). El conocimiento actual sobre este proceso es limitado debido al hecho de que la única medida reportada consiste en menos de cien interacciones registradas en 1978 por la cámara de burbujas del experimento Gargamelle. En esta tesis se presenta el primer estudio de este tipo de interacciones hecho con un experimento moderno de neutrinos mediante el análisis de datos de T2K recolectados por el detector ND280. Con este propósito, se ha desarrollado un nuevo algoritmo de selección de eventos en ND280. Los resultados preliminares constituyen la descripción más detallada de la naturaleza de este proceso. Además, la incertidumbre de la sección eficaz extraída es menos de la mitad de la utilizada actualmente en el AO de T2K y por ende, tiene el potencial de mejorar significativamente las futuras medidas de oscilación de neutrinos que se hagan en T2K.

Mejorar los instrumentos existentes es una tarea esencial para reducir las incertidumbres sistemáticas. Con este fin, el detector ND280 está siendo mejorado mediante la adición de tres nuevas tecnologías de detección: dos nuevas cámaras de proyección temporal (HATPCs), un novedoso detector de grano superfino (SuperFGD) y seis paneles de tiempo de vuelo (ToF). En esta tesis, se presentan contribuciones relevantes al desarrollo de estas tecnologías, que incluyen: estudios de sensibilidad basados en simulación, pruebas de validación de los módulos de lectura ERAM para las HATPCs, la caracterización de las señales y del potencial de identificación de partículas de SuperFGD usando un prototipo y el desarrollo de nuevos métodos de reconstrucción para SuperFGD y los paneles ToF basados en algoritmos de aprendizaje profundo.

Acknowledgements

This PhD has been a fantastic journey. Along these years I found my strength, my will and my dreams. It fills me with joy to think about the many incredible people I met on the way. I truly and deeply appreciate all the help I got and the many moments of true happiness that I have been able to share.

In the first place, I would like to state that none of the work presented here would have been possible without the generations of researchers who worked before me nor without the financial aid I got. Hence, I would like to acknowledge the help of everyone who contributed to this project, directly or indirectly.

Among the people I have met in science my supervisors stand out for their incredible support, knowledge and human quality. Federico, you gave me the opportunity that made all of this possible for which I will always be grateful. Since the early days in my master I found in you a role model and a beacon of hope. Thanks to you I found my passion which is that of doing research. You were the first person I ever met who works in a way that I understand and I can not emphasize enough how much that changed my life and shaped my current self. You have always listened, respected, supported and trusted me. You gave me a lot of your time even when you had none. You treated me as an equal and made me feel valuable and supported. You gave me everything I needed to grow up and to be happy in these crucial years of my life. Thorsten, you have been essential to me. You have been the perfect mentor, the balancing force I needed all along these years. You have been there for me, always. You have answered my endless questions and always pushed me to grow. You have taught me how academia is much broader than simply doing science and the value of organization and politics in pushing forward the experiments. You have encouraged me to pursue my own ideas and projects and you have given me as much freedom as I needed. From you I have learned the importance of setting up goals, to be always careful to anticipate events, to have always a back up plan and the value of materializing ideas into reality.

Through T2K and my stays abroad I have met outstanding people which have enormously contributed to my formation as a researcher and to my happiness. Davide, Claudio and Stephen you have been an inspiration to me. I deeply appreciate your invaluable support, guidance and help. Sergey, Dana, Christoph, Emanuele and Saúl it has always been a pleasure to work and learn from you. Sebastián, Caspar, Callum and M. Lamoreux, thank you all for your feedback and help. Special thanks to Danaisis, Sophie and Sasha for their help with HighLAND. Marc, Paula, Jordi, Elena and Miguel, I truly enjoyed our side projects. Lastly, to the many people I found on my stays: Carlos, Adri, Sergio, L. Pereira, Jesús, Stergios, Fabio, Marta, L. Munteanu, Pablo and Emily, thanks for all the moments we shared!

On a more personal note, I would like to highlight that the tricky path that got me to this point was seeded by my grandparents whom worked really hard throughout their lives with the goal of giving better starting chances to their kids. Similarly, nothing in my life would have been possible without the great efforts and deep love of my parents. Mom, I will always admire you. You taught me to persevere, to stay true to myself, to plan and to fight for my goals. I would never have dared reaching this far without you. Dad, you are my eclectic spark. You taught me to wonder, to think. You showed me the value of open mindedness, creativity and originality. Nietzsche said "You need chaos in your soul to give birth to a dancing star". You gave me the chaos that I most cherish.

To my friends. To Daniel Cañueto who will never be able to read this words but will always live in my memory. To Raúl, who got me excited about physics. To Marcel, Marc, Sergi and Claudia.

My backbone. I share with you some of the best moments in my life, a trend that I am decided to continue. To Elvis, Rubén and Nacho and to Bet, Julia and Uxue, you kept alive my faith in humanity. Your joy and kindness have made of me a happier and better self. To you all, thanks for being always by my side.

The last words are for you, Claudia. You made this possible. All of it. Your support, joy and strength are infinite. You made of these years, so far, the best of my life. You are the fuel that pushes me forward to pursue my dreams and to become, day after day, a better self. I have learned from you more than from anyone else in my life. Every single of these pages is impregnated with my enthusiasm and joy, which I found in you. You are my true inspiration and my hope. I hope to continue living this dream for many years to come, by your side. Either in Spain, at CERN, in Japan, or elsewhere, my heart will always be with you.

Contents

Abstract	II
Acknowledgements	IV
1 Introduction	1
1.1 Introduction	1
1.2 Organization	2
1.3 Contributions	3
I Theoretical background	6
2 Neutrino physics	7
2.1 Neutrino history	7
2.1.1 Proposal, early theory and discovery	7
2.1.2 The birth of the Standard Model	8
2.1.3 Neutrino oscillations	10
2.1.4 Overview of a new era: status and prospects	10
2.2 Neutrino theory	11
2.2.1 The neutrino in the Standard Model	11
2.2.2 The neutrino beyond the Standard Model	17
2.3 Neutrino oscillations	18
2.3.1 Oscillations in vacuum	19
2.3.2 Oscillations in matter	21
2.3.3 Solar neutrino oscillations	22
2.3.4 Accelerator and atmospheric neutrino oscillations	24
2.3.5 Reactor neutrino oscillations	26
2.3.6 Global analysis of 3ν data	27
2.3.7 Sterile neutrinos	31
2.4 Neutrino masses	33
2.4.1 Majorana signatures	35
2.4.2 Neutrino mass values	37
2.4.3 Direct mass searches	38
2.4.4 Cosmological bounds	39
3 Neutrino interactions	40
3.1 Introduction	40
3.1.1 Neutrino interactions and oscillations	40
3.1.2 Neutrino cross sections in the $E_\nu \approx 1$ GeV region	41
3.1.3 Experimental approach	41
3.2 Neutrino-nucleon scattering	42

3.2.1	Quasielastic neutrino scattering	43
3.2.2	Meson production in neutrino scattering	45
3.2.3	Deep inelastic neutrino scattering	46
3.3	Neutrino-nucleus scattering	48
3.3.1	Initial nuclear state	48
3.3.2	Additional nuclear effects	50
3.3.3	Final State Interactions (FSI)	50
3.3.4	Detector limitations	51
3.3.5	Interaction topologies	51
3.3.6	State-of-the-art challenges	52
3.4	Neutrino event generators	53
3.5	Neutrino scattering data	54
3.5.1	Early experiments	54
3.5.2	Modern experiments	54
4	Fundamentals of neutrino instrumentation	59
4.1	Relevant interaction processes	59
4.1.1	Charged particles	59
4.1.2	Photons	62
4.1.3	Neutrons	63
4.2	Time Projection Chambers (TPCs)	64
4.2.1	Working principle	64
4.2.2	Momentum reconstruction	65
4.2.3	Particle identification	66
4.3	Scintillation detectors	67
4.3.1	Light extraction in plastic scintillators	67
4.3.2	Energy reconstruction	68
4.3.3	Particle identification	68
4.4	Photomultipliers	69
4.4.1	Working principle	69
II	Study of $NC1\pi^+$ interactions in T2K	70
5	The T2K experiment	71
5.1	Introduction	71
5.1.1	Brief T2K's history	71
5.2	The T2K neutrino beam	73
5.2.1	The off-axis beam technique	76
5.2.2	The T2K beam prediction	77
5.3	The near detectors complex	80
5.4	The on-axis detector INGRID	80
5.5	The Off-Axis detector ND280	81
5.5.1	UA1 magnet	81
5.5.2	Side Muon Range Detector (SMRD)	82
5.5.3	Electromagnetic Calorimeter (ECal)	83
5.5.4	Pi-zero Detector (PØD)	84
5.5.5	Fine-Grained-Detectors (FGDs)	85
5.5.6	Time-Projection-Chambers (TPCs)	87
5.5.7	Electronics	91
5.5.8	DAQ and GSC	93

5.5.9	ND280 software	94
5.6	Super-Kamiokande	95
6	Motivations and analysis strategy	97
6.1	Introduction and motivations	97
6.1.1	Existing published measurements	98
6.1.2	NC1 π^\pm and T2K's oscillation analysis	99
6.1.3	Existing studies and constrains in T2K	99
6.2	Analysis overview	101
6.2.1	Datasets	102
6.2.2	Signal and background definitions	102
6.2.3	Initial look into the signal according to MC generators	103
7	The NC1π^+ Selection Algorithm and its Associated Systematic Uncertainties	108
7.1	The HighLAND2 framework	108
7.2	The NC1 π^+ selection algorithm	109
7.2.1	FGD1 fiducial volume definition	110
7.2.2	Event quality cut	111
7.2.3	FGD1-TPC multiplicity cut	111
7.2.4	Single positive track cut	111
7.2.5	Upstream vetos	111
7.2.6	Michel electron cut	112
7.2.7	TPC pion likelihood cut	112
7.2.8	Ecal pion likelihood cut	113
7.2.9	FGD1 MIP-like cut	114
7.3	Selection performance	116
7.3.1	Signal sample	116
7.3.2	$\bar{\nu}_\mu$ CC sideband	121
7.3.3	NC1 π^+ + 1 FGD1 track sideband	122
7.3.4	NC0 π sideband	123
7.4	Evaluation of systematic uncertainties associated to the selection	124
7.4.1	Detector systematics	125
7.4.2	OOFV systematics tuning	126
7.4.3	SINeutron systematics tuning	127
7.4.4	Computation of pile up corrections and systematics	127
7.4.5	Computation of FGDMIP-like variable corrections and systematics	129
7.5	Final detector systematics	131
7.6	Comparisons to data	132
8	Fitting and cross section results	134
8.1	Binned likelihood fitting	134
8.1.1	Likelihood definition	134
8.1.2	Cross-section extraction	136
8.1.3	Fitting framework	136
8.1.4	Binning for the reconstructed kinematics	137
8.1.5	Binning for the true kinematics	137
8.2	Nuisance parameters	139
8.2.1	Detector systematics	139
8.2.2	Flux model systematics	139
8.2.3	Cross section model systematics covariance	140
8.3	Normalization factors	143

8.3.1	Number of targets	143
8.3.2	Efficiency	143
8.3.3	Flux	143
8.4	Fake data studies	144
8.4.1	Asimov fit	144
8.4.2	Fake data studies	146
8.5	Data Fit	149
III T2K-II and the ND280 upgrade		151
9	T2K-II and the ND280 upgrade	152
9.1	Introduction	152
9.2	T2K's Beam upgrade	154
9.2.1	J-PARC main ring upgrades	154
9.2.2	Upgrade in the neutrino beamline	155
9.2.3	Monitoring upgrades	156
9.3	The WAGASCI-BabyMIND detector	156
9.3.1	WAGASCI	156
9.3.2	Proton module	157
9.3.3	NINJA	158
9.3.4	BabyMIND	160
9.3.5	Physics motivations	161
9.4	GADZOOKS!	162
9.5	Overview of the ND280 upgrade	163
9.5.1	The removal of the PØD	163
9.5.2	Physics Goals	164
9.5.3	The ND280 upgrade geometry	164
9.5.4	The ND280 upgrade expected physics performance	166
10	The High-Angle Time-Projection-Chambers	169
10.1	Introduction	169
10.2	Design and construction	170
10.2.1	The ERAMs	170
10.2.2	Readout electronics and DAQ	172
10.2.3	Field-cage box	173
10.2.4	Box prototyping	175
10.2.5	Cathode	177
10.2.6	Module frames	178
10.3	The ERAM0 prototype	179
10.3.1	Production	179
10.3.2	Beam test setup	179
10.3.3	Track reconstruction	180
10.3.4	Calibration and gas monitoring	180
10.3.5	Gain studies	182
10.3.6	Characterization of the charge spreading	184
10.3.7	dE/dx resolution	185
10.3.8	Spatial resolution	187
10.3.9	ERAM0 analysis conclusions	190
10.4	The ERAM1 prototype	190
10.4.1	Production	190

10.4.2	Beam test setup	190
10.4.3	Track reconstruction	191
10.4.4	Spatial resolution	192
10.4.5	dE/dx resolution	193
10.4.6	RC map characterization	196
10.4.7	ERAM1 analysis conclusions	197
10.5	Final ERAM production and testing	198
11	The SuperFGD	200
11.1	Introduction and overview	200
11.1.1	Cube production and detector assembly technique	202
11.1.2	Mechanical box	204
11.1.3	Fibers	205
11.1.4	Photosensors	206
11.1.5	Light calibration system	207
11.1.6	Readout electronics and DAQ	207
11.2	First prototypes	209
11.3	The $24 \times 8 \times 48$ SuperFGD prototype	210
11.3.1	Calibration	211
11.3.2	The 2018 beam test setup at CERN	212
11.3.3	Signal thresholds and noise	212
11.3.4	Hit amplitude uniformity	213
11.3.5	Optical crosstalk	214
11.3.6	Fiber light attenuation	216
11.3.7	Cube response	216
11.3.8	Time resolution	217
11.3.9	Particle identification	219
11.3.10	Electron-gamma separation	220
11.4	Track reconstruction and signal classification	221
11.4.1	2D to 3D matching	221
11.4.2	GNN voxel classification	223
11.4.3	SuperFGD simulation	224
11.4.4	Datasets	225
11.4.5	GNN training	225
11.4.6	Results	226
11.4.7	Systematic uncertainties associated to the GNN	229
11.5	Neutron detection in SuperFGD	229
11.5.1	Neutron measurements with the $24 \times 8 \times 48$ SuperFGD prototype	232
12	The Time-of-Flight panels	234
12.1	Overview and Motivations	234
12.2	Development of the ToF technology	235
12.3	The ToF panels for the ND280 upgrade	235
12.3.1	SiPMs amplifier board	236
12.3.2	DAQ	236
12.3.3	Performance tests with a single bar	237
12.4	Final tests at CERN	238
12.5	Data-driven detector signal characterization with constrained bottleneck autoencoders	238
12.5.1	Autoencoders	240
12.5.2	Methodology	242

12.5.3	Results and discussion	243
12.6	ToF status and future plans	246
IV	Conclusions	249
13	Conclusions	250
A	DUNE and the photon detection system of the protoDUNE-DP detector	252
A.1	Introduction	252
A.1.1	Working principle of LArTPCs	253
A.1.2	History and state-of-the-art of LArTPCs	253
A.2	The protoDUNE-DP detector	254
A.3	The photo-detection system of the protoDUNE-DP detector	255
A.3.1	PMT preparation	255
A.3.2	Installation	256
A.3.3	Performance results	257
B	ASTRA a novel range telescope for proton computerized tomography	258
B.1	Introduction	258
B.2	pCT design	259
B.2.1	The DMAPS-based tracker	259
B.2.2	ASTRA	259
B.3	Methodology	260
B.3.1	Tracking	260
B.3.2	Performance tests	262
B.4	Results	264
B.4.1	Radiography	266
B.4.2	Proton CT scan	267
B.5	Conclusions, status and plans	269

Chapter 1

Introduction

“What do I advise? Forget it all. Don’t be afraid. Do what you get the most pleasure from. Is it to build a cloud chamber? Then go on doing things like that. Develop your talents wherever they may lead. Damn the torpedoes - full speed ahead! If you have any talent, or any occupation that delights you, do it, and do it to the hilt.”

– RICHARD FEYNMAN

This Chapter works as an introduction for the thesis and summarizes its structure. Most of the studies here presented have been made in collaboration with other researchers and, consequently, this Chapter also reviews my individual contributions.

1.1 Introduction

High energy physics (HEP), i.e. the physics of the fundamental constituents of matter and its interactions, is a widely studied field of research. The incremental development of HEP knowledge over the years and its deep and diverse ramifications have created a whole scientific culture around it which spans from almost pure mathematics to the manufacture and operation of some of the most complex instruments developed by humankind. This incredibly rich environment has forced the field to evolve into a community divided into two main branches: experimental and theoretical HEP. Nowadays, most experiments are run by scientific collaborations whilst the mainstream theory has been grouped into the so-called Standard Model.

The work here presented focuses on the study of neutrinos, a type of elementary particles in the Standard Model. This thesis is devoted to the experimental determination of neutrino properties and, consequently, the bulk of the work has been carried out in the Tokai-To-Kamioka (T2K) neutrino experiment, a leading reference in the study of the neutrino physics and, in particular, in the measurement of neutrino oscillations.

The work here presented can be subdivided into two main blocks:

- On one hand, T2K data has been analyzed with the main goal to measure single positive pion production in neutrino neutral current interaction. The measurement, which is the first of its kind, aims to expand our knowledge on this type of processes, relevant for the study of neutrino oscillations in T2K.
- On the other hand, R&D has been made to upgrade the ND280 detector of the T2K experiment using three novel detector technologies. The work here presented has helped to validate the upgrade design and to push it from the conceptual stage to the construction of the final detectors.

Both of the former tasks complement each other encompassing the whole domain of experimental HEP: from detector instrumentation to HEP data analysis and all the gray areas in-between. Individually the results provide relevant information on how neutrinos behave and how to build improved neutrino detectors. Together, the results add up and contribute to the future performance of the T2K experiment and to our future understanding of neutrino physics.

1.2 Organization

The thesis is organized in three parts. The first of them, named *Theoretical background*, is dedicated to the review of existing knowledge and the introduction of concepts that are fundamental to contextualize and understand the studies in the rest of the Chapters.

- **Chapter 2:** It reviews the basics of neutrino physics presenting key concepts, definitions and useful formulae, especially concerning the phenomenon of neutrino oscillations. It describes the state-of-the-art of this field of research, its major challenges and future prospects.
- **Chapter 3:** It reviews the state-of-the-art theoretical and experimental knowledge on neutrino interactions especially concerning neutrino-nucleus scatterings at $E_\nu \approx 1$ GeV and their connection to the measurement of neutrino oscillations.
- **Chapter 4:** It reviews the fundamental processes associated to the passage of particles through matter and describes the basics of how Time-Projection-Chambers (TPCs), plastic scintillators and photosensors work.

The second part of the thesis, named *Study of $NC1\pi^+$ interactions in T2K*, is dedicated to the study of neutrino neutral-current interactions producing a single positive pion ($NC1\pi^+$). The study uses T2K's data measured in the near detector ND280.

- **Chapter 5:** It describes the T2K experiment. It presents its working principle and reviews one by one its main elements: the neutrino beam, the near detectors INGRID and ND280 and the far detector Super-Kamiokande.
- **Chapter 6:** It reviews the motivations to study $NC1\pi^+$ interactions in the context of T2K, outlines previously existing studies and outlines the analysis strategy.
- **Chapter 7:** It describes a new selection algorithm to identify $NC1\pi^+$ interactions in ND280, discusses its performance and details the evaluation of its associated systematic uncertainties.
- **Chapter 8:** It explains the fitting method and presents fit validation tests, fake data studies and the extracted cross section preliminary results.

The third part, named *T2K-II and the ND280 upgrade*, describes a series of upgrades and improvements for the T2K experiment. In particular, it focuses on the upgrade of the ND280 detector describing developments and tests for its three new sub-detector technologies: the High-Angle Time-Projection-Chambers (HATPCs) the Super-Fine-Grained-Detector (SuperFGD) and the Time-Of-Flight panels (ToF).

- **Chapter 9:** It reviews the motivations and plans for the upgrades of T2K including: the upgrade of its beam, the inclusion of a new near detector named WAGASCI-BabyMIND to the experiment, the addition of a Gadolinium salt to the water of Super-Kamiokande and overviews the upgrade of the near detector ND280 and its expected performances.

- **Chapter 10:** It presents the new HATPCs detectors. It reviews its design and presents the prototype testing of its field-cage box and novel readout technology. In particular, it describes the development, validation and characterization studies of the Encapsulated Resistive Anode Micromegas (ERAM) technology.
- **Chapter 11:** It describes the novel SuperFGD detector from its design to the prototype testing and its final construction. Several studies relative to this detector are presented: The validation and characterization of this technology using a beam of charged particles, the development of a novel deep learning method for signal classification and the study and measurement of neutrons with this technology.
- **Chapter 12:** It explains the new ToF detector from its construction to its ongoing final characterization. In this context, a novel deep learning method is presented to perform data-driven signal characterization.

Additionally, the thesis contains two Appendices presenting work that has been done out of the scope of the T2K experiment.

- **Appendix A:** It overviews the DUNE experiment and describes the protoDUNE-DP detector and the preparation and installation of its photo detection system.
- **Appendix B:** It presents simulation-based feasibility studies proposing a novel range telescope, named ASTRA, for proton computerized tomography.

1.3 Contributions

The background and introductory Chapters 1, 2, 3 and 4 correspond to the review and presentation of well-established knowledge necessary to contextualize and understand the upcoming Chapters and, consequently, the material there presented is extracted from previously existing sources, cited throughout the text. Nonetheless, the compilation of the information, its organization and the text itself are the result of my own understanding and insight on the topics discussed on them. Chapter 5, describes the T2K experiment. I am a member of the T2K collaboration since 2019. In 2018 and 2019 I took data with ND280 for T2K runs 9 and 10. Those Runs have already been used in the latest oscillation analyses and used to show for the first time a potentially large matter-antimatter asymmetry in neutrino oscillations [1, 2].

The possibility to study $NC1\pi^+$ interactions as part of this thesis was suggested by Prof. Federico Sánchez. The work of the $NC1\pi^+$ analysis, presented in Chapters 6,7 and 8, is my original work: The development of the selection algorithm, the evaluation and of its performance and systematics, the fitting tests, fake data studies and preliminary cross-section results. It must be noted that this study has been carried out within the T2K collaboration and, therefore, its outcome relies and has benefit on the previous work of many researchers as well as on the feedback and guidance of numerous T2K collaborators.

In Chapter 9, my contributions are relative to my participation to the refurbishments tasks of Super-Kamiokande in 2018 in preparation for the addition of the Gadolinium salt to the water and to the studies and confection of the ND280 upgrade Technical Design Report (TDR) [3]. As part of the ND280 upgrade simulations and reconstruction working group I played an important role in the development of the GEANT4 based simulation framework that was used to perform the TDR physics studies and the determination and validation of the final sub-detector envelopes. Concerning the physics studies, building upon the previous work of collaborators I calculated to final expected event rates, efficiencies and purities for the ν_μ CC studies.

Chapter 10 describes the work relative to the HATPC technology. Under the supervision of Dr. Thorsten Lux I joined the HATPCs project in 2018, when the overall HATPC design was still under discussion. As part of the ND280 TDR, I implemented the HATPC geometry in the simulation and used the early ν_μ CC studies to validate its design from the physics perspective. I participated in setting up the first beam test in 2018 at CERN and collected data with a first prototype of the new HATPCs readout, based on the ERAM modules. Later, I played a major role on the first analysis of its data, presented in Ref. [4], doing a significant fraction of the final studies (gas quality, gain, dE/dx) and substantially participating in others (pad uniformity, spatial resolution). In 2019, a second beam test was done at DESY to test a second ERAM prototype. The data was collected and analyzed by collaborators. Nonetheless, this new analysis was built upon the strategies and software solutions developed for the CERN beam test and, consequently, I continued actively involved in this study, specially at the beginning of the analysis, helping collaborators to adapt the existing tools to perform the second analysis which can be found in Ref. [5]. With respect to the field-cage development and construction, I attended to the construction of the first prototype box with which I took data at CERN in 2019. In 2020 a second box prototype was built and measured by collaborators in 2021 in a beam test at DESY. It was later also tested in a second beam test at CERN in which I participated. The data of these last two tests, not presented in Chapter 10, is still being analyzed by collaborators. The final detector production is ongoing. This includes the fabrication and commissioning of the final boxes and the manufacture of 40 ERAMs. Concerning the latter, I participated in the commissioning of the final ERAMs using a dedicated test-bench at CERN.

Chapter 11 describes the work relative to the SuperFGD technology. My first interaction with SuperFGD was in 2018, in the TPC beam test at CERN. On it, the final SuperFGD prototype took data in the same beam line, placed behind the TPC where the first ERAM prototype was being tested. Close to the finalization of the first ERAM prototype analysis and with the support of my thesis supervisors, I decided to join the team analyzing SuperFGD's prototype beam test data. I adapted the TPC analysis software tools to the necessities of the SuperFGD prototype analysis flow and I played a main role in the analysis of the data, producing a significant fraction of the results reported in Ref [6]. In particular, I was responsible for the attenuation, light yield and crosstalk measurements, for the search of gamma conversions, for the studies of the dE/dx of different particles and its resolution for MIPs, inspired on the ERAM studies. Also inspired by the ERAM analysis I proposed using a DBSCAN-based method to perform clustering in SuperFGD using time-slices of 2D hits in windows of 100 ns. These ideas have been later integrated in the final SuperFGD reconstruction flow. In that context, I made some of the first studies on 2D to 3D reconstruction in SuperFGD which, together with collaborators, lead to the development of a novel application of graph neural networks to perform 3D signal classification in SuperFGD. In those studies, reported in Ref [7], I developed the simulation environment to generate realistic detector signals, provided all datasets, designed all signal features to be input to the Network and participated in the strategy conceptualization and evaluation of the systematic uncertainties associated to the method. This method is also expected to be used in the final reconstruction chain. Regarding the detection of neutrons in SuperFGD, I have worked on it since its first studies. In 2019, as a continuation of the TDR physics studies, a project was suggested by collaborators to study the physics potential of measuring neutrons in SuperFGD-like detectors. I used the TDR simulation to estimate a realistic smearing for the reconstructed lepton kinematics and I participated in the discussion of the optimal description of the time resolution for neutrons. The results of the study are described in Ref. [8]. In 2020, the SuperFGD prototype was sent to LANL and exposed to a beam of neutrons. Neutron data was collected and analyzed using software tools adapted from those built to analyze the CERN beam test data the year before. As one of its main contributors, I helped in the transition from one project to the other. In 2021,

neutron data was collected again at LANL and I participated in the data taking remotely. Using 2020 and 2021 neutron beam test data, I suggested to Dr. Thorsten Lux to study the SuperFGD hits' time resolution dependence with the light yield. This project lead to a master thesis where this measurement was done under my co-supervision.

In Chapter 12, the work relative to the ToF detector is presented. In the summer of 2021 I started a one year stay at CERN and at the University of Geneva, where the final ToF hardware had been built. Under the guidance of Prof. Federico Sánchez and Dr Thorsten Lux, I decided to join the ToF working group where I supported diverse activities, such as taking data, setting up the analysis framework, doing installation tests, validating the DAQ, etc. As a result of the discussions on how to characterize the ToF waveform signals with Prof. Federico Sánchez, I developed a deep learning algorithm to perform data-driven detector signal characterization and evaluated its performance and potential, as described in Ref. [9].

Aside of my activities reported in the former chapters I participated in a number of side projects along the duration of the PhD. Together with Dr. Thorsten Lux I participated in the PHIL project where we studied a new method to perform liquid biopsy as reported in Ref. [10]. Also together with Dr. Thorsten Lux I joined activities related to the DUNE experiment, summarized in Appendix A. I worked partially for DUNE during the summers of 2018 and 2019 in two separate stays at CERN and became DUNE collaborator in 2019. In the first summer, along with collaborators, I coated and tested 40 PMTs with tetraphenyl butadiene (TPB) for the protoDUNE dual phase (DP) detector, as reported in Ref. [11]. In the second summer, the PMTs were installed inside the protoDUNE-DP cryostat. I participated in the final preparation of the cryostat and in the installation of the PMTs. The photo-detection system (PDS) of this detector is reported in Ref. [12] and a study of its performance can be found in Ref. [13]. In 2021, I attended remotely the International Neutrino Summer School where I made a project on Core-Collapse Supernova (CCSN) neutrinos. This experience lead me to suggest a master thesis project to Dr. Thorsten Lux with the aim to estimate the mass-hierarchy sensitivity of Hyper Kamiokande in the eventuality of a CCSN. The master thesis is currently ongoing under my co-supervision. In 2020, after conversations with a colleague working in proton computerized tomography (pCT) I realized that the necessities of the pCT community to track and reconstruct protons could be satisfied by recent hardware developments in the context of the ND280 upgrade. After feedback from Dr. Thorsten Lux I proposed a novel range telescope named ASTRA and a synergy started between IFAE, University of Birmingham and University of Geneva to evaluate the potential performances of this conceptual device using numerical simulations. The outcome of the study, in which I played a main role, is presented in Ref. [14] and summarized in Appendix B. Currently, plans to request funding and to build and test a first prototype are ongoing. As a result of this project in 2021 I suggested to Dr. Thorsten Lux a master thesis project to improve some of the initial reported performances using machine learning. The master thesis is currently ongoing under my co-supervision.

Part I

Theoretical background

Chapter 2

Neutrino physics

“We must not forget that when radium was discovered no one knew that it would prove useful in hospitals. The work was one of pure science. And this is a proof that scientific work must not be considered from the point of view of the direct usefulness of it. It must be done for itself, for the beauty of science, and then there is always the chance that a scientific discovery may become like the radium a benefit for humanity.”

– MARIE CURIE-SKŁODOWSKA

The work presented in this thesis focuses on studying neutrinos. Neutrino physics is a vast and well established field of research within the domain of high energy physics (HEP). Studying neutrinos has been key in shaping our current understanding on how nature works at its most elementary level and, still nowadays, plays a crucial role to push forward the theory. To understand why, this chapter reviews the history of this field of research, its most prominent theoretical features and our current experimental knowledge.

2.1 Neutrino history

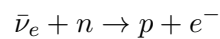
2.1.1 Proposal, early theory and discovery

At the beginning of the 20th century the observation of new experimental phenomena was piling up and an upraising quantum theory to explain it was under development. In particular, three sources of natural radioactivity were known and under study: α , β , and γ . A major issue to overcome was the apparent non-conservation of spin nor energy in β processes described as two body decays at that time. In 1930 Pauli proposed a new particle, the *neutrino*¹, ν , as a desperate solution to the problem [17]. If true, the neutrino would be a neutral particle carrying the missing energy and spin in β decays. In 1933, shortly after the neutrino was proposed and the neutron was discovered, Fermi developed a theory involving neutrons, protons, electrons and neutrinos to explain β decays [18]. It was the first precursor to the modern description of weak interactions². Remarkably, Fermi noticed already then that, due to the energy spectrum of β decays, neutrino masses should be either zero or much smaller than that of the electron [19]. Fermi’s description

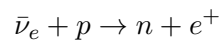
¹He called it neutron, but after the modern neutron was discovered by Chadwick in 1932 [15] Pauli’s neutron was re-named by Fermi and his student Amaldi to its final diminutive name neutrino [16].

²Fermi’s paper was such a breakthrough that was rejected by *Nature* ‘because it contained speculations too remote from reality to be of interest to the reader’. This in turn, motivated Fermi to move from theory to experimentation.

of the β decay considered only transitions where the outgoing particles have antiparallel spin. In 1936, Gamow and Teller [20] showed that Fermi interactions including transitions with outgoing particles with parallel spins are also possible. In 1934, using Fermi's theory, Bethe and Peierls calculated the cross-section for detecting neutrinos from β decays to be $\sigma < 10^{-44}$ cm [21]. Such a remarkably small value led them to conclude: 'It is therefore absolutely impossible to observe processes of this kind with the neutrinos created in nuclear transformations.' [21]. In 1936, the muon μ was discovered in cosmic rays by Anderson and Neddermeyer [22] and confirmed by Street and Stevenson [23] with no apparent connection to neutrinos. In 1938 muons from cosmic rays were observed to decay³ [25] and in 1940 evidence was found in cosmic rays⁴ for the emission of β particles in muon decays [28]. Given the mass difference between both, the presence of a neutrino in the decay was suspected. In 1949 the energy distribution of the decay electrons was measured to be continuous [29] suggesting the presence of not one but two neutrinos in the final state of the muon decay. In 1951 the cross-section for the free neutron decay was measured [30] allowing to have a reliable prediction $\pm 25\%$ [31]) for the cross section of the antineutrino capture by the proton. In 1953 Konopinski and Mahmoud [32] proposed the law of lepton number conservation which for the first time introduced a clear difference between neutrinos and antineutrinos and suggested that the two neutrinos emitted in muon decays could be different. The means to attempt an experiment would be provided by Fermi who, in the mid 1930s, had transitioned to experimental physics and following the recent findings from Joliot-Curie [33] started looking into inducing artificial radioactivity by bombarding heavy atoms with neutrons. Under the context of World War II, Fermi led the construction of the first human-made nuclear fission reactor which went critical on 1942 [34]. According to the theory it was known that nuclear reactors should be tremendous sources of neutrinos, allowing in the 1950s to attempt two experiments to finally detect the neutrino. On one hand, Davis tried to measure the neutrino for the first time in 1954 via the lepton number violating process:



without success [35]. On the other hand, an experiment led by Cowan and Reines in 1956 at the Savannah River Nuclear Plant succeeded measuring the process:



confirming the existence of the neutrino and the difference between neutrinos and antineutrinos [31]. Six years later, in 1962, the existence of a second neutrino flavor, the ν_μ , would be confirmed by Lederman, Schwartz and Steinberger [36].

2.1.2 The birth of the Standard Model

In the decade of the 1930s, while computing physical observables using early quantum electrodynamics (QED), unphysical results in the form of infinities were found [37, 38, 39]. This fundamental problem of the theory was overcome in the 1940s by Tomonaga, Schwinger and Feynman whom, in doing so, rebuilt the mathematical description of QED⁵. Their work was combined by Dyson in 1949 [41] directing HEP towards the theoretical formalism that continues being used today. During the 1950s Yang and Mills [42] illustrated the types of symmetries and invariances any field theory must satisfy. In 1955 Dirac described QED in a gauge-invariant formalism realizing that the symmetry group U(1) dictates the form of the interactions involving the electromagnetic

³Incidentally, the study of muon decays allowed to experimentally test special relativity predictions about time dilation for the first time [24].

⁴In the early 1940s Fermi [26] and Rossi [27] grounded the theory to study cosmic rays which would be seminal for the development of many important experimental techniques.

⁵A great insight on this process can be found on Feynman's Nobel Lecture [40].

field with the photon as the gauge boson [43]. Thus, QED was the first renormalizable theory to arise in a gauge invariant fashion. It provided excellent predictions for the behavior of fundamental particles and in consequence, it was regarded as a template to build up field theories able to describe all other types of interactions. In 1956 Lee and Yang proposed that parity could be violated in weak interactions to solve the so-called $\tau - \theta$ (modern kaon) puzzle [44]. This was proven experimentally to be correct by Wu in 1957 [45]. In 1958 the theory of weak interactions was casted into its modern V-A shape by Feynman and Gell-Mann [46]. In 1961 Glashow showed that QED and weak interactions could be united in a single electroweak description [47]. In 1961 Nambu [48] and Goldstone [49] paved the way for the description of the phenomena of spontaneous symmetry breaking in HEP⁶. In 1964 three teams formed by Brout and Englert [51], Higgs [52], and Guralnik, Hagen and Kibble [53] described what is known today as the Higgs mechanism. This culminated in 1967 with the work of Salam [54] and Weinberg [55] whom independently presented a full description of the electroweak interaction under the $SU(2)_L U(1)$ symmetry group spontaneously broken by the Higgs field which predicted three new bosons, W^\pm and Z^0 , as well as the existence of weak neutral currents. Weak neutral currents were observed in 1973 in neutrino interactions measured in the Gargamelle experiment [56], confirming the great success of the electroweak unification.

In the 1960s the advancements in accelerator technology had unraveled a confounding variety of particles, nicknamed the *particle zoo*, creating great confusion and disconcert. In 1964 Gell-Mann [57] and Zweig [58] proposed the $SU(3)$ gauge symmetry group to explain the particle zoo as arising from more fundamental constituents, named quarks by Gell-Mann, which at that time were thought to be three: up, down and strange. This new symmetry group required 8 gauge bosons, named gluons. The concept of color to intuitively represent $SU(3)$ was introduced in 1965 by Greenberg [59] and Han and Nambu [60], such that this theory would eventually be named Quantum Chromodynamics (QCD). In 1968, experiments at SLAC showed hints of a sub-structure in protons in deep inelastic collisions. An effective theory to study them, later extended by Bjorken [61], was originally developed by Feynman⁷ [62] who dubbed partons the inner-components of the nucleons⁸. In 1970 Glashow, Iliopoulos and Maiani [63] presented the so-called GIM mechanism to explain the experimental non-observation of flavor-changing neutral currents, this model predicted the existence of a new quark, the charm. In 1973 Kobayashi and Maskawa [64] extended the number of quarks to six to explain the experimental observation of CP violation. The two new quarks were named as top and bottom in 1975 by Harari [65]. In 1974 the quark model was finally accepted when two teams, led by Ting [66] and Richter [67], independently discovered the J/Ψ meson formed by a charm anticharm quark pair. Also in 1974, a team headed by Perl found the tauon τ at SLAC [68, 67], increasing the number of leptons from two to three and suggesting the existence of a tau neutrino ν_τ . In 1977 the bottom quark was experimentally found at Fermilab by a team led by Lederman [69], and that same year the term *generation* was coined by Harari [70]. The much more massive top quark was discovered in 1995 at Fermilab [71], and in 2000 the DONUT collaboration detected the tau neutrino [72]. The theory arising in the 1970s, including all of the former particles and their interactions, would eventually get to be known as the *Standard Model* (SM) of HEP [73]. The last missing piece of the Standard Model, the Higgs boson predicted in 1964, was finally discovered in the early 2010s by the CMS [74] and ATLAS [75] experiments at CERN.

⁶Described earlier in the context of superconductivity [50].

⁷The paper has deep implications on the experimental approach to measure accelerator collisions, e.g. in the paper the concept of *exclusive* and *inclusive* cross-section measurements, very much used later in this thesis, are introduced.

⁸Initially, the HEP community was reluctant to identify partons with quarks and gluons. However, the sub-structure observed at SLAC would eventually be identified as up and down quarks as further evidence piled up. Nonetheless, the two descriptions continue to be used today as they have complementary features.

2.1.3 Neutrino oscillations

Whereas from the 1960s to the 2000s the modern picture of HEP evolved with remarkable success, the phenomenology of neutrinos started to depart from that of massless particles as assumed in the SM. First, the idea of neutrino oscillations, only possible for massive neutrinos, arose in the theory. As early as 1937 Majorana realized that neutrinos might be their own antiparticles [76]. Building on this concept in 1957 Pontecorvo proposed neutrino-antineutrino oscillations in analogy with neutral kaon mixing [77]. This work was followed up in 1962 by Maki, Nakagawa and Sakata [78] and completed in 1967 by Pontecorvo [79] to describe the oscillatory transitions not from neutrinos to antineutrinos but among neutrinos of different flavors. To experimentally study neutrino oscillations three elements are needed: A source of neutrinos, a detection method and a prediction of the rate of interactions under the unoscillated hypothesis. A potential source was presented in 1939 when Bethe showed using Fermi's theory that the energy produced by the Sun might have its origin in thermonuclear reactions [80] such that a high flux of neutrinos would be produced in the Sun. In 1945, Pontecorvo realized that neutrinos coming from the Sun could transform ^{37}Cl nucleus it into an unstable ^{37}Ar allowing its direct detection [81]. It was not until the 1960s that the Homestake experiment, led by Davis, detected for the first time solar neutrinos [82] using Pontecorvo's method. Remarkably, this was achieved only a few years after the first discovery of the neutrino and signified the birth of neutrino astrophysics. There was, however, a caveat. A very significant neutrino deficit was found when comparing the expected number of neutrino interactions, calculated by Bahcall [83], to the measurements. This was the first historical hint for neutrino oscillations, however, it was not identified as such until other experiments reported additional measurements. In the 1990s, similar flux deficits were found in the GALLEX/GNO [84, 85] and the SAGE [86] experiments, which used Gallium instead of Chlorine, sensitive to lower neutrino energy detection thresholds. The appearance of Water Cherenkov detectors able to study neutrino interactions in an event-by-event basis was a major step forward in the study of neutrino oscillations. The first of this new type of detectors was the Kamioka Nucleon Decay (KamiokaNDE) experiment [87], built in the 1980s. Although it was originally designed to search for proton decay signatures, in 1985 it was upgraded and optimized for neutrino detection and became the world reference neutrino observatory⁹. In 1989 the Kamiokande experiment was able to prove that the measured flux of neutrinos was indeed coming from the Sun by measuring the recoil direction of electrons ejected by neutrino elastic scattering interactions and provided further evidence for the deficit of solar neutrinos [91]. In the 1990s Kamiokande also found a deficit in the predicted flux of atmospheric neutrinos [92], a major independent indication in favor of the true existence of neutrino oscillations. In 1996 an evolution of the Kamiokande experiment, the Super Kamiokande (SK) detector was built. Finally, in 1998 SK reported for the first time¹⁰ direct evidence of neutrino oscillations in atmospheric neutrinos [94]. In 2002, the solar neutrino problem was solved by the SNO experiment, which demonstrated that the deficit in the solar neutrinos flux was produced as the result of matter effects in neutrino oscillations¹¹ [96] earlier described by Wolfenstein [97] and Mikheyev and Smirnov [98] in the 1980s.

2.1.4 Overview of a new era: status and prospects

The discovery of neutrino oscillations proved that neutrinos are massive particles in disagreement with their Standard Model description. In addition to the unknown origin and value of their

⁹As a remarkable apart, in 1987 neutrinos coming from a Super Nova (SN 1987A) were measured for the first and only time in history in the Kamiokande [88], IMB [89] and Baksan [90] experiments.

¹⁰The eagerly expected results from SK were first presented by Kajita at the 1998 Neutrino conference [93].

¹¹To do so, SNO measured charge-current (CC), neutral-current (NC) and elastic scattering (ES) solar neutrino interactions. Whilst neutrinos of all flavors interact via NC, CC interactions were only sensitive to electron neutrinos. Moreover, CC and ES flux were also related by $\Phi_{ES} \approx \frac{4}{3} \Phi_{CC}$ [95]. All predictions matched the SNO observations. [96]

masses (m_1, m_2, m_3), four additional parameters consisting of three angles ($\theta_{12}, \theta_{13}, \theta_{23}$) and one CP violating phase (δ_{CP}) ruling the phenomenon of the oscillations were either largely or completely unknown. Thus, the main goal of the new era in neutrino physics, which is still ongoing, is to experimentally determine the value of the new degrees of freedom with high accuracy. In order to set up the grounds to study this parameters and contextualize their scientific significance, the next sections of this Chapter will review the most prominent features of HEP theory regarding neutrinos, as well as the current knowledge about their physics in light of the existing measurements. It is however useful to state from the beginning that the origin of the neutrino masses is currently unknown, that only upper bounds exist concerning the value of the neutrino masses and that their relative size ($m_2 > m_3$ or $m_3 > m_2$) is unknown. Although all of the three mixing angles have been measured to be different from zero, the value of δ_{CP} , potentially of crucial importance to understand the matter-antimatter asymmetry in the universe [99, 100], remains largely uncertain.

To tackle this questions there is an ambitious experimental program ongoing which will largely increase the experimental sensitivity in the next years. Specially relevant to understand neutrino masses will be the future results of the ongoing experiment KATRIN [101], the search for Majorana signatures at the many experiments described in section 2.4.1, and the results of the next-generation cosmological surveys. Regarding oscillations, major improvements are expected to come with the upgrades of T2K [3] discussed in this thesis and IceCube [102]. In addition, the construction of several new major neutrino oscillation experiments with unprecedented budgets is ongoing: KM3NeT [103] and Baikal-GVD [104] which will complement IceCube for a full sky view of high energy neutrinos, Hyper Kamiokande [105] which also opens the door to T2HK [106] (from 2027) and possibly T2HKK [107] further in the future, JUNO [108, 109] and DUNE [110, 12, 111, 112]. Therefore, as of today, the future of neutrino physics is bright.

2.2 Neutrino theory

Abundant literature exists discussing the theoretical grounds of neutrino physics, both in the context of the Standard Model and beyond. The following sections introduce a summary of the most prominent knowledge, equations and remarks that currently constitute the basics of this field of research. The reader might find additional details, demonstrations and insights in excellent available textbooks, out of which I highlight those in Refs. [113, 114, 115, 116, 117].

2.2.1 The neutrino in the Standard Model

The Standard Model of particle physics (SM) is a relativistic quantum field theory classifying and describing the properties of all the known elementary particles as well as their interplay through three of the four fundamental interactions we are aware of, i.e electromagnetic, weak and strong, but not gravitational. The SM calculations have shown for decades excellent agreement with experimental data. In addition, for its theoretical self-consistency several predictions were made that, over years, have been demonstrated to be correct. Consequently, the SM is nowadays nominally accepted by the HEP community as the best existing description of nature at its fundamental level. The SM describes the fundamental particles and its interactions as quantum fields of half-integer (fermions) or integer (bosons) spin belonging to the gauge symmetry group

$$G_{SM} = \underbrace{\text{SU}(3)_C}_{\text{color}} \times \underbrace{\text{SU}(2)_L}_{\text{weak isospin}} \times \underbrace{\text{U}(1)_Y}_{\text{hypercharge}} \xrightarrow{\text{SSB}} \underbrace{\text{SU}(3)_C}_{\text{QCD}} \times \underbrace{\text{U}(1)_{EM}}_{\text{QED}}. \quad (2.1)$$

G_{SM} is spontaneously broken (SSB) by the Higgs field. As in all gauge theories G_{SM} fixes the number and properties of the vector gauge bosons leaving only as free parameters the gauge couplings which need to be experimentally measured. In G_{SM} three different interaction types

(or forces) are described. The group $SU(3)_C$ has 8 massless generators, the gluons, carrying a charge referred to as color. The groups $SU(2)_L \times U(1)_Y$ are intertwined and have four generators that after the SSB can be identified with three massive (W^\pm and Z^0) and one massless (photon γ) gauge bosons.

In gauge theories the fermions and scalar bosons are left unconstrained, in the sense that they might, or might not, be realized in nature. If they do exist, however, they must transform under the G_{SM} symmetry group, and accordingly, their fundamental properties must be described by the representations of G_{SM} . In addition, not all choices of representations are allowed, as the sets occurring in nature must cancel anomalies out. Consequently, the fermion and scalar content of the SM is chosen heuristically to match up experimental evidence under the former rules. In its current description, the SM has a single scalar boson, the Higgs, and twelve fermions, encompassed in three groups of four, forming a hierarchical structure often referred to as fermion generations:

$$\underbrace{\begin{bmatrix} \nu_e & u \\ e & d \end{bmatrix}}_{\text{1st generation}}, \quad \underbrace{\begin{bmatrix} \nu_\mu & c \\ \mu & s \end{bmatrix}}_{\text{2nd generation}}, \quad \underbrace{\begin{bmatrix} \nu_\tau & t \\ \tau & b \end{bmatrix}}_{\text{3rd generation}}.$$

Each generation spans a copy of fermions, identical from the symmetry group perspective. The mass of their fermions, however, gradually grows as one moves from the first to the third generation¹². In each generation, two fundamentally different types of fermions can be found. On one hand, up, down, charm, strange, bottom and top (u, d, s, c, b, t) are known as quarks q , and are sensitive to all the SM interactions. On the other hand the electron, muon, tauon (e, μ, τ) and their associated neutrinos (ν_e, ν_μ, ν_τ) are known as leptons ℓ , insensitive to the strong force. Finally, an important difference exists among leptons. Whereas e, μ and τ interact via the electromagnetic and weak forces, the neutrinos only interact through the latter.

Fermions can form bound-states. In particular, u and d quarks are the constituents of protons (uud) and neutrons (udd) which together with electrons are the most abundant building blocks of matter in form of atoms. Bound-states of quarks are named, with generality, hadrons. Hadrons with three quarks, such as neutrons and protons, are called baryons whereas quark-antiquark bound-states are referred to as mesons where pions π are their lightest form.

The Standard Model Lagrangian

Observables, e.g. cross-sections and decay-rates, are functions of the probability amplitude \mathcal{M} of a given transition to happen between an initial and final state. In practice, such an amplitude is calculated from the action of the system which is a function of the Lagrangian density \mathcal{L} which contains the dynamical information of the system. For a given model, \mathcal{L} can be built writing up the most general expression invariant under the model's symmetries. In the case of the SM such a Lagrangian is \mathcal{L}_{SM} .

The electroweak Lagrangian before SSB

As neutrinos do not carry color charge for the sake of studying neutrino phenomenology it is enough to study the electroweak Lagrangian \mathcal{L}_{EW} , which before SSB is

$$\mathcal{L}_{SM} \supset \mathcal{L}_{EW} = \mathcal{L}_g + \mathcal{L}_f, \quad (2.2)$$

¹²A rule that might be broken exclusively by neutrinos, as later discussed in Sec. 2.3.1.

with

$$\mathcal{L}_g = - \sum_{a=1}^3 \frac{1}{4} W_a^{\mu\nu} W_{\mu\nu}^a - \frac{1}{4} B^{\mu\nu} B_{\mu\nu}, \quad (2.3)$$

and

$$\mathcal{L}_f = \sum_{i=1}^N \bar{Q}_i i \not{D} Q_i + \bar{u}_i i \not{D} u_i + \bar{d}_i i \not{D} d_i + \bar{L}_i i \not{D} L_i + \bar{e}_i i \not{D} e_i. \quad (2.4)$$

Here:

- \mathcal{L}_g is the kinetic term for the gauge bosons W_a^μ and B^μ , involving the field strength tensors $B_{\mu\nu}$ and $W_{\mu\nu}^a$ defined as

$$B_{\mu\nu} = \partial_\mu B_\nu - \partial_\nu B_\mu \quad \text{and} \quad W_{\mu\nu}^a = \partial_\mu W_\nu^a - \partial_\nu W_\mu^a - g\epsilon_{abc} W_\mu^b W_\nu^c. \quad (2.5)$$

- \mathcal{L}_f is the kinetic term for the fermions. The index i iterates over generations, Q and L are left-handed doublets

$$Q_{1,2,3} = \left(\begin{pmatrix} u_L \\ d_L \end{pmatrix}, \begin{pmatrix} c_L \\ s_L \end{pmatrix}, \begin{pmatrix} t_L \\ b_L \end{pmatrix} \right), \quad L_{1,2,3} = \left(\begin{pmatrix} \nu_{eL} \\ e_L \end{pmatrix}, \begin{pmatrix} \nu_{\mu L} \\ \mu_L \end{pmatrix}, \begin{pmatrix} \nu_{\tau L} \\ \tau_L \end{pmatrix} \right) \quad (2.6)$$

and u, d, e are right-handed singlets

$$u_{1,2,3} = u_R, c_R, t_R, \quad d_{1,2,3} = d_R, s_R, b_R \quad \text{and} \quad e_{1,2,3} = e_L, \mu_R, \tau_R. \quad (2.7)$$

Both left- and right-handed fermion fields being Weyl spinors. Feynman slashed notation is used such that $\not{D} = \gamma^\mu D_\mu$ where

$$D_\mu = \partial_\mu - i\frac{g}{2} Y B_\mu - i\frac{g'}{2} \sum_{a=1}^{a=3} T_a W_\mu^a \quad (2.8)$$

is the covariant derivative involving the generators of the $SU(2)_L$ and $U(1)$ groups, τ_a and Y respectively, with associated couplings g and g' .

The electroweak SSB

If a complex scalar doublet ϕ is included in the model additional terms need to be considered and the electroweak Lagrangian becomes

$$\mathcal{L}'_{EW} = \mathcal{L}_{EW} + \mathcal{L}_h + \mathcal{L}_y, \quad (2.9)$$

where \mathcal{L}_h and \mathcal{L}_y are defined as

$$\mathcal{L}_h = |D_\mu \phi|^2 - V(|\phi|) = |D_\mu \phi|^2 - \mu^2(|\phi|) - \lambda(|\phi|)^2, \quad (2.10)$$

$$\mathcal{L}_y = -y_u^i \phi^c \bar{Q}_i u_i - y_d^i \phi \bar{Q}_i d_i - y_e \phi \bar{L}_i e_i + h.c.. \quad (2.11)$$

Here:

- \mathcal{L}_h is the Higgs Lagrangian describing the interactions of the scalar doublet $\phi = \phi_1 + i\phi_2$ with itself and with the gauge bosons implicit in the covariant derivative. The potential V

has a set of minima defined by the circle equation

$$\phi_1^2 + \phi_2^2 = \frac{-\mu^2}{2\lambda}. \quad (2.12)$$

Notoriously, choosing a particular minimum spontaneously breaks the Lagrangian symmetry. A usual choice (convention) is, $\phi_1^{min} = v, \phi_2^{min} = 0$, where $v \equiv \sqrt{-\mu^2/2\lambda}$ is the so-called vacuum expectation value (VEV). In a physical scenario where $v = 0$, \mathcal{L}_h and \mathcal{L}_y vanish. However if $v > 0$, the symmetry is broken. The physical consequences of a non-null VEV are revealed in the former equations by the use of the field definitions $H \equiv \phi_1 - v, \xi \equiv \phi_2$ which upon substitution into $|D_\mu\phi|^2$ lead to a collection of new terms involving H, ξ and v . Then, the Lagrangian can be rearranged by redefining the gauge vector bosons (in the process some of them acquire mass) and ξ can be set to zero using gauge symmetry (this is the so-called unitarity gauge).

- \mathcal{L}_y contains couplings between the scalar doublet ϕ and the fermion fields. The Higgs doublet allows to connect left-handed and right-handed spinors which, through SSB, form the so-called Dirac mass terms. This can be readily seen by doing the matrix product of the multiplets in \mathcal{L}_Y and evaluating the Higgs field at its minimum

$$\mathcal{L}_y = \frac{y_u^i v}{\sqrt{2}} \bar{u}_L u_R + \frac{y_d^i v}{\sqrt{2}} \bar{d}_L d_R + \frac{y_e^i v}{\sqrt{2}} \bar{e}_L e_R + h.c. = \sum_{\psi=u,d,e} m_\psi^i \underbrace{(\bar{\psi}_L \psi_R + \bar{\psi}_R \psi_L)}_{\bar{\psi}\psi}. \quad (2.13)$$

Where for $m > 0$ the Weyl spinors $\psi_{L,R}$ get mixed into Dirac bispinors ψ . In general, Dirac bispinors, ψ , can be decomposed into two Weyl spinors by means of the projection operators

$$\psi_{L,R} = P_{L,R} \psi = \left[\frac{1 \mp \gamma_5}{2} \right] \psi. \quad (2.14)$$

In Eqs. 2.11 and 2.13 the index i iterates over generations and the parameters $y_{u,d,e}^i$ are the so-called Yukawa couplings. Remarkably, the masses $m_{u,d,e}^i$ are proportional to the couplings provided that v is identical for all fermions. Hence, one might expect that in the absence of an underlying mechanism that modifies the Yukawa couplings all masses would be similar. However, that is experimentally known to not be true, e.g. m_u/m_d is $O(1)$ but m_u/m_t is $O(10^{-5})$. Moreover, upon SSB a number of terms are generated from \mathcal{L}_y which contain both fermion fields and the Higgs, responsible for the Higgs-fermion interactions.

The electroweak Lagrangian after SSB

After spontaneous symmetry breaking, field redefinitions lead to the following gauge bosons:

$$W_\mu^\pm = \frac{1}{\sqrt{2}} (W_\mu^1 \mp iW_\mu^2) \quad \text{with mass} \quad m_W = g \frac{v}{2}. \quad (2.15)$$

$$Z_\mu^0 = \frac{1}{\sqrt{g^2 + g'^2}} (gW_\mu^3 - g'B_\mu) \quad \text{with mass} \quad m_Z = \frac{v\sqrt{g^2 + g'^2}}{2}. \quad (2.16)$$

$$A_\mu = \frac{1}{\sqrt{g^2 + g'^2}} (g'W_\mu^3 + gB_\mu) \quad \text{with mass} \quad m_A = 0. \quad (2.17)$$

As a result three gauge bosons are massive (W_μ^\pm, Z_μ^0) whereas the photon field (A_μ) remains massless. The covariant derivative becomes

$$D_\mu = \partial_\mu - i \frac{g}{\sqrt{2}} (W_\mu^+ T^+ + W_\mu^- T^-) - i \frac{g}{\cos \theta_W} Z_\mu (g^2 T^3 - g' 2Y) - ie A_\mu Q, \quad (2.18)$$

with $T^\pm = T^1 \pm iT^2$. The electroweak unification is explicit by means of

$$g = \frac{e}{\sin \theta_W}, \quad e = \frac{gg'}{\sqrt{g^2 + g'^2}} \quad \text{and} \quad Q = T^3 + Y, \quad (2.19)$$

where e is the electron's electric charge, θ_W is the Weinberg angle satisfying $m_W = m_Z \cos \theta_W$ and Q is the electric charge quantum number (-1 for electrons, 2/3 for up-type quarks, 1/3 for down-type quarks and 0 for neutrinos). Moreover, the Fermi constant can be written as a combination of the previous parameters, i.e $G_F = g/4\sqrt{2}m_W^2$.

With the previous modifications, the new terms in the electroweak Lagrangian can be grouped as

$$\mathcal{L}_{EW} = \mathcal{L}_K + \mathcal{L}_{NC} + \mathcal{L}_{CC} + \mathcal{L}_H + \mathcal{L}_V + \mathcal{L}_{HV} + \mathcal{L}_Y. \quad (2.20)$$

Here:

- \mathcal{L}_K is the kinetic term, containing the dynamic terms (those with partial derivatives) for all bosons and the mass terms for all the fermions, the Higgs, and the massive gauge bosons.
- \mathcal{L}_H contains the three-point and four-point Higgs interactions with itself.
- \mathcal{L}_V contains the three-point and four-point gauge vector boson interactions with themselves.
- \mathcal{L}_{HV} contains the Higgs interactions with the gauge vector bosons.
- \mathcal{L}_Y contains the Higgs interactions with the fermions.
- \mathcal{L}_{NC} and \mathcal{L}_{CC} are the neutral- and charged-current electroweak interactions. This terms arise from the multiplication of fermion fields with the gauge boson fields in the covariant derivative and are, for the study of neutrino physics, the most important ones as are the only interaction terms in the SM which involve neutrino fields. In particular, all interactions with neutrinos are described by

$$\begin{aligned} \mathcal{L}_{CC} \supset \mathcal{L}_L^{(W)} &= -\frac{g}{2\sqrt{2}} \left(\sum_{i=e,\mu,\tau} 2\bar{\nu}_L^i \gamma^\mu \ell_L^i \right) W^+ + h.c. \\ &= -\frac{g}{2\sqrt{2}} j_{W,L}^\mu W^+ + h.c. \end{aligned} \quad (2.21)$$

and

$$\begin{aligned} \mathcal{L}_{NC} \supset \mathcal{L}_L^{(Z)} &= \frac{g}{2\cos\theta_W} \left(\sum_{i=e,\mu,\tau} 2g_L^\nu \bar{\nu}_L^i \gamma^\mu \nu_L^i + 2g_L^\ell \bar{\ell}_L^i \gamma^\mu \ell_L^i + 2g_R^\ell \bar{\ell}_R^i \gamma^\mu \ell_R^i \right) Z_\mu \\ &= \frac{g}{2\cos\theta_W} j_{Z,L}^\mu Z_\mu, \end{aligned} \quad (2.22)$$

Fermions	g_V	g_A
ν_e, ν_μ, ν_τ	$g_V^\nu = \frac{1}{2}$	$g_A^\nu = \frac{1}{2}$
e, μ, τ	$g_V^\ell = -\frac{1}{2} + 2s_W^2$	$g_A^\ell = -\frac{1}{2}$
u, c, t	$g_V^U = \frac{1}{2} - \frac{4}{3}s_W^2$	$g_A^U = \frac{1}{2}$
d, s, b	$g_V^D = -\frac{1}{2} + \frac{2}{3}s_W^2$	$g_A^D = -\frac{1}{2}$

TABLE 2.1: Values of g_V and g_A for the fermion fields with $s_W \equiv \sin \theta_W$. The superscripts ν, ℓ, U, D indicate, respectively, a generic neutrino, charged lepton, up-type quark, and down-type quark.

with $j_{Z,L}^\mu$ and $j_{W,L}^\mu$ being the weak neutral and charged currents associated to leptons. The coefficients $g_L^\nu, g_L^\ell, g_R^\ell$ are in general for a fermion f described by

$$g_L^f = T_3^f + g_R^f \quad \text{and} \quad g_R^f = -q^f \sin^2 \theta_W. \quad (2.23)$$

Here T_3 is the third component of the weak isospin and q^f is the electromagnetic charge of the fermion such that using the definitions

$$g_V^f = g_L^f + g_R^f = T_3^f - 2q^f \sin^2 \theta_W \quad \text{and} \quad g_A^f = g_L^f - g_R^f = T_3^f \quad (2.24)$$

it is possible to write $j_{Z,L}^\mu$ as

$$j_{Z,L}^\mu = \sum_{i=e,\mu,\tau} \bar{\nu}^i \gamma^\mu (g_V^\nu - g_A^\nu \gamma^5) \nu^i + \bar{\ell}^i \gamma^\mu (g_V^\ell - g_A^\ell \gamma^5) \ell^i. \quad (2.25)$$

Notice that γ^μ transforms like a vector whereas $\gamma^\mu \gamma^5$ transforms like an axial-vector. Thus, the couplings g_V and g_A are respectively named the vector and axial couplings, such that the structure of weak interactions is often referred to as V-A. In the case of quarks, one finds

$$j_{W,Q}^\mu = \sum_{i=1,2,3} 2\bar{u}_L^i \gamma^\mu d_L^i \quad (2.26)$$

and

$$j_{Z,L}^\mu = \sum_{i=1,2,3} \bar{u}^i \gamma^\mu (g_V^U - g_A^U \gamma^5) u^i + \bar{d}^i \gamma^\mu (g_V^D - g_A^D \gamma^5) d^i. \quad (2.27)$$

To perform calculations it is useful to have in mind the values of g_V and g_A presented in Table 2.1.

The Standard Model parameters

The SM Lagrangian contains physical parameters, constants in \mathcal{L}_{SM} , not predicted by the theory but playing a fundamental role in the calculation of observables. In total, 26 free parameters can be identified, including 7 relative to neutrinos. Which ones to use is a matter of choice due to the existing relations connecting them. By specifying the values of these parameters one can control all SM predictions. A possible particular choice is:

- The electromagnetic, weak, and strong couplings g_e, g_w, g_s .
- The electroweak symmetry breaking scale v .
- The Higgs mass m_H .

- The three mixing angles θ_{12}^{CKM} , θ_{23}^{CKM} , θ_{13}^{CKM} and the CP violating phase δ_{CP}^{CKP} contained in the Cabibbo-Kobayashi-Maskawa (CKM) matrix, ruling quarks mixing.
- The three mixing angles θ_{12}^{PMNS} , θ_{23}^{PMNS} , θ_{13}^{PMNS} and the CP violating phase δ_{CP}^{PMNS} contained in the Pontecorvo-Maki-Nakagawa-Sakata (PMNS) matrix, ruling neutrino mixing.
- The twelve fermion masses $m_e, m_\mu, m_\tau, m_1^\nu, m_2^\nu, m_3^\nu, m_u, m_d, m_s, m_c, m_b$ and m_t .
- The angle Θ quantifying the amount of CP-violation in pure QCD interactions¹³.

The current experimental knowledge on this values, is collected and annually published by the Particle Data Group [119]. Notably, in the discussion presented up to now neutrinos have assumed to be massless. The motivations for this choice are two-fold. On one hand, all of the equations presented so far are with generality excellent approximations to perform electroweak calculations since neutrino masses are know to be small enough to be generally omitted without measurable consequences¹⁴. On the other hand a full description of neutrino masses is not available at the Lagrangian level as to do so extensions that go beyond the Standard Model are necessary.

2.2.2 The neutrino beyond the Standard Model

Since its inception the SM has been known to be, at most, an approximate theory surfacing from a more fundamental one. At least a fourth type of interaction is known to exist, gravity, for which there is not a successful description at the quantum level. Moreover, cosmology provides solid evidence of the existence of dark matter and dark energy in the Universe with still rather unknown properties. Even within the SM there are unsettling aspects. To quote some of the most relevant:

- The hierarchy problems. *Why is the gravity coupling strength so low with respect to the other interactions? Why the Higgs mass is so light compared to the Plank mass?*
- The structure of generations. *Is there an underlying theory to explain the observed fermion masses? Is there a fundamental explanation for the CKM hierarchical pattern? Why are there three generations?*
- The elementary charge. *Why quarks have multiples of 1/3 the charge of the electron?*
- The matter-antimatter imbalance. *Why is there much more matter than antimatter in the Universe?*
- The strong CP problem. *Why there is not (or extremely small) CP violation in pure QCD processes?*

These open questions have attracted the research efforts of many. On the theoretical end, researchers have sought for SM extensions either simplifying the current picture, looking for grand unification theories (GUTS) or including extra features, such as dark matter candidates. Those efforts have led to developments of generalized and powerful frameworks, such as Super Symmetry and String theory, each with its own appeals and caveats. However, so far, no new physics has been found and many theoretically appealing BSM models have already been excluded. On the experimental end, under the light of the initial LHC results it might very well be that new physics lies at an energy scale far from the reach of modern collider experiments, even if great hopes were placed in theories predicting new physics around the TeV scale. The LHC will continue taking data for another two decades during which it will continue to be undisputed as the most

¹³ Θ is experimentally tightly compatible with zero constituting the *strong CP* problem and motivating the experimental search for axions [118].

¹⁴The one exception is that of neutrino mixing.

powerful collider in the world. Along its operation it will continue to increase very significantly its accumulated data. Thus, the main hopes for finding new physics on collider experiments in the next decades remain in the discovery of SM-forbidden processes with very small cross-sections, or in the identification of tension in SM observables getting BSM corrections from physics at an upper energy scale.

The up to now scarce hints of new physics at collider experiments, which have for decades centralized the development of HEP, and the difficulty and economic cost of upgrading them beyond the TeV scale are approaching the field to a possible change of paradigm. Evidence of this transition can be found in the increasing amount of monetary resources directed to build non-collider experiments. In particular, one must highlight the proliferation of experiments seeking for hidden sector particles such as dark matter candidates, the construction of gravitational wave detectors, cosmological probes, and neutrino experiments. This new experimental trend is theoretically well-grounded. Dark matter candidates are known to exist and its discovery would greatly help to focus the theoretical efforts. The study of gravitational waves (GW) is an emerging field, providing completely new information about gravity, the less known of all forces. Cosmological probes provide a unique way to peer into otherwise unreachable energy scales by measuring data directly influenced by the super-hot start of the Universe.

Finally, neutrino experiments are interesting for a number of reasons. In contrast to all of the former research avenues, neutrinos are both directly connected to the HEP particle description (GW and cosmology are only indirectly informative of the microscopic behavior) and can be readily measured in experiments (finding dark matter in direct search experiments is not guaranteed). Moreover most current SM limitations have tentative connections with BSM neutrino physics. First, neutrino physics is a direct probe to the hidden sector, e.g. via PMNS unitarity, and therefore informative of possible dark matter candidates, such as sterile neutrinos. Second, neutrino masses are remarkably small and hence likely connected to otherwise inaccessible energies, e.g. via the see-saw mechanism. Third, the generational resemblance of quarks and leptons might be pointing into a higher energy scale, e.g. that of a possible leptoquark unification. If there is a fundamental link, informative patterns might emerge in the neutrino mass values, their hierarchy, and in resemblances on the CKM and PMNS angles. Fourth, the observed matter-antimatter asymmetry can not be explained with the measured amounts of CP violation in the quark sector, however, it might be explained if CP violation is large in neutrino oscillations. Finally, neutrinos are invaluable probes for cosmological and astrophysical research. The exploration of solar neutrinos, supernova neutrinos, supernova relic neutrinos and super high energy astrophysical neutrinos, united to the rising field of multi-messenger astronomy makes neutrinos key pieces to better understand microscopic phenomena in the domain of gravity.

2.3 Neutrino oscillations

Neutrino oscillations arise from the fact that neutrino flavor eigenstates (ν_e, ν_μ, ν_τ) are unequivalent to neutrino mass eigenstates (ν_1, ν_2, ν_3). Both bases, flavor and mass, are rotated such that a unitary transformation is needed to transform vectors from one basis to the other. Such transformations are encoded into an $n \times n$ unitary matrix U which is named in general the U_{PMNS} matrix after Pontecorvo, Maki, Nakagawa and Sakata. By convention U_{PMNS} is typically parametrized as

$$\begin{pmatrix} \nu_e \\ \nu_\mu \\ \nu_\tau \end{pmatrix} = \underbrace{\begin{pmatrix} 1 & 0 & 0 \\ 0 & c_{23} & s_{23} \\ 0 & -s_{23} & c_{23} \end{pmatrix} \cdot \begin{pmatrix} c_{13} & 0 & s_{13}e^{-i\delta_{CP}} \\ 0 & 1 & 0 \\ -s_{13}e^{i\delta_{CP}} & 0 & c_{13} \end{pmatrix} \cdot \begin{pmatrix} c_{12} & s_{12} & 0 \\ -s_{12} & c_{12} & 0 \\ 0 & 0 & 1 \end{pmatrix}}_{U_{\text{PMNS}}} \cdot \begin{pmatrix} \nu_1 \\ \nu_2 \\ \nu_3 \end{pmatrix}. \quad (2.28)$$

where $c_{ij} = \cos(\theta_{ij})$, $s_{ij} = \sin(\theta_{ij})$ and δ_{CP} is the CP-violating Dirac phase. In shorthand notation, flavor states $|\nu_\alpha\rangle$ can be written as superpositions of mass eigenstates $|\nu_i\rangle$ as

$$|\nu_\alpha\rangle = \sum_i U_{\alpha i}^* |\nu_i\rangle, \quad (2.29)$$

where $\alpha = e, \mu, \tau$ and $i = 1, 2, 3$. Mutatis mutandis,

$$|\nu_i\rangle = \sum_\alpha U_{\alpha i} |\nu_\alpha\rangle. \quad (2.30)$$

The mass eigenstates are solutions of the time-independent Schrödinger equation

$$\mathcal{H} |\nu_i\rangle = E_i |\nu_i\rangle, \quad (2.31)$$

where H is the Hamiltonian and E_i are the eigenvalues associated to the states $|\nu_i\rangle$.

2.3.1 Oscillations in vacuum

In vacuum, the Hamiltonian eigenvalues are

$$E_i = \sqrt{p^2 + m_i^2} \quad (2.32)$$

such that neutrino flavor states $|\nu_\alpha(t)\rangle$ evolve in time as

$$|\nu_\alpha(t)\rangle = \sum_i U_{\alpha i}^* e^{-iE_i t} |\nu_i\rangle. \quad (2.33)$$

Then, writing the mass states in the flavor basis follows

$$|\nu_\alpha(t)\rangle = \sum_i \sum_\beta U_{\alpha i}^* U_{\beta i} e^{-iE_i t} |\nu_\beta\rangle. \quad (2.34)$$

Therefore, a pure flavor state evolves with time t into a superposition of flavor states. The probability amplitude A for the transition of one flavor state into another, i.e. $\nu_\alpha \rightarrow \nu_\beta$, is

$$A(\nu_\alpha \rightarrow \nu_\beta)(t) = \langle \nu_\beta | \nu_\alpha(t) \rangle = \sum_i U_{\alpha i}^* U_{\beta i} e^{-iE_i t}. \quad (2.35)$$

Thus the measurable observable, the probability, is

$$P(\nu_\alpha \rightarrow \nu_\beta) = |A(\nu_\alpha \rightarrow \nu_\beta)|^2 = \sum_{i,j} U_{\alpha i}^* U_{\beta i} U_{\alpha j} U_{\beta j}^* e^{-i(E_i - E_j)t}. \quad (2.36)$$

Since neutrino masses are much smaller than their typical kinetic energies in all the existing neutrino oscillation experiments the approximations $t \approx L$ and $p_i = \sqrt{E^2 - m_i^2} \approx E - m_i^2/2E$ hold and, consequently, it is useful to rewrite the former expression as

$$P(\nu_\alpha \rightarrow \nu_\beta) = \sum_{i,j} U_{\alpha i}^* U_{\beta i} U_{\alpha j} U_{\beta j}^* \exp\left(-i \frac{\Delta m_{ij}^2 L}{2E}\right). \quad (2.37)$$

Where the definition $\Delta m_{ij}^2 \equiv m_i^2 - m_j^2$ has been used. Hence, the oscillation probability is parametrized by four PMNS values $\theta_{12}, \theta_{23}, \theta_{13}, \delta_{CP}$ (analogous to the CKM parameters), and two squared-mass differences Δm_{21}^2 and Δm_{31}^2 , (given that $\Delta m_{32}^2 = \Delta m_{21}^2 - \Delta m_{31}^2$) that modern

experiments try to precisely quantify.

The observation of neutrino oscillations has remarkable implications explicit in Eq.2.37. On one hand both non-null neutrino masses and oscillation angles are necessary and on the other hand lepton flavor is not conserved in oscillations. Moreover, neutrino oscillations might not conserve CP symmetry.

Experimentally, the mass differences are known to be of the order of 10^{-4} eV² and modern oscillation experiments often work with distances, L , on the order of kilometers and neutrino energies E of the order of the MeV or GeV. Consequently, the argument in Eq.2.37 in natural units ($c = \hbar = 1$) is often expressed in SI units as

$$\frac{\Delta m_{ij}^2 c^3 L}{4\hbar E} = 1.27 \frac{\Delta m_{ij}^2 L}{E} \left[\frac{\text{eV}^2 \cdot \text{Km}}{\text{GeV}} \right]. \quad (2.38)$$

In neutrino oscillation experiments two searches can be done: *appearance* ($\alpha = \beta$) and *disappearance* ($\alpha \neq \beta$) measurements, wherein the deficit or excess of ν_β is respectively studied. Notice that

$$P(\nu_\alpha \rightarrow \nu_\alpha) = 1 - \sum_{\beta \neq \alpha} P(\nu_\alpha \rightarrow \nu_\beta). \quad (2.39)$$

Albeit Eq.2.37 describes the whole phenomena of neutrino oscillations for the case of three active neutrinos, in some experimental conditions the probability for oscillations among two flavors

$$P(\nu_\alpha \rightarrow \nu_\beta) = \sin^2 2\theta \sin^2 \left(1.27 \frac{\Delta m^2 L}{E} \right) \quad (2.40)$$

is a valid and useful approximation to the three flavors probability. In two flavor neutrino mixing a single mass-splitting and angle are sufficient and CP symmetry is conserved. This simplification was used for decades before the oscillation experiments became sensitive to subdominant effects. In particular, one can find abundant literature under this paradigm for the study of solar ($\Delta m_{sol}^2, \theta_{sol}$) and atmospheric ($\Delta m_{atm}^2, \theta_{atm}$) neutrino oscillations. Under the three flavor mixing description Δm_{sol}^2 can be identified as Δm_{21}^2 and Δm_{atm}^2 as Δm_{31}^2 or Δm_{32}^2 . The experimental measurements reveal that

$$\Delta m_{21}^2 \ll |\Delta m_{31}^2| \simeq |\Delta m_{32}^2|. \quad (2.41)$$

Whereas the sign of Δm_{21}^2 can be chosen to be positive without loss of generality [120], this is not true for the sign of the largest mass splitting, which remains experimentally unknown. Hence, it is still unclear if masses follow a normal ordering (NO) with $m_1 < m_2 < m_3$, or an inverted ordering (IO) with $m_3 < m_1 < m_2$, see Figure 2.1.

Experimentally, it is also unknown if CP is violated in neutrino oscillations, i.e $\delta_{CP} \neq 0, \pi$. To study it, it is useful to rewrite Eq.2.37 as

$$P(\nu_\alpha \rightarrow \nu_\beta) = \delta_{\alpha\beta} - 4 \sum_{i>j}^3 \mathcal{R}(U_{\alpha i}^* U_{\beta i} U_{\alpha j} U_{\beta j}^*) \sin^2 \left(\frac{\Delta m_{ij}^2 L}{4E} \right) \quad (2.42)$$

$$\pm 2 \sum_{i>j}^3 \mathcal{I}(U_{\alpha i}^* U_{\beta i} U_{\alpha j} U_{\beta j}^*) \sin \left(\frac{\Delta m_{ij}^2 L}{2E} \right). \quad (2.43)$$

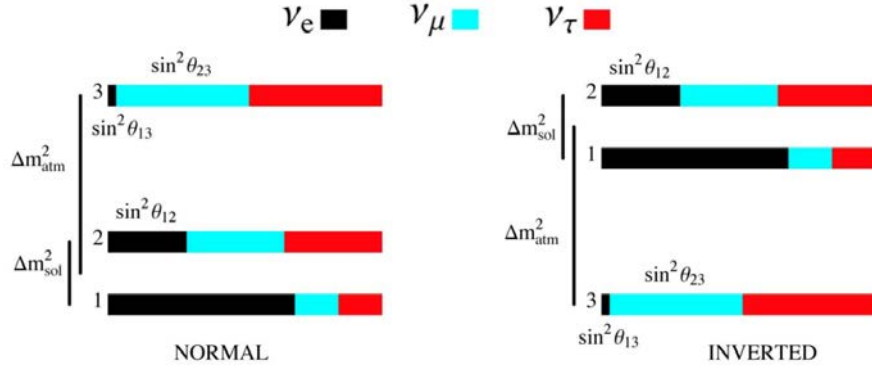


FIGURE 2.1: Possible mass orderings under the light of current experimental data. The PMNS angles $(\theta_{12}, \theta_{13}, \theta_{23})$ determine the flavor composition of each mass state. Two mass orderings are allowed. In the normal ordering the lightest neutrino mass state is ν_1 , which is mainly connected to ν_e and therefore to the lightest lepton, the electron. In the inverse ordering the lightest state would be ν_3 , which is the mass state with the smallest ν_e flavor contribution. Image Credit: FNAL.

The third term sign is positive (negative) for neutrinos (antineutrinos) due to $U \leftrightarrow U^*$. Hence, the amount of CP violation in neutrino mixing is characterized by

$$A_{CP}^{\alpha\beta} = P(\nu_\alpha \rightarrow \nu_\beta) - P(\bar{\nu}_\alpha \rightarrow \bar{\nu}_\beta) = +4 \sum_{i>j}^3 \mathcal{I}(U_{\alpha i}^* U_{\beta i} U_{\alpha j} U_{\beta j}) \sin\left(\frac{\Delta m_{ij}^2 L}{2E}\right) \quad (2.44)$$

$$= 16 J_{CP} \sum_{\gamma} \epsilon_{\alpha\beta\gamma} \sin\left(\frac{\Delta m_{21}^2 L}{2E}\right) \sin\left(\frac{\Delta m_{32}^2 L}{2E}\right) \sin\left(\frac{\Delta m_{31}^2 L}{2E}\right). \quad (2.45)$$

Here $\epsilon_{\alpha\beta\gamma}$ is the Levi-Civita tensor and J_{CP} is known as the Jarlskog invariant, defined as

$$J_{CP} = \frac{1}{8} \cos \theta_{13} \sin 2\theta_{12} \sin 2\theta_{23} \sin 2\theta_{13} \sin \delta_{CP}. \quad (2.46)$$

Notice that $A_{CP}^{\alpha\beta}$ is proportional to J_{CP} . Interestingly, as both quarks and neutrinos experience flavor mixing one can compare the experimental values of J_{CP}^{CKM} and J_{CP}^{PMNS} . Although δ_{CP}^{PMNS} is not yet accurately measured, current data suggests a CP violation three orders of magnitude larger in neutrinos than in quarks [1]. Moreover, it must be noted that only appearance measurements are sensitive to $A_{CP}^{\alpha\beta}$ since $\epsilon_{\alpha\beta\gamma} = 0$ if $\alpha = \beta$.

2.3.2 Oscillations in matter

When neutrinos travel across matter the interactions with the surrounding particles need to be accounted for. This is particularly relevant due to the fact that ordinary matter has a great amount of e^- , but neither μ^- , τ^- nor antimatter. As a result of it, ν_e and $\bar{\nu}_e$ can interact both through NC and CC whereas for all other neutrinos only NC is possible, as depicted in Figure 2.2.

Accordingly, to account for matter effects an effective potential acting on the electronic flavor needs to be included in the Hamiltonian

$$H = U \text{diag}\left(\frac{m_1^2}{2E}, \frac{m_2^2}{2E}, \frac{m_3^2}{2E}\right) U^{-1} + \text{diag}(V, 0, 0), \quad (2.47)$$

where V is the matter potential

$$V = \pm\sqrt{2}G_F N_e \simeq 7.6Y_e \frac{\rho}{10^{14}\text{g/cm}^3} \text{eV}. \quad (2.48)$$

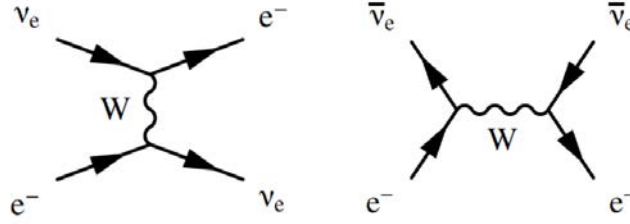


FIGURE 2.2: Feynman diagrams responsible for the matter effects.

Here G_F is the Fermi constant, N_e is the electron number density in the medium and the sign is positive for neutrinos and negative for antineutrinos. $Y_e = N_e/(N_p + N_n)$ is the relative electron number density with N_e, N_p, N_n being the number of electrons, protons and neutrons in the medium.

The Hamiltonian in Eq.2.47 can be written as

$$H = U \text{diag} \left(0, \frac{\Delta m_{21}^2}{2E}, \frac{\Delta m_{31}^2}{2E} \right) U^{-1} + \text{diag} (V, 0, 0) \quad (2.49)$$

by re-phasing the neutrino flavors by $\exp(-im_1^2/2E)$ and diagonalized using the effective mixing matrix in matter \tilde{U} , namely

$$H = \tilde{U} \text{diag} \left(0, \frac{\Delta m_{21}^2}{2E}, \frac{\Delta m_{31}^2}{2E} \right) \tilde{U}^{-1}. \quad (2.50)$$

In this manner, the number of physical parameters remains unchanged with respect to those in vacuum by defining effective mass-squared splittings and effective mixing angles. In the simpler case¹⁵ of two flavors mixing the effective mass splitting and angle in matter ($\Delta m_M^2, \theta_M$) are related to those in vacuum ($\Delta m^2, \theta$) by

$$\Delta m_M^2 = \sqrt{(\Delta m^2 \cos 2\theta - 2EV)^2 + (\Delta m^2 \sin 2\theta)^2} \quad (2.51)$$

and

$$\tan 2\theta_M = \tan 2\theta \left(1 - \frac{2EV}{\Delta m^2 \cos 2\theta} \right)^{-1}. \quad (2.52)$$

Notably, in the former equation there is a resonance ($\theta_M = \pi/4$) at

$$E^R = \frac{\Delta m^2 \cos 2\theta}{2V}. \quad (2.53)$$

Implicitly, E^R is a function of the matter electronic density. If the density is constant, the oscillation probability is well described by the equations in vacuum under the replacement of the vacuum parameters by the effective mass splittings and angles in matter. However, if the density is not constant along the neutrino propagation these variations need to be considered locally.

2.3.3 Solar neutrino oscillations

Solar neutrinos (ν_α is ν_e), which are produced in thermonuclear reactions in the core of the Sun with typical energies of few MeV, experience a change in the density of matter as they scape from the star. If the density variations are (not) smooth the neutrino oscillations are called *adiabatic* (*non-adiabatic*). In practice, the smoothness of the density transition can be quantified comparing

¹⁵For three neutrino flavors the discussion is analogous.

the oscillation length

$$L_M^{osc} = \frac{4\pi E}{\Delta m_{12}^2} \quad (2.54)$$

to the distance over which the density is changing. Thus, if the oscillation length, controlled by the size of Δm_{12}^2 , is significantly smaller (larger) than the Sun's core radius, which is $O(10^5)$ km, solar neutrino oscillations are adiabatic (non-adiabatic). In Adiabatic oscillations, the transition probability is

$$P_{\nu_e \rightarrow \nu_e}^{adiabatic} = \frac{1}{2} + \frac{1}{2} \cos 2\theta_M^i \cos 2\theta_M^f + \frac{1}{2} \sin 2\theta_M^i \sin 2\theta_M^f \cos \left(\int_0^L \frac{\Delta m_M^2(x)}{2E} dx \right), \quad (2.55)$$

where θ_M^i, θ_M^f refer to the oscillation angle in matter at the production and detection points respectively. Since for solar neutrinos the distance from the production to the detection point is much larger than the oscillation length, the integral term in Eq. 2.55 averages to zero. Accordingly, oscillations can not be observed, instead, an average survival probability is left which for adiabatic oscillations is

$$\bar{P}_{\nu_e \rightarrow \nu_e}^{adiabatic} = \frac{1}{2} + \frac{1}{2} \cos 2\theta_M^i \cos 2\theta_M^f. \quad (2.56)$$

For the non-adiabatic case an additional factor $0 \leq P_c \leq 1$ needs to be considered, leading to

$$\bar{P}_{\nu_e \rightarrow \nu_e}^{non-adiabatic} = \frac{1}{2} + \left(\frac{1}{2} - P_c \right) \cos 2\theta_M^i \cos 2\theta_M^f, \quad (2.57)$$

which is known as the Parke formula [121].

The overall behavior of these equations can be understood by studying the two limits $E_\nu \ll E^R$ and $E_\nu \gg E^R$ in Eq. 2.52. For simplicity, we consider the case where solar neutrinos reach a detector on Earth during the day, i.e. $\theta_M^f = \theta^{16}$. For low E_ν , $\theta_M^i = \theta$, such that Eq. 2.55 becomes

$$\bar{P}_{\nu_e \rightarrow \nu_e}^{adiabatic}(E \ll E^R) = \frac{1}{2} + \frac{1}{2} \cos^2 2\theta \geq 0.5, \quad (2.58)$$

which is identical to the vacuum survival probability. Conversely for large E_ν , $\theta_M^i = \pi/2$, such that

$$\bar{P}_{\nu_e \rightarrow \nu_e}^{adiabatic}(E \gg E^R) = \frac{1}{2} - \frac{1}{2} \cos 2\theta \leq 0.5. \quad (2.59)$$

Analogously, the same limits are found in non-adiabatic oscillations replacing $0.5 \rightarrow (0.5 - P_c)$. By comparing the predictions from the former equations to experimental data it is possible to determine the underlying unknown parameters θ_{12} and Δm_{12}^2 . However, it must be noted that, if the experimental data is limited, some degeneracies arise. For instance, for large values of Δm_{12}^2 (adiabatic behavior) and a large mixing angle θ_{12} , similar predictions are obtained at some energies to that of much smaller Δm_{12}^2 (non-adiabatic behavior) with small mixing angle θ_{12} . This possible solutions to explain the early experimental data were referred to as the Large Mixing Angle (LMA) and Small Mixing Angle (SMA) solutions to the solar neutrino problem, see Figure 2.3. Currently, the LMA solution is very much favored in view of data, as presented in Figure 2.4.

Additionally, it is illustrative to use Eq. 2.58 and Eq. 2.59 with the current best fit $\theta_{12} \sim 33^\circ$, which leads respectively to $\bar{P}_{\nu_e \rightarrow \nu_e}^{adiabatic}(E \ll E^R) \sim 0.58$ and $\bar{P}_{\nu_e \rightarrow \nu_e}^{adiabatic}(E \gg E^R) \sim 0.30$. This predictions are in nice qualitative agreement with the low and high energy limits in Figure 2.4.

¹⁶If the same is studied at night, solar neutrinos cross the Earth before reaching the detector, leading to additional matter effects, responsible for the so-called neutrino *regeneration*.

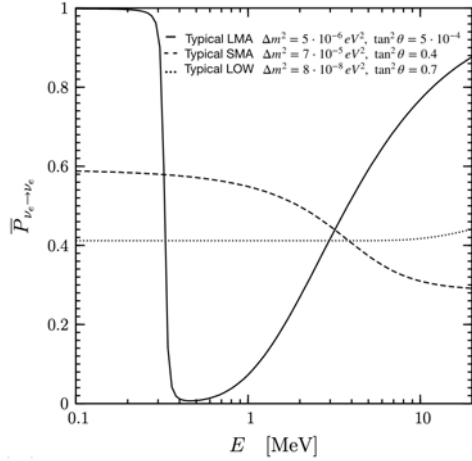


FIGURE 2.3: Predictions for the average survival probability for different parameter solutions. Figure from Ref. [113].

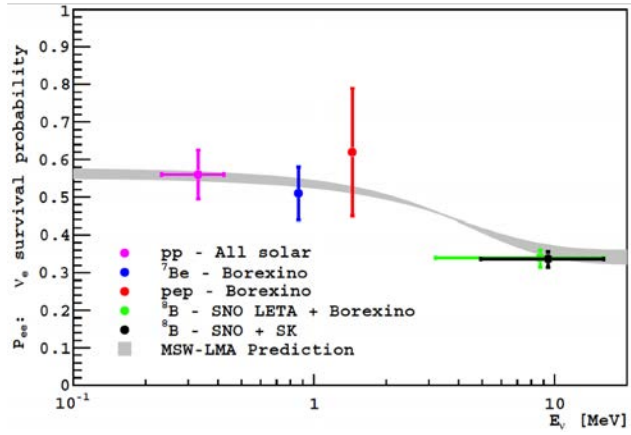


FIGURE 2.4: Survival probability of electron neutrinos as foreseen by the MSW-LMA model compared to experimental measurements. Figure from Ref. [122].

2.3.4 Accelerator and atmospheric neutrino oscillations

Atmospheric and accelerator neutrino oscillation experiments work with neutrino energies spanning from hundreds of MeV to few GeV, and oscillation distances of the order of hundreds to thousands of kilometers. As man-made beams ($\nu_\alpha = \nu_\mu$) allow for a better control of the experimental conditions, currently, the best constraints to the atmospheric parameters (θ_{23} , Δm_{23}^2) are set by accelerator experiments. For the simplified case of oscillations in vacuum and neglecting subdominant terms containing Δm_{12}^2 , follows

$$P(\nu_\mu \rightarrow \nu_\mu) \approx 1 - 4 \cos^2 \theta_{13} \sin^2 \theta_{23} (1 - \cos^2 \theta_{13} \sin^2 \theta_{23}) \sin^2 \frac{\Delta m_{23}^2 L}{4E}, \quad (2.60)$$

which as expected is explicitly insensitive to CP. Analogously,

$$P(\nu_\mu \rightarrow \nu_e) \approx \sin^2 2\theta_{13} \sin^2 \theta_{23} \sin^2 \frac{\Delta m_{23}^2 L}{4E} + J_{CP} \cos \left(\frac{\Delta m_{23}^2 L}{4E} \pm \delta_{CP} \right), \quad (2.61)$$

where δ_{CP} is positive (negative) for neutrino (antineutrino) oscillations.

As accelerator experiments allow to work with a highly pure muon neutrino or antineutrino beam under very similar conditions they are crucial to measure δ_{CP} . However, in both atmospheric and accelerator neutrino experiments neutrinos propagate through matter¹⁷. This plays a particularly important role when studying CP violation, since matter effects introduce an asymmetric dependence in neutrino and antineutrino probabilities, similar to δ_{CP} . To understand this, it is useful to rewrite Eq. 2.61 including matter effects. Keeping terms only up to second order in the small

¹⁷For atmospheric neutrinos measured from the sky, matter effects can be ignored. For atmospheric neutrinos crossing the Earth, the discussion is analogous to that of accelerator neutrinos presented in the text.

quantities α and θ_{13} , follows

$$\begin{aligned}
P(\nu_\mu \rightarrow \nu_e) &\simeq \sin^2 \theta_{23} \sin^2 2\theta_{13} \frac{\sin^2[(1 - \tilde{A})\Delta]}{(1 - \tilde{A})^2} \\
&\mp \alpha \sin 2\theta_{13} \xi \sin(\Delta) \frac{\sin(\tilde{A}\Delta)}{\tilde{A}} \frac{\sin[(1 - \tilde{A})\Delta]}{(1 - \tilde{A})} \sin \delta_{CP} \\
&+ \alpha \sin 2\theta_{13} \xi \cos(\Delta) \frac{\sin(\tilde{A}\Delta)}{\tilde{A}} \frac{\sin[(1 - \tilde{A})\Delta]}{(1 - \tilde{A})} \cos \delta_{CP} \\
&+ \alpha^2 \cos^2 \theta_{23} \sin^2 2\theta_{12} \frac{\sin^2 \tilde{A}\Delta}{\tilde{A}^2}, \tag{2.62}
\end{aligned}$$

with

$$\alpha \equiv \frac{\Delta m_{12}^2}{\Delta m_{31}^2}, \quad \Delta \equiv \frac{\Delta m_{31}^2 L}{4E}, \quad \xi \equiv \cos \theta_{13} \sin 2\theta_{12} \sin 2\theta_{23} \quad \text{and} \quad \tilde{A} \equiv \frac{2VE}{\Delta m_{31}^2}. \tag{2.63}$$

In Eq. 2.62 the sign of the second term is negative (positive) for neutrinos (antineutrinos).

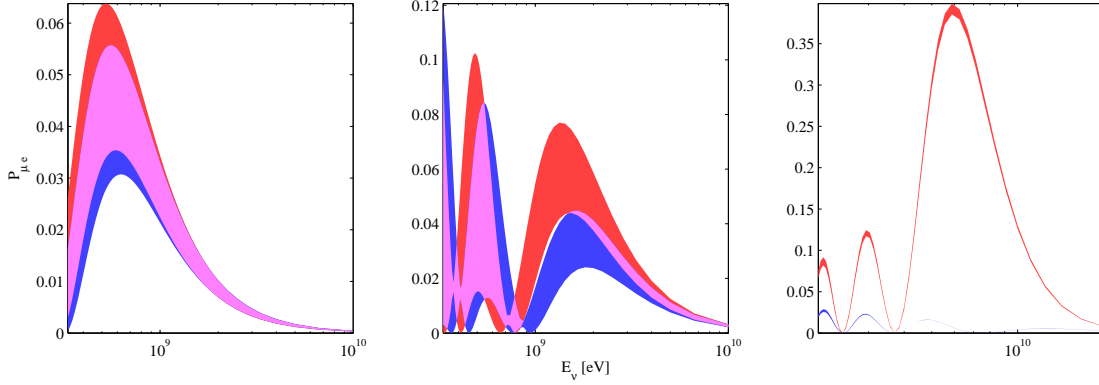


FIGURE 2.5: The electron appearance probability P_{ν_e} at baselines of 295 (left), 810 (middle), and 7500 km (right) as a function of the neutrino energy. These baselines correspond to those of T2K, NO ν A and the magic baseline. The red (blue) band corresponds to the normal (inverted) mass hierarchy and the band width is obtained by varying the value of δ_{CP} . The antineutrino probabilities look similar with the hierarchies interchanged. Note the different scales of the axes. Figure from Ref. [123].

In general, there is a complex interplay between the four terms as α , Δ and \tilde{A} are sign sensitive, which translates into degenerate solutions for δ_{CP} and the mass ordering. Moreover, the typical neutrino energy and the baseline of the experiments greatly change the relative importance of CP-violation and matter effects in the oscillation probability. On one hand, close to the resonance condition, where $\tilde{A} \sim 1$, the first term is enhanced¹⁸, leading to an increased sensitivity to the mass ordering. Given that $\tilde{A} \approx 2.95 \cdot 10^{-2} \frac{\rho}{[\text{g}\cdot\text{cm}^3]} \cdot E [\text{GeV}]$, and $\rho = 2.6 \text{ g/cm}^3$ in the Earth crust, the resonance happens at $E_\nu \sim 13 \text{ GeV}$. Thus, in general, the closer the typical neutrino energy in the beam is to the resonant energy, the more sensitive the experiment is to matter effects. On the other hand, all terms but the first one are proportional to $\sin(\tilde{A}\Delta)$ and since the product $\tilde{A}\Delta$ is energy independent the magnitude of the CP-violating terms depends on the baseline L . Remarkably, due to this it is possible to find baselines at which all terms but the first one cancel. The first one of these "magic" baselines is found at $L \sim 7360 \text{ km}$. Hence, as it can be seen in Figure 2.5, the larger the baseline in the interval from 0 to 7360 km, the larger the dominance of the matter effects.

For the study of disappearance, an analogous expression to Eq. 2.62 can be found by applying the

¹⁸ $\lim_{a \rightarrow 0} \sin^2(ax)/a^2 = x^2$, and $\lim_{a \rightarrow 0} \sin(ax)/a = x$.

same approximations and definitions, namely

$$\begin{aligned}
P(\nu_\mu \rightarrow \nu_\mu) = & 1 - \sin^2 2\theta_{23} \sin^2 \Delta + \alpha \cos^2 \theta_{12} \Delta \sin 2\Delta - \alpha^2 \sin^2 2\theta_{12} \cos^2 \theta_{23} \frac{\sin^2 \tilde{A} \Delta}{\tilde{A}^2} \\
& - \alpha^2 \cos^4 \theta_{12} \sin^2 2\theta_{23} \Delta^2 \cos 2\Delta - 4 \sin^2 \theta_{13} \sin^2 \theta_{23} \frac{\sin^2(\tilde{A} - 1)\Delta}{(\tilde{A} - 1)^2} \\
& + \frac{1}{2\tilde{A}} \alpha^2 \sin^2 2\theta_{12} \sin^2 2\theta_{23} \left(\sin \Delta \frac{\sin \tilde{A} \Delta}{\tilde{A}} \cos(\tilde{A} - 1)\Delta - \frac{\Delta}{2} \sin 2\Delta \right) \\
& - \frac{2}{\tilde{A} - 1} \sin^2 \theta_{13} \sin^2 2\theta_{13} \left(\sin \Delta \cos A \Delta \frac{\sin(\tilde{A} - 1)\Delta}{\tilde{A} - 1} - \frac{\tilde{A}}{2} \Delta \sin 2\Delta \right) \\
& - 2\alpha \sin \theta_{13} \sin 2\theta_{12} \sin 2\theta_{23} \cos \delta_{CP} \frac{\sin \tilde{A} \Delta \sin(\tilde{A} - 1)\Delta}{\tilde{A}(\tilde{A} - 1)} \\
& + \frac{2}{A - 1} \alpha \sin \theta_{13} \sin 2\theta_{12} \sin 2\theta_{23} \cos 2\theta_{23} \cos \delta_{CP} \\
& \sin \Delta \left(\tilde{A} \sin \Delta - \frac{\sin \tilde{A} \Delta}{\tilde{A}} \cos(A - 1)\Delta \right). \tag{2.64}
\end{aligned}$$

In general however, to study neutrino disappearance in matter it is enough to work in an effective two-flavor approximation [124].

2.3.5 Reactor neutrino oscillations

Reactor neutrino oscillation experiments study antineutrinos produced in the fission processes in nuclear reactors ($\bar{\nu}_\alpha = \bar{\nu}_e$). As the energy of these antineutrinos is typically of the order of a few MeV only disappearance studies are possible, ruled by the probability

$$\begin{aligned}
P(\bar{\nu}_e \rightarrow \bar{\nu}_e) = & 1 - \sin^2 2\theta_{12} \cos^4 \theta_{13} \sin^2 \frac{\Delta m_{21}^2 L}{4E} \\
& - \sin^2 2\theta_{13} \left[\cos^2 \theta_{12} \sin^2 \frac{\Delta m_{31}^2 L}{4E} + \sin^2 \theta_{12} \sin^2 \frac{\Delta(\Delta m_{31}^2 - \Delta m_{21}^2)L}{4E} \right], \tag{2.65}
\end{aligned}$$

plotted in Figure 2.6. Given that typical baselines and energies are low in reactor experiments, matter effects can be ignored. In Eq. 2.65 two regimes can be probed. On one hand, when the baseline is sufficiently short, i.e. hundreds of meters to few kilometers, $\sin^2(\Delta m_{21}^2 L/4E) \approx 1$, leading to

$$P^{\text{short}}(\bar{\nu}_e \rightarrow \bar{\nu}_e) \sim 1 - \sin^2 2\theta_{13} \sin^2 \frac{\Delta m_{31}^2 L}{4E}. \tag{2.66}$$

Since Δm_{31}^2 is experimentally well known from non-reactor experiments, this probability provides the best experimental way to pin down θ_{13} . On the other hand, for intermediate baselines of tens to hundreds of kilometers, $\sin^2(\Delta m_{21}^2 L/4E)$ changes significantly in the relevant span of antineutrino energies, so that Eq. 2.65 is well approximated by

$$P^{\text{medium}}(\bar{\nu}_e \rightarrow \bar{\nu}_e) \sim 1 - \cos^4 \theta_{13} \left[1 - \sin^2 2\theta_{12} \sin^2 \frac{\Delta m_{12}^2 L}{4E} \right], \tag{2.67}$$

providing a complementary way to study the solar sector. Finally, it is relevant to notice that the last term in Eq. 2.65 is potentially sensitive to the mass ordering as the sign of Δm_{31}^2 introduces

a retardment or advancement phase to the oscillation frequency, as illustrated in Figure 2.7. Measuring such a small effect has not been possible yet as an extremely good energy resolution is required. However, JUNO [109] is expected to have a sensitivity of about 3σ to the mass ordering by exploiting this method.

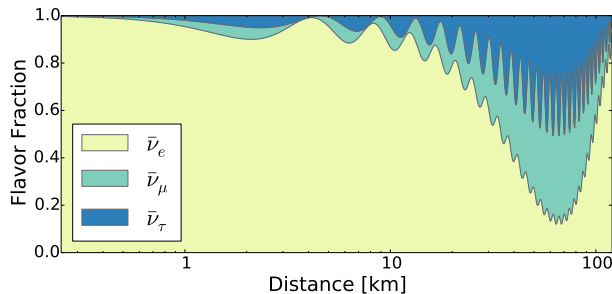


FIGURE 2.6: Oscillation probability for a typical electron antineutrino ($E_\nu = 4$ MeV) as a function of the baseline. Figure from Ref. [125].

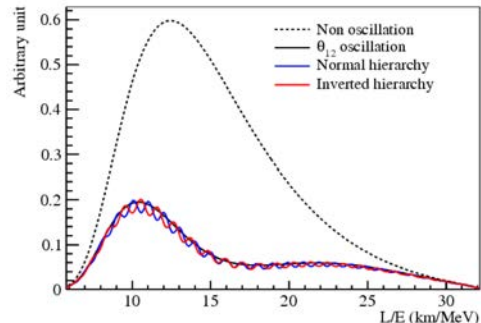


FIGURE 2.7: Expected number of neutrino interactions with and without oscillations, including the role of the mass hierarchy. Figure from Ref. [109].

2.3.6 Global analysis of 3ν data

The best current knowledge of the parameters ruling 3ν oscillations is provided by combining the information of the different solar, atmospheric, accelerator and reactor neutrinos by means of global fits¹⁹. In general, new global fits are published every time that significant updates are provided by the experiments. Currently there are different groups, e.g. those in Refs. [129, 130, 131], dedicated to perform global analysis. Although every group follows slightly different strategies and conventions, the overall results largely agree. In order to review the most updated status on the current knowledge of neutrino physics, hereafter, the main results of Ref. [132] and its follow-up Ref. [133], are summarized, as they provide the most widely cited and recently published²⁰ results (2020).

The contributions from different experiments to the determination of the atmospheric mass splitting and the angles θ_{13} and θ_{23} is presented in Figure 2.8. The results show a high overall agreement between the different datasets, as well as the leading role of T2K, NO ν A and Daya Bay in driving the current experimental precision of the aforementioned parameters. Concerning the determination of the solar parameters Δm_{12}^2 and θ_{12} , two different datasets are crucial, as presented in the left panel of Figure 2.9. On one hand, solar neutrino experiments, in combination with a given solar flux model, provide the best knowledge on the solar mass splitting. On the other hand reactor antineutrinos measured by KamLAND provide the best knowledge on θ_{12} . Although these two datasets have been in mild tension in the past, see the right panel of Figure 2.9, the most recent data from SK [134] has increased their compatibility. Namely, the best Δm_{21}^2 fit of KamLAND lies now at 1.1σ in the analysis with the GS98 fluxes. The global analysis results²¹ from Ref. [133] are presented in Fig 2.10 and in the associated Table 2.2.

In view of all the former results, some remarks must be made concerning the current most important unknowns: the mass ordering, the octant of θ_{23} and the value of δ_{CP} . In the first place,

¹⁹Further details can be found on Refs. [126, 127, 128].

²⁰As of now, i.e. 19/09/2021.

²¹As discussed in Ref. [132] the atmospheric measurements from SK (SK-atm) can not be included in the global analysis on the same footing as the data from other experiments. SK-atm dataset is, however, important to draw conclusions about the preferred mass ordering. Accordingly, the authors in Ref. [132] perform two global fits with and without the SK-atm data.

the NO is preferred at the 1.6σ level (2.7σ including SK-atm data). In the second place, the upper θ_{23} octant is preferred with the best fit point located at $\sin^2 \theta_{23} = 0.57$. Maximal mixing ($\sin^2 \theta_{23} = 0.5$) is disfavored at 1.6σ (2.0σ) without (with) SK-atm. Finally, the best fit point for δ_{CP} is at 195° , allowing CP-conservation at 0.6σ [133]. Despite the apparent tension in Figure 2.11, statistical tests show great compatibility between T2K, $\text{NO}\nu\text{A}$ and reactor data for both mass orderings [133]. Remarkably, if the data is restricted to the IO, the best fit point for δ_{CP} is close to maximal and CP-conservation is disfavored at around 3σ . Consequently, elucidating the mass ordering might be crucial to assess if CP is violated.

Lastly, in light of current data the following 1σ [3σ] level precision (interval/best-fit-point from Table 2.2) is obtained for the NO:

$$\begin{aligned} \theta_{12} &: 4.6\% [14\%], & \theta_{13} &: 2.9\% [9.0\%], & \theta_{23} &: 5.1\% [27\%], \\ \Delta m_{21}^2 &: 5.5\% [16\%], & |\Delta m_{3\ell}^2| &: 2.2\% [6.7\%], & \delta_{CP} &: 39\% [100\%]. \end{aligned} \quad (2.68)$$

All results but those for δ_{CP} are unchanged for the IO²². Remarkably, the current best fit for the PMNS parameters show a flavor pattern completely different to that in quarks, see Figure 2.12. While the CKM matrix elements are highly hierarchical, all PMNS matrix elements are of similar size.

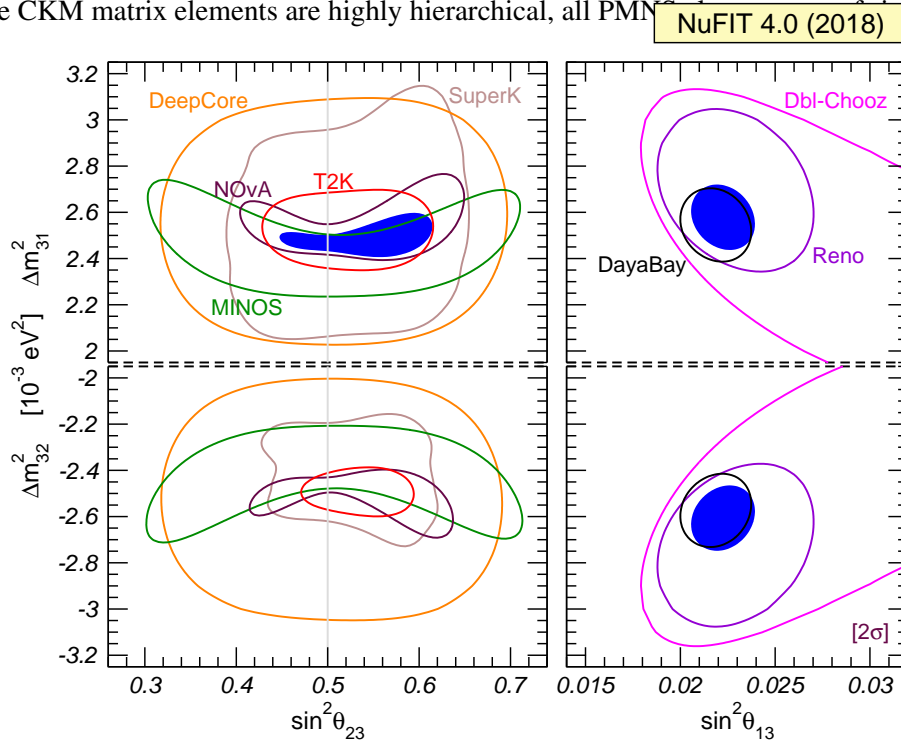


FIGURE 2.8: Determination of $\Delta m_{3\ell}^2$ at 2σ (2 dof), where $\ell = 1$ for NO (upper panels) and $\ell = 2$ for IO (lower panels). The left panels show regions in the $(\theta_{23}, \Delta m_{3\ell}^2)$ plane using both appearance and disappearance data. In the left panels the constraint on θ_{13} from the global fit (which is dominated by the reactor data) is imposed as a Gaussian bias. The right panels show regions in the $(\theta_{13}, \Delta m_{3\ell}^2)$ plane. In all panels Δm_{21}^2 and $\sin^2 \theta_{12}$ are fixed to the global best fit values and the blue colored region shows the combination of the data from the experiments in each plot. Contours are defined with respect to the global minimum of the two orderings. Figure from Ref. [132].

²²For IO, the δ_{CP} knowledge corresponds to 20% [100%] at 1σ [3σ].

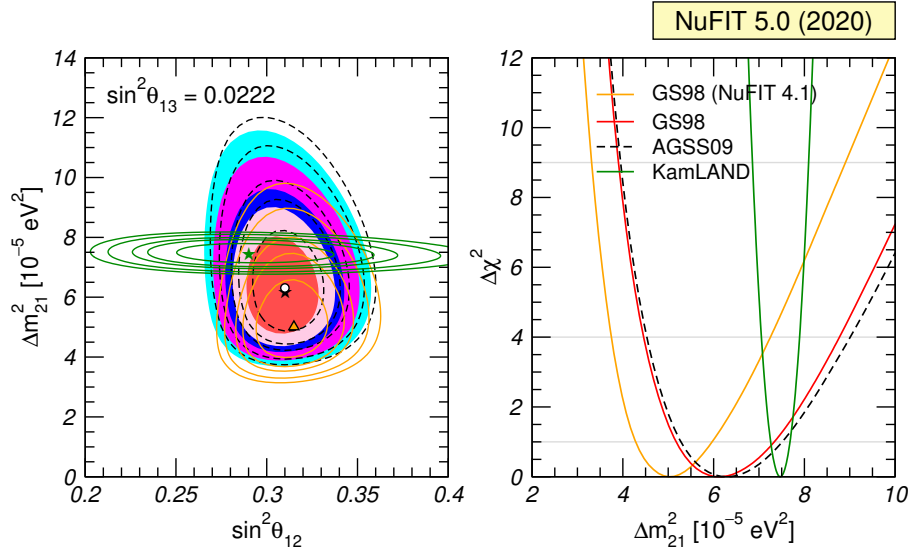


FIGURE 2.9: Left: Allowed parameter regions (at 1σ , 90%, 2σ , 99%, and 3σ CL for 2 *dof*) from the combined analysis of solar data for the GS98 model (full regions with best fit marked by black star) and the AGSS09 model (dashed void contours with best fit marked by a white dot), and for the analysis of KamLAND data (solid green contours with best fit marked by a green star) for fixed $\sin^2 \theta_{13} = 0.0224$ ($\theta_{13} = 8.6$). The orange contours feature the previous results (2018) of the global analysis for the GS98 model in Ref. [132]. Right: Δ^2 dependence on Δm_{21}^2 for the same four analyses after marginalizing over θ_{12} . Figure from Ref. [133].

		Normal Ordering (best fit)		Inverted Ordering ($\Delta\chi^2 = 2.7$ (1.6σ))	
		bfp $\pm 1\sigma$	3σ range	bfp $\pm 1\sigma$	3σ range
without SK atmospheric data	$\sin^2 \theta_{12}$	$0.304^{+0.013}_{-0.012}$	$0.269 \rightarrow 0.343$	$0.304^{+0.013}_{-0.012}$	$0.269 \rightarrow 0.343$
	$\theta_{12}/^\circ$	$33.44^{+0.78}_{-0.75}$	$31.27 \rightarrow 35.86$	$33.45^{+0.78}_{-0.75}$	$31.27 \rightarrow 35.87$
	$\sin^2 \theta_{23}$	$0.570^{+0.018}_{-0.024}$	$0.407 \rightarrow 0.618$	$0.575^{+0.017}_{-0.021}$	$0.411 \rightarrow 0.621$
	$\theta_{23}/^\circ$	$49.0^{+1.1}_{-1.4}$	$39.6 \rightarrow 51.8$	$49.3^{+1.0}_{-1.2}$	$39.9 \rightarrow 52.0$
	$\sin^2 \theta_{13}$	$0.02221^{+0.00068}_{-0.00062}$	$0.02034 \rightarrow 0.02430$	$0.02240^{+0.00062}_{-0.00062}$	$0.02053 \rightarrow 0.02436$
	$\theta_{13}/^\circ$	$8.57^{+0.13}_{-0.12}$	$8.20 \rightarrow 8.97$	$8.61^{+0.12}_{-0.12}$	$8.24 \rightarrow 8.98$
	$\delta_{CP}/^\circ$	195^{+51}_{-25}	$107 \rightarrow 403$	286^{+27}_{-32}	$192 \rightarrow 360$
	$\frac{\Delta m_{21}^2}{10^{-5}} \text{ eV}^2$	$7.42^{+0.21}_{-0.20}$	$6.82 \rightarrow 8.04$	$7.42^{+0.21}_{-0.20}$	$6.82 \rightarrow 8.04$
	$\frac{\Delta m_{3\ell}^2}{10^{-3}} \text{ eV}^2$	$+2.514^{+0.028}_{-0.027}$	$+2.431 \rightarrow +2.598$	$-2.497^{+0.028}_{-0.028}$	$-2.583 \rightarrow -2.412$

TABLE 2.2: Three-flavor oscillation parameters from the fit to global data. The numbers in the 1st (2nd) column are obtained assuming NO (IO). Note that $\Delta m_{3\ell}^2 \equiv \Delta m_{31}^2 > 0$ for NO and $\Delta m_{3\ell}^2 \equiv \Delta m_{32}^2 < 0$ for IO. Table from [133], where additional results including the tabulated SK-atm $\Delta\chi^2$ can be found. The addition of SK-atm data has a minor impact in all best fit points (bfp) and uncertainties, but disfavors the IO at 2.7σ .

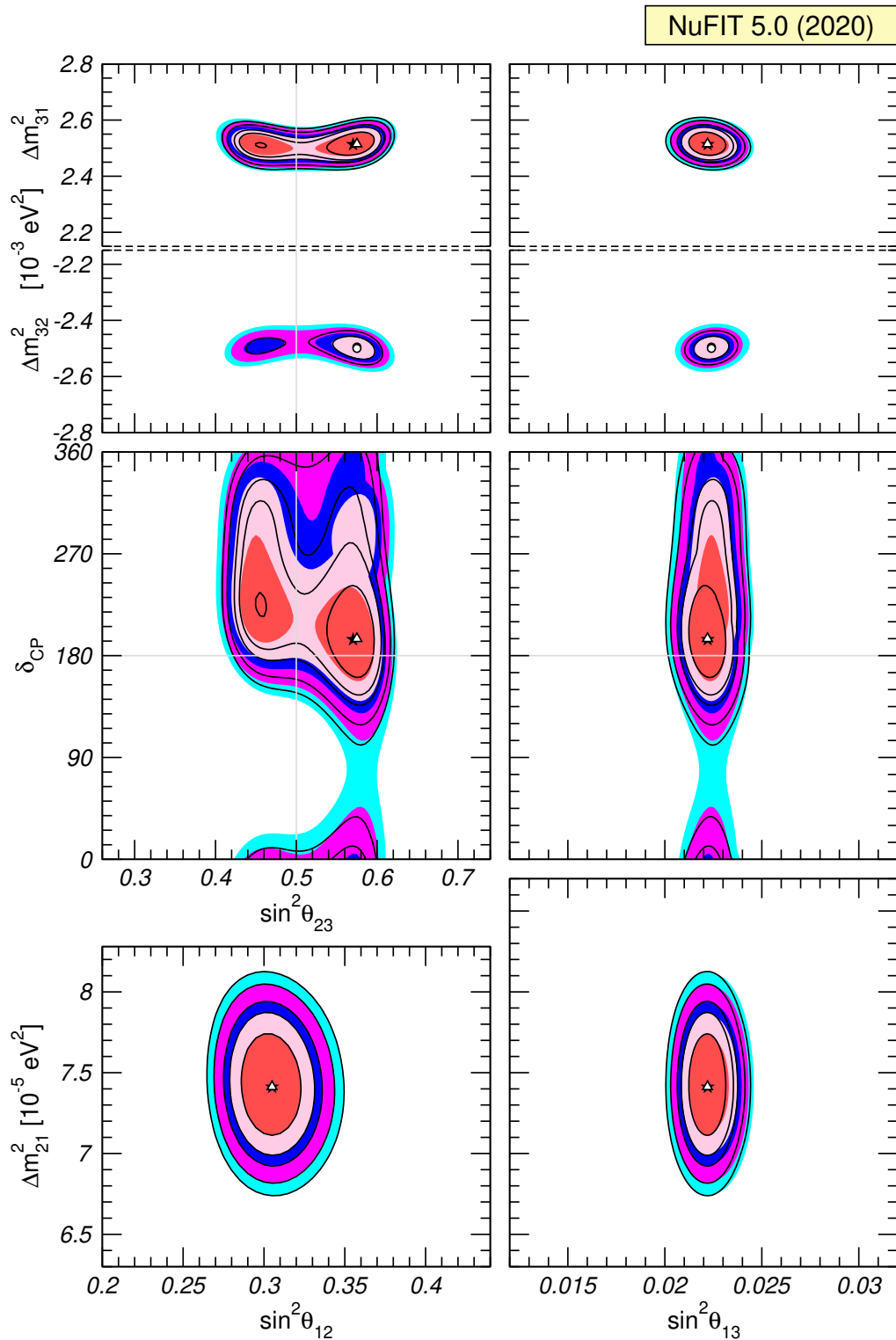


FIGURE 2.10: Global 3ν oscillation analysis. Each panel shows the two-dimensional projection of the allowed six-dimensional region after minimization with respect to the undisplayed parameters. The regions in the four lower panels are obtained from $\Delta\chi^2$ minimized with respect to the mass ordering. The different contours correspond to 1σ , 90%, 2σ , 99%, 3σ CL (2 *dof*). Colored regions (black contour curves) are without (with) adding the tabulated SK-atm $\Delta\chi^2$. Note that $\Delta m_{3\ell}^2 \equiv \Delta m_{31}^2 > 0$ for NO and $\Delta m_{3\ell}^2 \equiv \Delta m_{32}^2 < 0$ for IO. Figure from Ref. [133].

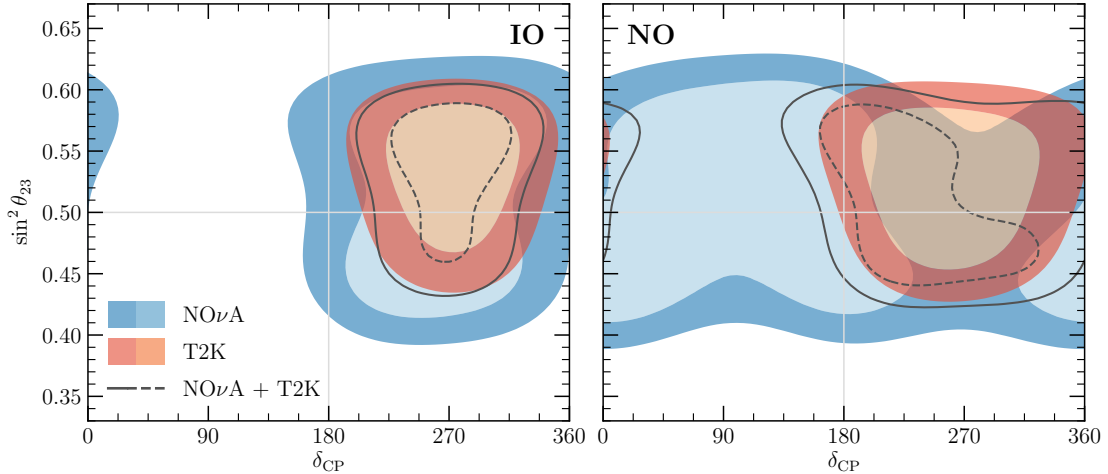


FIGURE 2.11: 1σ and 2σ allowed regions (2 dof) for T2K (red shading), NOνA (blue shading) and their combination (black curves). Contours are defined with respect to the local minimum for IO (left) or NO (right). The values $\sin^2\theta_{13} = 0.0224$, $\sin^2\theta_{12} = 0.310$, $\Delta m_{21}^2 = 7.40 \times 10^{-5} \text{ eV}^2$ are fixed, and the minimization is done with respect to $|\Delta m_{3\ell}^2|$. Figure from Ref. [133].

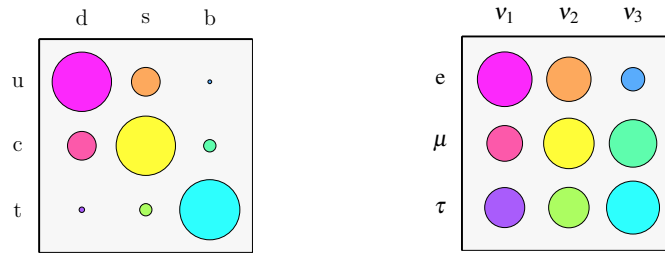


FIGURE 2.12: The areas of the circles represent the size of the mixing elements. For neutrinos, normal mass hierarchy is assumed. From top to bottom, from left to right: (a) quark mixing (CKM) elements $|V_{ud}|$, $|V_{us}|$, $|V_{ub}|$, $|V_{cd}|$, ...; (b) lepton mixing (PMNS) elements $|U_{e1}|$, $|U_{e2}|$, $|U_{e3}|$, $|U_{\mu 1}|$, ... in both panels, the mixing matrices are supposed to be unitary. The hierarchical structure of quark mixing elements contrasts with the one of lepton mixing elements. Figure from Ref. [135].

2.3.7 Sterile neutrinos

Although collider data places stringent constraints on the number of active neutrinos, i.e. those that interact weakly, being equal to three [136], in principle, additional sterile neutrinos, insensitive to the strong and electroweak forces, might exist. Due to its noninteracting nature, direct detection of sterile neutrinos can not be achieved. However, clear indirect signatures of their existence might be found on neutrino oscillations. In general, Eq. 2.29 can be expanded to include an arbitrary number of neutrino species, often regarded as $3+n$. For illustration, it is useful to review the $3+1$ scenario. As in the case of the solar sector and the atmospheric sector, which are quasi-decoupled due to their different Δm^2 values, a sterile sector (Δm_{14}^2) might be dominant for some values of L/E . Currently, most sterile searches have focused in studying ν_e and ν_μ disappearance and ν_e appearance at short baselines, described in the two-flavor approximation by

the following probabilities

$$P(\nu_\mu \rightarrow \nu_e) = \underbrace{4|U_{e4}|^2|U_{\mu4}|^2}_{\sin^2 2\theta_{\mu e}} \sin^2 \frac{\Delta m_{14}^2 L}{4E}, \quad (2.69)$$

$$P(\nu_e \rightarrow \nu_e) = 1 - \underbrace{4|U_{e4}|^2(1 - |U_{e4}|^2)}_{\sin^2 2\theta_{ee}} \sin^2 \frac{\Delta m_{14}^2 L}{4E}, \quad (2.70)$$

$$P(\nu_\mu \rightarrow \nu_\mu) = 1 - \underbrace{4|U_{\mu4}|^2(1 - |U_{\mu4}|^2)}_{\sin^2 2\theta_{\mu\mu}} \sin^2 \frac{\Delta m_{14}^2 L}{4E}. \quad (2.71)$$

Here U is a four-dimensional version of the PMNS unitary matrix, and $\theta_{\mu e}$, θ_{ee} and $\theta_{\mu\mu}$ are effective mixing angles. Remarkably, several experiments have probed these oscillations and intriguing but controversial anomalies have been found. On one hand, in the early 2000s the LSND experiment found significant hints, at the level of 3.8σ , for $\bar{\nu}_\mu \rightarrow \bar{\nu}_e$ transitions [137]. The MiniBooNE experiment has further explored this anomaly since 2002 using both neutrinos and antineutrinos. MiniBooNE has also found a significant excess of events in ν_e and $\bar{\nu}_e$ appearance, of 4.8σ [138, 139], compatible with LSND data. The MiniBooNE results however, are in conflict with a recent set of dedicated measurements by the MicroBooNE experiment [140, 141, 142]. On the other hand, both the GALLEX and SAGE experiments measured a deficit of ν_e generated in nearby radioactive sources. As both detectors used Gallium these results are known as the Gallium anomaly (GA) with a combined significance of 2.9σ [143]. Moreover, in 2011 two updates on the prediction of the reactor neutrino flux [144, 145] increased the expected detection rate, which turned out to be larger than the observed rate of interactions in several short-baseline reactor neutrino experiments. Since then, this deficit of $\bar{\nu}_e$ is known as the reactor antineutrino anomaly (RAA), with an overall significance similar to 3σ [146]. The significance of this anomaly could decrease if the flux normalization uncertainty was larger than the nominal one²³. Hence, the RAA remains controversial. To avoid reactor flux dependencies, some reactor experiments have focused on measuring the relative rate of $\bar{\nu}_e$ interactions at different distances in the search for oscillations. Particularly interesting are the results of NEOS [148] and DANSS [149], which have found hints for oscillations compatible with one another. Although other experiments such as Neutrino-4, have also recently claimed to observe sterile oscillations with great significance [150], their results have been promptly criticized [151, 152] and their preferred phase-space strongly disfavored by other recent experiments, such as STEREO [153] and PROSPECT [154]. Finally, ν_μ disappearance searches influenced by steriles have not found any significant signal in several experiments, including CDHSW [155], SciBooNE-MiniBooNE with neutrinos [156] and antineutrinos [157], IceCube [158] and MINOS&MINOS+ [159]. With all, the ν_e appearance and disappearance data, which hints for sterile signatures, is disfavored by ν_μ disappearance data, see Figure 2.13. The overall tension has been quantified by the goodness-of-fit to global data, with a p-value of 2×10^{-7} [143]. Interestingly, the consistency of the fit does not improve when more than one sterile neutrino is considered [160]. As noted in Ref. [146], although adding more sterile neutrinos adds extra freedom to the fit, the only qualitatively new feature that appears in 3+2 and 3+3 models compared to the simple 3+1 scenario is the possibility of CP violation at short baselines. However, since there is no tension between neutrino and antineutrino data, adding CP-violation does not improve the global fit.

²³There is evidence pointing in this direction, e.g. the so-called "5 MeV bump" [147].

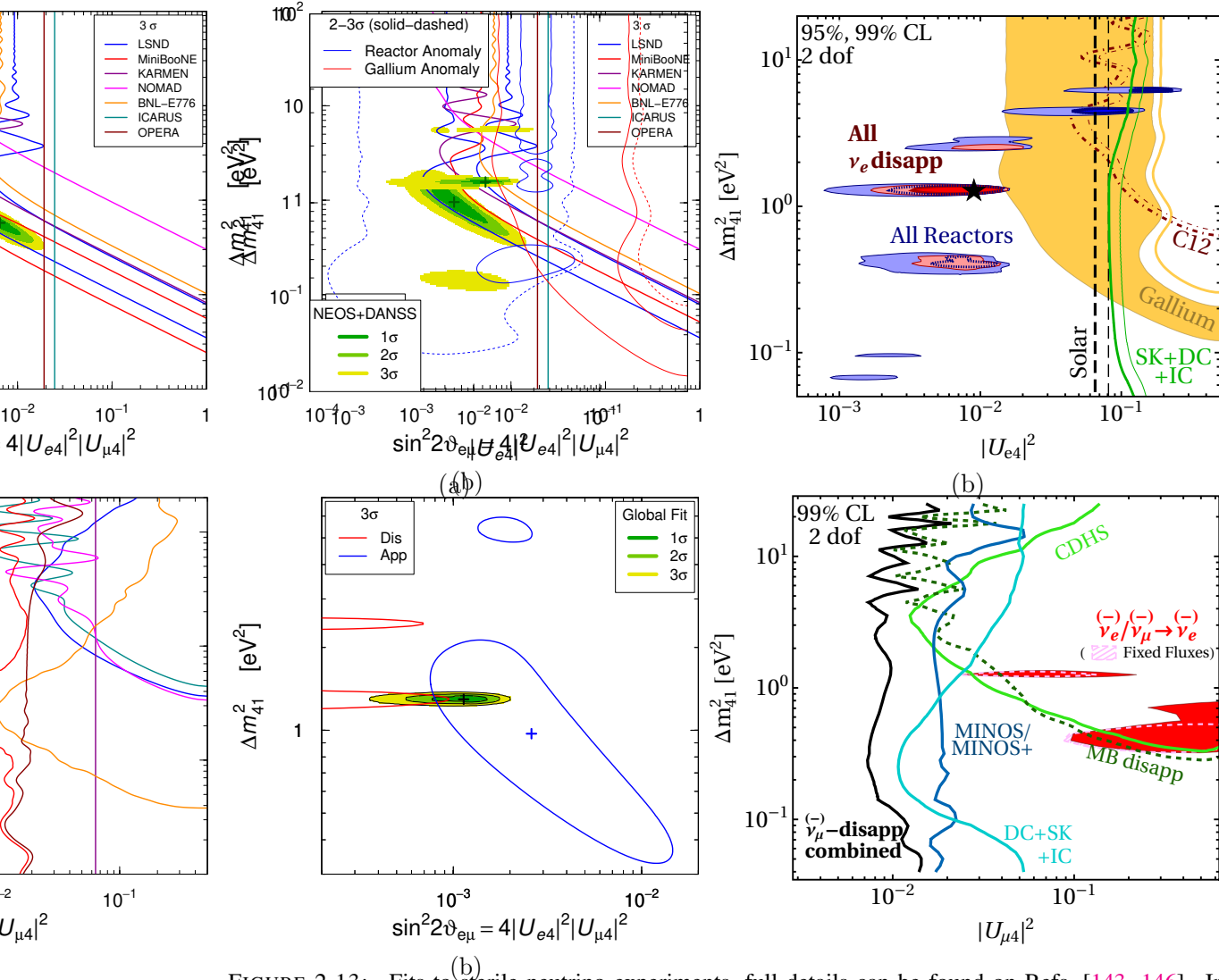


FIGURE 2.13: Fits to sterile neutrino experiments, full details can be found on Refs. [143, 146]. In all cases non-close lines exclude the region on their right. Top-left panel: Allowed regions and preferred phase-space according to ν_e and $\bar{\nu}_e$ appearance searches. Top-right panel: Allowed regions and preferred phase-space according to ν_e and $\bar{\nu}_e$ disappearance searches. The blue shaded regions include both flux normalization and spectral information from reactor experiments. The red shaded regions include additional constrains from Gallium, solar and atmospheric neutrino experiments. Bottom-left panel: Allowed regions and preferred phase-space according to ν_μ and $\bar{\nu}_\mu$ disappearance (Dis) and appearance (App) experiments. Bottom-right panel: Global fit to all data. The black exclusion line from ν_μ and $\bar{\nu}_\mu$ disappearance is in clear tension with the phase-space allowed by the remaining data, enclosed in the red-shaded regions.

2.4 Neutrino masses

In the SM, which only includes left-handed neutrinos, Dirac mass terms, i.e those in Eq. 2.13, can not be built. Explaining neutrino masses, known to exist due to the observation of neutrino oscillations, hence requires a SM extension. The simplest solution, known as neutrino minimal standard model (ν MSSM) [161], is to include right-handed neutrinos as new SM fermions. Since neutrinos can only interact weakly, and only left-handed chiral particles can sense the weak force, right-handed neutrinos would be G_{SM} singlets insensitive to all known forces but gravity. This solution is appealing in many senses. On one hand, a particle with this properties would constitute an excellent dark matter candidate. On the other hand, the SM would remain unchanged (from the symmetry group point of view) such that all the other predictions, so far correct, would not

be compromised. There is, however, an important setback. Neutrino masses are known to be much smaller than those of the next lightest SM particle, the electron, see Figure 2.14. Hence, explaining the low neutrino mass values is difficult under the assumption that all SM fermions get their mass values from the same underlying mechanism. The unique properties of neutrinos

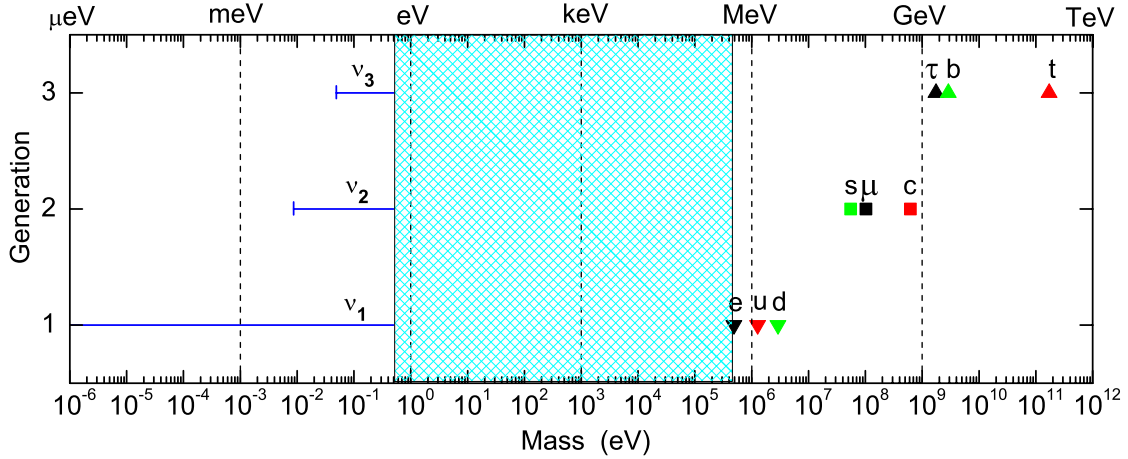


FIGURE 2.14: A schematic illustration of the fermion mass spectrum at the electroweak scale assuming NO. Figure from Ref. [162].

allow, however, for a different possibility not allowed to any other SM fermion. The trick consists in noting that charge conjugation reverses the field chirality as well as the field charges. Thus, one can use a charge conjugated left-handed field $\bar{\Psi}_L^c$ as a right-handed field in order to build a mass term. This was first noted by Ettore Majorana in 1937 [76], and is thus regarded as a Majorana mass term

$$L_{Majorana} = -m\bar{\Psi}_L^c\Psi_L + h.c. . \quad (2.72)$$

Remarkably, neutrinos are the only particles that might be Majorana fields. For all the other SM particles the Majorana condition $\bar{\Psi}_L^c = \Psi_L$ does not hold, given that, unlike neutrinos, they carry QCD and/or QED charges that get reversed by the charge conjugation operator. A crucial conceptual remark is to realize that Majorana particles are their own antiparticles.

Additionally, if right-handed neutrinos exist Majorana mass terms could also be built for them given that $\bar{\Psi}_R^c = \Psi_R$ is also possible. Although G_{SM} does not require it, lepton number conservation is an accidental symmetry of the SM and, accordingly, neutrinos do carry lepton charge. If neutrinos satisfy the Majorana condition, lepton-violating processes are expected, which constitute the major hope for their experimental search, as discussed later.

One of the most interesting things is that the Dirac mass term and the Majorana mass term are not mutually exclusive. In fact, one can describe neutrino masses with generality as a combination of both [163]. To do so, one can arrange N flavors of neutrinos as

$$n_L = \begin{bmatrix} \nu_L \\ (\nu_R)^c \end{bmatrix}, \quad (2.73)$$

where

$$\nu_L \equiv \begin{bmatrix} \nu_{eL} \\ \nu_{\mu L} \\ \nu_{\tau L} \\ \vdots \end{bmatrix} \quad \text{and} \quad (\nu_R)^c \equiv \begin{bmatrix} (\nu_{eR})^c \\ (\nu_{\mu R})^c \\ (\nu_{\tau R})^c \\ \vdots \end{bmatrix}. \quad (2.74)$$

The Lagrangian with both left- and right-handed neutrinos including Dirac and Majorana mass terms can be written as

$$\mathcal{L}_{M+D} = -\frac{1}{2}\overline{(n_L)^c}\mathcal{M}n_L + h.c. \quad \text{with} \quad \mathcal{M} = \begin{pmatrix} \mathcal{M}_L & \mathcal{M}_D^T \\ \mathcal{M}_D & \mathcal{M}_R \end{pmatrix}, \quad (2.75)$$

where \mathcal{M}_L and \mathcal{M}_R are $N \times N$ Majorana mass terms and \mathcal{M}_D is a $N \times N$ Dirac mass term. If non-degenerate, \mathcal{M} can be diagonalized by writing it as $\mathcal{M} = (U^\dagger)^T \hat{m} U^\dagger$ where \hat{m} is a diagonal matrix with $2N$ m_k diagonal values and U a unitary matrix. After diagonalization follows

$$\mathcal{L}_{M+D} = -\frac{1}{2} \sum_{k=1}^{2N} m_k \overline{(\tilde{n}_{kL})^c} \tilde{n}_{kL} + h.c. = -\frac{1}{2} \sum_{k=1}^{2N} m_k \bar{\phi}_k \phi_k, \quad (2.76)$$

with $n_k = U \tilde{n}_{kL}$ and $\phi_k = \tilde{n}_{kL} + \tilde{n}_{kL}^c = \phi_k^c$. Hence, in the general Dirac and Majorana scenario, the resulting physical states ϕ_k are clearly Majorana particles. The lepton-conserving Dirac description, where no Majorana terms are involved, is only recovered as a special case, corresponding to set all elements in the \mathcal{M}_L and \mathcal{M}_R matrices in Eq.2.75 to zero.

The see-saw mechanism

One of the most fundamental appeals of describing neutrinos as Majorana particles is provided by the so-called see-saw mechanism²⁴ [165]. Multiple hints point out that extended physics exist at a much higher, yet unexplored, energy scale. In that scenario, following the essence of the Higgs mechanism, one could have not one but multiple symmetry breaking scales each leading to particles with very different masses. In this way G_{SM} might be embedded in a larger GUT symmetry group, such as $SU(5)$, $SO(10)$ or $E(6)$. Currently many GUTs exist and for each of them a rich phenomenology can be derived, often involving very massive particles. If one considers Eq.2.75, it is easy to notice that diagonal and off-diagonal terms are of fundamentally different types. Whereas the Dirac masses m_D arise from the Higgs mechanism and hence are expected to be on the order of the mass of all other SM fermions, the Majorana masses m_L , m_R could lie in a different scale. If, as some GUT models predict, $m_L \ll m_D \ll m_R$, diagonalization of \mathcal{M}_L leads to two largely different neutrino masses, the currently observed ones $m_\nu \sim m_D/m_R$ and a much more massive undiscovered set with $m_N \sim m_R$.

2.4.1 Majorana signatures

Because of the importance of discovering Majorana neutrinos it is relevant to understand its phenomenological differences with Dirac neutrinos.

Oscillations of Majorana neutrinos

If neutrinos are Majorana particles, two extra physical phases (α_1, α_2) known as Majorana phases, need to be considered in Eq.2.28, such that the unitary transformation U becomes

$$U = U_{PMNS} \times \text{diag}(e^{i\alpha_1/2}, e^{i\alpha_2/2}, 1). \quad (2.77)$$

However, it is immediate to realize that Majorana phases cancel out in Eq.2.39 (due to $i \rightarrow -i$ for $U \rightarrow U^*$), and therefore neutrino oscillations are insensitive to the possible Majorana nature of the neutrinos.

²⁴Significant literature exists on this topic, for a review see Ref. [164].

Helicity flip

All SM fermions have a well defined chirality (left-handed or right-handed), a fundamental property related to how they transform under the Lorentz group. An intuitive way to understand chirality is by means of the helicity. The helicity is the projection of a particle's spin on its momentum. If the spin and the momentum are parallel (antiparallel) the particle has right (left) handed helicity. If the particle is massless then the momentum is invariant under Lorentz transformations and accordingly the helicity is fixed and equivalent to the chirality. However, if the particle is massive the helicity is no longer constant provided that it is always possible to find a reference frame where the momentum (and accordingly the helicity) is reversed. Therefore, in the massive case chiral states $\Psi_{L,R}$ can be written as combinations of helicity states $\chi(\pm)$ as

$$\Psi_{R,L}(x) = \frac{1}{\sqrt{2E}} \int \left[A(\pm)e^{-ikx} - B \dagger(\mp)e^{ikx} \right] \chi(\pm)\sqrt{E+k} \quad (2.78)$$

$$+ \frac{1}{\sqrt{2E}} \int \left[A(\mp)e^{-ikx} + B \dagger(\mp)e^{ikx} \right] \chi(\mp)\sqrt{E-k}, \quad (2.79)$$

where k is the momentum, A and B are respectively the particle and antiparticle creation operators, and \pm is positive (negative) for Ψ_R (Ψ_L) [166]. Notice that in the massless limit, this leads to

$$\Psi_{R,L}(x) = \frac{1}{\sqrt{2E}} \int \left[A(\pm)e^{-ikx} - B \dagger(\mp)e^{ikx} \right] \chi(\pm)\sqrt{2E}. \quad (2.80)$$

In Eq.2.80 four different combinations can be identified, $A(\pm)$ and $B(\pm)$, corresponding to the two possible helicity states both for particle and antiparticle states. This has well known effects. For instance, the charged pion decays $\pi^+ \rightarrow e^+ + \nu_e$, $\pi^- \rightarrow e^- + \bar{\nu}_e$ are disfavored when compared to their muon equivalents despite having (a priori) a larger available phase space. The underlying reason for this is that in two body decays each outgoing particle is forced to have parallel spin and momentum ($\chi(+)$), but only left-handed chiral fields weighted by $\sqrt{E-k}$ couple to the weak boson mediating the decay. Since the electron mass m_e is much smaller than the center of mass energy of the decay, $k \simeq E$ and therefore this weight is small. For the much more massive muons the wrong helicity state is far more likely, leading to a preference in the muonic channel for the π decay.

In the case of Majorana neutrinos particles are their own antiparticles, i.e. $A = B$ in the equations above. Hence a wrong helicity neutrino state is physically equivalent to an antineutrino. This leads a unique Majorana signature. In a CC interaction, a wrong helicity neutrino state produces an antilepton (instead of a lepton). The experimental observation of this phenomenon is, however, extremely unlikely [167]. Neutrino masses are known to be tiny (sub-eV in the most optimistic scenarios), thus, the wrong helicity amplitude can be approximated by $\sqrt{E-k}/\sqrt{2E} \approx m/4E$. Since this amplitude appears squared in all observables, Majorana signatures are proportional to $(m/E)^2$ whereas normal signatures are of order $1 - (m/E)^2$. To observe the antilepton the threshold energy for the reaction is $O(1 \text{ MeV})$, therefore, assuming (optimistically) that the lightest neutrino mass is $O(1 \text{ eV})$ the wrong helicity component is 10^{12} smaller than the standard one. Accordingly, this limitation is known as the practical Dirac-Majorana confusion theorem [168].

Neutrinoless double-beta decay

Due to their ambiguous particle-antiparticle nature, Majorana neutrinos allow lepton number violating processes. A particularly relevant one is that of the neutrinoless double-beta decay ($0\nu 2\beta$ decay), depicted in Figure 2.15. In a $0\nu 2\beta$ decay [170] the two final state antineutrinos from an ordinary $2\nu 2\beta$ decay [171, 172] get connected due to its Majorana nature such that the process becomes a two body decay. In this way, each of the two outgoing electrons gets exactly half of the

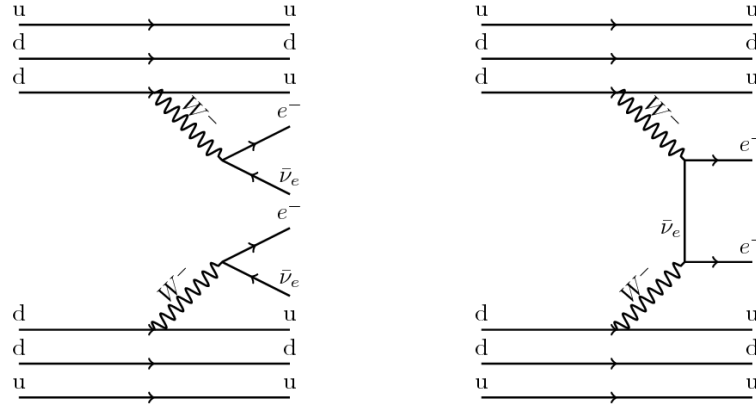


FIGURE 2.15: Feynman diagrams for the SM double-beta decay (left) and for the Majorana mediated neutrinoless double-beta decay (right). Figure from Ref. [169].

total available energy in the decay ($Q_{\beta\beta}$). This unique feature allows for searches with near to zero background, making $0\nu 2\beta$ decay to be widely regarded as the best candidate to experimentally test the hypothetical Majorana nature of neutrinos. The half-life for this process is [163]

$$\left[T_{1/2}^{0\nu}\right]^{-1} = G_{0\nu}(Q_{\beta\beta})|M_{0\nu}|^2\langle m_{\beta\beta}\rangle^2, \quad (2.81)$$

where $G_{0\nu}$ is a phase space factor, $M_{0\nu}$ is the nuclear matrix element and $\langle m_{\beta\beta}\rangle$ is the effective Majorana mass of the electron neutrino, given by

$$\langle m_{\beta\beta}\rangle = \left| \sum_k m_k U_{ek} \right| = \left| m_1 |U_{e1}|^2 + m_2 |U_{e2}|^2 e^{i(\alpha_1 - \alpha_2)} + m_3 |U_{e3}|^2 e^{i(-\alpha_1 - 2\delta_{CP})} \right|. \quad (2.82)$$

Notably, in addition to confirm neutrinos as Majorana particles measuring $T_{1/2}^{0\nu}$, would pin down the value of $\langle m_{\beta\beta}\rangle$ allowing to study the Majorana phases (α_1, α_2). However, one must notice that Eq. 2.82 has the freedom to be funneled to zero for a small parameter space of those phases. Thus, even if neutrinos are indeed Majorana particles solutions might exist that forbid or make exceedingly rare the neutrinoless double beta decay. It is interesting to note that if the Majorana phases are not fixed by a flavor symmetry and the lightest mass eigenvalue m_l is not driven to zero, the current data greatly disfavours this scenario [173], see Figure 2.16. Moreover, a significant fraction of the most relevant phase space will be probed by the next-generation of experiments [173, 174], such as LEGEND [175, 176], SuperNEMO [177, 178], CUPID [179, 180], CUORE [181], SNO+ [182, 183], KamLAND-Zen [184], nEXO [185], NEXT [186, 187] and PandaX-III [188], see Figure 2.17. Finally, if neutrino masses are proven to follow the IO the Majorana nature of neutrinos could be ruled out in the next decade.

2.4.2 Neutrino mass values

The weakly interacting nature of neutrinos paired to their extremely low mass values makes resolving their individual mass eigenstates highly challenging. As neutrino oscillation measurements inform about their relative mass differences, the experimental determination of a single mass eigenstate or of the sum of all neutrino masses would lead to the unambiguous determination, if the mass ordering is known, of all the neutrino mass values.

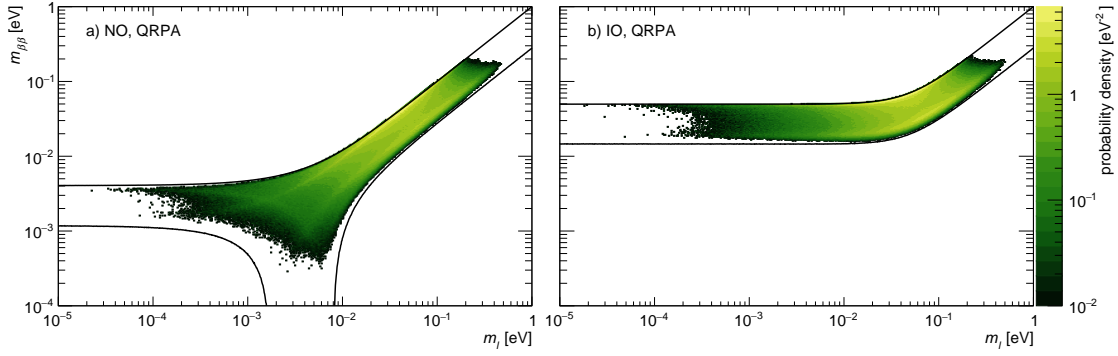


FIGURE 2.16: Marginalized posterior distributions for $m_{\beta\beta}$ and m_l for NO (a) and IO (b). The solid lines show the allowed parameter space assuming 3σ intervals of the neutrino oscillation observables from Ref. [131]. The plot is produced assuming the absence of mechanisms that drive m_l or $m_{\beta\beta}$ to zero. The probability density is normalized by the logarithm of m_l and of $m_{\beta\beta}$. Figure from Ref. [173].

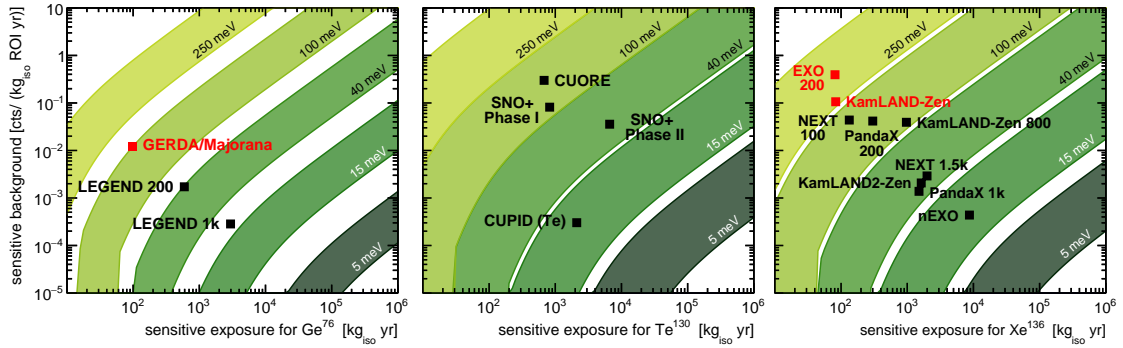


FIGURE 2.17: Discovery sensitivity for ^{76}Ge , ^{130}Te , and ^{136}Xe as a function of sensitive exposure and sensitive background. Contours in $m_{\beta\beta}$ are represented as bands spanning the range of considered nuclear matrix element values. The experimental sensitivities of future or running experiments are marked after 5 years of operation. Past or current experiments with published background level and energy resolution (red marks) are shown according to the average performance in their latest data taking phase. Figure from Ref. [173].

2.4.3 Direct mass searches

Direct mass searches are sensitive to the effective electron neutrino mass m_{β} , defined as

$$m_{\beta}^2 = \sqrt{\sum_i |U_{ei}|^2 m_i^2} = m_1 + |U_{e2}|^2 \Delta m_{21}^2 + |U_{e3}|^2 \Delta m_{31}^2. \quad (2.83)$$

Its value is explicitly dependent on the mass ordering since Δm_{31}^2 is positive (negative) for the NO (IO). As discussed in Ref. [189], since $|U_{e3}|$ and Δm_{21}^2 are known to be quite small the approximation $m_{\beta} \simeq m_1$ holds at the percent level or better down to 0.05 eV. In general, it is useful to introduce the quantity

$$m_{least} = m_1 \quad (NO), \quad m_{least} = m_3 \quad (IO). \quad (2.84)$$

which allows to define m_{β} as

$$\begin{aligned} m_{\beta}^2 &= m_{least}^2 + 7.74 \cdot 10^{-5} \text{ eV} \quad (NO) \\ &= m_{least}^2 + 2.47 \cdot 10^{-3} \text{ eV} \quad (IO). \end{aligned} \quad (2.85)$$

Notably, in the most challenging scenario (minimal $m_{least} = 0$) $m_\beta \approx 8$ meV ($m_\beta \approx 50$ meV) for NO (IO). The current best bound $m_\beta < 0.8$ eV has been recently settled by the KATRIN experiment [101, 190] which analyses the tritium β -decay's energy spectrum. The ultimate sensitivity of KATRIN is of $m_\beta < 0.2$ eV [189]. To probe even smaller masses novel experimental approaches are under study [191], with the potential to lower the m_β sensitivity to about 40 meV in the future [192]. Interestingly, the historical data on the improvement of the m_β bounds show a smooth logarithmic trend over the last 70 years [189]. According to this trend, roughly, the upper bound on m_β is decreased by half every 10 years.

2.4.4 Cosmological bounds

In cosmology, neutrinos are predicted to have played a significant role in the expansion history of the universe creating an imprint that can be measured by cosmological surveys. As neutrinos decoupled from matter about 1s after the Big Bang, a Cosmic Neutrino Background (C ν B) would have been created analogous to the Cosmic Microwave Background (CMB) created about 379.000 years later. Current measurements of the relic abundance of light elements [193], baryon acoustic oscillations [194, 195] and the CMB [196] support the existence of the C ν B. The analysis of this data can be used to bound the sum of all neutrino mass states $\sum \equiv \sum_i m_i$. Currently, $\sum < 0.111$ eV (95% CL) [197]. Since

$$\begin{aligned} \sum &= m_{least} + \sqrt{m_{least}^2 + \Delta m_{21}^2} + \sqrt{m_{least}^2 + \Delta m_{31}^2} \quad (\text{NH}) \\ &= m_{least} + \sqrt{m_{least}^2 - \Delta m_{32}^2} + \sqrt{m_{least}^2 - \Delta m_{31}^2} \quad (\text{IH}), \end{aligned} \quad (2.86)$$

this translates, mostly independently of the mass hierarchy, into a $m_{least} < 0.05$ eV. In the next years, the next generation of surveys will have sensitivity to $\sum > 2 \times 10^{-2}$ [198]. As this value is smaller than the value of \sum allowed for both mass orderings, cosmology is expected to provide a first determination of m_{least} . However, it has to be remarked that the cosmological determination of \sum might be affected by the existence of additional light particles, or non-standard neutrino interactions, and consequently this result will likely need to be understood more as a reference than as a definitive solution. Nonetheless, the cross-comparison of the independent direct mass search results and cosmological measurements is of great interest to validate our understanding of both theories.

Chapter 3

Neutrino interactions

“We are rather like children, who must take a watch to pieces to see how it works.”

– ERNEST RUTHERFORD

The fundamental behavior of the elementary particles, i.e. their interactions as asymptotic free states is, in general, very well understood. However, when particles form bound states, such as quarks in nucleons and nucleons in the atomic nucleus, the complexity of the system rapidly scales up. In accelerator based neutrino oscillation experiments, where neutrino energies are typically around 1 GeV, interactions are sensitive to a significant list of non-trivial nuclear effects. This Chapter reviews the state-of-the art knowledge on this topic, its relevance for neutrino oscillation experiments, the existing methods and modeling techniques to predict the expected neutrino interaction events rates and final state particle kinematics and provides a comprehensive list of the existing measurements.

3.1 Introduction

In the previous Chapter the oscillation probability $P_{\vec{\theta}}(\nu_\alpha \rightarrow \nu_\beta)(E)$, characterized by the PMNS parameters $\vec{\theta}$, has been presented from a theoretical standpoint. In order to determine $\vec{\theta}$ experimentally it is necessary to consider in addition how neutrinos interact in a detector.

3.1.1 Neutrino interactions and oscillations

For an initial set of neutrinos characterized by a flux $\Phi_{\vec{b}}(E)$, the expected number of selected neutrino interactions, N_{exp} , is affected by the oscillation probability as

$$\begin{aligned} N_{exp} &= \sum_i N_{exp}^i \\ &= P_{\vec{\theta}}(\nu_\alpha \rightarrow \nu_\beta)(E) n_{\vec{d}} \Phi_{\vec{b}}(E) \sum_i \sigma_{\vec{x}}^i(E) \epsilon_{\vec{d}}^i(E) S_{\vec{d}}^i(E, E^{reco}), \end{aligned} \quad (3.1)$$

where $\sigma_{\vec{x}}^i(E)$ is the exclusive scattering cross section for the i -th interaction channel selected with efficiency ϵ_i , n is the number of elementary targets and \vec{b} , \vec{x} and \vec{d} are the collection of nuisance parameters controlling respectively the functional form of the flux, cross section and detector models. In order to determine $\vec{\theta}$, the parameters on the former equation are adjusted¹ to maximize the similarity of N_{exp} to the observed number of selected interactions N_{obs} . Whereas the statistic

¹Additional comments on this topic are later presented in Sec. 8.1, in the context of the NC1 π^+ analysis.

error depends on the number of N_{obs} , the systematic errors depend on the knowledge of \vec{b} , \vec{x} and \vec{d} . Accordingly, to produce accurate measurements both a high number of observed events² and a precise knowledge of all model parameters is required.

3.1.2 Neutrino cross sections in the $E_\nu \approx 1$ GeV region

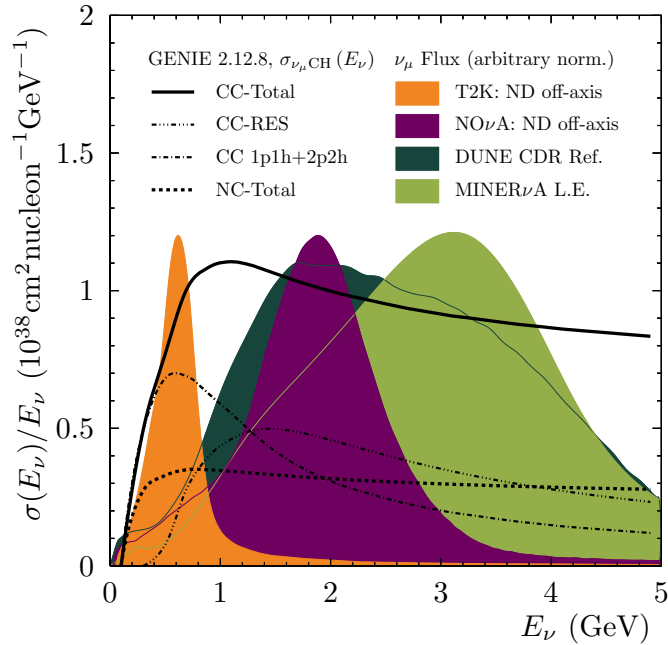


FIGURE 3.1: Neutrino fluxes, as a function of energy, of current and future accelerator-based neutrino experiments. Also overlaid are several cross sections divided by energy. Figure from Ref.[199].

Accelerator-based long-baseline neutrino oscillation experiments, which are the focus of this thesis, work with neutrino energies ranging from hundreds of MeV to few GeV, see Fig.3.1. At those energies, leptonic processes such as $\nu_\ell + e^-$ have cross sections that are much smaller ($\sigma \sim 10^{-43} \text{ cm}^{-2}$) than those of neutrino-nucleon interactions such as $\nu_\ell + p^+$ ($\sigma \sim 10^{-38} \text{ cm}^{-2}$). This introduces two complications. First, nucleons are bound-states of quarks such that neutrino-nucleon interactions are sensitive to QCD resonances. Second, modern neutrino detectors use heavy nuclei³ such that neutrino-nucleus interactions are affected by nuclear effects.

3.1.3 Experimental approach

The difficulty to model neutrino-nucleus interactions in the relevant energy region combined with the degeneracies⁴ arising in \vec{b} and \vec{x} make of the flux and cross section model parameters dominant sources of systematic error in current accelerator-based neutrino oscillation experiments. To address this, in the case of \vec{b} complementary experiments can be run to constrain the flux model uncertainties. For instance, if neutrinos are produced in pion decays $\pi^- \rightarrow \mu^- + \bar{\nu}_\mu$, a subset of \vec{b} can be constrained by studying the flux of μ^- . In the case of neutrino cross sections, there are in general two ways to constrain \vec{x} . On one hand it is possible to study scattering data that does not involve neutrinos, which are difficult to measure, and draw theoretical connections to constrain

²Unless otherwise noted, an *event* refers to a single neutrino interaction recorded in the detector.

³In this context anything with more than one proton.

⁴For instance, an increased number of events can be in general explained by a higher flux or by a higher cross section.

\vec{x} . On the other hand, some parameters in \vec{x} can only be constrained by studying neutrino interactions such as those related to the axial part of the interaction.

Since a significant number of the constrains are only valid under very specific circumstances (e.g. a given energy range and nuclear target) large portions of the model parameter space relevant to the experiments is often unconstrained a priori. Due to this, a common strategy in accelerator-based neutrino oscillation experiments is to use two neutrino detectors:

- A **near detector** is built close to the production point where the oscillation probability is negligible, such that Eq. 3.1 is independent of θ . In this way, the measurements on the observed event rates can be used to constrain the nuisance parameters \vec{b} and \vec{x} .
- A **far detector** is built far away from the production point where the oscillation probability is noticeable, such that N_{obs} can be used to determine $\vec{\theta}$.

Notably, selection criteria can be established to try to break degeneracies among \vec{x} and \vec{b} or to increase the sensitivity to a given subset of parameters. This feature is explicit in Eq. 3.1. For an idealized selection criteria satisfying $\epsilon_i = \delta_{ij}$ all the selected events are expected to belong to the i -th interaction mode. Since the flux and cross section parameters play different roles in each interaction type, studying individual channels improves the constraints on \vec{x} and \vec{b} .

3.2 Neutrino-nucleon scattering

Neutrino-nucleon scattering is characterized by the following interactions:

$$\text{CC: } \nu_{\ell}^{(-)} + N \rightarrow \bar{\ell}^{(-)} + X \quad \text{and} \quad \text{NC: } \nu_{\ell}^{(-)} + N \rightarrow \nu_{\ell}^{(-)} + X.$$

Where $N = n, p$ and X corresponds to the collection of hadronic particles produced in the interaction. The associated differential cross sections is

$$\frac{d^2\sigma}{dE_l d(\cos\theta_{\nu l})} = \frac{1}{32\pi^2 m_N} \frac{|\vec{p}_l|}{E_l} |\mathcal{M}|^2 \prod_X \frac{d^3\vec{p}_l}{(2\pi)^3 2E_X} (2\pi)^4 \delta^{(4)}(p_X - p_{\nu} - p_l - p_N). \quad (3.2)$$

where $l = \{\nu_{\ell}, \bar{\ell}\}$ is the neutral or charged final state lepton and p_l , E_l and $\theta_{\nu l}$ are the momentum, energy and angle of the final state lepton. The same is true for antineutrinos under the replacements $\nu \rightarrow \bar{\nu}$ and $l \rightarrow \bar{l}$. The Dirac δ ensures 4-momentum conservation and \mathcal{M} is the amplitude matrix which for neutrino-nucleon scattering takes the general form

$$\mathcal{M}_{\text{CC,NC}} = \frac{G_F}{\sqrt{2}} \epsilon_{NC,CC}^{\mu} \langle X | j_{\mu}^{\text{CC,NC}} | N \rangle, \quad (3.3)$$

where

$$\epsilon_{CC}^{\mu} = \bar{u}_{\ell}(\gamma_{\mu} - \gamma^5)u_{\nu}, \quad \epsilon_{NC}^{\mu} = \frac{1}{2}\bar{u}_{\nu}(\gamma_{\mu} - \gamma^5)u_{\nu} \quad (3.4)$$

and $\langle X | j_{\text{CC,NC}}^{\mu} | N \rangle$ characterizes the transition amplitude for the hadronic system, mediated by the weak charged or neutral hadronic current j^{μ} . In practice, the computation of \mathcal{M} depends strongly on the content of X , which in turn is influenced by the 4-momentum transfer q from the leptonic to the hadronic system. Under the definition $q^2 = (p_{\nu} - p_{\ell})^2 \equiv -Q^2$, one can identify three regions. For $Q^2 \ll m_N^2$ the cross section is dominated by quasielastic interactions, for intermediate energies $Q^2 \sim m_N^2$ the interactions are dominated by resonances and finally for $Q^2 \gg m_N^2$ the dominant process is deep inelastic scattering. These three regions can be seen in Fig.3.1, corresponding roughly to neutrino energies of $E_{\nu} \lesssim 1$ GeV, $1 \lesssim E_{\nu} \lesssim 3$ and $E_{\nu} \gtrsim 3$. Notice that, as these regions are highly overlapped, all of the former processes play

a significant role in the whole energy range studied in accelerator-based long-baseline neutrino oscillation experiments. Additionally, the relations

$$\sigma_{\nu q}^{\text{CC,NC}} \propto E_\nu \quad \text{and} \quad \sigma_{\nu q}^{\text{CC}} \approx 3\sigma_{\nu q}^{\text{NC}} \quad (3.5)$$

are good approximations above 1 GeV as it is explicit in Fig.3.1.

3.2.1 Quasielastic neutrino scattering

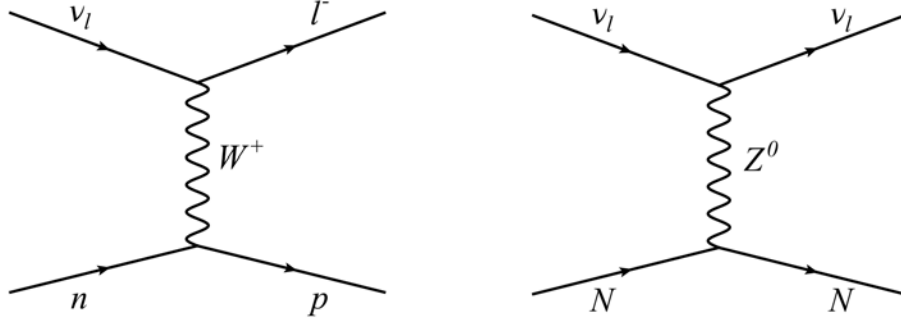


FIGURE 3.2: Feynman diagrams for CCQE (left) and NCE (right) neutrino interactions.

When in a neutrino-nucleon interaction the set of outgoing hadrons, X , can be identified with a single nucleon, see Figure 3.2, we have

$$\text{CCQE: } \nu_\ell^{(-)} + n(p) \rightarrow \ell^{(-)} + p(n) \quad \text{and} \quad \text{NCE: } \nu_\ell^{(-)} + N \rightarrow \nu_\ell^{(-)} + N.$$

For CC the nucleon changes to a different isospin state ($p \leftrightarrow n$). Given the mass difference between both nucleons, small compared to the energies we are considering, i.e. $O(1)$ GeV, the kinetic energy is almost unchanged by the interaction so the process is quasielastic (CCQE). For NC the same nucleon is found both in the initial and the final state, such that the process is elastic (NCE). For these processes the cross section is given by the Llewellyn-Smith model [200]

$$\frac{d\sigma_{\text{CC}}^{\nu p, \bar{\nu} n}}{dQ^2} = \frac{G_F^2 M_N |V_{ud}|^2}{8\pi E_\nu^2} \left[A(Q^2) \pm \frac{(s-u)}{M_N^2} B(Q^2) + \frac{(s-u)^2}{M_N^4} C(Q^2) \right], \quad (3.6)$$

with the Mandelstam variables

$$\begin{aligned} s &= (p_\nu + p_N)^2 & \xrightarrow{\text{lab frame}} & s = m_N^2 + 2m_N E_\nu \\ t &= (p_\nu - p_\ell)^2 \equiv -Q^2 & & t = m_\ell^2 - 2E_\nu(E_\ell - p_\ell \cos \theta) \\ u &= (p_\ell - p_N)^2 & & u = m_N^2 - 2m_N E_\nu + 2E_\nu(E_\ell - p_\ell \cos \theta). \end{aligned}$$

Here $s - u = 4m_N E_\nu - Q^2 - m_\ell^2$ and

$$\begin{aligned} A(Q^2) &= \frac{m_\ell^2 + Q^2}{m_N^2} \left[(1 + \eta) F_A^2 - (1 - \eta) (F_V^1)^2 + \eta(1 - \eta) (F_A^2)^2 + 4\eta F_V^1 F_V^2 \right. \\ &\quad \left. - \frac{m_\ell^2}{4m_N^2} ((F_V^1 + F_V^2)^2 + (F_A + 2F_P)^2 - 4(\eta + 1) F_P^2) \right], \end{aligned} \quad (3.7)$$

$$B(Q^2) = \frac{Q^2}{M_N^2} F_A (F_1 + F_2), \quad (3.8)$$

$$C(Q^2) = \frac{1}{4} (F_A^2 + F_1^2 + \eta F_2^2). \quad (3.9)$$

The definition $\eta \equiv Q^2/4m_N^2$ has been used, $F_V^{1,2}$ is the vector form factors and F_P and F_A are respectively the pseudoscalar and axial form factors. In general, a form factor is used to parametrize the unknown charge distribution of the object being scattered, such as [114]

$$\frac{d\sigma}{d\Omega} = \left(\frac{d\sigma}{d\Omega} \right)_{\text{point like}} |F(Q)|^2. \quad (3.10)$$

For nucleons the charge distribution is often assumed to be exponential ($\rho(r) = \rho_0 e^{-M_\lambda r}$) and, consequently, they are commonly described by dipole form factors $|F(Q)| = F(0)(1 + \frac{Q^2}{M_\lambda^2})^{-2}$ with parameters $F(0)$ and M_λ determined from fits to data.

The vector form factors $F_V^{1,2}$ are related to the electromagnetic form factors F_i^N [113] via

$$F_i(Q^2) = F_i^p(Q^2) - F_i^n(Q^2) \quad (i = 1, 2), \quad (3.11)$$

also known as the *Dirac* (F_1^N) and *Pauli* (F_2^N) form factors [201] which are connected to the so-called Sachs electric (G_E^N) and magnetic (G_M^N) form factors [202] through the conserved vector current (CVC) hypothesis [203, 47] by

$$G_E^N = F_1^N(Q^2) - \frac{Q^2}{4m_N^2} F_2^N(Q^2) \quad \text{and} \quad G_M^N = F_1^N(Q^2) + F_2^N(Q^2). \quad (3.12)$$

The Sachs form factors satisfy

$$G_E^p = G_D(Q^2), \quad G_E^n(Q^2) = 0. \quad (3.13)$$

$$G_M^p = \frac{\mu_p}{\mu_N} G_D(Q^2), \quad G_M^n(Q^2) = \frac{\mu_n}{\mu_N} G_D(Q^2). \quad (3.14)$$

The nuclear magneton is given by $\mu_N \equiv e\hbar/2m_p$ and μ_p, μ_n are respectively the proton and neutron magnetic moments. Also $G_D(Q^2) = (1 + Q^2/M_V^2)^{-2}$ and $M_V \simeq 0.84$ is the *vector mass* which is known from polarized electron-nucleon scattering [204].

The pseudoscalar form factor, F_P , is related to the axial form factor, F_A , through the partial conservation of the axial current (PCAC) [205, 206], by means of

$$F_P(Q^2) = \frac{2m_N^2}{Q^2 + m_\pi^2} F_A(Q^2), \quad \text{where} \quad F_A(Q^2) = \frac{F_A(0)}{(1 + \frac{Q^2}{m_N^2})^2}. \quad (3.15)$$

The value of $g_A \equiv F_A(0)$ is determined measuring the asymmetry of β -decays [207] and M_A , known as the *axial mass*, is the only free parameter in the Lewellyn-Smith model for CC interactions that needs to be determined via neutrino-nucleon scattering [208, 209]. Interestingly, as the second term in Eq. 3.7 is proportional to m_ℓ^2/m_N^2 it can be generally neglected for electrons, but not for muons. Accordingly the determination of the pseudoscalar form factor is important as it can introduce non-trivial differences between the cross sections for ν_e and ν_μ .

For NC, Eq. 3.6 holds under the following replacements: First, in NC there is no quark transition such that $|V_{ud}| \rightarrow 1$. Second, the final state lepton is now a neutrino and therefore $m_\ell = 0$, making the cross section for all neutrino flavors identical. Finally, the charged current form factors have to be replaced by the neutral current form ($F \rightarrow \tilde{F}$), defined by

$$\tilde{F}_i = \pm(F_i^p - F_i^n) - 2 \sin \theta_W F_i^N - F_i^{sN} \quad (i = 1, 2; N = p, n; \overset{(-)}{\nu} = \pm), \quad (3.16)$$

$$\tilde{F}_j = \pm \frac{1}{2} F_j - \frac{1}{2} F_j^{sN} \quad (j = A, P; N = p, n; \overset{(-)}{\nu} = \pm). \quad (3.17)$$

The new contributions $F_{1,2}^{sN}$, F_P^{sN} and F_A^{sN} are known respectively as the electromagnetic, the

pseudoscalar and the axial strange form factors for their association to the strange quark [210] and are estimated using lattice QCD in combination with neutrino scattering data [211, 212, 213].

3.2.2 Meson production in neutrino scattering

For increasing neutrino energies the momentum transfer to the hadronic system is large enough to produce additional mesons. This can happen through two different mechanisms. On one hand the production can be resonant, namely through the decay of a nucleon excited by a neutrino scattering

$$\nu + N \rightarrow N^* + l, \quad N^* \rightarrow m + N'. \quad (3.18)$$

Here m denotes a meson, typically a pion π and $l = \{\nu, \ell\}$. The lifetime of the resonant state is negligible (e.g $\sim 10^{-24}$ s for Δ^+) and in practice it is not observed. On the other hand the production can be non-resonant, if there is no intermediate state and the hadron is directly produced in the interaction.

To describe this complex phenomenon different models have appeared over the years each including further refinements. The first of them, presented in 1971, was the Feynman-Kislinger-Ravndal (FKR) model [214]. It was followed in 1981 by the seminal Rein-Seghal model [215, 216] which has been the standard reference for many years. In 2004, it was extended by the Kuzmin-Lyubushkin-Naumov (KLN) model [217] to account for massive leptons, mainly relevant for events involving ν_τ . Further improvements were achieved by using alternative vector and axial form factors [218, 219, 220] that accounted for pion-pole contributions to the hadronic axial current to better model the main resonance ($\Delta(1232)$), leading in 2007 to the KLN-Berger-Seghal (KLN-BS) model [221]. Also in 2007 a new approach to compute non-resonant contributions was presented, the Hernandez-Nieves-Valverde (HNV) model [222, 223]. In 2018, the Monireh Kabirnezhad (MK) model [224, 225] presented a full kinematic description of the Rein-Seghal model including the non-resonant diagrams of the HNV model and the modified form-factors of the KLN-BS model.

To compute the meson resonant production cross section, it is necessary to evaluate the matrix element

$$\epsilon_{NC,CC}^\mu \langle X | j_\mu^{\text{CC,NC}} | N \rangle = \underbrace{\langle X, \lambda_X | R, \lambda_R \rangle}_{\text{decay amplitude}} \underbrace{\langle R, \lambda_R | e^\mu j_\mu | N, \lambda_i \rangle}_{\text{production amplitude}}, \quad (3.19)$$

where λ refers to the helicity of the state. This requires the computation of the production amplitude for all the resonances, 17 in the MK model, by writing the matrix elements in terms of helicity-dependent vector and axial form factors. In total, there are $2 \times 2 \times 4 = 16$ vector (and 16 axial) form factors, accounting for the two possible initial and two possible final helicities and the 4 possible gauge boson polarizations. The decay amplitudes are functions of the isospin coefficients characterized by the Clebsch-Gordan rules, the branching ratios and the Breit-Wigner factor [226] accounting for the amplitude of each resonance. For neutrino energies below 1 GeV the only meson production channel that has a significant cross section is the single pion production. In this channel an additional dipolar axial form factor, C_A^5 , is needed to model the $\Delta(1232)$ resonance. This axial form factor depends on two parameters, $C_A^5(0)$ and M_A^{RES} , analogous to $F_A(0)$ and M_A , which are determined by analyzing pion production data in neutrino scattering [205]. The non-resonant terms are coherently included in the cross section [216] by evaluating the amplitude of the Feynman diagrams containing the relevant final state configurations, see Figure 3.3. Overall, the complete set of possible single pion production channels is:

• CC

$$\begin{aligned} \nu_\mu + p &\rightarrow \mu p \pi^+, \\ \nu_\mu + n &\rightarrow \mu p \pi^0, \\ \nu_\mu + n &\rightarrow \mu n \pi^+, \end{aligned}$$

$$\begin{aligned} \bar{\nu}_\mu + n &\rightarrow \mu^+ n \pi^-, \\ \bar{\nu}_\mu + p &\rightarrow \mu^+ n \pi^0, \\ \bar{\nu}_\mu + p &\rightarrow \mu^+ p \pi^-, \end{aligned}$$

• NC

$$\begin{aligned} \nu + p &\rightarrow \nu p \pi^0, \\ \nu + p &\rightarrow \nu n \pi^+, \\ \nu + n &\rightarrow \nu n \pi^0, \\ \nu + n &\rightarrow \nu p \pi^-, \end{aligned}$$

$$\begin{aligned} \bar{\nu} + p &\rightarrow \bar{\nu} p \pi^0, \\ \bar{\nu} + p &\rightarrow \bar{\nu} n \pi^+, \\ \bar{\nu} + n &\rightarrow \bar{\nu} n \pi^0, \\ \bar{\nu} + n &\rightarrow \bar{\nu} p \pi^-. \end{aligned}$$

An example of resonant diagram and all non-resonant diagrams relevant for single pion production are illustrated in Figure 3.3.

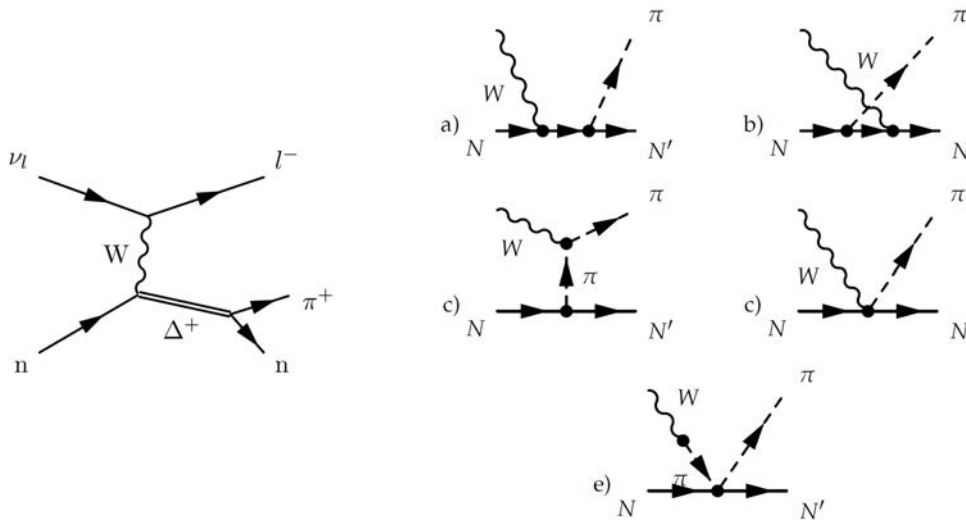


FIGURE 3.3: Left: The Δ^+ resonant diagram contributing to the CC single π^+ production. Right: Non-resonant pion production diagrams: (a) nucleon pole, (b) crossed nucleon pole, (c) pion-in-flight, (d) contact term, and (e) pion pole. Notice that $W = \{W^\pm, Z\}$ and $\pi = \{\pi^\pm, \pi^0\}$. Figure from Ref. [224].

3.2.3 Deep inelastic neutrino scattering

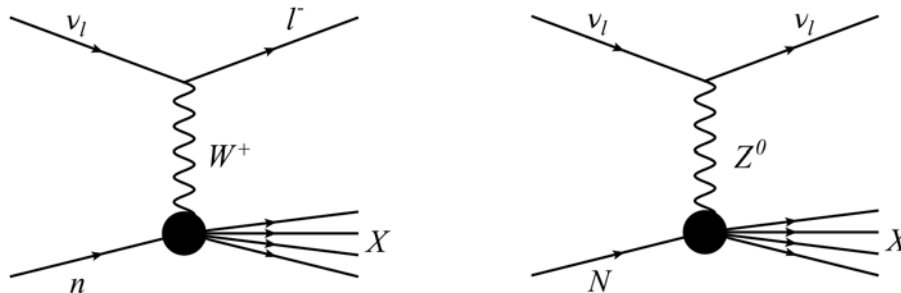


FIGURE 3.4: Conceptual Feynman diagrams for CC-DIS (left) and NC-DIS (right) neutrino interactions.

As presented in Figure 3.4, in deep inelastic neutrino scattering (DIS) the energy transfer from the lepton to the nucleus is large enough to produce multiple final state hadrons and mesons, namely

$$\text{CC-DIS: } \nu_{\ell}^{(-)} + N \rightarrow \ell^{(-)} + \sum_{i=0}^{N>1} X_i. \quad \text{NC-DIS: } \nu_{\ell}^{(-)} + N \rightarrow \nu_{\ell}^{(-)} + \sum_{i=0}^{N>1} X_i.$$

To study DIS interactions, it is customary to introduce the invariants

$$x \equiv \frac{Q^2}{2p_N \cdot q} \quad \text{and} \quad y \equiv \frac{p_N \cdot q}{p_N \cdot p_{\nu}}, \quad \text{related by} \quad xy = \frac{Q^2}{s - m_N^2}.$$

Commonly y is named as the inelasticity parameter whereas x is the Bjorken scaling variable. Then, the CC-DIS cross section is given by

$$\frac{d^2 \sigma_{\text{CC-DIS}}^{(-)}}{dx dy} = \sigma_{CC}^0 \left[xy^2 F_1^{W^{\pm}N} + (1-y) F_2^{W^{\pm}N} \pm \left(1 - \frac{x}{2}\right) F_3^{W^{\pm}N} \right], \quad (3.20)$$

where

$$\sigma_{CC}^0 = \frac{G_F^2}{2\pi} s \left(1 + \frac{Q^2}{m_W^2}\right)^{-2}. \quad (3.21)$$

The structure functions $F_i^{W^{\pm}N}$, defined as

$$F_i^{W^{\pm}N}(x) = \xi_i \sum_q f_q^N(x) + \bar{\xi}_i \sum_{\bar{q}} f_{\bar{q}}^N(x), \quad (3.22)$$

parametrize the interaction of the W^{\pm} bosons with the quark sub-structure in the nucleons. Here $q = \{d, s\}$ ($q = \{u, c\}$) and $\bar{q} = \{\bar{u}, \bar{c}\}$ ($\bar{q} = \{\bar{d}, \bar{s}\}$) for W^+ (W^-) and

$$\xi_1 = \bar{\xi}_1 = 1, \quad \xi_2 = \bar{\xi}_2 = 2x, \quad \xi_3 = -\bar{\xi}_3 = 2. \quad (3.23)$$

The probability density functions $f_q^N(x)$ are the so-called parton distribution functions (PDFs) [227] which quantify the probability of finding q with momentum $p = xp_N$.

Given the highly hierarchical structure of CKM elements, considering only the transitions among quarks of the same generation is a reasonable approximation. Under this simplified picture, Eq.3.20 becomes

$$\frac{d^2 \sigma_{\text{CC-DIS}}^{(-)N}}{dx dy} = 2x \sigma_{CC}^0 \left[\sum_{a=q(\bar{q})} f_a^N(x) + (1-y^2) \sum_{b=\bar{q}(q)} f_b^N(x) \right]. \quad (3.24)$$

This equation reveals the most important properties of the neutrino-nucleon DIS cross section: it scales linearly with the neutrino energy, explicit in σ_{CC}^0 , and for a given neutrino energy it scales linearly with x , a feature known as Bjorken scaling [61]. Since the second term has an additional factor $(1-y^2)$ the cross section is different for neutrinos than for antineutrinos. Upon integration, one gets $\sigma_{\nu}(E) \approx 2\sigma_{\bar{\nu}}(E)$ [228].

For NC-DIS, the cross section can be calculated following an analogous line of thought. Here, Eq.3.20 becomes

$$\frac{d^2 \sigma_{\text{NC-DIS}}^{(-)}}{dx dy} = \sigma_{NC}^0 \left[xy^2 F_1^{ZN} + (1-y) F_2^{ZN} \pm \left(1 - \frac{x}{2}\right) F_3^{ZN} \right], \quad (3.25)$$

where, as expected

$$\sigma_{NC}^0 = \frac{G_F^2}{2\pi} s \left(1 + \frac{Q^2}{m_Z^2} \right)^{-2}. \quad (3.26)$$

The form factors now get modified to account for the different interaction of the Z boson with the quarks. The allowed transitions are

$$WZq \rightarrow q \qquad WZ\bar{q} \rightarrow \bar{q}.$$

From the former expressions it is possible to derive the Paschos-Wolfenstein relation [229]

$$\frac{\sigma_{NC}^\nu - \sigma_{NC}^{\bar{\nu}}}{\sigma_{CC}^\nu - \sigma_{CC}^{\bar{\nu}}} = \frac{1}{2}(1 - \sin^2 \theta_W), \quad (3.27)$$

which provides either a way to measure θ_W or, if θ_W is fixed from some other measurement, a relation to constrain neutrino cross sections.

3.3 Neutrino-nucleus scattering

To model the fact that neutrinos interact with nucleons bound to an atomic nucleus, a series of additional effects are introduced sequentially, as presented in Figure 3.5. In the first place the neutrino interaction is assumed to happen with a free-nucleon at rest, as earlier described in Sec. 3.2. In a second step, the initial momentum of the nucleon is accounted for under the impulse approximation [230] which considers the nucleon momentum distribution to be unaffected by correlations with neighboring nucleons. Thirdly, nucleon correlations are introduced by ad hoc models. Lastly, additional effects are introduced to model final state interactions (FSI) affecting the particles escaping the dense nuclear medium.

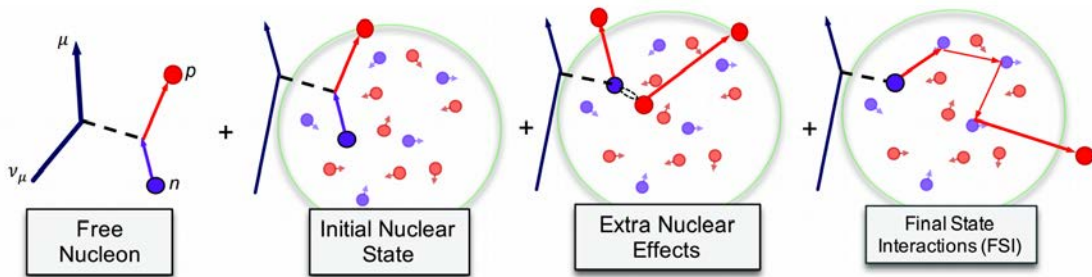


FIGURE 3.5: Modeling steps to compute realistic cross sections for neutrino-nucleus scattering. Figure from Ref. [231].

3.3.1 Initial nuclear state

The momentum distribution of the target nucleon can be modeled in different ways with different degrees of sophistication. In all cases the impulse approximation is used. The description of the initial nuclear state focuses on the characterization of the initial state kinematics for the target nucleon and in the inclusion of a binding energy E_B . The free parameters in these models are determined by fitting electron-nucleon scattering data [232, 233, 234]. A comparative view of the initial nuclear state models described below is presented in Fig.3.6.

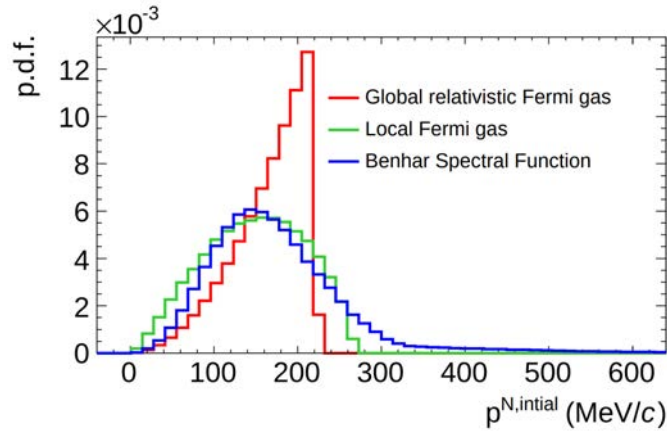


FIGURE 3.6: Initial nucleon momentum distribution on carbon for three different models. Figure from Ref. [235].

Relativistic Fermi Gas (RFG)

The simplest approach to describe the initial nucleon momentum is the global Relativistic Fermi Gas model (RFG) [236]. On it, nucleons are described as non-interacting fermions in a potential well. Due to Pauli's exclusion principle fermions can not be in the same quantum state, so that in order to fill the well nucleons need to be arranged in higher energy states each consisting of two antiparallel isospin states. The distribution is characterized by the Fermi momentum p_F which corresponds to the momentum of the nucleon in the highest energy level of the potential well. Because of this the RFG momentum distribution has a characteristic hard-cut at p_F , as it can be seen in Figure 3.6. For $^{12}_6\text{C}$, $p_F = 221$ MeV/c. This value is significantly different for lighter and heavier elements, for instance, for ^6_3Li and $^{208}_{82}\text{Pb}$ it is 169 MeV/c and 265 MeV/c respectively [233]. This model includes a constant binding energy E_B common to all nucleons, given by

$$E_B = [Z \cdot M_p + (A - Z) \cdot M_n - M_A] \cdot c^2, \quad (3.28)$$

where Z and A are the atomic and mass numbers respectively. This leads to a typical binding energy of 7-9 MeV [233].

Local relativistic Fermi Gas (LFG)

The RFG model assumes the nuclear medium to be uniformly dense which is an oversimplification. A better alternative is to consider the effect created by the local density of nuclear matter $\rho(r)$ on the potential well and modify the nucleon momentum distribution accordingly. This description is known as the Local relativistic Fermi Gas model (LFG) [237]. Under this model, the RFG distribution is modified to include a nuclear density dependence $p_F \propto \rho(r)^{1/3}$, smoothing the momentum distribution as presented in Figure 3.6. The binding energy is the same as in the RFG model.

Spectral Function (SF) models

It is well known that the LFG description is inaccurate as it does not consider strongly interacting nucleon pairs which influence significantly the initial state of the nucleon in about 10-20% of scatterings, according to electron scattering data [238]. To overcome this, the so-called Spectral Function models (SF) include a more elaborate description of the momentum and the binding energy by splitting the nucleon momentum distribution in two terms. On one hand, a mean field term describes single nucleons within the nucleus in a shell-like structure and, on the other hand,

a term considering short-range correlations accounts for nucleons in quasi-deuteron states [239]. This description has two consequences. First, the additional nucleon-nucleon interactions spread the momentum distribution to values significantly above p_F producing the characteristic high momentum tail in Figure 3.6. Second, the removal energy is no longer constant but can be tuned to resemble the spectroscopic structure observed in electron scattering data [240]. Although several SF models exist [241], few of them are implemented in neutrino interaction Monte Carlo models, making their comparison to data difficult. One of the most widely available models is the Benhar SF [239], others like the Effective Spectral function [242, 243] are implemented in NEUT. The relativistic shell model [244] and the relativistic Green's function approach [245] are implemented in GiBUU. Remarkably, even if SF models do not change significantly the integrated cross section, they do significantly change the shape of the cross section in some kinematic variables [246].

3.3.2 Additional nuclear effects

The existence of short-range correlations, discussed in the previous section, not only modifies significantly the distribution of the initial nucleon momentum but also allows to scatter out not one, but two or more tightly bound nucleons. This effect was known to be important in electron-nucleon scattering, especially in the transition gap between the quasi-elastic and resonant regions [238], but it was neglected for years in neutrino experiments as most detectors were insensitive to its effects. It was not until MiniBooNE measured a value of $M_A = 1.35 \pm 0.17$ [247], significantly higher than the world average of $M_A = 1.026 \pm 0.021$ [248] obtained with light nuclear targets, that 2-body currents in neutrino-nucleus scattering were seriously considered, see Fig.3.7. Currently, the most extended approaches to describe multi-nucleon knockouts are the Martini [249] and the Nieves [223] models, both using the LFG to describe the initial nuclear state. In this models the weak boson propagator gets self-energy corrections to account for multi-nucleon processes. The idea is that tree-level contributions, corresponding to CCQE, are mediated by the interaction with a single particle (nucleon) which after getting scattered creates a single hole in the nucleus (1p1h). In higher levels, the weak current gets contributions from interactions with 2 particles leaving two holes (2p2h), and so on. Recently, it has been estimated that 2p2h (3p3h) interactions contribute to about 20% (4%) of the total CCQE processes [250]. In addition, to correctly model the scattering with heavy targets long-range correlations with several nucleons also need to be considered. This is done by including random phase approximations (RPA) [249, 223] which introduce Q^2 dependent modifications of the electroweak coupling. This has a screening effect at low Q^2 and an enhancement at intermediate Q^2 , while it converges to the impulse approximation for large Q^2 .

3.3.3 Final State Interactions (FSI)

The outgoing particles produced in the processes reviewed in the former sections are created in a dense nuclear medium. Consequently, they might re-interact before leaving the nucleus, undergoing Final State Interactions (FSI), see Figure 3.8. Through FSI particles can significantly change their kinematics, e.g. change their momentum, be deflected, be absorbed by the nuclear medium or, in the case of hadrons, change its charge sign. These effects are important as they mix the output from different exclusive cross section channels. For instance, a true $\nu_n + n \rightarrow \mu^- + p + \pi^+$ interaction where the outgoing pion is absorbed due to FSI leads to a final state particle content indistinguishable from that produced in a true CCQE interaction. Thus, FSI constitute an important complication in the experimental study of neutrino interactions. It is worth noting that FSI are particularly relevant to study channels with subdominant cross sections, as their final state particle content can be outnumbered by interactions of other dominant channels undergoing FSI.

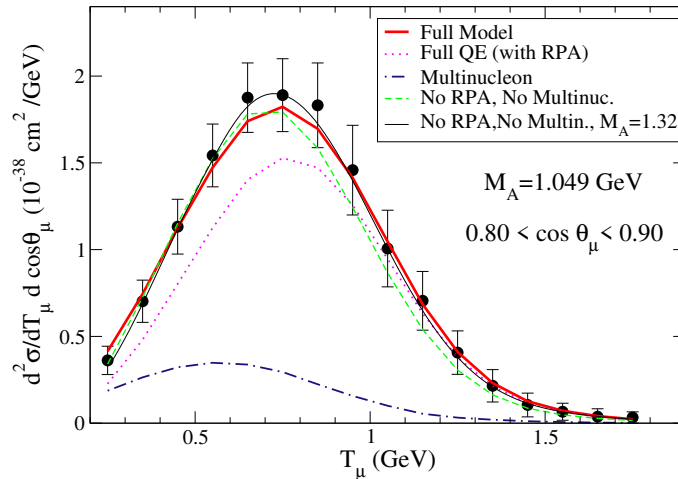


FIGURE 3.7: ν - ^{12}C double differential cross section averaged over the MiniBooNE flux as a function of the muon kinetic energy T_μ . The thick solid line stands for the full model Nieves model (LFG+RPA+2p2h). The dashed, dotted and dash-dotted lines show partial results for only LFG, LFG+RPA and only 2p2h, respectively. All these curves are obtained with $M_A = 1.049$ GeV (compatible with light-target data) while the thin solid line is calculated with the LFG and $M_A = 1.32$ GeV. Figure from Ref. [251].

3.3.4 Detector limitations

In addition to FSI, detector limitations also need to be considered when studying exclusive neutrino cross sections. For instance, most detectors are largely or completely insensitive to neutral particles in the final state, some others are insensitive to the charge sign and all of them have a minimum tracking threshold, which can change dramatically depending on the detector technology. Accordingly, among many other cases, for some detectors 1p1h and 2p2h are indistinguishable and some other experiments can not differentiate ν_ℓ from $\bar{\nu}_\ell$.

3.3.5 Interaction topologies

Since there is no way to prevent FSI in neutrino-nucleus scattering nor to overcome the final state degeneracies introduced by the limitations in the detector, in the recent years experiments have started to re-think how to study neutrino-nucleus interactions. Not so long ago it used to be the case that the experiments presented their predictions for theoretically well-defined processes, such as CCQE. However, the results reported by modern experiments, working with relatively heavy nuclei, often disagreed with those from bubble chamber experiments, working with deuterium, due to the significantly different role of nuclear effects [253]. This presented an important challenge as depending on the model assumptions the predictions in Eq. 3.1 changed noticeably, introducing large systematic uncertainties in the cross section and in the oscillation measurements. The reason for this was two-fold. On one hand, cross sections were unfolded [254] as a function of the neutrino energy. However, neutrino energy reconstruction depends intimately on the interaction mode as specified by the model under consideration. In the second hand, using different models lead to significant variations in the determination of \vec{x} and \vec{b} . In 2016, a seminal paper from the T2K collaboration [255] proposed a new approach to tackle this problem. Instead of working with interaction channels, experiments could use interaction topologies, more robust to model effects. An interaction topology is defined solely by the observable final state particles. For instance, all events created by a charged current interactions without detectable positive charged pions in the final state can be regarded as belonging to the CC0 π^+ topology. In this way both 1p1h and 2p2h interactions get enclosed into the same category making the measurements more independent to the multinucleon description of different models. Moreover, experiments

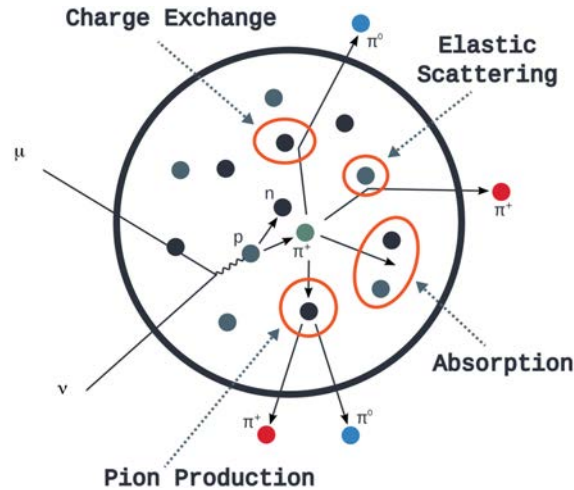


FIGURE 3.8: Sketch of FSI possible processes after a neutrino interaction: Elastic scattering modifies the kinematics of a pion; Charge exchange modifies the charge sign of a pion; A pion is absorbed by the nucleus; A pion re-interaction produces an additional pion. Extracted from Ref. [252].

could tune their own topology definitions to be more robust to their detector limitations. For example, detectors insensitive to final state neutrons can study interaction topologies which include any number of neutrons in the final state. Additionally, omitting the use of the neutrino energy when possible was proposed, using instead direct detector observables such as the angle θ_ℓ and the momentum p_ℓ of the outgoing charged lepton. For the near detector constrain, where knowing the neutrino energy is not directly needed, the event rate prediction can be directly written as a function of the detector observables, much better known, increasing the sensitivity to the cross section and flux nuisance parameters. Moreover, reporting measurements as functions of direct kinematic variables allows to compare data and models on the same footing, opposed to unfolded cross section measurements, providing valuable insights to further develop the theory behind neutrino-nucleus interaction models.

3.3.6 State-of-the-art challenges

The state-of-the-art knowledge on neutrino-nucleus interactions and the most urgent challenges in this field of research are thoroughly presented in a series of recent papers [252, 256, 257] by the Neutrino Scattering Theory-Experiment Collaboration (NuSTEC). The most important points are:

- There is great necessity on expanding our knowledge on the theoretical side. This includes: The creation of unified models that do not rely on breaking the nuclear description in a chain of steps; The development of fully differential cross section approaches even for multi-track topologies; It is necessary to find further refined constructions to model nucleon-nucleon correlations, to extend the reach of current ab initio computations and to improve lattice-QCD calculations on the nucleon form factors.
- For the sake of ensuring the success of future neutrino oscillation experiments complementary data sources are required, including: The development of new high-statistics hydrogen or deuterium scattering experiments to pin down the neutrino-nucleon model parameters; To increase neutrino and antineutrino Argon scattering data to better model interactions for DUNE and to study and support the option to build narrow energy muon-based neutrino beams, such as muon storage rings and intense electron neutrino beams.

- Bridges among theory and experiments need to be built and extended to ensure a more efficient and stronger collaboration. This includes: Defining a standardized format for neutrino event generators; To embed all existing neutrino models in neutrino event generators such that can be cross-validated with data and to work in global fits to all existing data to highlight tensions.
- Finally, it is desirable to increase in the future the current neutrino-nucleus scattering data in the widest possible range of energies, nuclear species and interaction types, and to measure their scattering distributions as a function of as diverse and complementary kinematic variables as possible, including their correlations.

3.4 Neutrino event generators

In order to model neutrino interactions and to compute event rate predictions, experiments use neutrino event generators. Event generators consist of an ensemble of neutrino interaction cross section models, such as those earlier reviewed in this Chapter, which, for a specific choice of model parameters, determines the probability density functions characterizing the rate of each neutrino interaction process and the kinematic distributions of its final state particles. Using Monte Carlo (MC) methods, event generators sample from this distributions in order to produce synthetic datasets. To work, neutrino event generators require to specify the flux shape, integral and flavor content as well as the detector geometry. With the former information, events are generated by means of the following steps:

1. Sample the target nuclei, its position in the detector and the neutrino energy and flavor according to the detector geometry, the neutrino flux and the inclusive cross sections.
2. Sample the exclusive interaction process considering the chosen target nuclei, neutrino energy and flavor.
3. Sample the initial four-momentum of the target nucleon according to the nuclear model describing the chosen target nuclei.
4. Sample the initial four-momentum for all the final state particles according to the exclusive cross section model given the former choices.
5. Simulate the trajectory of each final state particle in their path across the nuclear medium in a series of steps. At each step, the probability and effect of undergoing final state interactions is sampled according to the FSI model. If an interaction occurs, the state of the particle is changed. In the process particles can be created and destroyed. The process ends when all particles have escaped the nucleus.

The most common event generators used by neutrino oscillation experiments are GENIE [258], NEUT [259], GiBUU [260] and NuWro [261]. Due to their different formats, dedicated software like Nuisance [262] can be used to compare their outputs. Due to their easier integration to the experimental necessities T2K and NO ν A use NEUT and GENIE to perform their measurements on the oscillation parameters. A comparison, adapted from Ref. [263], of the models used by two generators, NEUT (version 5.4.0) and GENIE (version 2.8.0), used later in this thesis is provided below.

- **Nuclear Model:** NEUT uses the Benhar SF [239]. GENIE uses the Bodek-Ritchie implementation [264] of the RFG.
- **Quasi-Elastic Scattering:** Both generators use an implementation of the Llewellyn-Smith model [236] and the same parametrization for the vector form factors, called

BBBA05 [265]. However, they use a different value for the axial mass. NEUT (GENIE) uses $M_A = 1.21 \text{ GeV}/c^2$ ($M_A = 0.99 \text{ GeV}/c^2$).

- **2p2h:** NEUT uses the Nieves model [223], while GENIE does not include multinucleon knock-out⁵.
- **Meson Production:** NEUT uses the KLN-BS model [221] with a cut-off value for the invariant mass resonance of $W < 2.0 \text{ GeV}$. The axial resonant form factor uses $M_A^{RES} = 0.95 \text{ GeV}/c^2$ and $C_A^5(0) = 1.01$ [219]. The normalization of the non-resonant background is set to 1.30. GENIE uses the Rein-Seghal model [215] with a cut-off value for the invariant mass resonance of $W < 1.7 \text{ GeV}$, with $M_A^{RES} = 1.12 \text{ GeV}$ [267]. The Δ width is modified for in-medium effects and it is assumed that inside the nucleus 20% of Δ decays are pion-less.
- **Coherent Scattering:** Both generators use the Rein-Seghal model [215].
- **Deep Inelastic Scattering:** Both generators use the GRV98 PDF parametrization [268].
- **Hadronization:** For non-resonant hadron production in the low invariant mass region NEUT uses the Koba-Nielsen-Olesen (KNO) scaling [269] and GENIE uses the Andreopoulos-Gallagher-Kehayias-Yang (AGKY) model [270]. For high invariant masses both generators use the PYTHIA-JETSET model [271].
- **FSI:** Both generators include FSI using intranuclear cascade models. Whereas NEUT uses a custom model, GENIE uses the INTRANUKE package [272, 273].

3.5 Neutrino scattering data

Neutrino scattering data can be split as coming from early neutrino experiments or from modern neutrino experiments as the experimental approach and the detector technology has changed significantly from ones to the others.

3.5.1 Early experiments

In the decades of the 1970s and 1980s, several experiments were build with the goal to validate the, back to then recent, SM predictions about neutrino interactions. A summary of the existing results is presented in Table 3.1. Among them, ANL, BNL and BEBC worked with deuterium, such that their measurements still provide some of our best knowledge on neutrino interactions unaffected by nuclear effects. An excellent review on this data can be found on Ref.[303]. Summary plots are presented in Figure 3.9.

3.5.2 Modern experiments

In the early 2000s, after the discovery of neutrino oscillations, there was a new wave of neutrino scattering experiments, summarized in Table 3.2, which still last today. This was so because of two reasons. In the first place measuring neutrino oscillations requires to build detectors and a neutrino beam, such that indirectly, all the necessary elements required to study neutrino scattering are provided. In the second place, as earlier discussed in this chapter, improving our understanding on neutrino scattering is crucial to measure accurately neutrino oscillations and, consequently, large efforts have been devoted to analyze thoroughly the data produced by those experiments. Contrary to the early experiments, which typically consisted in in bubble chambers, modern experiments use and have used quite diverse technologies to study neutrino scattering:

⁵Multinucleon know-out has been included in GENIE-v3 [266].

Experiment	CCQE Measurements	π Production	Target(s)
Aachen	ν_μ [274]	NC [275]	Al
ANL	ν_μ [276, 277, 278]	CC [279, 280, 281, 282], NC [283, 284]	D ₂
BEBC	ν_μ [285]	CC [286, 285], NC [286, 285]	D ₂
BNL	ν_μ [287, 288], $\bar{\nu}_\mu$ [289]	CC [290], NC [291]	D ₂
FNAL	ν_μ [292]	CC [293], NC [294]	D ₂
GGM	ν_μ [295, 296], $\bar{\nu}_\mu$ [297]	NC [298, 299]	C ₃ H ₈ CF ₃ Br
SKAT	ν_μ [300], $\bar{\nu}_\mu$ [300]	CC [301]	CF ₃ Br
Serpukov	ν_μ [302], $\bar{\nu}_\mu$ [302]	-	Al

TABLE 3.1: Summary of cross section measurements made by early neutrino experiments broken down by neutrino target, experiment, and interaction type. The studies on CCQE measurements are separated in neutrino and antineutrino. The studies on π production do not differentiate between π^\pm and π^0 , are split in CC and NC, and include both ν_μ and $\bar{\nu}_\mu$ measurements.

Experiment	Beam	$\langle E_\nu \rangle, \langle E_{\bar{\nu}} \rangle$ GeV	Neutrino Target(s)	Run Period
ArgoNeuT	$\nu, \bar{\nu}$	4.3, 3.6	Ar	2009 – 2010
K2K	ν	1.3	CH, H ₂ O	2003 – 2004
MicroBooNE	ν	0.8	Ar	2015 –
MINER ν A	$\nu, \bar{\nu}$	3.5 (LE), 5.5 (ME)	He, C, CH, H ₂ O, Fe, Pb,	2009 – 2019
MiniBooNE	$\nu, \bar{\nu}$	0.8, 0.7	CH ₂	2002 – 2019
MINOS	$\nu, \bar{\nu}$	3.5, 6, 1	Fe	2004 – 2016
NOMAD	$\nu, \bar{\nu}$	23.4, 19.7	Fe	1995 – 1996
NO ν A	$\nu, \bar{\nu}$	2.0, 2.0	CH ₂	2010 –
SciBooNE	$\nu, \bar{\nu}$	0.8, 0.7	CH	2007 – 2008
T2K	$\nu, \bar{\nu}$	0.6, 0.6	CH, H ₂ O, Fe	2010 –

TABLE 3.2: Summary of the main modern neutrino scattering detectors. Adapted from Ref. [304].

from liquid argon TPCs, to liquid and plastic scintillators and water Cherenkov detectors. This of course, has pros and cons. On one hand modern experiments can accumulate several orders of magnitude more data due to their much more massive detectors. High statistics allows to isolate many event topologies and to study the event rate dependence to many variables. On the other hand, using C, O or Ar, needed to build such massive detectors, introduces significant nuclear effects. In order to understand them many cross section measurements have been made in recent years. The inclusive cross section measurements are summarized in Table 3.3. Studies on mesonless neutrino scattering are summarized in Table 3.4. Finally, studies on pion production induced by neutrino scatterings are presented in Table 3.5. Several remarks can be drawn in light of the existing measurements:

- So far, the two modern experiments leading the measurement of neutrino interactions cross sections have been MINER ν A and T2K. MINER ν A was a dedicated neutrino scattering experiment exploring the few GeVs region which finished its operation in 2019 and had the ability to change its target material to study scatterings against different nuclei. T2K, which continues operational, has centered its measurements in energies ranging from hundreds of MeV to slightly above 1 GeV, using different detector technologies: Super-Kamiokande, INGRID and ND280. Among them, ND280 is the most specialized detector for this task and accordingly is the detector that has produced most of the results. This trend is expected to continue in the next years by means of T2K's beam upgrade [305] and the upgrade of ND280 [3], later described in this thesis.
- Although electron neutrino cross sections are crucial to study electron neutrino appearance, and therefore to measure δ_{CP} , almost all current cross section knowledge is based on muon neutrino and antineutrino scattering. This stems from the fact that producing intense electron neutrino beams is technically difficult. Currently, the only modern experiments that have measured ν_e cross sections are T2K and MicroBooNE, and so far, only inclusive measurements are available. In the future, the upgraded ND280 detector and additional detectors in T2K's neutrino beamline such as the WAGASCI [306], NINJA [307] and possibly IWCD [308]), as well as Liquid Argon based detectors, such as MicroBooNE [309] and DUNE [110], are expected to mitigate this limitation.
- Despite NO ν A being today, with T2K, the most important accelerator neutrino oscillations experiment, NO ν A measurements on neutrino scattering are scarce, due to the fact that NO ν A does not have a magnet and its detectors are made up of coarse plastic scintillator bars that offer poor tracking and PID capabilities. This scenario contrasts with ND280, explained in Chapter 5, as it has excellent tracking and PID capabilities designed to study neutrino interactions.
- of studies have been published reporting pion production measurements in modern neutrino experiments, non of them have measured charged pion production in neutrino neutral current interactions. This gap in the literature is expected to be filled in the near future by the studies later presented in Chapters 6, 7 and 8.

Experiment	Measurement	Target(s)
ArgoNeuT	ν_μ [310, 311], $\bar{\nu}_\mu$ [311]	Ar
MicroBooNE	ν_μ [312, 313], $\nu_e, \bar{\nu}_e$ [314]	Ar
MINER ν A	ν_μ [315, 316, 317, 318], $\bar{\nu}_\mu$ [318], $\nu_\mu/\bar{\nu}_\mu$ [319]	CH, Fe, Pb
MINOS	ν_μ [320], $\bar{\nu}_\mu$ [320]	Fe
NOMAD	ν_μ [321]	C
SciBooNE	ν_μ [322]	CH
T2K	ν_μ [323, 324, 325, 326, 327], ν_e [328, 329, 330] $\bar{\nu}_e$ [330], $\nu_\mu/\bar{\nu}_\mu$ [331]	CH, H ₂ O, Fe

TABLE 3.3: Summary of inclusive cross section measurements by modern neutrino experiments. Adapted from Ref. [304].

Experiment	Measurement	Target(s)
ArgoNeuT	2p [332]	Ar
K2K	M_A [333]	H ₂ O
MicroBooNE	$\frac{d\sigma}{dQ^2}$, $\frac{d\sigma}{dp_{\mu,p}}$, $\frac{d\sigma}{d\cos\theta_{\mu,p}}$ [334]	Ar
MINER ν A	$\frac{d\sigma}{dQ^2}$ [335, 336, 337], 1p [338], ν_e [339] $\frac{d^2\sigma}{dp_T d\parallel}$ [340, 341], $\frac{d\sigma}{dp_n} \frac{d\sigma}{d\delta_{\alpha T}}$ [342], $\frac{d^2\sigma}{dE_{avail} dq_3}$ [343]	CH, Fe, Pb
MiniBooNE	$\frac{d^2\sigma}{dT_\mu d\theta_\mu}$ [344, 345], M_A [346], NC [347, 348]	CH ₂
MINOS	M_A [349]	Fe
NOMAD	$M_A, \sigma(E_\nu)$ [350]	C
Super-K	NC [351]	H ₂ O
T2K	$\frac{d^2\sigma}{dT_\mu d\theta_\mu}$ [255, 352, 353, 354, 355], $\sigma(E_\nu)$ [356], M_A [357] NC [358, 359], $\frac{d\sigma}{d\delta_{pT}} \frac{d\sigma}{d\delta_{\alpha T}}$ [360]	CH, H ₂ O

TABLE 3.4: Summary of quasielastic cross section measurements by modern neutrino experiments. Adapted from Ref. [304].

Experiment	π^\pm Measurement	π^0 Measurement	Target(s)
ArgoNeuT	CC [361]	NC [362]	Ar
K2K	CC [363, 364]	CC [365], NC [366]	H ₂ O
MicroBooNE	-	CC [367]	Ar
MINER ν A	CC [368, 369, 370, 371, 372]	CC [369, 373, 374], NC [375]	CH
MiniBooNE	CC [376, 377]	CC [378], NC [379, 380]	CH ₂
MINOS	-	NC [381]	Fe
NOMAD	-	NC [382]	C
NO ν A	-	NC [383]	C
SciBooNE	CC [384]	NC [385, 386]	CH
T2K	CC [387, 388, 389], NC [CJV]	NC [390]	CH ₂ , H ₂ O

TABLE 3.5: Summary of neutrino induced pion production cross section measurements by modern neutrino experiments. The tag [CJV] highlights the space meant to be filled by the study later presented in this thesis. Table adapted from Ref. [304].

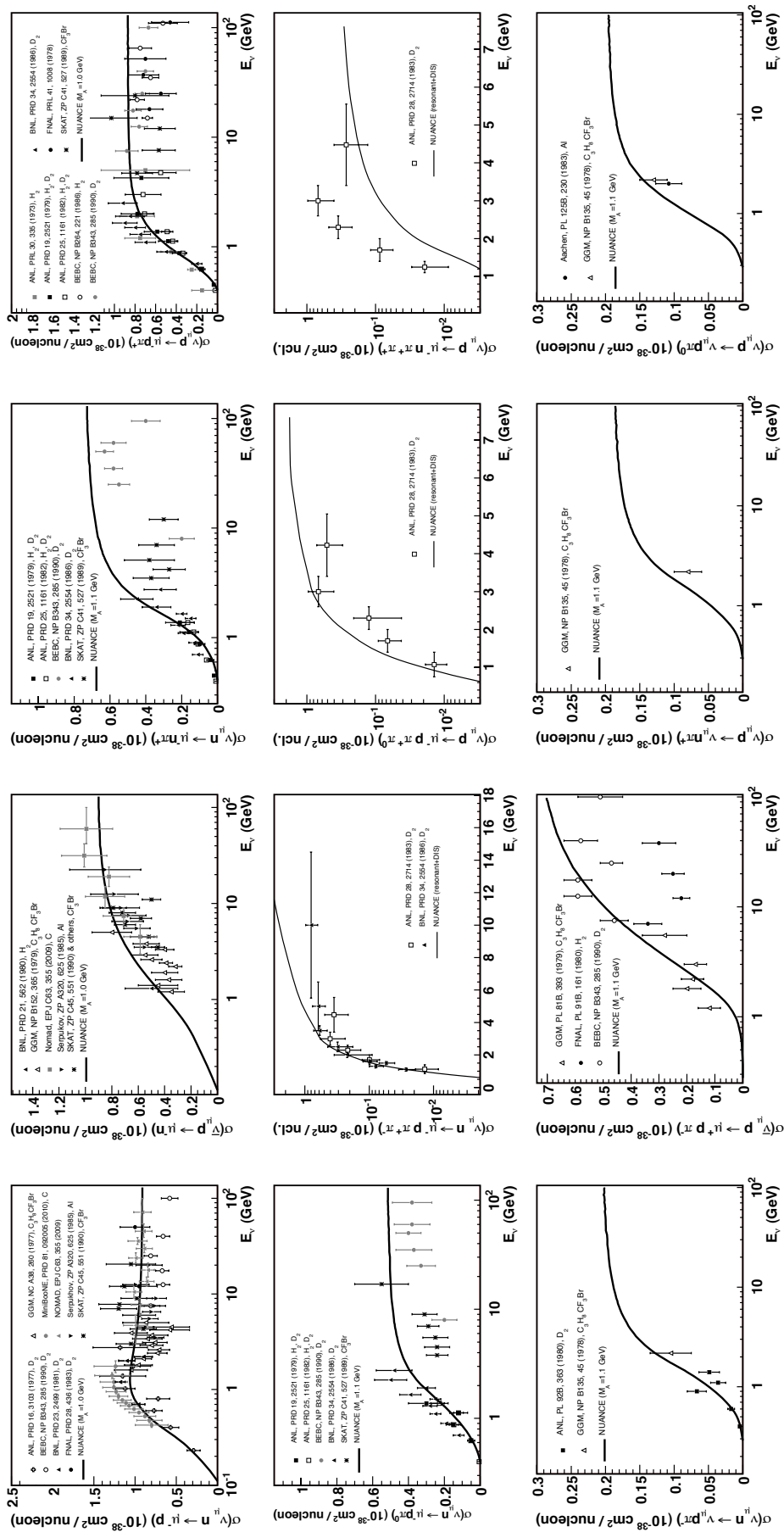


FIGURE 3: Summary plots presenting available cross section data from experiments operated in the 1970s and 1980s, sensitive in general to small nuclear effects. The solid line shows the prediction using the model from Ref.[391]. Figures from [303].

Chapter 4

Fundamentals of neutrino instrumentation

“I suppose I’m worried that someday there will be some exciting experiments to do, and there won’t be anyone around who knows what experiments are.”

– SHELDON LEE GLASHOW

To experimentally study neutrino physics it is necessary to build up particle detectors sensitive to the imprints of neutrino interactions. This Chapter reviews the most essential concepts regarding the interaction of particles with matter and describes the working principles of time-projections-chambers, scintillating materials and photomultipliers. Extensive and excellent literature exists dedicated to this topic. For an extended discussion on the subject the reader might find useful Refs. [392, 393, 394, 395, 396, 397, 398].

4.1 Relevant interaction processes

Due to their unusually low interaction cross sections neutrinos hardly ever interact with matter. In consequence, neutrinos generally propagate through matter without leaving any detectable trace. However, in the rare occasions when a neutrino interaction happens final state particles are produced which interact with the surrounding media frequently enough to create a pattern of signatures which can be measured and used to reconstruct information about the properties of the interacting neutrino. Hence, in order to understand what physical signatures a neutrino detector looks for and what detrimental effects might interfere with them it is necessary to understand the dominant processes affecting the typical particles produced in neutrino interactions. As reviewed in the former Chapter, for experiments working with $E \approx 1$ GeV, the final state particles typically consist of charged leptons, nucleons and light mesons. In regard of their interaction processes neutral and charged particles are nothing alike.

4.1.1 Charged particles

The most important processes affecting charged particles passing through a block of matter are inelastic collisions with the electrons and elastic scatterings with nuclei. Additionally, in some circumstances Cherenkov radiation and Bremsstrahlung are also important.

Inelastic collisions

A charged particle traveling through a block of material undergoes inelastic collisions with its electrons and, in doing so, transfers to them a part of its energy. As a result, the atomic electrons get excited or ionized. In some cases the energy transferred to the electron is large enough to produce significant secondary ionization. These high energy recoil electrons are commonly named δ -rays or δ -electrons. The inelastic collisions are statistical in nature with its associated energy loss well described by a Landau distribution. Since the number of interactions per macroscopic length is usually large the average energy loss per unit length is often a meaningful metric. This quantity is the so-called stopping power, or dE/dx , and it is characterized by the Bethe-Bloch formula. Such a formula, however, is different for light charged particles such as electrons and positrons, and heavy charged particles such as muons, pions, protons or alpha particles.

For heavy particles, the Bethe-Bloch formula, characterizing the dE/dx is:

$$-\frac{dE}{dx} = 2\pi N_a r_e^2 m_e c^2 \rho \frac{Z z^2}{A \beta^2} \left(\ln \frac{2m_e \gamma^2 v^2 W_{\max}}{I^2} - 2\beta^2 - \delta(\beta\gamma) \right) \left[\frac{\text{MeV cm}^2}{\text{g}} \right], \quad (4.1)$$

with

r_e : classical electron radius ,	ρ : density of absorbing material ,
m_e : electron mass ,	z : charge of incident particle in unit of e ,
N_a : Avogadro's number ,	β : v/c of the incident particle ,
I : mean excitation potential ,	γ : $1/\sqrt{1-\beta^2}$,
m_e : absorbing material atomic number ,	δ : density correction ,
N_a : absorbing material atomic weight ,	W_{\max} : max energy transfer per collision .

The density correction δ accounts for the fact that the incident particle electric field polarizes the material along its path, producing a shielding effect that reduces the energy loss for increasing energies. This effect gets enhanced for denser materials and because of that it is called *density* effect. Tables with values for δ for different materials can be found in Ref. [399]. For an incident particle of mass M , W_{\max} is given by

$$W_{\max} = \frac{2m_e c^2 \eta^2}{1 + 2s\sqrt{1 + \eta^2 + s^2}}, \quad (4.2)$$

where $s = m_e/M$ and $\eta \equiv \beta\gamma$. The mean excitation potential I is well approximated using the semi-empirical formulas

$$\frac{I}{Z} = 12 + \frac{7}{Z} \text{ [eV]} \quad \text{for } Z < 13, \quad \text{and} \quad \frac{I}{Z} = 9.76 + 58.8Z^{-1.19} \text{ [eV]} \quad \text{for } Z \leq 13. \quad (4.3)$$

The typical behavior of Eq. 4.1 is presented in Figure 4.1. For non-relativistic energies the dE/dx is dominated by terms $1/\beta^2$ and it decreases until about $\beta \simeq 0.96$ where a minimum is reached. Particles at this point are often referred to as *minimum ionizing particles* or MIPs. As the minimum depends on the mass of the particle it is worth to bear in mind that muons and pions (protons) are MIPs when they have momenta of about 0.3 GeV (2 GeV). Interestingly, the MIP point is quite universal across materials.

In the case of light particles, i.e. electrons and positrons, the incident particle no longer remains undeflected due to its low mass. Moreover, in the case of electrons the collisions are between identical particles so that the calculation must consider their indistinguishability. This leads to the

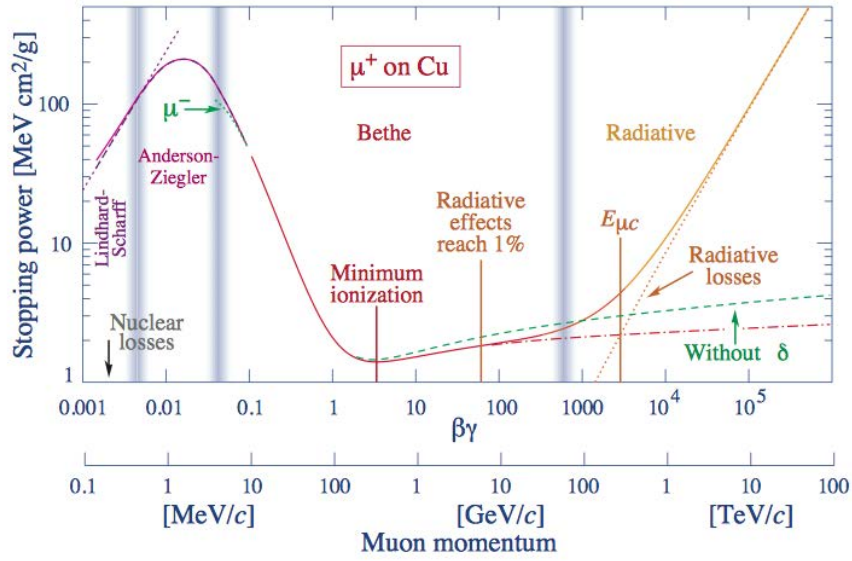


FIGURE 4.1: Stopping power for positively charged muons in copper as a function of $\beta\gamma$. Figure from Ref. [400].

following modified Bethe-Bloch formula

$$-\frac{dE}{dx} = 2\pi N_a r_e^2 m_e c^2 \rho \frac{Z}{A} \frac{1}{\beta^2} \left(\ln \frac{\tau^2(\tau+2)}{2(I/m_e c^2)^2} + F(\tau) - \delta(\beta\gamma) \right) \left[\frac{\text{MeV cm}^2}{\text{g}} \right], \quad (4.4)$$

where τ is the kinetic energy of the particle in units of $m_e c^2$ and

$$F(\tau) = 1 - \beta^2 + \frac{t^2/8 - (2r+1) \ln 2}{(\tau+1)^2} \quad \text{for } e^-,$$

$$F(\tau) = 2 \ln 2 - \frac{\beta^2}{12} \left(23 + \frac{14}{\tau+2} + \frac{10}{(\tau+2)^2} + \frac{4}{(\tau+2)^3} \right) \quad \text{for } e^+.$$

Bremsstrahlung

Bremsstrahlung consists in the emission of light produced by the deceleration of a charged particle when deflected. As it is clear in Figure 4.1, for particle momenta ranging from hundreds of MeV to few GeV, the Bethe-Bloch description is enough to accurately characterize the stopping power of heavy particles, such that radiative losses, i.e. Bremsstrahlung, can be ignored. However, for electrons and positrons Bremsstrahlung becomes relevant for energies above few MeV. Unlike inelastic collisions, which take place many times per path length, losses by bremsstrahlung are characterized by the emission of few high energy photons. Accordingly, depending on the material and its density the probability to undergo losses by Bremsstrahlung can change dramatically. The Bremsstrahlung losses are characterized by the so-called radiation length, X_0 , which describes the distance over which the energy of an electron is expected to be reduced by a factor $1/e$ exclusively due to radiation losses. For air $X_0 \simeq 300$ m, for polystyrene $X_0 \simeq 43$ cm and for lead $X_0 \simeq 0.56$ cm. Therefore, Bremsstrahlung losses can be typically ignored in gases whereas in liquids and solids they are relevant.

Cherenkov radiation

Cherenkov light is produced when a charged particle travels faster than the velocity of light in the medium. The emission happens at an angle given by

$$\cos \theta = \frac{1}{n\beta}, \quad (4.5)$$

where n is the refractive index for the medium, and $\beta = v_p/c$ is the ratio of the velocity of the particle and the speed of light in the vacuum. Provided that $\cos \theta \leq 1$, $\beta = 1/n$ defines the so-called Cherenkov threshold, namely the minimum velocity for which the particle will emit Cherenkov light. In a water Cherenkov detector, where $n=1.33$, this corresponds to a momentum threshold of about 0.6 MeV/c, 120 MeV/c, 160 MeV/c and 1.05 GeV/c for an electron, muon, charged pion and proton respectively. Since the light emission happens at a given angle, a light cone is formed around the track trajectory. In water, if $\beta \approx 1$, the cone opening angle is $\theta \approx 41^\circ$.

4.1.2 Photons

In the case of photons relevant for neutrino detectors, i.e. visible, UV, X-rays and γ -rays, the main processes that need to be considered are the photoelectric effect, Compton scattering and pair-production, with the magnitudes and energy dependences presented in Figure 4.2.

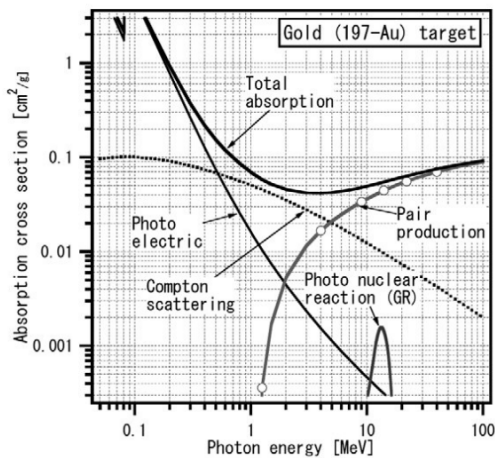


FIGURE 4.2: Photon exclusive cross sections in gold. Figure from Ref. [401].

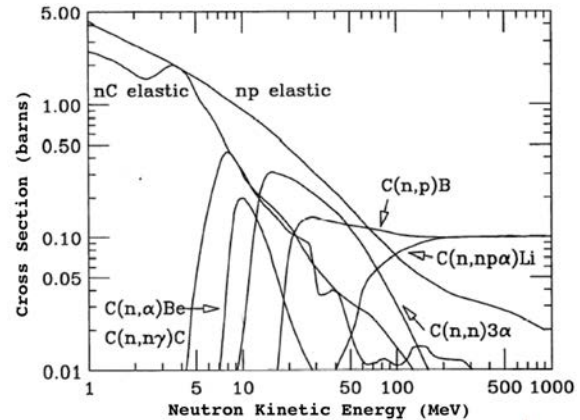


FIGURE 4.3: Neutron exclusive cross sections in carbon. Figure adapted from Ref. [402].

Photoelectric effect

In the photoelectric effect an incident photon is absorbed ionizing an atomic electron. To be allowed, the photon energy must be equal or higher to the electron binding energy. The cross section for this process grows as the energy of the incident photon approaches that of the highest electric binding energy of the atom, known as the K-shell. If the energy of the photon is lower, the K-shell electrons become insensitive to the photoelectric effect producing a sudden drop in the cross section known as the K absorption edge, which can be seen in Fig 4.2. The cross section rises and dips again as it approaches and passes the necessary energy to ionize the next shells (L,M,etc).

Compton and Rayleigh scattering

Compton scattering describes the incoherent scattering of photons with free¹ electrons. By means of Compton scattering a photon gets deflected and changes its energy while ionizing a high energy electron. The maximum energy for this outgoing electron is when the photon and the electron are back-to-back. As at this value there is a sharp cutoff in the outgoing electron energy spectrum this energy is known as the Compton edge. Electrons ejected with energies between zero and this value are often referred to as belonging to the Compton continuum.

Rayleigh scattering describes the elastic scattering of photons by atoms as a whole. In Rayleigh scattering the light is deflected without changing its energy. Despite of this, Rayleigh scattering is sometimes significant as it can change the typical photon travel distance from the production to the detection point.

Pair production

For energies above some MeV pair production becomes the dominant interaction channel. Through it, photons produce in the presence of a third body such as a nucleus, an electron-positron pair. Given that two electrons are created in the process there is a threshold energy of $2 m_e$. The typical distance for pair-production to happen is characterized by the mean free path λ_{pair} , which is related to the radiation length by $X_0 = 9/7 \lambda_{pair}$.

Electron-photon showers

As earlier reviewed, when electrons cross a block of material with a thickness comparable or larger than its radiation length a significant loss of energy happens in the form of Bremsstrahlung photons. Since this photons can create additional electrons and positrons by means of pair production, in general, when radiation losses are significant an avalanche process, known as an electron-photon shower, is triggered: The more electron-positron pairs are created the more Bremsstrahlung photons are emitted. The shower keeps growing exponentially until the mean energy of its constituents is sufficiently low for the Bremsstrahlung cross section to drop.

4.1.3 Neutrons

Due to its lack of electric charge neutrons interact much less frequently with matter than massive charged particles. The most relevant interaction processes for neutrons are: elastic or inelastic scattering from nuclei, neutron capture, nuclear reactions and hadron shower production. Due to the high dependence of the cross section with the neutron kinetic energy it is usual to find in the literature the following terminology:

meV	→	0.25 eV	←	100 keV	→	10 MeV	→	100 MeV	→
Cold		Thermal		Epithermal		Fast		High Energy	

In neutrino interactions, final state neutrons are either fast or high energy. At this typical energies, the main processes affecting neutrons are scattering and nuclear reactions, see Figure 4.3. In the case of inelastic scattering, the neutron transfers some energy to the target nucleus. Consequently, the nucleus recoils creating a short (< few cm) but intense ionization track. If the scattering is inelastic, additionally, a gamma is emitted. In nuclear reactions the neutron knocks out one or several nuclei, typically a proton or an α particle, from the target nucleus. The outgoing charged hadrons produce a highly ionizing track with a length ranging from short to moderately long (some cm) depending on the particle type and the neutron momentum transfer.

¹As the photon energy is relatively high compared to the atomic electron binding energy the latter can be neglected.

4.2 Time Projection Chambers (TPCs)

Time Projection Chambers (TPCs) are a widely extended and highly successful type of ionization detectors. Ionization detectors are based on the direct collection of the ionization electrons and ions produced in a gas or liquid by passing radiation. Among early ionization detectors one can find ionization chambers, proportional counters and Geiger-Müller counters. Their modern use in experiments is very limited. In the 1960s the multi-wire proportional chamber (MWPC) was invented by Charpak [403]. A MWPC is made up arranging anode wires in a gas volume between of two cathode planes. Each anode wire collects the ionized electrons providing a signal proportional to the particle stopping power. In this way, studying the pattern of signals in different wires allows to determine the particle trajectory and its local ionization. Because of this, the MWPC provided for the first time the possibility to study a track trajectory with excellent precision using an all-electronic device, replacing older detector technologies such as photographic emulsions and bubble chambers that required storing the event information in films. Early after the development of the MWPC it was realized that measuring the drift time of electrons from their production point to the wire could be used to obtain additional spatial information [404]. In this way, drift chambers measured the track position by studying the electrons drift time. The combination of the working principles of the MWPC and the drift chambers finally lead to the development of the TPC [405]. TPCs provide simultaneously 3D tracking information and dE/dx measurements of high precision. Since its invention, TPCs have been used in numerous high energy physics experiments and it remains a fundamental instrument.

4.2.1 Working principle

The working principle for the TPCs is illustrated in Figure 4.4. A constant electric field is applied to a gas or liquid volume which is enclosed by a box. Typically, one side of the box is the cathode and the opposite side is the anode. Once a charged track crosses the TPC volume ionizing it, the ions drift towards the cathode and the electrons towards the anode where the signal readout is installed. The readout typically consists of several planes of parallel wires rotated in different angles or it is made up of modules segmented in pads. Either solution provides both ionization and spatial information. The third spatial coordinate is then reconstructed by the drift time to the anode. In addition, a magnetic field is often used in parallel to the electric field, with the goal of bending the tracks trajectories allowing the identification of its charge.

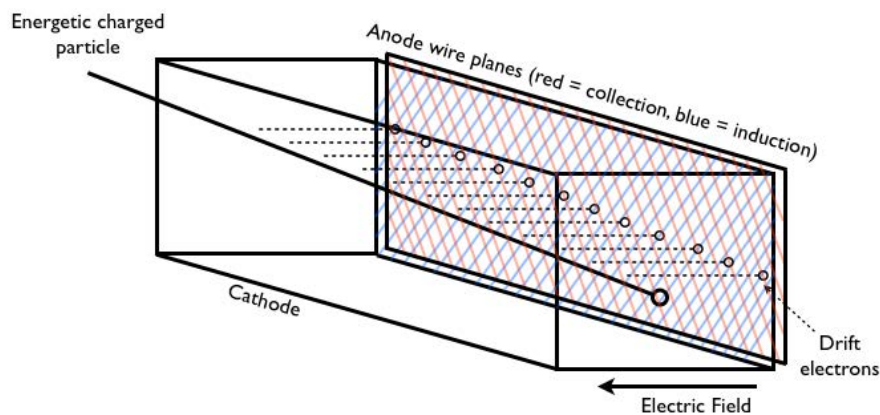


FIGURE 4.4: Drawing of the TPC working principle. In this particular example the readout consists of wire planes. Figure from Ref. [406].

Drift velocity

The drifting charges in the TPC volume suffer gradual energy losses in collisions with the atoms along their way. However, they acquire energy due to the presence of the electric field. A balance is met between these two effects leading to a constant electron drift velocity. The drift velocity is known to be maximal when the electron wavelength is equal to the width of the electric potential in which it travels, known as the Ramsauer–Townsend effect [407]. Consequently, TPCs are often operated at the electric field where this maximum is reached.

Diffusion

The scattering of the ionization electrons by the gas atoms randomly diffuses their trajectory towards the anode. The diffusion is known to be proportional to \sqrt{L} , where L is the drift distance. In general, the diffusion has a negative impact in the determination of the particle trajectory and consequently often using short drift distances is preferred.

Charge attenuation

Ionization electrons can be captured by the gas molecules progressively reducing the amount of charge drifting towards the anode. The severity of the electron attenuation depends on the electron affinity of the gas, which is the amount of energy released when an electron is attached to a neutral atom or molecule to form a negative ion. The attachment for noble gases is very small and can be neglected, however, the presence of impurities in the gas, e.g. Oxygen, can play a significant role. To ensure a good operation performance the TPC gas quality needs to be monitored and kept within nominal values by the use of purifiers and the circulation of fresh gas. As in practice the attenuation is never zero it is measured and corrected for.

Amplification

If the electric field is high enough ($O(10^4)$ V/cm) the electrons may reach sufficient energy between collisions to ionize the gas and trigger an avalanche. The amplification factor, also called gain, is often determined experimentally. TPCs are operated at a lower electric field, in the so-called proportional mode. Namely, after correcting for the attenuation the number of electrons reaching the anode plane should correspond to the number of electrons ionized by the track being measured. In the anode plane, the electric field intensity is typically higher leading to an amplification of the signal. Since the amplification distance is always the same, once the gain is determined, the charge measurement can be translated into a dE/dx for the track. During the avalanche process photons are also created with enough energy to produce additional ionizations. As photons might reinteract at different points in the amplification gap, they might lead to a loss of the proportionality. To prevent this, photon quencher molecules (e.g. CO₂, methane or isobutane), characterized by their large photon absorption cross sections, are usually added in small fractions to the gas mixture.

4.2.2 Momentum reconstruction

Under the influence of a magnetic field $\vec{B} = (0, 0, B_z)$, a particle with initial momentum $B = (p_x, p_y, p_z)$ describes a helicoidal trajectory as long as $p_t = \sqrt{(p_x^2 + p_y^2)} \neq 0$. Under the assumption of constant momentum magnitude, which is generally true, the curve of the trajectory in the plane perpendicular to the magnetic field is a circle arc of radius

$$R = \frac{p_t}{eB}. \quad (4.6)$$

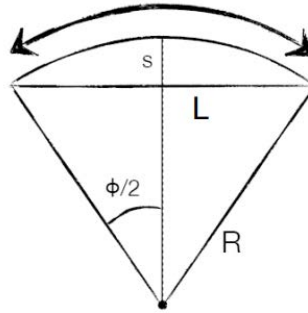


FIGURE 4.5: Schematics of the track parameters in the transverse plane. R is the circle radius, L is the track length and s is known as the sagitta. Figure from Ref. [408].

With the radius in meters, the momentum in GeV/c and the magnetic field in Teslas, one gets the useful equivalence $p_t \approx 0.3Br$.

For N_p equidistant points, and neglecting multiple scattering, the transverse momentum resolution σ_{p_t} is given by the Glückstern formula [409]

$$\frac{\sigma_{p_t}}{p_t} = \sigma_{xy} \frac{p_t}{eBL^2} \sqrt{\frac{720}{N_p + 4}}, \quad (4.7)$$

where σ_{xy} is the point resolution on the transverse plane and L is the length of the track, as illustrated in Figure 4.5. The track momentum is determined by measuring the polar angle θ between \vec{p} and \vec{B} , as:

$$p = \frac{p_t}{\sin \theta} \quad (4.8)$$

where the resolution on θ is given by

$$\frac{\sigma_\theta}{\theta} = \frac{\theta_z}{L} \sqrt{\frac{12(N_p - 1)}{N_p(N_p + 1)}}. \quad (4.9)$$

4.2.3 Particle identification

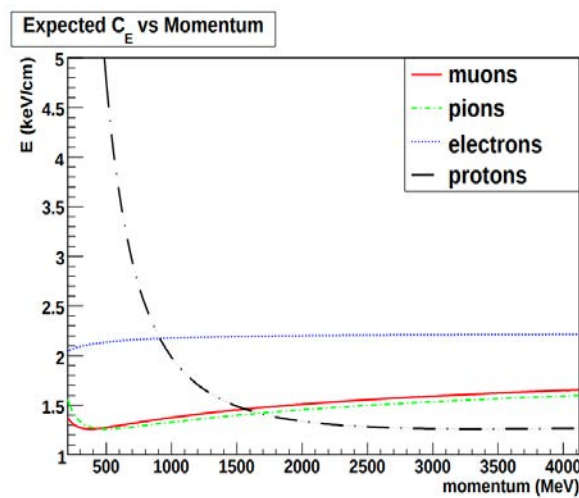


FIGURE 4.6: Expected energy loss (C_E) for different particles in the T2K TPCs. Figure from Ref. [410].

The strategy to perform particle identification (PID) in the TPCs is the following. In the first place the expected ionization C_E , see Figure 4.6, can be computed by using the Bethe-Bloch formula for each given particle hypothesis (electron, muon, charged pion or proton) using the reconstructed momentum and the known (measured) TPC gain. In the second place the expected distribution of measured values C_M is characterized by a certain width σ_E that is a function of the charge resolution of the detector, the gain and the diffusion and it needs to be determined experimentally. With the former, pull variables δ can be built for each particle hypothesis i as

$$\delta(i) = \frac{C_M - C_E(i)}{\sigma(i)}, \quad (4.10)$$

where

$$\sigma(i) = \sqrt{\sigma_E^2(i) + (dC_E/dp)^2 \sigma_p^2} \quad (4.11)$$

accounts both for the charge resolution σ_E and the propagation of the momentum resolution σ_p on the prediction of the central value C_E .

4.3 Scintillation detectors

Whereas ionization detectors such as the TPC focus on measuring the energy loss of tracks by measuring its ionization, scintillation detectors are devoted to measure the light arising from the de-excitation processes induced by charged tracks traveling through matter. While many scintillating materials exist not all of them are adequate to build detectors. In general, a good scintillating material must exhibit high efficiency for converting excitation energy to fluorescent light and it should be transparent to its fluorescent radiation. The most important classes of scintillators are the noble gases, inorganic crystals (e.g. NaI or CsI), liquid organic scintillators, and polycyclic hydrocarbons (plastics). Nowadays, noble gases, in particular Argon and Xenon, are being used in liquid form to build detectors where both the ionization and the scintillation are measured. Inorganic crystals, despite of their high economic cost, provide the largest light yield and are therefore of extended use for precision measurements and nuclear medicine. Plastics constitute the most extended class of scintillators due to their overall good performance, cheap industrial production, robustness and mechanical stability. Finally, organic liquid scintillators provide a mechanical alternative to plastics with similar scintillating performance. Additionally, the de-excitation time of different materials needs to be often considered. Whereas plastic scintillators have a fast response, scintillating on a time-scale of nanoseconds, some inorganic crystals can provide higher light yields but de-excitations might take tens or hundreds of nanoseconds [411].

4.3.1 Light extraction in plastic scintillators

The plastic scintillator is optically isolated from the surroundings, often using a reflector, to prevent that photons get in or out of the detector volume. Thus, once the scintillation light is produced the photons start bouncing on the scintillator surfaces. In order to detect them, it is necessary to use a light-sensitive device, such as a photomultiplier, presented later. The simplest way to transfer photons to the photosensor is to leave free of optical insulator some areas of the plastic surface and use these openings to couple light sensors directly to the scintillator bulk. A common alternative is to use wavelength-shifting (WLS) fibers inserted in the plastic volume or located in one of its sides. The light entering the fiber is converted into a longer wavelength and it is internally reflected until it reaches one of its ends where the photosensor is installed. The use of WLS fibers has a number of pros and cons. On one hand, the wavelength shift helps to reduce the light attenuation and to increase the photosensor response uniformity and performance. In addition, collecting the light by means of fibers allows to precisely guide the light into the photosensor surface which is crucial to use photosensor solutions with a small sensible area. On the other

hand, the use of the fibers reduces the time resolution of the system. Hence, both solutions are attractive depending on the detector purpose and intended geometry.

4.3.2 Energy reconstruction

The spatial resolution in plastic scintillators is typically several times worse than that of a TPC, such that using the method in Sec. 4.2.2 is impractical. However, an alternative method can be used. A crucial difference between gaseous and liquid/solid detectors is the stopping power. As earlier presented, the dE/dx is proportional to the density of the matter being crossed by the track. Accordingly, whereas in a gas a MIP typically loses some keV/cm, in a liquid/solid the stopping power is of MeV/cm. The much increased energy loss makes that, often, tracks will stop within the plastic scintillator volume. The full containment of tracks has two advantages. In the first hand it is possible to measure the range in which the track stops. For a given kinetic energy, the expected range can be computed from the energy losses predicted by the Bethe-Bloch formula allowing to reconstruct the initial particle kinematics. In the second hand, if the track stops in the scintillator volume, and no neutrals escape the detector, the total energy deposit in the detector corresponds to the initial particle energy. Hence, as the light yield is correlated to the energy deposit, the particle energy can also be reconstructed by calorimetry, i.e. measuring the total energy deposited in the detector. Of course, range and calorimetric information can also be combined.

Light yield linearity

For the purpose of correctly mapping the measured light yield to an associated energy deposit it is crucial to know how both are related. Although the relation is mostly linear for high dE/dx the signal is quenched and corrections are necessary to model the light output of highly ionizing tracks. This is done by using the semi-empirical Birks model [412] which relates the light output per unit length, dL/dx to the stopping power by

$$\frac{dL}{dx} = \frac{A \frac{dE}{dx}}{1 + \kappa_B \frac{dE}{dx}}, \quad (4.12)$$

where A is the absolute scintillation efficiency and κ_B is a parameter known as the Birks constant which is fit to experimental data.

4.3.3 Particle identification

Plastic scintillators are denser than gaseous TPCs and consequently the dE/dx of particles usually changes significantly as they travel through them making impractical the use of the method earlier described in Sec. 4.2.3. For stopping particles, a common strategy is to build PID variables based on its dE/dx profile. Protons slow down much faster than μ and π^\pm creating a unique signature that allows to set them apart of μ and π^\pm . Additionally, decay electrons, often named Michel electron [413], are produced at the endpoint of most of μ and π^\pm decays with a typical decay time of 2.2 μ s allowing to differentiate them from protons. Separating μ from π^\pm is often the most complicated task. Their similar mass creates for them a very similar dE/dx pattern. A difference that sometimes is exploited is the fact that pions, due to their hadronic nature, undergo inelastic interactions with nuclei leading to the formation of kinks in the particle trajectory. Electrons and photons trigger electron-photon showers which are easy to identify and to differentiate from all other particle signatures. Nonetheless, separating photons from electrons is challenging. An approach to deal with it is to identify the formation of a primary e^+e^- pair at the beginning of the shower. Additionally, if the γ energy is known, e.g. for $\pi^0 \rightarrow \gamma\gamma$, photons can be identified using calorimetry. Finally, fast and high energy neutrons produce isolated energy deposits delayed by

few nanoseconds with respect to the other detector hits providing a unique signature for their identification.

In summary, PID in plastic scintillator detectors can exploit a larger range of possibilities than those available in gaseous TPCs. However, in order to build high quality PID variables, plastic scintillators need to be finely segmented, provide good calorimetric information and good time resolution.

4.4 Photomultipliers

Photomultipliers (PMs), are devices which convert light into a measurable electric current.

4.4.1 Working principle

When photons reach the sensitive surface of a PM electrons can be emitted due to the photoelectric effect. PMs amplify this primary electrons into a measurable signal. The process depends greatly on the PM design.

Photomultiplier Tubes (PMTs)

The first type of photomultipliers, that are still widely used, were PMTs. A PMT consists on a photocathode, placed on one end of the tube, where the photons are converted into electrons. The electrons are then accelerated and directed by the electric field towards a series of amplification stages, that consists of small strings, named dynodes. The dynodes are set in increasing voltage such that the primary electrons, produced in the cathode, go dynode after dynode until they reach the anode. When the electrons hit each dynode, enough energy is transferred by the primary electron to produce secondary electrons, triggering an avalanche effect. As the final current is proportional to the number of primary electrons, measuring the total current in the anode allows to quantify the number of incident photons. The main advantage of PMTs is that the photocathode can cover very large areas up to tens of cm^2 , e.g. Ref. [414], which is ideal to instrument large detector surfaces.

Silicon Photomultipliers (SiPMs)

With the development and the cost decrease of silicon-based technologies, SiPMs, aroused as an alternative to PMTs [415, 416]. SiPMs consist on Single-Photon Avalanche Diodes (SPADs) that are semiconductor p-n junctions operated at high reverse bias voltage. When a photon reaches a SPAD an electron avalanche is produced in the semiconductor bulk creating a measurable signal. As the area of a single SPAD can be as low as few hundreds of μm^2 , several thousand SPADs can be placed in a single mm^2 forming a pixel grid [417]. The number of SPADs with currents above a certain threshold corresponds to the number of measured photons, which in this context are often named photoelectrons (PE). Because of this working principle pixelated SiPMs are also referred to as Multi-Pixel Photon Counters (MPPCs). Compared to PMTs, MPPCs can be operated at much lower voltages (tens or hundreds of volts instead of thousands) have a much more compact size and are robust to external magnetic fields [415].

Part II

Study of NC1 π^+ interactions in T2K

Chapter 5

The T2K experiment

“It is perhaps difficult for a modern student of Physics to realize the basic taboo of the past period (before 1956). It was unthinkable that anyone would question the validity of symmetries under space inversion, charge conjugation and time reversal. It would have been almost sacrilegious to do experiments to test such unholy thoughts.”

– CHIEN-SHIUNG WU

This Chapter reviews the original setup of the T2K experiment as commissioned in 2009. This Chapter is relevant for the two main topics presented in this thesis. On one hand, the details of the T2K experiment here presented have been used to collect the data and to perform the analysis discussed in Chapters 6, 7 and 8. On the other hand, such setup is the starting point for the upgrades later presented in Chapters 9, 10, 11 and 12. This Chapter describes the main elements of the T2K experiment: the beam, the near detectors and the far detector. Due to its central importance for this thesis, the ND280 detector is explained with special detail.

5.1 Introduction

The Tokai-to-Kamioka (T2K) experiment¹ [418] is a long-baseline neutrino experiment located in Japan, see Figure 5.1. Using a neutrino beamline installed in the proton accelerator J-PARC a highly pure ν_μ or $\bar{\nu}_\mu$ beam is produced in Tokai, Ibaraki. The beam is directed towards Kamioka, Toyama, where the far detector Super-Kamiokande is located, 295km away from J-PARC. T2K uses the off-axis beam technique, namely, the T2K beamline intentionally misses the center of Super-Kamiokande by 2.5° providing a narrow energy beam. In order to characterize the beam a set of near detectors are located at 280m from the beam production point. On one hand, INGRID sits on-axis and its main role is to monitor the beam direction and its stability. On the other hand, ND280 is placed off-axis and is used to measure the beam flux and the neutrino cross section properties at the relevant energy and target materials for T2K.

5.1.1 Brief T2K’s history

Since the 1990s the Super-Kamiokande detector was operative and showed excellent performance studying both solar and atmospheric neutrinos. It was an ideal far detector candidate to build a long-baseline neutrino experiment, a concept that was then just arising. Using the KEK’s proton synchrotron in Tsukuba, a neutrino beam was manufactured by the KEK-to-Kamioka (K2K)

¹General information is publicly available at <https://www.t2k-experiment.org/>

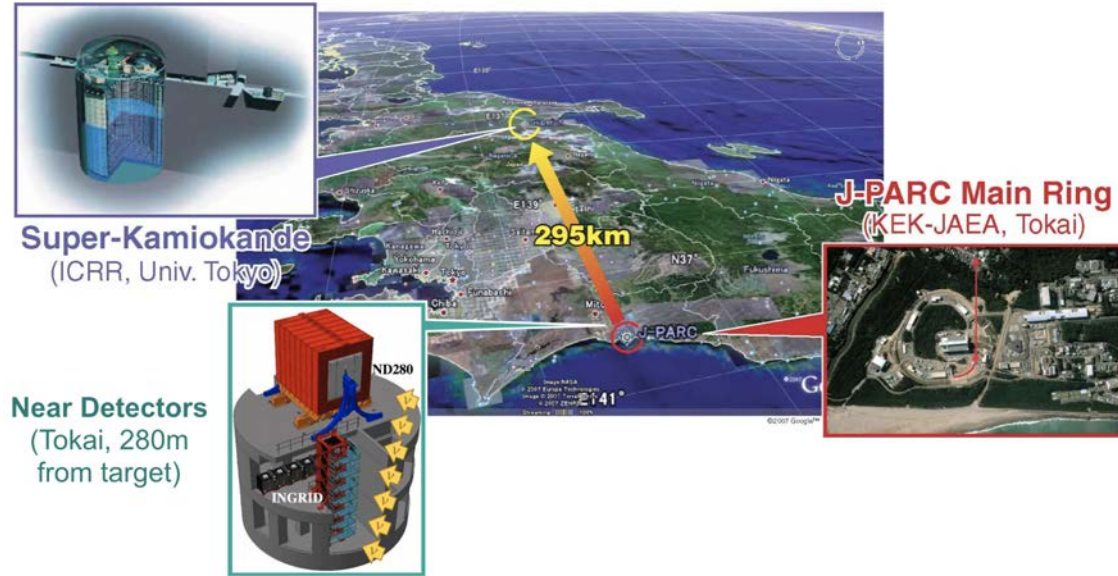


FIGURE 5.1: Sketch of the T2K experiment. Image credit: T2K collaboration.

experiment, which started collecting data in 1999. K2K was the first experiment to measure neutrino oscillations with full experimental control on both the source and the detectors [419] and provided evidence for ν_μ disappearance with a significance of 4.3σ [420]. It was a seminal experiment. About that time a new, more powerful proton beam facility, J-PARC, was being built in Tokai. This opened the door to build the Tokai-To-Kamioka (T2K) experiment which would combine the K2K expertise and the superior J-PARC facilities to design a next-generation experiment. A letter of intent outlining the T2K experiment was written in the year 2000 [421]. The T2K international collaboration, nurtured by a significant number of researchers with experience in the K2K and Super-Kamiokande experiments, was born soon after and wrote a second letter in 2003 presenting the conceptual designs for the necessary elements to be built [422]. The same year, T2K was approved and funds were granted. In 2006, the T2K collaboration presented a technical proposal with the final form of the necessary beam facilities and new detectors to be built with the following physics goals [423]:

1. The discovery of $\nu_\mu \rightarrow \nu_e$. The goal was to extend the search down to $\sin^2(2\theta_{13}) > 0.008$. This was critical since θ_{13} was the last experimentally unknown mixing angle. This measurement was also necessary to elucidate if measuring δ_{CP} would be possible in T2K.
2. Precision measurements of θ_{23} and Δm_{23}^2 via $\nu_\mu \rightarrow \nu_\mu$. In particular a measurement with 1% uncertainty for the oscillation minimum, comparable to the Cabibbo angle uncertainty in the quark sector, and 3% for the mass squared difference, namely $\delta(\Delta m_{23}^2 = 10^{-4} \text{ eV}^2)$ and $\delta(\sin 2\theta_{23} = 0.01)$.
3. Searches for $\nu_\mu \rightarrow \nu_\tau$ in the far detector measuring neutral current neutrino interactions.

The experiment was finally commissioned in 2009 and has been taking data and providing results since then becoming one of the world-wide leading experimental references in studying neutrino oscillations. T2K indicated electron neutrino appearance soon after its construction in 2011 [424], and published a confirmation of the observation in 2013 [425]. Disappearance measurements have also been reported since 2012 [426, 427, 428, 2]. The most recent of this studies is the most accurate existing measurement on θ_{23} . In 2016, T2K was awarded the Breakthrough Prize in Fundamental Physics [429]

For the fundamental discovery and exploration of neutrino oscillations, revealing a new frontier beyond, and possibly far beyond, the Standard Model of particle physics.

Additionally, T2K has measured $\nu_\mu \rightarrow \nu_\mu$, $\nu_\mu \rightarrow \nu_e$ and its anti-neutrino equivalents $\bar{\nu}_\mu \rightarrow \bar{\nu}_\mu$, $\bar{\nu}_\mu \rightarrow \bar{\nu}_e$ to study CP-violation in neutrino oscillations [428, 430, 431]. The accumulation of data over 10 years of operation and the iterative refinements in the data analysis allowed T2K to be, in 2020, the first experiment to report precise measurements of δ_{CP} rejecting almost half of the phase space at the 3σ level and excluding the particularly relevant values $\delta_{CP} = \{0, \pi\}$ with 2.4σ significance [1]. This measurement, presented in Figure 5.2, was highlighted by the journal Nature as one of the ten remarkable scientific discoveries of 2020 [432]. Moreover, while pursuing better experimental control, the T2K experiment has become a referent in the study of neutrino-nucleus cross sections, as reviewed in the previous Chapter. In 2022, the second phase of the experiment (T2K-II²) is in preparation and T2K will continue operational as it is until 2026. In 2027 with the conclusion of the construction of the Hyper-Kamiokande (HK) detector, T2K's beam and near detectors will continue to be used as part of HK's accelerator-based neutrino program [106].

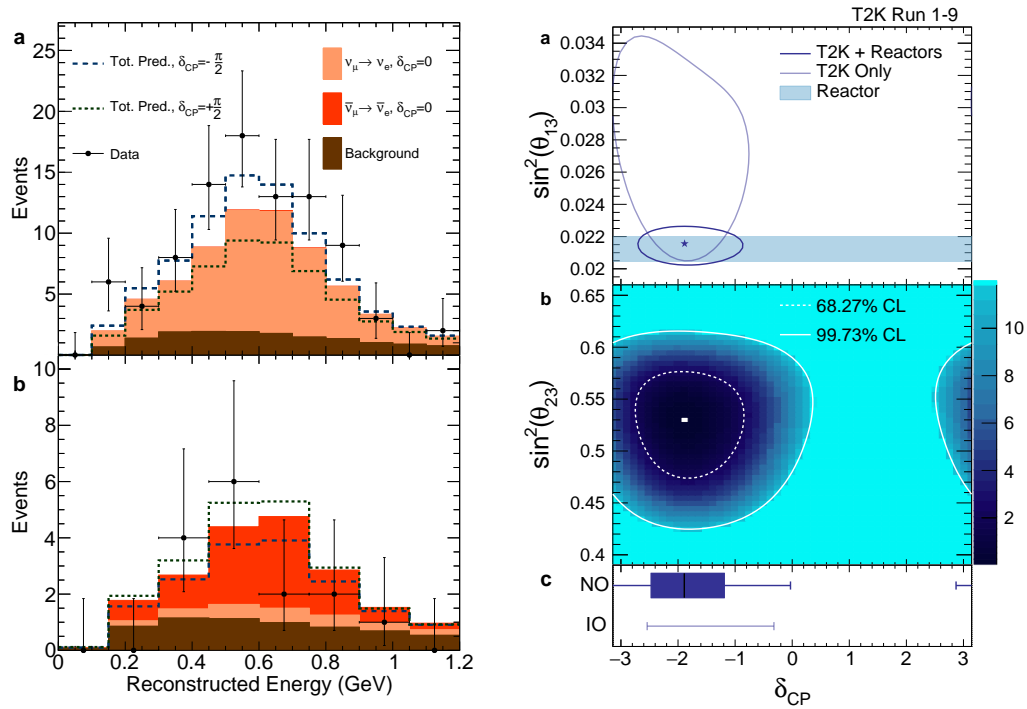


FIGURE 5.2: Left-panel: MC predictions and observed ν_e and $\bar{\nu}_e$ candidate events at SK for: a) ν beam mode b) $\bar{\nu}$ beam mode. Right-panel: Constraints on PMNS oscillation parameters: a) shows the T2K measurement unconstrained and constrained using reactor data; b) shows the result at 1σ and 3σ in the $\sin^2 \theta_{23}$ - δ_{CP} plane assuming normal ordering; c) presents the 1σ and 3σ confidence intervals for normal (NO) and inverted (IO) neutrino mass orderings. Figures from Ref. [1].

5.2 The T2K neutrino beam

The Japan Proton Accelerator Research Complex (J-PARC) in Tokai, Ibaraki, consists of three parts: a linear accelerator (LINAC) a rapid-cycling synchrotron (RCS) and a main ring (MR),

²It must be noted that T2K-II is not an official name, and it is only being used in the context of this thesis when it contributes to clarify the explanations.

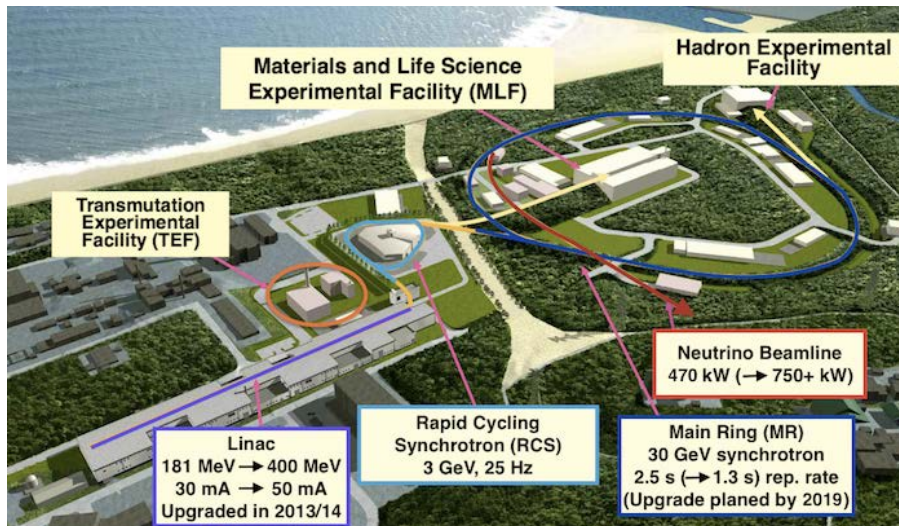


FIGURE 5.3: Drawing of the J-PARC facilities, highlighting its main elements. Figure from Ref. [305].

Beam kinetic energy	30 GeV
Beam power	750 kW
Beam intensity	3×10^{14} p/spill
Spill interval	2.3 s
Number of bunches	8/spill
Bunch interval	581 ns
Bunch width	58 ns

TABLE 5.1: Machine design parameters of the J-PARC main ring at the fast extraction point. These settings determine the T2K neutrino beam structure. Table from Ref. [418]

sketched in Figure 5.3. The MR has two extraction points, a slow extraction for the hadron beamline³ and a fast extraction for the neutrino beamline used by T2K with nominal values summarized in Table 5.1. In the neutrino beamline two different sections can be identified, as presented in

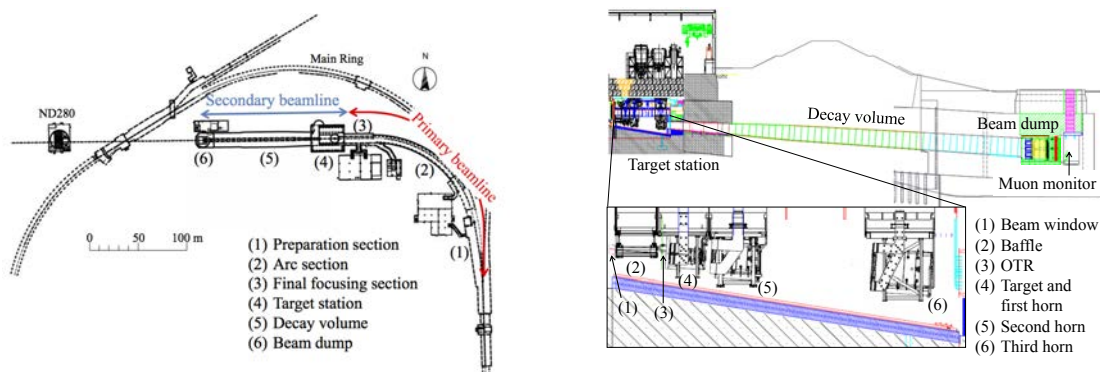


FIGURE 5.4: Left-panel: Neutrino beamline in J-PARC. Right-panel: Detail on the secondary beamline. Figures from Ref. [433].

Figure 5.4. The primary beamline bends the beam into its final direction, using a set of dedicated magnets [418, 434, 435]. The secondary beamline is responsible to convert the beam of protons

³More information about its ongoing research program is available at: <http://j-parc.jp/c/en/for-researchers/hadron.html>.

into a beam of neutrinos. It is divided in three subsections all contained inside a helium gas vessel at 1 atm to reduce the number of particle re-interactions.

- The target station contains a baffle which protects the magnetic horns; an optical transition radiation monitor (OTR) to monitor the proton beam profile upstream to the collision; a cylindrical graphite target of 91.4cm long, 2.6cm diameter, and 1.8g/cm^3 density, to generate secondary tracks out of proton collisions; and three magnetic horns. The first of the horns acts as a collimator collecting⁴ charged particles and directing them forward. The next two magnetic horns are used to select tracks of a given charged sign enhancing the purity of the beam. The polarity of this magnets can be reversed. In Forward Horn Current (FHC), also known as neutrino beam mode, positive (negative) particles are focused (defocused) providing a highly pure ν_μ beam. Conversely, in Reverse Horn Current (RHC), also known as antineutrino beam mode, a beam populated mainly by $\bar{\nu}_\mu$ is produced.
- The decay volume is a 96m long chamber located immediately after the target station. On it, mesons, mainly pions, decay via $\pi^+ \rightarrow \mu^+ + \nu_\mu$ above 0.9998% of the times⁵. Decays involving ν_e are helicity suppressed contributing greatly to create a highly pure ν_μ beam. Kaon decays also play a sizable role. Due to the off-axis configuration they contribute significantly to the high energy tail of the ν_μ flux. In addition, kaons are important sources of ν_e as kaon decays lead to the production of ν_e about 10% of the times. In addition to meson decays, muon decays are relevant to ν_e . Details are presented in Figure 5.5.

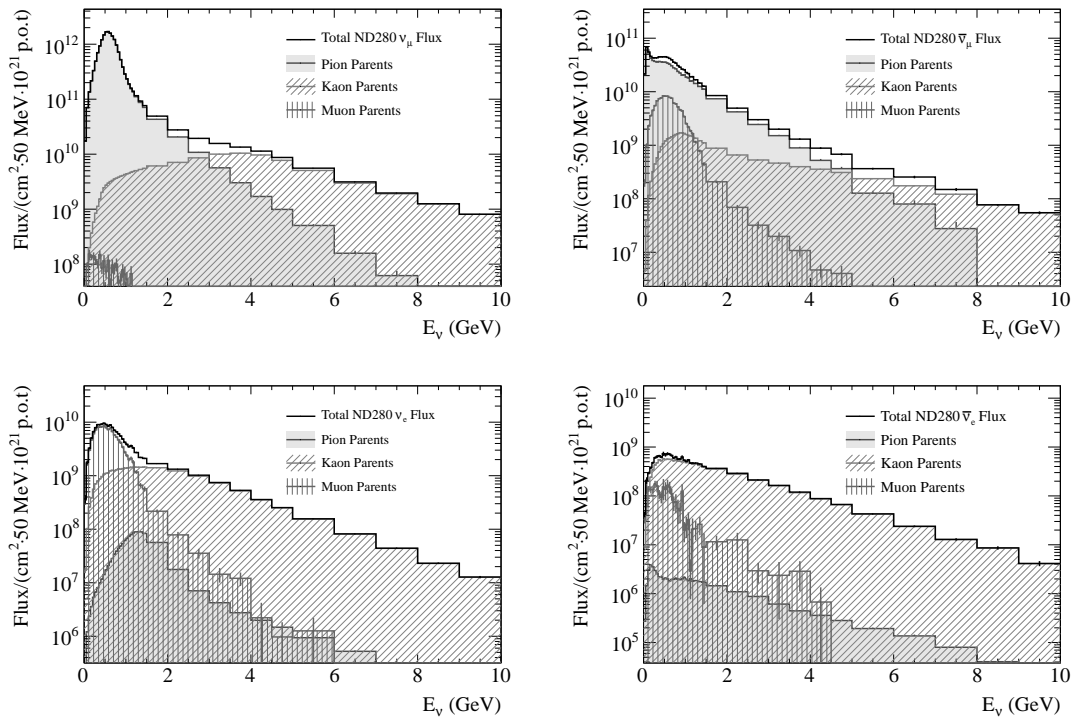


FIGURE 5.5: Predicted neutrino flux at ND280 by decay parent. Figure from Ref. [433].

- The beam dump is located immediately after the decay volume. It stops all beam particles but neutrinos and muons above 5 GeV which are used to monitor the neutrino beam using the MUMON module.

⁴At a maximum 2.1 T field the first horn enhances the neutrino flux at SK by 16-fold compared to 0 T.

⁵For RHC the dominant decay is $\pi^- \rightarrow \mu^- + \bar{\nu}_\mu$.

Immediately after the vessel, the muon monitor (MUMON) [436] analyzes the neutrino beam intensity and direction on a bunch-by-bunch basis by measuring the distribution profile of the high energy muons crossing the beam dump. The neutrino beam direction is determined to be the direction from the target to the center of the muon profile. The MUMON is located 118 meters downstream to the target immediately behind the beam dump. It is designed to measure the beam direction with a precision better than 0.25 mrad. It also provides an intensity estimate with a precision better than 3%. Additionally, a nuclear emulsion detector installed downstream to the MUMON measures the absolute muon flux as well as its momentum distribution. MUMON and INGRID are complementary as the first measures muons and the second neutrinos. The measured beam stability, for Runs 1 to 9, is presented in Figure 5.6.

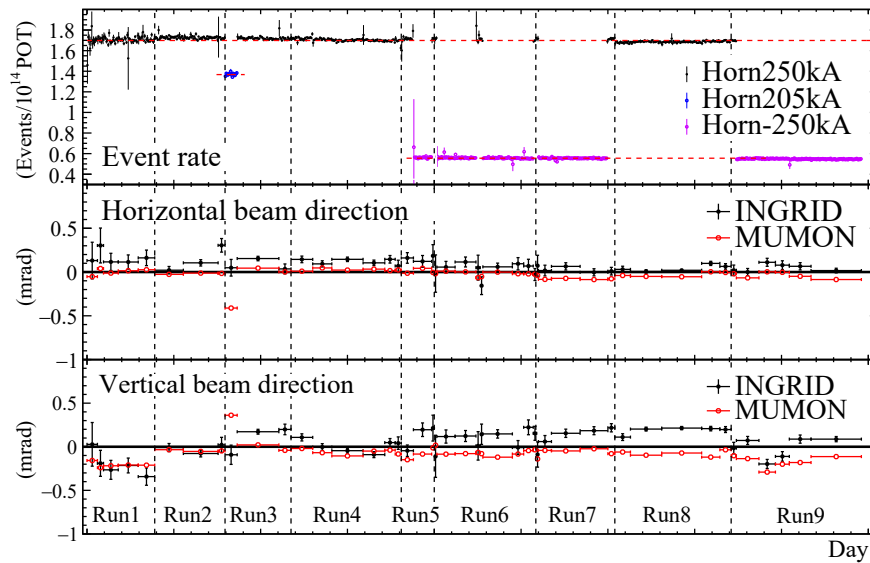


FIGURE 5.6: Data from MUMON and INGRID for runs 1-9. The top row shows the event rate in both detectors. The middle and bottom rows show the horizontal and vertical beam alignment. Figure from Ref. [2].

5.2.1 The off-axis beam technique

T2K oscillation measurements are mainly based on CCQE interactions. To maximize the fraction of this type of events, see Figure 5.7, T2K uses a narrow energy beam. To achieve it T2K is the first experiment using the off-axis beam technique⁶. The idea is to exploit the pion decay kinematics in the dominant pion decay $\pi^+ \rightarrow \mu^+ + \nu_\mu$. Since it is a two-body decay the neutrino energy satisfies

$$E_\nu = \frac{m_\pi^2 - m_\mu^2}{2(E_\pi - p_\pi \cos \theta)} \xrightarrow{\text{rest frame}} E_\nu^{\text{RF}} = \frac{m_\pi^2 - m_\mu^2}{2m_\pi} \sim 30 \text{ MeV}. \quad (5.1)$$

In the pion rest frame the outgoing tracks are emitted isotropically. In the laboratory frame, where the pion decays in flight, the maximum angle that can be reached for a given pion momentum is that where the neutrino in the pion rest frame is emitted perpendicular to the beamline. This maximum angle is smaller for increasing pion kinetic energies. Because of this geometrical constraint the neutrino energy spectrum is different at each off-axis angle, with a maximum neutrino energy given by

$$E_\nu \leq E_\nu^{\text{RF}} / \tan \theta. \quad (5.2)$$

⁶Originally proposed in Ref. [437].

At the nominal off-axis angle of 2.5° , see Figure 5.7, the neutrino energy from the former decays is limited to be below 682 MeV, such that T2K's flux peaks at 0.6 GeV, energy for which the disappearance and appearance probabilities are maximal in the far detector. In this way, the J-

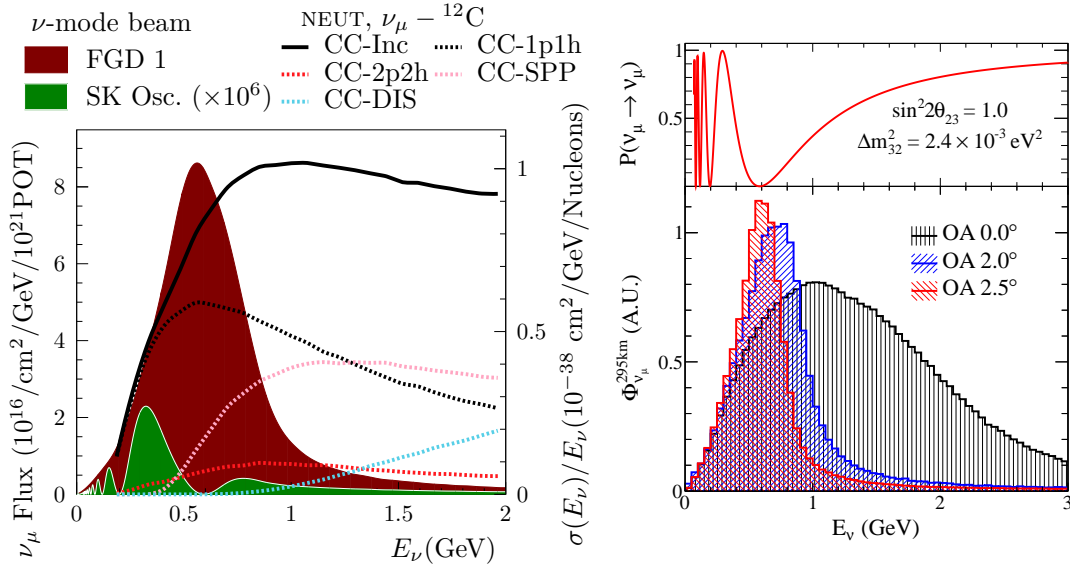


FIGURE 5.7: Left-panel: ν_μ survival probability for 295km and ND280 flux for different off-axis angles. Figure from Ref. [433]. Right-panel T2K flux in the ND280 and SK compared to the cross section predictions from NEUT 5.3.3. Figure from Ref. [2].

PARC neutrino beamline is monitored on-axis by the MUMON and the INGRID detectors, but is used for the oscillation analysis off-axis, with two detectors placed at 2.5° off-axis: the near detector ND280, and the far detector Super-Kamiokande. See the sketch in Figure 5.8.

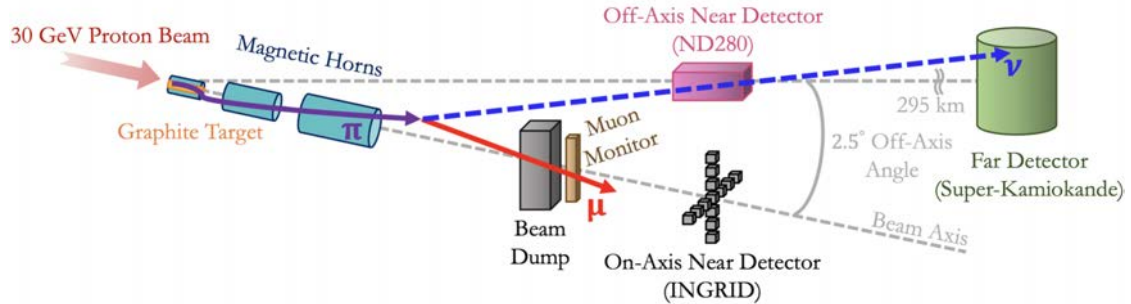


FIGURE 5.8: Sketch of the main elements along the T2K's neutrino beamline. Figure from Ref. [438]

5.2.2 The T2K beam prediction

To draw conclusions on the oscillation parameters from the observed number of events it is necessary to model the flux on each of the detectors. In order to do so, a full Monte Carlo simulation chain, described in Ref. [433], is used. First, the initial proton interactions of the J-PARC beam with the target and baffle are simulated with FLUKA [439, 440]. For each interaction the information on the outgoing tracks is stored and transferred to JNUBEAM. JNUBEAM is a GEANT3 [441] Monte Carlo simulation including all elements in the secondary beamline based on its final mechanical drawings. In JNUBEAM the initial tracks are propagated upstream using the GCALOR [442] package. Neutrinos from particle decays and their distributions are saved. In addition, the kinematic information of the initial proton and full interaction chain producing the

neutrino are saved to allow for re-weighting of the proton beam profile and hadron interactions which is used to quantify the impact of their uncertainty in the flux prediction. The initial proton beam parameters are tuned using data from the proton beam monitors. Data from the fixed-target experiment NA61/SHINE [433, 443, 444], located at the CERN SPS, measures particle production in nucleus and hadron collisions with a large acceptance spectrometer. This includes measurements of the meson distributions and production yields outgoing the collisions of 31 GeV protons with graphite, see Figure 5.9. These data are then used to tune the production rate, distributions and re-interactions of secondary particles and ultimately to constrain the flux model parameters. In 2018, NA61/SHINE used a T2K replica target [444] significantly reducing T2K's flux uncertainty. The 2020 predictions for the neutrino beam are presented in Figure 5.10 and its associated uncertainties in Figure 5.11.

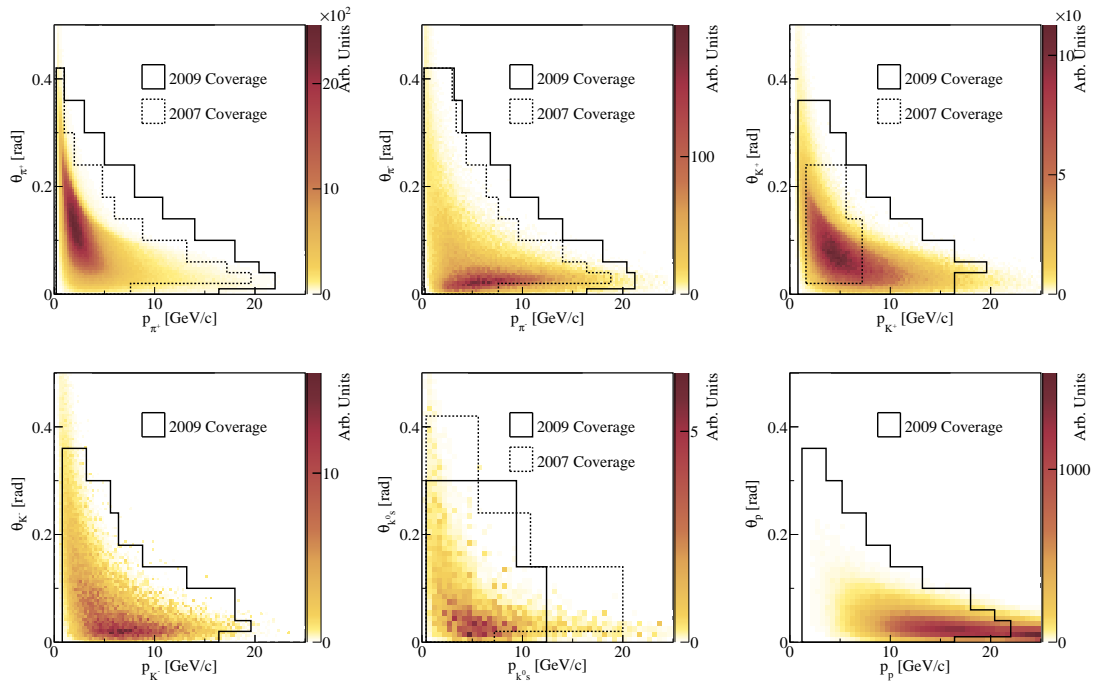


FIGURE 5.9: NA61/SHINE coverage in the θ - p phase space for the pions, kaons and protons contributing to the neutrino flux prediction at SK. Figure from Ref. [443].

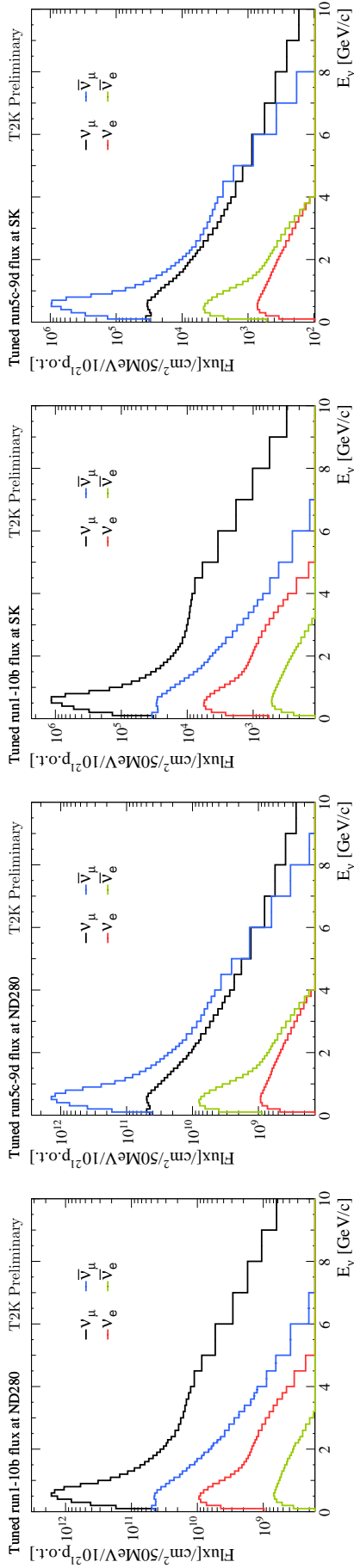


FIGURE 5.10: Flux prediction for ND280 FHC and RHC, and SK FHC and RHC. Figures from T2K-TN354 [445].

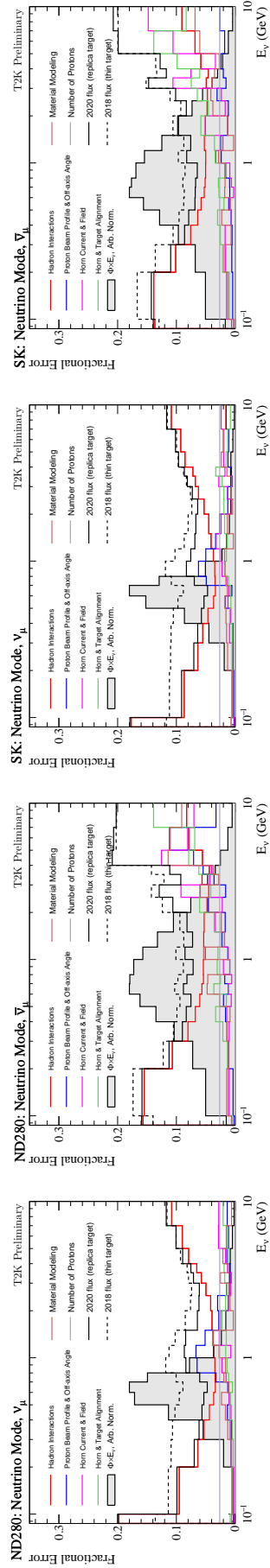


FIGURE 5.11: Fractional error for the flux prediction for ND280 ν_μ in FHC and $\bar{\nu}_\mu$ in FHC and SK ν_μ in FHC and $\bar{\nu}_\mu$. As it can be seen using T2K's replica target significantly reduced the flux prediction uncertainty. Figures from T2K-TN354 [445].

5.3 The near detectors complex

The T2K near detectors are located into a dedicated facility at 280 meters from the production point, see Figure 5.12. Its main goal is to characterize the beam of neutrinos prior to any

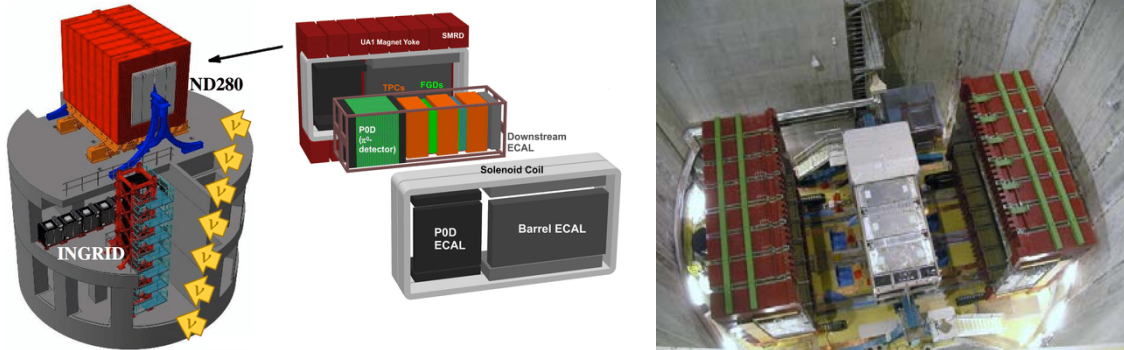


FIGURE 5.12: Left: Sketch of the near Detector pit. Right: View from above the pit of the ND280 detector. The UA1 magnet is open revealing the inner elements within the basket. Images Credit: T2K collaboration.

signification oscillation. Given that the T2K beam goes below the surface, to account for the Earth curvature in its path to the far detector, the near detectors are placed into a 30m deep concrete pit with several floors at different off-axis degrees. The first floor contains the ND280 detector which can be seen from above in Figure 5.12. The ND280 cabling is grouped underneath the detector where it is guided to the floor below using dedicated feedthroughs. The second floor from the top contains racks with the necessary equipment to operate ND280. The top modules of INGRID also sit in the second floor. Finally, the ground floor allows to access the lower modules of INGRID. Immediately next to the pit building, there is another building which serves both as a workshop and control room. The workshop provides space for detector testing and commissioning and to store material and spares for repairs. The control room is used to operate and monitor the near detectors when T2K is taking data. The near detector complex is completed by a series of barracks close to the two former buildings which host the gas bottles and gas mixing room used to supply gas to the ND280's TPCs.

5.4 The on-axis detector INGRID

The INGRID (Interactive Neutrino GRID) detector [446], is the main on-axis detector of the T2K experiment. INGRID consists of 16 identical modules, 14 of them arranged in a cross-like grid as sketched in Figure 5.13. Two additional modules, off the main cross shape, are used to check the beam axial symmetry. All INGRID modules, are composed by 11 tracking scintillator planes interleaved with iron plates and surrounded by veto scintillator planes used to reject interactions from outside the module. Each of the iron plates has a size of $124 \times 124 \times 6.5 \text{ cm}^3$. The scintillator planes are made of 24 polystyrene vertical and 24 horizontal $1 \times 5 \times 120.3 \text{ cm}^3$ scintillator bars. The light in each of them is collected by a single WLS fiber and read-out by an MPPC. Each of the planes is mounted in an independent box with an electronics front-end board on one side. INGRID has a total iron weight of 7.1 tons. This provides a large enough target mass to precisely monitor the beam in a daily basis with 0.4 mrad precision, see Figure 5.6.

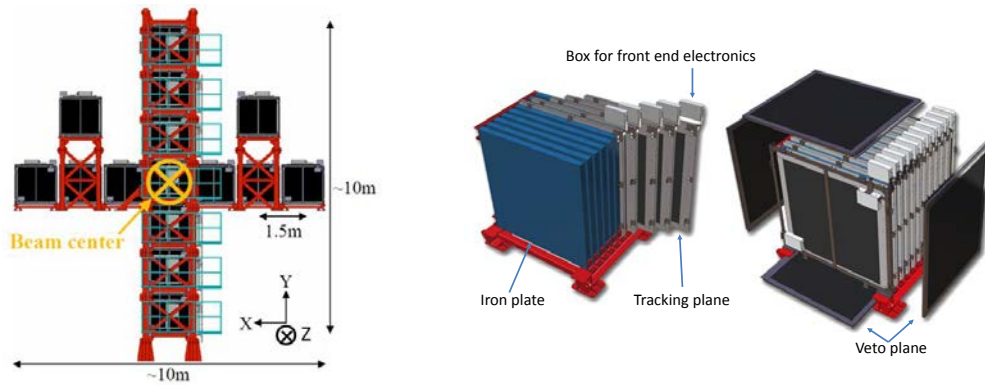


FIGURE 5.13: Left: Sketch of the INGRID detector. Right: Detail of a single INGRID module.

5.5 The Off-Axis detector ND280

The Near Detector at 280 meters (ND280) is the main off-axis near detector of the T2K experiment, see Figure 5.14. ND280 was designed to:

- Study both ν_e and ν_μ interactions.
- Differentiate ν from $\bar{\nu}$ CC interactions.
- Study both CC and NC interactions.
- Reliably identify long ranged particles, such as leptons and pions.
- Measure interactions using both plastic and water targets.

To achieve it, the center of the ND280 detector was filled with high performance modules with specific tasks, complementing one another. All central modules are located in a rectangular steel frame known as the basket, sketched in Figure 5.16. The basket is fully surrounded by an electromagnetic calorimeter which provides additional information for tracks escaping the basket, works as a veto for external tracks and helps to identify signatures associated to neutral particles. To identify the charge sign of the tracks the calorimeter is enclosed by the UA1 magnet, depicted in Figure 5.15, which has plastic scintillator insertions in the air gaps of its yoke, acting as a Side-Muon-Range-Detector (SMRD). Within the ND280 basket two well differentiated elements can be found. Upstream, a Pi-Zero Detector (PØD) is used to study neutrino NC interactions. Downstream, a sandwich of fine-grained detectors (FGDs) and time-projection chambers (TPCs) is used to study neutrino CC interactions. To study the differences in neutrino interactions occurring in plastic and water, the PØD and FGD2 have water-fillable bags.

5.5.1 UA1 magnet

ND280 uses the magnet of the UA1 experiment⁷ after it was donated by the NOMAD collaboration [447]. It provides a 0.2 T magnetic field orthogonal to the beam direction when operated at the nominal current of 2900 A. The magnet consists of four water-cooled aluminum coils which create the horizontally oriented dipole field and a flux return yoke to homogenize the magnetic field. The yoke is made up of 16 C-shaped segments organized in two mirror-symmetric halves. Each of the yoke segments is made up of low-carbon steel plates. The UA1 magnet dimensions are $7.6 \times 5.6 \times 6.1 \text{ m}^3$ ($7.0 \times 3.5 \times 3.6 \text{ m}^3$) for a total weight of 850 tons [418]. The main goal of the magnet is to bend the tracks such that their charge sign can be identified and their momentum reconstructed measuring its curvature. After ND280 was built the UA1 magnetic field was

⁷As a historical remark, the UA1 experiment located at CERN was key for the discovery of the W and Z bosons.

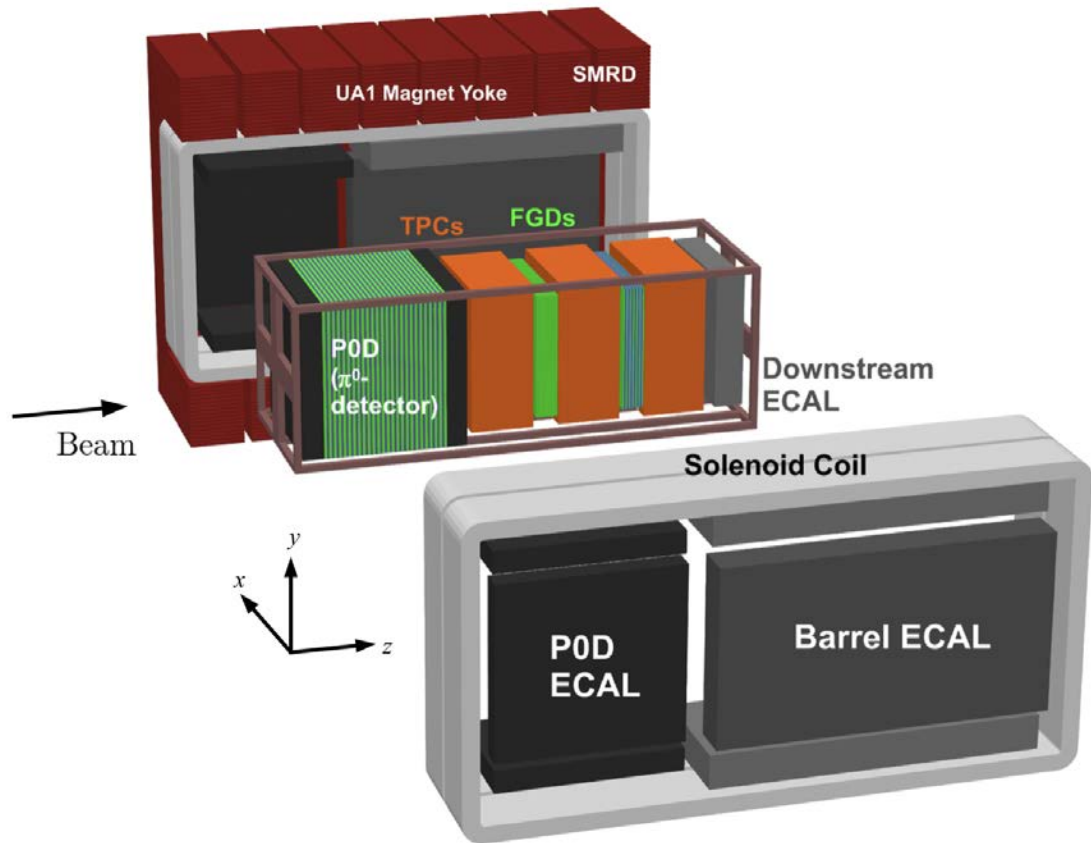


FIGURE 5.14: Exploded drawing of the ND280 detector. Figure from Ref. [418].

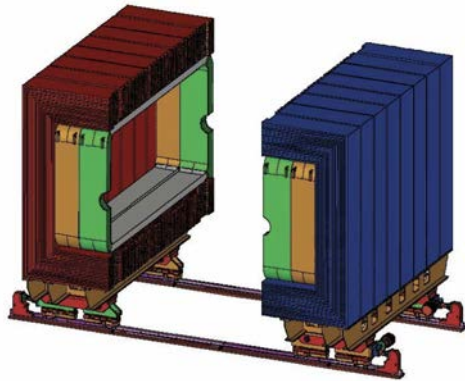


FIGURE 5.15: Sketch of the UA1 magnet. The magnet can be opened to access the inner modules. Figure from Ref. [423].



FIGURE 5.16: Sketch of the ND280 basket. Figure from Ref. [423].

mapped, see Figure 5.17, and an excellent uniformity was achieved for all the field components, see Figure 5.18.

5.5.2 Side Muon Range Detector (SMRD)

The SMRD consists of 440 scintillator modules placed in the air gaps between the iron plates of the magnet yoke, see Figure 5.19. Each module, see Figure 5.20, is a plastic scintillator plane made up of four or five thin plastic scintillator bars of $875 \times 167 \times 7 \text{ mm}^3$ [448], crossed by a WLS fiber attached to an MPPC read by Trip-T front-end boards. The SMRD is used to trigger

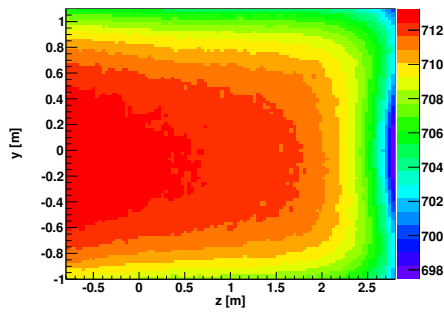


FIGURE 5.17: Slice of the measured ND280 magnetic field magnitude in Gauss in the TPC region (at the basket central plane, $x=0$). The neutrino beam is entering the picture from the left. Figure from Ref. [418].

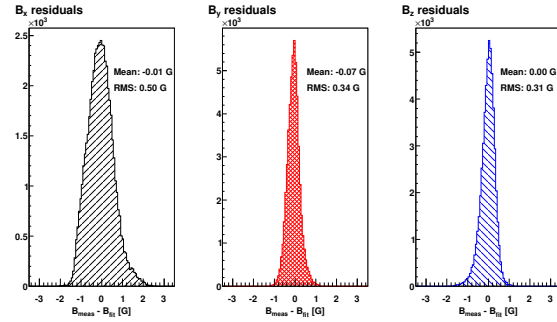


FIGURE 5.18: . Residuals between a fit of the magnetic field data and the actual measurements for each B-field component (x,y and z respectively). The RMS of the distributions is taken as a measure of the systematic uncertainty of the mapping. Figure from Ref. [418].

on cosmic ray tracks, to veto interactions starting in the magnet and to assist the momentum reconstruction of very high energy particles, typically muons.

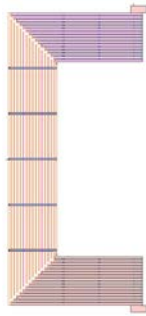


FIGURE 5.19: Drawing of a yoke segment of the UA1 magnet. The iron plates are hold by bolts dividing each yoke into 4 horizontal, 4 vertical and 2 corner sections. Sketch from Ref. [448].

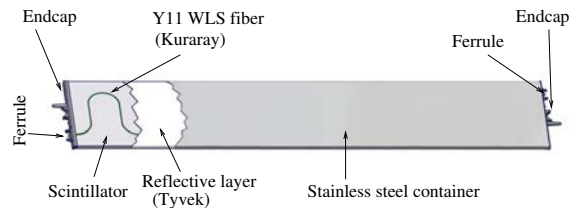


FIGURE 5.20: . Sketch of an SMRD module. Figure from Ref. [448].

5.5.3 Electromagnetic Calorimeter (ECal)

The electromagnetic calorimeter (ECal) [449] provides a near-hermetic coverage for tracks escaping the basket. In total, there are 13 ECal modules. Six surround the sides of the PØD parallel to the beam (PØDECAL), six cover the sides of the tracking elements of the basket parallel to the beam (BarrelEcal) and one is placed at the downstream exit of the basket in perpendicular to the beam (DsEcal). Having two modules on the top and bottom sides of the PØDECAL and BarrelEcal following the magnet division allows to open ND280 to access to its inner elements. Each module is made up of polystyrene scintillator bars with a cross section of $4.0 \times 1.0 \text{ cm}^2$ interleaved with lead sheets of 1.75mm for the BarrelEcal and the DsEcal and 4mm for the PØDECAL. A WLS fiber inserted in the center of each bar collects the light which is measured by an MPPC in one or both ends depending on the fiber length and it is read-out by Trip-T front-end boards. The main goal for the ECal is to complement the capabilities of the tracking elements within the basket. Thanks to the lead layers it is highly opaque to photons. This is of great importance to identify $\pi^0 \rightarrow \gamma\gamma$ events which constitutes the main background to study ν_e interactions. In addition, the ECal is often used in the absence of TPC PID information or to complement it.



FIGURE 5.21: Picture from the original installation of the ECal in ND280. In the image, half of the ECal can be seen with the three PØDE-Cal modules on the left, and the three BarrelE-Cal modules on the right. Part of the magnet yoke (top, red) is visible. Figure from Ref. [449].

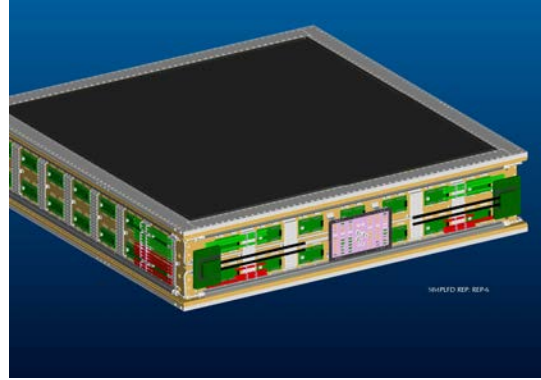


FIGURE 5.22: . Render of one ECal module. The scintillator bars run horizontally inside the module as shown. The readout electronics, signal and power cables, and cooling pipes can be seen mounted on the aluminum plates on the sides of the module. Figure from Ref. [418]

5.5.4 Pi-zero Detector (PØD)

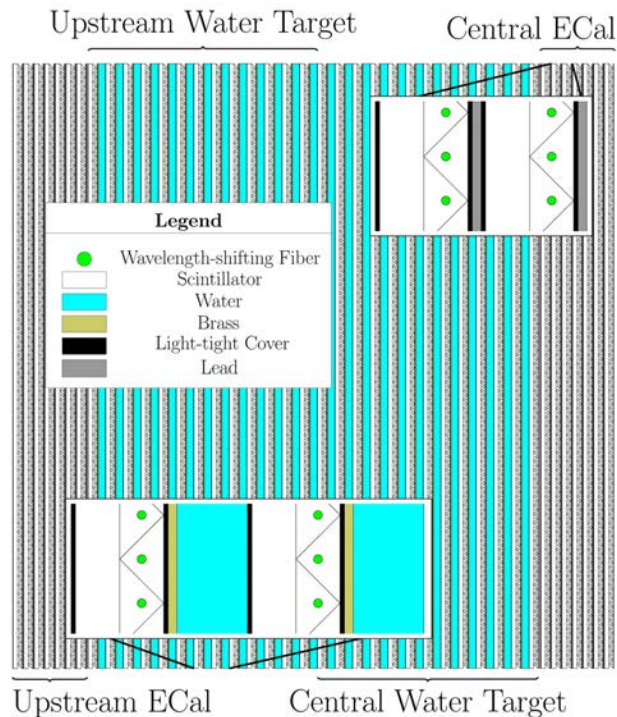


FIGURE 5.23: Sketch of the PØD detector. The beam enters from the left of the image. Figure from Ref. [418].

The Pi-zero Detector (PØD) [450], sketched in Figure 5.23, is the most upstream sub-detector within the basket. The PØD can be sub-divided in four regions (Super-PØDules): the Upstream ECal, the Upstream Water Target, the Central Water Target and the Central ECal. Each of this regions is made up of smaller modules (PØDules). A PØDule consists on two layers made up of doped polystyrene triangular scintillator bars; The bars in each layer are oriented respectively along the x and y axis and each of them is traversed by a WLS attached to an MPPC read-out by Trip-T front-end cards. The most upstream and downstream Super-PØDules have 7 PØDules

and each of them is interleaved with stainless steel clad lead sheets (4 mm thick). The other two Super-PØDules have a total of 26 PØDules interleaved with fillable water bags (28 mm thick) and brass sheets (1.5 mm thick). The detector size is $2103 \times 2239 \times 2400 \text{ mm}^3$ for a total mass of 16.1 tons and 13.3 tons with and without water respectively. As its name suggests, the PØD detector was optimized to measure interactions involving π^0 s. Using the PØD ν_e events can be separated from its main background, which are electromagnetic cascades triggered by $\pi^0 \rightarrow \gamma\gamma$ decays. The PØD has been used to measure the ν_e component in the T2K beam [451] and to measure for the first time the cross section of ν_e interactions with water [329]. The PØD has also been used to constrain the ratio of $\nu/\bar{\nu}$ cross sections [331] and to measure the π^0 production cross section in NC interactions with water [390].

5.5.5 Fine-Grained-Detectors (FGDs)

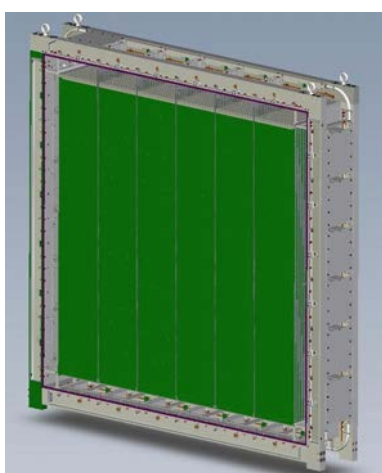


FIGURE 5.24: Render of an FGD with the front cover removed. XY scintillator modules (green) hang perpendicular to the direction of the neutrino beam. Along the top, six mini-crates with electronics can be seen without their cooling lines, while on the right side the cooling lids covering the mini-crates are shown. Figure from Ref. [418].



FIGURE 5.25: . Photograph of the XY modules inside the FGD1 dark box. Busboards carrying photosensors are mounted along all four sides of each module. Ribbon cables connect each busboard to the backplanes (not visible in this photo) on the sides of the dark box. Figure from Ref. [452].

The FGDs [452], shown in Figures 5.24 and 5.25, are made of $(9.61 \times 9.61 \times 1864.3 \text{ mm}^3)$ plastic scintillator bars arranged in layers of 192 bars oriented alternately along the x and y axis. Each bar contains a WLS fiber, mirrored on one end, and attached to an MPPC with specifications summarized in Table 5.2 and shown in Figures 5.26 and 5.27. The bars, see Figure 5.28, are co-extruded with 0.25mm thick TiO_2 reducing the optical crosstalk from bar to bar to $0.5 \pm 0.2\%$. From upstream to downstream they are named FGD1 and FGD2. In order to measure the differences in the interactions with plastic and water the two FGDs are different. FGD1 is made up of 30 layers organized in 15 modules of 2 layers, known as XY modules. FGD2 has 7 XY modules interleaved with 6 water modules (2.5 mm thick). All modules hang inside a light-tight mechanical frame known as the dark box. Each dark box has an external (internal) size of $2300 \times 2300 \text{ mm}^2$ ($2069 \times 2069 \text{ mm}^2$) perpendicular to the beam and a thickness of 365 mm (352 mm) along the beam.

To account for small bar-to-bar variations in the light yield, arising on the slightly different MPPC responses, fiber treatment quality and MPPC-fiber alignments, the light yield of each individual bar in FGD was calibrated and correction factors were computed, as presented in Figure 5.29. In

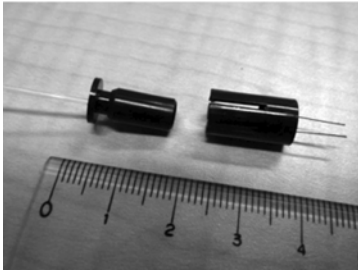


FIGURE 5.26: WLS fiber (left) and MPPC connector (right). Figure from Ref. [452].

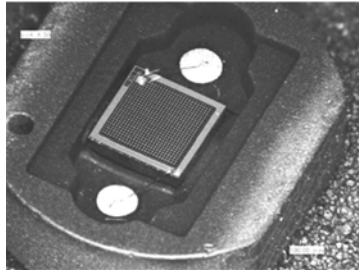


FIGURE 5.27: Picture of a S10362-13-050C MPPC. Figure from Ref. [452].

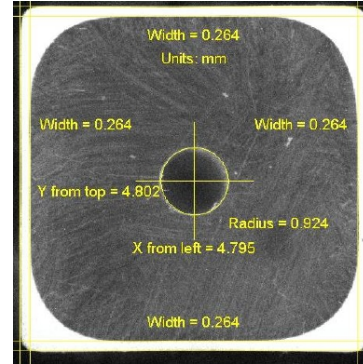


FIGURE 5.28: cross section of an FGD bar. Figure from Ref. [452].

Active area	$1.3 \times 1.3 \text{ mm}^2$
Pixel size	$50 \times 50 \text{ } \mu\text{m}^2$
Number of pixels	667
Operation voltage	70 V (typ.)
PDE @ 550 nm	(>15%)
Dark Count (>0.5 pe) [@ 25°C]	< 1.35 Mcps
Dark Count (>1.2 pe) [@ 25°C]	< 0.135 Mcps

TABLE 5.2: Specifications of the Hamamatsu S10362-13-050C MPPCs used in both FGDs.

addition, the light is attenuated while travelling inside the WLS fiber, following the equation

$$I = Ae^{-x/L} + Be^{-x/S}, \quad (5.3)$$

such that distance-dependent attenuation factors need to be computed. In order to do this, the attenuation in multiple fibers was measured, see Figure 5.30. Unlike the SMRD, the ECal and the PØD which have electronics based on TFB cards, the FGD electronics are based on the AFTER chip [453]. Using the AFTER chip the MPPC charge is sampled 511 times every 20 ns providing a 10.2 μs waveform for each bar. Each MPPC is read by two readout channels, one working with high-gain and the other with low-gain. The high-gain channel saturates at 80 photo-electrons (PE) such that it can measure accurately the light yield of MIP tracks, which is typically 25-30 PE. Searching for multi-peak structures in the waveforms allows to identify Michel electrons (ME), as presented in Figure 5.31, with an efficiency in data (Monte Carlo) of $56.5 \pm 0.94\%$ ($56.4 \pm 0.16\%$) in FGD1 and 42.8 ± 0.11 ($41.4 \pm 0.70\%$) in FGD2 [454]. The time resolution is slightly dependent on the light yield and asymptotically approaches about 3 ns resolution for high light yields, see Figure 5.32. This resolution is high enough to provide good separation between forward and backward going events between FGD1 and FGD2.

The FGDs are essential elements in ND280 playing multiple roles. On one hand, they provide a sufficient target mass for the neutrinos to interact in them at a significant rate. On the other hand, they work as trackers and are used to reconstruct the neutrino vertex position and its outgoing tracks. The FGDs provide light yield information which is used to perform particle identification, specially separating protons from muons and pions when they are fully contained, see Figures 5.33, 5.34 and 5.35. In addition, the FGDs are used in combination with other sub-detectors to determine the tracks sense of motion by time-of-flight.

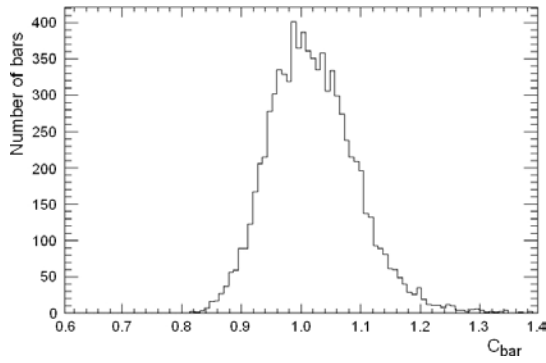


FIGURE 5.29: FGD bar-to-bar light yield correction factors. Figure from Ref. [452].

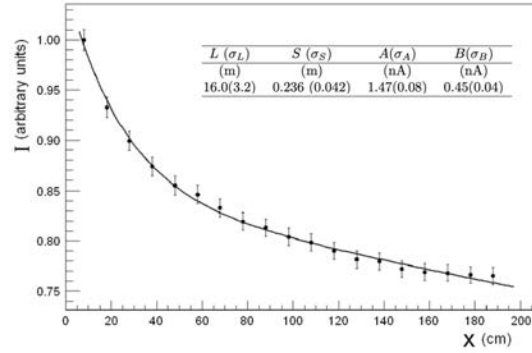


FIGURE 5.30: Light yield attenuation dependence and fitted parameters for Eq. 11.2 using multiple FGD fibers. Figure from Ref. [452].

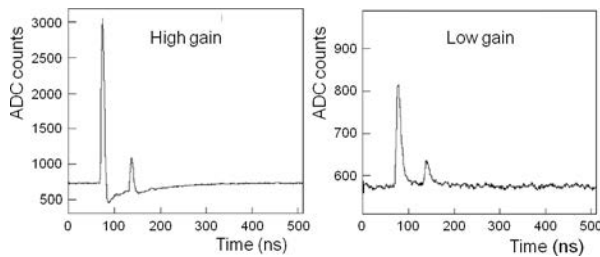


FIGURE 5.31: FGD waveform example showing a Michel electron signal in both the high and low gain processing paths. Each bin is 20 ns. Figure from Ref. [452].

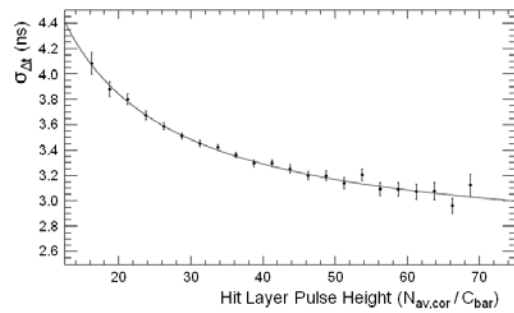


FIGURE 5.32: Time resolution as a function of the light yield. Figure from Ref. [452].

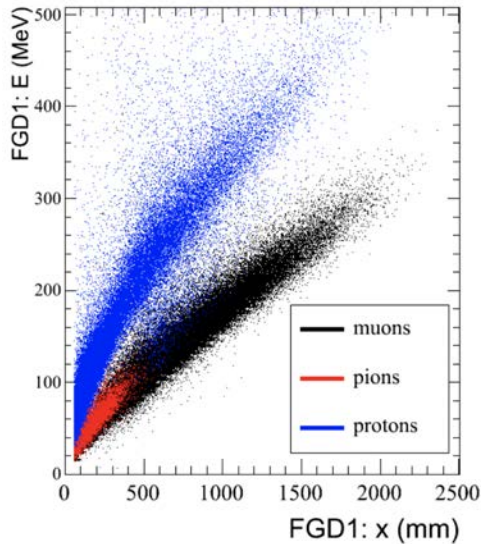


FIGURE 5.33: Reconstructed energy deposit vs track length in FGD1 for fully contained tracks, using MC. Figure from Ref. [455].

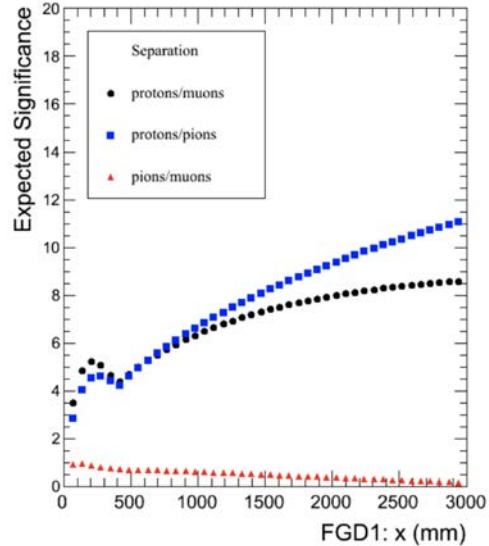


FIGURE 5.34: Pull separation obtained for different particle hypothesis using fully contained FGD1 tracks, using MC. Figure from Ref. [455].

5.5.6 Time-Projection-Chambers (TPCs)

The ND280 TPCs [456], see Figure 5.36, consist of two rectangular boxes one inserted within the other, with the innermost volume divided in two halves by a central cathode. The inner box, see Figure 5.37, made of copper-clad G10, contains the drift volume. The inward looking panels

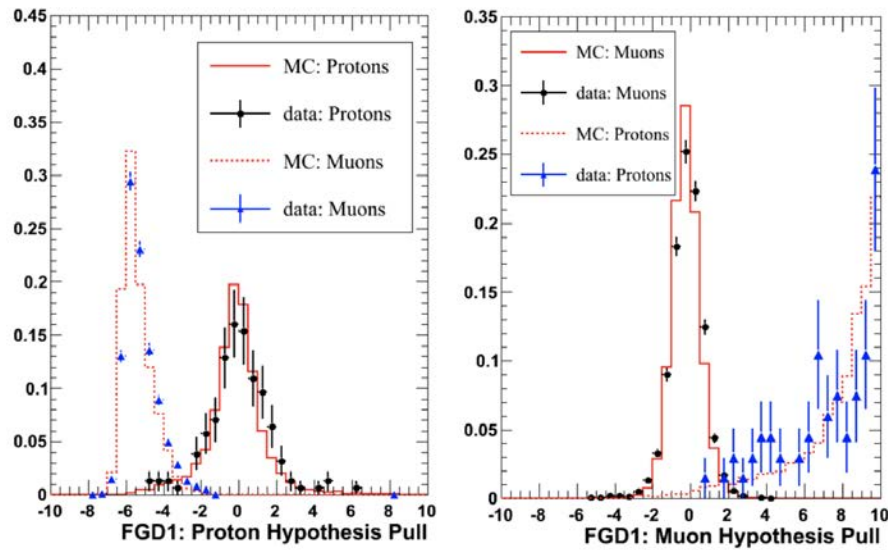


FIGURE 5.35: FGD1 pulls showing excellent agreement in data vs MC and great separation for different particle types. Figure from Ref. [455]

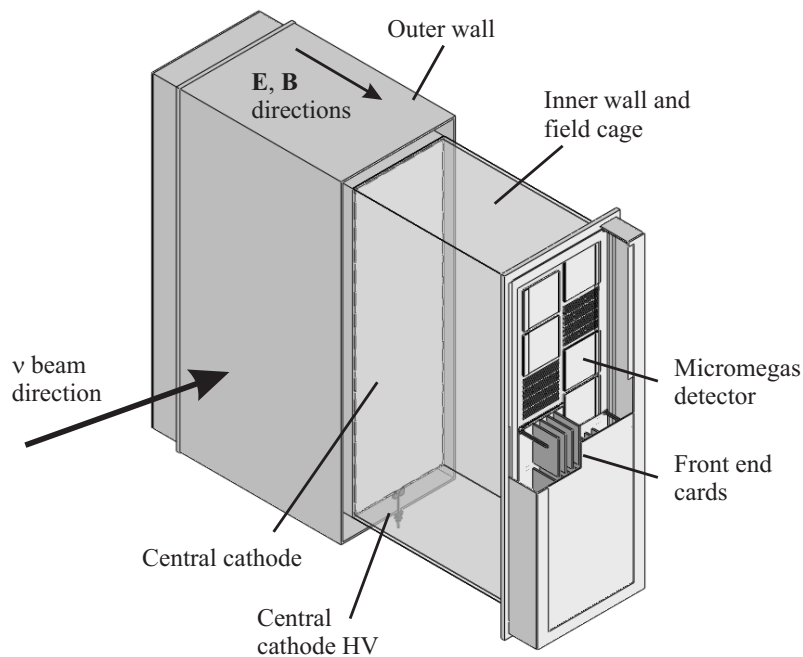


FIGURE 5.36: Sketch of one of the ND280 TPCs. Figure from Ref. [418].

of this box were machined to form an 11.5 mm pitch copper strip pattern which, in conjunction with the cathode produces a uniform electric drift field in the drift volume parallel to the ND280's magnetic field. Surrounding this volume, an outer aluminum chamber, see Figure 5.38, is filled with CO_2 acting as an electrical insulator. The main characteristics of the TPCs are summarized in Table 5.3. The readout system is based on bulk Micromegas [457, 458], see Figures 5.39 and 5.40, with $6.9 \times 9.7 \text{ mm}^2$ (vertical \times horizontal) anode pad segmentation, for a total of 1728 pads per module. Two of the pads in one corner are dedicated to provide the mesh high voltage. In total, ND280 uses three identical TPCs, each with 12 bulk Micromegas in both readout planes for a total of 72 Micromegas in the detector. T2K is the first experiment to use Micromegas in a

Outer dimensions	$2.5 \times 2.5 \times 1 \text{ m}^3$
Maximum dirt distance	90 cm
Gas mixture	Ar:CF ₄ :iC ₄ H ₁₀ (95:3:2)
Cathode High Voltage	25 kV $\rightarrow E = 280 \text{ V/cm}$
Drift speed	7.9 cm/ μ
Transverse diffusion coefficient	$237 \mu/\sqrt{\text{cm}}$
Total number of readout channels	124272
Pad dimensions	$6.9 \times 9.7 \text{ mm}^2$
MicroMegas High Voltage	-350 V $\rightarrow \sim 27 \text{ kV/cm}$
MicroMegas Gain	~ 1500 (at -350 V)
ASIC peaking time	200 ns

TABLE 5.3: TPCs parameters under nominal running conditions. Table from Ref. [410].

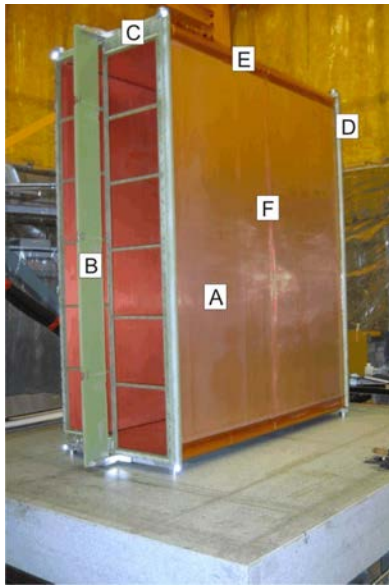


FIGURE 5.37: TPC inner box. A: Inner box walls; B: module frame stiffening plate; C: module frame; D: inner box end-plate; E: field-reducing corners; F: central cathode location. Figure from Ref. [456].



FIGURE 5.38: TPC outer box. A: one of the outer box walls; B: service spacer; C: one of the Micromegas modules inserted into the module frame. Figure from Ref. [456].

physics experiment, which has now become a well established technology. The 12 modules per plane are placed in two vertical columns with a small offset, reducing the inactive regions between the modules. The signal of each module is processed using six front-end electronic cards each with six AFTER ASICs. The inner drift volume has a total volume of 3000 L and is filled with a gas mixture made of Ar:CF₄:iC₄H₁₀ (95:3:2) chosen for its high speed, low diffusion, and good compatibility with Micromegas. Under normal operating flow (10 L/min) the 3000 L drift volume is flushed five times per day. To reduce operation costs a dedicated purifier system recycles about 90% of the drift gas. The gas purity is controlled using two dedicated monitoring chambers. On them, see Figures 5.41 and 5.42, the drift velocity (gain) is measured using ⁹⁰Sr (⁵⁵Fe) radioactive sources, placed at known distances. Additionally, the concentration of contaminants such as O₂ and H₂O is also controlled. Under normal operational conditions both are kept below 2 ppm at the output of the purifier. Prior to its installation, the T2K bulk MicroMegas were studied in a testbench, doing a ⁵⁵Fe scan of the pads. The energy resolution at 5.9 keV was measured to be better than 9%, see Figure 5.43. The gain grows exponentially with the mesh voltage, see

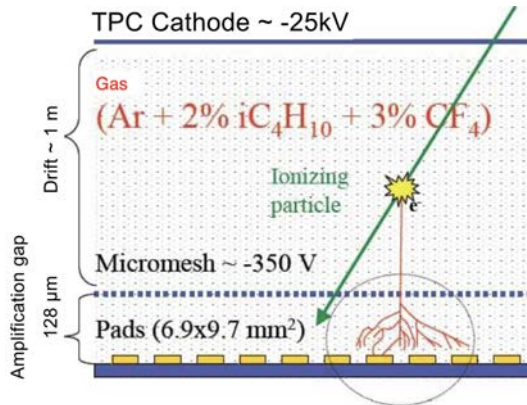


FIGURE 5.39: Schematic view of the Micromegas detector used in T2K. Adapted from Ref. [410].

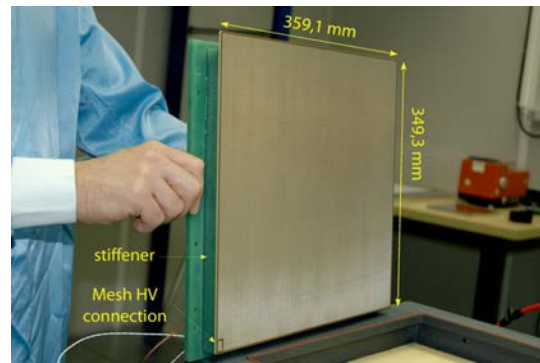


FIGURE 5.40: A bulk Micromegas for the T2K TPCs. Figure from Ref. [456].

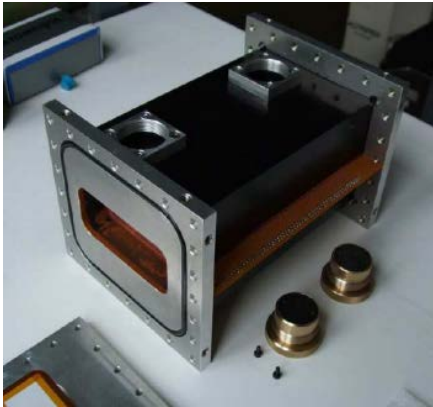


FIGURE 5.41: Picture of one of the monitoring chambers. Figure from Ref. [410].

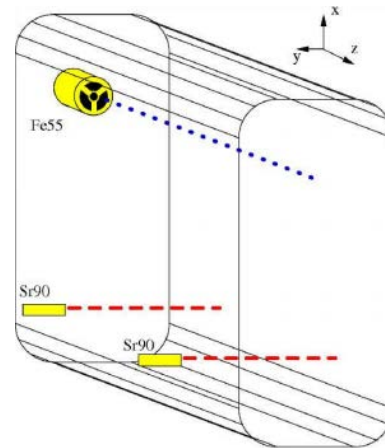


FIGURE 5.42: Radioactive source placements in the monitoring chambers. Figure from Ref. [410].

Figure 5.44, reaching about 1500 with a low spark rate (below 0.1/h) at the nominal mesh voltage of -350V. An excellent pad-to-pad gain uniformity was achieved, as presented in Figure 5.45, with a charge collection resolution better than 3%, presented in Figure 5.46.

The three TPCs in ND280 are identical. They play two main roles in ND280. On one hand, they provide highly precise tracking information for the charged tracks crossing them. This allows to associate a momentum to each reconstructed track by measuring its curvature under the known magnetic field. On the other hand, they measure very precisely the ionization of the tracks providing the best particle identification variables in ND280. Therefore, the two main figures of merit are: the spatial resolution, see Figure 5.47, directly linked to the momentum resolution by the Glückstern formula [409], and the resolution on the energy loss, presented in Figure 5.48. The spatial resolution is below 1 mm for most TPC tracks. It degrades slightly for tracks very close to the anode whose electrons, due to the small drift, experience very little diffusion, reaching fewer number of pads. Although for high $\tan \phi$ values the resolution worsens noticeably, it is necessary to bear in mind that all ND280 analysis select events starting in either the PØD or the FGDs, such that events with tracks with $\tan \phi > 45$ are very rare. The resolution achieved for minimum ionizing tracks crossing 72 rows is 7.8 %, significantly better than the design goal of 10 %. This allows excellent electron-muon separation, see Figure 5.49, crucial to estimate precisely the ν_e component of the T2K beam.

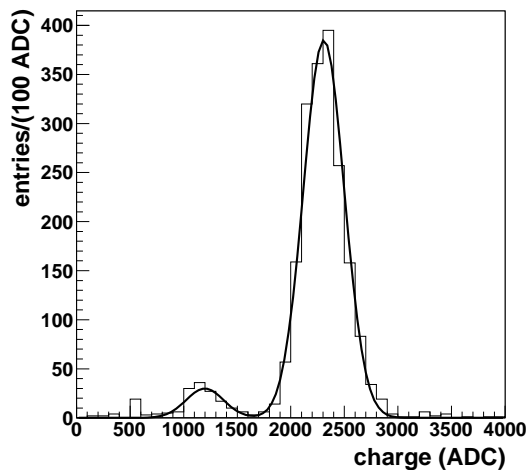


FIGURE 5.43: Measured ^{55}Fe spectrum with a single pad. Figure from Ref. [456].

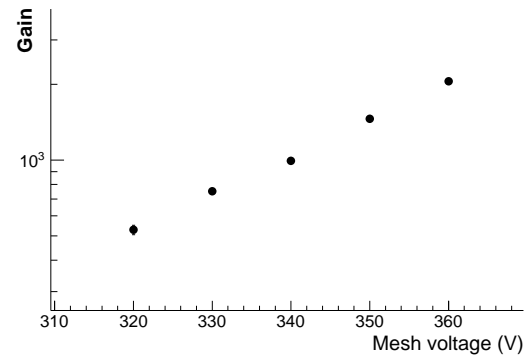


FIGURE 5.44: Gain dependence with the mesh voltage. Note the log-scale in the Y-axis. Figure from Ref. [456].

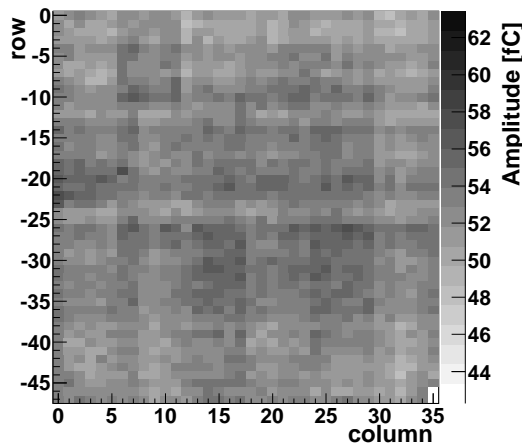


FIGURE 5.45: Gain uniformity, measured as the mean ^{55}Fe charge collected by pad. Figure from Ref. [456].

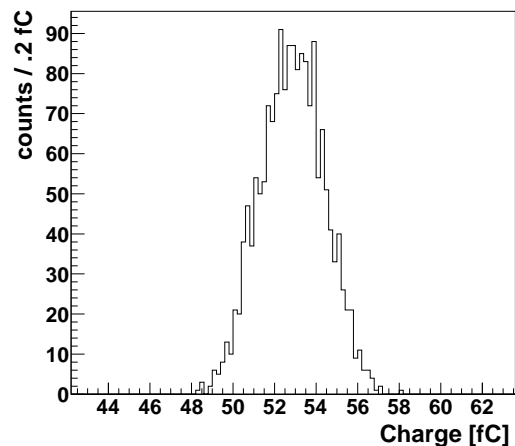


FIGURE 5.46: Distribution of the amplitude values in Figure 5.45. The uniformity is about about 3%. Figure from Ref. [456].

5.5.7 Electronics

ND280 electronics rely on two different chips: The Trip-T [459] and the AFTER [453] ASICs. On one hand, the PØD, the SMRD and the ECal modules have Trip-T based electronics, and so does the whole INGRID detector. On the other hand the TPCs and the FGDs use electronics build around the AFTER chip.

Trip-T based front-end electronics

Trip-T based modules use custom Trip-T Front-end Boards (TFBs) each with four ASICs reading 64 MPPCs. In order to increase the dynamic range of the electronics the signal of each MPPC is split (1:10) and routed to two separate channels of the ASIC, providing a low gain and a high gain output signal. The Trip-T chips integrate the charge in programmable cycles of at least 50 ns, for a total of 23 cycles. The signal is digitized by dual-channel 10-bit ADCs (1024 values). The high gain signals are routed to a programmable (0 to 5 p.e.) discriminator which is used to compute trigger primitives to collect cosmic rays data. The TFBs periodically collect temperature

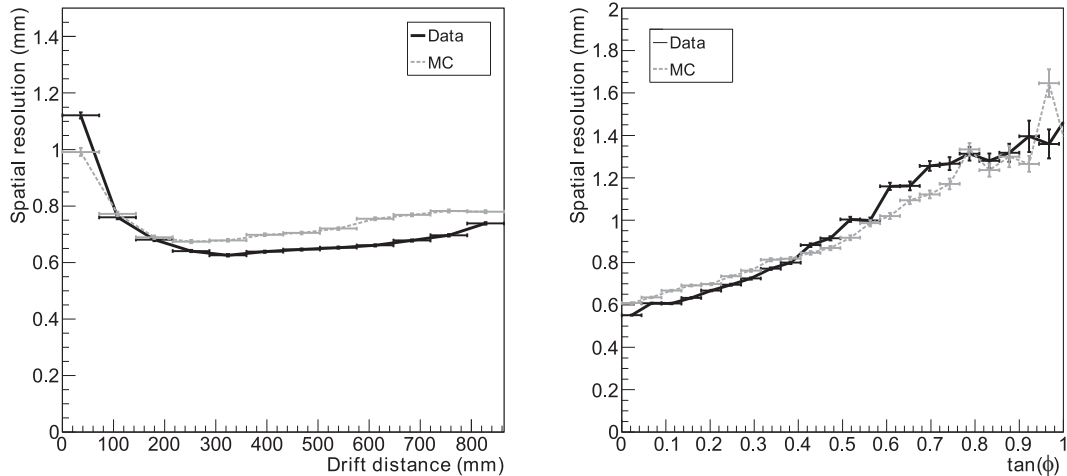


FIGURE 5.47: TPCs spatial resolution for data and MC as a function as the drift distance and the azimuth angle. Figure from Ref. [456].

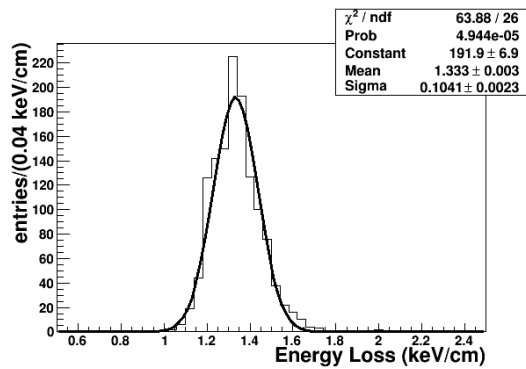


FIGURE 5.48: Distribution of the energy loss in the TPCs for negatively charged particles with momenta between 400 and 500 MeV/c. Figure from Ref. [456].

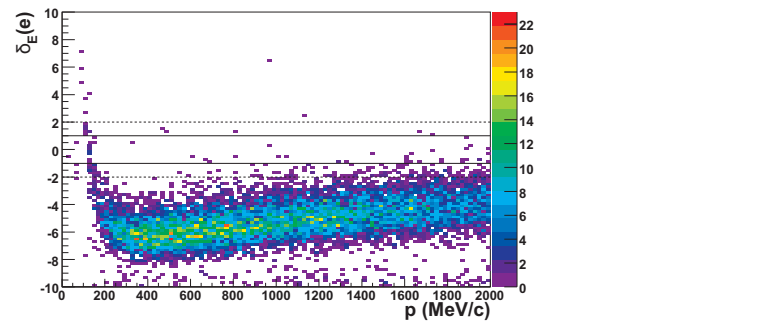


FIGURE 5.49: TPC electron hypothesis for a sample of through going muons of different momenta. Solid and dash lines correspond to a pull of 1 and 2 σ respectively. Figure from Ref. [456].

and voltage information and are controlled by an FPGA which timestamps the signal with an accuracy of 2.5 ns.

FGD and TPC front-end electronics

Although the FGD and the TPC electronics have in the AFTER chip their cornerstone, their front-end electronics are different.

- The FGDs use Front-End Boards (FEBs) containing two AFTER ASICs. In order to cover the whole dynamic range each MPPC is routed to two different channels, such that each FEB can read at most 72 MPPCs. Groups of four FEBs are organized in mini-crates together with a Crate Master Board (CMB). Each FGD is readout by a total of 24 mini-crates. For FGD1 (FGD2) 240/288 (112/288) of the possible channels are used, for a total of 5760 (2688) channels equivalent to 192 bars per layer organized in 30 (14) layers. Although not using all the possible channels might seem sub-optimal, in practice using the same layout for both detectors reduces the system design customization reducing production costs and facilitating the detector maintenance.

- For the TPCs, Front-End Cards (FECs) are used, organized in groups of six connected to a single Front-End Mezzanine (FEMs) card directly mounted on the back of a Micromegas detector. Each FEC handles 288 channels, such that in total each FEM can read exactly the 1728 channels of one Micromegas module. Unlike the FGDs, the TPCs do use a single gain per channel, as it is enough to cover the whole dynamic range. Both the FEBs and the FECs are equipped with 12-bit ADCs (4096 values) sampling the signal at a rate of 50 MHz for the FGDs and of 20 MHz for the TPCs, in both cases providing waveform of 511 samples.

The digitized signals, together with asynchronous control voltage and temperature measurements are sent from the CMBs and the FEMs to the Data Collector Cards Cards (DCCs).

Back-end electronics

The back-end electronics consists of Readout Merger Modules (RMMs), Cosmic Trigger Modules (CTMs), Slave Clock Modules (SCMs) and a Master Clock Module (MCM), all of them using a Vertex II Pro FPGAs from Xilinx, clocking at 100 MHz. The ND280 detector can take data in different modes. When the detector runs on beam mode the master clock module gets signals from the J-PARC accelerator determining when the neutrino spill happens and from a GPS-based clock later used to synchronize the electronics to UTC. In order to collect cosmic data, signals from up to 192 TFBs, including all of the 128 SMRD TFBs and 48 FGD CMBs can be used to trigger using the CTMs. Finally, the electronics of each sub-detector can be configured independently via the SCMs, such that, if necessary, ND280 can run operating only a subset of them. The INGRID detector is run independently from ND280, using an additional MCM and one CTM. A summary sketch is presented in Figure 5.50.

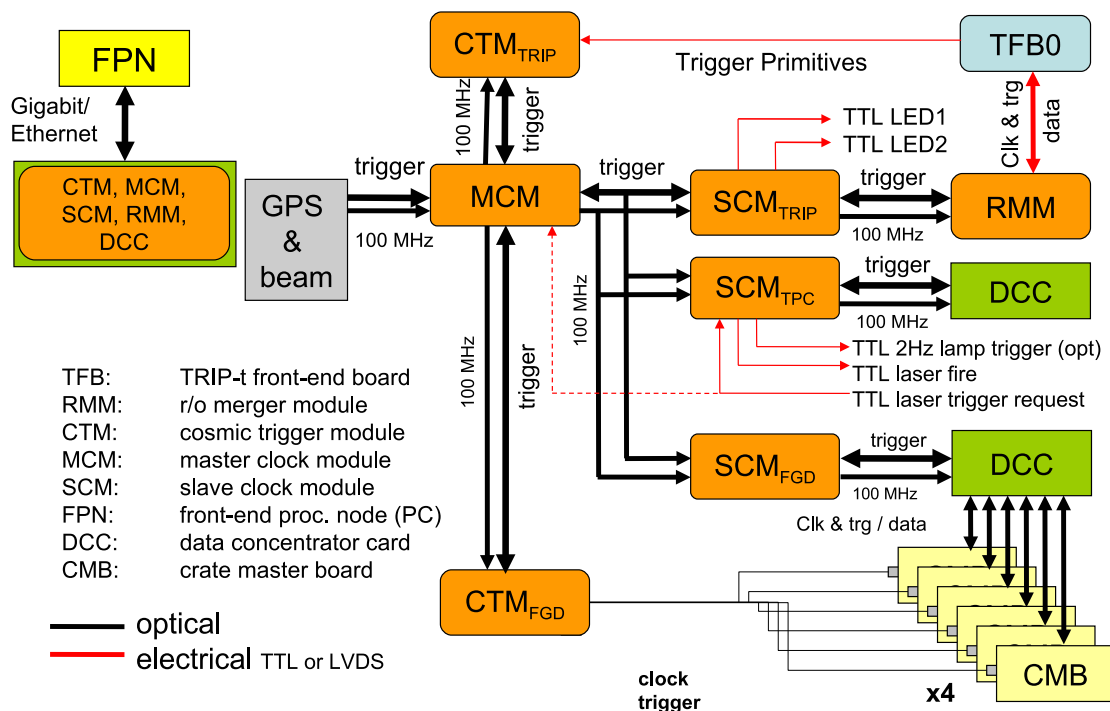


FIGURE 5.50: Layout of the ND280 electronics. Figure from Ref. [418].

5.5.8 DAQ and GSC

The ND280 DAQ and Global Slow Control (GSC) are controlled by a single software application developed using the Maximum Integration Data Acquisition System (MIDAS) package [460].

It runs on commercially available computing machines with the Scientific Linux operating system. MIDAS is interfaced to the hardware via custom C/C++ applications and is used to collect and assemble the event information from the event fragments provided by the different detector submodules. A custom online-monitor allows to display events in real time and access control plots to monitor the data quality. The GSC is built around a central shared memory database named ODB which contains the settings of the electronics and the data of the periodic control measurements (voltage, temperature, status, etc). The ODB data is stored regularly in a MySQL database which is later used to perform offline calibration tasks. MIDAS provides easy access to the status of the detector and allows to modify it interacting with the ODB. A series of alarms and warnings are integrated in MIDAS to ensure a safe and efficient operation of the detector. The GSC is complemented by an electronic logbook system (Elog).

5.5.9 ND280 software

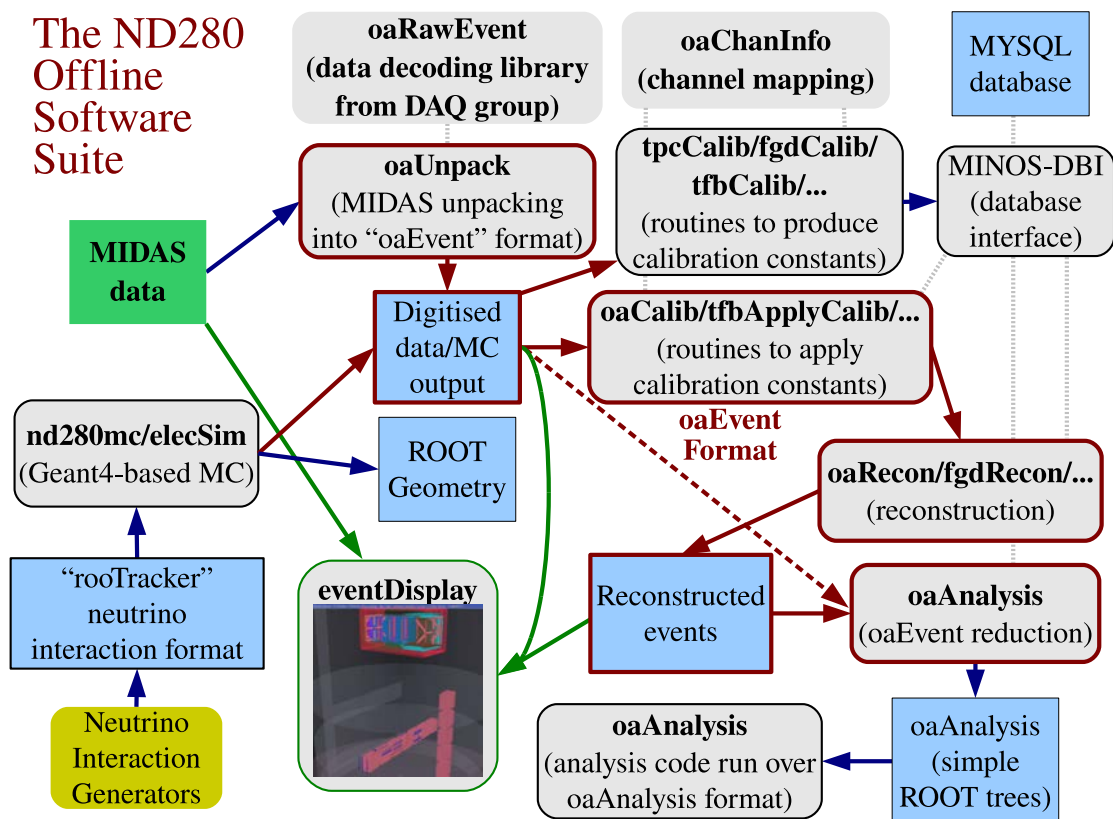


FIGURE 5.51: Simplified diagram of the ND280 Software. Figure from Ref. [418].

The ND280 Software, see Figure 5.51, is built using ROOT [461] as its underlying framework and data storage model. To perform physics simulations the GEANT4 toolkit [462] is used. Although the software was originally managed and built using CMT [463] and CVS [464] was used for version control, in 2021, under the context of the ND280 upgrade they were replaced by more up-to-date solutions, such as CMake [465] and Git [466] respectively.

The ND280 software decodes the DAQ raw data, converts into the ND280 data format, the so-called `oaEvents`, and sequentially performs actions of them, such as applying calibrations based on the associated MySQL GSC data, and applying reconstruction algorithms to build up high level information. The fully-processed reconstructed `oaEvents` are converted into data-reduced

ooAnalysis files which contain the information as ROOT TTrees. The software is automatically documented using Doxygen, which generates files from comments embedded in the code⁸. An event display using the ND280 software is presented in Figure 5.52.

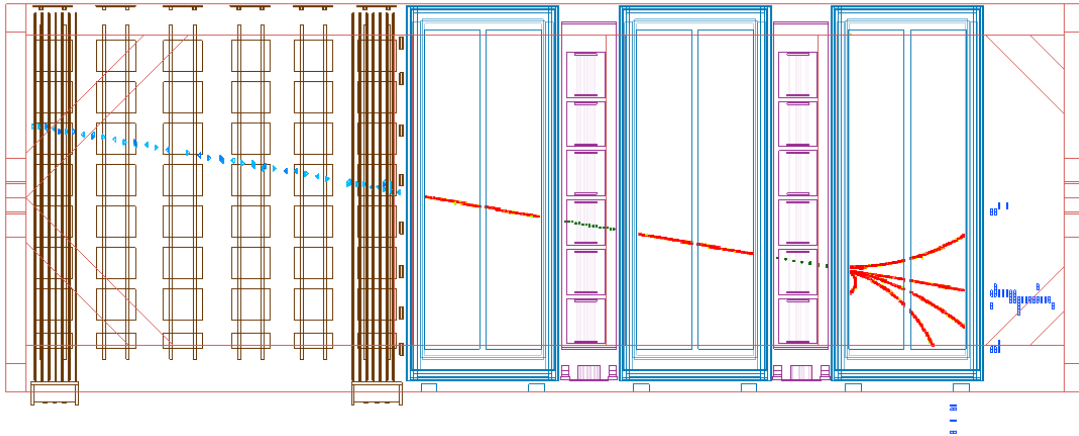


FIGURE 5.52: Event display of a muon crossing in the ND280 basket. The muon enters from the left, and crosses several sub-detectors, creating secondary tracks which are stopped in the ECal. Figure from Ref. [418].

5.6 Super-Kamiokande

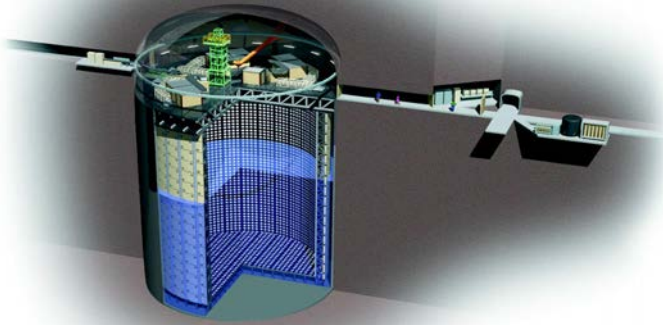


FIGURE 5.53: Computer drawing of the Super-Kamiokande detector. Figure from Ref. [467].

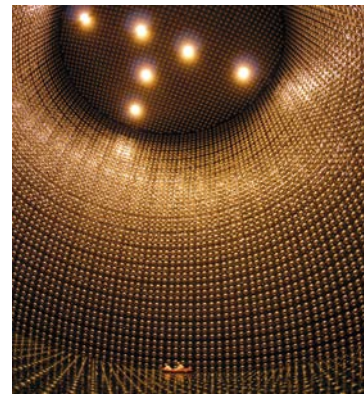


FIGURE 5.54: Picture of Super-Kamiokande's inner detector volume showing most of the inward-facing PMTs. Figure from Ref. [468].

Super-Kamiokande (SK), depicted in Figure 5.53 is T2K's far detector. It is located in the Mozumi mine excavated under mount Ikeno, close to the city of Gifu, in the Japanese prefecture of Gifu, at a distance of 295 km from the neutrino beam production point. Super-Kamiokande is the largest Water Cherenkov detector in the world. It consists of a cylindrical stainless steel tank with a height of 41.4 m and 39.3 m in diameter containing a smaller cylindrical structure with a height of 36.2 m and a diameter of 33.8 m. The innermost cylinder consists of a stainless steel scaffold

⁸The documentation is available for T2K collaborators at: <https://git.t2k.org/nd280/wiki/nd280-wiki/-/wikis/home>.

of about 50 cm wide covered with plastic sheets which optically separate the detector in two volumes, known as the inner detector (ID) and the outer detector (OD). SK is instrumented using PMTs that are placed in all surfaces of the cylindrical scaffold. There are 11,129 inward-facing 50 cm diameter PMT's measuring light in the ID and 1,885 outward-facing 20 cm diameter PMTs in the OD. SK's volume is filled with highly pure water to have good optical transparency. Its total volume is of 50 kT and its fiducial volume is of 22.5 kT.

SK studies neutrinos measuring the Cherenkov light of the final state particles produced by neutrino scatterings in the water. Since the Cherenkov light emission happens at a given angle, a light cone is formed around the track propagating in the detector. When the cone intersects the detector surface it produces a characteristic light-ring pattern. The main strategy to identify the neutrino flavor in SK is to study the light patterns of the rings. Due to its lower mass, electrons are more affected by Coulomb scatterings than muons, such that their rings appear more fuzzy. This is used to build highly powerful particle identification variables, as presented in Figure 5.55

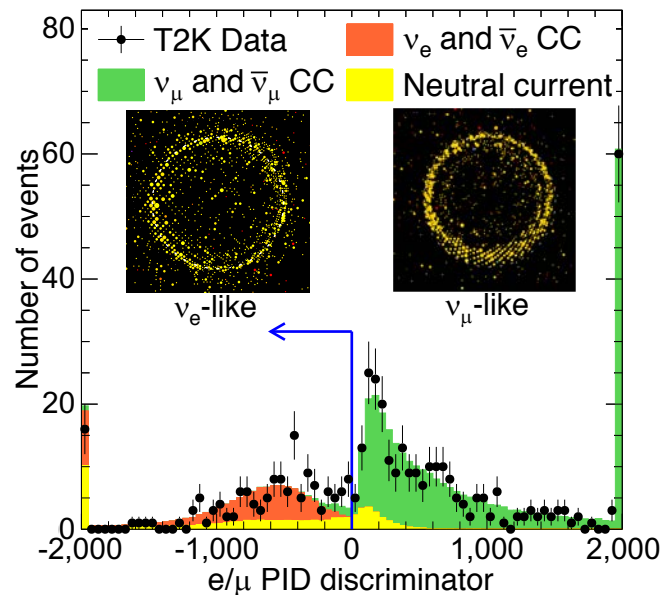


FIGURE 5.55: Electron/Muon discrimination at SK based on light-ring patterns. Figure from Ref. [1].

Chapter 6

Motivations and analysis strategy

“Science in textbooks is not fun. But if you start doing science yourself, you will find delight.”

– MASATOSHI KOSHIBA

This Chapter discusses the motivations to study $\text{NC}1\pi^+$ interactions and reviews the state-of-the-art knowledge and existing measurements for this process. In addition, the strategy and key concepts to perform a new analysis using T2K data are outlined.

6.1 Introduction and motivations

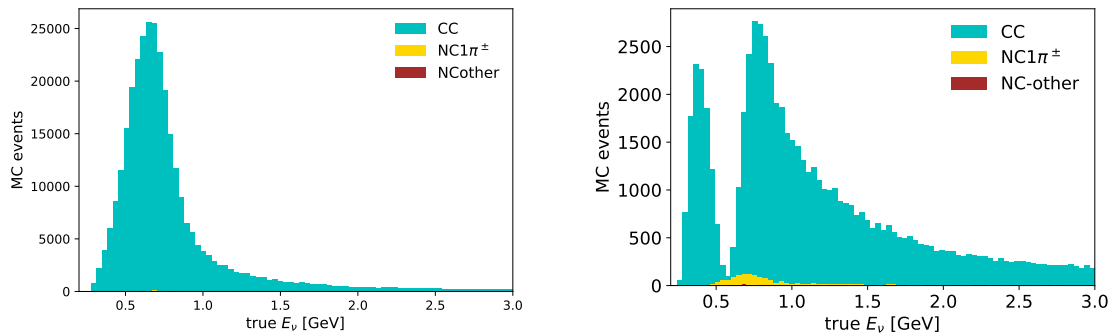


FIGURE 6.1: Selected events in SK for the 1- μ ring sample using the cuts described in T2K-TN399 [469] without (left) and with (right) oscillation weights applied ($\theta_{23} = 45^\circ$, $\Delta m_{23}^2 = 2.5 \cdot 10^{-3}$ eV).

Neutrino NC interactions producing a single charged pion in the final state ($\text{NC}1\pi^\pm$) are an important background for the study of θ_{23} and Δm_{23}^2 via $\nu_\mu \rightarrow \nu_\mu$ (and $\bar{\nu}_\mu \rightarrow \bar{\nu}_\mu$) oscillations in T2K. Since T2K has world-wide leading sensitivity to these parameters, constraining as much as possible its associated uncertainty is of great interest. In $\text{NC}1\pi^\pm$ interactions, the outgoing pion can mimic the muon signal in Super-Kamiokande (and in the future in Hyper-Kamiokande), such that $\text{NC}1\pi^\pm$ interactions are difficult to separate from ν_μ $\text{CC}0\pi$ events, the main signal topology. The energy spectrum of the neutrinos measured in Super-Kamiokande depends both on the oscillation probability and the interaction cross section. NC interactions are insensitive to the oscillation probability. Hence, given that the predominant flavor in T2K’s far detector is ν_τ that is unable to undergo CC for typical T2K neutrino energies, the event rate of the $\text{NC}1\pi^\pm$ background is non negligible when compared to the ν_μ CC signal. To show this effect, Figure 6.1

compares the selected events in the 1-R μ sample with and without applying oscillation weights.

In T2K, the far detector event rate predictions are constrained by measurements in the ND280 detector. However, in ND280 the oscillation probability is negligible such that the fraction of NC1 π^\pm interactions only accounts for few percent of the total. Because of that, isolating a statistically significant sample of NC1 π^\pm interactions with good purity is a very challenging problem. This is also true for all other existing neutrino detectors and, consequently, no measurements have been published for NC1 π^\pm interactions in modern neutrino experiments, as earlier reviewed in Sec. 3.5.2. Some studies were published about four decades ago (two for NC1 π^- [284, 298] and one for NC1 π^+ [298]) using bubble chamber detectors and a methodology significantly different from that being used in modern neutrino experiments. In consequence, no constrains from that data are in use in T2K. The scarcity of existing results, the large uncertainty associated to these processes and its important role in the study of neutrino oscillations in T2K and HK in the future, motivate this new study.

6.1.1 Existing published measurements

As it will be later presented in Sec. 6.2.3, the major fundamental process contributing to the NC1 π^+ topology is $\nu + p \rightarrow \nu + n + \pi^+$. For SK, both NC1 π^+ and NC1 π^- are relevant. However, due to isospin symmetry NC1 π^+ and NC1 π^- process are expected to have similar cross sections. Hence, constraining one would help to constrain both. In any case, it is worth noting that, in analogy to NC1 π^+ , for NC1 π^- the dominant fundamental process contributing to this topology is $\nu + n \rightarrow \nu + p + \pi^-$ interactions.

In total there are three published measurements for this processes, two involving negative pions and the other involving positive pions. In the first place, $\nu + n \rightarrow \nu + p + \pi^-$ interactions were measured at the Argonne National Laboratory (ANL) [284] in 1980 scattering using deuterium target. In the second place, both $\nu + n \rightarrow \nu + p + \pi^-$ and $\nu + p \rightarrow \nu + n + \pi^+$ interactions were measured in 1978 by the Gargamelle experiment (GGM) using a C₃H₈-CF₃Br (propane-freon) target [298].

Among them, the one most closely related to the NC1 π^+ topology studied in this thesis is the only existing $\nu + p \rightarrow \nu + n + \pi^+$ measurement. In this study, a wide energy neutrino beam peaking at 2 GeV was used and total of $1.21 \cdot 10^{18}$ POT were collected. The main goal for the analysis was to demonstrate that Δ resonances were produced in neutrino NC interactions and therefore the results focused on demonstrating that a significant amount of this events were observed over background. In this sense, no cross section measurement was reported and instead event rates were presented. GGM reported 104 events selected as $\nu + p \rightarrow \nu + \pi^- + n$ interactions, which after corrections and background subtractions were estimated to contain 88.4 ± 11.6 true signal events. This error is almost equivalent to the statistical error (± 9.4 events) of the selected sample and therefore does not seem to include a full treatment of the systematic uncertainties associated to the measurement. Nonetheless, this measurement is of great importance as it demonstrated that this types of interactions are likely occurring in nature and it is, moreover, the only published study for this process.

The reported event numbers by the GGM experiment were used more than 20 years later to produce cross section estimates for this process. The estimates were presented at the NuInt02 conference and can be found in Ref. [470]. The quoted values are as follows:

$$\begin{aligned}\sigma_{\text{nuc}}^{\text{GGM}}(E_\nu = 2.0 \text{ GeV}) &= 0.056 \pm 0.011 \cdot 10^{-38} \text{ cm}^2 \\ \sigma_{\text{cor}}^{\text{GGM}}(E_\nu = 2.0 \text{ GeV}) &= 0.08 \pm 0.02 \cdot 10^{-38} \text{ cm}^2\end{aligned}$$

where $\sigma_{\text{nuc}}^{\text{GGM}}$ is the raw cross section result and $\sigma_{\text{cor}}^{\text{GGM}}$ is an associated model-dependent free-nucleon cross section. Unfortunately, no details about the methodology employed to calculate

this values and its associated errors are available in the proceedings, significantly limiting its interpretation.

6.1.2 NC1 π^\pm and T2K's oscillation analysis

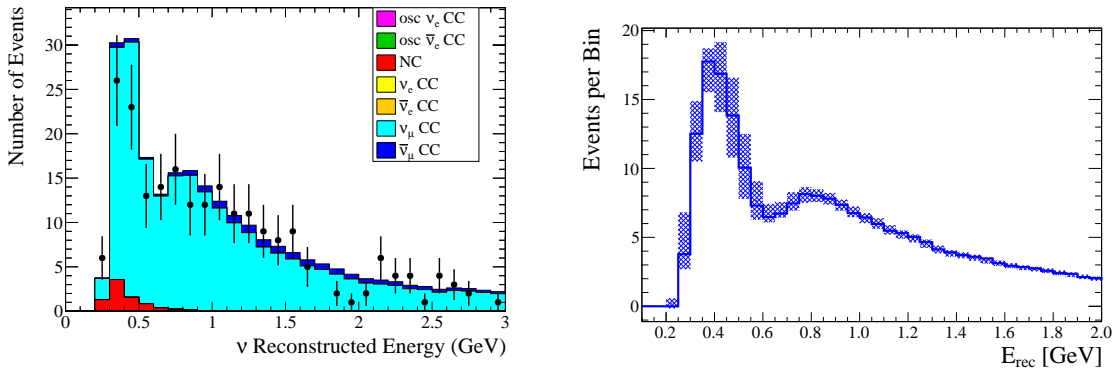


FIGURE 6.2: Expected selected events in SK for the 1 R- μ sample compared to data for T2K OA (2021) and the ND280-constrained binned systematic errors. Notice that the range and binning of the two plots is not the same. Figures from Ref. [2].

The uncertain true value of the NC1 π^\pm cross section is covered in T2K's OA, see Ref. [2], by generous systematic errors. Currently, as later presented, such uncertainty is similar to 59% [471]. This large error budget has a significant impact to T2K's OA sensitivity, specially in disappearance studies, however, quantifying this impact numerically is not trivial¹. In the latest published T2K OA (2021) [2], in the most important signal sample (1 R- μ) a total of 268 events (210 CC0 π) were expected to be selected according to MC. Out of them, 6.4 events (2.4%) are expected to belong to the NC1 π^\pm topologies. Consequently, CC0 π (NC1 π^\pm) events which have a systematic uncertainty similar to 3% (59%) lead to a total event rate uncertainty of ± 6.3 (± 3.8) events. Accordingly, one might think that NC1 π^\pm interactions have only a sub-leading effect to the OA sensitivity. However, NC1 π^\pm interactions pile-up at low reconstructed neutrino energy bins and, consequently, most of their systematic uncertainty is contained on them, making it comparable to the systematic uncertainty for the signal² in those bins. The result is that the total systematic uncertainty in bins before the disappearance dip is much larger than that of the high-energy tail. This effect can be observed in Figure 6.2.

Notably, this uncertainty affects primarily the bins which are more informative of the disappearance parameters. To show this effect, illustrative plots are presented Figure 6.3. In the first place, the depth of the dip determines the value of θ_{23} , being maximal for $\sin^2 \theta_{23} = \pi/4$. In the second place, the neutrino energy reconstruction method relies heavily on the assumption that events are generated by true CCQE interactions. Consequently, true NC1 π^\pm events are migrated towards lower reconstructed energy values, shifting the position of the dip which determines the value of Δm_{23}^2 .

6.1.3 Existing studies and constrains in T2K

To reduce its role in the oscillation analysis, dedicated studies on NC1 π^\pm have been made in T2K in the past both using ND280 and SK. As early as 2012, a study was made using ND280,

¹Mainly because bin to bin and model parameter correlations are important and to get correct numbers would require to run multiple OA fits on fake data (computationally demanding) while varying the systematic error associated to the NC1 π^\pm events.

²The signal uncertainty in those bins is also expected to be larger due to 2p2h among other effects.

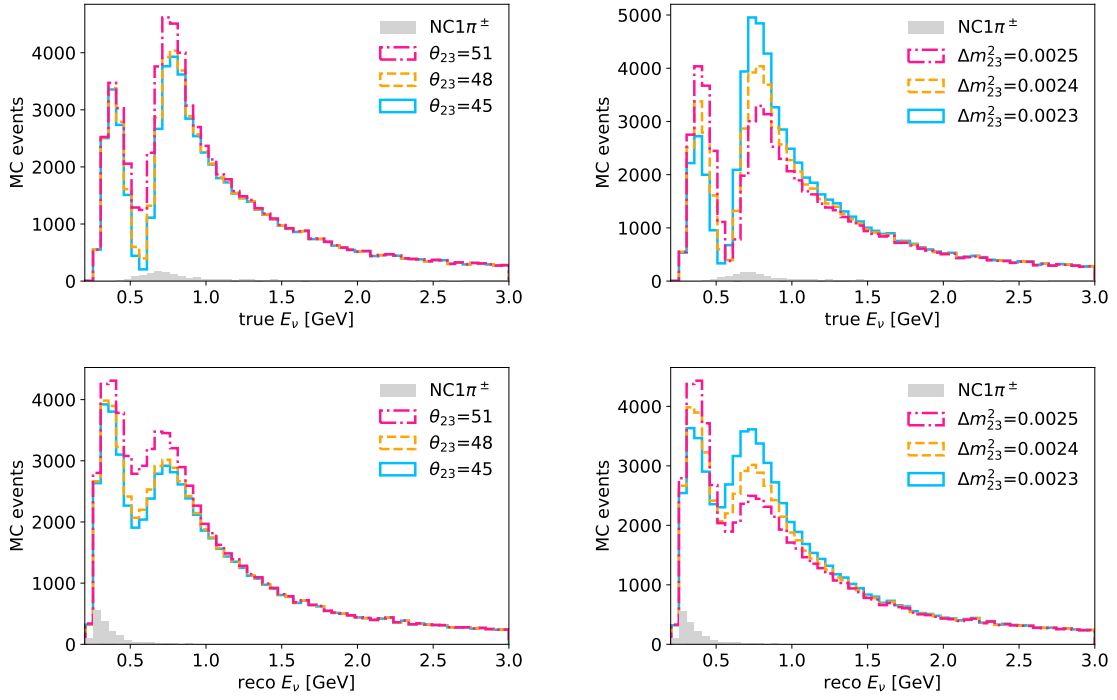


FIGURE 6.3: Expected selected events in SK for the 1- μ ring sample with current OA cuts (described in TN-399) for different disappearance parameters as a function of the true (top) and reconstructed (bottom) neutrino energy. For the left (right) plots $\Delta m_{23}^2 = 2.4 \cdot 10^{-4}$ ($\theta_{23} = 48^\circ$).

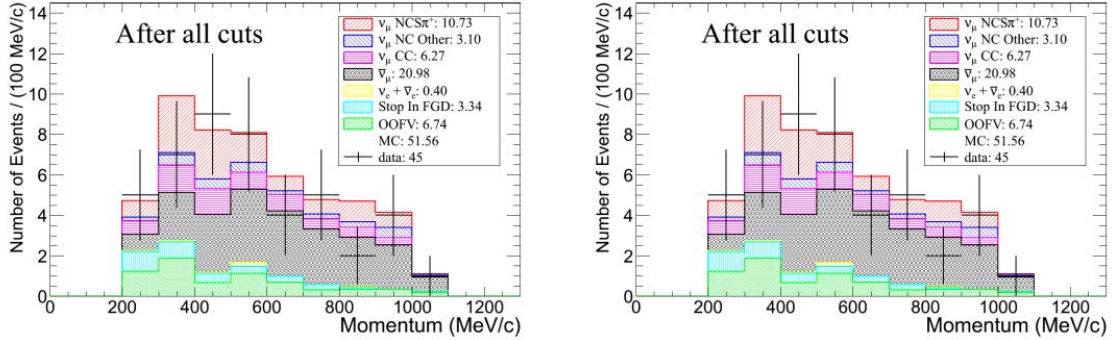


FIGURE 6.4: Final selection results from the first T2K study on $\text{NC}1\pi^+$ (here named $\text{NCS}\pi^+$) as a function of the π^+ momentum (left) and angle (right). Figure from Ref. [455].

described in T2K-TN129 [472]. In this study a total of $1.077 \cdot 10^{20}$ POT (Run 1 and 2) with analyzable quality were used. The signal topology was defined as interactions with only $1\pi^+$ and no other mesons nor protons in the final state with any number of other neutral particles (neutrons and photons) allowed. The cross section was extracted in the reduced kinematic space satisfying $\cos\theta_{\pi^+} > 0$ and $p_{\pi^+} \in [0.2, 1.1]$ GeV. Under this conditions, a selection was developed for which 10.73 signal events were expected, with 20.8% purity and 39% integrated efficiency. The selection results are presented in Figure 6.4. The study reported the following results:

$$\sigma^{\text{data}}/\sigma^{\text{MC}} = 0.382 \pm (\text{stat})_{-0.890}^{+0.852} (\text{syst}) \quad (6.1)$$

$$\sigma^{\text{data}}/\sigma^{\text{MC}} < 1.43 \text{ (68\% C.L.)} \quad (6.2)$$

$$\sigma < 4.3 \cdot 10^{-40} \text{ cm}^2/\text{nucleus (68\% C.L.)} \quad (6.3)$$

This first study allowed to ensure that the 100% normalization uncertainty, used at that time for T2K's OA, was conservative. In particular, it was demonstrated that $\sigma^{\text{data}}/\sigma^{\text{MC}} < 2$ (87% C.L.). The results were not published as the low number of expected signal events and the low purity in the selected sample limited the range of conclusions that could be extracted.

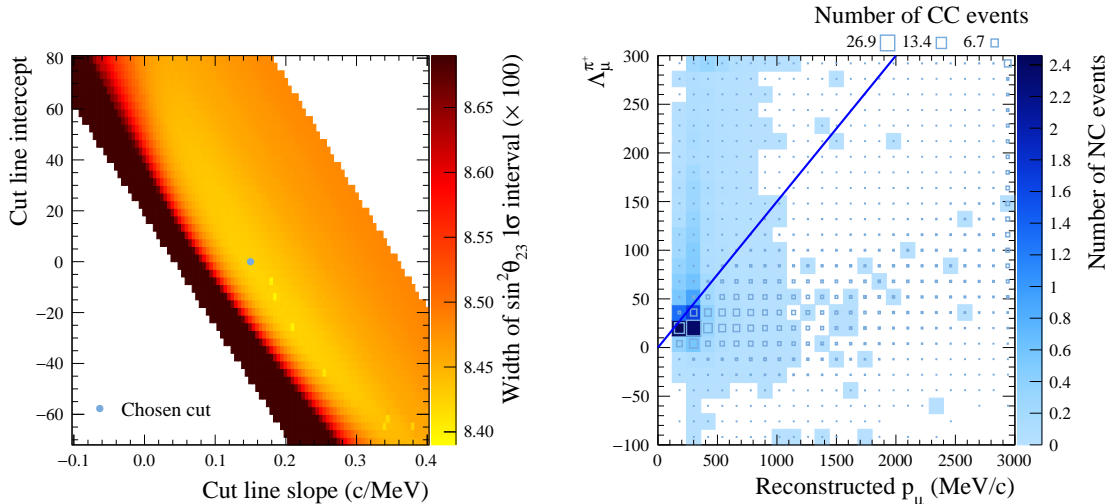


FIGURE 6.5: Left: Reconstructed values of δ_{23} for different cut slopes. Right: NC1 π^\pm chosen cut together with the event distributions of NC1 π^\pm and CC events selected in SK 1- μ ring sample. Figure from Ref. [2].

In 2013 further studies were made involving NC1 π^\pm interactions, this time using atmospheric data in SK. This studies selected a NC1 π^\pm enriched data sample and, comparing the data to MC predictions the systematic uncertainty for the overall normalization for this process was reduced from 100% to 59.19%, the value currently in use. This analysis is presented in detail in T2K-TN159 [473].

Given the large systematic uncertainty for this process, in 2017 a new cut to reject NC1 π^\pm events in SK samples was developed optimizing the cut value to maximize the sensitivity for θ_{23} . A full description of this studies can be found in T2K-TN319 [471]. The cut is presented in Figure 6.5. As of now (2022), this cut is being used in T2K OA, together with the rest of cuts detailed in T2K-TN399 [469].

Currently, considering data up to Run 8, 1.16 POT $\cdot 10^{21}$ POT have been collected with good analysis quality in ND280 for neutrino beam mode³. In this way, there are now about $\times 10.8$ more data than in the former NC1 π^+ analysis using ND280, opening the door to a new analysis with the potential to study this process in detail for the first time in history.

6.2 Analysis overview

The goal of the analysis is to provide a new selection algorithm which preserves the largest statistical sample of NC1 π^+ events ever collected with sufficient purity to draw relevant physical conclusions on this process. In particular, the end-goal is to measure the cross section for this process and to constrain it as much as possible to improve the future oscillation analysis in T2K and Hyper-Kamiokande.

The selection algorithm and the evaluation of its associated systematic errors are presented in detail in the following Chapter. Due to the large increase of available data it was decided to develop a new selection criteria from scratch. The selection aims to identify events generated by

³During runs 10 and 11 ND280 magnet was off due to technical problems such that those runs were mainly intended to collect data with the far detector, and cannot be used for the study here discussed.

the neutrino interaction occurring in FGD1 and therefore it studies interactions of neutrinos with hydrocarbon (C_8H_8). Extending the study to FGD2, which has a fraction of inactive water mass, was not considered in this first attempt as FGD2 tracking capabilities are significantly worse than those of FGD1 and would have required to eliminate some of the most critical selection cuts applied in FGD1. The development of the selection algorithm was blind to the collected data. Namely, it was designed and optimized studying only Monte Carlo generated events and it was compared to data only once the selection criteria had been validated and fixed.

6.2.1 Datasets

In total, three different datasets have been used, two MC samples and the ND280 data. The MC samples consist on ND280 production 6T (6B) which is based on events generated with NEUT 5.4.0 (GENIE 2.8.0). Details on this models have been previously presented in Sec. 3.4. The ND280 data consists of Runs 2,3,4 and 8. The total good POT for this three datasets is summarized in Table 6.1.

Dataset		POT ($\times 10^{21}$)
NEUT	MC p6T	12.9994418552
GENIE	MC p6B	20.3562710541
Data	Runs 2,3,4 & 8	1.1602768366

TABLE 6.1: Summary of the datasets and their associated POT used in the $NC1\pi^+$ analysis.

6.2.2 Signal and background definitions

Defining the true signal and background topologies is crucial for the design of the selection algorithm. For this study the signal, highlighted in color, and the background topologies are defined based on its collection of final state particles (after FSI) in the following way:

- ν_μ **CC0 π** : ν_μ interactions with a muon and without mesons in the final state.
- ν_μ **CC1 π^+** : ν_μ interactions with a muon and a positive pion and no other mesons in the final state.
- ν_μ **CC-other**: ν_μ interactions with a muon which are not included in other topologies.
- $\bar{\nu}_\mu$ **CC**: $\bar{\nu}_\mu$ interactions with an antimuon in the final state.
- $\nu_e/\bar{\nu}_e$ **CC**: ν_e and $\bar{\nu}_e$ interactions interactions with an electron or positron in the final state.
- **NC0 π** : ν and $\bar{\nu}$ interactions without charged leptons nor mesons in the final state.
- **NC1 π^+ 0p**: ν and $\bar{\nu}$ interactions without charged leptons, a single positive pion and no other mesons nor other charged particles in the final state.
- **NC1 π^+ Np**: ν and $\bar{\nu}$ interactions without charged leptons, a positive pion at least one proton and no other mesons in the final state.
- **NCX π^0** : ν and $\bar{\nu}$ interactions without charged leptons and a neutral pion in the final state.
- **NC-other**: ν and $\bar{\nu}$ interactions without a charged lepton that are not included in any other topology.

In addition, we will differentiate between events occurring within the detector volume of interest, often referred to as Fiducial Volume (FV), and events Out Of the Fiducial Volume (OOFV). Hence, all events arising from interactions with a true vertex OOFV will be labeled as OOFV regardless of its true interaction topology.

A major decision was to split the $\text{NC1}\pi^+$ topology in events without protons ($\text{NC1}\pi^+ 0p$, signal) and events with any number of protons ($\text{NC1}\pi^+ Np$ background). This criteria is identical to that in the former study with ND280, earlier presented in Sec. 6.1.3. Events with and without protons are both backgrounds for SK and therefore, ideally, one would want to study both. However, as it is discussed in the next section and throughout the following Chapter, there are strong motivations driving this choice, the key factor being the necessity to use a particular cut that removes numerous background events with signatures very similar to those of $\text{NC1}\pi^+$ events with final state protons.

6.2.3 Initial look into the signal according to MC generators

Before starting the design of a new selection algorithm, it is necessary to understand the signal and background topologies. For this, looking into the fundamental interaction channels contributing to each topology is of great help. A break down of the processes associated to all neutrino interactions occurring in the FGD1 volume, i.e. before any selection cut, is presented for NEUT in Table 6.2 and for GENIE in Table 6.3. To focus only in the most relevant processes, only those producing more than 0.5% of the interactions are shown individually. As it can be seen, both for NEUT and GENIE, ν_μ CC events are by far the most abundant topology in ND280. There are, however, notable differences between NEUT and GENIE. For instance, whereas NEUT predicts more $\text{CC}0\pi$ events, GENIE has a relatively larger contribution of $\text{CC}1\pi$ events. NEUT includes $2p2h$ (about one in every seven $\text{CC}0\pi$ events), whilst GENIE does not. At least in part, this differences can be attributed to the fact that nowadays, neutrino generators get constant updates to better match the insights revealed by experimental measurements over years and, in this regard the p6T (NEUT 5.4.0) uses a much more recent generator than p6B (GENIE 2.8.0). In this sense, a comparison with GENIE v3 would likely show a better agreement, however, fully validated ND280 MC productions based on this generator are not yet available. Nonetheless, the significant difference between both models allows to perform stringent tests on how much neutrino interaction model differences can affect the analysis results.

On the regard of the $\text{NC1}\pi^+$ events without protons (signal) and with protons (background) the predictions for both generators are rather different, as detailed in Table 6.4. GENIE predicts that in a large fraction of events the ejected neutron scatters out a proton, an effect only minor for NEUT. In consequence, for GENIE a large fraction of events are $\text{NC1}\pi^+-Np$ instead of $\text{NC1}\pi^+-0p$. Notably, in the restricted phase space where $\cos\theta > 0.3$ and $p_{\pi^+} > 200$ MeV/c, which is the one that can be better probed with ND280, the difference is much less relevant for both generators. In any case, as neutrino interactions continue to be studied in the next years, the discrepancy in the role of FSI effects for both generators are likely to shrink.

Having this in mind, the studies presented later in Chapter 8 provide a direct (indirect) constraint on the rate of $\text{NC1}\pi^+$ interactions without (with) protons, which, even for GENIE, are about 70% of the total.

To visualize the data a stacked histogram is presented in Figure 6.6. The total fraction of events for each topology, in connection with Table 6.2, is included in the legend. This compact visual representation will be use extensively in the next Chapter. Unless otherwise specified the MC statistics are scaled to the data POT.

Signal and background considerations

From Figure 6.6 and the tables presented earlier a number of conclusions can be extracted which settle the frame to take decisions regarding the analysis strategy.

Topology	Process	Events	[%]
CC0 π	$\nu + n \rightarrow \ell^- + p$	37200.9	36.8
	$\nu + n + X \rightarrow \ell^- + p + X$ (X=(n or p))	5573.1	5.5
	$\nu + p \rightarrow \ell^- + p + \pi^+$	2517.5	2.5
	$\nu + n \rightarrow \ell^- + p + \pi^0$	771.6	0.8
	$\nu + n \rightarrow \ell^- + n + \pi^+$	688.6	0.7
	Others	220.8	0.2
	Total	46972.6	46.4
CC1 π^+	$\nu + p \rightarrow \ell^- + p + \pi^+$	9549.0	9.4
	$\nu + n \rightarrow \ell^- + n + \pi^+$	2946.0	2.9
	$\nu + (n \text{ or } p) \rightarrow \ell^- + (n \text{ or } p) + \text{mesons}$	578.3	0.6
	Others	1184.1	1.2
	Total	14257.4	14.1
CC-other	$\nu + p \rightarrow \ell^- + p + \pi^+$	653.1	0.6
	$\nu + n \rightarrow \ell^- + p + \pi^0$	2850.4	2.8
	$\nu + (n \text{ or } p) \rightarrow \ell^- + (n \text{ or } p) + \text{multi } \pi$	4961.3	4.9
	$\nu + n \rightarrow \ell^- + p + \eta^0$	665.3	0.7
	$\nu + (n \text{ or } p) \rightarrow \ell^- + (n \text{ or } p) + \text{mesons}$	4517.7	4.5
	Others	606.6	0.6
	Total	14254.5	14.1
NC0 π	$\nu + p \rightarrow \nu + p$	7281.6	7.2
	$\nu + n \rightarrow \nu + n$	2358.4	2.3
	Others	1959.1	1.9
	Total	11599.1	11.5
NC1 π^+ 0p	$\nu + p \rightarrow \nu + n + \pi^+$	1092.2	1.1
	Others	209.2	0.2
	Total	1301.3	1.3
NC1 π^+ Np	Total	425.3	0.4
NCX π^0	$\nu + n \rightarrow \nu + n + \pi^0$	1404.3	1.4
	$\nu + p \rightarrow \nu + p + \pi^0$	1727.4	1.7
	$\nu + (n \text{ or } p) \rightarrow \nu + (n \text{ or } p) + \text{multi } \pi$	911.9	0.9
	$\nu + (n \text{ or } p) \rightarrow \nu + (n \text{ or } p) + \text{mesons}$	965.6	1.0
	Others	650.6	0.6
	Total	5659.7	5.6
NC-other	$\nu + n \rightarrow \nu + p + \pi^-$	1023.2	1.0
	$\nu + (n \text{ or } p) \rightarrow \nu + (n \text{ or } p) + \text{multi } \pi$	614.7	0.6
	$\nu + (n \text{ or } p) \rightarrow \nu + (n \text{ or } p) + \text{mesons}$	528.6	0.5
	Others	671.8	0.7
	Total	2838.3	2.8
$\bar{\nu}_\mu$ CC	$\bar{\nu} + p \rightarrow \text{LEpTOn} + n$	1059.9	1.0
	Others	1297.8	1.3
	Total	2357.7	2.3
$\nu_e/\bar{\nu}_e$ CC	Total	1519.4	1.5

TABLE 6.2: Break down of the true interaction topologies of neutrino interactions in FGD1 FV according for the NEUT dataset prior to any selection cut. All interaction modes accounting for less than 0.5% of the events are grouped in a special category named *Others*. Events are normalized to $1.16 \cdot 10^{21}$ POT.

In the first place, the signal topology accounts for only 1.29% of the total number of events in the FGD1 FV. This number is remarkably low when compared to other studies in ND280. For instance, when one considers CC0 π and CC1 π^+ , the two most studied channels in ND280, their relative frequency in the total number of interactions is, according to NEUT, of about 46% and 14% respectively. Sub-dominant processes which have been measured, like ν_e are only about 1.5%. However, ND280 was designed to differentiate very effectively ν_e and ν_μ events, with TPC

Topology	Process	Events	[%]
CC0 π	$\nu + n \rightarrow \ell^- + p$	37513.0	37.8
	$\nu + p \rightarrow \ell^- + p + \pi^+$	2255.1	2.3
	$\nu + n \rightarrow \ell^- + p + \pi^0$	764.6	0.8
	$\nu + n \rightarrow \ell^- + n + \pi^+$	742.3	0.7
	Others	287.9	0.3
	Total	41562.9	41.9
CC1 π^+	$\nu + p \rightarrow \ell^- + p + \pi^+$	11331.6	11.4
	$\nu + n \rightarrow \ell^- + n + \pi^+$	3945.6	4.0
	Others	1467.8	1.5
	Total	16745.0	16.9
CC-other	$\nu + p \rightarrow \ell^- + p + \pi^+$	611.1	0.6
	$\nu + n \rightarrow \ell^- + p + \pi^0$	3593.0	3.6
	$\nu + (n \text{ or } p) \rightarrow \ell^- + (n \text{ or } p) + \text{multi } \pi$	3506.8	3.5
	$\nu + (n \text{ or } p) \rightarrow \ell^- + (n \text{ or } p) + \text{mesons}$	4372.1	4.4
	Others	623.9	0.6
	Total	12706.9	12.8
NC0 π	$\nu + p \rightarrow \nu + p$	7724.8	7.8
	$\nu + n \rightarrow \nu + n$	3266.3	3.3
	Others	1960.0	2.0
	Total	12951.1	13.1
NC1 π^+ 0p	$\nu + p \rightarrow \nu + n + \pi^+$	900.4	0.9
	Others	144.0	0.1
	Total	1044.4	1.1
NC1 π^+ Np	Total	614.0	0.6
NCX π^0	$\nu + n \rightarrow \nu + n + \pi^0$	1953.2	2.0
	$\nu + p \rightarrow \nu + p + \pi^0$	2036.9	2.1
	$\nu + (n \text{ or } p) \rightarrow \nu + (n \text{ or } p) + \text{multi } \pi$	897.8	0.9
	$\nu + (n \text{ or } p) \rightarrow \nu + (n \text{ or } p) + \text{mesons}$	1105.2	1.1
	Others	821.9	0.8
	Total	6815.0	6.9
NC-other	$\nu + n \rightarrow \nu + p + \pi^-$	1597.6	1.6
	$\nu + (n \text{ or } p) \rightarrow \nu + (n \text{ or } p) + \text{multi } \pi$	512.8	0.5
	$\nu + (n \text{ or } p) \rightarrow \nu + (n \text{ or } p) + \text{mesons}$	508.0	0.5
	Others	313.9	0.3
	Total	2932.3	3.0
$\bar{\nu}_\mu$ CC	$\bar{\nu} + p \rightarrow \text{LEpTO}n+ + n$	1070.6	1.1
	Others	1256.7	1.3
	Total	2327.2	2.3
$\nu_e/\bar{\nu}_e$ CC	Total	1422.1	1.4

TABLE 6.3: Break down of the true interaction topologies of neutrino interactions in FGD1 FV according for the NEUT dataset prior to any selection cut. All interaction modes accounting for less than 0.5% of the events are grouped in a special category named *Others*. Events are normalized to $1.16 \cdot 10^{21}$ POT.

PID variables able to separate muon from electron tracks at the 3σ level. Hence, the low relative rate of ν_e interactions is overcome by the design of ND280, which was tailored for this purpose. In the case of NC1 π^+ this is not the case, at least not straightforwardly. Muons and pions are in most cases very difficult to separate in ND280. Hence, pions from NC1 π^+ events and muons from CC interactions, several times more numerous, are very difficult to tell apart. However, the ND280 magnet rescues some chances to measure NC1 π^+ in ND280. In ν_μ CC interactions the outgoing muon is negative whereas in NC1 π^+ events a positive pion is produced. This is of fundamental importance as the charge identification directly separates the signal from the majority of the most

Topology	full PS Process	NEUT		GENIE	
		Events	[%]	Events	[%]
NC1 π^+0p	$\bar{\nu} + p \rightarrow \bar{\nu} + n + \pi^+$	49.0	2.8	60.3	3.6
	$\nu + n \rightarrow \nu + n + \pi^0$	84.0	4.9	30.9	1.9
	$\nu + p \rightarrow \nu + n + \pi^+$	1092.2	63.3	900.4	54.3
	$\nu + (n \text{ or } p) \rightarrow \nu + (n \text{ or } p) + \text{mesons}$	51.4	3.0	32.4	2.0
	Others	24.8	1.4	20.4	1.2
NC1 π^+Np	$\nu + n \rightarrow \nu + n + \pi^0$	18.2	1.1	27.5	1.7
	$\nu + p \rightarrow \nu + p + \pi^0$	102.9	6.0	15.3	0.9
	$\nu + p \rightarrow \nu + n + \pi^+$	139.4	8.1	37.1	2.2
	$\nu + (n \text{ or } p) \rightarrow \nu + (n \text{ or } p) + \text{multi } \pi$	79.1	4.6	421.4	25.4
	$\nu + (n \text{ or } p) \rightarrow \nu + (n \text{ or } p) + \text{mesons}$	27.7	1.6	67.5	4.1
	$\nu + p \rightarrow \nu + p$	22.8	1.3	17.0	1.0
	Others	35.2	2.0	28.2	1.7
NC1 π^+0p	Total	1301.3	75.4	1044.4	63.0
NC1 π^+Np	Total	425.3	24.6	614.0	37.0

Topology	$\cos \theta > 0.3$ & $p_{\pi^+} > 200$ MeV/c Process	NEUT		GENIE	
		Events	[%]	Events	[%]
NC1 π^+0p	$\bar{\nu} + p \rightarrow \bar{\nu} + n + \pi^+$	25.8	3.3	33.6	3.8
	$\nu + p \rightarrow \nu + n + \pi^+$	541.5	68.9	495.5	56.4
	$\nu + (n \text{ or } p) \rightarrow \nu + (n \text{ or } p) + \text{mesons}$	32.7	4.2	27.5	3.1
	Others	25.8	3.3	21.6	2.5
NC1 π^+Np	$\nu + p \rightarrow \nu + p + \pi^0$	19.5	2.5	-	-
	$\nu + p \rightarrow \nu + n + \pi^+$	59.3	7.5	198.3	22.6
	$\nu + (n \text{ or } p) \rightarrow \nu + (n \text{ or } p) + \text{multi } \pi$	41.0	5.2	43.1	4.9
	$\nu + (n \text{ or } p) \rightarrow \nu + (n \text{ or } p) + \text{mesons}$	20.9	2.7	15.3	1.7
	Others	19.4	2.5	43.0	4.9
NC1 π^+0p	Total	625.8	79.6	578.1	65.9
NC1 π^+Np	Total	160.1	20.4	299.7	34.1

TABLE 6.4: Break down of the true processes contributing to the NC1 π^+0p and NC1 π^+Np topologies according to NEUT and GENIE. Only events with a true vertex contained in the FGD1 fiducial volume are considered. The top (bottom) part of the table shows the results in the (restricted) full phase space.

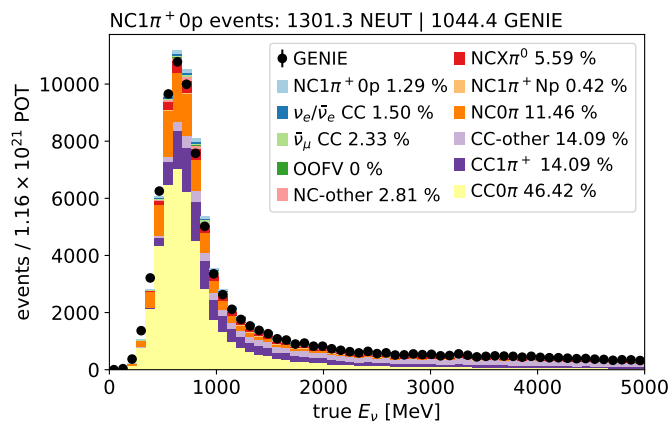


FIGURE 6.6: Stacked histogram with the number of expected events with a true vertex position contained in the FGD1 fiducial volume prior to any selection cut. Notice that there is no OOFV by definition.

numerous background. Notably, due to this discrimination criteria ND280 is not well suited to identify NC1 π^- events with good purity in neutrino beam mode and, consequently, the study here reported is focused on the NC1 π^+ topology.

Even after keeping only those events with tracks reconstructed as positive the scarcity of the signal events allows to envision potential challenges for the selection which are listed below:

- Negative backward-going particles bend in the same way as positive forward-going tracks, potentially escaping the charge identification criteria. Hence, it is necessary to come up with a method to differentiate forward-going from backward-going tracks associated to OOFV.
- In some background events, e.g. $CC1\pi^+$, π^+ are generated in addition to the muons. Hence, finding strategies to tag the additional charged particles in this topologies is crucial to reject this events.

This challenges, later presented in detail in Sec 7.2.9, drove the decision to separate the $NC1\pi^+$ topology in events with (background) and without (signal) protons and to limit this studies to FGD1, which has much better tracking capabilities when compared to FGD2.

In addition, it is worth noting that about 2% (11%) of the total interactions are $\bar{\nu}_\mu$ CC ($NC0\pi$) events. For both of these topologies, often, a single charged particle is produced in the final state, making them relevant backgrounds.

Signal kinematics and ND280 acceptance

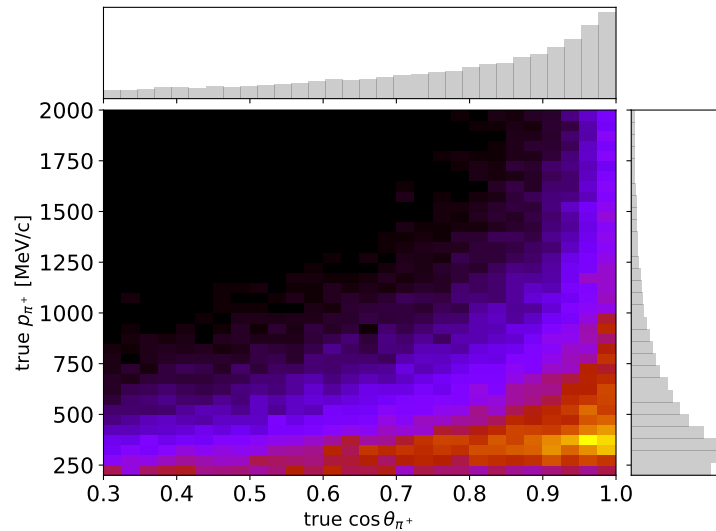


FIGURE 6.7: Density of events in the true kinematic variables of the outgoing π^+ for signal topology. Marginal 1D distributions are also presented for shape-only visualization.

When measuring interactions the acceptance of the detector needs to be considered. In ND280, most FGD1 tracks starting with low momentum or high angle do not reach the TPCs. When this happens, insufficient information is available to identify reliably the $NC1\pi^+$ signal events. Due to this, our study aims primarily to select efficiently and with good purity events with relatively horizontal angles ($\cos \theta_{\pi^+} > 0.3$) and not too low momenta ($p_{\pi^+} > 200$ MeV/c). Interestingly, only about 50% of the signal events satisfy the former conditions. Illustrative distributions of the true π^+ kinematics for signal events starting in the FGD1 FV prior to any selection cut are presented in Figure 6.7. The results show that most pions are expected to be emitted very forward with a typical momentum similar to 300 MeV/c and consequently, ND280's acceptance is well suited to probe the most relevant kinematics phase space of this process at T2K's typical neutrino energies.

Chapter 7

The $\text{NC1}\pi^+$ Selection Algorithm and its Associated Systematic Uncertainties

“En España podrá faltar el pan, pero el ingenio y el buen humor no se acaban.”

– RAMÓN MARÍA DEL VALLE-INCLÁN

This Chapter describes the $\text{NC1}\pi^+$ selection algorithm, its performance and its associated systematic uncertainties. Using the selection algorithm, comparisons between MC and data are presented and discussed at the end of the Chapter.

7.1 The HighLAND2 framework

The selection algorithm was developed within the High-Level ANalysis and Development (HighLAND2¹) framework. HighLAND is a C++/ROOT toolkit built by the T2K collaboration which provides the necessary software infrastructure to perform most of the common tasks needed to perform data analysis using ND280 data. The framework’s core is built upon a series of abstract base classes which perform tasks common to all analysis. In this sense, all ND280 studies are centered around the following loop:

- Load events either from MC or data, spill by spill and bunch by bunch.
- For each event apply corrections.
- For each MC event create an ensemble of *toy* events by random sampling from the underlying detector variables uncertainty distributions.
- For each toy MC event (or data event) iterate over selection algorithms.
- Store the results.

This is steered in code by the parent class `AnalysisLoop` from which all ND280 selection algorithms stem via inheritance. In this way, the logic is preserved through the use of virtual methods in the base classes which guarantee that all analyses share the same logic². This allows to standardize the analysis procedure and organically increase the number of selections and update them over time with a high degree of homogeneity, easing the maintenance of the code, the reproducibility of results over time and to share tools among different studies. In part, this is also

¹For convenience, it is named simply HighLAND hereafter.

²In practice, this is such a standard task that most selections inherit from the higher-level class `baseAnalysis`, stemming from `AnalysisLoop`, which includes basic implementation solutions for most of its virtual methods. Similar examples can be found throughout HighLAND.

motivated by the necessity of stacking up and running in coordination multiple selection algorithms that are used in the oscillation analysis (OA). In consequence, the framework has evolved to consist of two parts, HighLAND, which works as a developing framework interface, often used in cross section analysis and Psyche, a module closely related to HighLAND that contains all the validated selections that are used in the OA.

As earlier presented in Sec 5.5.9, ND280 provides data in `oaAnalysis` format which has been already calibrated and reconstructed. HighLAND provides utilities to unpack the `oaAnalysis` information into the custom HighLAND objects that are the building blocks of HighLAND. In this sense, at this stage the analyzer deals already with vertices and tracks and most hit-level information is unavailable. Three main groups of information are passed onto HighLAND: Reconstructed information, Truth information (for data files it is empty) and Beam information (Beam power, number of spills, total POT, etc). The objects containing the previous information have, in general, a list of methods which allows to read their information, e.g. a track's reconstructed starting position or momentum, and interconnect them. In general, developing a selection algorithm consists in combining these high-level inputs to perform cuts which select a sub-sample of events in order to identify event topologies of interest (signal) and reject the others (background) as effectively as possible. The selection algorithms runs on classes which contain only reconstructed information such that they can be applied in the same manner to both MC and data files. However, in addition, for MC a link³ is provided between the reconstructed objects being handled by the analyzer and the true physical objects producing the detector signatures under investigation. In this way, for a given reconstructed track or vertex, it is possible to check if it has an associated true object and access its information, e.g. true momentum, particle type, etc. Then, true information can be used to run diagnostics on the performance of the algorithm and to get insights on the underlying physics. Notably, vertices true information is passed from the neutrino generator onwards so that the true vertex information can be used during the analysis. This is crucial as it allows to customize the topology definition at the analysis level. Finally, HighLAND output consists of the following blocks:

- A *default* TTree⁴ containing information about the selection effect on each event, e.g. the highest cut reached by the event, and containing as many reconstructed variables as defined by the analyzers such as, for instance, the main track (typically a lepton, for us the π^+ candidate) kinematics.
- A *truth* TTree with a structure analogous to that of the default TTree but containing exclusively true information. The truth TTree contains information of all neutrino interactions occurring in the detector(s) FV, such that it can be used to characterize the efficiency of the selection.
- A *header* TTree with the beam information and that can be used later to normalize the different datasets, e.g. MC and data, by rescaling MC to the data POT.
- A collection of TTrees containing information of the detector systematic uncertainties.

7.2 The $\text{NC1}\pi^+$ selection algorithm

The selection algorithm applies a series of sequential cuts to create a signal enriched sample and three control regions, often referred to as sidebands. All the samples are exclusive, such that events can only be selected in either none or one of them. A summary sketch is presented in Figure 7.1.

Before reviewing the selection steps it must be noted that all plots are normalized to the data

³This is done at the reconstruction level, so it is already fixed at this analysis stage

⁴A TTree is a ROOT [461] object which represents a columnar dataset. Any C++ type can be stored in its columns.

POT (1.16×10^{21} POT). Often, both NEUT and GENIE information is presented. In general, one generator (typically NEUT) is used to provide information broken down either by true topology or true PDG. The other generator is shown as a black dot containing aggregated information, playing the role of fake data.

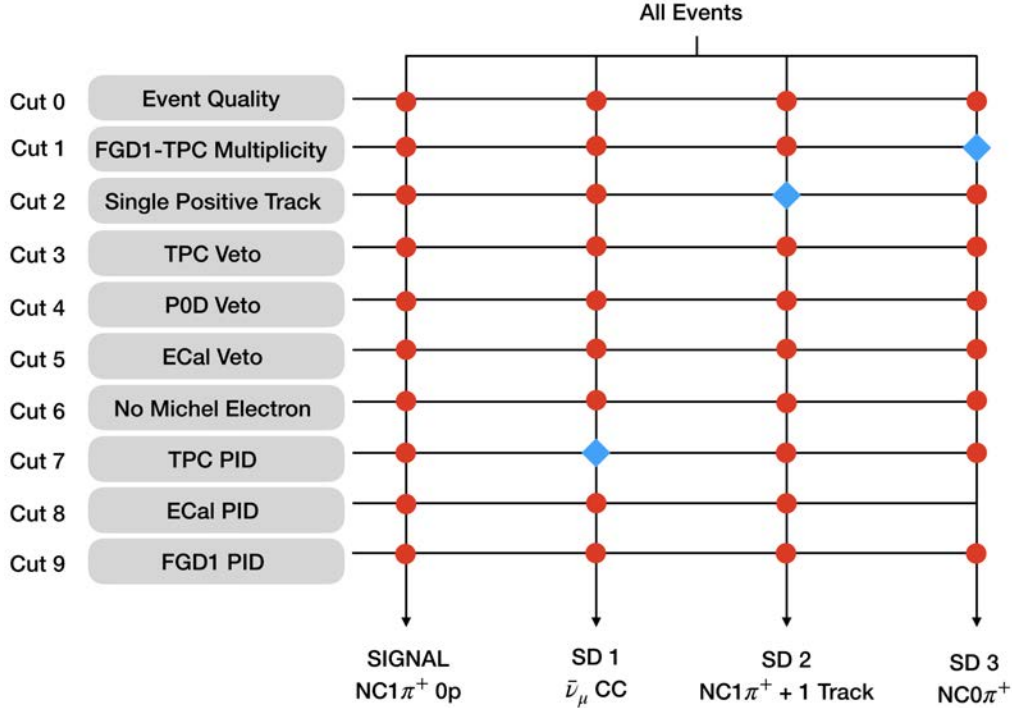


FIGURE 7.1: Diagram of the selection algorithm. Nominal cuts are depicted by red circles whereas alternative cuts are illustrated by blue diamonds. The output consists of four samples: 1 signal sample and three sidebands (SD).

7.2.1 FGD1 fiducial volume definition

The fiducial volume (FV) defines the region of the detector where we want to select neutrino interactions. The use of a FV smaller than the active size of the detector allows to reject troublesome backgrounds leading to a cleaner measurement. In most FGD1 selections the FGD1 active volume is reduced by 57.66 mm (6 bars) on the sides to reduce the number of FGD1-barrelECal OOFV events. Along the beam direction the choice of the FV depends on the analysis. For selections working both with backward- and forward-going tracks, often, no additional FV restrictions are applied. For selections focused on the study of forward-going tracks further downsizing the FGD1 FV allows to reduce the role of OOFV tracks entering to FGD1 from its upstream side. This is particularly important for the study of signals with a low cross section, such as $NC1\pi^+$ interactions, as otherwise OOFV events can significantly outnumber the signal in this part of the detector. Consequently, the first two layers (first FGD1 module) are excluded from the FV definition. Lastly, events starting in the most downstream layer provide insufficient tracking information to apply the last cut of the selection reliably and accordingly the last FGD1 layer is also excluded. In this way, the FGD1 FV is defined by the volume given by:

- $-932.17 < x < 932.17$ [mm] exclude 6 bars left and right
- $-929.51 < y < 819.51$ [mm] exclude 6 bars top and bottom
- $125.843 < z < 437.157$ [mm] exclude 2 bars upstream and 1 bar downstream

7.2.2 Event quality cut

The event quality cut is customary for all ND280 selections. It ensures that all ND280 systems were working under nominal conditions and that the event time is consistent with the beam structure.

7.2.3 FGD1-TPC multiplicity cut

The selection aims to identify events starting in FGD1. In addition, to select $NC1\pi^+$ events with good purity having TPC information is necessary. Since for the signal topology a single track is expected, all events that do not have a single track with both FGD1 and TPC segments⁵ are rejected. If the event is selected, the track satisfying the former condition is the π^+ candidate track.

7.2.4 Single positive track cut

This cut rejects all events for which:

- The largest TPC segment does not contain at least 19 Micromegas clusters. This criteria is standard in ND280 selection as it ensures a reliable interpretation of the TPC information.
- The π^+ candidate track, assuming that it is forward-going, is reconstructed as a negative particle according to the TPC information.
- The π^+ candidate track, assuming that it is forward-going, starts out of the FGD1 FV.
- There are additional FGD1 reconstructed segments. In our signal topology a single charged track is expected in the final state such that additional FGD1 segments are in a very high proportion background events. To control the rejection of true signal events by this last condition all events with only one additional FGD1 segment are selected in SD 2.

In other ND280 analysis time-of-flight⁶ (ToF) information is used to better assess the tracks sense of motion. However, due to time synchronization problems in many sub-runs of Run 8, the ToF information is not reliable in about 45% of the ND280 data intended for this analysis. As backward going tracks are very efficiently separated by the last cut of this selection, which can not be applied to most of the other analysis⁷, the decision was taken to do not use ToF information in this selection as it is not detrimental for the final performance of the algorithm.

Additionally, it was attempted to sub-classify all events at this stage depending on where they were stopping in ND280 (FGD2, Barrel ECal, DsECal or elsewhere) with the aim of tailoring specific selection conditions for each of them based on the available detector information at the stopping point. However, early validation tests revealed that such strategy lead to a cumbersome selection efficiency as a function of the π^+ kinematics and, as no notable performance improvements were achieved, this alternative approach was discarded.

7.2.5 Upstream vetos

Since the selection aims to keep forward going events starting in FGD1 three vetos are applied in order to reduce OOFV events generated by neutrino interactions happening upstream to the FGD1:

- **TPC veto:** Events with TPC1 segments are rejected.
- **ECal veto:** Events with a barrel ECal segment with one of its ends upstream to the end of FGD1 ($z < 447.375$) are rejected.
- **PØD veto:** Events with PØD or PØDECAL segments are rejected.

⁵A track segment is a reconstructed object at the local sub-detector level. Namely, there are TPC1 track segments, FGD1 segments, etc. A global track consists of a collection of matching track segments.

⁶This refers to the time that it takes to a particle to flight from one point of the detector to another.

⁷The last cut works under the assumption that the signal has a single charged track in the final state.

7.2.6 Michel electron cut

Michel electrons (ME) measured in the FGD1 are indicative of a muon or a pion stopping in FGD1, a signature not expected for the signal events. Hence, all events with tagged Michel electrons are rejected. As studied in T2K-TN104 [454], ME in the FGD1 are tagged with a $64.2 \pm 2.0\%$ efficiency, allowing only for a partial rejection of backgrounds with a true ME.

7.2.7 TPC pion likelihood cut

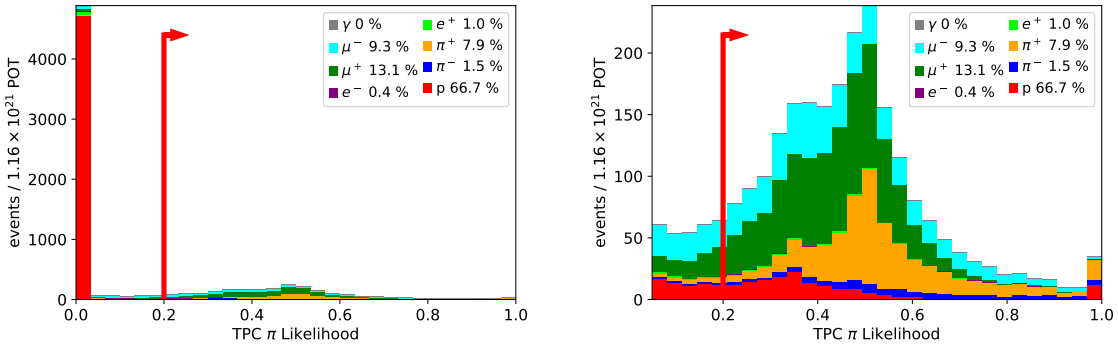


FIGURE 7.2: TPC pion likelihood cut in the whole range of values (left) and limited to $L_{\pi^+} \geq 0.05$ (right).

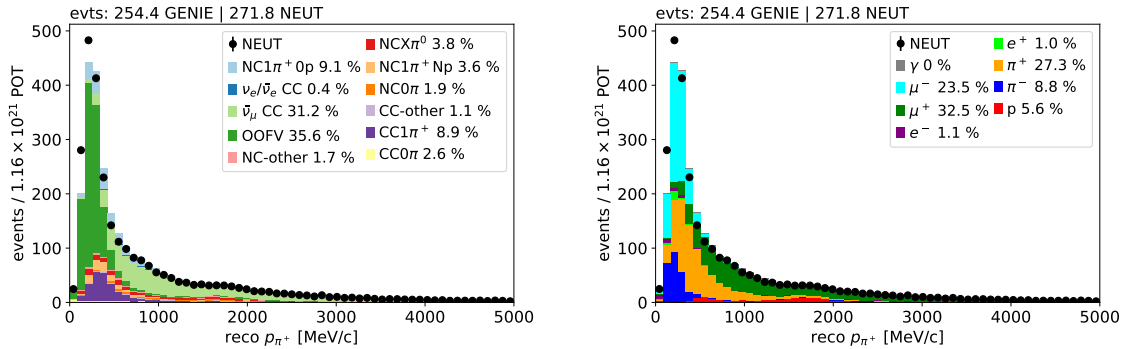


FIGURE 7.3: Selection output after the TPC pion likelihood PID cut as a function of the momentum broken down by true topology (left) and true π^+ candidate PDG (right).

At this stage, about 2/3 of the selected π^+ candidates are protons and only about 8% of them are positive pions. Consequently, to rise the purity of the signal topology it is necessary to increase the purity of the selected particle type. To achieve this, events with a π^+ candidate with a low TPC pion likelihood are rejected.

The cut value was selected by studying its impact directly on the final selection performance on a range of reasonable cut values. This range is defined as follows. The likelihood ranges from 0 to 1 and it gives a fractional score to each track to be an electron, a muon, a pion or a proton. At low momentum, muons and pions have similar behavior such that both get similar scores, which are typically much higher than those of being an electron or a proton, as it can be seen in Figure 7.2. For high momentum, i.e. above 1 GeV/c, protons become less ionizing and muons, pions and protons get similar TPC likelihood scores, much higher than those of being an electron. Accordingly, for both low and high momentum, a true pion is expected to get, at least, a likelihood of $L_{\pi} \leq 0.33$. As the cut on the TPC likelihood has an implicit dependence on the momentum, one needs to be careful to cut on values that do not introduce a kinematic dependence on the efficiency. Due to this, relaxing this cut to values slightly lower than 33% is of potential interest.

A compromise was found cutting at $L_\pi > 0.2$, a value for which the final efficiency is flat in momentum but effectively removes proton tracks with momentum below 1 GeV/c.

The events rejected by this cut, can be used to constrain the $NC0\pi$ background effectively. Hence, rejected events by this cuts are accepted in SD 3. In addition, as the negative of the TPC PID also includes a significant fraction of muons and electrons, in SD 3 additional cuts are applied, namely $L_e \leq 0.3$ and $L_\mu \leq 0.3$.

The results of this cut in the signal sample are presented in Figure 7.3. A major improvement is achieved, as most of the proton backgrounds below 1 GeV/c are rejected. Notably, about 5% of the selected π^+ candidates are still protons, almost entirely selected above 1 GeV/c.

Thanks to the effective rejection of protons, from this point onwards, the main selection backgrounds become OOFV events created by backward going tracks and $\bar{\nu}_\mu$ CC producing forward going muons.

7.2.8 ECal pion likelihood cut

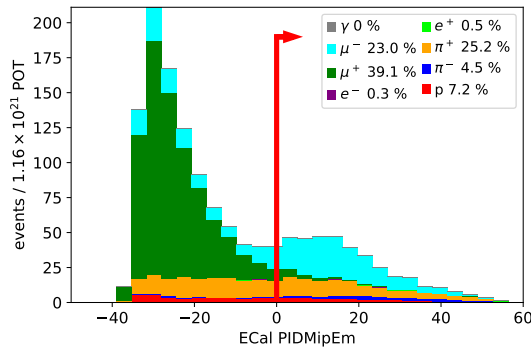


FIGURE 7.4: ECal PID_{MipEm} cut showing the true PDG of particles.

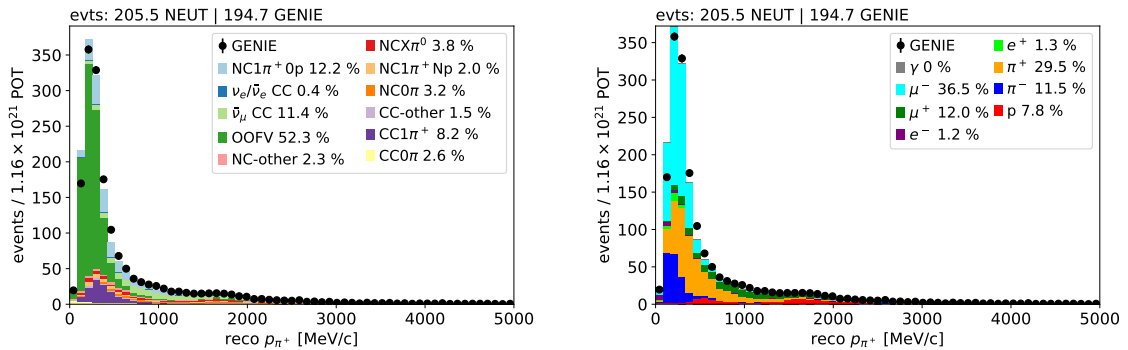


FIGURE 7.5: Selection output after the ECal PID_{MipEm} cut as a function of the momentum broken down by true topology (left) and true π^+ candidate PDG (right).

A majority of the forward going tracks selected at this point are either true positive pions or positive antimuons. Despite both of them producing similar signatures on the TPC due to their close mass values, muons and pions can be in some circumstances separated as they stop.

A particularly well suited detector for this task is the ECal. Pions stopping on the ECal, unlike muons, undergo hadronic interactions producing shower patterns. A variable characterizing this information is the so-called PID_{MipEm} value reconstructed for all ECal segments. This variable is standard in ND280 selections as it has been used for years to tell apart muons and pions in CC selections. As it was constructed, tracks with negative (positive) PID_{MipEm} values are more

track-like (shower-like). Consequently, the selection algorithm separates π -like events from μ -like events using the cut presented in Figure 7.4. On one hand, events without ECal information or with a positive $PID_{MIP}Em$ value are accepted in the signal sample. On the other hand, all events not passing the former condition, i.e. those with negative values for $PID_{MIP}Em$, are rejected in the signal branch but are kept in the $\bar{\nu}_\mu$ CC sideband. The results of the accepted events in the signal sample are presented in Figure 7.5. As it can be seen, this cut very significantly reduces the $\bar{\nu}_\mu$ CC background as intended.

For SD 3, the tracks selected prior to this cut consists already primarily of protons. In consequence, this cut is not used for SD 3.

7.2.9 FGD1 MIP-like cut

At this point, most of the accepted events in the signal sample consist of an event with only one long-ranged track, the π^+ candidate, which in about 30% of the cases is indeed a true positive pion. However, the purity of the signal sample is still low, mainly because of two reasons.

- **Backward-going tracks:** A large population of OOFV events is being selected at low momentum. These events, correspond to negative backward-going particles identified as forward-going pions.
- **CC backgrounds:** A significant amount of CC events starting in the FGD1 FV is being selected. These events, are typically associated to interactions where a positive particle is emitted, which is identified as the π^+ candidate. Most CC events are expected to produce, in addition to the final state lepton, one or more partner charged tracks in the final state. However, in a small fraction of the CC events this partner track is expected to be short ranged or emitted collinearly with the lepton, such that only one FGD1 segment is reconstructed.

In both of the former cases, FGD1 ionization information can allow to reject a significant fraction of these background events, whilst keeping most of the signal. In the case of backward going tracks (pion-like tracks stopping in FGD1), their FGD1 dE/dx is expected to be significantly higher than in the case of forward going π^+ tracks. Similarly, for events where a partner charged track has been untracked in a significant number of occasions its energy deposit is expected to be merged to the π^+ candidate, increasing the ionization of the FGD1 segment.

Albeit a dE/dx -based variable exists for FGD1, the so-called FGD pulls which play a role similar to that of the TPC PID likelihoods, this variable was designed for FGD1 contained track segments, and consequently, it is not well suited for this analysis. Therefore, a new variable to separate signal and background was designed to exploit this information for the case of particles not contained in the FGD1.

Variable definition and cut

The main goal of this variable is to relate the π^+ candidate total energy deposit with its range and to use it to identify MIP-like particles according to their FGD1 information. Consequently, this variable has been named $FGD1MIPLike$.

The correlation between the FGD1 segment energy and range, for all the π^+ candidates in the signal sample prior to this cut, is presented in Figure 7.6. As it can be seen and as expected, whereas a single region is populated by signal events, a second populated region over a blurry scatter distribution are present in background events. The nature of the different distributions is well understood. On one hand, the signal and some backgrounds with a single charged track in the final state, particularly $\bar{\nu}_\mu$ CC background events, follow a similar trend which can not be separated by this method. This trend is that of the expected dE/dx for a single outgoing particle with a MIP-like behavior, which can be visualized clearly on the left panel in Figure 7.6. On the

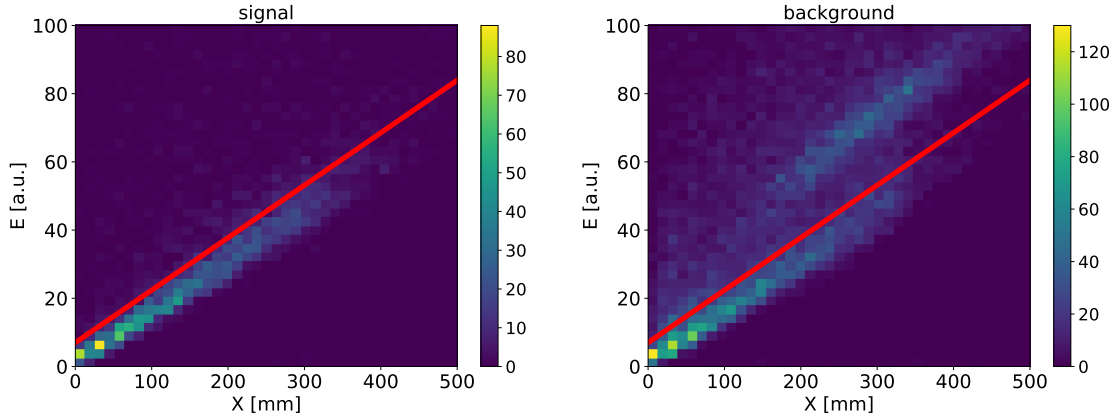


FIGURE 7.6: Energy and range of the FGD1 segments for signal and background events prior to FGD1MIPLike cut. The red line indicates the cut.

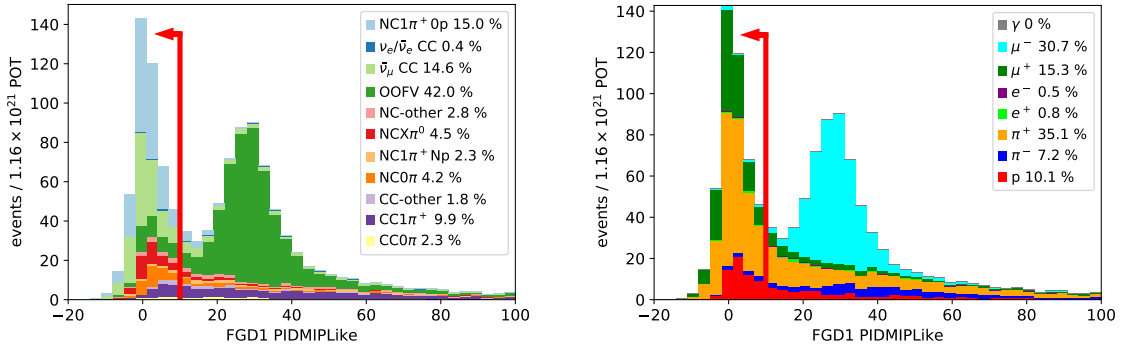


FIGURE 7.7: FGD1 low ionization cut broken down by topology (left) and PDG (right).

other hand, the numerous OOFV events produce a second well defined band with higher dE/dx in the right panel of Figure 7.6, consisting on the dE/dx expected for backward going particles (mostly μ^- and π^-) stopping in FGD1. Finally, also in the right panel of Figure 7.6 a blurry scatter can be seen, associated to events where an untracked charged particle has been merged to the π^+ candidate.

Given the clear and linear trend in Figure 7.6 it is possible to use a linear cut to discriminate signal from background:

$$\text{FGD1MIPLike} \equiv E - \beta X_{\text{cut}} < \alpha \quad (7.1)$$

where E and X are the FGD1 segment energy and range respectively. The coefficients of the variable were set as follows. The slope $\beta = 1/6.5$ ensures the parallelism of the cut with the signal trend. The intercept $\alpha = 10$ was chosen to adjust closely the signal distribution without accounting for significant efficiency losses. The choice of the intercept is later further motivated in Sec 7.4.5 when discussing the validation of this variable using dedicated control samples.

Alternative choices for the parameters were studied via optimization techniques. However, the results using optimization targets such as the purity or a combination of the purity and the efficiency were not completely satisfactory and were disfavored compared to the choices above. The reason for this behavior is that optimization strategies tend to prefer more aggressive cuts that reject more signal events at higher range, where the background is more dense. However, a cut affecting differently tracks with different ranges is difficult to control from the systematic uncertainty point of view, hindering the reliability of the cut.

Under the former definitions, events with $\text{FGD1MIPLike} < \alpha$, i.e. below the line in Figure 7.6 can be considered to be MIP-like according to the FGD1 information and the other way around.

Hence, this cut consists on rejecting all events where the π^+ candidate is not MIP-like in FGD1. The separation power of this variable is presented in Figure 7.7. As it is clear, the variable works as expected, rejecting very efficiently OOFV and CC events and, consequently, this last cut is essential for the final performance of this selection algorithm.

Lastly, it is worth noting that this cut must be used carefully. If the signal definition allows multiple charged particles in the final state, such as any number of protons, then this cut would make the prediction model-dependent. To avoid this problem, in the analysis here presented $\text{NC}1\pi^+0\text{p}$ events and $\text{NC}1\pi^+\text{Np}$ are treated differently. Interestingly, a similar strategy could be used in the future in CC samples to constrain the role of some nuclear effects. For instance, in $\bar{\nu}_\mu$ CCQE interactions, a positive muon and no other charged particles are expected in the final state. Hence, by studying the proportion of events with a MIP-like FGD1 PID one could constrain the amount of neutron to proton FSI, which is one of the main discrepancies between NEUT and GENIE concerning the prediction of $\text{NC}1\pi^+$, as earlier discussed in Sec. 6.2.3.

7.3 Selection performance

As earlier anticipated the selection provides one signal sample and three sidebands. The results for each of them is presented in the kinetic variables of interest, i.e. the π^+ candidate momentum and angle. The efficiency and purity of each sample is also reported as a function of each selection cut.

7.3.1 Signal sample

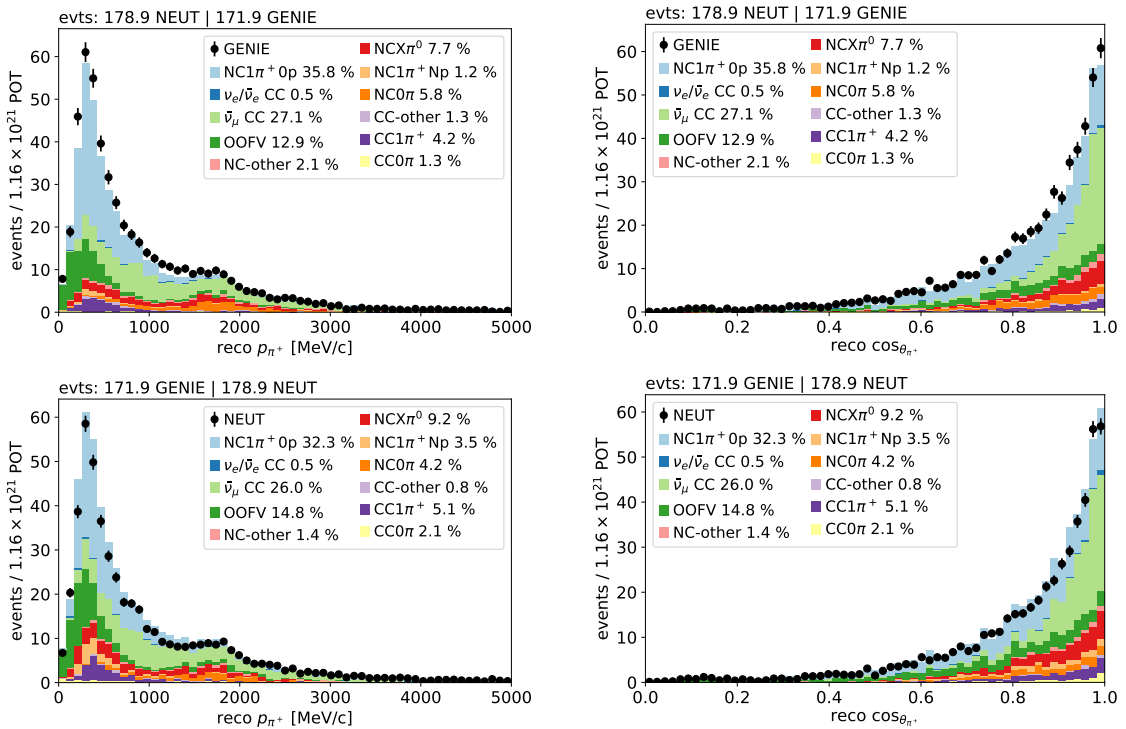


FIGURE 7.8: Signal sample results of the selection as a function of the π^+ candidate momentum (left) and angle (right). The results are broken down by topology with purity detailed in the legend and are presented both for NEUT (top) and GENIE (bottom).

The signal sample has been designed to be enriched in protonless $\text{NC}1\pi^+$ interactions. The results are presented in Figure 7.8. Both MC datasets show good overall agreement, both in the in the

distribution shapes and in the total number of final selected events, which in the full kinematic phase space is similar to 175 events. Slight variations can be observed for NEUT and GENIE as it is expected given the pre-selection event rate predictions presented in Sec. 6.2.3. The selected signal events have typically low momenta and near horizontal trajectories. However, keeping the high-momentum tail in the signal sample is also important as it provides a useful kinematic region to constrain some background topologies which are primarily selected at high momenta.

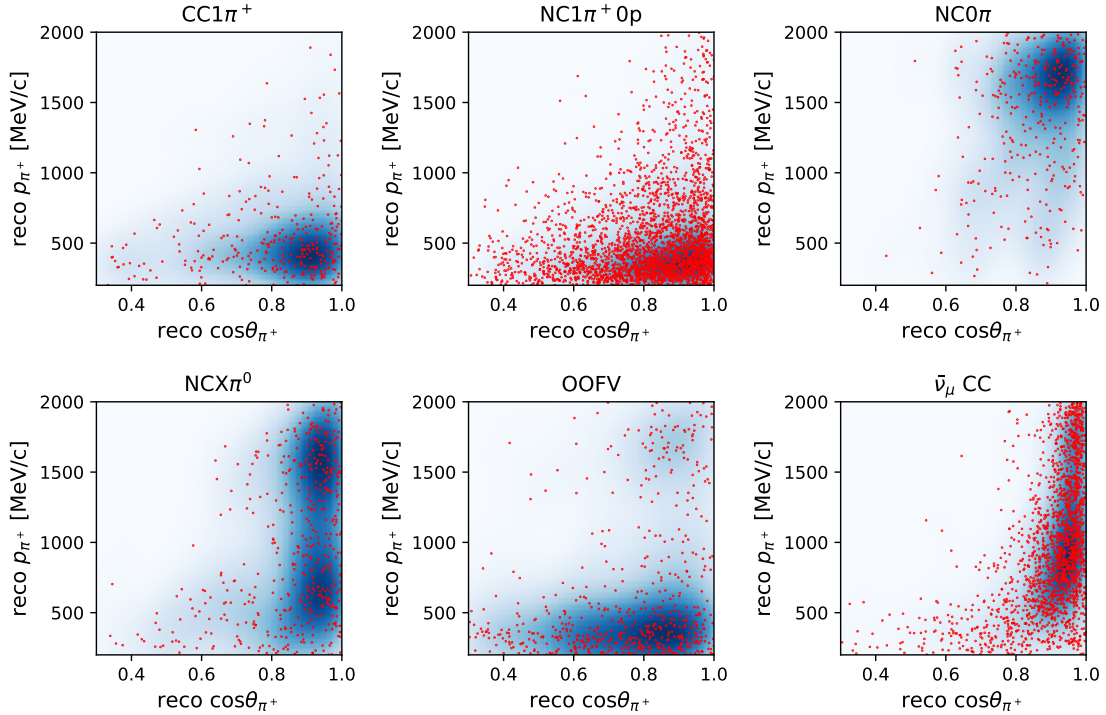


FIGURE 7.9: Distributions of selected events in the kinematic variables of interest for the six most abundant topologies in the signal sample.

The distributions of momentum and angle for the π^+ candidate in the signal sample are presented in Figure 7.9. As it can be seen, a very good separation is achieved in 2D, especially between signal and $\bar{\nu}_\mu$ CC which is the dominant background topology. The signal events are highly localized in the kinematic phase space where $\cos\theta_{\pi^+} > 0.3$ and $0.2 < p_{\pi^+} < 1.0$ GeV/c, so that the selection performance is particularly relevant for events satisfying those conditions. The selection purity for both NEUT and GENIE is presented in Figure 7.10. As it can be seen, the purity is particularly high, about 60% (50%) for NEUT (GENIE), in the bins where most signal is selected and it is generally well above 30% for $\cos\theta_{\pi^+} > 0.3$ and $0.2 < p_{\pi^+} < 1.0$ GeV/c. This is remarkable, as the selection algorithm has its best performance in the most relevant signal region and, consequently, its output can be expected to be highly informative about the signal cross section. For high momentum and angle the purity gradually degrades reaching values similar to 10-20%.

Signal sample composition

A break down of the processes contributing to the signal topology in the signal sample, restricted to $\cos\theta_{\pi^+} > 0.3$ and $0.2 < p_{\pi^+} < 1.0$ GeV/c, is presented in Table 7.1. About 95-97% of the events are expected to be generated by ν_μ . If one considers both neutrinos and antineutrinos, both generators agree in that 96% of the selected events are produced by the true process $\bar{\nu} + p \rightarrow \bar{\nu} + n + \pi^+$ and, accordingly, only the remaining 4% of the selected events arise

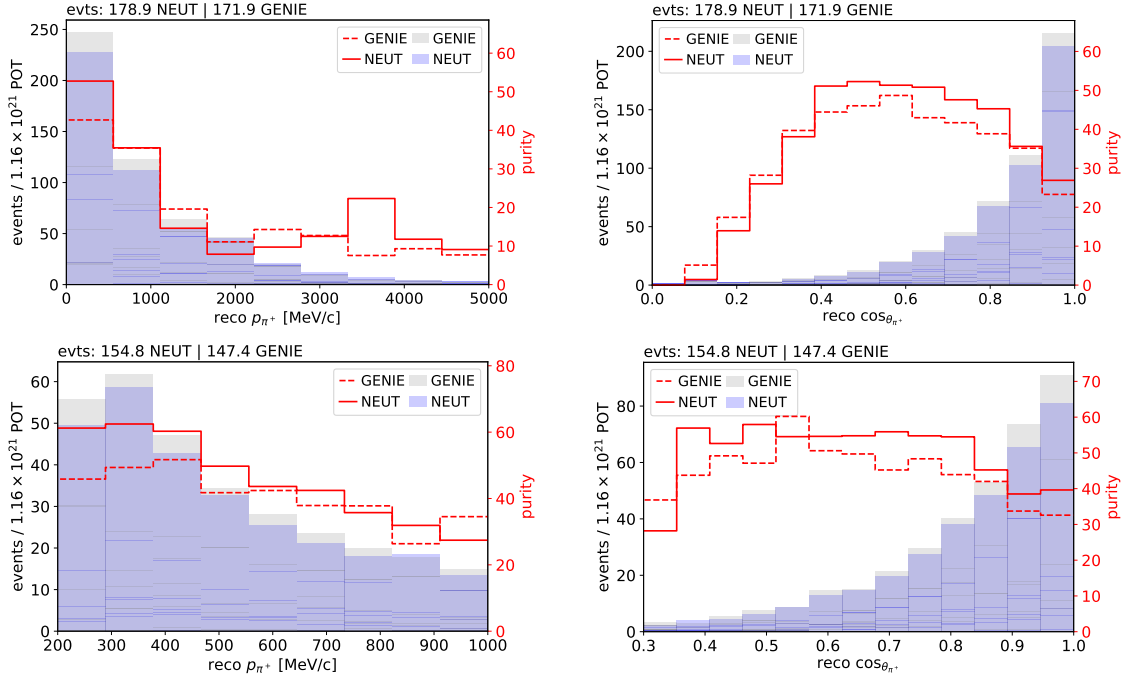


FIGURE 7.10: Purity for the selected signal sample for both NEUT and GENIE. The top (bottom) row shows the results in the unrestricted (restricted) phase space ($\cos\theta_{\pi^+} > 0.3$ & $0.2 < p_{\pi^+} < 1.0$ GeV/c). For a direct comparison the distributions of selected events for NEUT and GENIE is also presented.

Topology	Process	NEUT		GENIE	
		Events	[%]	Events	[%]
NC1 π^+0 p	$\bar{\nu} + p \rightarrow \bar{\nu} + n + \pi^+$	5.75	3.73	8.01	5.47
	$\nu + n \rightarrow \nu + n + \pi^0$	2.90	1.88	2.49	1.70
	$\nu + p \rightarrow \nu + n + \pi^+$	142.60	92.44	133.05	90.88
	$\nu + (\text{n or p}) \rightarrow \nu + (\text{n or p}) + \text{multi } \pi$	1.99	1.29	0.98	0.67
	$\nu + (\text{n or p}) \rightarrow \nu + (\text{n or p}) + \text{mesons}$	1.02	0.66	1.87	1.28

TABLE 7.1: Processes contributing to the signal topology in the signal sample, restricted to $\cos\theta_{\pi^+} > 0.3$ and $0.2 < p_{\pi^+} < 1.0$ GeV/c, by number of events scaled to data POT ($1.16 \cdot 10^{21}$) and by percentage.

from other processes where the particle content has been influenced by FSI. This results are of great importance, as they show a very consistent signal prediction for both generators despite their initial preselection differences and supports the signal topology definition as a robust choice against modeling dependencies. In addition, even if one attributes a large uncertainty to FSI events, the selected sample provides a strong handle on the cross section of the fundamental process $\bar{\nu} + p \rightarrow \bar{\nu} + n + \pi^+$.

Information relative to the processes contributing to the background topologies is presented in Table 7.2. Overall, consistent prediction for both generators are observed with few notable exceptions such as the amount of NC1 π^+ -Np events predicted by GENIE that is studied in the next Chapter.

Topology	Process	NEUT		GENIE	
		Events	[%]	Events	[%]
CC0 π	$\nu + n \rightarrow \ell^- + p$	2.28	1.33	4.00	1.89
CC1 π^+	$\nu + p \rightarrow \ell^- + p + \pi^+$	2.45	1.43	8.28	3.91
	$\nu + n \rightarrow \ell^- + n + \pi^+$	13.32	7.79	11.84	5.59
	$\nu + O(16) \rightarrow \ell^- + O(16) + \pi^+$	1.65	0.97	3.20	1.51
CC-other	$\nu + (n \text{ or } p) \rightarrow \ell^- + (n \text{ or } p) + \text{multi } \pi$	2.56	1.50	1.16	0.55
	$\nu + (n \text{ or } p) \rightarrow \ell^- + (n \text{ or } p) + \text{mesons}$	0.85	0.50	0.71	0.34
NC0 π	$\nu + p \rightarrow \nu + p$	8.88	5.20	7.39	3.49
	$\nu + n \rightarrow \nu + n$	-	-	0.71	0.34
NC1 π^+ Np	$\bar{\nu} + p \rightarrow \bar{\nu} + n + \pi^+$	-	-	0.89	0.42
	$\nu + p \rightarrow \nu + n + \pi^+$	3.24	1.90	14.95	7.06
	$\nu + (n \text{ or } p) \rightarrow \nu + (n \text{ or } p) + \text{multi } \pi$	0.57	0.33	-	-
NCX π^0	$\bar{\nu} + (n \text{ or } p) \rightarrow \bar{\nu} + (n \text{ or } p) + \text{multi } \pi$	0.91	0.53	-	-
	$\nu + n \rightarrow \nu + n + \pi^0$	-	-	0.62	0.29
	$\nu + p \rightarrow \nu + p + \pi^0$	2.11	1.23	2.58	1.22
	$\nu + (n \text{ or } p) \rightarrow \nu + (n \text{ or } p) + \text{multi } \pi$	10.82	6.33	18.87	8.91
	$\nu + (n \text{ or } p) \rightarrow \nu + (n \text{ or } p) + \text{mesons}$	6.83	4.00	7.30	3.45
NC-other	$\nu + n \rightarrow \nu + p + \pi^-$	0.57	0.33	-	-
	$\nu + (n \text{ or } p) \rightarrow \nu + (n \text{ or } p) + \text{multi } \pi$	3.64	2.13	1.87	0.88
	$\nu + (n \text{ or } p) \rightarrow \nu + (n \text{ or } p) + \text{mesons}$	0.68	0.40	1.07	0.50
OOFV	$\bar{\nu} + p \rightarrow \ell^+ + p + \pi^-$	-	-	0.89	0.42
	$\bar{\nu} + n \rightarrow \ell^+ + n + \pi^-$	-	-	1.33	0.63
	$\bar{\nu} + p \rightarrow \ell^+ + n$	0.85	0.50	1.25	0.59
	$\nu + n \rightarrow \ell^- + p$	2.39	1.40	1.96	0.92
	$\nu + p \rightarrow \ell^- + p + \pi^+$	0.85	0.50	2.31	1.09
	$\nu + n \rightarrow \ell^- + p + \pi^0$	0.57	0.33	1.42	0.67
	$\nu + n \rightarrow \ell^- + n + \pi^+$	3.13	1.83	6.05	2.86
	$\nu + (n \text{ or } p) \rightarrow \ell^- + (n \text{ or } p) + \text{multi } \pi$	3.13	1.83	2.94	1.39
	$\nu + (n \text{ or } p) \rightarrow \ell^- + (n \text{ or } p) + \text{mesons}$	4.84	2.83	8.90	4.20
	$\nu + n \rightarrow \nu + n + \pi^0$	1.37	0.80	1.60	0.76
	$\nu + p \rightarrow \nu + p + \pi^0$	-	-	1.07	0.50
	$\nu + n \rightarrow \nu + p + \pi^-$	0.74	0.43	1.60	0.76
	$\nu + p \rightarrow \nu + n + \pi^+$	1.99	1.17	2.31	1.09
	$\nu + (n \text{ or } p) \rightarrow \nu + (n \text{ or } p) + \text{multi } \pi$	1.31	0.77	1.69	0.80
	$\nu + (n \text{ or } p) \rightarrow \nu + (n \text{ or } p) + \text{mesons}$	2.16	1.27	3.29	1.55
$\nu + n \rightarrow \nu + n$	2.28	1.33	2.14	1.01	
$\bar{\nu}_\mu$ CC	$\bar{\nu} + p \rightarrow \ell^+ + n + \pi^0$	1.76	1.03	3.20	1.51
	$\bar{\nu} + n \rightarrow \ell^+ + n + \pi^-$	4.04	2.37	3.47	1.64
	$\bar{\nu} + p + X \rightarrow \ell^+ + n + X$ ($X=(n \text{ or } p)$)	8.08	4.73	-	-
	$\bar{\nu} + p \rightarrow \ell^+ + n$	67.52	39.51	77.70	36.68
$\nu_e/\bar{\nu}_e$ CC	$\nu + n \rightarrow \ell^- + n + \pi^+$	0.68	0.40	-	-

TABLE 7.2: Processes contributing to the background topologies in the signal sample, restricted to $\cos\theta_{\pi^+} > 0.3$ and $0.2 < p_{\pi^+} < 1.0$ GeV/c, by number of events scaled to data POT ($1.16 \cdot 10^{21}$) and by percentage. Only processes contributing to at least 0.5 events are considered.

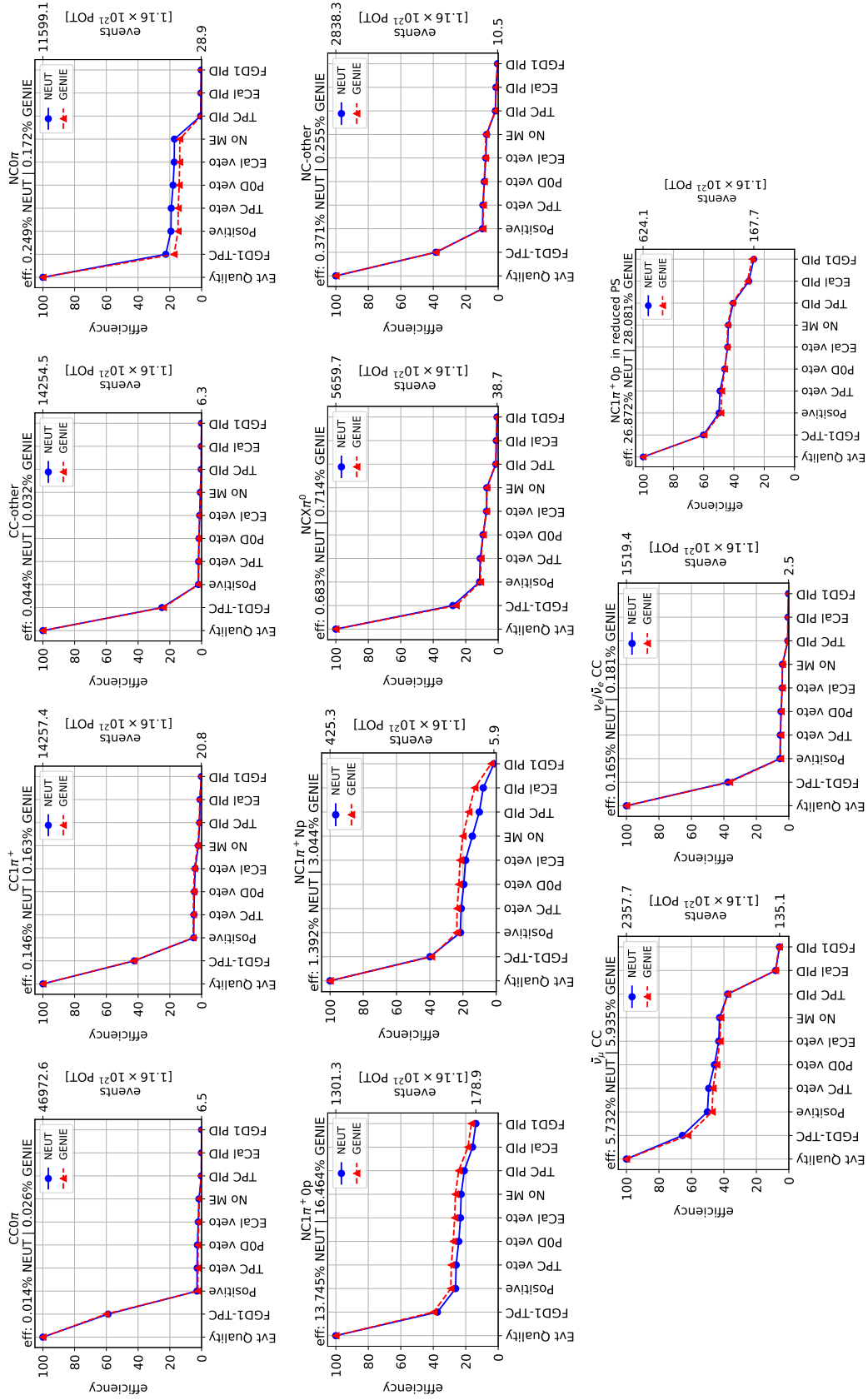


FIGURE 7.1.1: Selection efficiency for each topology in the signal sample. For scale the number of events prior to any cut and after all cuts is shown in the right vertical axis. All plots consider events in the full kinematic phase space with the exception of the bottom right plot that is limited to events where $\cos\theta_{\pi^+} > 0.3$ and $0.2 < p_{\pi^+} < 5.0$ GeV/c.

Efficiency

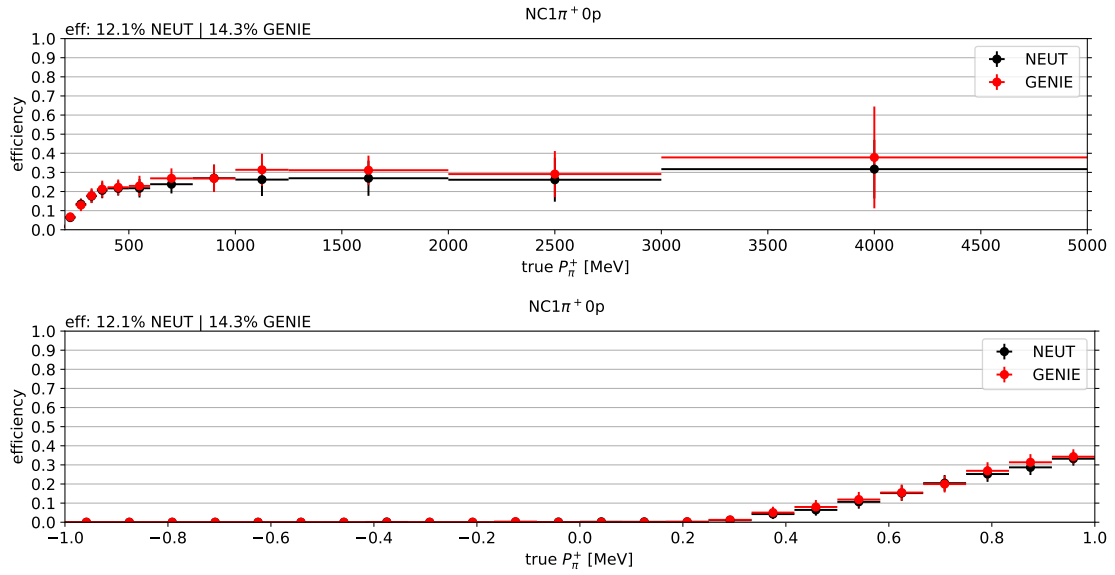


FIGURE 7.12: Selection efficiency for the signal topology in the signal sample in the kinematically unconstrained phase space in bins of momentum and angle.

To show the background rejection power of the selection and to study the role of each cut on all topologies, efficiency plots for different cut levels are presented in Figure 7.11. As it can be seen the background reduction is drastic, with selection efficiencies well below 1% for most background topologies. Even for background topologies with very similar overall properties to those of the signal, e.g. $NC1\pi^+ - Np$ and $\bar{\nu}_\mu$ CC, the selection efficiency is very low. For the signal topology, the overall efficiency is of 13.7% (16.5%) according to NEUT (GENIE). As intended, this efficiency is several times larger than that for any background topology, proving that the selection cuts are effective in discriminating signal from background signatures. When constrained to events satisfying $\cos\theta_{\pi^+} > 0.3$ & $0.2 < p_{\pi^+} < 1.0$ GeV/c in true kinematic space, the efficiency rises to 26.9% (28.1%) for NEUT (GENIE).

Regarding the signal selection efficiency, it is important to understand its behavior to ensure a reliable cross section extraction. As it can be seen in Figure 7.12 the selection algorithm efficiency is very smooth and follows a well understood trend. On one hand, the efficiency rises with momentum until 300 MeV/c, where the efficiency becomes flat. This pattern is the result of the necessary minimum momentum that the pions need to have in order to escape the FGD1 and enter in the TPC1 without curling on themselves. For small momentum only those pions produced in the most downstream layers of FGD1 are selected, decreasing the overall efficiency for those momentum bins. As this momentum rises more layers contribute to the selected sample, until for a momentum of around 300 MeV/c this is no longer a sensible effect and the efficiency stabilizes into a plateau. On the second hand, the efficiency decreases for increasing pion angles with respect to the beam axis. This trend is generated by the forward acceptance of the TPC and it is a well known effect in ND280 also affecting CC selections. Hence, the results show that the selection treats evenly all events without any significant fine tuning nor kinematic dependent cuts ensuring a good reproducibility on data.

7.3.2 $\bar{\nu}_\mu$ CC sideband

In the signal sample, about 2/3 of the selected events are either signal or $\bar{\nu}_\mu$ CC events. The $\bar{\nu}_\mu$ CC sideband was created to constrain this dominant background and to validate its overall modeling

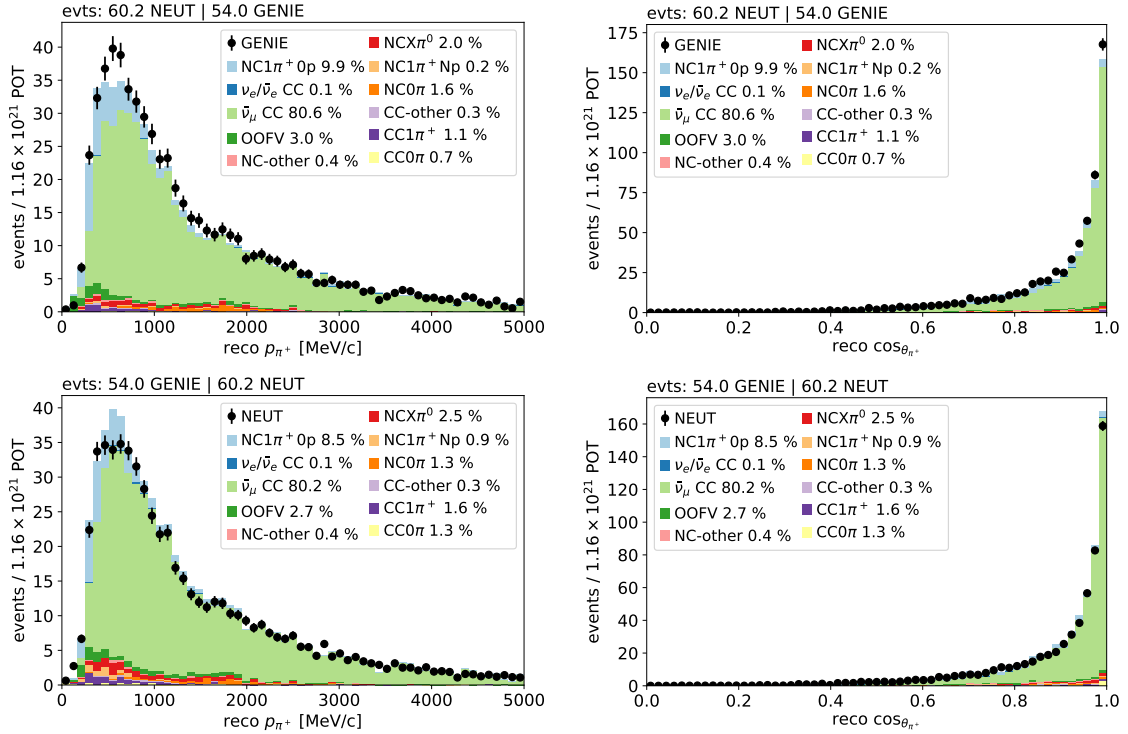


FIGURE 7.13: $\bar{\nu}_\mu$ CC sample results of the selection as a function of the π^+ candidate momentum (left) and angle (right). The results are broken down by topology with purity detailed in the legend and are presented both for NEUT (top) and GENIE (bottom).

by directly comparing it to data. As earlier explained in Sec. 7.2.8, this sideband is created by applying all the cuts in the signal sample but reversing the ECal PID cut. The results, presented in Figure 7.13, show overall good agreement between NEUT and GENIE predictions and have a high purity of $\bar{\nu}_\mu$ CC events, similar to 80% for the whole sample, including a very pure high momentum tail. In total, about 500 $\bar{\nu}_\mu$ CC events are expected to be selected in this sideband. In addition, it must be noted that despite its low overall purity of about 10% (9%) an additional set of 60 (54) signal events are expected to be selected according to NEUT (GENIE).

7.3.3 $NC1\pi^+$ + 1 FGD1 track sideband

The main goal of this sideband is to provide a means to constrain two particularly important types of events. On one hand, signal events were the outgoing neutron reinteracts in the FGD1 FV and creates a track long enough (> 5 FGD1 bars) to create an independent FGD1 segment. On the other hand, the amount of background topologies which, despite of producing an additional charged particle in the final state, are not rejected by the other cuts.

This sideband consists of the same selection algorithm applied to the signal sample with only one but significant difference. Whereas in the signal sample only events with 1 FGD1 segment are kept the events that have an additional FGD1 contained segment are kept in this sideband. Hence, this sideband is particularly intended to constrain events where a π^+ -like particle is produced and selected according to TPC and ECal PID variables but where the final state has an additional particle detected in FGD1. The results are presented in Figure 7.14.

As it can be observed in Figure 7.14, very few events are selected in this sideband given that those events with multiple charged particles in the final state are expected to be typically rejected by the FGD1 PID cut. Interestingly, both NEUT and GENIE show similar results on the amount of signal events, about 9, migrated to this sideband.

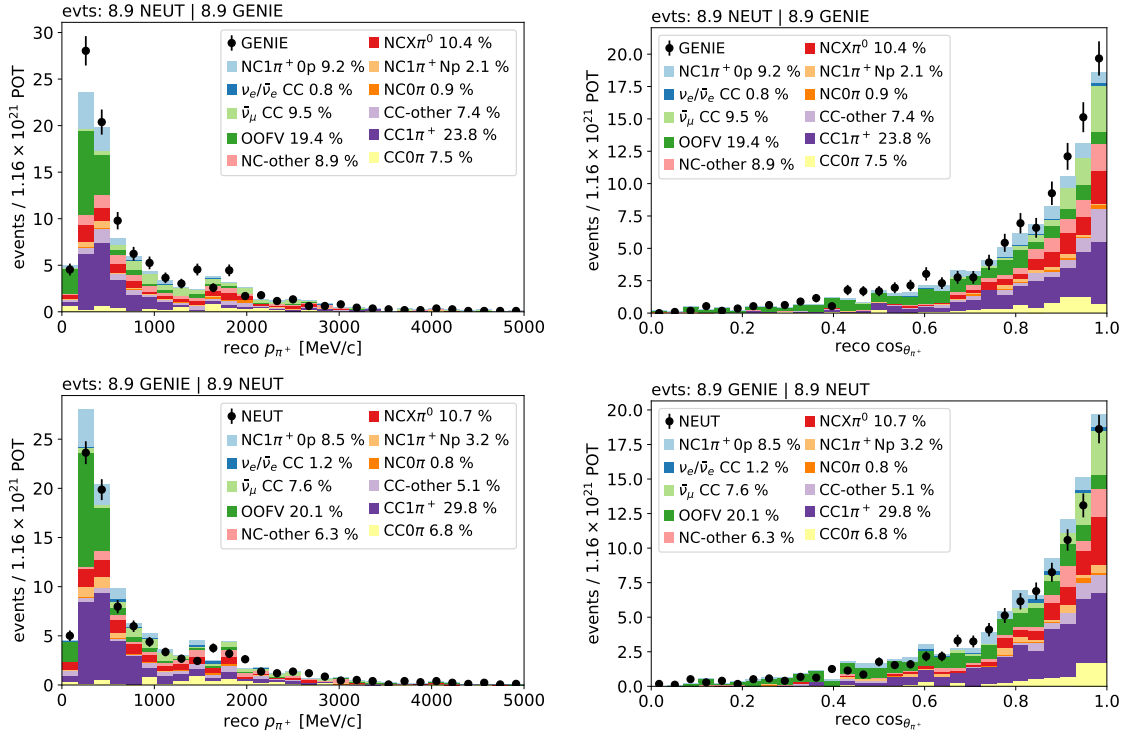


FIGURE 7.14: $\text{NC}1\pi^+ + 1$ FGD1 track sideband results of the selection as a function of the π^+ candidate momentum (left) and angle (right). The results are broken down by topology with purity detailed in the legend and are presented both for NEUT (top) and GENIE (bottom).

7.3.4 $\text{NC}0\pi$ sideband

Topology	Process	NEUT		GENIE	
		Events	[%]	Events	[%]
$\text{NC}0\pi$	$\bar{\nu} + p \rightarrow \bar{\nu} + p$	4.90	1.76	2.67	1.03
	$\nu + n \rightarrow \nu + n + \pi^0$	2.33	0.84	1.78	0.69
	$\nu + p \rightarrow \nu + p + \pi^0$	2.22	0.80	3.11	1.20
	$\nu + n \rightarrow \nu + p + \pi^-$	6.26	2.25	10.77	4.15
	$\nu + p \rightarrow \nu + n + \pi^+$	0.68	0.25	0.80	0.31
	$\nu + p \rightarrow \nu + p + \gamma$	-	-	0.62	0.24
	$\nu + p \rightarrow \nu + p + \eta^0$	-	-	1.51	0.58
	$\nu + (n \text{ or } p) \rightarrow \nu + (n \text{ or } p) + \text{mesons}$	0.85	0.31	-	-
	$\nu + p \rightarrow \nu + p$	240.41	86.55	221.96	85.44
	$\nu + n \rightarrow \nu + n$	19.75	7.11	16.29	6.27

TABLE 7.3: Processes contributing to the $\text{NC}0\pi$ topology in the signal sample by number of events scaled to the data POT and by fraction for both NEUT and GENIE. Only processes contributing to at least 0.5 events are considered.

The $\text{NC}0\pi$ topology is interesting in itself. Although its cross section is expected to be larger than that of $\text{NC}1\pi^+$ interactions, $\text{NC}0\pi$ interactions pose problems for their study similar to those earlier presented for the study of $\text{NC}1\pi^+$ events. There is, however, an important difference for both regarding T2K's OA. In Super-Kamiokande, only protons above 2 GeV/c produce enough Cherenkov light to be selected and given the relatively low typical neutrino energy in T2K's flux, very few of these background events are expected to be selected. Conversely, in ND280 $\text{NC}0\pi$ events generate detectable imprints even for low proton momenta. Since in ND280 the pion-proton separation is limited for tracks with momentum above 1 GeV/c, some $\text{NC}0\pi$ events are

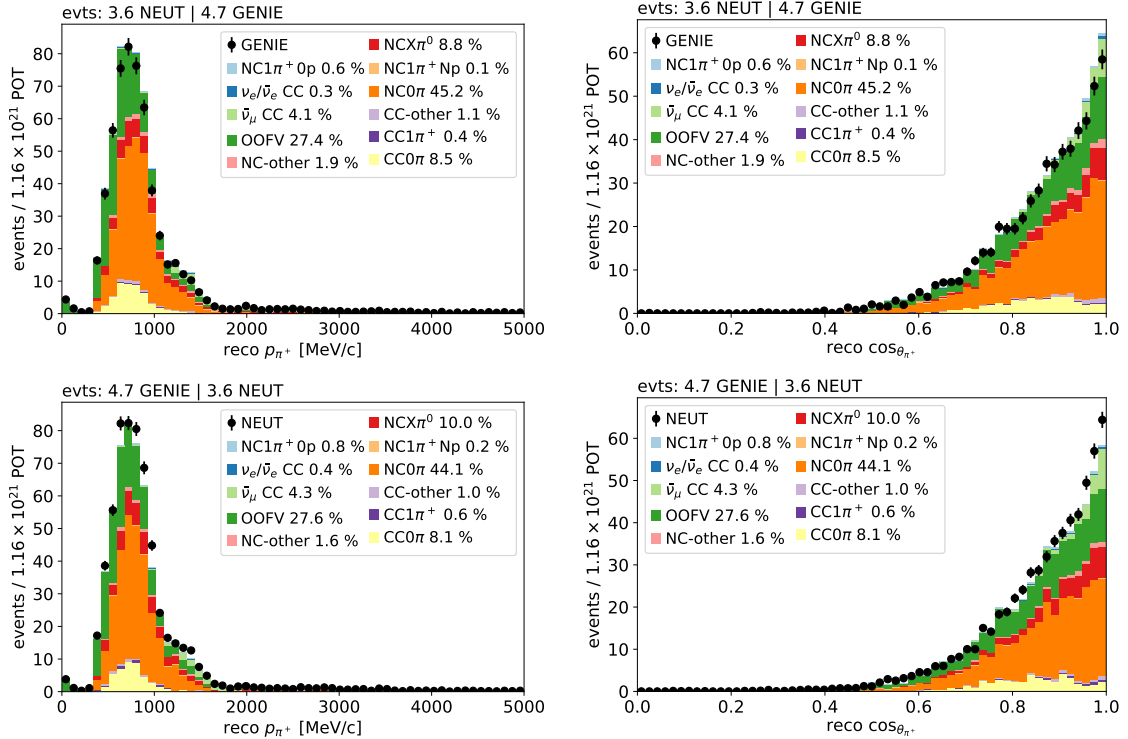


FIGURE 7.15: NC0 π sample results of the selection as a function of the π^+ candidate momentum (left) and angle (right). The results are broken down by topology, with purity detailed in the legend, and are presented both for NEUT (top) and GENIE (bottom).

expected to be selected as NC1 π^+ signal. As earlier presented in Figure 7.8, about 6% (4%) of the events in the signal sample are true NC0 π according to NEUT (GENIE) and consequently, the main purpose of this control region is to validate and constrain the generators prediction for this background.

The results for this sample are presented in Figure 7.15. The proton purity in the selected events is of 93.9% (92.8%) according to NEUT (GENIE). For both generators about 270 NC0 π events are expected to be selected with a purity of about 45%. The second most abundant topology are OOFV events (about 27%) primarily generated by OOFV neutrons ejecting a proton in FGD1.

A breakdown of the processes contributing to the NC0 π topology in this sideband are presented in Table 7.3. Interestingly, about 95% (92%) of the events are true NCE according to NEUT (GENIE). As earlier presented in Sec. 3.5, NCE interactions have been studied twice by Mini-BooNE [347, 348]. A measurement was also made using Super-Kamiokande [351] although it is not directly comparable since the selection criteria was built around the identification of γ de-excitations. In any case, the performance metrics of the NC0 π sideband here presented open the door to also study this channel in the future in T2K using ND280.

7.4 Evaluation of systematic uncertainties associated to the selection

In order to compare the results of the selection algorithm in MC and data and draw physics conclusions it is essential to evaluate the systematic uncertainties associated to the MC prediction. In the following, we review the list of systematic uncertainties associated to the detector model that play a role in the NC1 π^+ selection.

7.4.1 Detector systematics

Detector Systematic	Accounts for	Comments
BFieldDist	B field non-uniformities	T2KTN-212
Momentum Resolution	TPC spatial resolution	T2KTN-212
Momentum Scale	TPC response (affecting momentum)	T2KTN-212
FGD1Mass	Uncertain mass of FGD1	T2KTN-212
TPC PID	TPC response (affecting dE/dx)	T2KTN-212
TPCclusterEff	Cluster loss in TPC segment with 19 clusters	T2KTN-212
ChargeConf	Charge miss identification	T2KTN-212
FGDHybridTrackEff	FGD-TPC matching efficiency	T2KTN-212
MichelElectronEff	Michel Electron tagging efficiency	T2KTN-212
TPCECalMatchEff	TPC-ECal matching efficiency	T2KTN-212
ECalTrackEff	ECal tracking efficiency	T2KTN-212
EcalPID	EcalPIDMIP variations	T2KTN-212
SIPion	Uncertainties on the interactions of pions	T2KTN-212
SIProton	Uncertainties on the interactions of protons	T2KTN-212
SINeutron	Uncertainties on the interactions of neutrons	Tuned
OOFV	OOFV uncertainties	Tuned
PileUpTPC	TPC veto effect on pile up coming	New
PileUpPØD	PØD veto effect on pile up	New
PileUp ECal	ECal veto effect on pile up	New
FGD1MIPLike	Uncertainty associated to FGD1PIDMIPLike variable	New

TABLE 7.4: List of the detector systematics taken into account for the $NC1\pi^+$ analysis. They can be divided in three groups: Pre-existing and taken as defined in T2KTN-212 [474], pre-existing but tuned for this analysis, and developed particularly for this analysis.

There are different ways in which detector systematics play a role. In the first place, some detector variables in MC follow slightly different distributions to those observed in data. When a selection criteria is based on cuts applied to these variables, the MC-data discrepancies might lead to variations in the MC prediction. Accordingly, variation systematics account for this effect by varying the MC to cover any reasonable discrepancy with data in order to quantify its impact in the event rate predictions. In the second place, some detector uncertainties might change directly the event rate prediction, such as the FGD1 mass or material composition. When this happens the weight associated to each event is varied within the uncertainty of the unknown variable and, consequently, this type of systematics are referred to as weight systematics.

A list of all the detector systematics relevant for this selection are summarized in Table 7.4. An important point is that the $NC1\pi^+$ selection was designed, from the beginning, having in mind the list of variables and effects with well understood systematic uncertainties in ND280. In this sense, the selection cut choices were often driven to minimize the impact of systematic uncertainties in the selection and by the possibility of re-using as much as possible existing well controlled variables in ND280, covered by systematics studied in the past in the context of other ND280 analyses. Consequently, 14 systematic uncertainties have been used as detailed in T2KTN-212 [474] to account for the effects listed in Table 7.4.

In some other cases, however, pre-existing systematics have been tuned for the particular needs of this selection, as it is the case of the OOFV and SINeutron systematics. On other cases, the solution has been to implement new systematic uncertainties to cover for reasonable variations of some cuts on the selection output. This includes three new systematics associated to the veto cuts and one systematic to cover for MC-data discrepancies in the new FGD1MIPLike variable described earlier in Sec. 7.2.9.

7.4.2 OOFV systematics tuning

The OOFV systematic uncertainty varies the weight of OOFV background events to cover for some detector effects which are not well controlled within known uncertainties. We can differentiate between two different types of OOFV events. On one hand, some OOFV events happen within the FGD1 volume, but out of its FV. In the $NC1\pi^+$ analysis, this corresponds to only about 5 of the total 32 selected OOFV events. For them, the reconstruction uncertainty presented in Figure 7.5 is applied depending on its origin. These numbers, are taken from T2KTN-212 [474], where they were calculated. Using this number is considered to be a safe approach even if they were computed using CC events. The reason is that they characterize reconstruction effects that should be relatively independent of the type of interaction. Due to this, this numbers were also used in the past in ν_e studies as detailed in T2KTN-282 [475], much different from CC than $NC1\pi^+$ interactions.

category of OOFV event	Reconstruction Uncertainty
OOFV inside the FGD	0%
In tracker upstream	0%
In the tracker downstream	5%
From neutral parent	0%
Backward event	0%
High angle event	33%
Last module failure	35%
Double skipped layers	55%
Hard scattering	32%

TABLE 7.5: Reconstruction uncertainty associated to each OOFV event starting FGD1 depending on its true category. Values from T2KTN-212 [474].

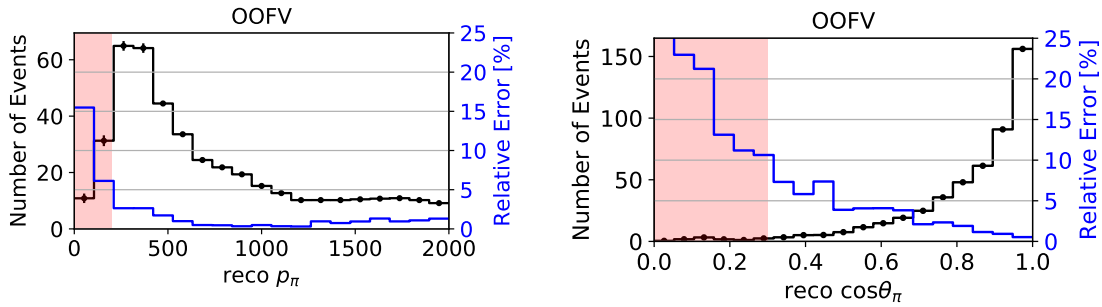


FIGURE 7.16: OOFV systematic uncertainty for the signal sample shown as 1D marginal distributions as a function of the reconstructed π^+ momentum (left) and angle (right). The regions where $\cos\theta_{\pi^+} < 0.3$ is covered by a red shadow. The number of events for the full MC statistics are also shown.

For those events occurring elsewhere in the detector a rate uncertainty is applied, in order to cover for scaling effects of the cross section with materials different to that of Carbon, such as the iron in the magnet and the metal in the electronic boards. In T2KTN-212 [474], detector specific uncertainties were derived for each sub-detector where the OOFV event could be produced. Those tuned numbers are not used for the $NC1\pi^+$ selection, as one can expect that their individual values would change noticeably as a result of the fact that the topologies contributing to the selected OOFV events in any CC selection and the ones relevant for the selection here presented are not the same. Hence, for the evaluation of the OOFV background uncertainties we use the conservative approach of using a 25% rate uncertainty for all OOFV interactions happening outside of FGD1. This value is larger than any rate uncertainty calculated in T2KTN-212 [474], being the

largest of them 24%. As presented in Figure 7.16, the OOFV systematic uncertainty for the most relevant phase-space is below 2%. The uncertainty only increases considerably for events with low momentum where we do not intend to extract physics conclusions on the behavior of the signal.

7.4.3 SINeutron systematics tuning

The cross section of neutron inelastic interactions has an associated uncertainty at the level of 10% and consequently its effect in the GEANT4 propagation of neutron tracks must be interpreted carefully. To account for this, an existing SINeutron systematic was available in HighLAND which calculates for each neutron the probability to undergo a secondary interaction in the surrounding detector media and combines the result with the GEANT4 uncertainty.

In the $\text{NC1}\pi^+$ selection, not all events with neutrons are sensitive to these effects since undergoing a secondary interaction (SI) is not problematic by itself in regard of the selection cuts. On the contrary, it is only relevant for those events where the neutron interaction is able to produce a secondary particle with a range long enough to produce an FGD1 segment. When this happens, the event is migrated from the signal sample to the $\text{NC1}\pi^+1$ FGD1 track sideband. To account for this, the SINeutron systematic has been tuned to be applied only to those events with an FGD1 segment generated by a neutron or by a particle with a neutron parent. As it can be seen in Fig-

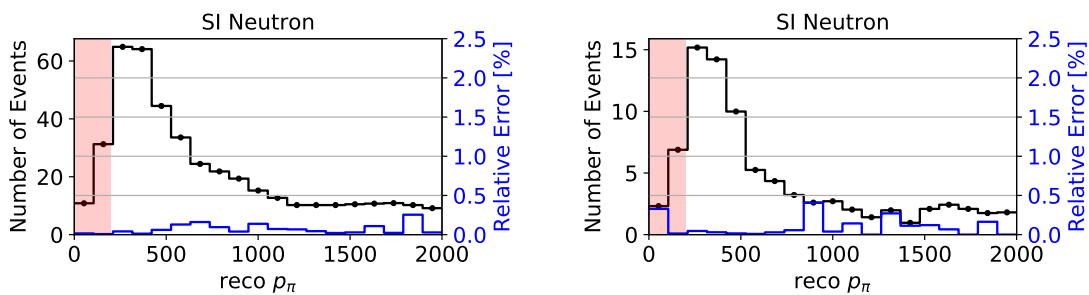


FIGURE 7.17: SINeutron systematic uncertainty for the signal sample shown as 1D marginal distributions as a function of the reconstructed π^+ momentum for the signal sample (left) and for SD 2. OOPS regions are highlighted using red shadows. The number of events for the full MC statistics are also shown.

ure 7.17, this systematic has, overall, a small effect generally below 0.5%, and it is generally flat for events with different π^+ candidates momenta. To be reconstructed, FGD1 segments must have at least 5 bar hits which means that the track needs to have a range of at least 5 cm. However, the vast majority of ejected neutrons are expected to have very low kinetic energy making the production of long-range segments unlikely. This assumption is supported by the very small migration of signal events observed in SD 2, which is similar to 5% of the amount of signal events in the signal sample. Accordingly, one would expect at most a systematic error of about 10% (if all neutrons would experience secondary interactions) of a 5%, namely a 0.5%, consistent with the results observed in Figure 7.17.

7.4.4 Computation of pile up corrections and systematics

The strategy to compute correction factors arising from pile up effects on the upstream vetos and its associated systematic errors have been computed with a method analogous to that developed and presented in T2KTN-282 [475]. The $\text{NC1}\pi^+$ selection uses three veto cuts (TPC, PØD, ECal) with the goal of removing a significant fraction of OOFV interactions. When a sand muon, i.e. a muon generated by a neutrino interaction in the vicinity of ND280, produces an interaction in

Run	TPC C_{pileup}	TPC σ_{pileup}	PØD C_{pileup}	PØD σ_{pileup}	ECal C_{pileup}	ECal σ_{pileup}
Run 2a	0.00730738	0.00268142	0.000169371	0.00670109	0.000153909	0.0295607
Run 2w	0.00623801	0.00207692	0.000144585	0.00860249	0.000131386	0.0257142
Run 3	0.00778612	0.00273778	0.000180468	0.00882905	0.000163993	0.0311638
Run 4a	0.0100351	0.00319593	0.000232595	0.0112634	0.000211361	0.038705
Run 4w	0.00882092	0.00259052	0.000204453	0.0116906	0.000185788	0.0348582
Run 8a	0.0202205	0.00206329	0.000468674	0.0185339	0.000425888	0.0671406
Run 8w	0.0174775	0.00213982	0.000405095	0.0202903	0.000368114	0.0596319

TABLE 7.6: Pile up correction weights and associated uncertainties for each run and for all the vetos in the $NC1\pi^+$ selection.

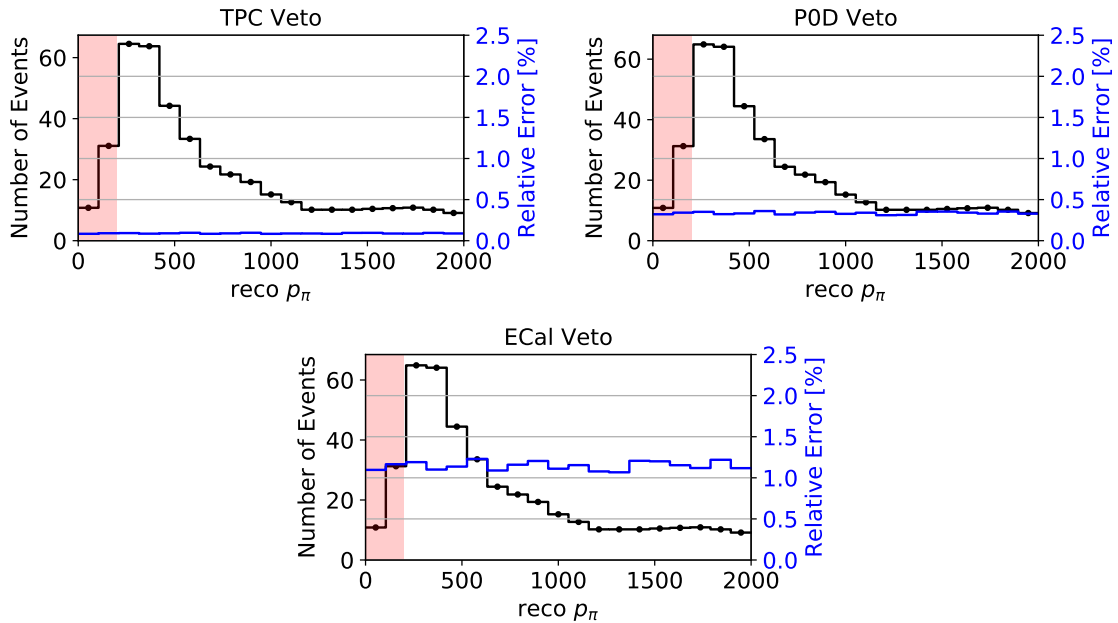


FIGURE 7.18: Systematic uncertainties associated to the veto cuts due to pile up effects for the signal sample shown as 1D marginal distributions as a function of the reconstructed π^+ momentum. OOPS regions are highlighted using red shadows. The number of events for the full MC statistics are also shown.

coincidence with an ND280 event it can trigger the veto cuts and account for selection inefficiencies. Sand muons are not included in the ND280 MC simulation and therefore need to be explicitly corrected for in a later stage by the use of event weights.

To assess the effect of these vetos a specific `PileUpSelection` was developed which counted how many times each veto was activated in the absence of any other cut. To avoid double counting, variables were filled to inform of how many times each veto was activated individually.

To compute adequate weights the `PileUpSelection` was run for all p6T MC runs (NEUT), for data and for a specific MC dataset only containing sand muon events, developed for this particular purpose in the past. For a fair comparison all datasets were scaled to the same number of POT.

The computed weights consist of correction factors, which correct the weight of the events by the proportion of times that events are expected to be lost due to a triggered sand muon in coincidence with the event and an uncertainty, which covers the difference of the observed number of vetos triggered in data compared to the sum of $\nu_{MC} + \text{sand}_{MC}$ vetos.

The corrections and uncertainties are calculated by run, as it is expected that periods with different beam powers account for small run-to-run variations. The numbers are presented in Table 7.6.

The systematic uncertainty associated to each veto is calculated by varying the weight of each event according to its run and the numbers presented in Table 7.6. The total effect of each of this veto uncertainties is presented in Figure 7.18. As it can be seen its error is similar or lower than 1% all across the kinematic space.

7.4.5 Computation of FGDMIP-like variable corrections and systematics

The `FGD1MIPLike` variable computed with FGD1 information is new and therefore it required both a study to validate its performance and to asses its associated systematic uncertainty arising from a possible data-MC mismatch. As this variable aims to primarily separate particles outgoing from the FGD1 from particles stopping in the FGD1 a control sample of outgoing MIPs and a control sample of stopping MIPs were developed and studied. To study the stopping particles, an existing HighLAND selection was used and adapted, named `StoppingControlSamples`, developed to perform other validation studies in the past. This algorithm selects particles that stop in FGD1 according to ToF information. Using it, a sample of negative particles stopping in FGD1 was identified, that according to true MC information is made up of negative muons, our primary interest, with a purity exceeding 99%. Then, for this sample of stopping muons the `FGD1MIPLike` variable was calculated and used to fill distributions for both MC and data.

An analogous procedure was applied to study outgoing particles with a MIP like behavior. For this task another existing HighLAND selection was used an adapted, named `numuCCZeroPiAnalysis`, which has been used in the past to study $CC0\pi$ events. Using it, a sample of $CC0\pi$ events without protons was identified. In addition, to ensure that no other particles were merged to the outgoing μ^- candidate and that its information was truly equivalent to that of a MIP, a vertex activity cut was applied ($VA_{5\times 5} < 250$) which ensured that in a 5×5 FGD1 box of hits around the reconstructed vertex the light yield was low enough to consider that no additional charged particles were influencing the light yield associated to μ^- track.

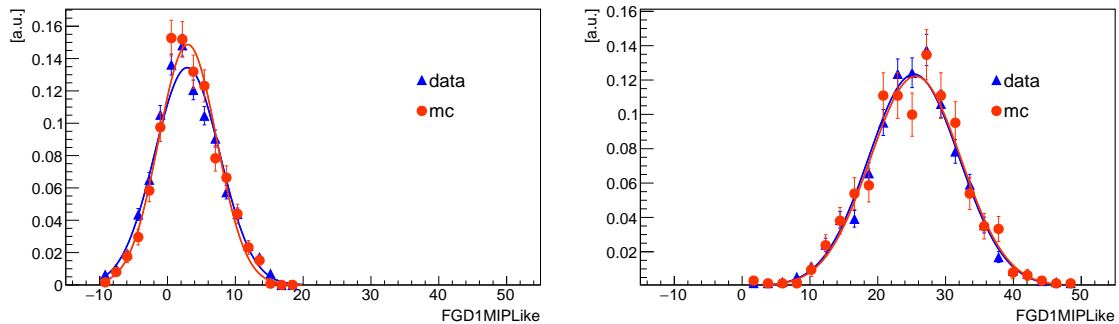


FIGURE 7.19: Data and MC distributions for the `FGD1MIPLike` variable for a control sample of FGD1 outgoing (left) and stopping (right) muons.

Data vs MC comparisons for this two samples are presented in Figure 7.19. As it can be seen, overall, a very good agreement between MC and data is seen prior to any correction. Nonetheless, to further optimize the agreement of this distributions a correction was applied that shifts the mean of each distribution in MC to resemble that of data. In addition, a variation systematic was implemented that accounts for the different widths of each distribution. The coefficients from the fits, used to perform this adjustments are presented in Table 7.7. The corrections and systematics are implemented separately to particles outgoing the FGD1 or stopping on it according to the true MC information. It must be noted the great separation between the two samples. The sample of stopping particles almost extinguishes for values of `FGD1MIPLike` smaller than 10, supporting the decision of cutting at this value.

The uncertainty associated to this cut is presented in Figure 7.20. As it can be seen, due to the

	Mean MC	Mean MC error	Mean Data	Mean Data error
Outgoing	2.3371	0.1006	2.5906	0.0967
Stopping	25.5436	0.1563	25.7045	0.2040
	Width MC	Width MC error	Width Data	Width Data error
Outgoing	4.2650	0.1007	3.9893	0.0966
Stopping	6.3315	0.2023	6.9876	0.2220

TABLE 7.7: Mean, width and their associated errors in the distribution of $FGD1MIPLike$ values observed for outgoing and stopping muons both for MC and data.

good agreement between MC and data its overall level is small and it is only significant for very high-angle tracks and momentum below 200 MeV/c.

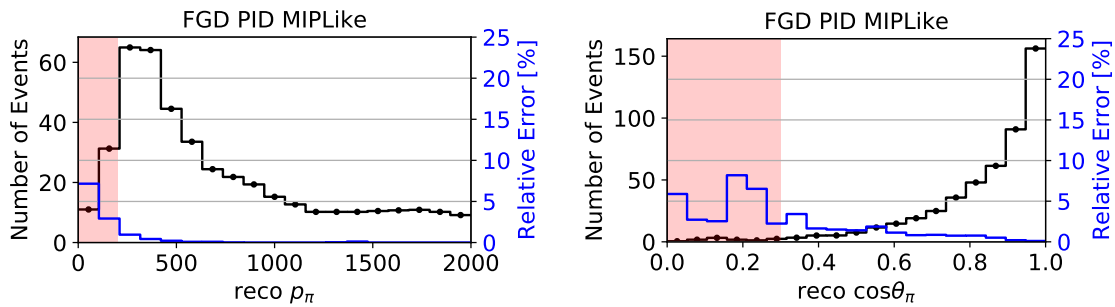


FIGURE 7.20: FGD1 MIP-like systematic uncertainty for the signal sample shown as 1D marginal distributions as a function of the reconstructed π^+ momentum (left) and angle (right). The regions where $\cos \theta_{\pi^+} < 0.3$ is covered by a red shadow. The number of events for the full MC statistics are also shown.

7.5 Final detector systematics

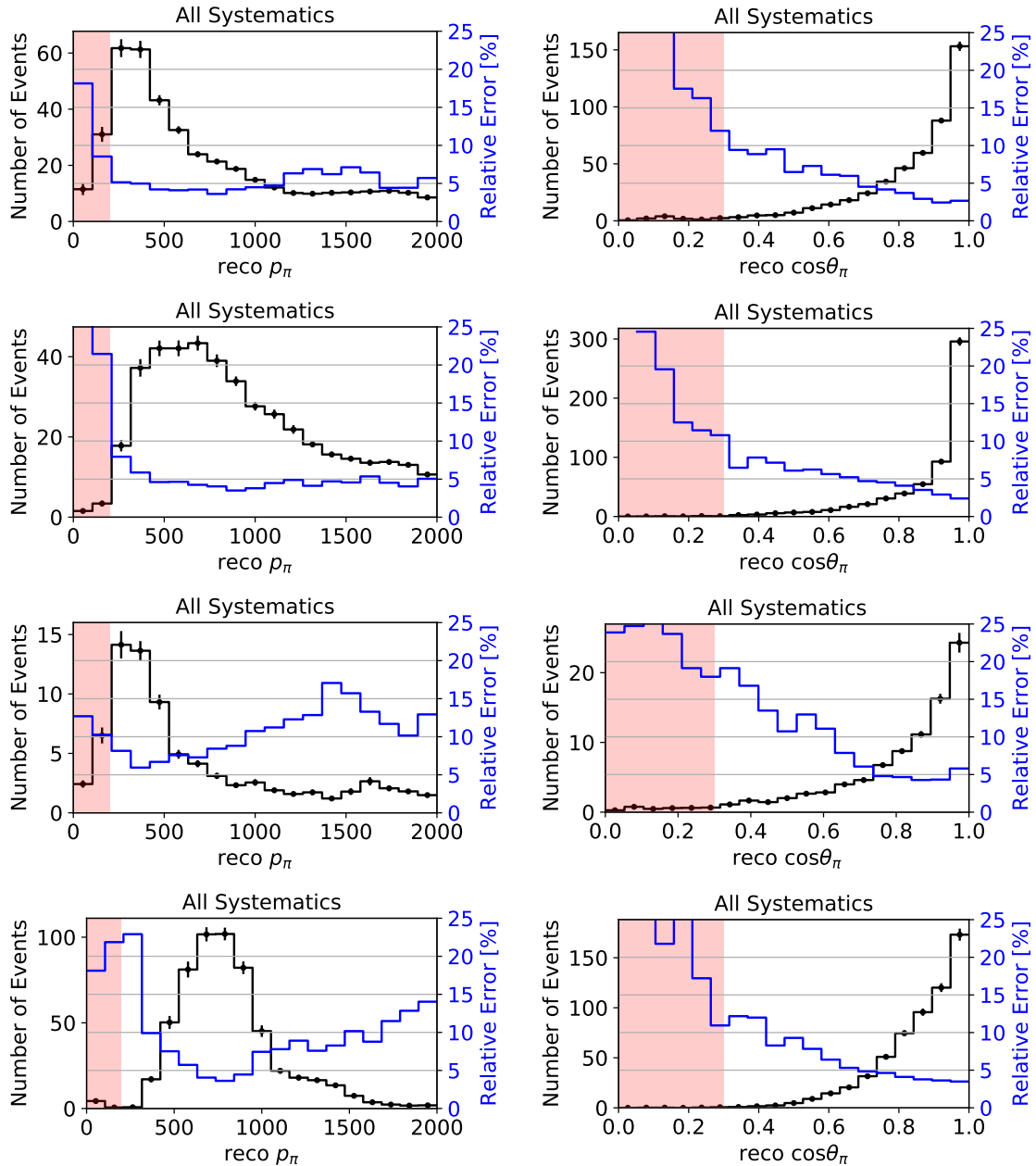


FIGURE 7.21: From top to bottom, total systematic error for the signal sample and SD 1, SD 2 and SD 3. The uncertainty is shown as a function of the reconstructed π^+ momentum. OOPS regions are highlighted using red shadows. The number of events are shown for the full MC statistics.

The effect of each detector systematic considered in the selection, integrated in the momentum range from 200 MeV/c to 1 GeV/c, is summarized in Table 7.8. As it can be seen, in this restricted kinematics the total systematic error is, for the signal sample, of 4.9%. This error budget is overall small and no individual source of uncertainty drives the final result, leaving few room for future improvements.

The kinematic dependence of all the systematics combined is presented in Figure 7.21 both for the signal and the sidebands. The trend is similar for all samples reaching the lowest error levels in the most relevant kinematic region. For high momentum, the error gradually increases due to

Systematic	Sample 0 Error [%]	SD 1 Error [%]	SD 2 Error [%]	SD 3 Error [%]
All Systematics	4.929%	4.706%	9.487%	5.803%
SI Pion	1.993%	0.796%	3.773%	0.388%
SI Proton	0.299%	0.151%	0.665%	0.941%
B Field	0.668%	0.994%	1.423%	0.714%
Momentum Scale	1.399%	1.373%	2.526%	1.749%
Momentum Resolution	1.473%	1.364%	3.434%	1.041%
TPC PID	1.985%	1.103%	2.227%	3.056%
Charge ID	0.157%	0.120%	0.192%	0.181%
FGD Tracking Eff	0.042%	0.020%	0.530%	0.022%
FGD-TPC Matching	0.090%	0.082%	0.042%	0.520%
FGD Mass	0.535%	0.578%	0.494%	0.433%
Michel Electron Eff	0.205%	0.064%	0.226%	0.010%
TPC Tracking Eff	0.010%	0.008%	0.006%	0.003%
TPC-ECal Matching	0.413%	2.837%	0.474%	1.144%
ECal PID	1.951%	2.010%	2.203%	0.633%
SI Neutron	0.067%	0.061%	0.185%	0.222%
TPC Veto	0.089%	0.088%	0.092%	0.089%
ECal Veto	1.148%	1.126%	1.171%	1.140%
POD Veto	0.337%	0.330%	0.343%	0.335%
FGD PID MIPLike	0.275%	0.038%	0.669%	0.063%
OOFV	1.498%	0.315%	3.229%	3.542%

TABLE 7.8: Integrated error in the momentum range from 200 MeV/c to 1 GeV/c for the signal (sample 0) and the different sidebands.

the difficulty to reconstruct the particle momentum reliably, which introduces large uncertainties via the momentum scale and momentum resolution systematics.

7.6 Comparisons to data

Comparisons of MC and data distributions are presented in Figure 7.22. As it can be seen, in general, good agreement can be seen between the MC predictions and the data distributions. For the signal region, and without applying any kinematic cuts, NEUT (GENIE) predicts a total of 500 (532) events, in good agreement with the 493 events observed for data. Remarkably, good agreement is also observed in the shapes of the distributions with few notable exceptions.

- For the most populated momentum bin in the signal region a significantly lower number of data events is observed.
- In all samples data shows a relative deficit compared to the MC when it comes to the most forward bin. Interestingly, this same deficit has been observed in the past in CCQE studies, e.g. Refs. [312, 324], as it is in this most forward region where nuclear effects are expected to play the largest relative role.
- The total number of entries in SD 2 is notably smaller for data. Despite the important role of statistical fluctuations in the sample, this mild discrepancy might indicate that the $CC1\pi$ contribution to this bins is smaller than predicted by the generators. Poor modeling in this region is reasonable as the $CC1\pi$ events being selected in this region corresponds to the particular corner of its phase-space where muons are emitted with very low momentum such that only the outgoing π^+ is observed.
- Overall, in SD 3 a slightly smaller number of events is observed for data, which might be symptomatic of a slightly smaller cross section for the $NC0\pi^+$ topology than currently predicted by the generators.

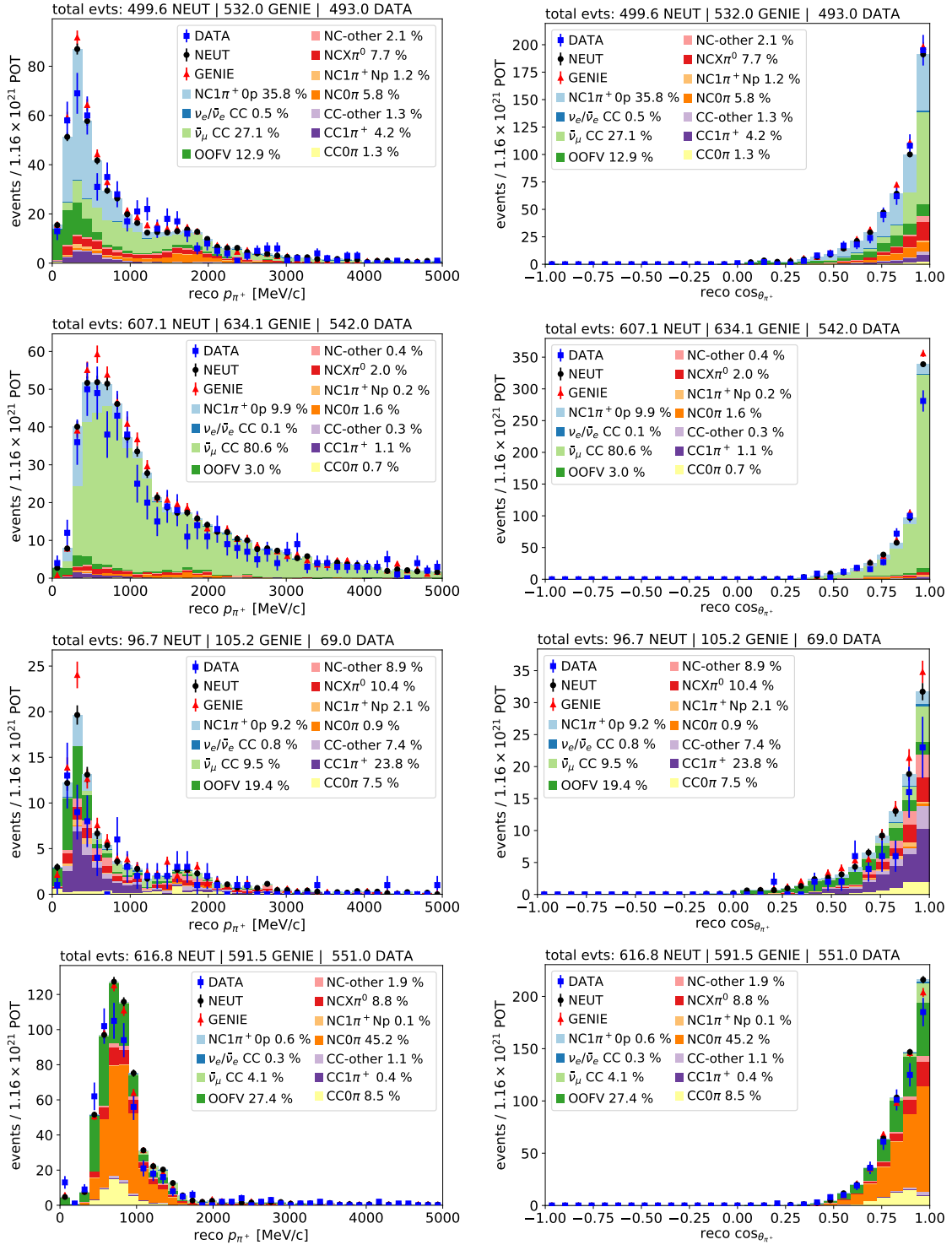


FIGURE 7.22: Comparisons of MC and data scaled to the same number of POT (1.16×10^{21} POT). From top to bottom each row corresponds to the momentum and angle distributions of the only FGD1-TPC track in the event for the signal sample and SD1, SD2 and SD3 respectively.

Finally, the good agreement, particularly in the signal sample, allows to anticipate that the extracted cross section for the signal topology must be reasonably similar to that predicted by the generators.

Chapter 8

Fitting and cross section results

“I remember my friend Johnny von Neumann used to say, with four parameters I can fit an elephant and with five I can make him wiggle his trunk.”

– ENRICO FERMI

This Chapter describes how to draw conclusions on the output samples obtained with the NC1 π^+ selection algorithm presented in the previous Chapter. First, the binned likelihood fitting technique is reviewed as a cross section extraction method, second, all the necessary inputs to the fitter are presented and discussed and finally, fits to different data sets are provided. The fits can be divided into two categories. On one hand, validation fits have been made on fake data to assess the correct fitter performance and the robustness of the selection to neutrino interaction modeling. On the other hand, a fit between MC and data has been made to measure the preliminary NC1 π^+ -0p cross section, in review by the T2K collaboration.

8.1 Binned likelihood fitting

A well known procedure to draw statistical conclusions from a physical model is to perform a binned likelihood fit where the binned distributions of the model expectations are adjusted to those observed in data. To do this, first, the experimental observables are chosen. Then, the distributions of the observables are binned in N-dimensions and the collection of bins is used to build a likelihood function L that characterizes the overall probability of observing the data distribution for a given choice of parameters controlling the model prediction. Finally, the model is adjusted to maximize the likelihood, i.e. the agreement between model and data.

To measure the cross section of the NC1 π^+ -0p topology the output samples of the NC1 π^+ selection algorithm presented in the former Chapter will be used. The bins will be defined as 2D regions of angle and momentum in the distribution of the kinematics for the outgoing π^+ candidate track¹.

8.1.1 Likelihood definition

The total likelihood L_{TOT} depends both on the statistical and systematic uncertainty associated to the predicted distributions, namely

$$L_{\text{TOT}} = L_{\text{STAT}} \times L_{\text{SYST}} . \quad (8.1)$$

¹For SD3, which aims to select NC0 π events, the proton candidate track kinematics will be used instead.

Since the logarithm is a monotonic function it is easy to see that the configuration that maximizes the likelihood is the same that maximizes the logarithm of the likelihood. Dealing with the later is numerically easier and, therefore, hereafter we focus on the $\log L$. Moreover, most numerical optimizers are built to perform minimizations, such that it practice to maximize the log likelihood the $-\log L$ is minimized. Finally, it must be noted that the addition of a constant does not change the result of the optimization and accordingly, for reasons later discussed, we concentrate on the minimization of $-2 \log L$.

The statistical likelihood corresponds to the product of the individual statistical probabilities of each bin which are Poissonian in nature², hence

$$\begin{aligned} \max_{\vec{\theta}} L_{\text{STAT}} &= \min_{\vec{\theta}} (-2 \log L_{\text{STAT}}) = \min_{\vec{\theta}} \left(-2 \sum_i \log \frac{N^{\text{exp}} N^{\text{obs}} e^{-N^{\text{exp}}}}{N^{\text{obs}}!} \right) \\ &= \min_{\vec{\theta}} \left(2 \sum_i \log N^{\text{obs}}! + N^{\text{exp}} - N^{\text{obs}} \log N^{\text{exp}} + C \right). \end{aligned} \quad (8.2)$$

Here $\max_{\vec{\theta}}$ ($\min_{\vec{\theta}}$) corresponds to the list of fit parameters $\vec{\theta}$ which maximize (minimize) the function, N^{exp} is the number of expected events, N^{obs} is the numbers of observed events and C is a constant that has been added for convenience. Notice that implicitly N^{exp} depends on $\vec{\theta}$. Then, if we define

$$C = - \sum_i \log \frac{N^{\text{obs}} N^{\text{obs}} e^{-N^{\text{obs}}}}{N^{\text{obs}}!} \quad (8.3)$$

follows

$$\begin{aligned} \max_{\vec{\theta}} L_{\text{STAT}} &= \min_{\vec{\theta}} \left(\log \frac{L_{\text{STAT}}(N^{\text{obs}}, N^{\text{exp}})}{L_{\text{STAT}}(N^{\text{obs}}, N^{\text{obs}})} \right) \\ &= \min_{\vec{\theta}} \left(2 \sum_i N^{\text{exp}} - N^{\text{obs}} - N^{\text{obs}} \log \frac{N^{\text{obs}}}{N^{\text{exp}}} \right). \end{aligned} \quad (8.4)$$

In the limit where N^{exp} is not too small

$$-2 \log L \approx \chi^2, \quad (8.5)$$

which is known as the Wilks Theorem [477]. Thus, in the high statistics limit maximizing the likelihood corresponds to minimizing the χ^2 .

Concerning the parameters $\vec{\theta}$, if constrains exist on their values they can be added to the likelihood using

$$-2 \log L_{\text{SYST}} \approx \chi_{\text{SYST}}^2 = (\vec{\theta}_i - \vec{\theta}_i^{\text{prior}}) V_{ij}^{\text{cov}} (\vec{\theta}_j - \vec{\theta}_j^{\text{prior}}), \quad (8.6)$$

where V_{ij}^{cov} is the covariance matrix characterizing the prior knowledge on $\vec{\theta}$.

²Additional insights and step-by-step demonstrations can be found on Ref. [476].

8.1.2 Cross-section extraction

If a set of events are labeled as signal and the rest are labeled as background, the MC event rate prediction is given by

$$\begin{aligned} N_j^{\text{exp}} &= N_j^{\text{signal}} + N_j^{\text{bkg}} \\ &= \sum_i^{\text{true bins}} \left[c_i \left(N_i^{\text{signal}} \prod_{\alpha}^{\text{model}} w(\alpha)_i^{\text{signal}} \right) + \left(N_i^{\text{bkg}} \prod_{\alpha}^{\text{model}} w(\alpha)_i^{\text{bkg}} \right) \right] U_{ij} r_j^{\text{det}} \sum_n^{E_\nu} w_n^i f_n. \end{aligned} \quad (8.7)$$

Here:

- c_i are the so-called template parameters which are our primary interest as they allow to modify the cross-section prediction in a true bin-by-bin basis and therefore its postfit value is informative of the true cross-section of the signal.
- $w(\alpha)_i$ are weighting functions of cross section model nuisance parameters α , e.g. C^5_A , that specify how changes on α translate in changes on the MC prediction.
- U_{ij} is the detector smearing matrix which maps the event rate predictions in a true bin i to a reconstructed bin j .
- r_j^{det} are nuisance parameters characterizing the detector uncertainty in each reconstructed bin j .
- w_n^i are weights characterizing the contribution of each neutrino energy bin n to the true kinematic bin i and f_n are the associated flux model nuisance parameters.

Hence, the postfit information consists of a set of best fit values for the template and nuisance parameters alongside their covariance, which can be used to estimate the number of expected signal events N_i^{signal} in each true kinematic bin i as

$$N_i^{\text{signal}} = \left[c_i \prod_{\alpha}^{\text{model}} w(\alpha)_i^{\text{signal}} \sum_j^{\text{reco bins}} r_j^{\text{det}} (U_{ij})^{-1} \sum_n^{E_\nu} w_n^i f_n \right] N_i^{\text{MC signal}}. \quad (8.8)$$

Finally, the differential cross-section $d\sigma/dx_i$ in the i -th kinematic bin is obtained normalizing the number of signal events by the bin size Δx_i , the detector efficiency ϵ_i^{obs} , the number of targets in the fiducial volume n^{FV} and the integrated neutrino flux Φ . Namely,

$$\frac{d\sigma}{dx_i} = \frac{N_i^{\text{signal}}}{\epsilon_i N^{\text{obs}} \Phi n^{FV}} \times \frac{1}{\Delta x_i}. \quad (8.9)$$

8.1.3 Fitting framework

In order to do the fit, an existing fitting framework³ was used. This framework, named `xslhFitter`, is the mainstream binned likelihood fitting resource for T2K cross section analysis, and its development and implementation is the result of the sequential progress done by multiple T2K collaborators, covered in a set of T2K technical notes [478, 479, 480, 481, 482, 483, 484].

The `xslhFitter` provides:

- A converter to transform HighLAND output into a simplified `xslhFitter` input.

³<https://gitlab.com/cuddandr/xsLLhFitter>

- A tool to calculate the detector model covariance directly from HighLAND output.
- A generic fitter implementation which handles the evaluation and the maximization of the likelihood. It is designed to work modularly allowing to use, or not, the detector, flux and cross section model parameters in addition to the template parameters. The core of the fitter is based on the MIGRAD and HESSE algorithms from Minuit2 [485, 486]. MIGRAD performs the multidimensional minimization of the χ^2 using a variable metric method based on the Davidon-Fletcher-Powell algorithm [487]. Hesse uses the method of finite differences to calculate the Hessian matrix around the best-fit point found by MIGRAD, which is then inverted to obtain the covariance matrix for the fit parameters. Additional details can be found in Ref. [484].
- Utilities to calculate the extracted cross section from the fit result.

8.1.4 Binning for the reconstructed kinematics

In total, as presented in Sec. 7.2, the NC1 π^+ selection algorithm provides four output samples, one for the signal and three sidebands. Each of them is treated separately and, in consequence, an independent list of bins is defined for each sample. To choose the binning, some guidelines must be followed:

- At least 1 MC event must be expected in each bin, to avoid divisions by zero in the likelihood calculation.
- The bins must not be finer than the detector resolution in the variables being binned, to limit the event migration among neighbor bins.
- Among the whole possible set of bins choices it is desirable to choose a set of bins which adjusts closely the signal distribution such that variations in their expected and observed number of events are informative of where in the phase space these tensions are more notable.

Having this in mind, the binning presented in Figure 8.1 was chosen. In total, there are 114 bins of reconstructed variables organized in 43, 29, 11 and 31 bins for the signal sample and SD 1, SD 2 and SD 3 respectively. In general, all samples have a set of coarse bins dedicated to cover the reconstructed momentum region from 0 to 200 MeV/c, and the reconstructed angles $\cos\theta < 0.3$. For the regions with more events the bins become finer, being the smallest momentum ($\cos\theta$) steps of 100 MeV/c (0.1). Except for the bins at very low momentum and angle, the number of expected events scaled to the data POT is always similar or larger than 10 events. To deal with bins in different samples the bin indices are chained such that the first bin index in a sample follows the numeration of the last bin in the former sample.

8.1.5 Binning for the true kinematics

The binning for the true kinematics defines the regions in which the cross section will be extracted. As presented in Figure 8.2, in total, 15 true bins have been defined to cover regions where the efficiency is expected to be nearly flat. Among them, 11 bins are contained in the region where the π^+ kinematics satisfy $\cos\theta > 0.3$ and $0.2 \text{ GeV}/c < p_\pi < 1 \text{ GeV}/c$, which is the target phase space for the cross section measurement. In the other 4 bins the cross section will be extracted but kept aside, namely, these bins will be treated equally to all others but the cross section extracted on them will not be interpreted in equal terms. The motivations for taking this approach are the following:

- As reviewed in Sec. 7.3, the purity in these regions is low making the extracted cross section more dependent on the accurate modeling of the background. Albeit the fit includes

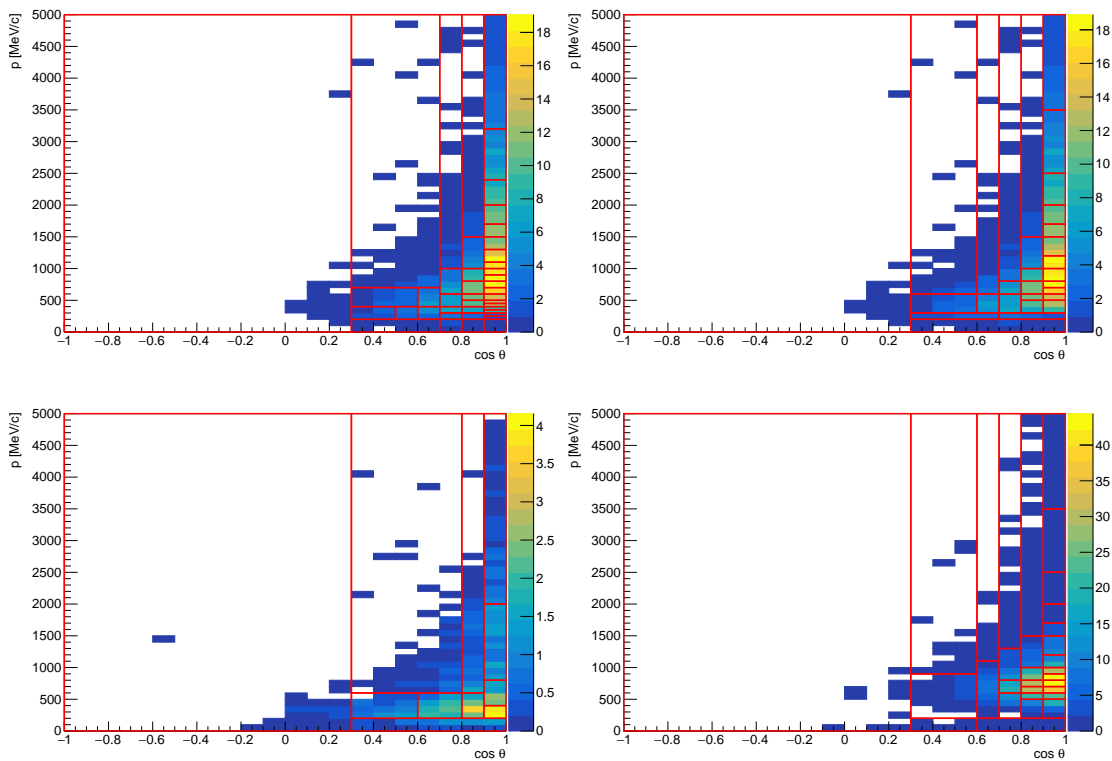


FIGURE 8.1: Binning for the reconstructed variables in the signal sample (top left), SD 1 (top right), SD 2 (bottom left) and SD 3 (bottom right). The colormap shows the number of expected events according to NEUT MC scaled to the data POT.

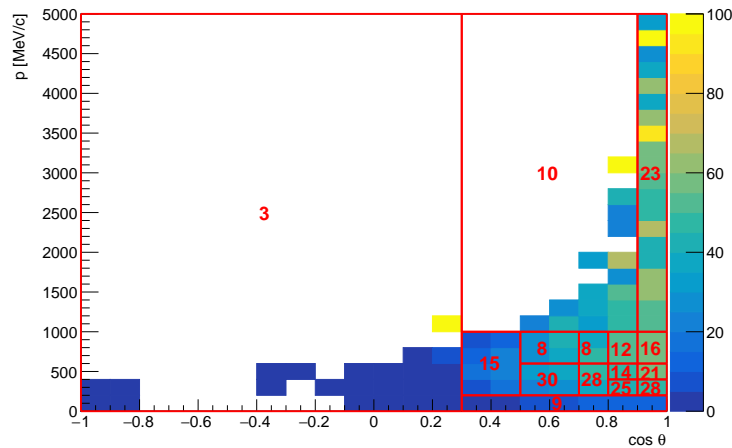


FIGURE 8.2: True binning for the cross section extraction. The colormap represents the efficiency in percentage. The number of expected true signal events according to NEUT MC scaled to the data POT are shown on top of each bin written in red.

cross section modeling uncertainties which allow to tweak the background event rate predictions, assuming a perfect background model parameterization is unrealistic. Hence, if some processes are not well captured by the model the posfit template parameters in bins with low purity might be driven by those effects. Therefore, conservatively, the decision is taken of not drawing physical conclusions from bins with a large proportion of background.

- The efficiency in some bins, e.g. those where $\cos\theta < 0.3$ or $p_{\pi^+} < 200$ MeV/c, is nearly 0%. Consequently, it seems unreasonable to assume that the physics of the signal in those bins is fully captured by such a low proportion of selected events.
- Even if the results in some bins will not be interpreted in physics terms, keeping them in the fit is recommended as it allows to evaluate the effect of migrating events from this bins to all the others and vice versa.

8.2 Nuisance parameters

As anticipated in Sec. 8.1.2, there are three types of nuisance parameters related to the detector, the flux and the cross section models.

8.2.1 Detector systematics

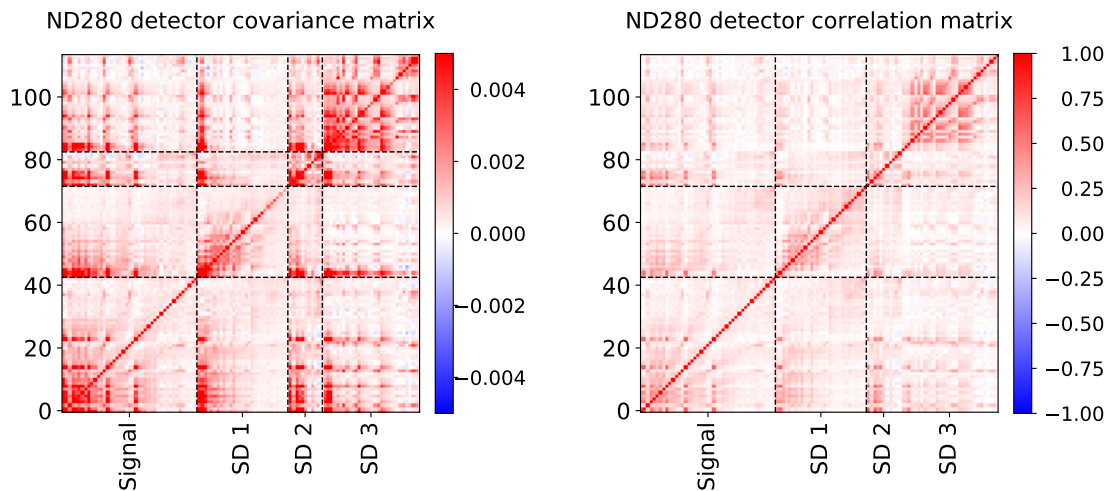


FIGURE 8.3: Detector model covariance (left) and correlation (right) matrices. The different samples are divided by dashed lines.

The origin and magnitude of the detector systematics influencing the event rate prediction have been presented earlier in Sec. 7.4. To account for these uncertainty in the binned likelihood fit one nuisance parameter per reconstructed bin is used. Each of them has a prior value equal to one, i.e. the nominal detector prediction according to the simulation. Its variations are constrained by an associated covariance matrix which characterizes how the number of events predicted in each reconstructed bin varies with that predicted in all other bins. The covariance matrix has been calculated running 500 toy experiments in which the weight of each event and all variables used to define cuts have been sampled randomly from their uncertainties. The result is presented in Figure 8.3.

8.2.2 Flux model systematics

The flux model systematics are calculated by a dedicated working group within T2K which provide flux covariance matrices that characterize how the number of expected neutrinos in the flux covary in different bins of neutrino energy and flavor. Then, in analogy with the detector systematics, a nuisance parameter for each bin of neutrino flavor and energy is included with a prior value of one constrained by the flux model covariance matrix. Since the NC1 π^+ output results are mainly sensitive to the ν_μ and the $\bar{\nu}_\mu$ components of the FHC flux prediction, both are included in

the fitter, each contributing with a total of 20 nuisance parameters covering bins spanning the same neutrino energies, summarized in Table 8.1. The flux covariance matrix is presented in Figure 8.4. It corresponds to the flux release 13av7 [488] that includes T2K replica target measurements done by the NA61/SHINE experiment.

Index	Flavour	Index	Flavour	E_ν [MeV/c]
0	ν	20	$\bar{\nu}$	0 - 100
1	ν	21	$\bar{\nu}$	100 - 200
2	ν	22	$\bar{\nu}$	200 - 300
3	ν	23	$\bar{\nu}$	300 - 400
4	ν	24	$\bar{\nu}$	400 - 500
5	ν	25	$\bar{\nu}$	500 - 600
6	ν	26	$\bar{\nu}$	600 - 700
7	ν	27	$\bar{\nu}$	700 - 800
8	ν	28	$\bar{\nu}$	800 - 1000
9	ν	29	$\bar{\nu}$	1000 - 1200
10	ν	30	$\bar{\nu}$	1200 - 1500
11	ν	31	$\bar{\nu}$	1500 - 2000
12	ν	32	$\bar{\nu}$	2000 - 2500
13	ν	33	$\bar{\nu}$	2500 - 3000
14	ν	34	$\bar{\nu}$	3000 - 3500
15	ν	35	$\bar{\nu}$	3500 - 4000
16	ν	36	$\bar{\nu}$	4000 - 5000
17	ν	37	$\bar{\nu}$	5000 - 7000
18	ν	38	$\bar{\nu}$	7000 - 10000
19	ν	39	$\bar{\nu}$	10000 - 30000

TABLE 8.1: List of the flux bins.

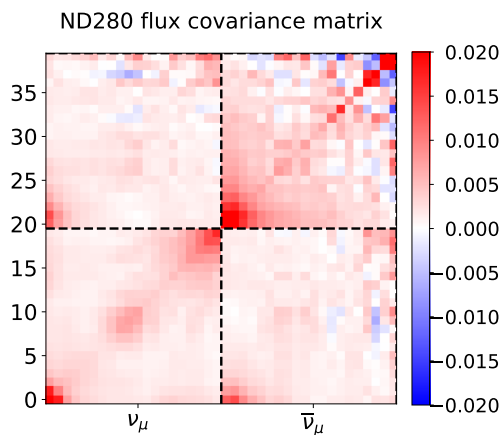


FIGURE 8.4: Flux covariance matrix from the flux release 13av7 [488]. Vertical lines separate the two neutrino flavors under consideration.

8.2.3 Cross section model systematics covariance

The cross section model systematic errors arise from the uncertainties of the parameters governing the MC model predictions. To characterize how varying these parameters affects to the prediction of the event rate a special package, known as T2KReWeight, is used to calculate reweighting functions describing these variations. The parametric form of these functions is calculated as follows:

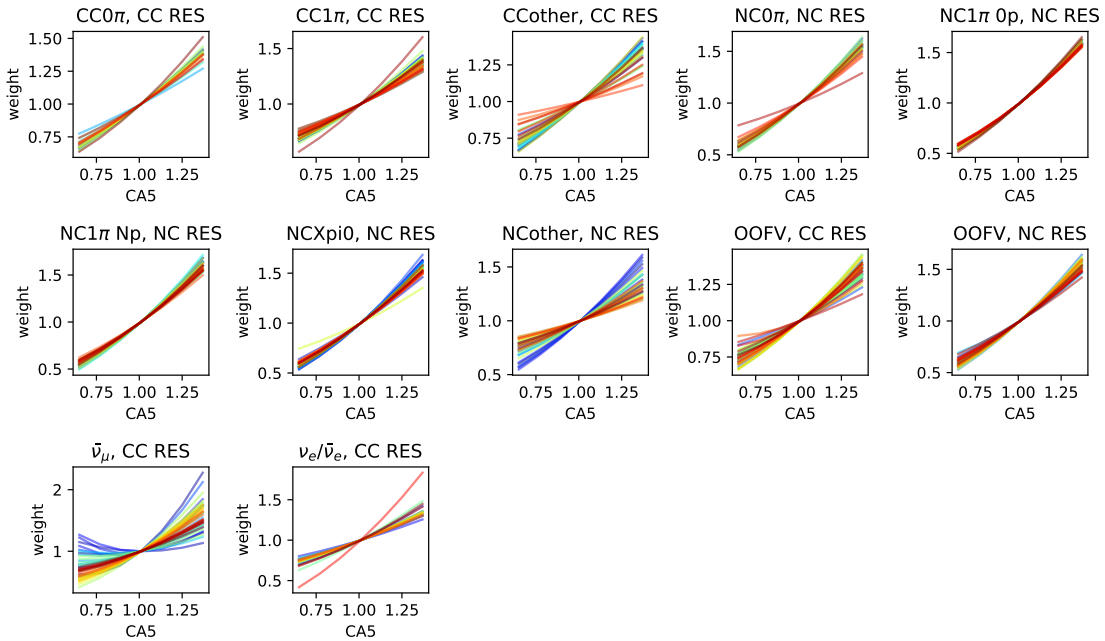


FIGURE 8.5: Non-trivial splines for the C_A^5 model parameter, presented in Sec. 3.2.2. Each panel represents a bin in topology and reaction, indicated in the panel title, and each line represented with a different color describes how the weights for the events must change in a given kinematic bin.

- All the selected events are grouped by their topology and reaction.
- Kinematics bins are defined. For this purpose the bins for the reconstructed kinematics earlier presented in Sec. 8.1.4 are used.
- For each model parameter, for each topology, reaction and kinematic bin the events are reweighted using `T2KReWeight` to compute how varying that model parameter changes the number of events in that bin. In total, 7 values are considered for each parameter ranging from -3σ to $+3\sigma$ of its nominal value, moving in steps of 1σ .
- The final function are obtained interpolating the results at every step by means of splines.

In total 11 topologies are used, i.e. those enumerated in Sec. 6.2.2, and a total of 7 reactions have been defined⁴: CCQE, CCRES, CCDIS, CCCoh, NCE, NCRES and NCDIS. Considering that 43 kinematics bins are used, a total of 3311 splines have been computed for each model parameter. Since in most cases a model parameters acts only in some reactions and typically each topology has only a subset of reactions most splines are trivial, namely, their value is equal to one in the whole domain. For illustration, examples of all the non-trivial splines for the C_A^5 model parameter are presented in Figure 8.5.

To fit the signal, 20 model parameters have been considered, summarized in Table 8.2. The possible variations of these parameters are constrained by the existing knowledge on each of them, encoded in the covariance matrix presented in Figure 8.6 provided by T2K's Neutrino Interaction Working Group (NIWG).

⁴The reactions have been named as follows: CC and NC characterize reactions arising from charged and neutral current interactions respectively. CCQE and NCE are associated to quasi-elastic and elastic scattering, RES stands for resonant pion production, Coh for coherent pion production and DIS for deep inelastic scattering. Details on these processes have been earlier presented in Sec. 3.3.

Index	Parameter	Type
0	M_A^{QE}	shape
1	2p2h norm	normalization
2	2p2h shape	shape
3	M_A^{RES}	shape
4	C_A^5	shape
5	I12RES	normalization
6	CC1 π $E_\nu < 2.5\text{GeV}$	normalization
7	CC1 π $E_\nu > 2.5\text{GeV}$	normalization
8	DIS	shape
9	CC DIS	normalization
10	CC Multi- π	normalization
11	CC Coherent on C	normalization
12	NCE	normalization
13	NC RES π^0	normalization
14	FSI Inelastic $< 0.5\text{GeV}$	shape
15	FSI π absorption	shape
16	FSI Charge exchange, $< 0.5\text{GeV}$	shape
17	FSI Inelastic, $> 0.5\text{GeV}$	shape
18	FSI π production	shape
19	FSI Charge exchange, $> 0.5\text{GeV}$	shape

TABLE 8.2: Summary of cross section model parameters. Normalization parameters change the overall event production scale whilst shape parameters modify the shape of the event distributions.

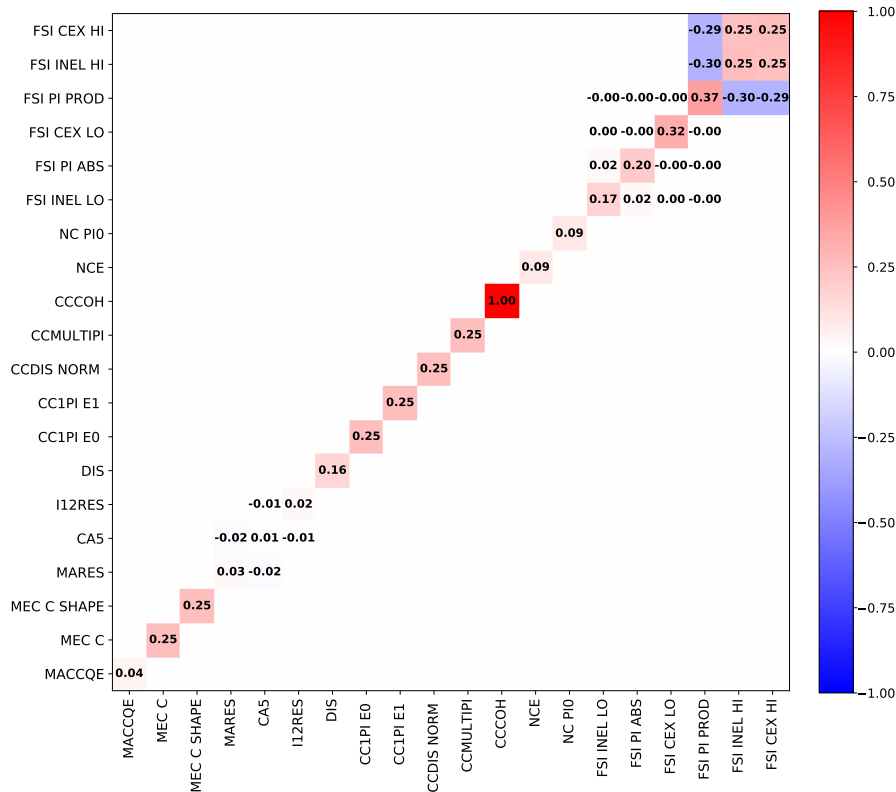


FIGURE 8.6: Covariance matrix for the cross section model nuisance parameters.

8.3 Normalization factors

To extract the signal cross section, see Eq. 8.9, it is necessary to calculate the selection efficiency in each true kinematic bin, the number of targets in the fiducial volume, the integrated flux and to account for their uncertainties. To do so, 1000 toy sets of N_i^{signal} are sampled from the fitter output covariance matrix. For each, the cross section is extracted using normalization factors sampled from their uncertainty distributions. The results characterize the extracted cross section and its uncertainty.

8.3.1 Number of targets

The number of target nucleons in FGD1 has been calculated in the past to be of $5.53 \cdot 10^{29} \pm 0.67\%$ nucleons [484]. The calculation was made using the same X and Y fiducial volume restrictions but using all FGD1 layers. In the NC1 π^+ selection, however, only 27 FGD1 layers are considered. To account for this difference, the number of nucleons has been scaled proportionally to the number of FGD1 layers and, conservatively, the error has not been scaled but kept as 0.67%. Consequently, we use

$$n^{FV} = 4.977 \cdot 10^{29} \pm 0.67\% \quad \text{nucleons.} \quad (8.10)$$

8.3.2 Efficiency

The efficiency in the kinematics bins described in Sec. 8.1.5 is calculated from MC. Whereas the total number of signal events is fixed the number of selected events is specified by N_i^{signal} . Hence, the efficiency is calculated independently for each toy fit result. For illustration, the efficiency for the best fit point N_i^{signal} associated to the Asimov fit later presented in Sec. 8.4.1, is presented in Figure 8.7.

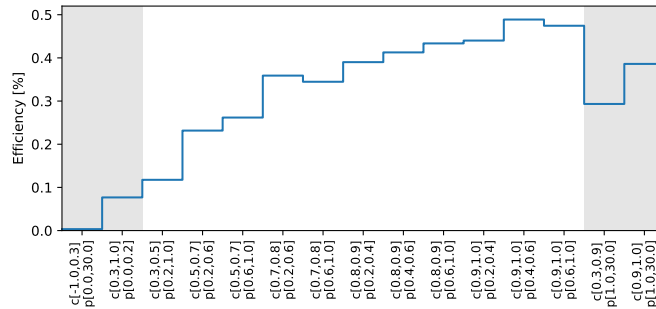


FIGURE 8.7: Selection efficiency calculated for the best fit point of the fit later presented in Sec. 8.4.1. The region covered by each bin is detailed in the x-axis, where c and p stand for the $\cos\theta$ and p_{π^+} intervals respectively. All the bins out of the phase space of interest are covered by gray shades.

8.3.3 Flux

The T2K beam prediction has been presented earlier in Sec. 5.2.2. To calculate the flux integral and account for its posfit uncertainty the nominal T2K flux prediction is reweighted using the flux model parameter values in each toy fit result. Importantly, in order to keep a clean flux normalization definition, in the fit, among all NC1 π^+ -0 μ events only those arising from ν_{μ} interactions are treated as signal. Consequently, the flux integral corresponds to the reweighted ν_{μ} flux prediction.

8.4 Fake data studies

8.4.1 Asimov fit

To validate the basic performance of the fitter and illustrate how to evaluate the fit results the NEUT MC prediction scaled to the data POT is fit to itself, in what is known as an Asimov Fit. The results are presented in Figure 8.8. The plot consists of four panels each containing a distinct block of information. The prefit central values are all set to one and their uncertainty bands reflect the prior knowledge on these parameters. The posfit central values and errors are the outcome of the fitter.

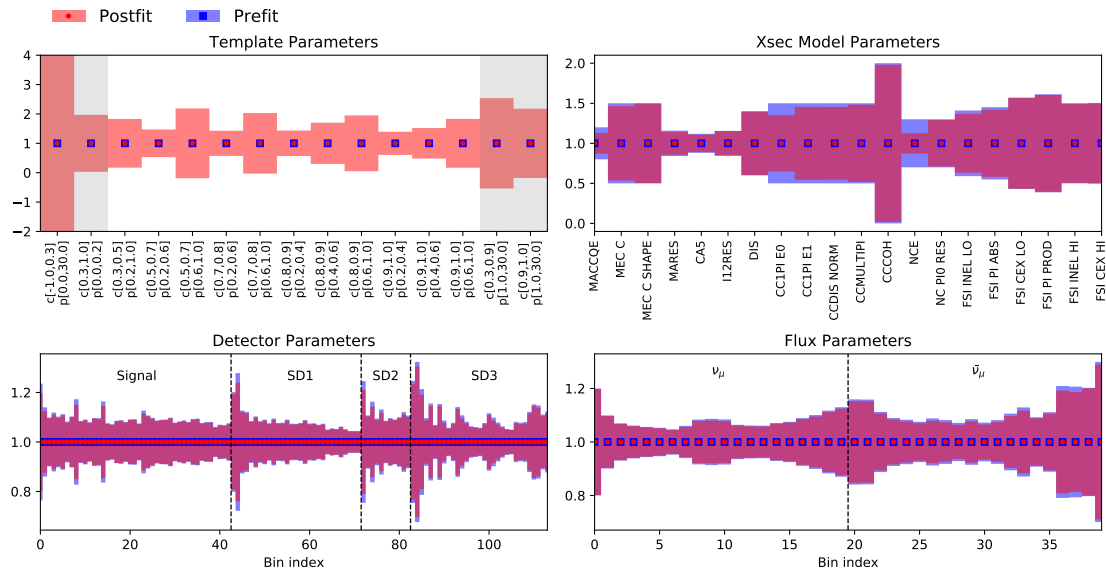


FIGURE 8.8: Prefit and Posfit parameters and errors for the Asimov Fit split in template parameters and the nuisance parameters divided in cross section, detector and flux model parameters. For the template parameters the region covered by each bin is detailed in the x-axis, where c and p stand for the $\cos \theta$ and p_{π^+} intervals respectively. All the bins out of the phase space of interest are covered by gray shades.

In the case of an Asimov fit the expected and observed distribution of events are identical such that the set of parameters that maximizes the likelihood corresponds to their prior values. In consequence, a successful Asimov fit has posfit central values exactly at their prefit location and has nuisance parameter posfit uncertainties equal or smaller than the prefit as the good agreement between expectation and observation constrains the parameter uncertainties.

To extract the cross section, the fit output is stored in the form a covariance matrix. The correlation matrix for the Asimov fit discussed above is presented in Figure 8.9. As it can be seen template parameters, indicative of the signal cross section, are in general anticorrelated to flux parameters. This is expected since for a given number of observed events increasing the flux decreases the size of the cross section necessary to predict it. Likewise, template parameters and detector parameters are typically anticorrelated. In some cases, however, this correlation is instead positive. This is because reducing the detector parameters allows in some cases to decrease the background predictions by tweaking the cross section model, such that to explain the same number of observed events higher template parameters are needed.

The cross section results obtained for the Asimov fit are presented in Figure 8.10. As it can be seen, when fitting NEUT to itself the extracted cross section matches, by definition, the nominal NEUT prediction. For comparison, the GENIE nominal prediction is also shown. Interestingly, at the current level of error both NEUT and GENIE are compatible in all bins within uncertainties. To extract the cross section in a single bin defined by $\cos \theta_{\pi^+} > 0.3$ and $0.2 < p_{\pi^+} < 1.0$ GeV/c

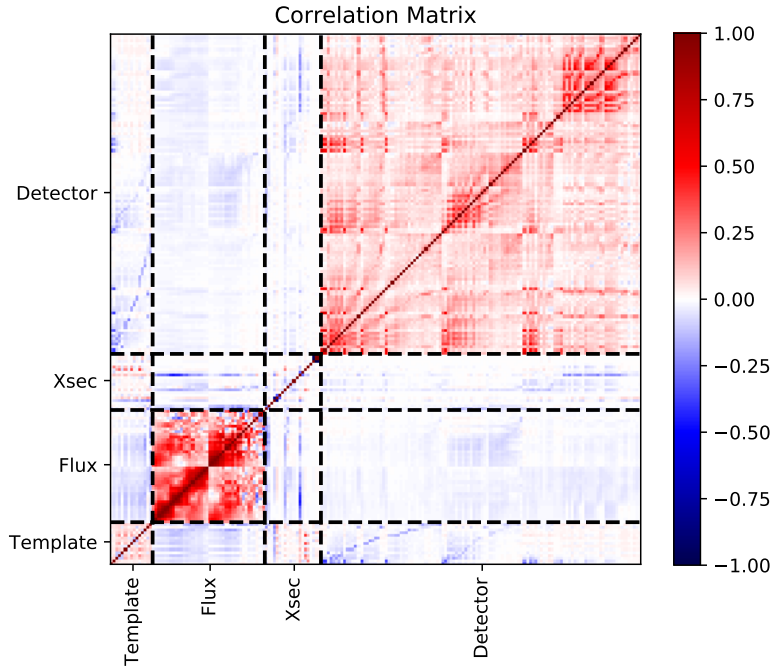


FIGURE 8.9: Posfit correlation matrix for the Asimov fit.

we merged the cross section results in all the bins there contained using the covariance matrix of the extracted cross section, leading to the following result:

$$\sigma_{\text{NC1}\pi^+ 0p}^{\text{Asimov NEUT}} = 1.26 \pm 0.31 \text{ (stat+syst)} \frac{10^{-40} \text{ cm}^2}{\text{nucleon}} \quad (8.11)$$

Hence, for $1.16 \cdot 10^{21}$ POT we expect a measurement with a 24.6% uncertainty. Interestingly, the Asimov fit can be done disabling different subsets of parameters, which allows to assess their contribution to the total uncertainty. The results are presented in Table 8.3. As it can be seen the dominant uncertainties arise, primarily, from the statistical and cross section model uncertainties. As all of the parameters are correlated, increasing the number of events would not only reduce the statistical error but all contributions to some extent. To show the potential of the NC1 π^+ selection algorithm samples, a very high statistics asimov fit has been done in which the full MC dataset with $20.35 \cdot 10^{21}$ POT has been used without scaling it to the data POT. This corresponds to a hypothetical increase of about $\times 17.5$ more data. The results render a 15.4% total uncertainty, showing that, in the future, a significantly tighter constrain on this process can be obtained by simply accumulating more data.

Parameters	Uncertainty [%]	Stat. Subtracted [%]
Template	14.0%	-
Template & Flux	15.8%	6.6%
Template & Detector	16.5%	8.7%
Template & Cross Section	21.2%	15.9%

TABLE 8.3: Cross section uncertainty measured using Asimov fits with different subsets of parameters enabled. Using only template parameters allows to estimate the statistical contribution alone. The individual contribution of the flux, detector and cross section model parameters is evaluated by disabling the other nuisance parameters and subtracting the statistical uncertainty in quadrature.

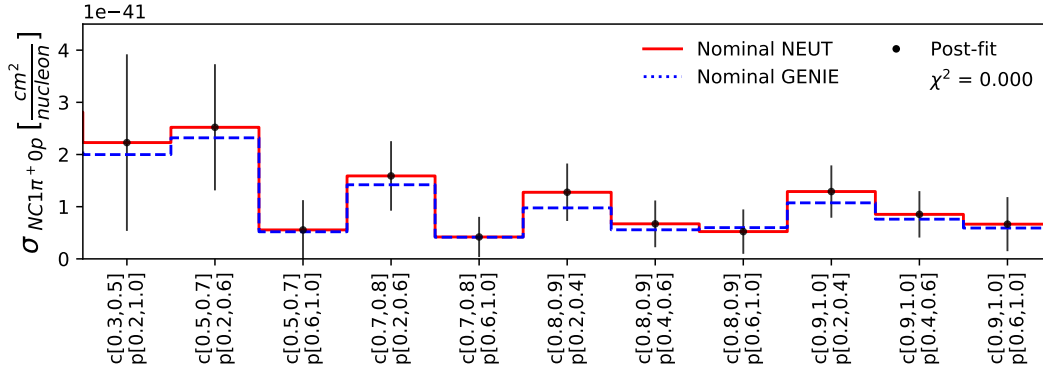


FIGURE 8.10: Extracted cross section in each true bin using the Asimov Fit results using the complete set of nuisance parameters. The fit results are compared to NEUT and GENIE nominal predictions. The region covered by each bin is detailed in the x-axis, where c and p stand for the $\cos \theta$ and p_{π^+} intervals respectively. Only bins enclosed by $\cos \theta_{\pi^+} > 0.3$ and $0.2 < p_{\pi^+} < 1.0$ GeV/c are presented.

8.4.2 Fake data studies

To test the robustness of the fitter to variations which might happen in reality, related to MC miss-modelings of the true physics observed in the detector, a set of fake data studies have been made to evaluate the reaction of the fitter to such controlled tests. In each of this fake data studies, a sub-set of events is reweighted to simulate, in a controlled manner, a particular effect. The results are summarized in Table 8.4.

Fake dataset	Cross section		
	$[\frac{10^{-40} \text{ cm}^2}{\text{nucleon}}]$	Ratio	χ^2
Nominal (NEUT)	1.26 ± 0.31	-	0.000
OOFV $\times 1.3$	1.26 ± 0.30	1.00	0.013
CC1 π^+ $\times 0.8$	1.16 ± 0.31	1.00	0.003
$\bar{\nu}_\mu$ CC $\times 1.2$	1.28 ± 0.31	1.02	0.152
signal $\times 1.2$	1.53 ± 0.33	1.21	0.004
signal $\times 0.8$	0.99 ± 0.25	0.79	0.007
NCE $\times 0.8$	1.26 ± 0.30	1	0.037
NC1 π^+ Np $\times 5$	1.34 ± 0.31	1.06	0.258

TABLE 8.4: Summary of fake data studies. All fake data sets have been obtained by weighting a subset of events as indicated in the first column, fitting them with the nominal NEUT MC prediction and extracting the cross section for the postfit. The quantify the variation of the result its value as a ratio to the true cross section in the fake data study is also presented. Finally, the χ^2 for the 11 bins being considered is included.

The extracted cross section for the different fake datasets indicate that, in general, the model is robust to background variations. This is particularly relevant for OOFV and $\bar{\nu}_\mu$ CC which constitute a significant fraction of the events selected in the signal sample. The only mild exception to this rule is the fake dataset consisting of NC1 π^+ Np $\times 5$, which generates an upshift in the cross section similar to 6%. Arguably, the increase of the background in that test is drastic (500%), however, it is also true that this is the level of discrepancy observed in this topology for NEUT and GENIE, as earlier presented in Sec. 7.3.1. Nonetheless, it is important to realize that the 6% shift is well below the total level of uncertainty.

In the studies where only the signal is increased or decreased by 20% very similar extracted cross section variations to those expected are observed.

Lastly, it is worth to mention that the calculated χ^2 values using the extracted cross section covariance matrix are generally very small, specially if one considers the number of degrees of freedom (11 bins). This is expected, since in these tests controlled variations are applied on the nominal prediction without statistical fluctuations and therefore the posfit solution is expected to be in very good agreement with the observed event rates, translating into a small χ^2 given the current uncertainty levels.

GENIE

The most demanding test concerning fake data studies is that of fitting NEUT MC to GENIE MC with both scaled to the data POT. As earlier presented in Sec. 7.3.1 NEUT and GENIE have significant differences in their background predictions. In addition, the two generators have a sensibly different cross section in the region defined by $\cos\theta_{\pi^+} > 0.3$ and $0.2 < p_{\pi^+} < 1.0$ GeV/c, namely⁵

$$\sigma_{\text{NC}1\pi^+0p}^{\text{GENIE}} = 1.12 \frac{10^{-40} \text{ cm}^2}{\text{nucleon}} \quad (8.12)$$

which is 11% smaller than that for NEUT, see Eq. 8.11.

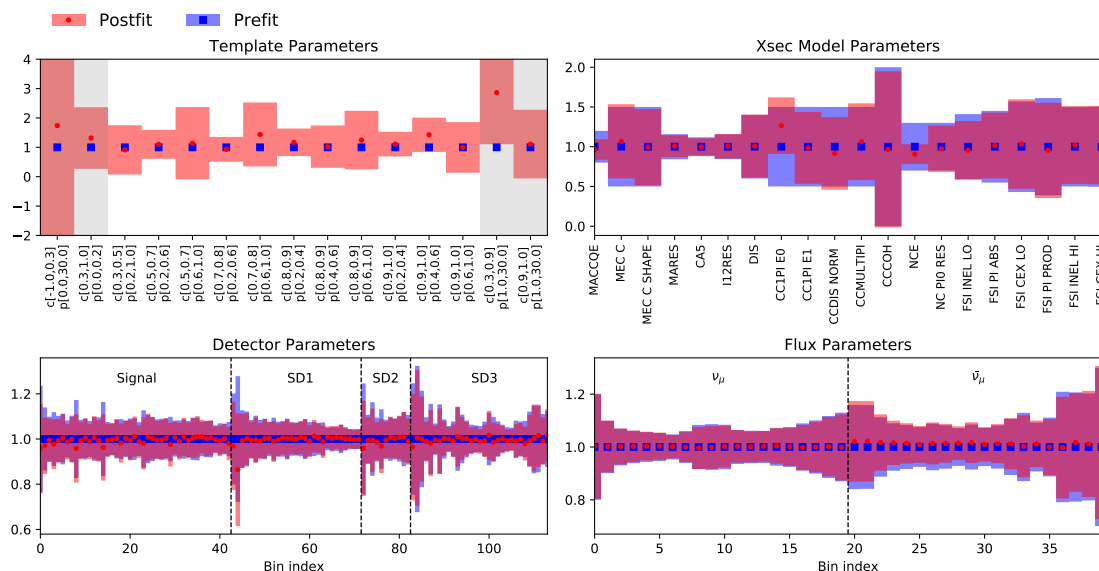


FIGURE 8.11: Prefit and Posfit parameters for the fit to the GENIE MC dataset split in template parameters and the nuisance parameters divided in cross section, detector and flux model parameters. For the template parameters the region covered by each bin is detailed in the x-axis, where c and p stand for the $\cos\theta$ and p_{π^+} intervals respectively. All the bins out of the phase space of interest are covered by gray shades.

The results of the GENIE fake data fit are presented in Figure 8.11. Overall, most posfit features are reasonable if the differences in NEUT and GENIE described in Sec. 7.3 are considered.

- Concerning the cross section model parameters, the most notable posfit results are that CC1 π for $E_{\nu} < 2.5$ GeV is pulled up (CC1PI E0) and NCE is pulled down. These results are reasonable in light of the NEUT and GENIE predictions for SD2 and SD3.

⁵To avoid computing splines for GENIE, the nominal GENIE cross section is estimated doing an Asimov fit to the GENIE MC dataset using only template and flux parameters. This leads to a valid calculation of the nominal GENIE cross section in the relevant bins but for consistency the uncertainty is not quoted.

- Regarding the flux parameters, the ν_μ flux is preferred at its prefit values whilst the $\bar{\nu}_\mu$ is increased in most bins by few percent, a trend which matches the fact that GENIE predicts more events in SD1 than NEUT. In fact, a similar flux increase is observed in the $\bar{\nu}_\mu$ CC $\times 1.2$ fake data study. Ideally, it would be better to control $\bar{\nu}_\mu$ CC variations by pulling cross section model parameters and leaving the flux parameters unchanged. However, the variations of these parameters do not seem enough to fully describe the discrepancies in NEUT and GENIE. Nonetheless, it is interesting to notice that the posfit M_A^{QE} parameter is a mildly lower than the prefit, a trend that goes in line to NEUT and GENIE implementation differences, reviewed in Sec. 3.4.
- The posfit detector parameters remain generally close to their prefit values. In general, this is expected as detector parameters are pulled to compensate MC-data detector mismodelings which are not present in this MC vs MC fake data study. In addition, detector parameters often absorb random statistical fluctuations. However GENIE MC dataset scaled to data POT has small statistical fluctuations, requiring smaller pulls to accommodate them.
- Finally, the template parameters remain either at their prefit values or are slightly pulled up, indicating a preference for a cross section larger than that of the nominal NEUT prediction.

The cross section results extracted from the fit to the GENIE dataset are presented in Figure 8.12. As it can be seen the observation matches the posfit parameters with a low $\chi^2 = 1.004$. The results, however, overestimate the cross section slightly in some bins leading to the combined result for $\cos \theta_{\pi^+} > 0.3$ and $0.2 < p_{\pi^+} < 1.0$ GeV/c of:

$$\sigma_{\text{NC}1\pi^+0p}^{\text{GENIE, from NEUT}} = 1.36 \pm 0.30 \frac{10^{-40} \text{ cm}^2}{\text{nucleon}} \quad (8.13)$$

Interestingly, this result is both higher to the nominal cross section of NEUT ($1.26 \frac{10^{-40} \text{ cm}^2}{\text{nucleon}}$) and GENIE ($1.12 \frac{10^{-40} \text{ cm}^2}{\text{nucleon}}$). However, when the measurement uncertainty is considered, the extracted cross section for GENIE using NEUT predictions matches the nominal GENIE cross section at the 0.8σ level. Consequently, this fake study indicates that the fit is able to estimate the signal cross section effectively even when the signal and background components are fairly different.

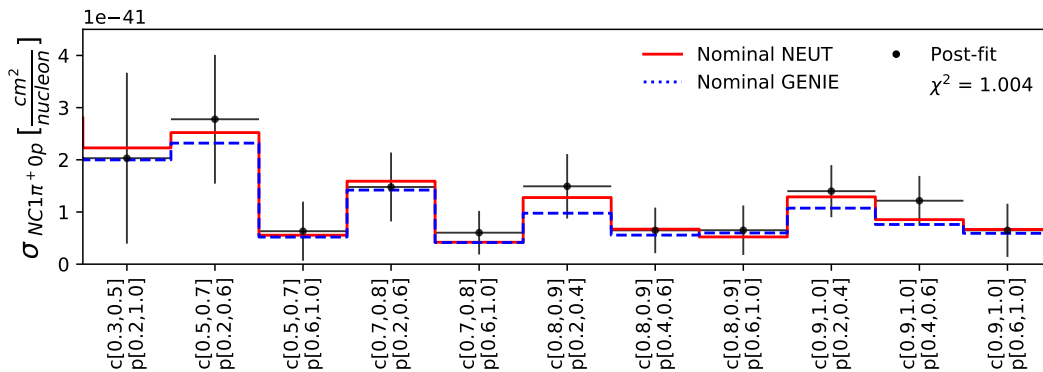


FIGURE 8.12: Extracted integrated cross section in each true bin for the GENIE fake data fit. The fit results are compared to NEUT and GENIE nominal predictions. The region covered by each bin is detailed in the x-axis, where c and p stand for the $\cos \theta$ and p_{π^+} intervals respectively. Only bins enclosed by $\cos \theta_{\pi^+} > 0.3$ and $0.2 < p_{\pi^+} < 1.0$ GeV/c are presented.

8.5 Data Fit

Lastly, the MC is fit to the data in order to measure the $\text{NC1}\pi^+$ cross section. The fit results are presented in Figure 8.13. The fit results show a set of interesting features:

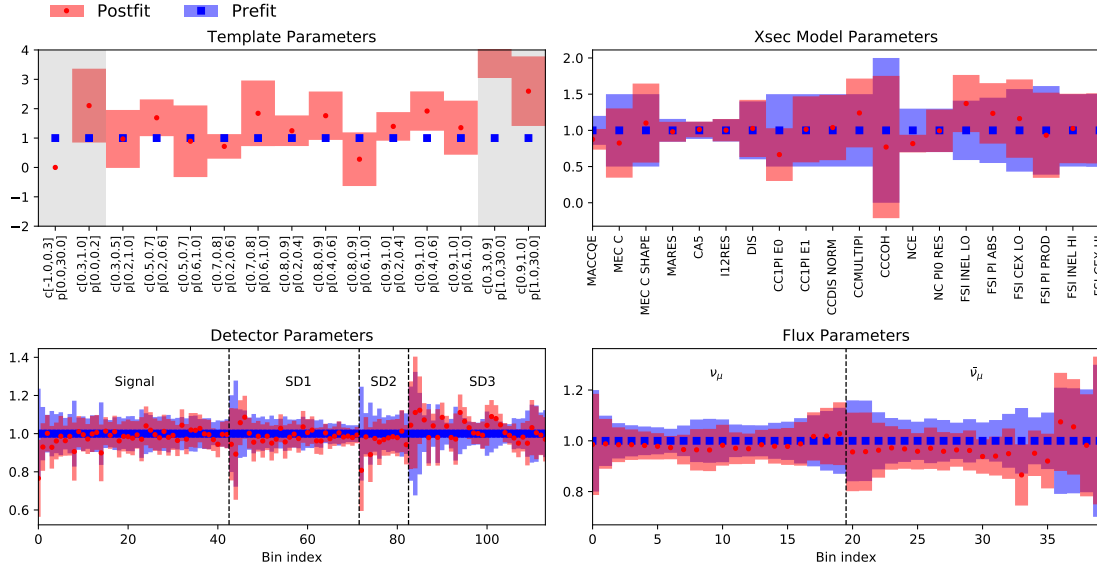


FIGURE 8.13: Prefit and Postfit parameters and errors for the fit to data split in template parameters and the nuisance parameters divided in flux, detector and cross section model parameters.

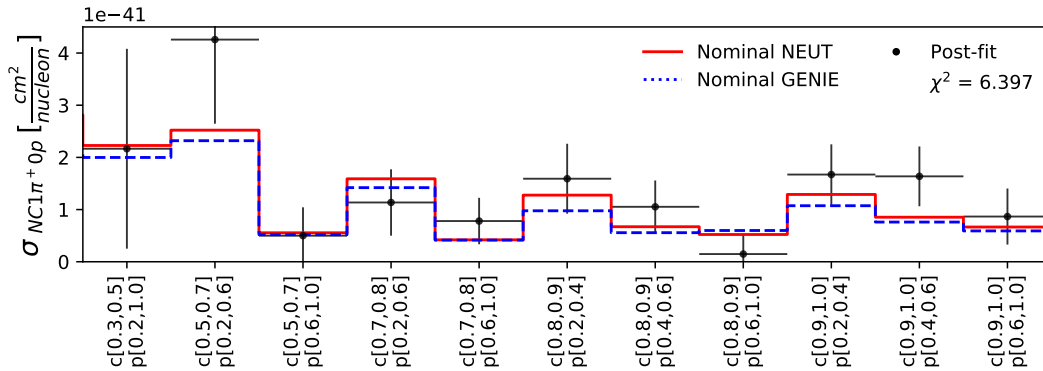


FIGURE 8.14: Extracted integrated cross section in each true bin for the ND280 data. OOPS bins are not shown nor used in the calculation of the χ^2 .

- Whilst the prefit ν_μ beam prediction is very close to the prefit, in general, the $\bar{\nu}_\mu$ beam prediction is pulled down, to about 90% of its original value in most flux bins.
- Several cross section model parameters are pulled down significantly: the CC1PI E0 dial responsible for the CC1 π for $E_\nu < 2.5$ GeV normalization; the NCE dial controlling the NCE normalization; and the M_A^{QE} and 2p2h normalization dials affecting the CCQE and 2p2h predictions respectively. Interestingly, some cross section parameters are also pulled up, particularly CCMULTIPI related to the production of multiple pions, and three FSI parameters, related to the amount of inelastic interactions for low energy particles, the amount of π absorption and FSI charge exchange.
- No major effects are observed in the detector nuisance parameters, which is indicative of an overall good description of the detector effects in the nominal simulation across all bins.

Some posfit detector parameters are pulled slightly up and down but their anarchic pattern is likely induced by statistical fluctuations.

- Concerning the template parameters, in general, posfit values are equal or higher than one, indicating a preference for a larger signal cross section than in the nominal NEUT simulation.

The cross section results are presented in Figure 8.14. As anticipated from the template posfit values, in general, a cross section larger than the nominal NEUT and GENIE predictions is preferred. The posfit agreement between prediction and observation is good with a $\chi^2 = 6.066$ for 11 degrees of freedom. The cross section for $\cos \theta_{\pi^+} > 0.3$ and $0.2 < p_{\pi^+} < 1.0$ GeV/c is:

$$\sigma_{\text{NC}1\pi^+ 0p}^{\text{DATA}} = 1.58 \pm 0.34 \text{ (stat+syst)} \frac{10^{-40} \text{ cm}^2}{\text{nucleon}} \quad (8.14)$$

This result is compatible with the nominal NEUT prediction with less than 1σ and with GENIE at the 1.4σ level. Overall, the fit indicates, with weak statistical confidence, that a larger cross section than predicted by both models is preferred.

Lastly, it is worth noting that the posfit uncertainty is of 21.5%. Notably, even if this number is only informative of the protonless NC $1\pi^+$ events, which as discussed in Sec. 6.2.3 are expected to be at least 70% of the total, an almost $\times 3$ improvement is achieved when compared to the 59% [473] uncertainty currently used for this type of interactions in T2K's OA.

Part III

T2K-II and the ND280 upgrade

Chapter 9

T2K-II and the ND280 upgrade

“At some point we have to give up and say that’s just the way it is. Or, not give up and push on.”

– LEONARD SUSSKIND

9.1 Introduction

The originally approved T2K running period expired in 2020, with an expected number of $7.8 \cdot 10^{21}$ POT. In 2016, a number of arguments supported the continuation of the experiment:

- In 2013, T2K discovered ν_e appearing from $\nu_\mu \rightarrow \nu_e$ [425]. This demonstrated that θ_{13} was large enough for T2K to be sensitive to the value of δ_{CP} .
- Although having small sensitivity, in 2015 using $6.6 \cdot 10^{20}$ POT, T2K’s oscillation analysis revealed a mild preference for CP being maximal [428], also favoring a potential determination of the CP non-conservation hypothesis.
- In 2013 tests were made to make Super-Kamiokande sensitive to neutrons by means of dissolving a Gd salt on the water started [489], leading to positive results in 2016 and the intention to implement this solution in SK in 2018 [490].
- On 2016, the NA61/SHINE experiment measured the meson production yields on a T2K replica target [444] significantly reducing the beam prediction related systematics.
- In 2011, a first letter of intent for the Hyper-Kamiokande project was launched [491]. In 2013, a study of the HK physics potential was published [492] followed up in 2014 by the first studies presenting the possibility of a future T2HK experiment [493].

In consequence, in 2016 the T2K collaboration presented a proposal to extend its operation [494]. The second phase of T2K, hereafter named T2K-II, would have the following goals:

- Upgrade the beam and operate at the power of 1.3 MW before the start of HK.
- Improve the selection efficiency by $\sim 50\%$ by means of software improvements and the inclusion of new data samples.
- Reach enough sensitivity to reject the CP conservation hypothesis at the 3σ level, assuming its true value to be $-\pi/2$.
- Determine the oscillation parameters θ_{23} and Δm_{23}^2 with a precision of 1.7° or better and 1% respectively.

- Deepen in the knowledge of neutrino-nucleus cross section and continue to supply data for the development of further refined interaction models, crucial for the next generation of experiments.

For this to be achieved, two necessary conditions were presented:

- To upgrade the beam and get sufficient beam time per year to accumulate about $2 \cdot 10^{21}$ POT by 2026.
- To decrease the uncertainties on the neutrino rate predictions from 5-6%, to about 4 %.

The plan was to progressively increase the beam power through two main upgrades, one in 2021 and the other in 2024, reaching 1.3 MW in 2026. The projected sensitivity to δ_{CP} with the improved efficiency and systematics is shown in Figure 9.1. The projected reach to Δm_{23}^2 and θ_{23} are presented in Figure 9.2 and Figure 9.3 respectively. Remarkably, as presented in Figure 9.3, for a true value of $\sin^2 \theta_{23} = 0.6$ the octant degeneracy would be resolved with more than 3σ .

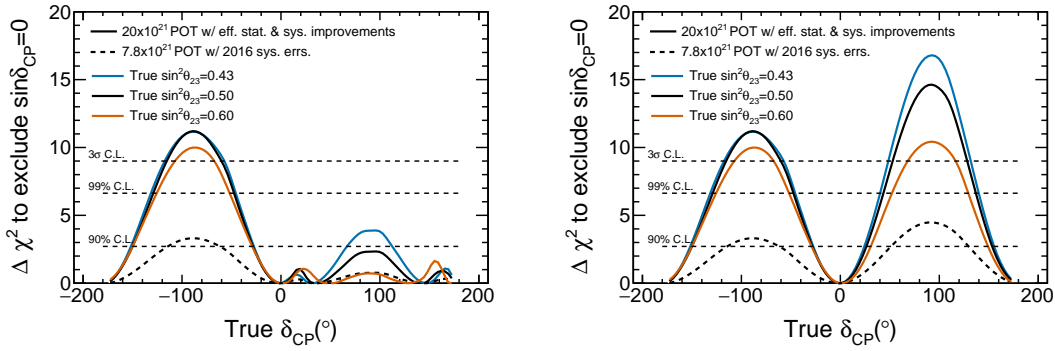


FIGURE 9.1: Projected sensitivity to exclude CP conservation depending on its true value. The plot is obtained re-scaling the systematics to 2/3 of its value in 2016 such that a $\sim 4\%$ level systematics are considered and assuming a selection efficiency increase of 50%. The results are shown for different values of θ_{23} and assuming that the mass hierarchy is not known, left, and known, right. Figure from Ref. [494].

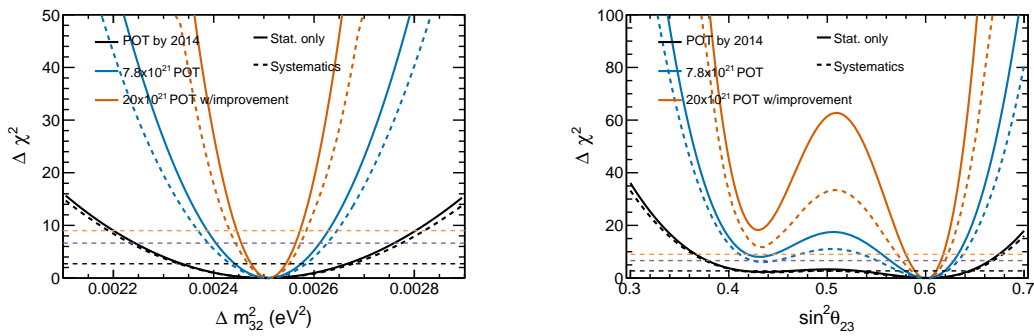


FIGURE 9.2: Expected improvement in the determination of Δm_{23}^2 , for a true value of $\sin^2 \theta_{23} = 0.6$. Figure from Ref. [494].

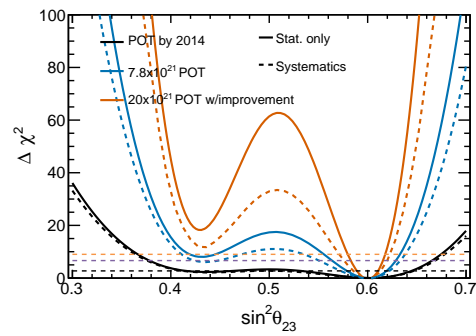


FIGURE 9.3: Expected improvement in the determination of $\sin^2 \theta_{23}$, for a true value of $\sin^2 \theta_{23} = 0.6$. Figure from Ref. [494].

In order to reach an overall $\sim 4\%$ level in the systematics a major concern was to be able to control with good precision the modeling on neutrino-nucleus interactions. A breakdown of the 2016 systematics are presented in Table 9.1. The systematics on the cross section modeling were evaluated by measuring the variation in the results running different interactions models. With the data collected in 2016 the observed changes were small compared to the total error, however, this

Error Type	$\delta_{N_{SK}}/N_{SK}$ (%)				
	1-Ring μ		1-Ring e		
	ν mode	$\bar{\nu}$ mode	ν mode	$\bar{\nu}$ mode	$\nu/\bar{\nu}$
SK Detector	3.9	3.3	2.5	3.1	1.6
SK Final State & Secondary Interactions	1.5	2.1	2.5	2.5	3.5
ND280 Constrained Flux & cross section	2.8	3.3	3.0	3.3	2.2
$\sigma_{\nu_e}/\sigma_{\nu_\mu}, \sigma_{\bar{\nu}_e}/\sigma_{\bar{\nu}_\mu}$	0.0	0.0	2.6	1.5	3.1
NC 1γ cross section	0.0	0.0	1.5	3.0	1.5
NC Other cross section	0.8	0.8	0.2	0.3	0.2
Total Systematic Error	5.1	5.2	5.5	6.8	5.9
External Constraint on $\theta_{12}, \theta_{13}, \Delta m_{21}^2$	0.0	0.0	4.1	4.0	0.8

TABLE 9.1: Breakdown of the systematic errors associated to 2016 event rate predictions in Super-K muon and electron ring samples in neutrino (ν -mode) and antineutrino beam mode ($\bar{\nu}$ -mode). Uncertainties arising from multinucleon effects (2p2h) are not included. Table from Ref. [494].

was known to be a temporal solution as the poor knowledge on the nucleon initial state and of 2p2h interactions would become a more prominent systematic with increased data [494]. Moreover, when T2K was being built up in the late 2000s, 2p2h interactions in neutrino scattering had never been studied and were not foreseen to play a meaningful role in neutrino oscillation experiments. It was only after some neutrino experiments, including T2K, found data-MC discrepancies in the mid 2010s that 2p2h started to be regarded as a major nuisance. This experience illustrated the importance of deepening in the understanding on neutrino-nucleus interactions with the goal to uncover potential unknowns. Accordingly, possible upgrades for the ND280 detector were under consideration.

9.2 T2K's Beam upgrade

The T2K beam upgrade can be separated into the main ring upgrades, which will allow to deliver and increased beam power and the neutrino beamline upgrades necessary to handle it. A complete report on these two upgrades was presented in the J-PARC neutrino beamline upgrade technical design report [305], published in 2019.

9.2.1 J-PARC main ring upgrades

J-PARC was designed having in mind a possible upgrade which would reduce the beam repetition cycle from 2.48 s to 1.32 s, such that at the expected beam intensity of 2.0×10^{14} protons per pulse (ppp) the beam would reach a power of 750 kW. However, in 2021 T2K was running with a beam power of 511 kW using 2.6×10^{14} ppp, higher than originally planned. Thus, by maintaining the pulse intensity and upgrading the repetition cycle as expected, J-PARC would reach a beam power of about 960 kW. An initial set of upgrades were performed along 2021 and consisted on the following tasks:

- Upgrade all power supplies for the main ring magnets.
- Upgrade all main ring radiofrequency (RF) cavities.
- Upgrade of the injection and extraction devices.
- Increase the main ring collimator capacity.
- Upgrade of a subset of the main ring quadrupole magnets to increase their aperture.

The roadmap for the future is to achieve 1.3 MW through a series of upgrades planned around 2024:

- Upgrade the main ring RF cavities power supply.
- Install two additional RF cavities.
- Upgrade the main ring beam position monitors.
- Upgrade the main ring fast extraction kicker magnet.

Necessary to reach 3.2×10^{14} ppp and a slightly faster cycle rate of 1.16 s. A summary of the main parameters for the current and proposed beam powers is presented in Table 9.2. In 2021, T2K-I

Beam power	511 kW (achieved)	960 kW (proposed)	1.3 MW (proposed)
Beam energy	30 GeV	30 GeV	30 GeV
Beam intensity (ppp)	2.6×10^{14}	2.6×10^{14}	3.2×10^{14}
Repetition cycle	2.48 s	1.32 s	1.16 s

TABLE 9.2: Summary of the MR operation parameters for the current and proposed beam power.

stopped collecting data to proceed with the beam and near detector upgrades, reaching a total of 3.82×10^{21} POT. This was lower than originally planned (7.8×10^{21} POT) due to a number of reasons that range from the increase in prices in electricity in Japan originated by the progressive nuclear reactors shut down after 2011's earthquake to the maintenance tasks in SK to load it with Gadolinium and the Sars-Cov2 pandemic. Currently, the plan is to reach $1 \cdot 10^{22}$ POT by 2026, before the start of Hyper-Kamiokande.

9.2.2 Upgrade in the neutrino beamline

All beamline elements were designed to deal with, at least, 750 MW. Additionally, the instruments in the primary neutrino beamline were found to be able to operate at 1.3 MW without modifications. However, several elements in the secondary beamline needed to be upgraded, as summarized in Table 9.3. Consequently, the following upgrades were performed in 2021:

- Improve the target titanium container to allow higher helium pressures to increase the helium flow rate ($\times 2$).
- Design and install a new beam window with an improved cooling capacity.
- Upgrade the horns power supplies and their cooling system with the goal to reach a horn pulsed current of 320 kA at a rate of 1 Hz. This is expected to increase to flux by an additional $\sim 10\%$.
- Improve the hydrogen removal system by implementing a recombination system in the water cooling system of the horns. Hydrogen is flammable and is produced by water radiolysis.
- Improve the cooling capacity of all components in the secondary beamline.
- Increase the radiation shielding installing additional concrete blocks.
- Upgrade the radioactive water disposal system. This includes reducing the volume of water in the cooling systems and install a larger disposal tank (400 m^3). The main contaminant is tritium ($T_{1/2} = 12.32$ years).

Component	Limiting factor	Current acceptable value
Target	Thermal shock	3.3×10^{14} protons/pulse
	Cooling capacity	0.9 MW
Beam window	Thermal shock	3.3×10^{14} protons/pulse
	Cooling capacity	0.75 MW
Horn	Conductor cooling	2 MW
	Stripline cooling	0.75 MW
	Cooling capacity	0.98 MW
	Hydrogen removal	1 MW
	Operation current and cycle	250 kA, 2.48 s
Target Station helium vessel	Thermal stress	4 MW
	Cooling capacity	1 MW
Decay Volume	Thermal stress	4 MW
	Cooling capacity	1 MW
Beam Dump	Oxidization of graphite blocks	3 MW
	Cooling capacity	1 MW
Radiation	Radiation shielding	0.75 MW
	Radioactive water disposal	8.4×10^{20} POT/year

TABLE 9.3: Summary of the acceptable values for beam operation before the upgrades. Table from [305].

9.2.3 Monitoring upgrades

With respect to the monitoring systems two major upgrades have been made. On one hand the MUMON sensors, based on silicon PIN photodiodes and ion chambers, would have degraded too fast in the high intensity environment of the upgraded beam. Several options to replace them were considered and Electron Multiplier Tubes (EMTs) were identified as the best performing alternative [495]. EMTs structure mimics that of PMTs with the difference that the cathode is covered with aluminum such that they are only sensitive to charged particles. On the other hand, a new Beam Induced Fluorescence (BIF) monitor was placed at the primary beamline. It will measure the beam in a non-destructive way detecting the fluorescent light induced by the beam in nitrogen gas [496].

9.3 The WAGASCI-BabyMIND detector

A new near detector, the WAGASCI-BabyMIND detector, has been installed at 1.5° off-axis. It was commissioned in 2020 and it already took data during the last T2K-I run (Run-11) accumulating, so far, a small statistical sample of $2 \cdot 10^{20}$ POT. Work to integrate WAGASCI-BabyMIND selection samples to the OA are ongoing with the intention to have a multi-near detector fit running for T2K-II. The detector, presented in Figure 9.4, is formed by WAGASCI, the proton module, the wall Muon Range Detector (Wall MRD), NINJA, and BabyMIND. However, for short, it is often named the WAGASCI-BabyMIND detector.

9.3.1 WAGASCI

The Water Grid And SCIntillator detector (WAGASCI) was first proposed in 2014 [498] as a detector to study Water/Plastic neutrino cross sections using T2K's beam with an accuracy similar to 3 % [499]. WAGASCI, illustrated in Figures 9.5 and 9.6, is a neutrino detector consisting of 1280 plastic scintillator bars of $3 \times 25 \times 1020$ mm² forming a 3D grid-like structure immersed in a water tank. The total water mass of 0.6 tons accounts for 80 % of WAGASCI's fiducial volume. The

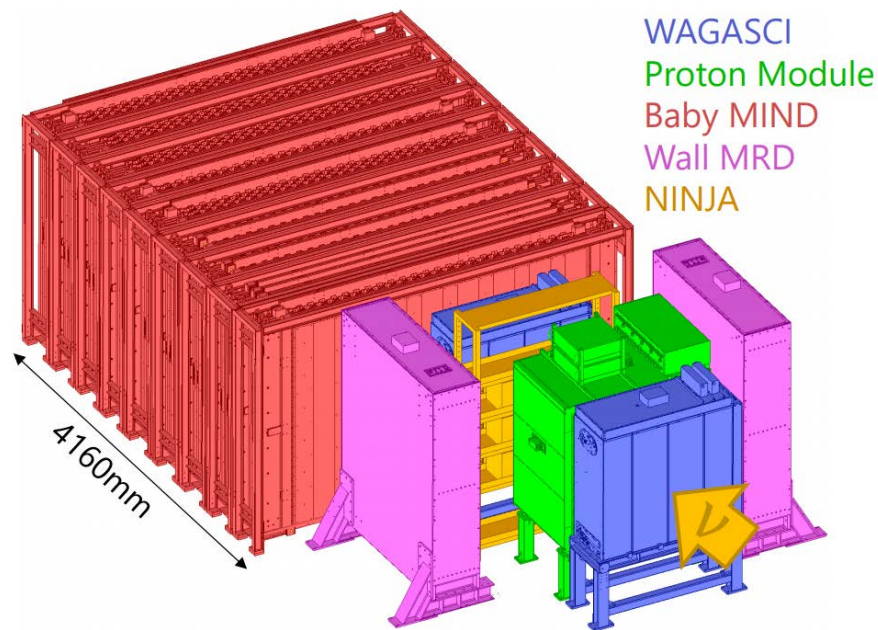


FIGURE 9.4: Computer image of the modules in the new T2K off-axis detector. Figure from Ref. [497].

scintillator bars are traversed by wavelength shifting fibers and read by the recently developed Silicon PM Integrated Read-Out Chip (SPIROC) which is a 36-channels auto-triggered front-end ASIC. In total, WAGASCI has 16 tracker planes, each made up of 80 scintillators, 40 in parallel and 40 in perpendicular to the neutrino beam.

Before finally being paired with BabyMIND, WAGASCI was considered as a possible sub-module for the ND280 upgrade [500]. Prior to being installed in its final location, WAGASCI was commissioned in J-PARC collecting data together with INGRID in 2018, and the proton module, leading to a ν_μ cross section measurement in water, carbon, iron and their ratios [325].

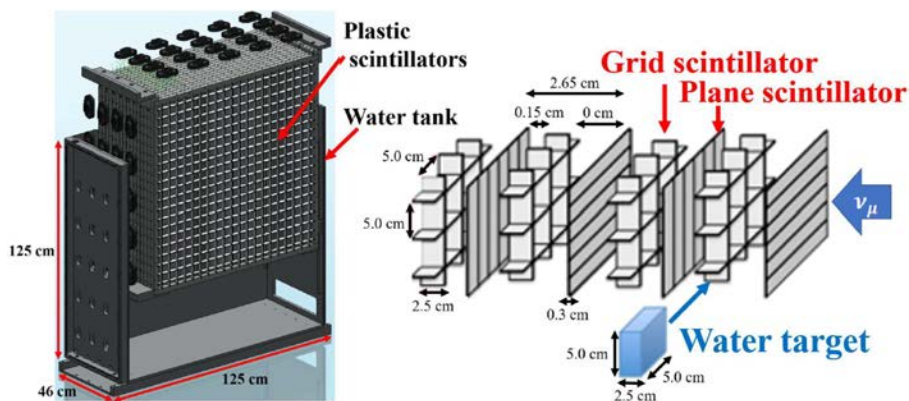


FIGURE 9.5: Computer drawing of the WAGASCI module (left) and schematic of its scintillator structure (right). Figure from Ref. [501].

9.3.2 Proton module

The Proton Module [326], presented in Figure 9.7, was originally designed as an extra module for INGRID, placed between its horizontal and vertical arms. It is similar to the standard INGRID



FIGURE 9.6: Pictures of the WAGASCI plastic scintillator 3D grid-like structure. The dimensions of each cell are $5 \times 5 \times 2.5 \text{ cm}^3$. Figure from Ref. [499].

modules but it is fully active since it has no iron. This allows to identify, in addition to the outgoing muon, pions and protons generated by CC neutrino interactions. The Proton Module consists in 36 layers made up of 32 scintillator bars of different size. The 16 innermost (outermost) bars have a size of $2.5 \times 1.3 \times 120 \text{ cm}^3$ ($5 \times 1 \times 120 \text{ cm}^3$), forming layers of $120 \times \text{cm}^2$, see Figure 9.8. In the Proton Module, analogously to the structure of the standard INGRID modules, the bars in alternate layers are oriented in the horizontal and vertical directions allowing to perform 3D tracking. The bars are intersected by WLS fibers measured on one end by an MPPC and read by TFBs. The proton module was installed in INGRID between Run 1 and Run 2 where it has collected on-axis data for years. In 2019, it was moved to its new location to become an additional element in the WAGASCI-BabyMIND detector.

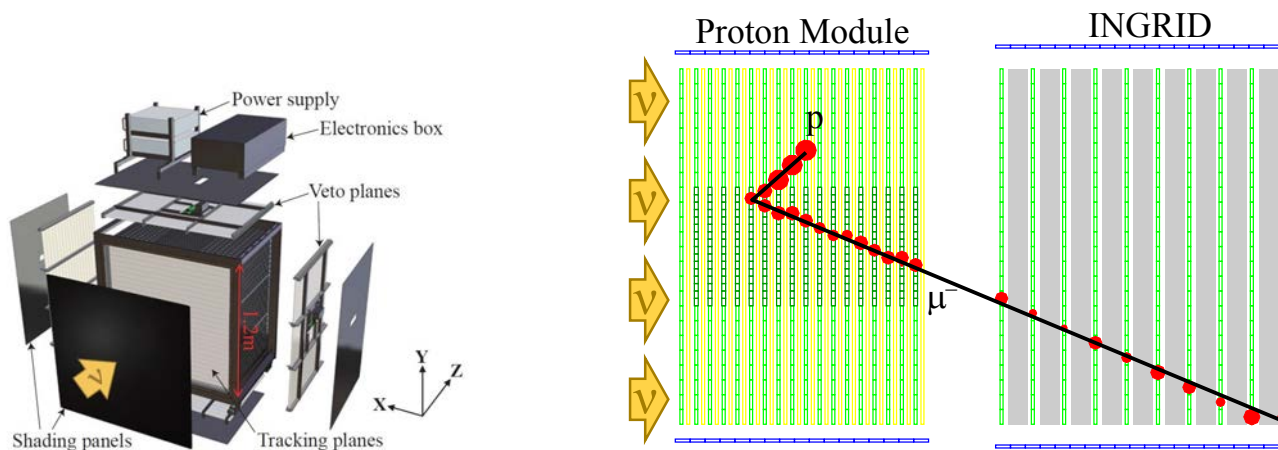


FIGURE 9.7: Exploded view of the Proton Module. Figure from Ref. [326].

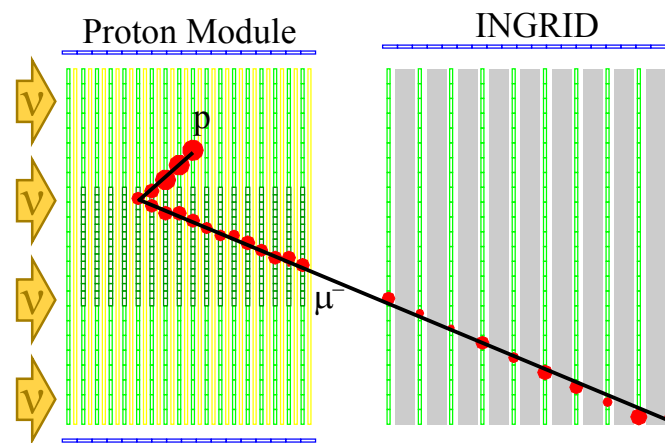


FIGURE 9.8: Event display of a neutrino interaction in the Proton Module. Light (Dark) green cells represent the thick (thin) scintillator bars. Elements in yellow correspond to layers in the vertical direction. Adapted from [326].

9.3.3 NINJA

The Neutrino Interaction research with Nuclear emulsion and J-PARC Accelerator (NINJA) experiment is an emulsion-based detector, see Figure 9.9. It consists of Emulsion Cloud Chambers (ECCs) which are tracking detectors made of emulsion films interleaved with iron plates. Each of the films has a surface of $25 \times 25 \text{ cm}^2$ and a thickness of $350 \mu\text{m}$. The iron plates have the same area and a thickness of $500 \mu\text{m}$. The emulsion film consists of gel and dispersed AgBr (silver bromide) crystals. When a charged particle passes through the emulsion film it ionizes the AgBr along its path leaving a trace of silver grains that can be visualized with the help of a microscope and used to reconstruct the event [504]. An example of the imprint of a neutrino interaction in NINJA is presented in Figure 9.10. The main advantage of emulsion based detectors

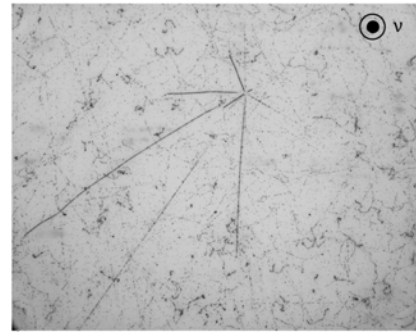
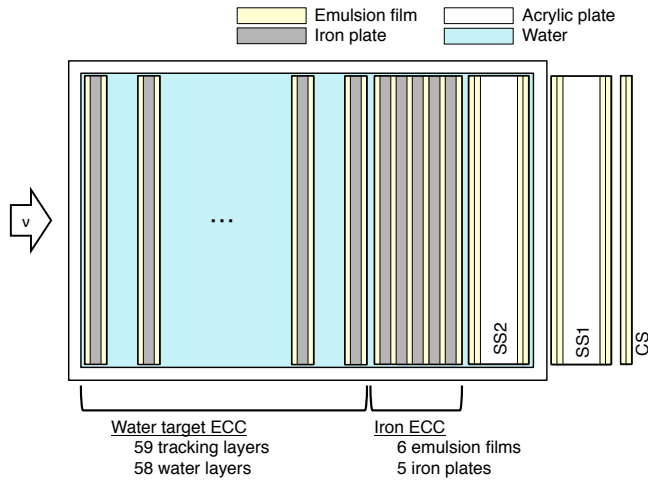


FIGURE 9.9: Structure of the emulsion-based NINJA tracker. The special sheets (SS) and changeable seat (CS) are special layers used to achieve better angular resolution and track separation. Figure from Ref. [502].

FIGURE 9.10: Image of a neutrino interaction in an emulsion layer. Figure from Ref. [502].

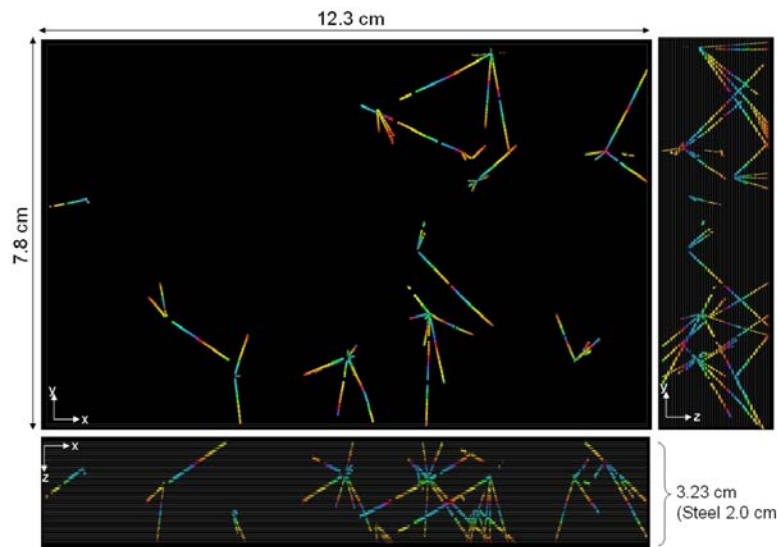


FIGURE 9.11: Reconstructed accumulated neutrino events in NINJA. Figure from Ref. [503].

is their unparalleled spatial resolution which allows to identify and study tracks with momenta above very low thresholds, e.g. 200 MeV/c ($E=20$ MeV) for protons [307]. The analysis of the trajectories on the film allows to reconstruct the tracks ionization [505] and momentum [506, 507] such that different particle types can be identified. For high momentum tracks escaping NINJA's tracker volume complementary detectors are needed in order to determine the momentum precisely. Emulsion based detectors have been successfully used in the past in other experiments, such as DONUT and OPERA, to discover the existence of ν_τ [508] and observe $\nu_e \rightarrow \nu_\tau$ oscillations for the first time [509]. In the case of NINJA, the tracker films are interleaved with 2 mm thick water layers such that the neutrino-water scattering properties can be studied with unprecedented precision, allowing:

- To measure exclusive neutrino-water cross sections.
- To determine the hadron multiplicities and their kinematics in neutrino-water interactions.
- To constrain 2p2h interactions in the scattering of neutrinos with water.

A demonstrator for NINJA, named J-PARC T60, was built in 2014 with the main goal to test the ECCs. NINJA first data taking started in 2016 and lasted until 2018 [503]. During this period NINJA used INGRID as a muon tracker and the collected data lead to two physics results: A neutrino-iron cross section measurement (65 kg of iron target mass, $4 \cdot 10^{19}$ POT) [510] and a study of kinematic distributions and particle multiplicities for neutrino and antineutrino interactions in water (3 kg of water target mass, $7.1 \cdot 10^{20}$ POT) [511]. In 2019, NINJA was moved to work in coordination with the WAGASCI-BabyMIND detector and its water target mass was increased¹ to 75 kg. Since emulsion films do not provide time information all tracks during the beam exposure are accumulated, as exemplified in Figure 9.11. The position resolution of BabyMIND (1-20 cm) is insufficient to connect the recorded high momentum tracks from babyMIND to the vertices in the ECCs. Thus, NINJA uses two auxiliary detectors designed for this task. On one hand, an emulsion shifter, consisting of both moving and fixed emulsion films, provides rough timing information (hours-few days) but highly accurate position information. On the other hand, a scintillator tracker made of partially overlapping plastic scintillator bars records accurate beam bunch timing information and better position resolution than BabyMIND.

Notably, the NINJA detector does not belong to the T2K collaboration. Despite of this, there is a memorandum of understanding between both collaborations [512]. Currently, there are plans to extend this relation and the possibility of including NINJA's data in T2K's near detector fit is under study. The addition of NINJA to the oscillation analysis could significantly help to constrain important systematic uncertainties, such as $2p2h$ in water, thanks to the unique detail of the emulsion images. Similarly, NINJA studies profit from T2K detectors and flux predictions.

9.3.4 BabyMIND



FIGURE 9.12: Picture of a BabyMIND magnet module. Figure from Ref. [513].

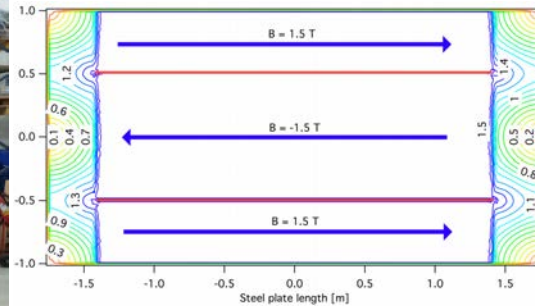


FIGURE 9.13: Magnetic field in one of the BabyMIND magnet modules. Figure from Ref. [513].

BabyMIND was first proposed in 2014 as a prototype for a larger Magnetized Iron Neutrino Detector (MIND) [514] which could be used in the LBNO experiment [515]. However, in 2015 it was finally decided to use BabyMIND in coordination with WAGASCI, driving a set of design modifications constrained, among other factors, by the installation conditions in Japan [513], leading to a new magnet set up [516]. In its final design, babyMIND consists of 33 magnet modules interspersed with scintillator tracker planes staggered in perpendicular to the beam. Each magnet module is made of steel with two slits in the middle and magnetized by Aluminum windings assembled around them in a sewing pattern. An illustrative picture is presented in Figure 9.12. This configuration provides a homogeneous 1.5 T magnetic field with opposite vector directions alternating in the three regions divided by the slits, as illustrated in Figure 9.13. The scintillator modules have a size of 2×3 m² and are made up of 95 horizontal bars and 16 vertical bars which are mounted in two halves in an overlapping pattern in order to provide a better position

¹For 75 kg several thousands of CC interactions are expected for every 10^{21} POT.

resolution, see Figure 9.14. The vertical (horizontal) bars have a size of $2880 \times 31 \times 7.5 \text{ mm}^3$ ($1950 \times 210 \times 7.5 \text{ mm}^3$). All bars are intersected by a wavelength shifting fiber measured by MP-PCs. In total, BabyMIND has 3996 channels readout by electronic boards based on the CITIROC chip [517]. The weight of each magnet module (tracker plane) is nearly 2 tons (0.4 tons) for a total weight of about 80 tons. BabyMIND construction was finalized in 2017 at CERN [518] where it was exposed to a beam of charged particles in the summer [513]. The detector was then transported to its final location in the near detector complex in J-PARC where it has been taking neutrino data since 2019. Currently, the analysis of the first neutrino data is ongoing [497, 306, 519], some neutrino event displays in BabyMIND are presented in Figure 9.15.



FIGURE 9.14: Pictures of: One half of a scintillating module being assembled (left), two half modules being brought together (middle) and a finished scintillating module covered by an Aluminum cover (right). Figure from Ref. [513].

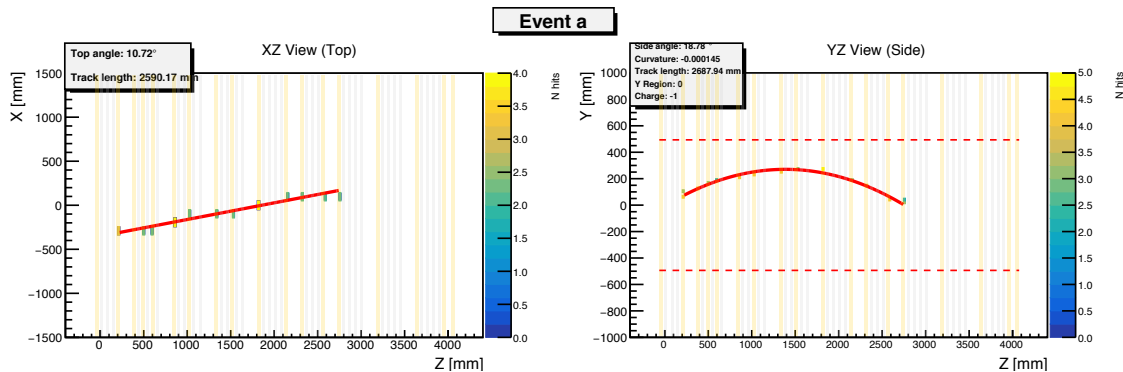


FIGURE 9.15: : Top view and side view of a ν_μ CCQE candidate event with a μ^- bending downwards in the central magnet region. Adapted from [519].

9.3.5 Physics motivations

So far, all T2K detectors have been placed either on-axis or 2.5° off-axis. INGRID is used to monitor the beam, and ND280 is used to constrain the flux model and the cross section model parameters. Although this strategy has been proven to work, breaking the fit degeneracies in the flux and cross section parameters is difficult if a single off-axis value is studied. Adding INGRID to the BANFF is not expected to make a significant difference as INGRID has limited segmentation and PID capabilities and no magnet. The WAGASCI-BabyMIND detector does not share this limitations and will provide data at an off-axis of 1.5° , where the neutrino energy spectrum peaks at about 0.8 GeV. This is expect to reduce the flux and cross section model co-dependencies and lead to an overall improved near detector constrain. In addition, further understanding neutrino interactions might be possible by developing narrow energy spectrum selections which statistically remove the contamination from the low-energy or high-energy tails by taking a linear subtraction of the ND280 and WAGASCI-BabyMIND spectra, as presented in Figure 9.16. Thanks to the fact that both ND280 and WAGASCI-BabyMIND will have plastic and water targets it will be possible

study differences in this materials by using the different off-axis spectrum. Moreover, WAGASCI is more finely segmented and contains more water mass than FGD2, such that more refined samples with high statistics of neutrino-water interactions will be possible, complementing ND280.

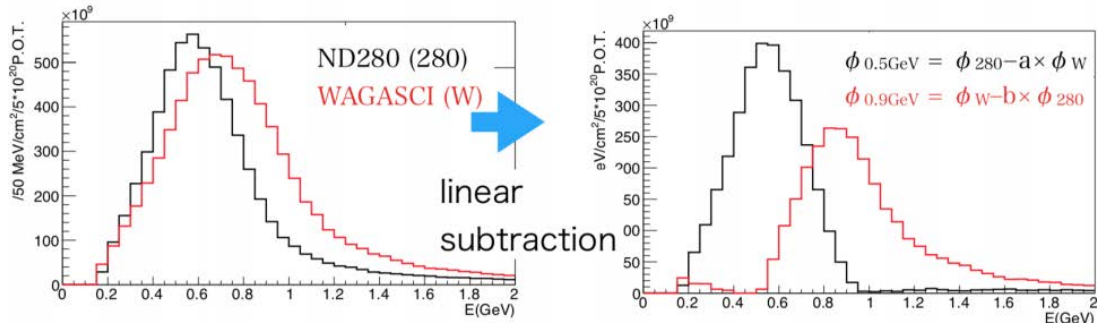


FIGURE 9.16: Simulated fluxes at ND280 and WAGASCI (left) and linear subtraction of the fluxes using two coefficient choices to suppress and enhance the high energy tail contribution. Figure from Ref. [497].

9.4 GADZOOKS!

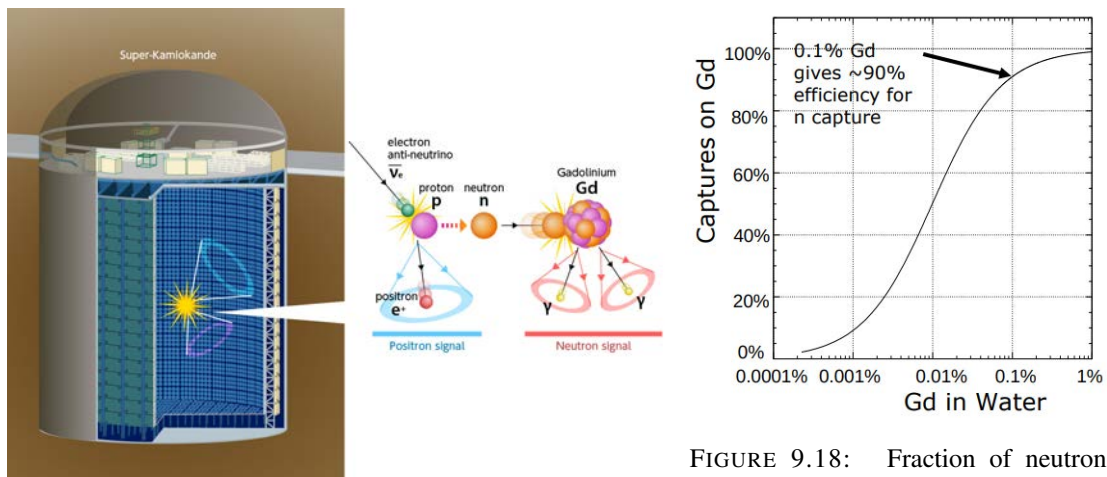


FIGURE 9.17: Sketch of the working principle of neutron tagging using gadolinium in the SK detector.

FIGURE 9.18: Fraction of neutron captures as a function of the amount of gadolinium dissolved in water. Figure from Ref. [520].

In 2004 a letter was published presenting the potential benefits of tagging neutrons in Water Cherenkov detectors by means of dissolving a Gadolinium salt to water [521]. Neutrino interactions, such as inverse beta decay, produce final state neutrons. In water, neutrons quickly lose energy and become thermal and continue to propagate until they are captured. Gd is known to have an exceptionally high neutron capture cross section². Upon neutron capture, over 90% of the times Gd emits a gamma of about 8 MeV, which produces a gamma cascade. As the capture in Gd occurs in about 20 μ s and about 4 cm, the delayed detection of a gamma cascade near to the position of a reconstructed neutrino interaction vertex is a unique signature of a neutron detection. The stages in the development of this method, for which the most relevant details are presented in the following paragraph, can be found in Ref. [522]. The concept was named GADZOOKS! (Gadolinium Antineutrino Detector Zealously Outperforming Old Kamiokande, Super!). Making neutrons visible would enrich the end-state interaction information, potentially leading to a

²For thermal neutrons this cross section is of 49000 bars for Gd compared to 0.3 bars on free protons.

very large background reduction in some physics searches. In particular, the detector response to supernova neutrinos (both galactic and diffuse) and to reactor antineutrinos would greatly improve. Moreover, this addition would benefit proton decay searches, as well as the study of solar, atmospheric and long-baseline neutrino oscillations. A main challenge however, was to prove that dissolving Gd would not affect the transparency of the water, damage the detector instruments nor leak into groundwater. To test the viability of the project, in 2009, a new experimental chamber was excavated in the Kamioka mine to install a dedicated large-scale (200-ton model of SK) Gd facility, named EGADS (Evaluating Gadolinium's Action on Detector Systems) [523]. EGADS worked as originally predicted [524] and, consequently, along 2018 and 2019 the Super Kamiokande detector was drained and refurbished, in preparation for the loading of the Gd salt. Finally, on July 14th 2020 the first Gd sulfate, i.e. $\text{Gd}_2(\text{SO}_4)_3$, was dissolved and injected into the SK tank and the concentration was increased over time reaching in August 17th 2020 the 0.01% target (13.2 tons of the salt). As presented in Figure 9.18 this concentration translates into about 50% of neutrons being captured. To validate the successful integration of the gadolinium salt in the water of SK, a neutrino-emitting calibration source was deployed at various positions in the SK tank, confirming the fraction of visible neutron captures as well as the uniformity of the gadolinium loading in the detector. In November of 2020 the Gd loading of EGADS was increased to 0.03%. The tests worked as expected and validated the increase of Gd concentration in SuperK to 0.03%, a value that is expected to be reached in 2022.

9.5 Overview of the ND280 upgrade

As early as 2016, when the extension of T2K was proposed, possible upgrades for ND280 were under consideration. One of the first studies consisted in the review of the status of the existing ND280 sub-detectors. It was found that the aging of most modules, including its electronics, was minor so that they could continue to operate without major maintenance at least until the end of T2K-II [494]. Working groups were formed to study possible modifications for ND280 and three constraints drove the effort from the beginning:

- The ND280 detector was already existing and this imposed design constraints in terms of the space availability, the accessibility for the installation of the new modules and the complementarity between the preexisting detector modules and the new modules to be installed.
- The project cost should be kept low. Accordingly, the modifications should maximize the impact on the performance while leaving most of the detector unchanged. In addition, the new detector technologies should be affordable in terms of the material choices, manufacture, operation and maintenance costs.
- The ND280 upgrade should be the results of sub-detector R&D projects. This was a necessary condition to attract a sufficiently large group of researchers and institutions to ensure the viability of the project.

9.5.1 The removal of the PØD

In the last decade major progress has been made in the research of neutrino interactions with energies around 1 GeV. Out of the experience of T2K-I, and given the current state-of-the-art of the field, it was identified that replacing the PØD by new sub-detectors could significantly improve the overall ND280 performance in terms of maximizing its usefulness for T2K. On one hand, the PØD was originally build to estimate the production yields of π^0 in neutrino interactions, in order to constrain this background for the oscillation studies involving ν_e . This measurements, after collecting data for 10 years, were limited by systematic errors such that taking more data with the PØD would not translate into any significant improvement. On the second hand, over

years, analysis improvements have significantly diminished the role of this background in SK selection samples. Furthermore, tagging π^0 in a small detector volume involves using materials with a high radiation length such as lead. In consequence, the PØD tracking and PID capabilities were limited, making it a not well suited detector to study CC interactions, crucial for the OA. Finally, the PØD occupied a large volume in the ND280 basket such that removing it would free a significant volume and allow to install new modules with the potential to significantly improve the overall ND280 performances whilst minimizing the amount of modifications to the other ND280 elements.

9.5.2 Physics Goals

With the available space freed by the PØD removal the ND280 upgrade was meant to meet the goals:

- Increase significantly the target mass within the ND280 basket able to study CC interactions with the aim to accumulate an even larger data sample and to further profit from the beam upgrade.
- Largely improve the angular acceptance of the detector with the aim to increase the selections efficiency, but most importantly, to make the detector acceptance more similar to that in SK, see Figure 9.19, to allow for a better modeling constrain in the whole phase-space of interest.

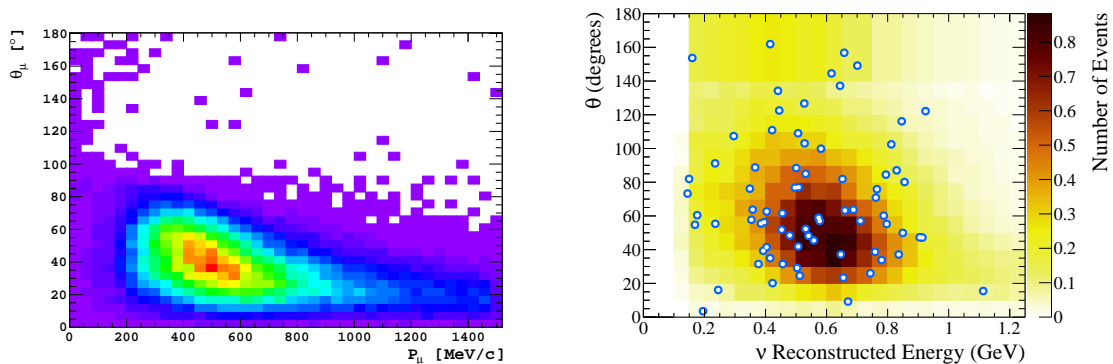


FIGURE 9.19: Reconstructed momentum and angle for muons in ND280 (left) and electrons in SK (right). The comparison shows the depletion of selected events in ND280 for high angle and backward angles as a result of the low efficiency of the detector in this phase-space. Figures from Ref. [3] (left) and Ref. [2] (right).

- Provide new tracking capabilities able to reconstruct and identify short tracks of low energy hadrons close to the interaction vertex. The aim is to study neutrino interactions with high statistics at an unprecedented detail, both enhancing the selection samples for the OA and providing hints for the future refinement of neutrino interactions models.

9.5.3 The ND280 upgrade geometry

With all, a solution meeting all the requirements above was finally presented in 2019 in the ND280 upgrade TDR [3]. The upgraded ND280, see Figure 9.20 and Figure 9.21, includes three new sub-detector technologies: Two High-Angle-Time-Projecting-Chambers (HATPCs), a new fully active plastic target named Super-Fine-Grained-Detector (SuperFGD) and six Time-Of-Flight (ToF) panels. All of these new sub-detectors are reviewed in detail in the following Chapters. One of the four PØD modules, the so-called upstream ECal, is left in place such that all tracking elements,

old and new, are surrounded by electromagnetic calorimeters. The old TPCs-FGDs sandwich remains in the basket unaltered playing the same role as originally, i.e. being a horizontal tracker for neutrino CC interactions. The new SuperFGD-HATPCs sandwich, fully surrounded by the six ToF panels, is placed upstream to them and stacked vertically, transforming ND280 into an efficient horizontal and vertical tracker. All other elements, namely the barrel ECal, the downstream ECal the SMRD and the UA1 magnet are unchanged.

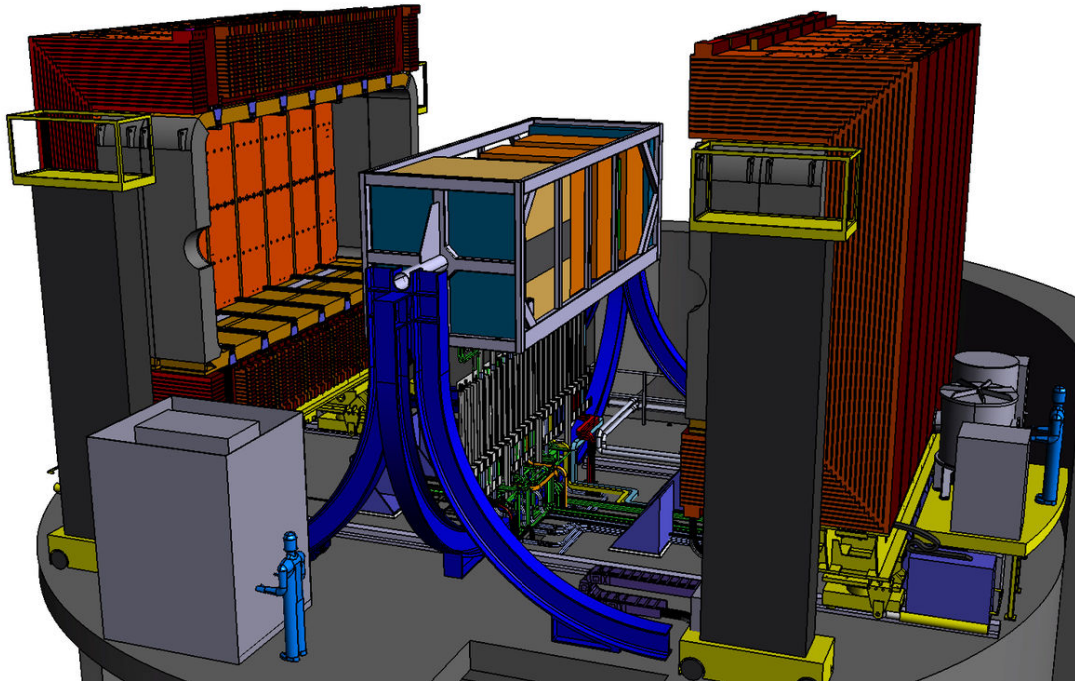


FIGURE 9.20: Computer drawing of the upgraded ND280 detector. Figure from Ref. [3].

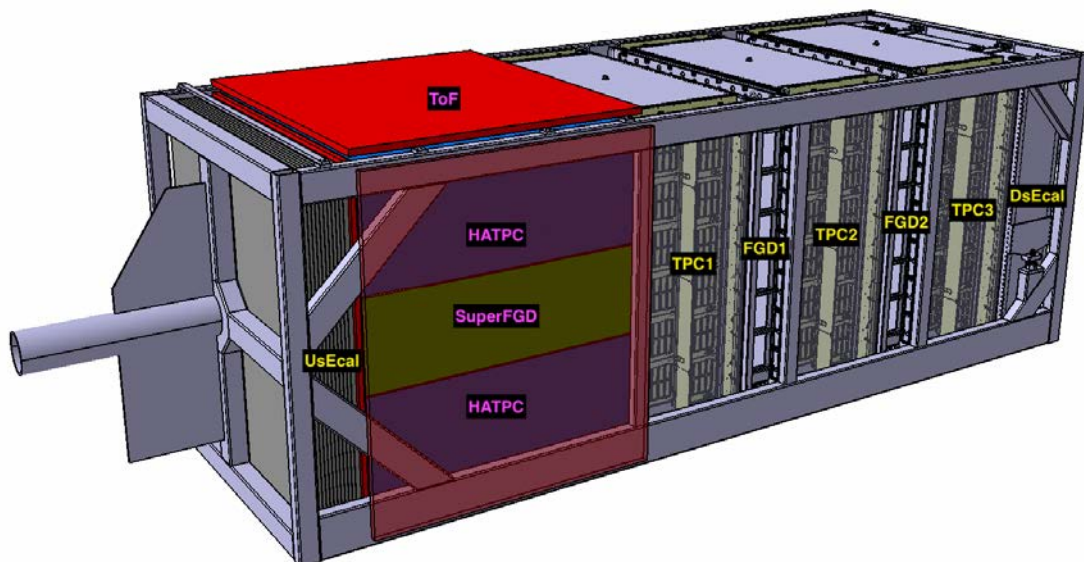


FIGURE 9.21: Computer drawing of the ND280 basket after the upgrade. Figure from Ref. [3].

9.5.4 The ND280 upgrade expected physics performance

The ND280 upgrade is expected to largely improve the angular acceptance of the detector with respect to its original configuration. Whereas tracks escaping the FGDs only enter into a TPC if they have a low-angle with respect to the beam axis, tracks outgoing neutrino interactions occurring in SuperFGD will have TPC information either if they are produced forward or at a high-angle with respect to the beam axis. In order to numerically quantify this increase in the acceptance and its impact in the oscillation analysis, a dedicated Monte Carlo simulation was developed from the standard ND280 simulation software ³.

Geometry details and reconstruction criteria

The ND280 upgrade geometry was adapted from the original ND280 geometry by realizing in software the same modifications that were expected to be later implemented in the detector's hardware. First, the necessary segments of the PØD were removed. Second, the new detector volumes were included, following the geometrical specifications detailed in the next chapters. For the sake of understanding the studies in the TDR, however, it is enough to anticipate the following details: SuperFGD consisted of a plastic volume of $192 \times 184 \times 56 \text{ cm}^3$. Tracks were assumed to be reconstructed in SuperFGD if they had a length of, at least, 20 cm, which was expected to be a very conservative criteria. For the PID in SuperFGD the also very conservative assumption of using the same response of the FGDs was taken. The HATPCs were simulated as gas volumes of $2140 \times 740 \times 1780 \text{ mm}^3$. A track was considered to be reconstructed in a HATPC if its true length projected in the readout plane was larger than 20 cm, in analogy to the reconstruction criteria in use for the original ND280 TPCs, also referred to as vertical TPCs or vTPCs. The tracking efficiency in the HATPCs was assumed to be perfect and no charge miss-identification was simulated. Both of this assumptions were known to have a very small effects in general, and in particular for the studies under consideration. The track momentum and ionization measured in the HATPCs were smeared to offer performances similar to those in vTPCs and were used to build PID variables analogous to those in the vTPCs. The ToF panels were only used to flip the tracks sense of motion according to their simulated time-of-flight information using time resolutions tuned to match beamtest data [525].

Muon neutrino studies

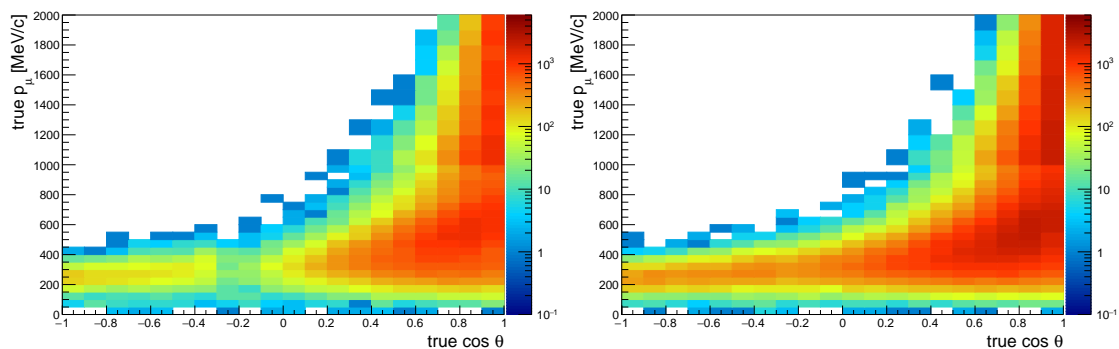


FIGURE 9.22: Current (left) and upgraded (right) ND280 efficiency for ν_μ -CC inclusive interactions in neutrino beam mode as a function of the true muon momentum and angle. Figures from [3].

To study the potential of the upgrade a simple selection was developed to select ν_μ ($\bar{\nu}_\mu$) events using an adapted version of the HighLAND analysis framework, earlier explained in Sec. 7.1.

³<https://github.com/t2k-nd280-upgrade/t2k-nd280-upgrade>

The selection algorithm consisted in tagging, for each event, the most energetic negative (positive) track as the muon candidate. The event was kept if the muon candidate was reconstructed in a TPC (here TPCs means either horizontal or vertical TPCs) and if it was identified as a muon according to the TPCs PID algorithms. High angle tracks were also included if the muon candidate was not selected in a TPC but entered into the ECal and was classified as a muon according to the standard ND280 ECal PID. If a muon was selected, then, other tracks produced in the interaction, such as pions and protons, were classified according to their TPC information if they had it. If they did not, tracks were reconstructed and classified according to SuperFGD reconstruction and PID assumptions.

		# of events (/10 ²¹ POT)	Purity (%)		
			CC0 π	CC1 π	CC Other
current	FGD 1	50507	72.5%	64.0%	68.2%
	FGD 2	50125	71.5%	62.3%	63.8%
upgrade	FGD 1	52655	72.9%	64.1%	64.7%
	FGD 2	51460	71.6%	62.9%	63.3%
	SuperFGD	95490	72.5%	70.3%	72.7%

TABLE 9.4: Predicted total number of selected ν_μ -CC events in neutrino mode for the current and upgraded ND280 configurations in each available neutrino target detector. The purity for each event topology is shown. The prediction corresponds to 1×10^{21} POT. The OOFV and the wrong-sign backgrounds are not included as they are expected to give have minor contributions. Table from Ref. [3].

Under the former procedure, the expected 2D efficiencies were computed using tracks selected in any of the ND280 targets (FGD1, FGD2, or SuperFGD). The results are presented in Figure 9.22. The associated number of events and the purity of the reconstructed topologies, is presented in Table 9.4. Using the upgraded ND280 geometry the amount of useful data per POT is expected to be doubled while keeping, at least, similar purities to those provided by the current FGDs. In addition, the ND280 upgrade will transform the 2D efficiency by allowing to select a significant fraction of events with high-angle and backward going muons.

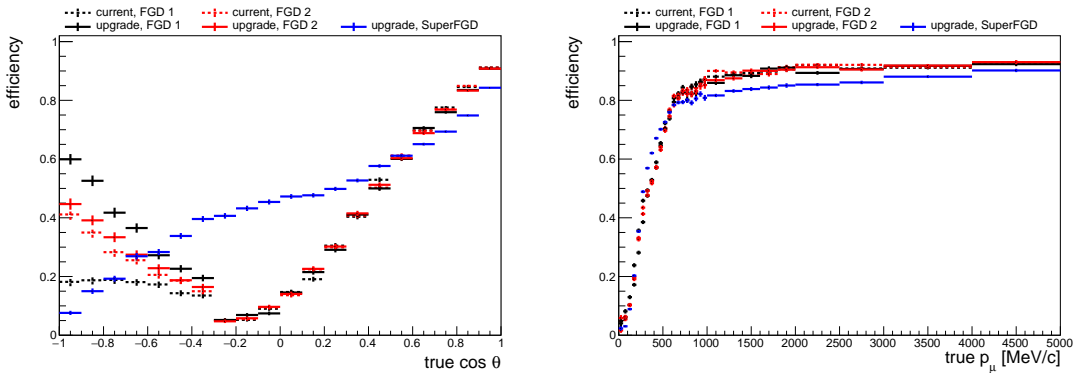


FIGURE 9.23: Efficiency for ν_μ -CC inclusive interactions in neutrino beam mode splitted by target and presented as a function of the true muon momentum and angle. Figures from [3].

To study the contribution of different targets to the total efficiency, 1D projected efficiencies in the muon angle and momentum are presented in Figure 9.23. The results show that the FGD1 selection efficiency is expected to significantly increase in the backward region due to the addition of upgrade elements whilst the inclusion of SuperFGD will provide a sample of data with good efficiency both for forward and high-angle tracks.

With the former selections, an Asimov BANFF-like fit⁴ was performed in order to estimate the improvement on the constraints in the current systematic uncertainties. The most significant results are presented in Table 9.5, and Figure 9.24. The error on most of the systematic parameters was reduced by about 30%. In some cases, such as in the FSI parameters, a larger reduction was achieved due to the significantly improved angular coverage and the lower hadron detection momentum thresholds.

In any case, it must be noted that this studies were intended to be only an orientation, to show that new geometry would translate into a better angular efficiency and in an increased event rate and to illustrate how this improvements could help to constrain the cross section model systematic uncertainties. Nonetheless, the real improvement of the ND280 upgrade is expected to be significantly better than the lower bound set by these studies as the expected reconstruction thresholds and PID quality of SuperFGD, which are among the most crucial improvements of the ND280 upgrade, were chosen to be greatly conservative.

Parameter	Current ND280 (%)	Upgrade ND280 (%)
SK flux normalization ($0.6 < E_\nu < 0.7$ GeV)	3.1	2.4
MA_{QE} (GeV/ c^2)	2.6	1.8
ν_μ 2p2h normalization	9.5	5.9
2p2h shape on Carbon	15.6	9.4
MA_{RES} (GeV/ c^2)	1.8	1.2
Final State Interaction (π absorption)	6.5	3.4

TABLE 9.5: Sensitivity to flux and cross section parameters of interest for the current ND280 and the upgrade configuration. Table from Ref. [3].

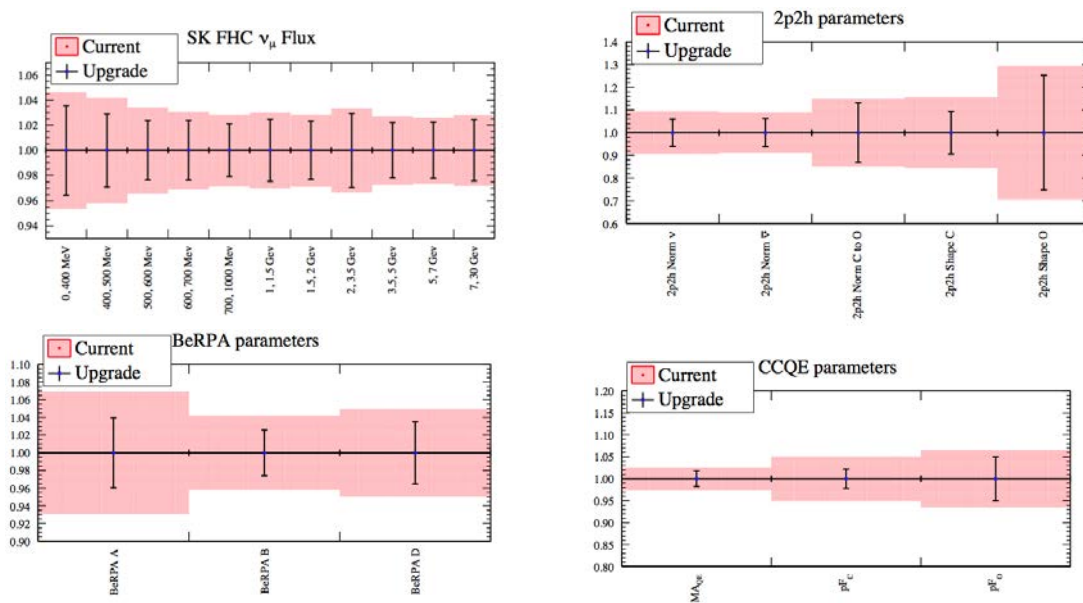


FIGURE 9.24: Post-fit uncertainties with the same POT for parameters associated to the far detector flux, CCQE, Random Phase Approximation (RPA) and 2p2h using ND280 before (blue dots) and after (red bars) the upgrade. Figure from Ref. [3].

⁴The near detector fit for T2K's OA is carried out by the so-called Beam and Near detector Fit task Force (BANFF), such that this fits are often referred to as BANFF-fits. BANFF fits resemble the logic described in Sec. 8.1 with one important difference: In BANFF fits, no is treated as signal such that template parameters are not used. The output of the BANFF is a posfit covariance matrix, that can be used to constrain the far detector fit.

Chapter 10

The High-Angle Time-Projection-Chambers

“I was 24 and I learned then to make instruments. Why? Because I had. In the laboratory we didn’t have instruments, we had to build them by ourselves. And I learned physics that way. Though why I have a special connection to physics through the channel of detectors, because I had to detect particles, I was in a nuclear physics laboratory. What do you do in a nuclear physics laboratory? You detect particles. So I imagined detectors.”

– GEORGES CHARPAK

Two new High-Angle Time-Projection-Chambers (HATPCs) will be installed in ND280 as part of its upgrade. This Chapter presents its design and construction method and reviews the study of prototypes that have been used to validate and characterize this technology. In particular, the development and characterization of the novel Encapsulated Resistive Anode Micromegas (ERAM) readout, discussed in Refs. [4, 5], is presented.

10.1 Introduction

The main goal of the HATPCs is to reconstruct with high precision the trajectory of charged tracks and their ionization in order to reconstruct their momentum and to create particle identification (PID) criteria. As earlier presented, the new HATPCs need to fit within two tight envelopes placed above and below the SuperFGD detector. Consequently, the new HATPCs boxes, acting as the electric field-cage, were designed to be as compact as possible. For comparison, whereas the original TPCs in ND280 have walls of about 10 cm the HATPCs have walls of about 4 cm. This ambitious plan was not exempt of challenges and required the construction of several prototypes until a final design and a manufacture method was finally accepted. Concerning the readout technology, the original ND280 TPCs were the first ever using bulk Micromegas, a decision which has proven to be excellent over the years. Because of to this, re-using the same readout concept would have been a natural decision as this choice straightforwardly met the desired performances while being an affordable and reliable solution. However, doing R&D to improve the current T2K Micromegas performances and decrease its production cost was appealing. In this way, a great compromise was found in using the Encapsulated Resistive Anode Micromegas (ERAM) readout

technology. ERAMs are expected to outperform bulk Micromegas, e.g. by providing much improved spatial resolution at short drift distances, at a lower production cost and, once installed in the upgraded ND280 detector, T2K will become the first experiment using this technology.

10.2 Design and construction

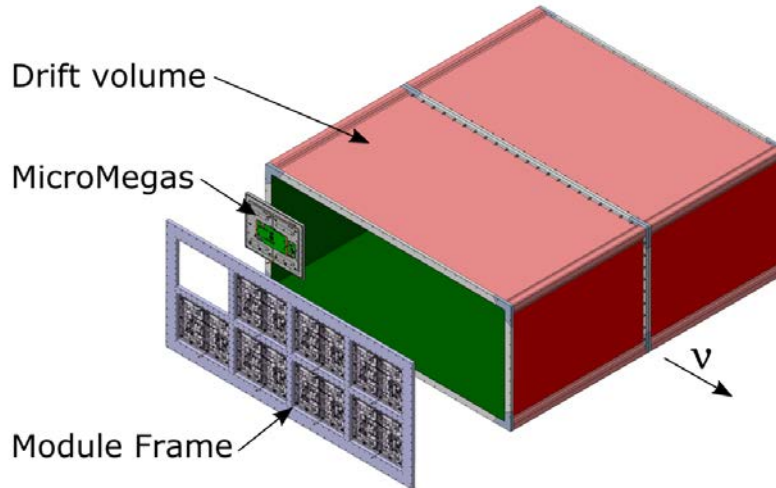


FIGURE 10.1: Sketch of a HATPC. Figure from Ref. [3].

The HATPC design was first proposed in the ND280 upgrade TDR [3]. Each of the two HATPCs is identical and, as sketched in Figure 10.1, consists of a drift volume enclosed by a field-cage, separated in two halves by a central cathode. At the two ends opposite to the cathode module frames are mounted each holding a total of eight ERAMs, acting as the anode. The electric field uniformity is provided by a series of copper strips in the inner surface of the box, connected by means of resistors forming a voltage divider defining a precise field gradient. The two internal volumes are communicated via open gaps at the cathode edges allowing the gas to flow. The most relevant parameters of the HATPCs are summarized in Table 10.1.

Drift Parameters	Value	Readout Parameters	Value
Overall $x \times y \times z$ (m)	$2.0 \times 0.8 \times 1.8$	Micromegas gain	1000
Drift distance (cm)	90	Micromegas dim. $z \times y$ (mm)	340×410
Electric field (V/cm)	275	N pads	36864
Gas Ar-CF ₄ -iC ₄ H ₁₀ (%)	95-3-2	Pad $z \times y$ (mm)	10×11
Drift Velocity (cm / μ s)	7.8	Sampling frequency (MHz)	25
Transverse diffusion (μ m/ $\sqrt{\text{cm}}$)	265	N time samples	511

TABLE 10.1: Main parameters of the HATPC. Table adapted from Ref. [3].

10.2.1 The ERAMs

As described in Ref. [5], the bulk Micromegas technology in use in the three original ND280 TPCs was invented in 2004 by a collaboration between the CERN/EP-DT-EF PCB workshop and CEA-IRFU [457]. It provides an easy and robust manufacturing with very limited dead area. However, in bulk Micromegas, the ionization charge often reaches a single pad, such that the position resolution is limited to the width of the pad over $\sqrt{12}$. An improvement for this

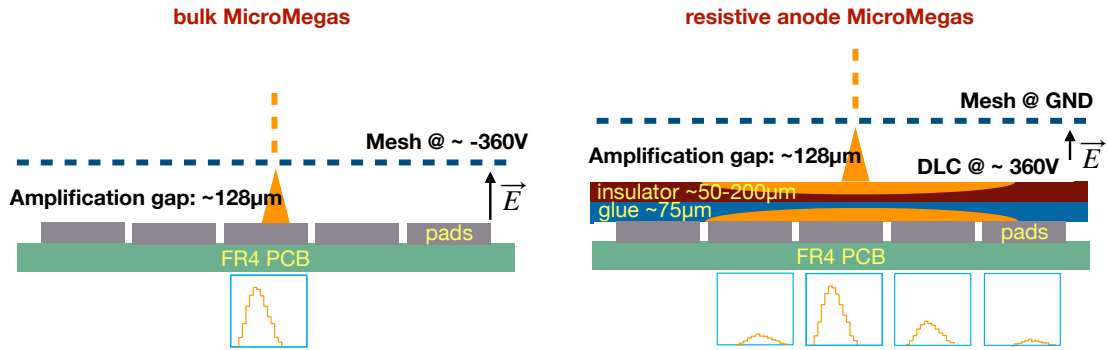


FIGURE 10.2: Comparative sketch of the bulk and the resistive MicroMegas technologies. Figure from Ref. [527].

In ERAMs, the anode, segmented in pads, is covered by a foil of insulating material, which has a thin resistive layer on its top side. The ERAM detector uses a Diamond-Like Carbon (DLC) thin layer sputtered on a 50 μm thick APICAL (Kapton) insulator sheet. The avalanche is then naturally quenched because the potential difference locally drops in presence of a high charge density. The resistive layer acts like a 2D RC network and the charge deposited by the avalanche induces a signal also on the adjacent pads, looking as if the charge spreads naturally with time following a Gaussian behavior. For a point charge deposited at $r = 0$ and $t = 0$, the charge density as a function of radius r and time t is given by

$$\rho(r, t) = \frac{RC}{4\pi t} e^{-\frac{r^2}{4tRC}}, \quad (10.1)$$

where R is the resistivity per unit area and C is the capacitance per unit area. The capacitance C is defined by the distance between the resistive layer and the grounded pads (glue thickness plus APICAL foil). The insulating layer thickness determines the width of the induced charge spread σ_t at a given time. When measured, due to integration of the charge collected by a front-end electronics of shaping time t , this spread is of the order of $\sigma_t = \sqrt{2t/RC}$.

Using ERAMs has a number of benefits:

- Due to the charge spread in the ERAMs, depicted in Figure. 10.2, the signal is spread over multiple pads, improving the position resolution.
- Alternatively, due to the spreading, ERAMs are able to match the performances of a bulk MicroMegas using a significantly reduced number of readout channels allowing to reduce production costs.
- ERAMs use a new high-voltage powering scheme where the mesh is set to ground allowing to get rid of the cumbersome anti-spark protection circuitry necessary for the standard bulk MicroMegas.
- The anode encapsulation provides a detection plane fully equipotential since the grounded mesh is at the potential of the detector frame and supporting mechanics. This leads to a better field uniformity in the TPC, especially near the module edges, minimizing track distortions.
- The grounding scheme provides more flexibility in the detector operation, allowing the high-voltage of a module to be set to a different value than its neighbors without degrading

the drift field uniformity. In this way, if necessary, a full module can be disconnected without affecting the drift field.

For the HATPCs, the ERAMs consist of an array of 32×36 pads of $10.09 \times 11.18 \text{ mm}^2$ printed on an PCB of $420 \times 340 \text{ mm}^2$. Hence, in total there are 1152 pads per module, which corresponds to exactly $2/3$ of 1728, the number of pads in current T2K bulk Micromegas.

10.2.2 Readout electronics and DAQ

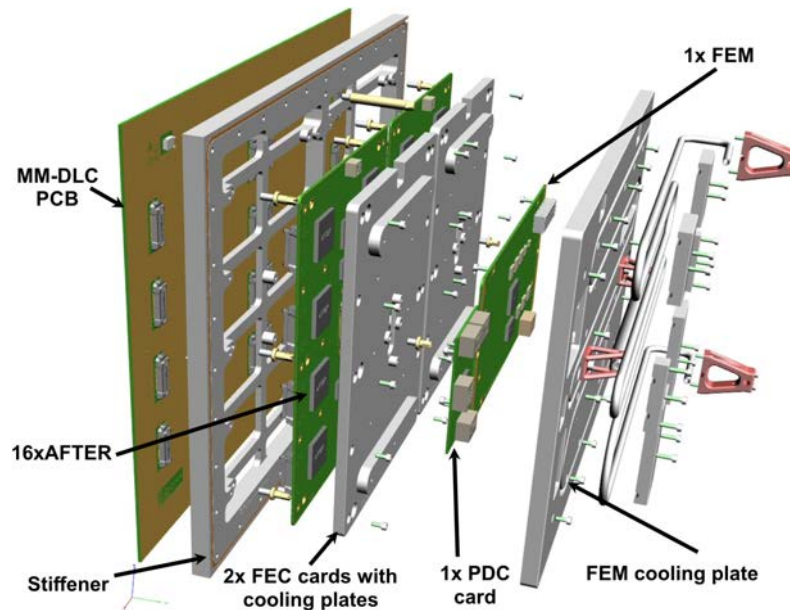


FIGURE 10.3: Exploded view of one ERAM module. Figure adapted from Ref. [3].

Each detector module, see Figure 10.11, consists of a DLC coated Micromegas PCB glued onto an aluminum stiffener. The stiffeners increase the mechanical stability of the modules ensuring high planarity and robustness. In addition, the aluminum is machined to include structural elements which allow to screw the ERAM modules into the module frames with high precision. To minimize the degradation of the highly sensitive detector analog signals and to reduce the high economic cost of cables the electronic boards are mounted directly on the back-plane of the ERAMs, surrounded by water cooling pipes. This solution is equivalent to that in the existing ND280 TPCs with two main differences. In one hand the electronics have been redesigned to read a reduced number of pads. In the other hand, the anti-spark protection circuits have been omitted, as the ERAMs naturally suppress sparking. Thanks to this simplifications, the boards will now be mounted in parallel to the Micromegas instead of the perpendicular integration in the existing TPCs, allowing to achieve a significantly more compact layout.

The electronics of each ERAM module consist of three different types of boards:

- Two Front-End Cards (FECs), each with 576 channels. The two FECs acquire the analog signals of the 1152 pads and convert them into digital signals using an octal-channel analog-to-digital converter (ADC). In order to do so, each FEC hosts eight 72-channel AFTER ASICs, the same chips in use in the original ND280 TPCs. Further details on the AFTER chip has been earlier presented in Chapter 5.
- A Front-End Mezzanine (FEM) card. The FEMs control the two FECs and perform elementary data processing tasks such as baseline offset corrections, zero-suppression and buffering.

- A Power Distribution Card (PDC). It converts the external input voltage into the nominal voltages used to operate the FECs and the FEM.

The pre-processed digital output of each detector module is transported outside of ND280 via an optical fiber to a back-end unit called the Trigger and Data Concentrator Module (TDCM). Each TDCM aggregates the data of the 16 ERAM modules of one HATPC and distributes the global clock and trigger signal to the FEMs using a dedicated return path on the corresponding optical link. The TDCMs are controlled via the MIDAS interface running the ND280 DAQ. A scheme of the overall readout architecture is presented in Figure 10.4.

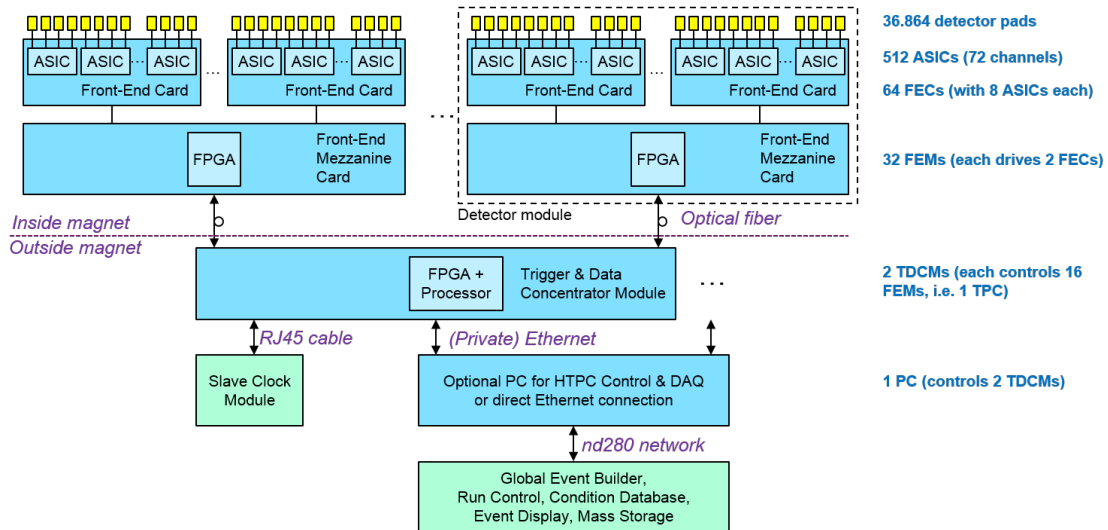


FIGURE 10.4: Scheme of the HATPC readout architecture. Figure from Ref. [3].

10.2.3 Field-cage box

The HATPCs boxes were designed to meet the following constraints [3]:

- Low-density and low-Z materials to reduce multiple scattering and conversion processes. The field-cage wall thickness must not exceed 4% radiation lengths.
- High structural integrity against over-pressure, gravitational and thermal loads.
- High degree of electric field uniformity. Manufacturing imperfections should not modify the reconstructed track positions by more than 0.2 mm.
- Good inner-surface smoothness and field-cage walls uniformity to prevent electric discharges. The electric field must be kept within 30% of the nominal breakdown value.
- Very low permeability to atmospheric gas components having a negative impact on the drift of electrons (O_2 , N_2 and H_2O). In particular the O_2 level must be at most 10 ppm.
- Negligible vapor pressure of contaminants emanating from the HATPC materials.

Given the target thickness of the box walls and its stringent mechanical and electrostatic tolerances composite multilayered materials were identified as the best option to build them. Composite materials are commonly used in the industry as they provide unparalleled stability-to-mass ratios at an affordable production cost. Different composite stacks were studied via finite element analysis simulations and validated via dedicated tests on small scale samples of the box. The final solution consists of a sandwich structure with a core made of 25 mm thick aramid honeycomb surrounded by two laminate skins of aramid fiber fabric (Twaron) with an approximate thickness of 2 mm. The innermost skin incorporates a Kapton foil with copper coated strips on both sides whereas

the outermost skin is covered in its outer surface by a copper foil. The detailed stack sequence of the layers with its associated radiation lengths, is presented in Table 10.2.

Layer of the wall	material	thickness d (mm)	average X_0 (mm)	d/X_0 (%)
1 (Inner layer)	Double layer strip foil	~0.05	143	0.08
2	Polymide film (Kapton)	0.01	285	<0.01
3	Aramid Fiber Fabric (Twaron)	2.0	~240	0.70
4	Aramid honeycomb panel (Nomex)	25	14300	0.17
5	Aramid Fiber Fabric (Twaron)	2.0	~240	0.07
6 (Outer layer)	Copper foil	0.01	143	0.07
Total		~30		1.7

TABLE 10.2: Field-cage wall materials composition and radiation lengths. Table extracted from Ref. [3].

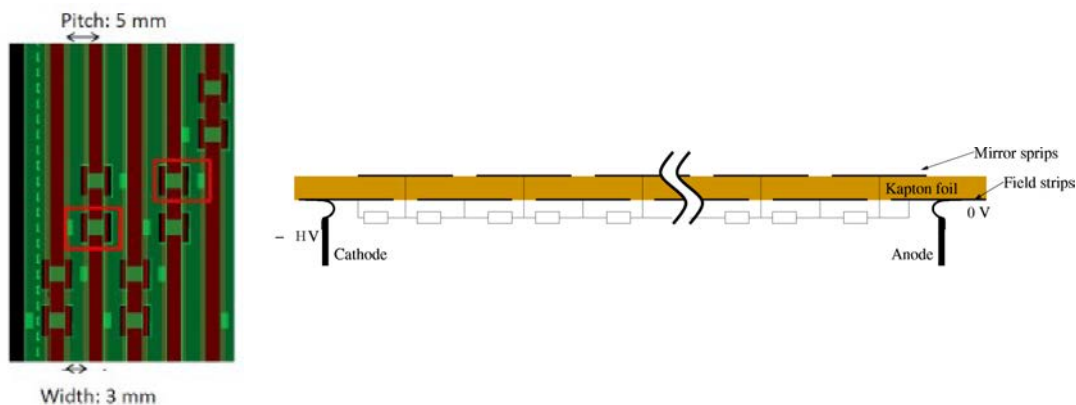


FIGURE 10.5: Drawing of the field-cage inner strips and connection pads (green) on the Kapton foil (brown). Right panel: Electric circuit formed by the strips. Figure from Ref. [3].

The copper strips in the inner surface of the HATPC boxes are designed to provide a smooth electric field within the box. The strips pitch is of 5 mm, with a gap between adjacent strips of 2 mm. In total, this requires of 110 strips in the inner side and 109 strips in the other side, referred to as mirror strips. The strips on opposite Kapton foil surfaces are staggered so that they overlap by 0.5 mm. Pads are included along the strips with a via to connect the mirror strips with the inner strips by means of a resistor to form a voltage divider, as sketched in Figure 10.5. For redundancy, strips are connected using two resistors connected in parallel. To satisfy the physics requirements, it was determined via finite elements simulations that the resistor pairs should be matched within a root-mean-squared (RMS) of 0.1%.

To ensure the mechanical stiffness of the box four bars made of thermoplastic (POM-C type), called angular bars, were initially included in the design. A second set of eight bars and eight corner parts, referred to as the flanges, were also initially included. The main goal of the flanges is to seal the box in a reliable and gas-tight manner and to provide a smooth and precise machinable surface.

Due to the high necessary planarity and parallelism of the box walls a precision mold is required in the fabrication process. It consists of a rectangular structure made up of four precision machined cast Aluminum plates held by L-shaped angular profiles. A figure of the molding process is presented in Figure 10.6.

The mold works as an inner structure for the box, on top of which the layers are stacked one by one manually. Between layers, special resins are applied to hold the layers together. Due to this,

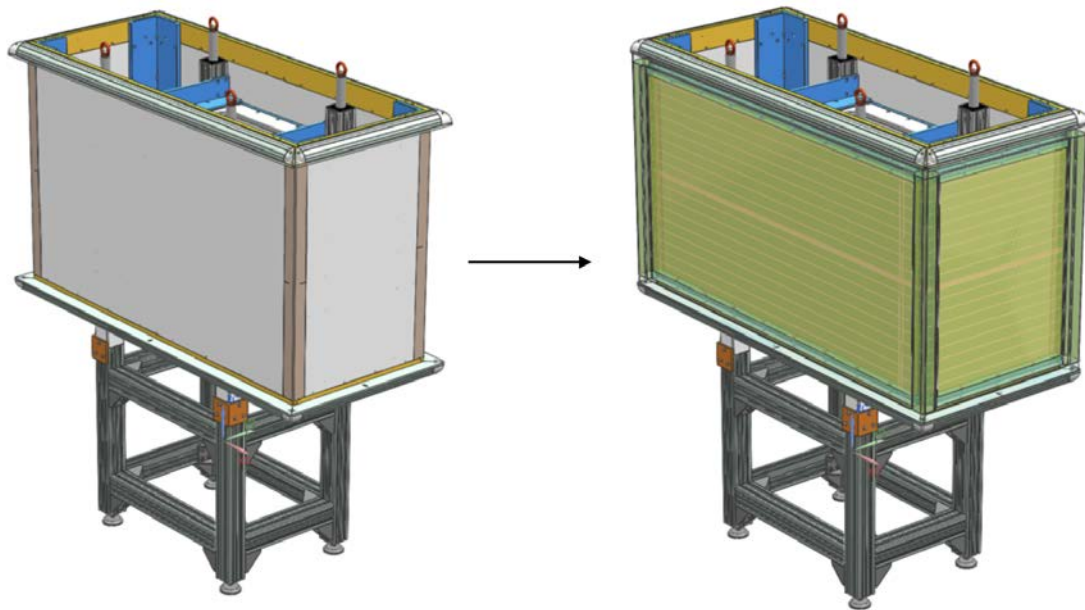


FIGURE 10.6: Drawing of the mold before (left) and after (right) the manufacture of a HATPC box half.

the material is cured in a high pressure autoclave. Once the field-cage is finished, the mold is dismantled from the inside and can be prepared for its next use.

10.2.4 Box prototyping

Two companies were selected for the fabrication of the HATPC field-cages. NEXUS¹, in Spain, would be responsible for the manufacture of the boxes and ORVIM², in Italy, would provide the copper-clad G10 cathode. As the HATPC boxes are custom made it was important to define early on a production plan that would allow to validate the designs and to develop and test the necessary manufacture steps to ensure an optimal end-product. With this goal, it was decided that the first milestone should be the production and validation of a smaller field cage prototype of $0.5 \times 0.5 \times 1 \text{ m}^3$.

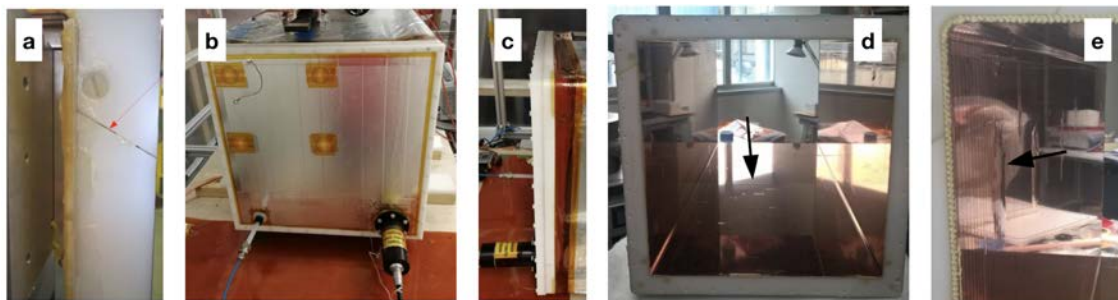


FIGURE 10.7: Pictures of the first small field-cage prototype: a) flange detail showing sub-optimal sealing b) detail of the cathode c) the cathode from the side d) and e) inner surface of the prototype showing bubbles in the Kapton foil hosting the strips.

The first field-cage prototype was built and tested at the end of 2019, see Figure 10.7. Stable operation of the TPC prototype was achieved at a cathode voltage similar to 20 kV. No sparks

¹<http://nexusprojectes.com>

²<http://www.orvim.com>

were observed in the voltage divider, however, discharges were initially seen in the cathode region. The origin of the sparks was understood and corrected by properly shaping the external grounded shielding at the cathode. A stable leak was measured due to insufficient sealing on the flanges. Small irregularities and blisters were observed in the inner Kapton foil with the strips which required postprocessing corrections.

Based on these experiences and the feedback from the companies involved it was decided to perform a series of updates in the original design:

- The box structural bars of POM-C thermoplastic would be replaced by stiffer and easier to glue G10 bars manufactured by ORVIM. This included the replacement of the eight flanges pieces, four per side, which would be replaced by a single flange part per side sealed with pured-on resin to reduce potential leaks.
- A new first layer positioning system would be used as suggested by NEXUS. The goal was to avoid crevices or blisters. The method consisted in removing the air trapped under the Kapton foil vacuum pumping through a sealed glass yarn. The method was proved to be effective in dedicated tests.
- A new Kapton layer would be added between the strip layer and the Twaron layer for additional insulation. This had a negligible impact in the total thickness and radiation length of the walls.
- The Twaron layers would use compensated fabrics with 45° and -45° instead of 0° and 90° as originally tested.
- The mold shape was updated including slight shape modifications in the corners to avoid damaging the box during the mold dismounting.
- The aluminum mold would be hard anodized to increase its robustness making it durable for its subsequent uses.
- The cathode high-voltage plug was redesigned.

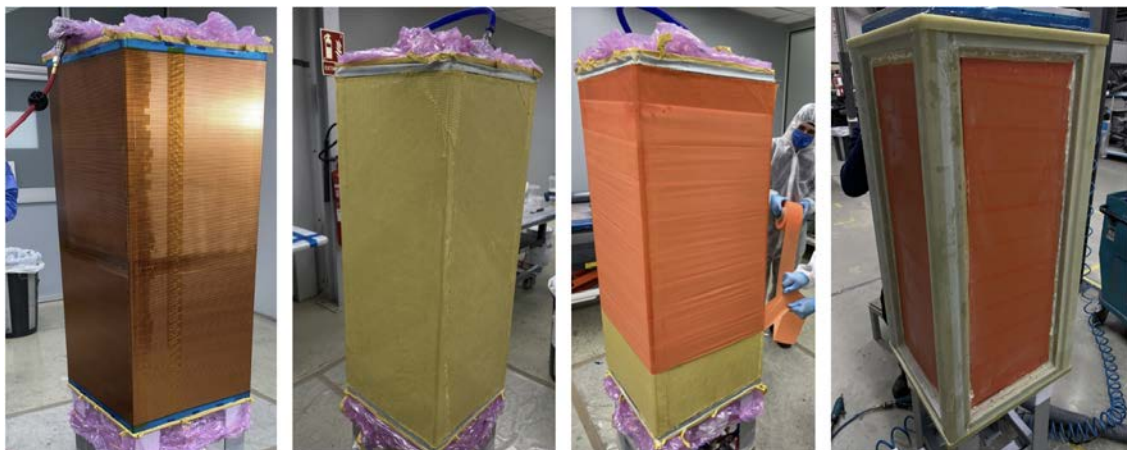


FIGURE 10.8: Pictures of the first steps of the fabrication process of one prototype box. From left to right the Kapton foil with the strips is installed, a resin layer is applied, the first Twaron fiber is glued and the G10 structural frames are mounted.

A second box prototype was built and tested in 2020. Pictures of the composite material fabrication and the installation of the structural bars are presented in Figure 10.8. The new prototype, see Figure 10.9, showed excellent results.

The mechanical tolerances were satisfied validating the molding technique. The Kapton foil with the strips was flat without significant imperfections. The strips in the Kapton foil were nicely

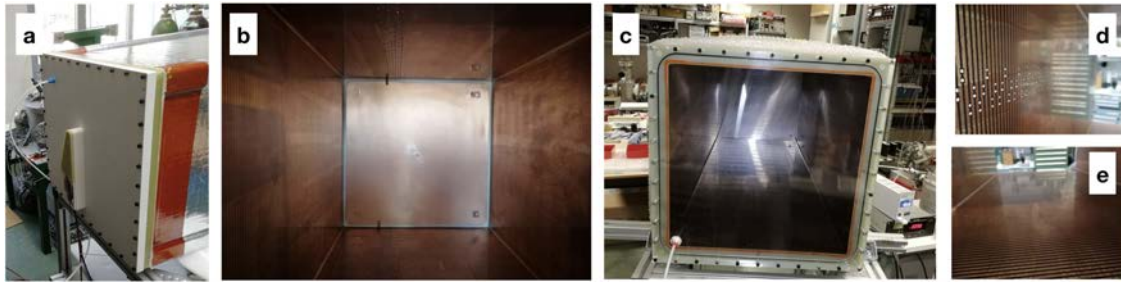


FIGURE 10.9: Pictures of the second small field-cage prototype: a) cathode detail with new high-voltage plug b) flat Kapton foil with good strips alignment c) view of the front flange through a transparent end-cap e) and d) details of the strips.

aligned within hundreds of μm thanks to the updated first layer deposition technique. The box had excellent gas tightness and mechanical resistance, enduring pressure variations of up to ± 80 mbar, validating the new flange design and the replacement of the POM-C bars by G10. The cathode was also successfully tested up to -35 kV in argon gas. In general, the second prototype validated the box design.

10.2.5 Cathode

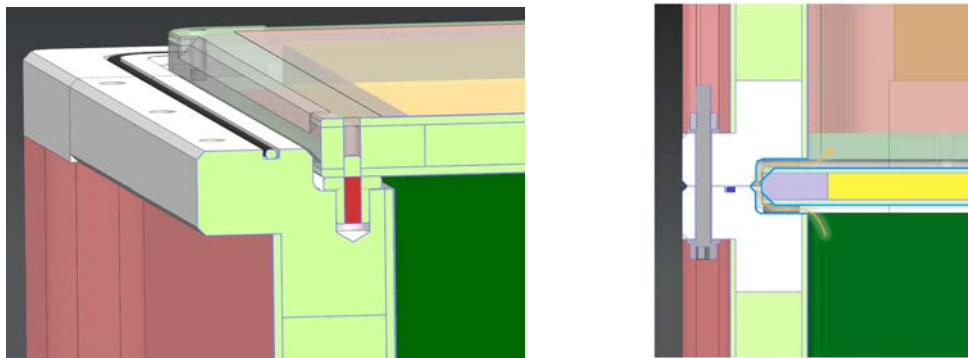


FIGURE 10.10: The left panel shows a closeup of the cathode supported through a spacer on the grooved flange in the box. The right panels depicts the cathode positioned between the flanges of the two field-cage boxes. The gas flow path, allowed by the gap between the cathode edge and the inner flange grooved surface and by the wedged cathode edge, is highlighted by a yellow arrow. Figures from Ref [3].

The central cathode is a Copper-clad G10/Nomex panel. It is constructed by laminating 1 mm copper-clad G10 onto both surfaces of a 10 mm thick Nomex honeycomb leading to a cathode with a nominal thickness of 12 mm. The cathode frame is built using G10 bars machined to match the Nomex thickness. The copper-clad G10 sheets are laminated at the same time on a granite flat table. As depicted in Figure 10.10 the internal side of the flanges is machined to include a 8×18 mm groove which hosts the edges of the cathode protruding 16 mm into the groove. The 2 mm gap between the cathode edge and the inner surface in the groove allows the gas to flow between the two field-cage box volumes. The gas flow is further enhanced by milling the cathode frame along the sides, except for a few cm around the corners, making a 45° wedge. The alignment of the cathode and the end-plate planes needs to be better than 0.1 mm. To achieve it, spacers are precisely machined. Finally, a high-voltage feedthrough is included in one of the flange corners to allow a high voltage connection to the cathode. The electrical connection between the cathode and the first field-cage strip is achieved manually soldering fine wires.

10.2.6 Module frames

The module frames main goal is to conceal the gas in the box whilst holding each eight ERAM modules, depicted in Figure 10.11, organized in two rows of four modules, as presented in Figure 10.12. The module frames were designed to cope with the following tolerances:

1. Precise ERAMs positioning, with tolerances of $100 \mu\text{m}$.
2. Global flatness within $\pm 0.1 \text{ mm}$ under the nominal overpressure of 4 mbar.
3. No plastic deformation under the gas tightness tests overpressure of 10 mbar.
4. Excellent gas tightness and negligible out-gassing from the module frame materials.

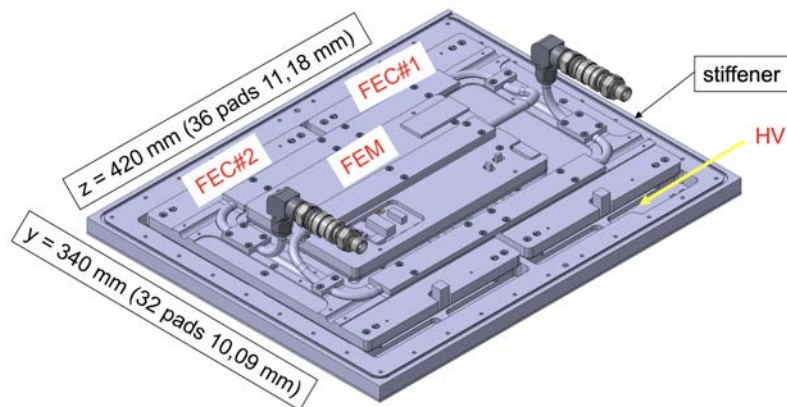


FIGURE 10.11: 3D drawing of a single ERAM module ready for installation in the module frame. The module includes the resistive Micromegas PCB glued onto its aluminum stiffener, all the electronic boards and cooling pipes.

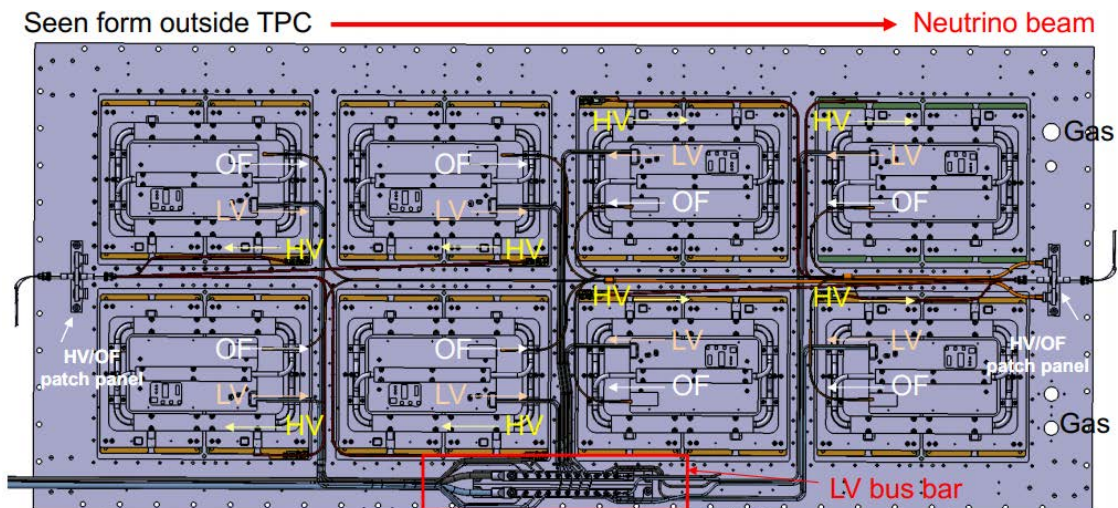


FIGURE 10.12: Drawing of the final module frame with all of its eight ERAM modules installed. The low-voltage (LV) and high-voltage (HV) distribution schemes are highlighted, as well as the optical fibers (OF) used for data transfer and the gas feedthroughs.

Aluminum was chosen as the best fitting option as it provides excellent structural performance in an economic and easily machinable material. The module frames include eight rectangular openings which allow to mount the ERAMs from the inner side reducing the gaps between the sensitive surface of the modules to about 1 mm. The ERAM modules, including the DLC coated

Micromegas PCB, the front-end electronics, and the cooling pipes, are concealed within an aluminum stiffener reinforced by mountable aluminum plates. Once installed in the module frame, a low-voltage distribution bus, and patch panels holding optical-fibers and high-voltage cables provide the necessary connections to operate and readout the ERAMs. The water-based cooling system is intended to dissipate the heat power of about 28 W produced during normal operation ($\Delta_{\text{water,module}} = 0.35^\circ \text{C}$). A drawing of the final module frames design, highlighting all of the former elements, is presented in Figure 10.12.

10.3 The ERAM0 prototype

To demonstrate that the ERAM scheme with grounded mesh was functional and could meet the expected performances, a first ERAM prototype, named ERAM0, was built and tested. The tests and performance studies were presented in Ref. [4]. Accordingly, this section summarizes and reproduces the most significant studies there described.

10.3.1 Production

The ERAM0 was developed on the basis of the already existing Micromegas PCB used in the original ND280 TPCs. Therefore, the module had a sensitive area of $36 \times 34 \text{ cm}^2$ and was covered by pads of $0.98 \times 0.70 \text{ cm}^2$. The pad surface was covered by a $200 \mu\text{m}$ insulating layer and a $50 \mu\text{m}$ Kapton (Apical) with a thin Diamond-Like-Carbon (DLC) layer. The resistivity was measured to be of $2.5 \text{ M}\Omega/\square$. On top of this surface, a bulk Micromegas was built, with a $128 \mu\text{m}$ amplification gap. The electronics were the same developed and in use for the T2K TPCs, based on the AFTER chip [453].

10.3.2 Beam test setup

To study the performances of the ERAM0 module a beam test was set up during the summer of 2018 at the T9 beamline at CERN. For the test, the ERAM0 module was installed in the HARP TPC field-cage [528], see Figure 10.13. The HARP TPC consists on a cylindrical volume of 2 m long and a diameter of 0.8 m, providing a drift distance of 1.5 m. The cathode is located at one of the cylinder ends at about 50 cm from the edge of the external cylinder. During normal data taking the cathode voltage was set to 25 kV creating a drift field of 167 V/cm from the cathode to the anode. On the anode, located in front of the cathode, a circular flange closed the cylinder and held the ERAM0 module.

The HARP TPC was filled with T2K's gas mixture, namely Ar:CF₄:iC₄H₁₀ (95:3:2), via a simple

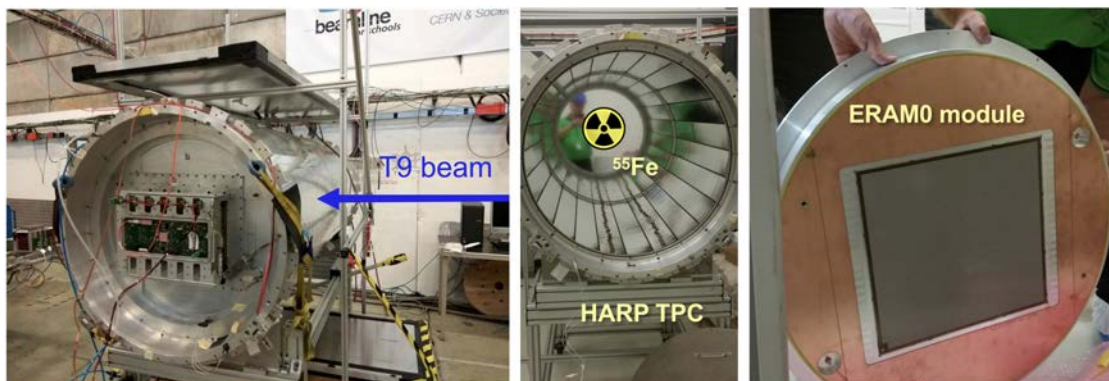


FIGURE 10.13: Images of the instrumented HARP TPC (left), the location of the ^{55}Fe radioactive source in the cathode (center) and ERAM0 module prior to installation (right).

gas system consisting of a single line. Before the start of the data taking, the TPC was extensively flushed with Nitrogen gas to remove impurities. Later, it was flushed with the final gas mixture with a volume of gas equivalent to 3 or 4 TPC volumes. The nominal flow rate during operation was kept at about 25 L/h. Temperature measurements on the exhaust line were also taken to monitor the environmental conditions affecting the gas density.

The HARP TPC was placed in the T9 beamline at CERN using a copper target to have an hadron enriched beam configuration. For the studies here described positively charged particles from the beam were collected as well as cosmic rays and signals from a ^{55}Fe radioactive source located in a Mylar window at the cathode. A series of instruments along the beamline were used in order to build a trigger system. It consisted of three plastic scintillators and two Cherenkov detectors. A selection criteria for the different particle types was done by combining the signals from those detectors.

In standard conditions, the ERAM0 was operated at 340 V. The settings chosen for the AFTER chip were a sampling time of 80 ns, a shaping time of 600 ns and the charge to saturate the ADC was 120 fC, providing a sufficiently large dynamic range for all the studies. Data was taken at different drift distances of 10, 30 and 80 cm by shifting the location of the TPC in perpendicular to the beam. Additionally, a scan of the ERAM was made varying its voltage in the range from 330 to 380 V.

10.3.3 Track reconstruction

Each data run consisted of a mixture of beam tracks, cosmic rays and ^{55}Fe signatures. Therefore a simple 3D track reconstruction algorithm was developed in order to remove noise and to separate cosmic and beam tracks. The selection algorithm looked for connected groups of pads, i.e. pad clusters, at the beginning and at the end of the module. If connecting the clusters on both sides was possible through a straight line of hits, the track was accepted. An example of reconstructed tracks is show in Figure 10.14.

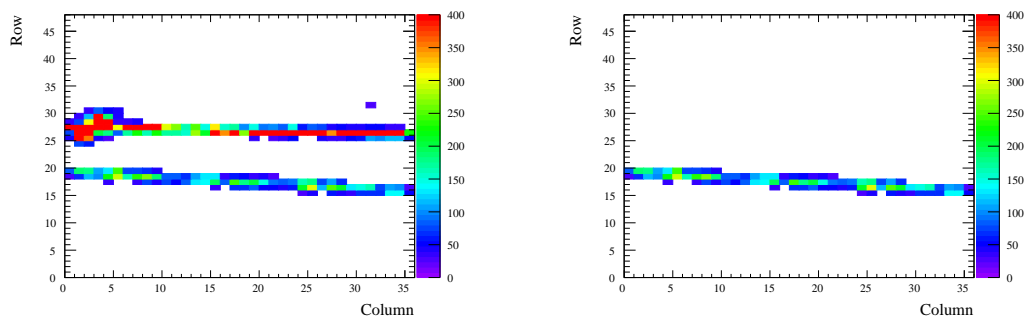


FIGURE 10.14: Example of the selection algorithm performance on a single data event showing a raw event (left) and a selected track (right). Figures from Ref. [4].

In addition, a reconstruction algorithm based on the DBSCAN clustering algorithm [529] was also tested as a potential solution for the final HATPCs reconstruction. An example of one event reconstructed using the DBSCAN-based algorithm is presented in Figure 10.15.

10.3.4 Calibration and gas monitoring

The attenuation length of electrons in the gas was measured as a function of the time elapsed since the start of the beam test. To do it, vertical cosmic tracks at different drift distances were selected. At each distance the average measured charge was computed and the resulting distribution fitted with an exponential function as presented in Figure 10.16. The results are shown in Figure 10.17.

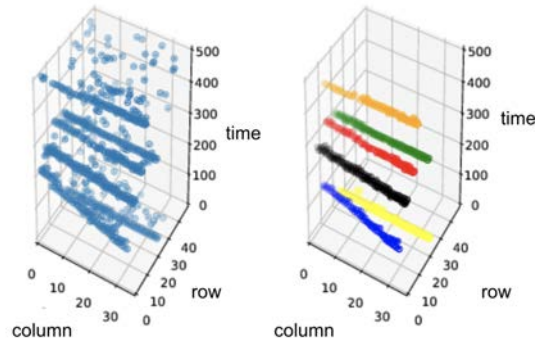


FIGURE 10.15: Example of the DBSCAN 3D matching algorithm performance for the raw event (left) and the reconstructed tracks (right). The time is expressed in units of 80 ns. Figure from Ref. [4].

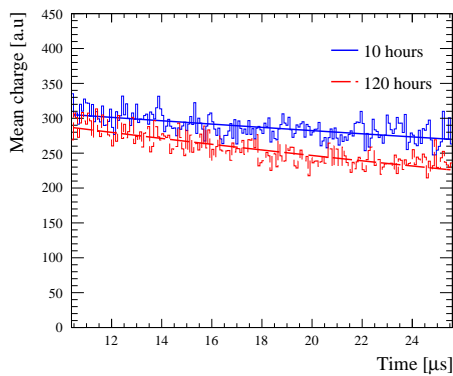


FIGURE 10.16: Average charge versus drift time for 2 sets of data taken at the beginning and at the end of the test beam period. Figure from Ref. [4]

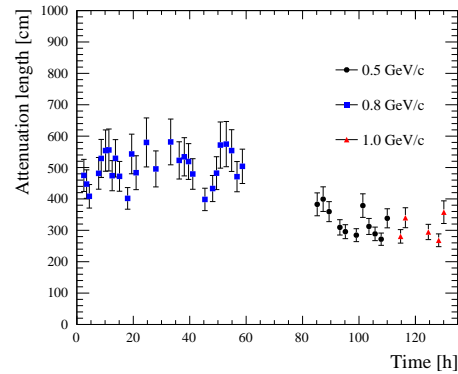


FIGURE 10.17: Evolution of the signal attenuation length during the data taking. Figure from Ref. [4]

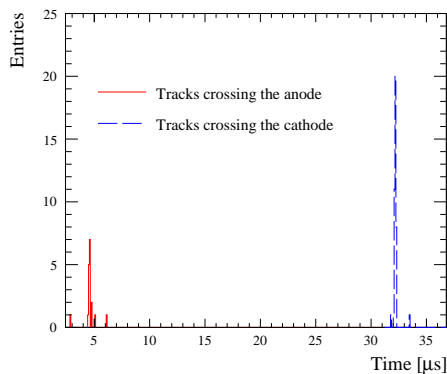


FIGURE 10.18: Time distribution of tracks crossing the end caps of the chamber for a set of 25k triggers. Figure from Ref. [4]

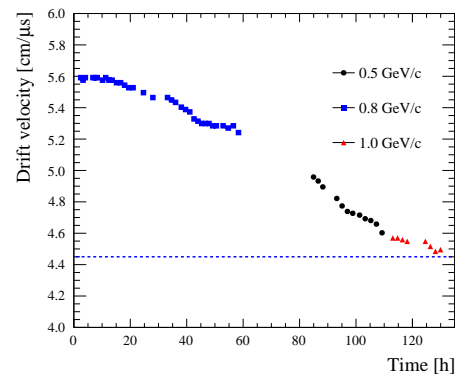


FIGURE 10.19: Drift velocity time evolution, the dashed blue line is set at the minimum measurable value. Figure from Ref. [4].

A reduction of the attenuation length was observed indicating a progressive degradation of the gas quality. The attenuation length, however, was reasonably small along all runs, as it was always at least twice the maximum drift length in the HARP TPC.

The drift velocity of the ionized electrons was computed using the time difference in signals generated by cosmic tracks crossing the cathode and the anode divided by the drift length, as

illustrated in Figure 10.18. A smooth reduction of the drift velocity can be observed in Figure 10.19. After a maximum was reached in the gas quality following the initial TPC gas purge an insufficient flow rate lead to a progressive deterioration of the gas quality. Eventually, the drift velocity was low enough (below 4.45 cm/ μ s) for the tracks near the cathode to not be recorded, as the electronics only collected data for short time windows. This experimental conditions were not planned. Consequently, investigations were made to better understand the origin of the gas quality degradation. For T2K's gas mixture at the electric field of 167 V/cm simulations lead to an expected drift velocity of 6.8 cm/ μ s. However the maximum measured drift velocity was instead of 5.6 cm/ μ s. Simulations showed that the observed reduction of the drift velocity was compatible with the presence of H₂O in the gas. A possible increase over time from 1500 ppm to 3000 ppm could explain the measured values. The presence of water in the gas would also explain the mild degradation observed in the attenuation length, which would have been much severe if instead of H₂O the contaminant would have been O₂. Hence, data suggests that the HARP TPC field cage progressively released water vapor into the drift volume. A large humidity on the inner side of the field cage is likely due to the fact that the HARP TPC was stored in air for several years. However, the role of humidity was underestimated and the TPC was not dried before bringing it back to operation. Hence, under this possible interpretation, the initial TPC purge removed most of the water vapor, however, the nominal flow rate of about 30 L/h was not enough to effectively remove the constant release of water molecules from the TPC walls which kept on increasing its concentration over time.

Nonetheless, the gas quality degradation did not significantly affect the main goal of this studies which was to validate the performance and functionality of the resistive Micromegas. The presence of contaminants in the gas reduces the amount of ionization reaching the Micromegas and therefore, any measured performances constitute a lower bound of the expected performances under optimal running conditions. In any case, the decision was taken to center the analysis in 0.8 GeV/c runs, which had the best working conditions.

10.3.5 Gain studies

The Micromegas gain and its uniformity are key elements for successful particle identification in the TPC. The gain of the resistive Micromegas module was measured using ⁵⁵Fe signatures. The uniformity of the gain was measured with cosmic rays.

The measured spectrum of the ⁵⁵Fe source is presented in Figure 10.20a. Both the 2.9 keV and the 5.9 keV photon emissions are visible. For the larger peak an energy resolution of 8.9% was obtained. Despite being measured on significantly more challenging conditions, this result is comparable to that in T2K's bulk Micromegas [456]. The ⁵⁵Fe 5.9 keV signatures can be used to compute the gain by computing the ratio of primary to secondary electrons. The primary number of electrons is known by dividing 5.9 keV by the mean ionization energy for the TPC gas mixture. The secondary number of electrons is extracted by converting the ADC mean counts into electrons via the known electronics specifications. The dependence of the gain and of the resolution with the ERAM voltage, is presented in Figure 10.20b, revealing the expected exponential dependence. The voltage scan was performed at the end of the beam test, when the gas quality was lower, affecting both the gain and the energy resolution. To illustrate the role of this degradation, data taken at -340 V at the beginning of the data taking is also shown. As expected, the decrease in the gas quality translated into a progressive reduction of the gain, see Figure 10.20d.

To study the gain uniformity, i.e. the uniformity in the gain measured in individual pads, cosmic tracks were used. The underlying reason for this was that due to the placement of the ⁵⁵Fe source it only illuminated the central region of the ERAM. The uniformity was studied by measuring the average charge on each pad. To reduce the effect of tails to this charge distributions a truncated average was used such that only the 70% of hits with lower charge from each track were used to fill the distributions. The results are presented in Figure 10.21. Except for the pads at the edge

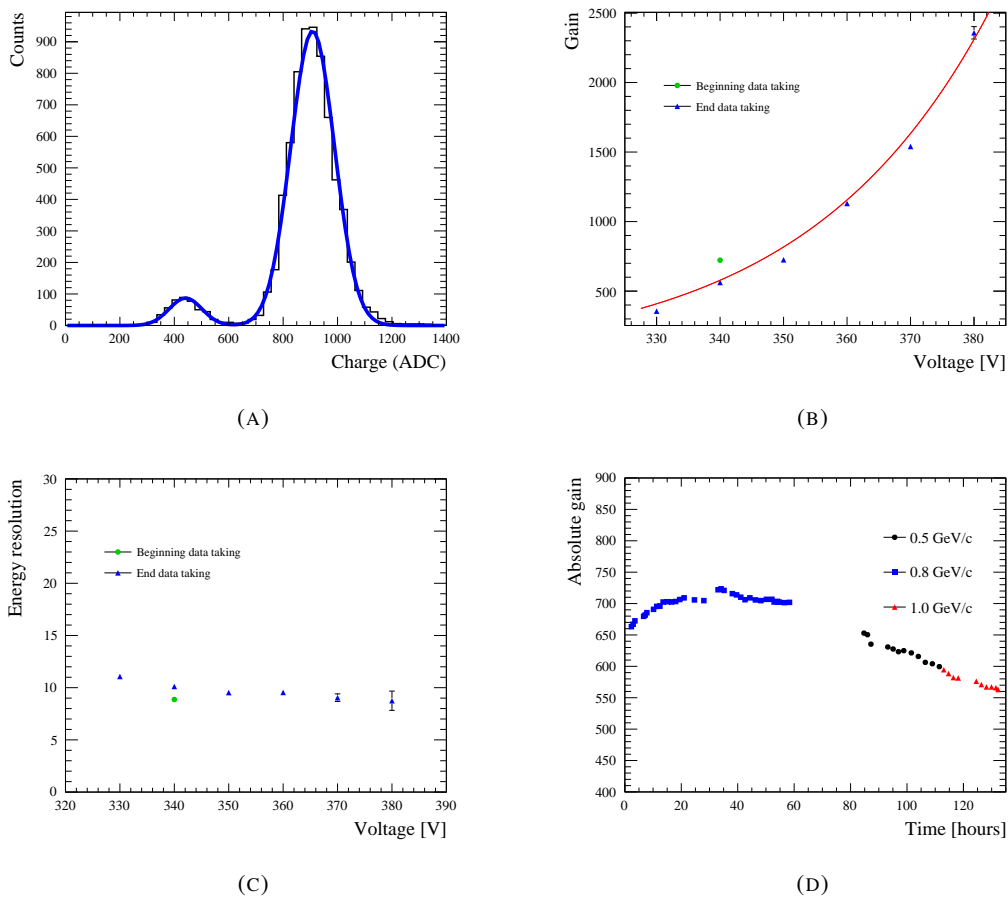


FIGURE 10.20: a) X-ray energy spectrum. The energy resolution at 5.9 keV is 8.9%. b) Micromegas gain for different micromesh voltages. c) 5.9 KeV resolution for different micromesh voltages. d) Time evolution of the gain during the data taking. Figures from Ref. [4].

of the Micromegas, which collect roughly half of the typical charge due to the smaller number of surrounding pads contributing to the signal spreading on the measured pad, the gain uniformity was better than 3%.

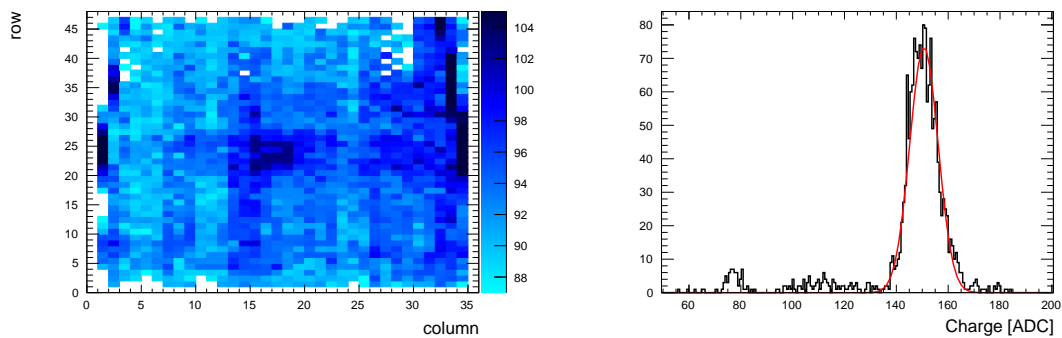


FIGURE 10.21: Gain calculated using cosmic rays represented as a 2D map (left) and as a 1D histogram with a Gaussian fit used to calculate to gain uniformity (right). Figures from Ref. [4].

10.3.6 Characterization of the charge spreading

The main difference in the ERAM when compared to the traditional bulk technology is the spreading of the charge signal, a phenomenon described in Ref. [530]. The spreading can be clearly observed in the ERAM0 signal waveforms of adjacent pads. As presented in Figure 10.22, the pads adjacent to the one collecting most of the charge contain a signal smaller in amplitude and longer in time. In order to characterize the size and the timing of the signal spread nearly horizontal tracks were selected.

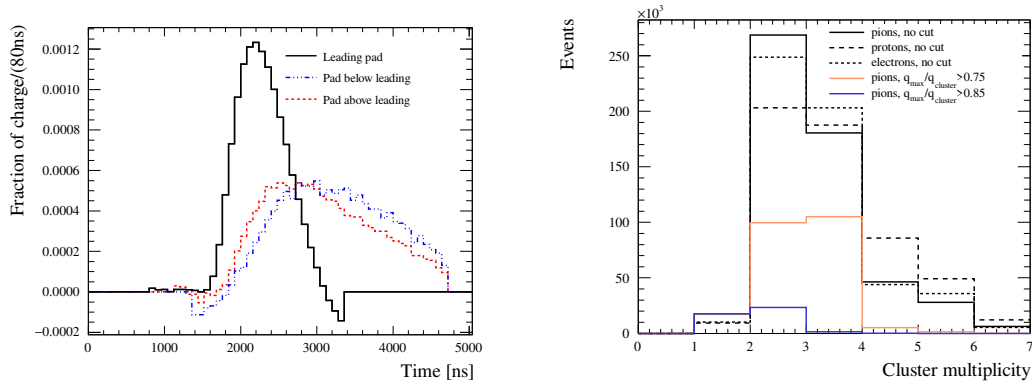


FIGURE 10.22: Pad multiplicity in the cluster (left) and fraction of the cluster charge that is collected in the pad with largest signal (right). The histograms for pion, electron and proton clusters are normalized to the same area. Figures from Ref. [4].

A cluster is defined as the set of fired pads on the same column (row for vertical tracks) and the pad multiplicity as the number of pads in a given cluster. The pad multiplicity per cluster and the fraction of charge in the pad with largest signal ($q_{max}/q_{cluster}$) are presented in Figure 10.22.

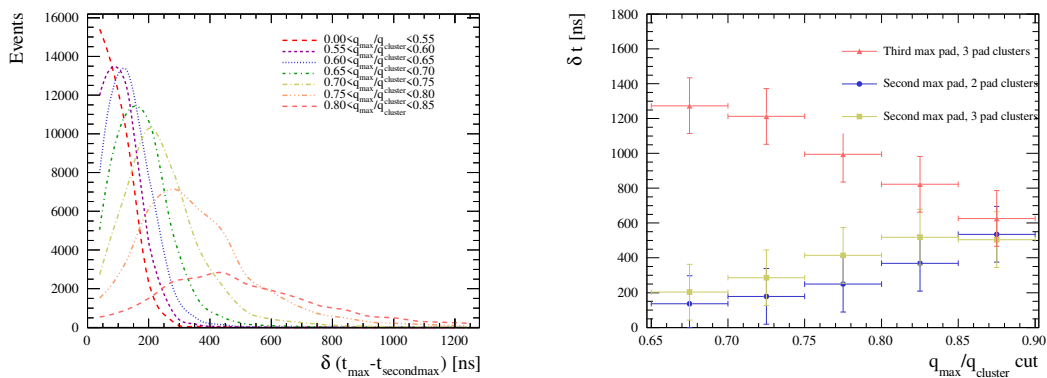


FIGURE 10.23: Left panel: Time difference in the waveform maximum between the leading and the second pad for 2-pads clusters. Right panel: Typical time difference as a function of the cut value. The error bars corresponds to two time-bins of 80 ns. Figures from Ref. [4].

Figure 10.23 shows the difference in peak time between the leading pad and the other pads. The delay of the charge spreading can be up to few μ s for clusters with a pad multiplicity of three. In Figure 10.23 the time difference between the leading and the second (third) pad is also presented as a function of the fraction of signal in the leading pad. Such fraction is a proxy for the position of the track. Decreasing the fraction corresponds to move closer to (away from) the second (third)

pad, and therefore, it can be used to extract an estimation of the velocity of the charge spreading. In the limit of large charge fraction in the leading pad the difference in time peak between the second and the third pad should converge to the same value, which corresponds to the time needed by the charge to spread along half a pad width. From these considerations, a charge spreading velocity of about $0.6 \text{ cm}/\mu\text{s}$ was measured.

10.3.7 dE/dx resolution

As the TPC's PID criteria is built upon momentum and dE/dx measurements, achieving high resolution in this two figures-of-merit is crucial. In particular, the new ERAMs are expected to provide a dE/dx resolution similar to 8% for minimum ionizing particles crossing the full length of two ERAM modules.

To study the dE/dx capabilities of the ERAM0 the truncated mean method, also used in current ND280 TPCs, was employed. Namely, the clusters of each track were sorted from lower to higher total charge, and only a fraction of them with the lower charge was used to compute the mean deposited energy. To avoid potential biases, clusters on the edges of the Micromegas were ignored. The result of using the truncated mean method is presented in Figure 10.24. An optimal truncation factor of keeping the lowest 62.5% clusters was used, corresponding to retain 21 clusters of a possible maximum of 34.

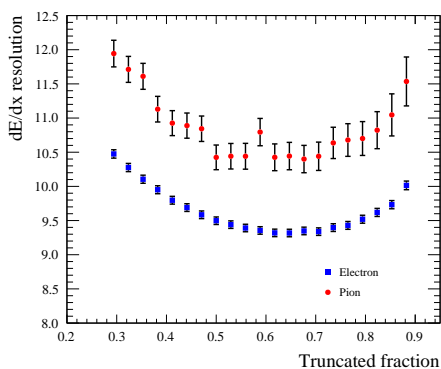


FIGURE 10.24: Resolution on the energy deposit per unit of track length for different truncation values. Figure from Ref. [4].

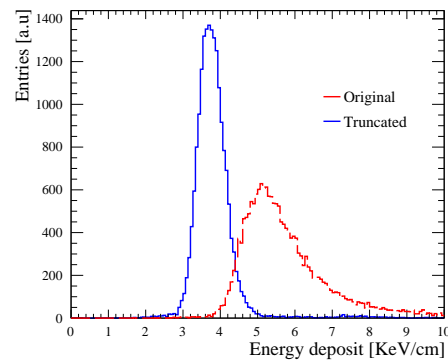


FIGURE 10.25: dE/dx on the same beam sample of positrons at $0.8 \text{ GeV}/c$ with and without applying the truncation mean method. Figure from Ref. [4].

The deposited energy distribution for different triggers is presented in Figure 10.26a. The double peaked spectrum of the distribution with pion trigger indicates a low purity on the selected tracks since a large fraction of them were positrons. Such a low purity is attributed to the sub-optimal performance of the Cherenkov trigger modules. Figure 10.26b shows the deposited energy for pion triggers taken at different drift distances. After applying corrections to account for the different gain and attenuation lengths comparable dE/dx spectra were obtained, see Figure 10.27.

Deposited energy resolutions in the interval from 9.0% to 11.2% were measured. These values account for drift distances up to 85 cm, similar to the maximal drift distance of the HATPCs. Such resolutions, correspond to the performance expected from tracks creating 34 clusters in the ERAM. However, depending on the angle a lower or higher number is expected in the HATPCs, where an array of 2×4 ERAMs is used. To extrapolate the recorded performances, the deposited energy resolution was measured as a function of the number of clusters used to computed the

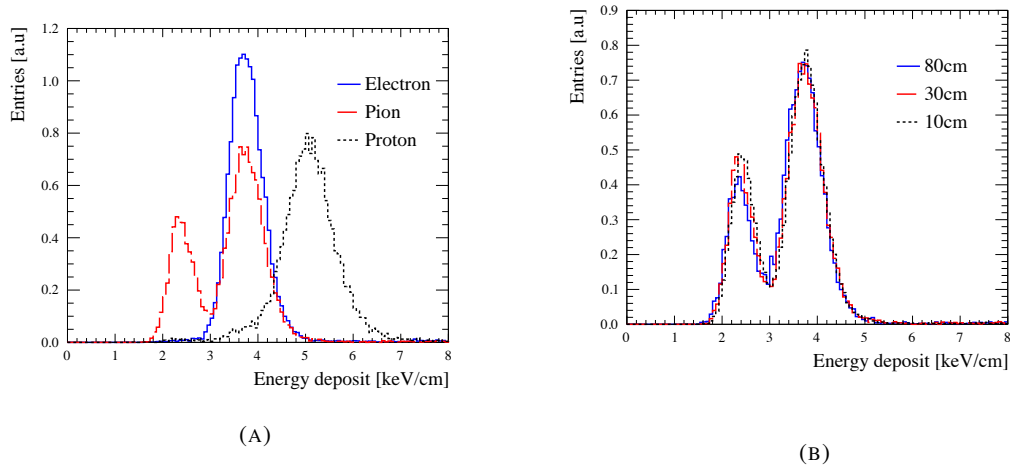


FIGURE 10.26: a) Energy deposited for three different triggers. The particles crossed the chamber at 30 cm from the Micromegas module. b) Energy deposited using pion trigger at 10, 30, and 80 cm drift distance. The two peaks visible in the pion trigger at attributed to the sub-optimal performance of the Cherenkov module in the trigger system. Figure from Ref. [4].

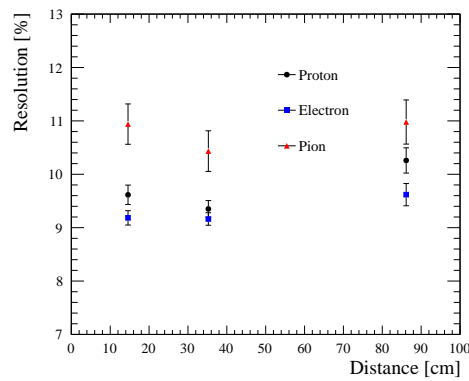


FIGURE 10.27: dE/dx resolution for 0.8 GeV/c positrons, pions, and protons at different drift distances. Figure from Ref. [4].

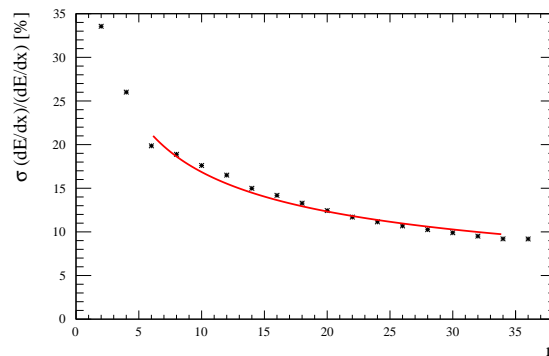


FIGURE 10.28: dE/dx resolution versus number of clusters for positrons at 30 cm of drift distance. Figure from Ref. [4].

truncated mean. The results are presented in Figure 10.28. The trend is fitted with

$$\frac{\sigma(dE/dx)}{(dE/dx)} = A n^B \quad (10.2)$$

Where n is the number of clusters and A and B are free parameters with best fit values presented in Table 10.3. In light of this results, with two ERAMs an excellent dE/dx resolution similar to 7% was expected.

trigger	momentum [GeV/c]	drift distance [cm]	A	B
positron	0.8	80	51.9 ± 2.9	-0.46 ± 0.02
	0.8	30	47.5 ± 2.6	-0.45 ± 0.02
	0.8	10	46.2 ± 2.5	-0.44 ± 0.02

TABLE 10.3: Values of A and B for different triggers. Table from Ref. [4].

10.3.8 Spatial resolution

The main advantage of the ERAMs technology is the charge spread, which allows to better estimate the track path. To do so, it is necessary to combine the measurements of multiple pads in the same cluster and to map their outcome into a position estimate. Such map, however, is not easy to build as the discretization of the true charge profile into pads of finite size induces position dependent biases. Due to this, the barycentric mean of the pad position, i.e the center of charge (CoC) of the cluster, is a limited estimator of the position. A more refined approach is to parametrize the spreading over the pads via the Pad Response Function (PRF) method, defined as

$$Q_{pad}/Q_{cluster} = PRF(x_{track} - x_{pad}), \quad (10.3)$$

where x_{pad} is the pad center, Q_{pad} is the charge on the pad and $Q_{cluster}$ is the total charge on the cluster containing the pad. The PRF was parametrized using the ratio of two symmetric 4th order polynomials, as proposed in Ref. [531]

$$PRF(x, \Gamma, \Delta, a, b) = \frac{1 + a_2x^2 + a_4x^4}{1 + b_2x^2 + b_4x^4}. \quad (10.4)$$

The coefficients a_2 and a_4 , and b_2 and b_4 can be expressed in terms of the full width half maximum Γ , the base width Δ of the PRF, and two scale parameters a and b .

To infer the position of the track, the χ^2 between $Q_{pad}/Q_{cluster}$ and $PRF(x_{track} - x_{pad})$ was minimized using

$$\chi^2 = \sum_{pads} \frac{Q_{pad}/Q_{cluster} - PRF(x_{track} - x_{pad})}{\sqrt{Q_{pad}/Q_{cluster}}}. \quad (10.5)$$

The analysis was performed in several iterations. In the first iteration the CoC method was used to extract the track position. Then, based on the CoC, the track was fitted with a straight line. The PRF scatter plot was filled and the distribution of $Q_{pad}/Q_{cluster}$ was obtained for each bin in $x_{track} - x_{pad}$. The peak and the full width half maximum were then taken as estimators of $Q_{pad}/Q_{cluster}$ and its uncertainty. This procedure is shown in Figure 10.29.

The spatial resolution is defined with the residuals $x_{track} - x_{fit}$ for each cluster. The obtained distribution was fit with a Gaussian and the σ was considered as the final spatial resolution. The improvement obtained with the PRF method compared to the CoC method is shown in Figure 10.30. Hence, using the PRF method, an outstanding spatial resolution at the level of 300 μm was achieved for horizontal tracks over the whole Micromegas.

To study the angular dependence of the spatial resolution cosmic tracks were used, since beam tracks were highly horizontal. The dependence of the spatial resolution on the angle in the detector plane, using the CoC method, is shown in Figure 10.31. Due to the limited geometrical acceptance of the cosmic trigger only tracks with drift distances between 50 and 100 cm and with angles between 0 and 20 degrees were used for this study. The rectangular shape of the pads

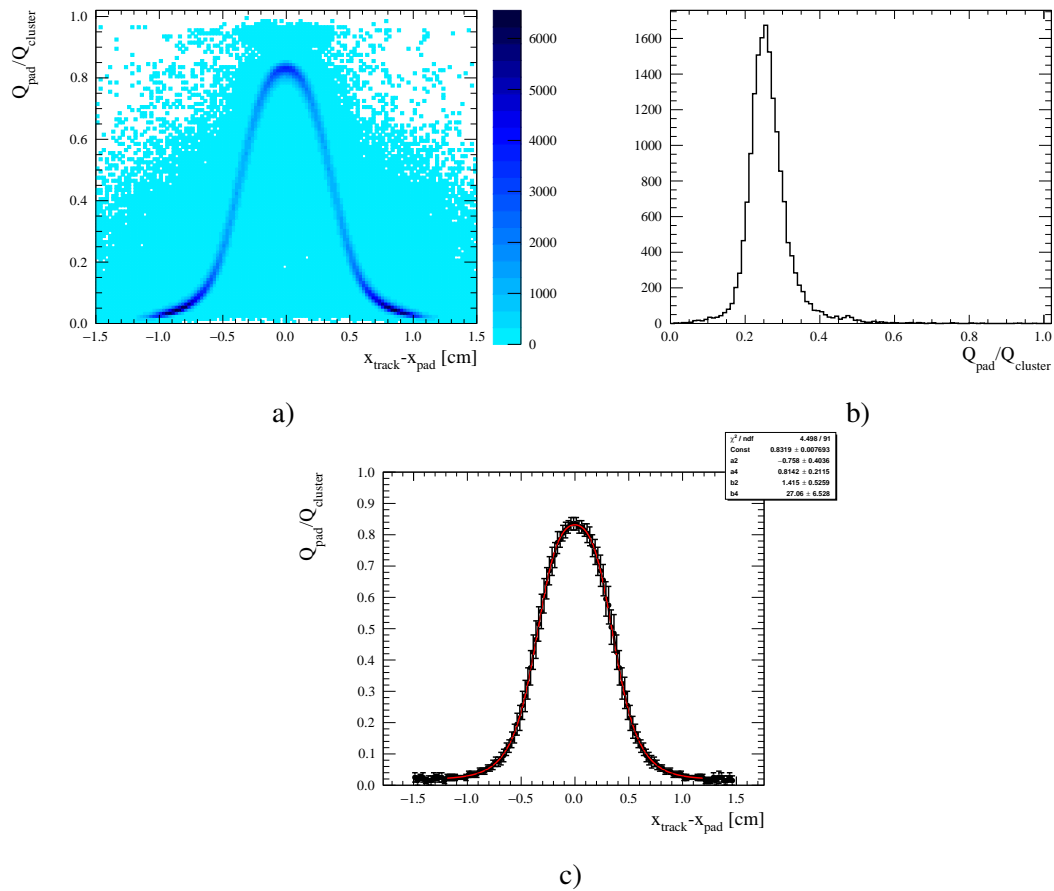


FIGURE 10.29: PRF results using 1 GeV/c pion triggers, 30 cm drift distance and 360 V in the ERAM: a) 2D histogram, b) example of the 1D histogram for $x_{\text{track}} - x_{\text{pad}} = -0.5$, c) final PRF plot with errors and fit with analytical function. Figure from Ref. [4].

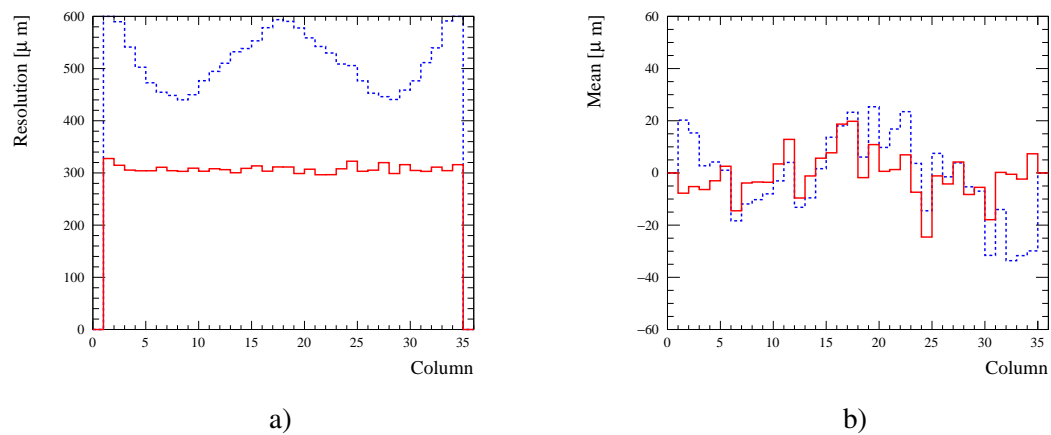


FIGURE 10.30: Spatial resolution comparison between PRF method (red solid line) and CoC method (blue dashed line). a) sigma of the residual as a function of the column number, b) mean of the residual as a function of the column number. Figures from Ref. [4].

($0.98 \times 0.70 \text{ cm}^2$) accounts for the different performance results for beam and cosmic tracks. The impact of the drift distance on the spatial resolution was studied. Ionization electrons traveling longer distances are expected to be more affected by the transverse and longitudinal diffusion.

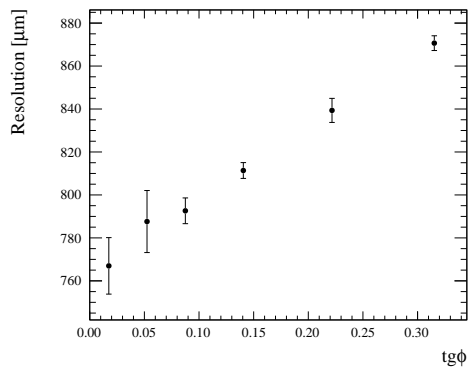


FIGURE 10.31: Spatial resolution as function of the track angle using the CoC method. Figure from Ref. [4].

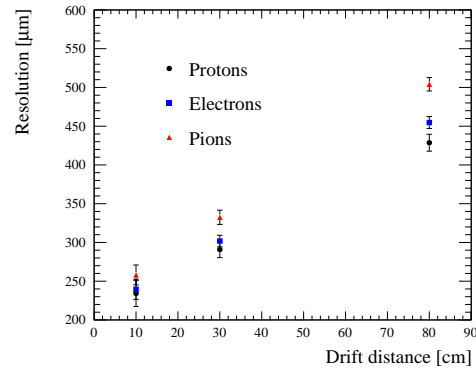
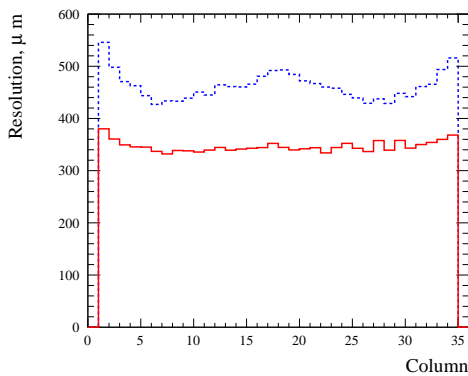
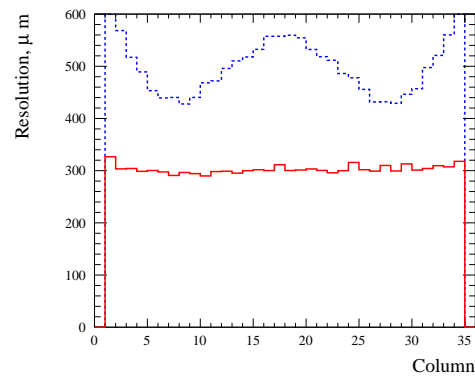


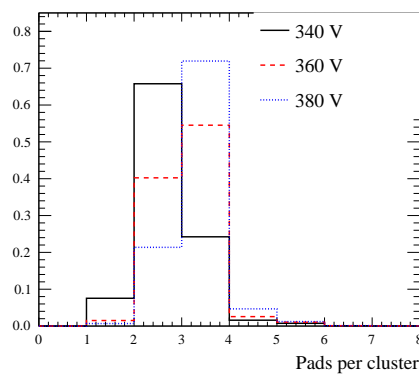
FIGURE 10.32: Average spatial resolution in each column for different particles at different drift distances. Figure from Ref. [4].



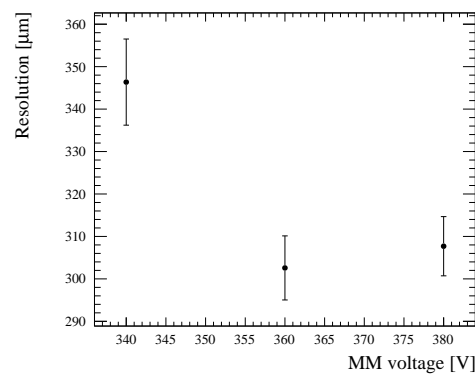
340 V



360 V



Multiplicity



Summary

FIGURE 10.33: Pad multiplicity and spatial resolution versus the ERAM voltage for 1 GeV/c pion samples at a drift distance of 30 cm. Blue dashed (red solid) line corresponds to the CoC (PRF) method. The summary was made with the PRF method. Figure from Ref. [4].

The average spatial resolution for pions, positrons and protons at different drift distances is presented in Figure 10.32 showing an acceptable level of degradation along the drift distance. The spatial resolution was also studied for different Micromegas voltages using only with 1 GeV/c pion triggers at a drift distance of 30 cm. For higher voltages larger gains are achieved such that enough charge reaches pads further away to increase the pad multiplicity of the clusters. A larger

multiplicity is then translated into better spatial resolutions as presented in Figure 10.33.

10.3.9 ERAM0 analysis conclusions

The performances of the ERAM0 module were excellent and validated the use of this technology in the HATPCs. The measured dE/dx resolution and uniformity were compatible to those in the bulk Micromegas. Finally, the spatial resolution was proven to be greatly improved in the ERAM.

10.4 The ERAM1 prototype

After the successful tests of the ERAM0 module, a new module, named ERAM1, was built and test using beam tracks at DESY in 2019. The main goal of the ERAM1 prototype was to characterize the performance of the ERAM technology using the final readout electronics and layout of pads.

10.4.1 Production

In fall 2018, after the ERAM0 beam test data was collected, the global design of HATPCs was finished. The sub-detector envelops were defined and the size of the ERAM modules set to be $420 \times 340 \text{ mm}^2$ with 32×36 rectangular pads of size $10.09 \times 11.18 \text{ mm}^2$. The ERAM1 module used this final layout and had a DLC foil resistivity of $200 \text{ k}\Omega/\square$, close to the final value. The resistivity of the foil was measured at critical steps of the manufacture process, which showed non-uniformities at the level of 20%. The detector readout electronics consisted on the final boards for the ERAMs and were mounted following the final expected design, earlier presented in Sec. 10.2.2. Remarkably, whereas the ERAM0 consisted of 1728 pads the ERAM1 consisted of 1152 pads and, therefore, the ERAM1 tests had also as a goal to validate the total pad number reduction.

10.4.2 Beam test setup

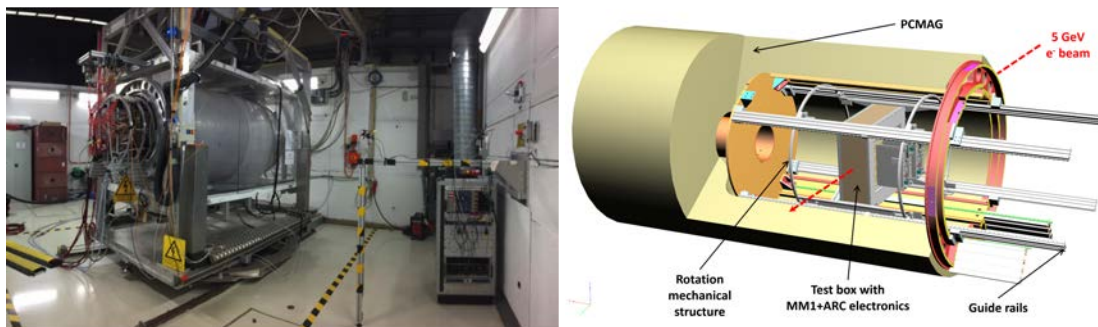


FIGURE 10.34: View of the experimental setup for the ERAM1 beam test at DESY. Figure from Ref. [5].

The prototype was mounted on a short TPC with a 15 cm drift distance and was exposed to an electron beam at the DESY II test beam facility [532]. DESY II provides electron beams of $1 - 6 \text{ GeV}/c$. In the test beam area a large solenoid was available and it was able to provide a magnetic field of up to 1.25 T. However, the solenoid was set up to provide 0.2 T since this is the nominal magnetic field in ND280. The magnet was mounted on a movable platform allowing to precisely change the TPC position both horizontally and vertically. Additionally, it allowed to precisely change the rotation angle. An image and a sketch of the setup is presented in Figure 10.34. A magnetic field of 0.2 T, perpendicular to the beam axis, was used in most of the collected data. The TPC holding the ERAM1 was operated with T2K gas mixture the quality of

which was constantly monitored during the data taking. The oxygen contamination was kept at around 30 ppm and the gas conditions were good all along the beam test. As the beam consisted only of electrons a simple trigger configuration was used. It consisted of a set of four consecutive scintillation counters mounted in front of the magnet. The coincidence between them was used as a beam trigger. Additionally, a second set of counters placed above and below the magnet was used to collect cosmic tracks.

Under nominal conditions the prototype was operated at a voltage of 360 V, a sampling time of 40 ns, a peaking time of either 200 ns or 412 ns and a gain of 120 fC. The momenta of selected electrons varied from 0.5 to 5 GeV/c. Several scans were carried out changing the drift distance, the ERAM voltage, the peaking time and switching on and off the magnetic field. The standard T2K drift field of 275 V/cm was used, significantly larger than that of 167 V/cm used in the ERAM0 tests, and a stable drift velocity of 7.68 ± 0.03 cm/ μ s was measured and validated by the use of a gas monitoring chamber identical to those used in the original ND280's gas system.

10.4.3 Track reconstruction

The DBSCAN-based reconstruction algorithm developed in the study of ERAM0 test beam data was used to reconstruct tracks for the ERAM1 prototype. A track was selected if it crossed the whole detector length without breaks or splits, namely events with more than one cluster in a given column were rejected. Events with more than one track crossing the detector close to one another were also rejected by applying a cut on the pad multiplicity in each cluster. The multiplicity cut was optimized for different voltages and electronic shaping times. Examples of the event displays are shown in Figure 10.35.

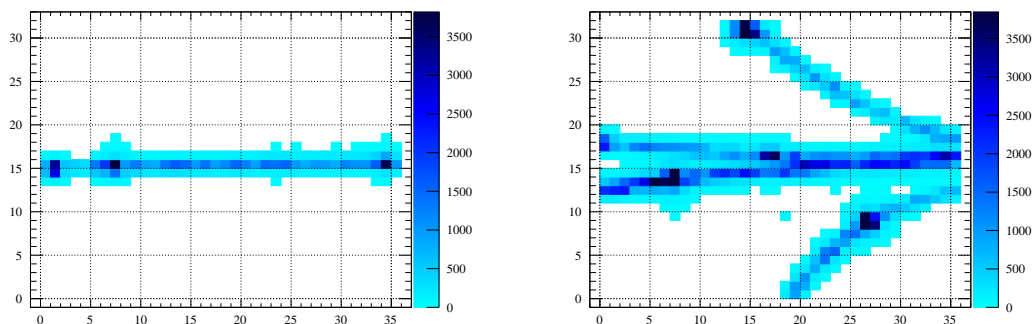


FIGURE 10.35: Displays of an accepted single track event and a rejected multi-track event. Figure from Ref. [5].

In the ERAM0 prototype tests only horizontal tracks were considered. In reality, however, tracks will enter the HATPC with different angles. For tracks projections in the pad plane which are parallel to the sides of the pads transverse spreading is defined precisely within the given column. However, for tracks entering the ERAM at an arbitrary angle the longitudinal and transverse spreading, i.e. the spreading along or in perpendicular to the track direction, are intertwined. In order to distinguish these two contributions the cluster patterns were generalized in the study of the ERAM1 prototype, as presented in Figure 10.36. Then, depending on the track angle, one of the former patterns was chosen and repeated to pave the whole set of pads in order to divide each track into clusters.

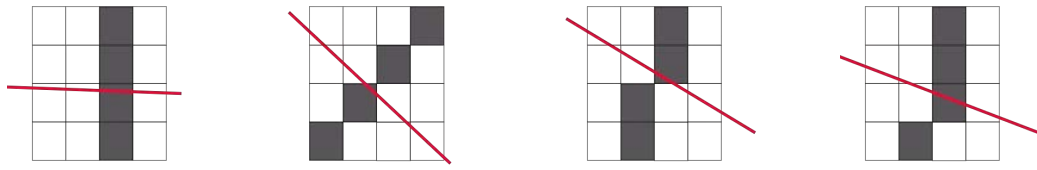


FIGURE 10.36: The different cluster patterns that can be used depending on the track (red line) angle. Figures from Ref. [5].

10.4.4 Spatial resolution

The PRF method, earlier described in Sec. 10.3.8, was built using an iterative method. Results are presented in Figure 10.37.

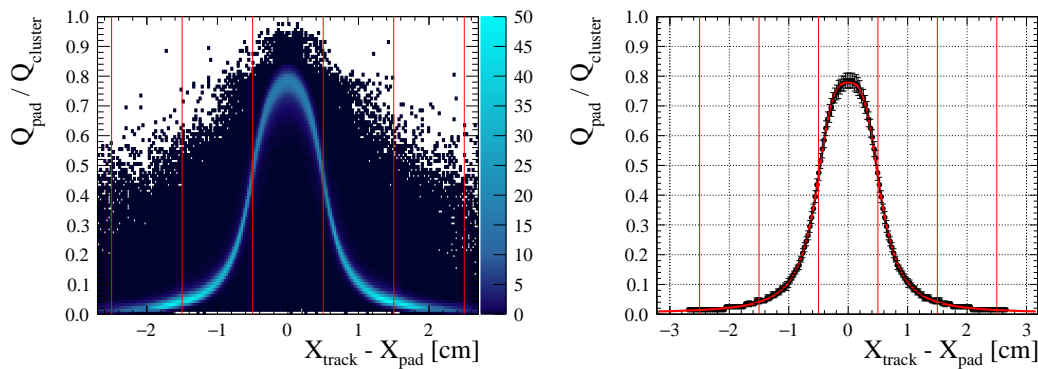


FIGURE 10.37: PRF scatter plot (left) and final fitted PRF function (right). The red vertical lines correspond to the pad borders. Figures from Ref. [5].

The spatial resolution was studied for different samples. In the first place, its dependence with the drift distance is presented in Figure 10.38a, showing a mild degradation with the drift, as expected. In the second place, the position resolution for different voltages is presented in Figure 10.38b. In both cases, excellent performances were obtained.

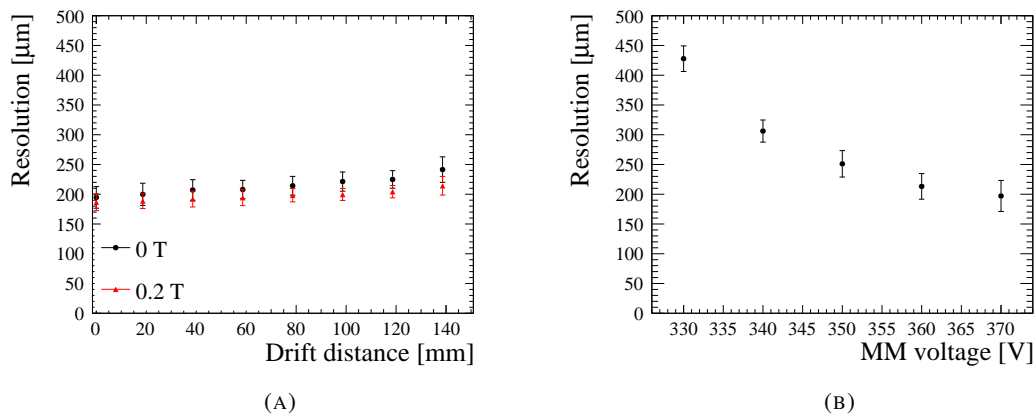


FIGURE 10.38: Spatial resolution dependence with the drift distance (a) and the ERAM voltage (b). The points and their errors correspond respectively to the mean of the spatial resolution across the ERAM columns and its RMS. Figures from Ref. [5].

The spatial reconstruction of inclined tracks is expected to be worse than for horizontal ones. In the current ND280 TPCs, see Sec. 5.5.6, the resolution degrades as a function of the track angle

from 600 μm to values slightly above 1 mm [456]. In order to study this dependence in the ERAMs, the spatial resolution was computed for tracks at different angles using the different cluster patterns earlier presented in Figure 10.36. The results, presented in Figure 10.39, revealed that for regular column clusters the spatial resolution degrades with the track slope. However, using alternative cluster patterns translated into significant performance improvements. It is worth noting that the rectangular pad shape makes of the diagonal pattern a better choice for 48° tracks than for 45° tracks. Therefore, tracks inclined with 50° were reconstructed better than 40° tracks. Remarkably, by taking the best clustering algorithm at each angle a spatial resolution better than 600 μm can be achieved for all inclinations significantly outperforming the bulk Micromegas even with a reduced number of pads.

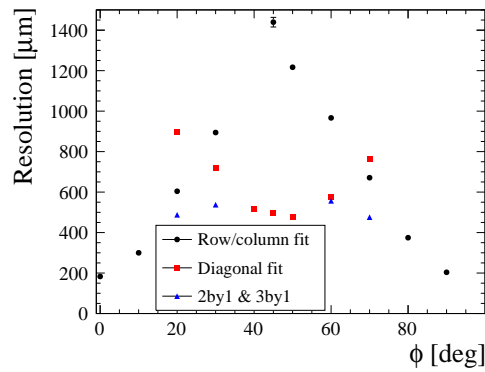


FIGURE 10.39: Spatial resolution w.r.t. track angle within the MM side obtained with different cluster definitions. Figure from Ref. [5].

The mean value of the residuals was also an important metric as it defines the position reconstruction biases. These biases arise due to the finite segmentation of the pads and therefore it is particularly interesting to analyze the dependence of the biases with respect to the track position in the pad. The results are presented in Figure 10.40. Individual PRFs were used for each column. The resolution oscillates with the track position as tracks closer to one of the leading pad borders produce larger signals in the neighboring pads enhancing the position reconstruction. Figure 10.41 presents the results of the reconstructed position biases. In general, the observed biases were smaller than the spatial resolution and therefore are expected to be negligible. This is only not true in the most downstream part of the detector where larger biases were observed. This was attributed to non-uniformities in the resistive foil which are going to be discussed later.

10.4.5 dE/dx resolution

The analysis of the ERAM1 prototype introduced a new method to characterize the energy deposition in each cluster. Instead of using Q_{sum} , i.e. the sum of the waveforms' maximum for all pads in the cluster, a new estimator named WF_{sum} was tested, consisting on using the maximum of the summed waveforms. The new method has the advantage to prevent double counting the charge being spread.

As in the case of the ERAM0 analysis the truncated mean method was used to study the energy deposit of tracks. Optimizations analogous to the previous analysis were made to determine an optimal truncation which kept the lower 70% of signals from each track.

Results of the dE/dx resolution for the two estimators described above are presented in Figure 10.42. As expected, the WF_{sum} method gives a better dE/dx resolution similar to 9.0%. In addition, the results were robust to changes in the shaping time.

The dE/dx resolution was also studied for tracks crossing the ERAM at an arbitrary angle. As earlier discussed, different cluster patterns can be used to have an improved segmentation of the

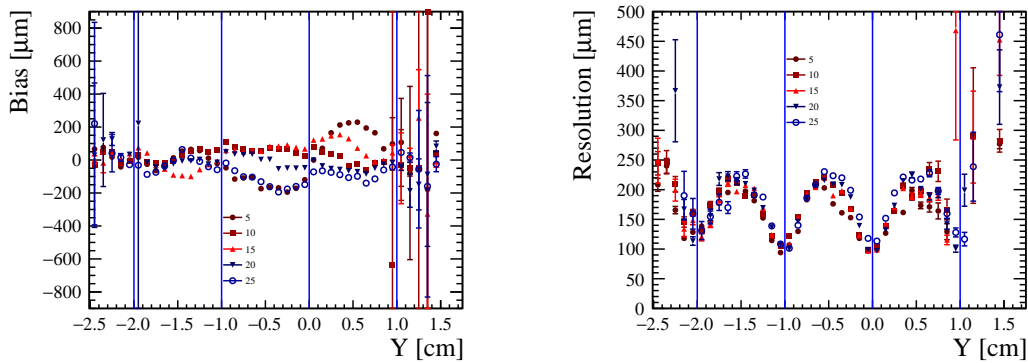


FIGURE 10.40: The resolution and the bias of the track reconstruction over the position in the pad for various columns. The pad borders are represented with vertical lines. In this coordinate system, the beam is centered around $Y = -0.5\text{cm}$, but tracks are also measured on the neighbor pads due to the beam spread. Figure from Ref. [5].

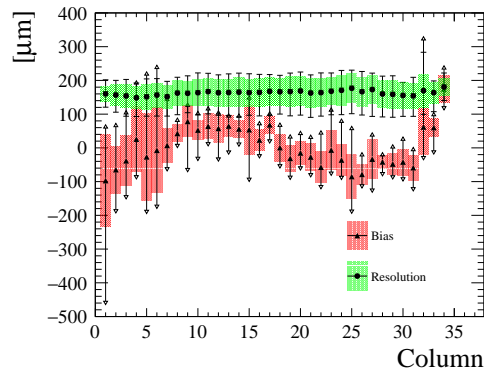


FIGURE 10.41: The spatial resolution and bias fluctuations observed for the different position of the track in the pad. Dots represent the mean value in a given column, filled areas correspond to the RMS, and error bars represent minimum and maximum values. Figure from Ref. [5].

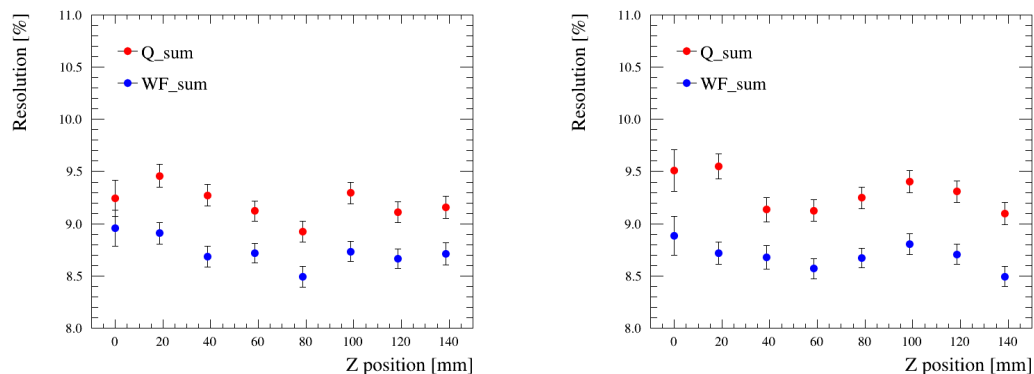


FIGURE 10.42: dE/dx resolution dependence with the drift distance using a magnetic field of 0.2 T and peaking times of 200 ns (left) and 412 ns (right). Q_{sum} method consists in summing the maximum of the waveform in each pad of the cluster while WF_{sum} corresponds to maximum of the summed waveforms in a cluster. Figures from Ref. [5].

track in clusters. However, the track path length in an irregular cluster might change as a function of its true position. In the fully vertical or horizontal rectangular clusters straight tracks with the

same angle have always the same dx . However, for diagonal clusters dx can vary between 0 and the diagonal length of the pad. This is shown in Figure 10.43 where the distribution of the charge as a function of the dx for tracks at an angle of 45 degrees is presented showing a non-linear dependence. This arises from the fact that each cluster sees not only the direct charge due to the primary ionization but also is affected in a non-trivial way by the charge spreading in its neighbor pads.

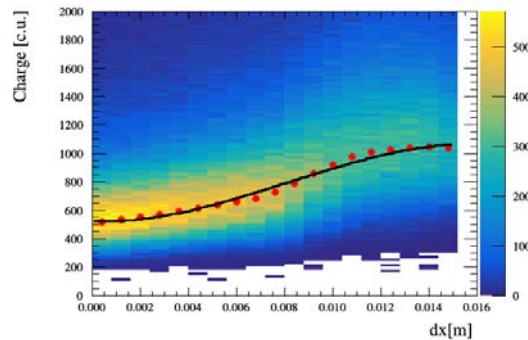


FIGURE 10.43: Charge distribution as a function of dx for 45° tracks. Figure from Ref. [5].

In order to correct the dx in each cluster, the charge in each slice of dx was fit with a Landau function and characterized by its most probable value (MPV). The distribution of the MPVs as a function of dx was then parametrized with a third degree polynomial, see Figure 10.43. The estimated charge in each cluster is weighted by the corrected dx and then the truncated mean method was applied. Examples showing the role of this correction are presented in Figure 10.44.

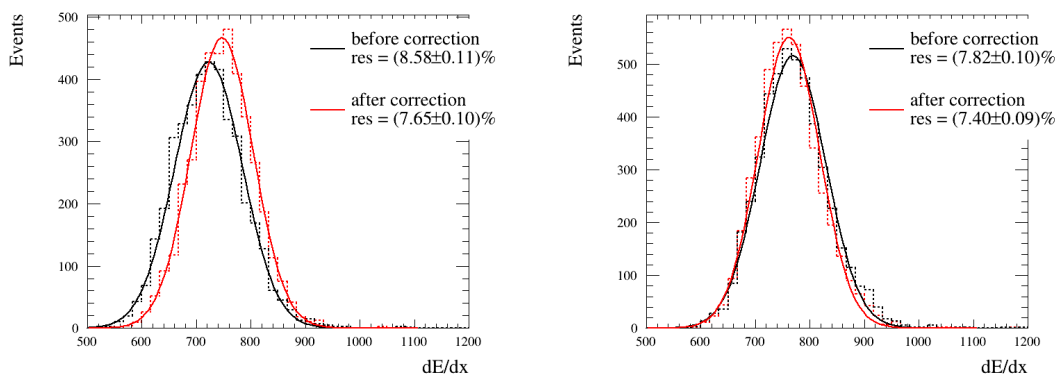


FIGURE 10.44: dE/dx distributions and resolutions for 40° tracks with and without correcting for the dx using a peaking time of 200 ns (left) and 412 ns (right). Figures from Ref. [5].

The deposited energy resolution as a function of the track angle is shown in Figure 10.45. As expected the diagonal clustering, after the dx correction, provides the best resolution thanks to the larger amount of clusters in which the track is sampled.

To study the expected performance with two modules the dE/dx resolution dependence on the number of clusters was studied, in a fashion analogous to that earlier presented for the ERAM0 prototype. The results are presented in Figure 10.46. In view of the results and using the fitted functions for tracks crossing the length of two ERAM modules an energy resolution similar to 6% is expected for all possible angles.

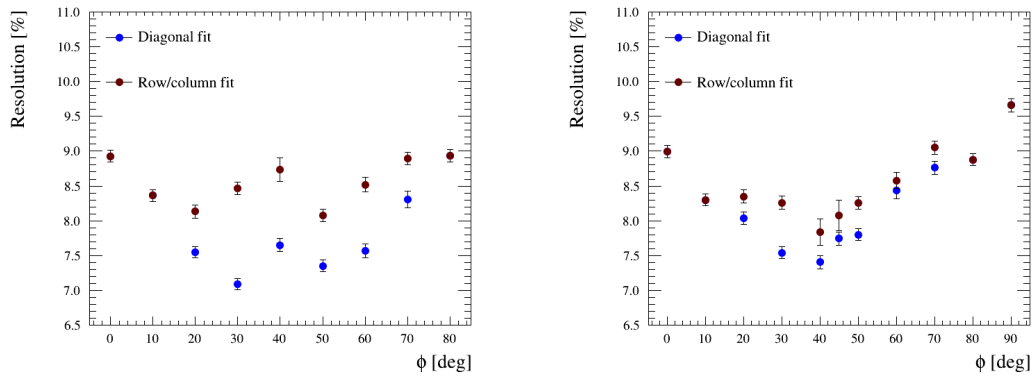


FIGURE 10.45: Angular dependence of the dE/dx resolution. Column clustering was used from 0° to 40° , otherwise row clustering was used. The shaping time in the left (right) plot was set to 200 ns (412 ns). Figures from Ref. [5].

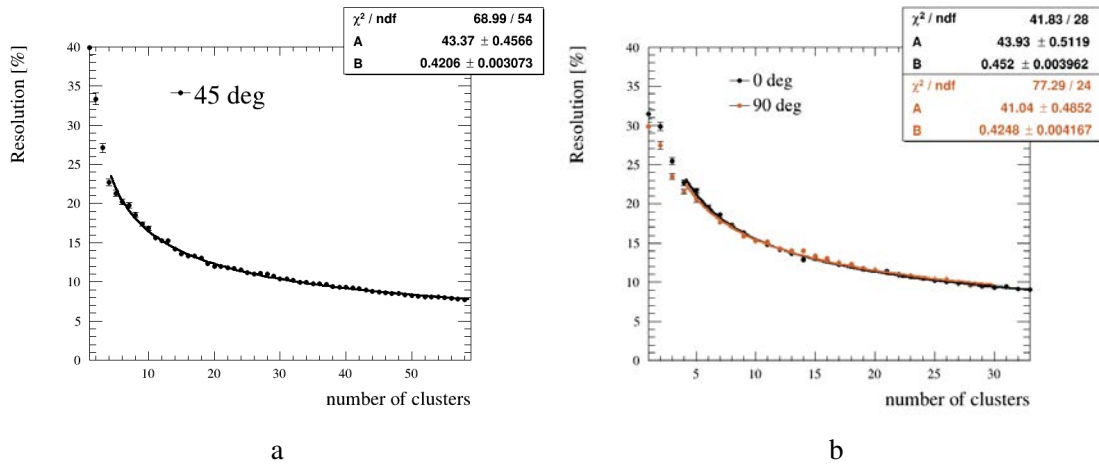


FIGURE 10.46: dE/dx resolution versus the number of clusters for 45° tracks (left) and for 0° and 90° tracks (right) using a peaking time of 412 ns and a magnetic field of 0.2 T. The data is fit with Eq. 10.2. Figures from Ref. [5].

10.4.6 RC map characterization

As anticipated in Sec. 10.2.1, the RC product determines the charge spreading behavior. An RC map was reconstructed using horizontal tracks from data taken doing scans in the y -direction at a peaking time of 412 ns. The RC values were extracted from an analytical model of the charge dispersion adjusted to the waveforms measured in the pads. Such analytical model relies on the fact that the total induced charge on a rectangular pad is given by the integral of the charge density function over its area [526]:

$$Q(t) = \frac{q_e}{4} \left[\operatorname{erf}\left(\frac{x_{\text{high}} - x_0}{\sqrt{2}\sigma(t)}\right) - \operatorname{erf}\left(\frac{x_{\text{low}} - x_0}{\sqrt{2}\sigma(t)}\right) \right] \times \left[\operatorname{erf}\left(\frac{y_{\text{high}} - y_0}{\sqrt{2}\sigma(t)}\right) - \operatorname{erf}\left(\frac{y_{\text{low}} - y_0}{\sqrt{2}\sigma(t)}\right) \right] \quad (10.6)$$

where q_e is the initial charge, (x_0, y_0) is the track position and x_{high} , x_{low} , y_{high} and y_{low} are the pad boundaries. The time-dependent spread width is $\sigma(t) = \sqrt{(2t/RC) + \omega^2}$ where ω sizes the transverse diffusion. The longitudinal diffusion was neglected as the maximum drift distance was only of 15 cm.

The former equation describes only the spread of the charge on the foil, however, to translate it into the measured waveforms it is necessary to account for the characteristics of the electronics. To parametrize the electronics shaping time effects $I(t)$ dedicated simulations were used. The final waveform prediction by the model was then given by a numerical convolution of $Q(t)$ and $I(t)$.

For this studies, horizontal tracks were used. To calculate the RC first the waveform of the leading pad was fit with $I(t)$ and then the two neighbor pads were fitted simultaneously using a convolution of $I(t)$ with $Q(t)$. Using the resulting RC, a second simultaneous fit of the two neighboring pads waveform was done using separate $Q(t)$ functions to account for the possible different track distances to each of the two pads. Since horizontal tracks were considered only the y_0 -position of the track was fit and no constraints were imposed to the x -position. The track position y_0 is obtained with the PRF χ^2 minimization method earlier presented in Eq. 10.5. Figure 10.47 shows an example set of waveforms associated to a single cluster with the fit results for the leading pad and its two side neighbors.

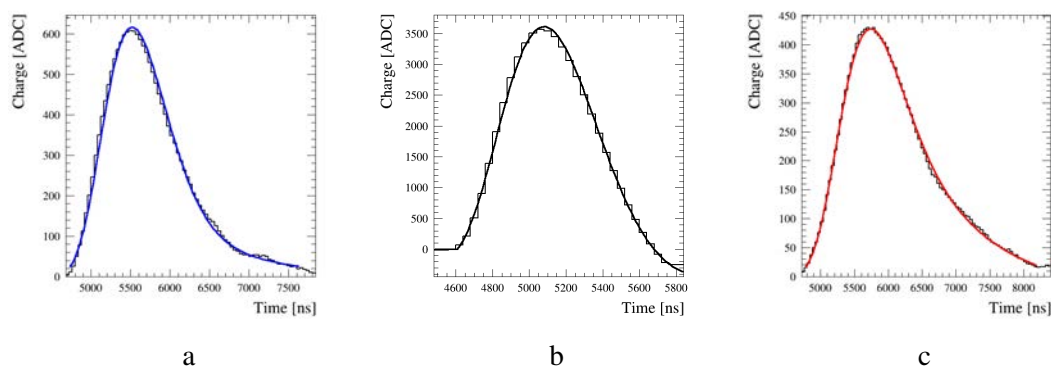


FIGURE 10.47: Example of waveform fit results for the leading pad (b) and its neighbors (a) and (c) in a given cluster. Figures from Ref. [5].

A second method was used to compute and validate the RC values extracted with the analytical model described above. The alternative procedure was built upon the strategy described in Sec 10.3.6 to measure the spread velocity. It used the time delay $\Delta t_{1,2} = t_{\text{Leading Pad}} - t_{\text{Neighbor}}$ and the ratio of amplitudes of the neighbor pads and the leading pad to estimate the track position y_0 . Then, the RC was extracted using:

$$\Delta t_1 - \Delta t_2 = RC \times L \times y_0 \quad (10.7)$$

where L is the pad length.

The reconstructed RC maps using the two models described above are presented in Figure 10.48. Both methods led to similar results. An RC non-uniformity of about 30% was measured with both methods.

10.4.7 ERAM1 analysis conclusions

The study and characterization of the ERAM1 performances validated the final ERAM layout using 2/3 of the pads in T2K's bulk Micromegas and the use and configuration of the new electronic boards. From the point of view of the physics performances excellent dE/dx resolutions, similar to 6% for the length of two ERAMs, were achieved for all possible angles. The measured spatial resolution was also excellent, being better than 600 μm for all angles. Remarkably, this translates into a worse spatial resolution in the ERAMs comparable to the best one in the T2K's bulk Micromegas. Additionally, it was proven that the RC map of the prototype could be reconstruction using tracks and its uniformity was measured to be similar to 30%.

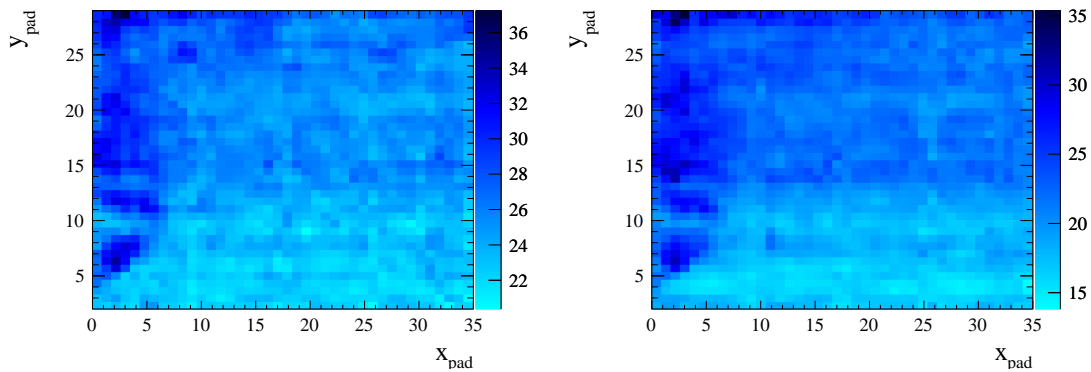


FIGURE 10.48: The RC (ns/mm^2) map obtained using the fit from the analytical model (left) and the time difference method (right) described in the text. Figures from Ref. [5].

10.5 Final ERAM production and testing

The production of the final ERAMs to be used in the HATPCs started in the second half of 2021, and it is currently ongoing. In total, 40 ERAMs will need to be manufactured consisting of 32 ERAMs to instrument the two HATPCs plus 8 spares. For the upcoming discussion it is worth noting that the structure of an ERAM module has been presented earlier in Figure 10.11.

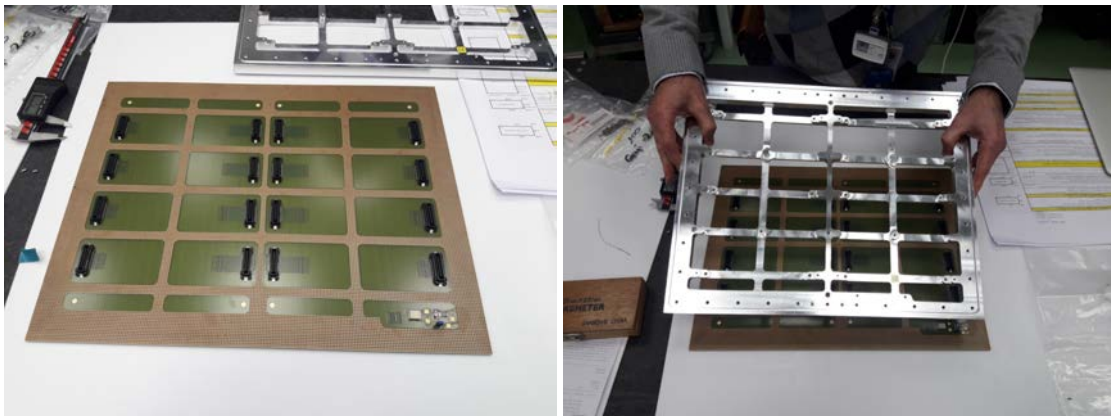


FIGURE 10.49: The picture on the left shows an ERAM PCB which is being glued to the stiffener in the picture on the right.

For the commissioning a dedicated test bench was mounted at CERN towards the end of 2021. The procedure is analogous to that made over 10 years ago to commission the bulk Micromegas modules, for which further details can be found in Ref. [456]. In the ongoing test bench, for each module the ERAM PCB, an example of which is presented in Figure 10.49, is manufactured at CERN and delivered to the test bench facility. Then, the PCB undergoes an initial round of validation tests. First, the mesh is powered up to 350-360 V to verify that the PCB can withstand high voltages. Second, the electronics are connected and used to collect pedestal runs, i.e. noise waveforms for each channel, the values of which are checked to be within reasonable intervals. Lastly, input squared signals are pulsed onto the mesh and the induced signal response in the ERAM pads is measured to check its uniformity and the absence of dead pads. If all of the former checks are successful, the PCB is glued into the aluminum stiffener, as presented in Figure 10.49. The gluing process is irreversible such that the verification of the ERAM quality needs to be definitive prior to this step. After the gluing is done, new pedestal runs and mesh pulsing tests are made in order to ensure that the module has not been damaged during the gluing process. Finally,

each ERAM is installed into the test bench TPC, see Figure 10.50. It consists of a flange with a single ERAM, a short drift volume with a depth of 35 mm and a robotic arm hosting a 355 MBq ^{55}Fe radioactive source. The radioactive source is collimated to illuminate a single pad and the robotic arm is used to perform a scan of all the pads on the plane. The result is an ^{55}Fe spectrum measured in each pad of the ERAM. An example of such a spectrum is presented in Figure 10.51. The set of spectra is used to validate the final module performance and it is considered as good if no outliers are observed. A full scan result is presented Figure 10.52. In this case, a grid-like structure is observed as a result of a non uniformity of the amplification gap, an effect which was corrected in the production of the subsequent ERAMs.

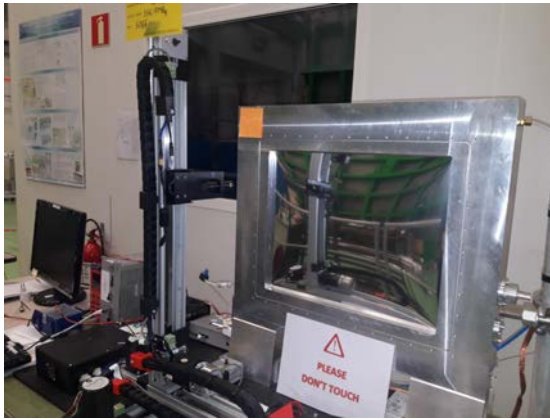


FIGURE 10.50: The picture on the left shows the test bench TPC setup. The picture on the right shows

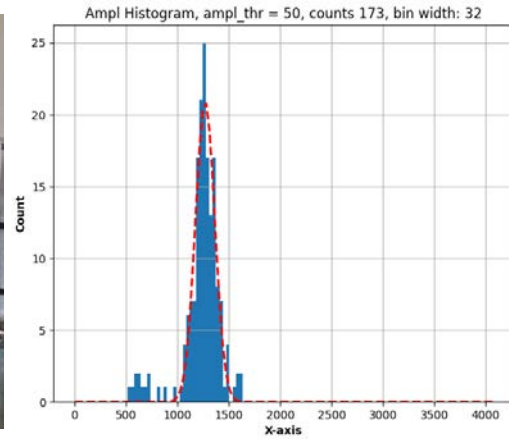


FIGURE 10.51: Spectrum of the ^{55}Fe source measured in a single pad with the test bench setup.

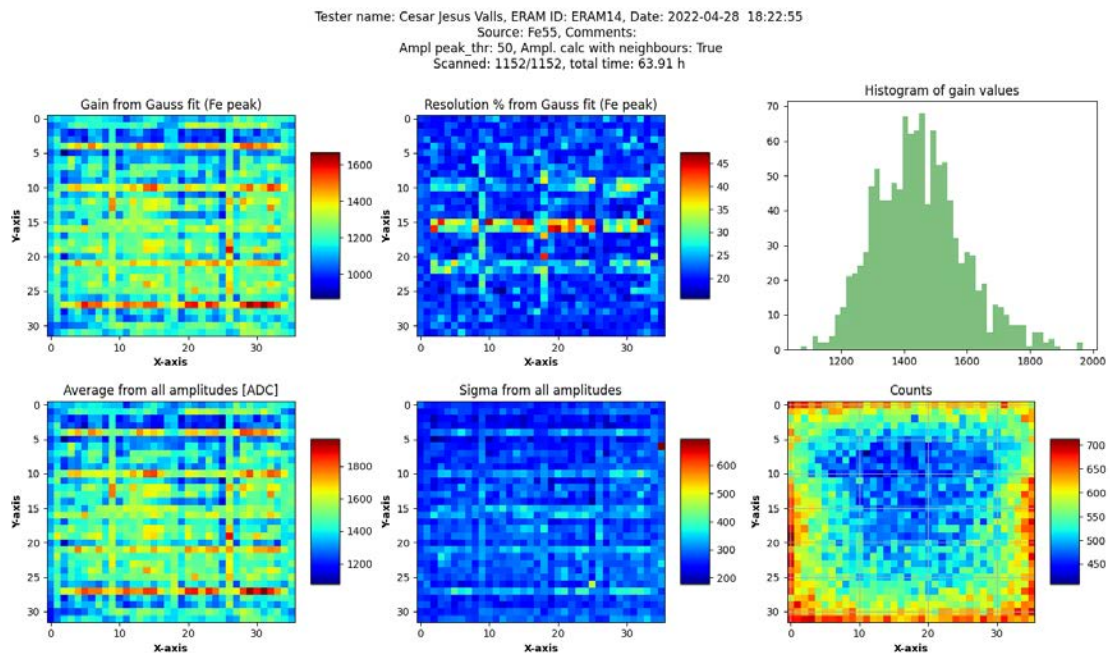


FIGURE 10.52: Summary plot of the ^{55}Fe scan of one of the final ERAM module.

Chapter 11

The SuperFGD

“The most exciting science requires the most complex instruments.”

– BARRY BARISH

SuperFGD is a novel neutrino target to be installed in ND280 as the cornerstone of its upgrade [3]. This Chapter reviews the characteristics of this technology, first presented in 2017 [533], and describes its final design and construction method. The validation tests and results from small prototypes [533, 534] and the final characterization of this technology using a larger prototype [6] are presented. This Chapter also reviews a novel reconstruction technique for SuperFGD consisting in the classification of three-dimensional signals using a Graph Neural Network [7]. Finally, this Chapter shows how SuperFGD is expected to identify neutrons and measure their kinematics [8].

11.1 Introduction and overview

Since the early stages of planning for an upgrade of the ND280 detector lowering the momentum thresholds to detect hadrons was identified as a priority. In particular, the aim was to develop a novel fully active neutrino target able to much better separate and identify short final state tracks ending close to the neutrino interaction vertex. In addition, it was clear that the new detector should have an isotropic acceptance as hadrons are oftentimes produced at high angles with respect to the neutrino beam or even backwards in contrast to the typically forward going muons. An evolution of the current ND280 FGD targets was proposed able to supersede almost all of their current limitations. This novel detector, which would be much finely segmented than the FGDs, was named SuperFGD. SuperFGD is based on the same instrumentation principles that made of the FGDs successful detectors. However, the characteristics that are expected to greatly improve its performance impose also very challenging technical problems relative to how to build the detector.

Instead of being based on layers made up of long plastic scintillator bars intersected by a single WLS fiber along its length, such as in the FGDs, SuperFGD is made up of an array of $184 \times 56 \times 192$ plastic scintillator cubes of 1 cm^3 , see Figure 11.1. Therefore, in total SuperFGD consists of almost 2 million cubes each weighting about 1 gram for a total active mass of 2 tons, similar to the mass of FGD1 and FGD2 together. Each cube is intersected by three orthogonal WLS fibers. One end of each fiber illuminates an MPPC, such that SuperFGD is read out on three orthogonal 2D planes by a total of 56384 electronic channels. In turn, combining this images allows to form a 3D representation of the event, as depicted in Figure 11.2. On the other end, the fibers are exposed to a LED light injection system used to calibrate the detector.

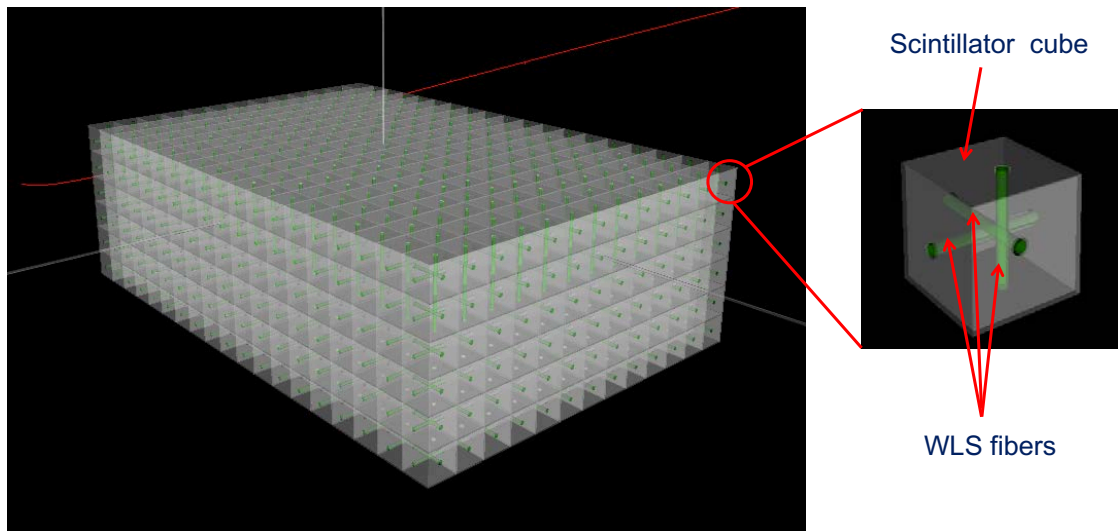


FIGURE 11.1: Sketch of SuperFGD showing a zoom in of a single cube. Figure from Ref. [3].

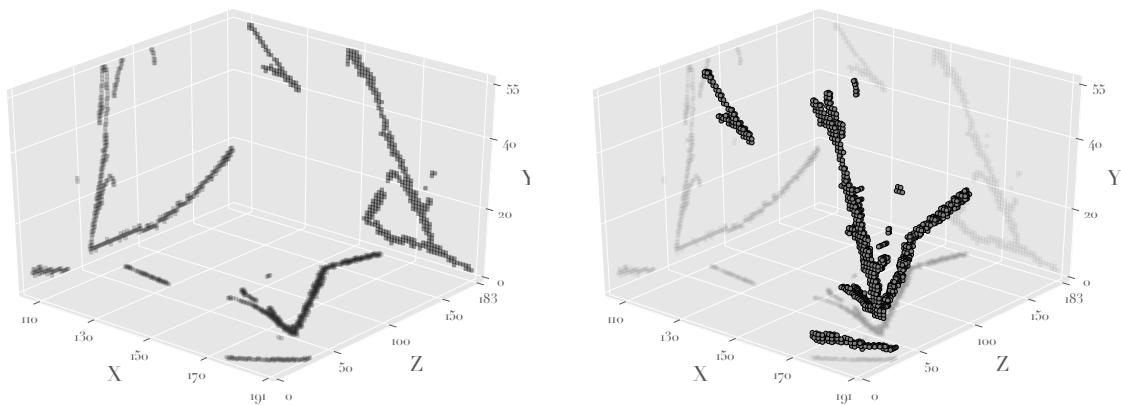


FIGURE 11.2: Left: Visualization of the SuperFGD 2D signals measured in the three orthogonal planes of MPPCs. Right: Reconstructed 3D view of the event by matching the projected 2D hits. For simplicity the visualization is colorless, in reality, each MPPC hit will have an associated a signal amplitude indicative of the tracks energy deposits. Figures from Ref. [7].

SuperFGD's design offers a number of immediate benefits. In the first place, its fine 3D segmentation allows to much better identify short tracks and its homogeneous segmentation provides isotropic angular acceptance and accurate track range and vertex position estimates. In the second place, the complementary measurements of the energy deposits from three fibers paired with the increased scintillation light yield and the dedicated calibration system will provide excellent calorimetric information allowing to build powerful PID variables. For instance, for a single MIP hit the FGD light yield statistical fluctuations are similar to 20% whilst for SuperFGD are expected to be 5-10%. In the third place, SuperFGD will use custom electronics able to size the light yield detected by the photosensors at a fast rate of 400 MHz (8 times faster than the current FGDs) with no deadtime. This will boost SuperFGD's ability to identify delayed signals which is critical for the identification of neutrons and Michel electron decays. Finally, the 3D granularity of SuperFGD paired with its excellent time resolution performances will open the possibility to identify neutrons (never attempted with FGDs) and to reconstruct their kinematics by time-of-flight.

Due to all of the above, SuperFGD is expected to have a major role in pushing T2K's physics measurements to the next level. However, in order to meet such high expectations many remarkable challenges have been faced. In one hand, SuperFGD requires two million plastic scintillator

cubes. For the 3D assembly to work very stringent tolerances in the cube production process have been met. Moreover, a novel assembly technique has been developed. The heavy weight of SuperFGD will be held in place by a box which has not only to withstand challenging static gravitational loads but also to endure the Japanese seismic activity. The box will be made of thin walls (about 4 cm thick) allowing particles to escape the detector with minor disturbances and its panels will be drilled with 110k holes to allow optical connections from outside with the fiber ends. The calibration system and readout interface (electronic boards, cables layout, crates) are custom made. Finally, the detector elements need to be highly reliable as in many cases their replacement will be virtually unfeasible once installed in ND280.

11.1.1 Cube production and detector assembly technique

The cubes, see Figure 11.3, were produced and assembled in Russia. Uniplast company (Vladimir, Russia) was responsible for the cube manufacture via injection molding. The plastic scintillator material consists of polystyrene doped with 1.5% of paratherphenyl (PTP) and 0.01% of POPOP. In order to optically insulate its surfaces, the cubes undergo an etching process with a chemical agent. This process creates a layer of micropores in the external surface of the polystyrene which significantly reduces its transparency. The cube fabrication is completed by drilling three orthogonal through going holes with a diameter of 1.5 mm. The center of the holes is placed at 3 mm in perpendicular from the closest two surfaces. The holes are by design significantly wider than the 1 mm WLS fibers to facilitate the detector assembly.

Cube metrology

To determine the precision of the cube fabrication metrology studies were made using a digital micrometer on 192 cubes. The measurements revealed that the etched surface increases by 60-70 μm the cube size which, after the etching, is typically of 10.17 mm. The variation of the side-to-side width was estimated to be similar to 30 μm . The positioning of the holes was studied calculating the hole coordinates from microscope images of the cubes. The hole center distance to the cube surface has a typical variation of 40 μm and the parallelism of the holes with respect to a given surface is similar to 50 μm .

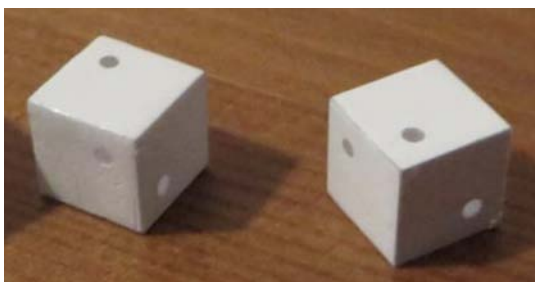


FIGURE 11.3: Picture of two SuperFGD cubes.

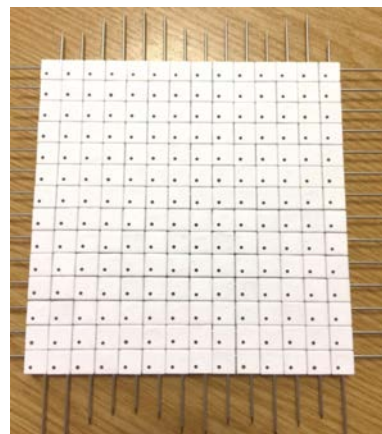


FIGURE 11.4: Picture of a 14×14 array of cubes inserted with 1.4 mm diameter needles to check their manufacture quality.

Fishing line method

Given the small but non-negligible cube manufacturing non-uniformities it was necessary to develop an assembly method able to distribute and absorb the cube variations along the cube grid such that all of the $\sim 60k$ WLS fibers could successfully cross the 2 million cubes and have their ends at predictable positions allowing to align them with the box holes.

With this goal the *fishing line method* was developed to assemble SuperFGD. The idea consists on building the array of cubes using flexible plastic threads of 1.3 mm in diameter. This has two obvious advantages. First, during the assembly process no damage is inflicted to the cubes given the elasticity of the fishing lines, and second, once the fishing lines are removed and sequentially replaced by WLS fibers the different diameter provides enough margin to ensure the smooth pass of the fibers without damaging them.

Assembly



FIGURE 11.5: Steps for SuperFGD assembly. First (left) the fishing line is inserted sequentially in the array of cubes held together by the needles. Second (middle) 184 strings of 192 cubes are accumulated. Third (right) a full plane is made up joining together two half planes of 92 strings held together by spokes.

The cube quality is checked empirically by forming 14×14 cube arrays using needles with a diameter of 1.4 cm, see Figure 11.4. Strings of 192 cubes are formed using fishing lines and grouped in planes of 192×184 cubes, as illustrated by pictures in Figure 11.5.

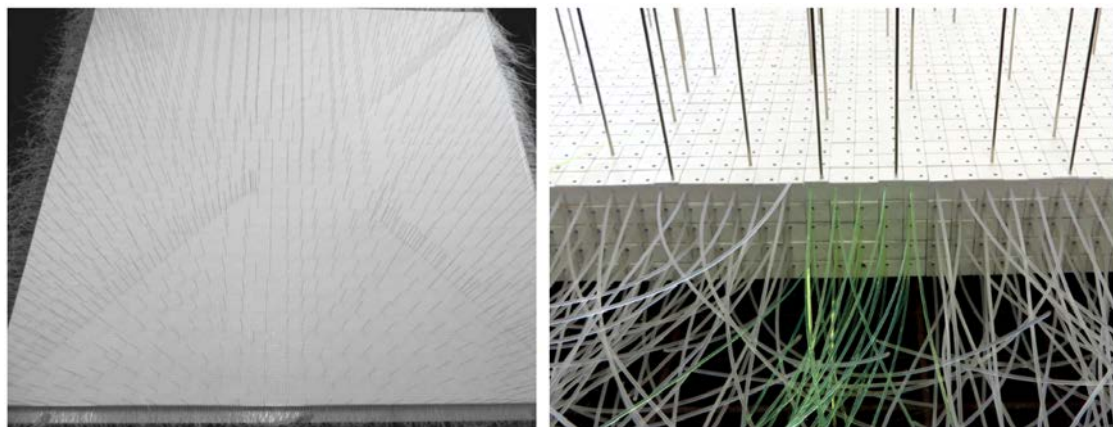


FIGURE 11.6: Left: An upper view of the stack of 5 layers of 184×192 cubes with vertical needles inserted. Right: Close up view of the same stack of cubes from one side showing some fishing lines (white) replaced by WLS fibers (green).

To perform the 3D assembly the planes are aligned using an Aluminum profile corner. The planes are held together in place by the insertion of needles at random positions and the WLS fibers are sequentially inserted in the aligned holes. To validate the 3D assembly a series of tests were made to align 2D planes. First, five planes of 184×192 cubes were stacked, and the alignment of its holes successfully verified, see Figure 11.6. A higher wall was built on top of it on one

side to reach the expected height of 56 layers. While being built 19 cm long needles of 1.4 cm in diameter were inserted and removed always successfully. The final height of 56 cm was pierced by 1 m long spokes with a diameter of 1.2 mm without blocks. Finally, 1 mm fishing lines were inserted in all holes without problems. Additionally, tests were made to replace some fishing lines by WLS fibers, always with a positive outcome.

The $15 \times 56 \times 192$ cube array was used to study the potential effect of the structural deformations due to the gravitational load of the cubes. In order to do so, the array was placed on top of a flexible structure that allowed the cube array to be deformed creating a sag of up to 2 cm. Even in this conditions, much more demanding than those foreseen in the final detector where the SuperFGD box will allow a sag similar to 0.5 cm, no stress nor damage was observed in the bended fibers.

Metrology

The former assembly prototypes were used to do metrology tests in order to settle the final SuperFGD box dimensions. The five x-y plane of 184×192 cubes resulted in a typical outer size of $1895 \times 1977 \text{ mm}^2$. The wall of $15 \times 56 \times 192$ cubes was used to measure the z-coordinate which was of 577 mm. Consequently, the average cube size without gaps of 10.17 mm increased to an effective size, with gaps, similar to 10.30 mm for all of the measured axis and, accordingly, the typical gap size is of 60-70 μm at each side of the cube.

Final production and assembly



FIGURE 11.7: The final 56 layers for SuperFGD, divided in two groups of 11 and 45 layers.

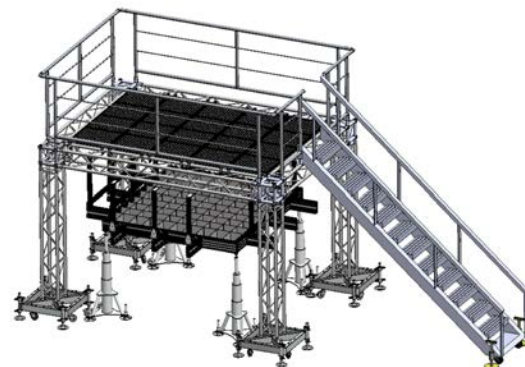


FIGURE 11.8: CAD drawing of the assembly platform for the final detector construction. The platform allows to comfortably and safely access all of SuperFGD surfaces.

The successful validation of the assembly technique led to the manufacture of the 2 million cubes, starting in summer 2019, and finalizing at the end of 2020. The assembly of the 56 planes of 184×192 cubes was completed at the beginning of 2021, see Figure 11.7, and stored for their final installation. For their adequate placement in the SuperFGD box and to allow to safely and efficiently do the installation from all of its sides a dedicated platform has been designed, see Figure 11.8. The final cubes assembly is expected to take place in Japan in the second half of 2022.

11.1.2 Mechanical box

The mechanical box holding the SuperFGD cubes and hosting its photosensors, light calibration system and electronics is made up of composite material panels of rectangular shape. The panel structure consists of a 36 mm core of Divinycell H250 sandwiched between two carbon

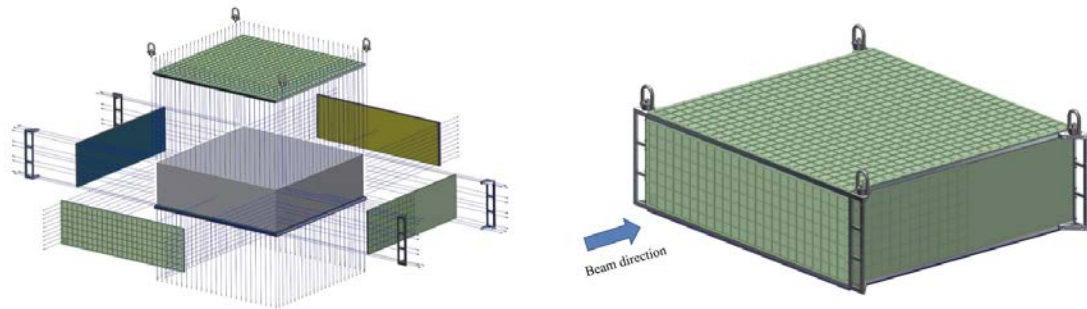


FIGURE 11.9: Left: Exploded view of the SuperFGD box. The blue (yellow) surface is a G10-datum (EPDM foam) layer. The green surface is the external G10 mounting layer showing pockets in the surfaces where the photosensor PCBs are installed and flat surfaces where the calibration system will be placed. The central gray volume corresponds to the cube envelope. Right: external view of the closed box. The four lifting fixtures in the top corners will be removed after installing the box in ND280.

fiber planes of 2 mm each for a total width of 40 mm. Aluminum frames are mounted on the sides of each Divinycell core forming a rigid skeleton that can be held together using screws, see Figure 11.9. On top of the carbon fiber layer, in its inner surface, the plates are finished in two different ways. Three of them (bottom, left and upstream) have an additional hard G10 layer, named G10-datum layer, that creates a coordinate reference for the array of cubes. The other three (top, right and downstream) have a soft EPDM foam to gently compress the cubes to their final position. In its outer surface G10 mounting plates are glued. Two different shapes can be found for them. The top and upstream planes host only MPPC boards and therefore its G10 external surface has pockets to host the 8×8 photosensor boards. The bottom and downstream planes hold exclusively the light calibration system and its G10 layers are designed to mount an interface for the fiber ends. The left and right plates have half of its surfaces dedicated to photosensors with the other half dedicated to the calibration system. The holes are drilled in each plate after the different layers are glued. Each hole has an external diameter of 3 mm but to help guiding the fibers and reduce the impact of fiber-hole misalignments they are tapered on its inner side reaching a diameter of 4 mm.

11.1.3 Fibers

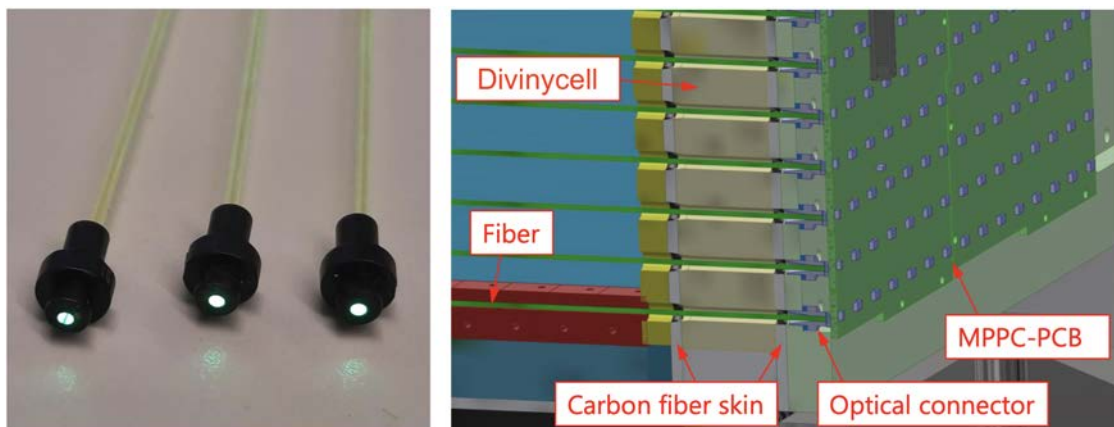


FIGURE 11.10: Left: Y11 WLS fibers with glued connectors on one end. Right: CAD drawing of a SuperFGD slice showing the cubes, the box profile and the fibers crossing the holes with connectors one their end installed in close contact with the MPPCs.

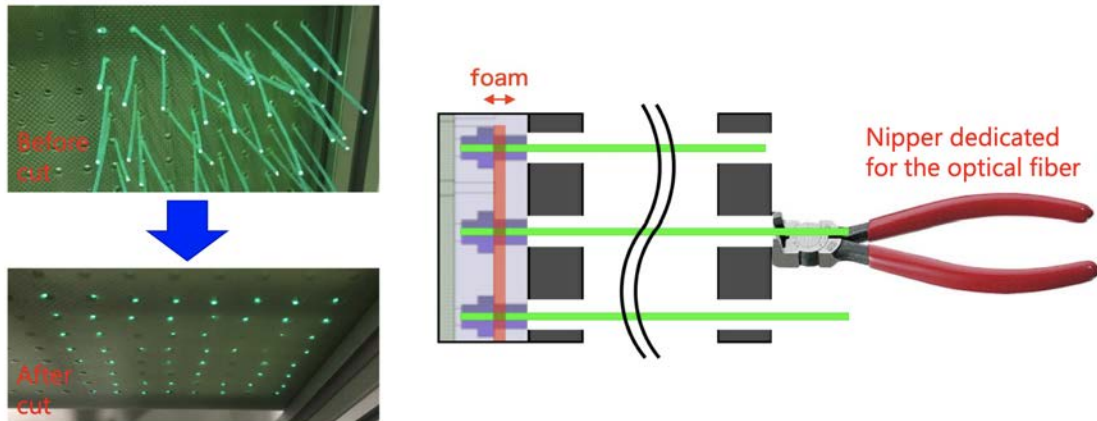


FIGURE 11.11: The pictures on the left show prototype tests of fibers protruding through a mock up box before (top) and after (bottom) being cut. The sketch on the right illustrates the procedure.

The WLS fibers will consist in Y11 WLS fibers from Kuraray, the same model currently in use in all of the scintillators in ND280, with a diameter of 1 mm. The purpose of the fibers is to collect the scintillation light from the cubes, shift it towards the green and transport it due to total internal reflection towards its ends only slightly attenuating the signal. On the end of the fiber which illuminates the photosensor an optical connector is glued, as presented Figure 11.10, with the help of a dedicated jig. The purpose of this connector is to hold the fiber in place and to ensure good alignment between the fiber and the photosensor, crucial to ensure a high-quality light yield determination with good uniformity across channels. To enhance the light emission the fiber end is smoothed using a polisher before gluing it to the connector. On the opposite end, the fibers are cut using a specialized nipper, see Figure 11.11, leaving the fiber exposed to the light emitted by the calibration system.

11.1.4 Photosensors

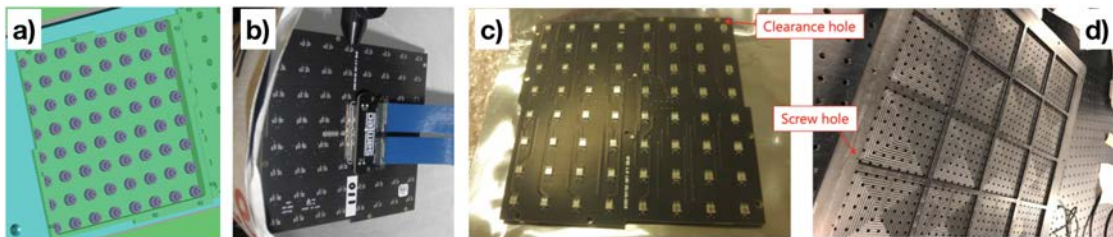


FIGURE 11.12: a) CAD drawing of a group of 64 WLS fibers held in a G10 frame pocket using optical connectors. b) picture of the backplane of an MPPC PCB. c) picture of the front-plane of an MPPC PCB. d) Picture of a G10 prototype frame showing the pockets and drilled holes. The screw mounting points are highlighted using red arrows and labels.

The light in each fiber is measured using an MPPC (Hamamatsu Photonics S13360-1325PE). Each MPPC consists of a pixel array of 2668 pixels in a $1.3 \times 1.3 \text{ mm}^2$ surface. The MPPC signal is proportional to the number of pixels fired by photons. The MPPCs are grouped in sets of 64 organized in 8×8 arrays using a custom PCB. In the contact surface the 64 MPPCs are placed right on top of the fiber ends. In the opposite surface, a single connector is installed used to power the MPPCs and read out their signals. The PCBs are attached to the G10 pockets using screws. To allow all the PCBs to fit in the G10 frame without overlaps the boards are shaped forming a puzzle pattern. Pictures are presented in Figure 11.12.

11.1.5 Light calibration system

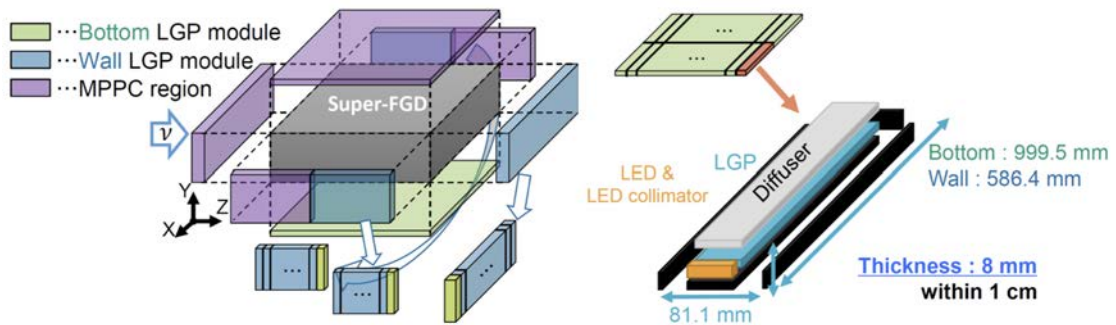


FIGURE 11.13: Left: Sketch of the light calibration system placements in the SuperFGD box. Right: Detail of a single calibration module.

The light calibration system will be mounted on half of the SuperFGD box surfaces opposed to the MPPC boards, see Figure 11.13. It will consist of calibration modules of two different sizes. Each module is made up of a transparent light guide plate (LGP) with notches on its bottom surface, a diffuser, a LED collimator and a set of blue LEDs. The bottom (wall) LGP modules will have a length of 999.5 mm (568.4 mm). The working principle is illustrated in Figure 11.14. An array of blue LEDs is installed in one side of the module, within a light collimator which is used to improve the light uniformity. The LEDs illuminate the LGP where a set of notches reflect a small fraction of the light in perpendicular to the plate. The diffuser board then distributes this light over a larger surface to reach all fiber ends. When the LED blue photons enter into the fibers they are shifted to a greenish wavelength and transported towards the other end where the MPPCs measure them. For each individual channel a histogram of the signal amplitude collected by the MPPC is built. This histograms have a set of peaks associated to the typical signal amplitudes produced by a given number of photons creating a pattern that is often referred to as a *finger plot*, later presented. Studying the position of these peaks and the spacing between them allows to calibrate the system. Therefore, it is not necessary that each fiber gets exposed to the same amount of light, but instead, it is sufficient that enough light reaches each fiber to generate a finger plot.

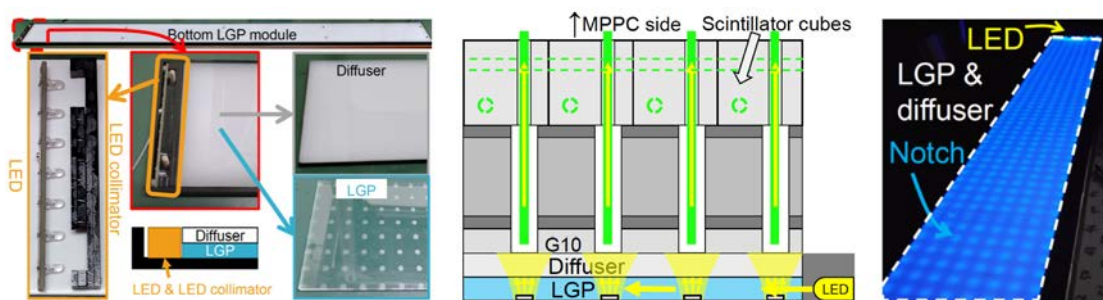


FIGURE 11.14: Left: Pictures of the different elements of a calibration module. Center: Sketch of the LED calibration system working method. Right: Picture of an assembled calibration module with the LEDs switched on.

11.1.6 Readout electronics and DAQ

The SuperFGD front-end cards (FEBs) responsible to read the detector signals are built around the CITIROC ASIC [517].

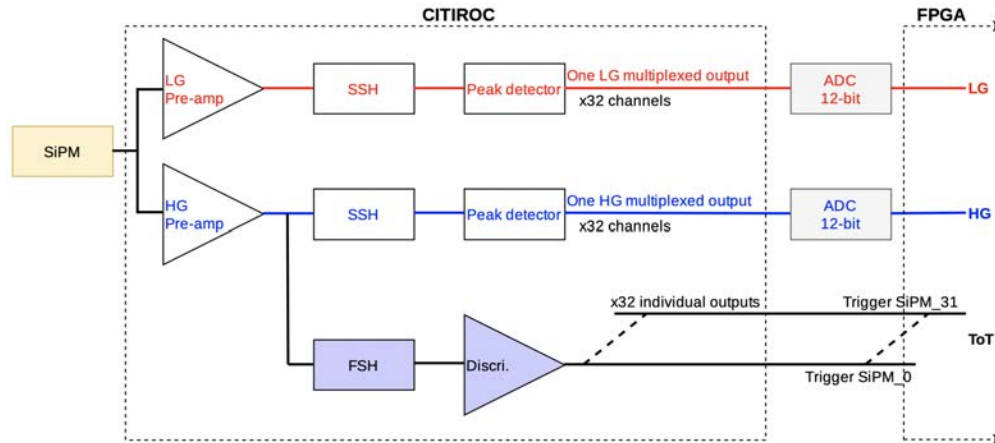


FIGURE 11.15: Sketch of the main elements within the CITIROC ASIC. For each channel the MPPC signal is split into a low-gain (LG) and a high-gain (HG) paths. Slow shapers are used to process the signal amplitude sensed by peak detectors and digitized using 12-bit ADCs. A fast shaper (FSH) in the HG path provides time information for the hit. Figure from Ref. [6].

The CITIROC

CITIROC-based electronics have also been recently used to readout the BabyMIND detector. The CITIROC chip, see Figure 11.15, reads a total of 32 channels. The signal of each channel is split in two paths set at two different gains, low-gain (LG) and high-gain (HG), covering a large dynamic range. Slow shapers connected to peak detectors digitized by 12-bit ADCs are used to characterize the signal amplitude. A fast shaper is used to provide time information for the hit. Additionally, the time of the signal rising edge (RE) and falling edge (FE) are measured. The difference between the RE and the FE defines the time-over-threshold which is also indicative of the signal amplitude. Consequently, each SuperFGD hit consists of a time stamp and LG, HG and ToT amplitude estimates. Notably, the acquisition of signals starts a hold of about $10 \mu\text{s}$. In this hold the signals of all channels are processed. However, if two different signals are produced in the same channel during the hold its HG and LG amplitude estimates are known to be unreliable. Nonetheless, the ToT information can be used to spot this situations by identifying multiple REs in the same channel and hold. When this happens, multiple hits are created for the channels with the signal amplitude given by ToT. Due to the low rate of neutrino events and the sparsity of triggered channels this situations are expected to be rare, however, having this information is expected to be crucial, for instance, to identify reliably Michel electrons.

The FEBs, MIBs and OCBs

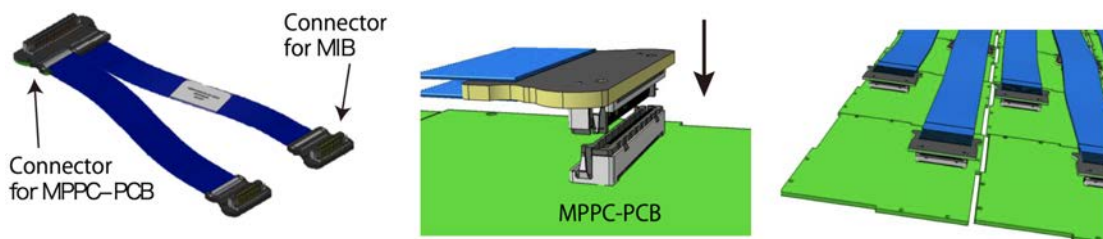


FIGURE 11.16: Left: Cable to connect the MPPC boards with the FEBs. Center: Detail of the MPPC boards connector. Right: Drawing of multiple cables being collected towards one side of the detector.

Each Front-end board has 8 CITIROCs each reading 32 channels. In total 221 FEBs are required organized in crates placed on the sides of SuperFGD. Eight crates will be installed per side organized in two rows of four columns. Each crate will contain 12 FEBs as well as two Optical Concentrator Board (OCB). The DAQ software will run on a hybrid Xilinx FPGA on the OCBs with an integrated core computer running Linux. Each OCB will control the settings of 6 FEBs and will be responsible for their data concentration and transfer. The MPPC PCB boards will be connected to the FEBs using the cables shown in Figure 11.16. These cables, often referred to as flat cables, have a single connector on one end that is attached to the PCB board and it is split into two connectors on the other end. This allows to guide all cables towards the sides without folding them, as illustrated in Figure 11.18.

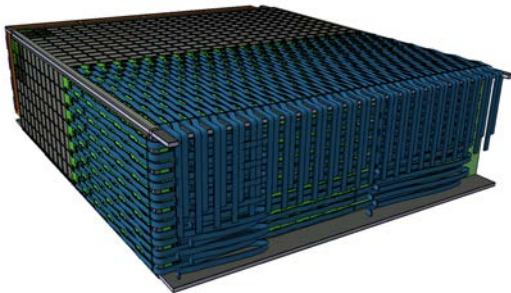


FIGURE 11.17: CAD drawing of half of the SuperFGD cables being routed towards one side.



FIGURE 11.18: CAD drawing of the crates of one side installed in the SuperFGD box.

The flat cables will be connected to the FEBs using custom MPPC Interface Boards (MIBs). The MIBs will work as an intermediate step guiding 8 cables, associated to 4 MPPC boards, to a single FEB. Illustrative drawings and pictures are presented in Figure 11.19.

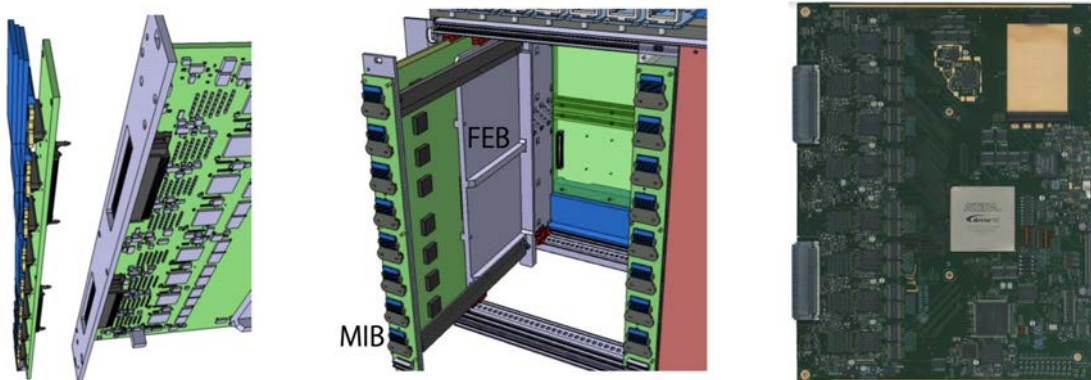


FIGURE 11.19: Left: A MIB being connected to an FEB. Center: A FEB with an MIB in place being inserted in one crate. Right: Picture of the first final FEB.

11.2 First prototypes

The SuperFGD detector concept was first proposed in 2017 in Ref. [533]. On it, the first cube prototypes were studied, and the cube array concept based on three orthogonal WLS fibers was presented, see Figure 11.20. Via simulations, it was shown that the muon and proton tracking efficiency of the detector could significantly outperform that of a bar-based scintillators, like the FGDs. The article presented also the first cube prototypes and measurements involving an array of eleven of those cubes. In particular, the light yield at the end of the WLS fibers was demonstrated to be high, of about 50 PE per MIP, when measured with 1 m long WLS fibers, validating the

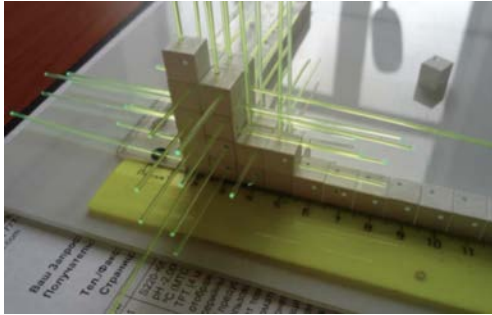


FIGURE 11.20: Picture of the SuperFGD detector concept from Ref. [533].

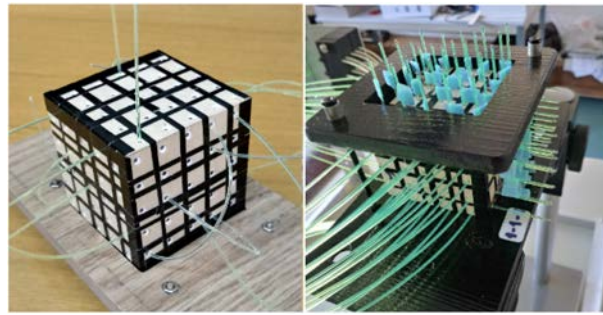


FIGURE 11.21: Pictures of the $5 \times 5 \times 5$ prototype from Ref. [534].

readout concept. Also, the optical crosstalk between cubes, this is, the amount of light from the initial cube flowing to each of its neighbors, was estimated to be similar to 2.9%, small enough to show that the chemical etching was effective in containing most of the light in the original cube. Finally, the intrinsic time resolution of the signals was measured to be similar to 0.9 ns using a 5 GHz digitizer.

The next prototype, built soon after, consisted on an array of $5 \times 5 \times 5$ cubes and its results were presented in Ref. [534]. In general, the new prototype further validated the original concept by reading a larger number of channels. The most significant difference was that the $5 \times 5 \times 5$ prototype was exposed to a beam consisting of a mixture of charged particles (mainly positrons and protons) with a momentum of 6 GeV/c. Using the beam the surface of the cube was scanned and the light yield was proven to be quite uniform regardless of the distance from the particle trajectory to the fiber. Moreover, for the first time some data was collected using CITIROC-based electronics, in particular using BabyMIND front-end cards.

11.3 The $24 \times 8 \times 48$ SuperFGD prototype

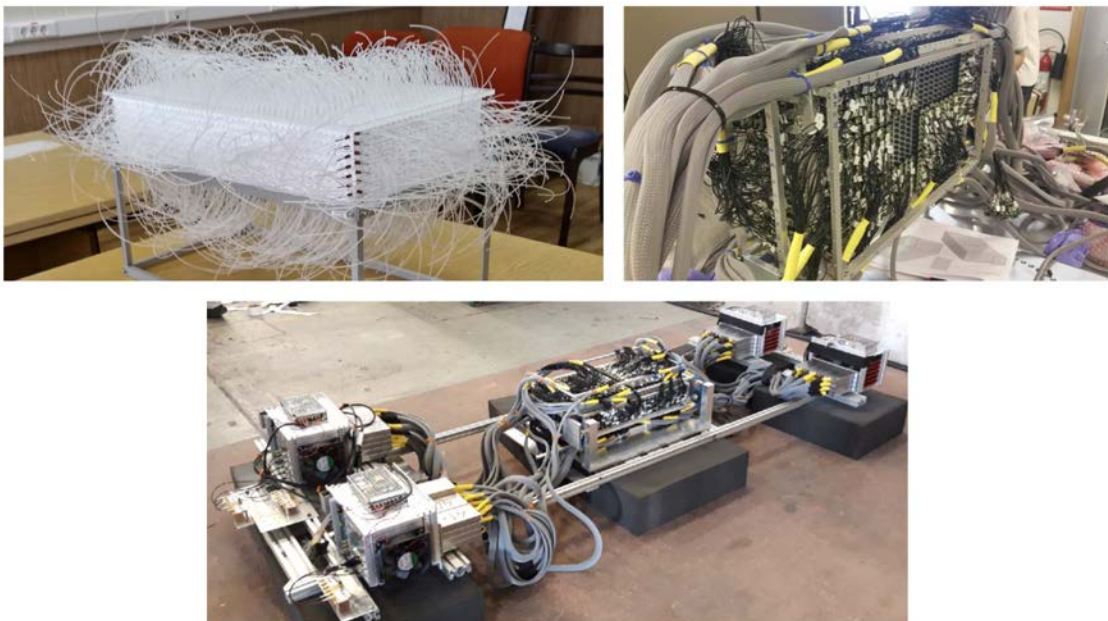


FIGURE 11.22: Pictures of the $24 \times 8 \times 48$ prototype, including an image of the cube array held by fishing lines (left), the prototype instrumented with the WLS fibers and MPPCs (right) and a view of the whole prototype including the four minicrates on the sides.

Description	Type I	Type II	Type III
Manufacturer ref.	S13360-1325CS	S13081-050CS	S12571-025C
No. in Prototype	1152	384	192
Pixel pitch [μm]	25	50	25
Number of pixels	2668	667	1600
Active area [mm^2]	1.3×1.3	1.3×1.3	1.0×1.0
Operating voltage [V]	56–58	53–55	67–68
Photon detection eff. [%]	25	35	35
Dark count rate [kHz]	70	90	100
Gain	7×10^5	1.5×10^6	5.15×10^5
Crosstalk probability [%]	1	1	10

TABLE 11.1: Specifications of the three MPPC types installed on the SuperFGD prototype. Table from Ref. [6].

The final test for this technology was to build a detector consisting of an array of 9216 cubes organized in an array of $24 \times 8 \times 48$ cubes, see Figure 11.22. The detector was built using the fishing line method earlier described and had only a significant difference with respect to the final detector: Between the 8 layers of 24×48 cubes reflective Tyvek layers were placed to study their potential benefit in reducing the optical crosstalk.

The prototype was instrumented with three different types of MPPCs named type-I, type-II and type-III, with specifications summarized in Table 11.1. Notably, type I has been selected as the final choice for SuperFGD. The MPPCs were instrumented on the surfaces of the prototype following the layout presented in Figure 11.23. The end of each fiber was glued to a custom connector and attached with 3 CITIROCs ($32 \times$ read the whole prototyp

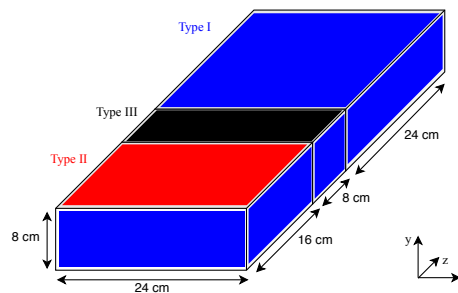


FIGURE 11.23: Distribution of MPPC types over the SuperFGD prototype. Figure from Ref. [6].

11.3.1 Calibration

The detector was calibrated using a custom LED system. The calibration consisted in building finger plots for each channel using different MPPC gains and extracting from them HG amplitude conversion factors into a number of PE. An example for one channel is presented in Figure 11.24. Then, a map was built using beamline data to relate the HG amplitudes to the LG and ToT amplitudes, see Figure 11.25. The trend was parametrized using polynomial fits. In this way, the final light yield of a hit was set based on the following criteria: If the signal amplitude was below 100 PE according to the HG amplitude, then the HG value was used, else, the LG was used. In the case that more than one hit was recorded in the same hold the ToT amplitude was used. Overall, this calibration scheme worked nicely, as presented later, and consequently a similar strategy

will be used in the final detector using the built-in LED light injection system earlier described in Sec. 11.1.5.

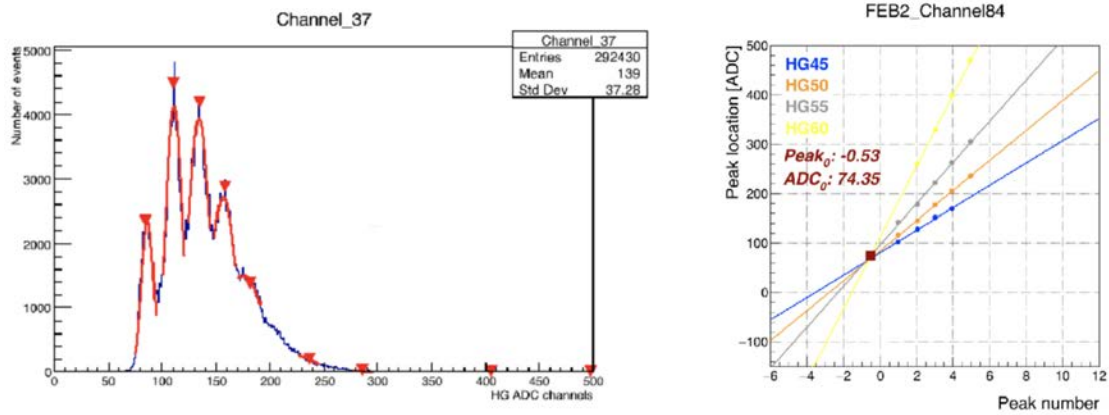


FIGURE 11.24: Left: Finger plot for a single SuperFGD prototype channel. Right: Channel calibration combining the peak positions of several finger plots at different high gain values.

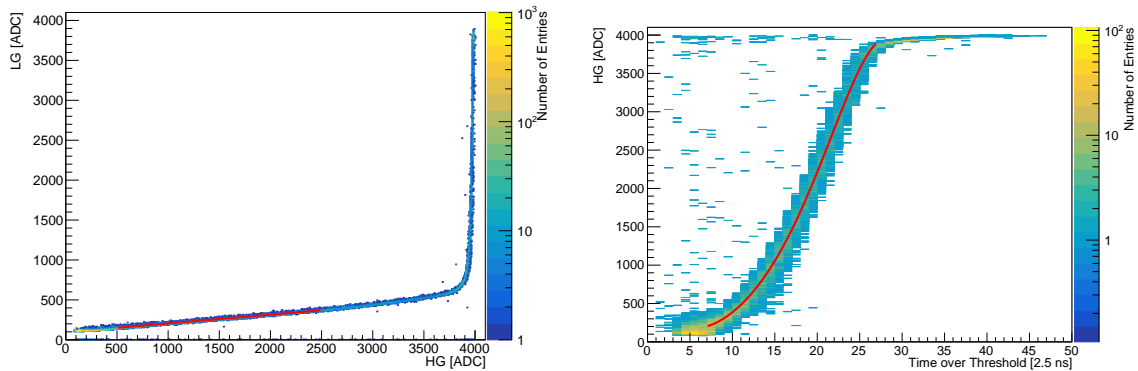


FIGURE 11.25: Amplitude correlation between the HG and LG amplitudes (left) and the HG and ToT amplitudes (right). Figures from Ref. [6].

11.3.2 The 2018 beam test setup at CERN

In the summer of 2018 the $24 \times 8 \times 48$ SuperFGD prototype took data in the T9 beamline at CERN together with the HARP TPC during the ERAMO tests presented in the previous Chapter. The SuperFGD prototype took data in parasitic mode, namely, it was placed behind the TPC and it recorded tracks crossing its field cage. The same trigger system earlier described in Sec. 10.3.2 was used and stored using few channels of an additional FEB. The prototype was placed inside a general purpose dipole magnet available at the T9 beamline and data was collected using the nominal magnetic field intensity in ND280 of 0.2 T.

11.3.3 Signal thresholds and noise

Two thresholds were used to suppress noisy signals. First, a common threshold value for all FEBs was set up. Second, an additional threshold was fixed per CITIROC based on the results of dummy runs acquired prior to the beam test. The threshold effects were checked empirically by measuring the minimum recorded HG amplitudes. The results are presented in Figure 11.26.

FEBs reading MPPCs of type I and type II had thresholds slightly above 1 PE whereas for type III a much larger threshold of around 5 PE was necessary.

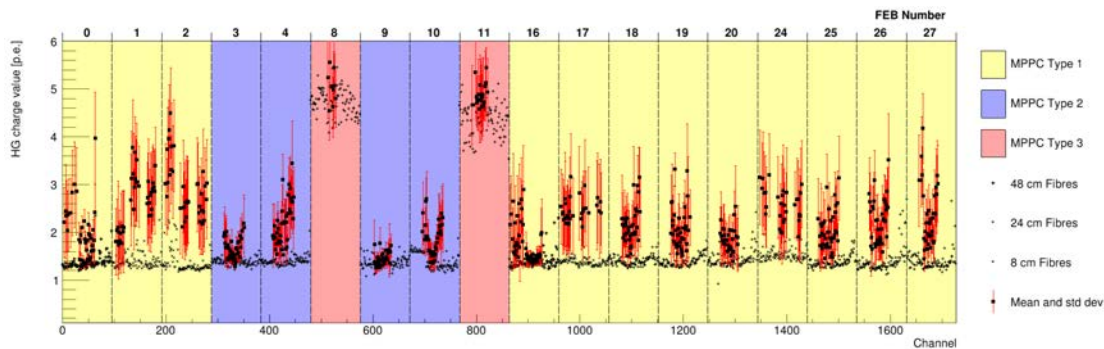


FIGURE 11.26: Measured minimum HG hit amplitudes per channel. The mean HG value in each channel per spill is shown if its standard deviation is below 1 PE. Figure from Ref. [6].

The time structure of the recorded hits was also studied, see Figure 11.27. The analysis consisted in determining the accumulated time distribution of hits for a given MIP run relative to the trigger signal. The observed distribution of hits presented a dominant peak associated to the hits generated by triggered beam tracks. A much weaker structure of unknown origin was observed, with a period similar to 300 ns. The remnant structure of hits was effectively suppressed vetoing out-of-trigger events using dedicated light yield cuts. For MPPCs of type I and II the remaining hits had a nice time structure virtually free of noise hits. For MPPC type III noisy hits were often recorded even at a threshold of about 5 PE.

The time structure shows an additional important feature. The width of the main peak, similar to 100 ns, is indicative of the recovery time of the electronics, crucial to understand the potential of SuperFGD to identify delayed signals such as those from neutrons and specially from Michel electron decays. Assuming that two hits can be measured reliably if separated by 100 ns or more, the Michel electron identification was estimated to be of 95%, significantly higher than that of 64% in FGD1 [454].

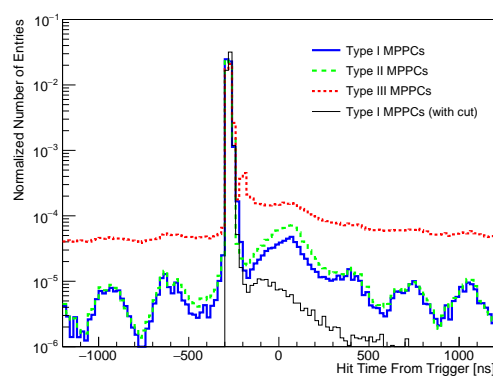


FIGURE 11.27: Time distribution of all hits in a single run relative to the external trigger time split by MPPC type. For MPPC type I the result of cutting off track-like events is also presented. Figure from Ref. [6].

11.3.4 Hit amplitude uniformity

The hit amplitude uniformity was studied in two different ways presented in Figure 11.28. In one hand the amplitudes provided by the HG, LG and TOT outputs in each individual channel

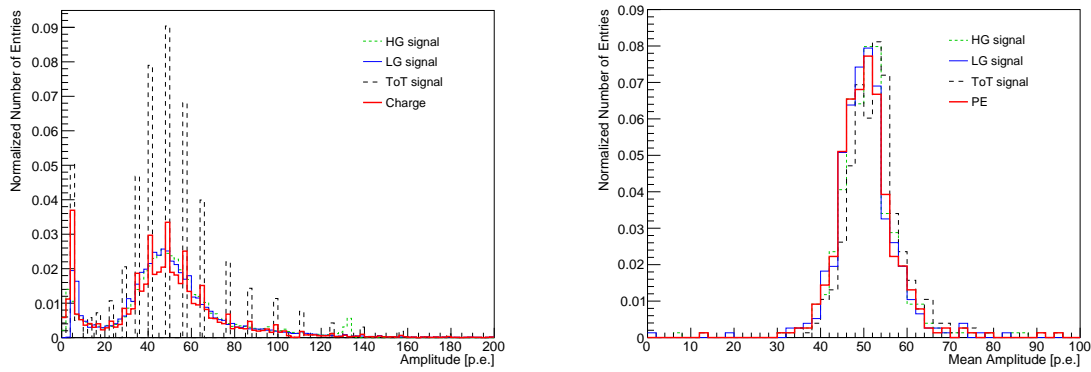


FIGURE 11.28: Left: HG, LG and ToT amplitudes for a single channel. Right: Average amplitudes for 384 channels read by X-fibers. Figure from Ref. [6].

were studied. In the other hand the distribution of the mean amplitude across channels was measured. The results showed overall good performance. In the first place, the calibration method was proven to work since all CITIROC outputs lead to similar amplitude distributions and no outliers were identified. It is worth noting in Figure 11.28 that the ToT amplitude is significantly less precise than the HG and LG estimates as the ToT is limited by the discretized time structure of the hits. In the second place, the distribution of mean amplitudes was reasonably narrow and followed a Gaussian-like trend without significant tails showing a uniform response across channels. Notably, channel-to-channel variations are attributed, at least partially, to misalignments in the fiber-to-MPPC connection. Consequently, the uniformity might increased in the final SuperFGD detector due to its better mechanics and by means of the application of channel-to-channel intercalibration factors derived from data.

11.3.5 Optical crosstalk

One of the main difficulties in handling the reconstruction of SuperFGD-like detectors is to be able to deal with the signal spreading created by cube-to-cube optical crosstalk and with the potential ambiguities that arise when combining the three 2D images into a single 3D view. This particular topic is discussed later in detail in Sec. 11.4. The amount of this ambiguities rapidly grows with the number of nearby hits in the 2D images and therefore a large fraction of crosstalk complicates the event reconstruction and hinders the detector performance. In order to deal with crosstalk it is necessary to understand its behavior and magnitude. Early prototypes, see Sec. 11.2, reported a crosstalk fraction similar to 3%, defined as the ratio of the light yield in the crosstalk hit relative to the light yield of the main hit. Those studies, however, studied a very limited number of cubes and were limited exclusively to low ionizing particles. With the $24 \times 8 \times 48$ prototype this measurements where significantly extended. It is important to recall that Tyvek layers were placed in-between the XZ planes such that different crosstalk values were measured for X- and Y-fibers, being the first one the most relevant for the final SuperFGD.

To identify main hits and crosstalk hits a simple selection criteria was applied. First, only events with straight going tracks were selected. The central row of hits was required to be consistent to the expected light yield associated to tracks by imposing a simple cut at a value much above of the typical light yield for crosstalk hits, i.e. above 20 PE (40 PE) for MIPs (protons). The results for X-fibers and Y-fibers, using only MPPC type I data, are presented in Figure 11.29. For 0.8 GeV/c protons, typically stopping within the prototype, the light yield changes significantly as they travel through the detector. Due to this, the light yield was studied for protons far from the stopping point, immediately before the stopping point and at the stopping point. The results show that MIPs produced a typical light yield in the main hit similar to 50 PE. For protons this

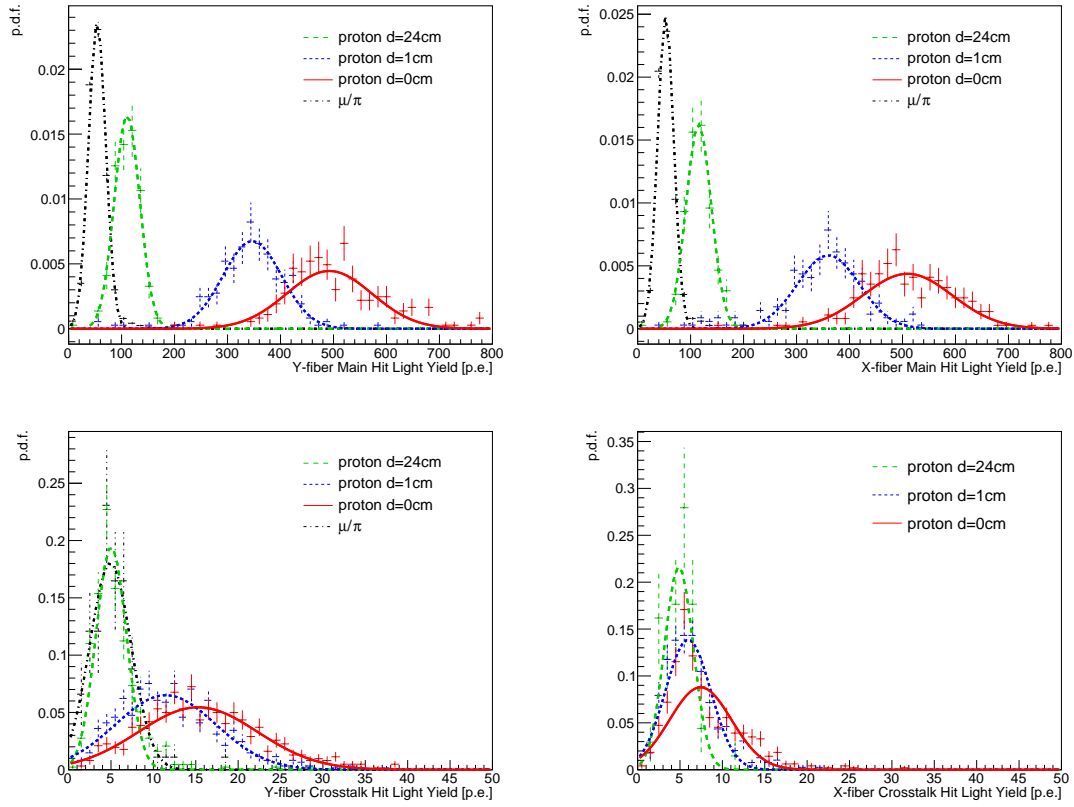


FIGURE 11.29: Light yield distributions for main hits (top) and crosstalk hits (bottom) using 0.8 GeV/c proton and 2.0 GeV/c μ/π triggers. In the left (right) the results are presented for 8 cm (24 cm) long Y-fibers (X-fibers) perpendicular (parallel) to Tyvek sheets. Figures from Ref. [6].

value was significantly larger, similar to 100 PE (500 PE) far from (at the) stopping point. For X-fibers the associated crosstalk hits had a much smaller light yield similar to 5 PE (15 PE) far from (at) the stopping point. This light yield was even smaller for Y-fibers showing the effect of Tyvek in further optically isolating cubes. In general, the absence of tails, the narrow crosstalk light yield distributions and the resemblance of their width to its associate main hit distributions proved that the set of etched surfaces in the detector cubes had a very uniform effect in containing the scintillation light.

The light yield distribution of crosstalk hits is affected by the threshold settings. Signals close to the threshold have a smaller probability to be recorded and therefore the reconstructed light yield distribution is shifted towards larger values. Due to this, to determine the fraction of crosstalk, κ , flowing from the original cube to a single neighbor cube, crosstalk hits at the proton stopping point were used as their light yield distribution is the less sensitive one to threshold effects. Finally, to estimate κ it is necessary to find a relation between the 2D hits that we are measuring and the light yield at the cube level. Thus, we need to account for the light that has flown outwards or inwards a given cube. On one hand, light escapes from the original cube six times, one per surface. On the other hand, the cube gets crosstalk light from two adjacent cubes along the particle trajectory. Moreover, the fiber that we use to do the measurement collects crosstalk light from two additional cubes. Consequently, a factor $2M_{\text{xtalk}}$, see Figure 11.30, is included in the denominator to correct for this six-to-four imbalance, leading to

$$\kappa = \frac{M_{\text{xtalk}}}{M_{\text{main}} + 2M_{\text{xtalk}}} \quad (11.1)$$

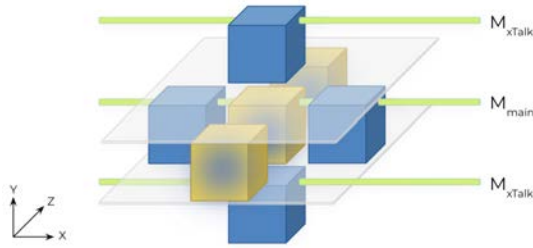


FIGURE 11.30: Sketch of the main cube (blue) surrounded by four crosstalk cubes (green) and its associated MPPC measurements M_{main} and M_{xtalk} . Tyvek sheets are depicted as horizontal thin surfaces.

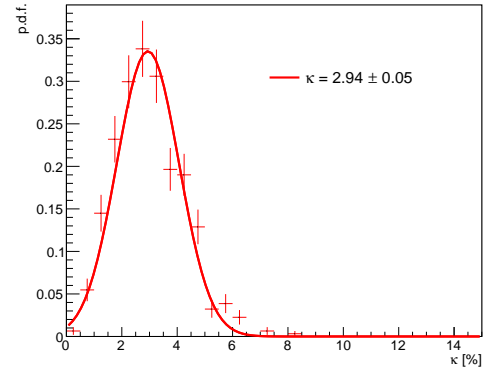


FIGURE 11.31: Left: Measurement of the crosstalk fraction defined in Eq. 11.1. Figure from Ref. [6].

Finally, as presented in Figure 11.31, the crosstalk fraction was found to be $\kappa = 2.94 \pm 0.05\%$ and the use of Tyvek was associated to crosstalk reduction similar to 50-60%.

11.3.6 Fiber light attenuation

Fiber attenuation is known to happen in the WLS fibers and therefore it needs to be corrected for in order to get a sensitive energy estimate for the tracks regardless of their distance to the readout plane. The attenuation process is known to be described by the equation [452]:

$$y(d) = LY_0 \left(\alpha e^{\frac{-d}{L_S}} + (1 - \alpha) e^{\frac{-d}{L_L}} \right), \quad (11.2)$$

where the unattenuated light yield is represented by LY_0 , α is a relative weighting factor, L_S and L_L are the short and long attenuation constants respectively and the distance d is measured from the center of the cube to the MPPC. To correctly assess d an offset of 2.3 mm was considered. For Y11 Kuraray WLS fibers the value of $L_L = 4$ m is known from the manufacturer specifications. However, L_S depends on the specific length of the fiber. Using prototype data the attenuation in the 8 cm and 24 cm fibers was measured by selecting tracks parallel to the Z-fibers and determining the X and Y track coordinates from the XY plane such that d was always known both for X- and Y-fibers. The results were averaged for all channels in the XZ and YZ planes. For the 24 cm long fibers a fit of Eq. 11.2 to the average light yield was made setting $L_L = 4$ m as a constant. The results are presented in Figure 11.32. Overall, a smooth trend was measured which was well fit by Eq. $L_S = 63 \pm 19$ cm and $\alpha = 0.14 \pm 0.03$. The light yield at $d = 0$ was measured to be $LY_0 = 59.6 \pm 2.2$ PE for 0.8 GeV/c muons, a large improvement for a single channel ($\approx \times 2$) compared to the FGDs [452].

11.3.7 Cube response

The uniformity of signals was also studied at the cube level. For this study, the XYZ coordinates of each cube were determined using the same selection method employed in the attenuation studies above. For each cube, distributions of the measured light yield, corrected for the expected attenuation, were filled with data from a run of 0.8 GeV/c muons and pions. A histogram of the average of the light yield in each cube is presented in Figure 11.33. The results are split in measurements with X-fibers (horizontal) and Y-fibers (vertical).

The measurements show a cube uniformity similar to 12% (13%) for X-fibers (Y-fibers). Slight differences in the width of the distributions is observable as the likely result of the different roles

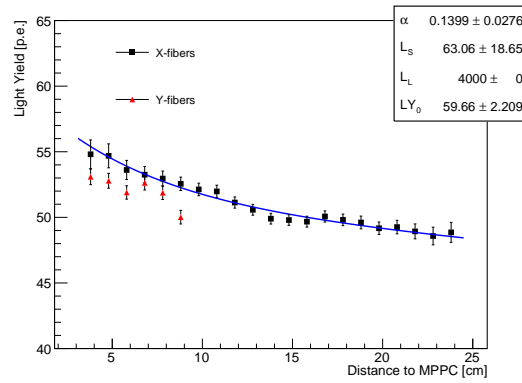


FIGURE 11.32: Light yield attenuation in 8 cm (24 cm) long Y-fibers (X-fibers). Eq. 11.2 is fit to X-fibers data, using $L_L = 4$ m as a constant. Figure from Ref. [6].

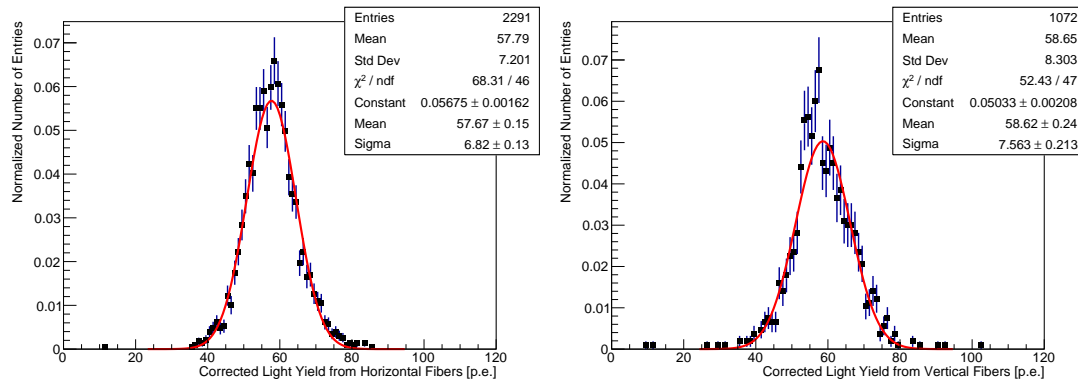


FIGURE 11.33: Left (Right): Light yield for 2291 (1072) cubes using X-fiber (Y-fiber) measurements after attenuation corrections. Figures from Ref. [6].

of optical cross-talk for both planes, which was not corrected for. Of special relevance is the fact that virtually no outliers in this trend were identified signaling a homogeneous cube response to the beam tracks.

11.3.8 Time resolution

The single hit time resolution was studied in the early SuperFGD prototypes for which an intrinsic time resolution similar to 0.95 ns was measured when using a fast 5 GHz digitizer. In the $24 \times 8 \times 48$ prototype these measurements were repeated using CITIROC based electronics and the final sampling rate of 400 MHz. Additionally, the time resolution was measured in multiple fibers for events crossing different sets of cubes in order to determine its uniformity at the channel level. To do so, first, the time walk of hits was corrected for. This consisted on parameterizing the time-delay of hits as a function of its light yield and correct this dependence for every hit. The time of the hit in the 24th Z-layer was used as a time reference. The time of all other hits subtracted by the reference was used to fill a distribution per channel. The width of these distributions characterized the time resolution for two channels, the one being measured and the reference. Consequently, the time resolution for a single channel was computed dividing the width of each distribution by $\sqrt{2}$ under the assumption that each channel had a time resolution identical to the reference, which was a reasonable approximation. The results, using a set of low ionizing tracks from a 2 GeV/c μ/π run, are presented in Figure 11.34. Notice that only the central channels in the XZ plane were used as those were the only channels populated by a

sufficiently large number of events due to the beam spread and incident position.

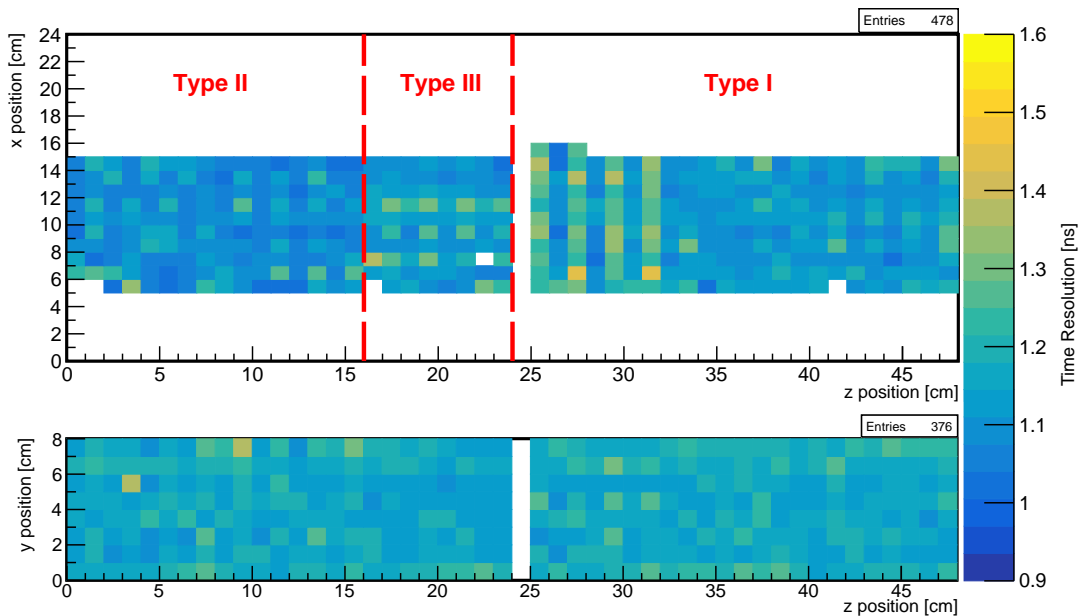


FIGURE 11.34: The time resolution across channels in the XZ and YZ planes. Figure from Ref. [6].

The time resolution in different channels was combined in order to draw more general conclusions, as presented in Figure 11.35. The channels in FEB 18 were not included as they were noticeably larger pointing out a potential synchronization problem with the master clock board. In the prototype the channels with odd and even Z were read in opposite detector surfaces such that a straight track might produce signals at two different delays in the reference channel and the one being measured. This effect was corrected for accounting for the travel time of the light from the cubes to the MPPCs. Despite of the correction a small discrepancy was observed between the time resolutions from hits in the XZ and YZ planes. Since the YZ plane was only instrumented with type I MPPCs the time resolution was studied as a function of the MPPC type. The results showed that whereas type I and II had similar resolutions type III had a worse performance. Interestingly, type III MPPCs had a typical light yield 20% lower than the type I and II. Consequently this results pointed towards a light yield dependence of the time resolution. This dependence is in

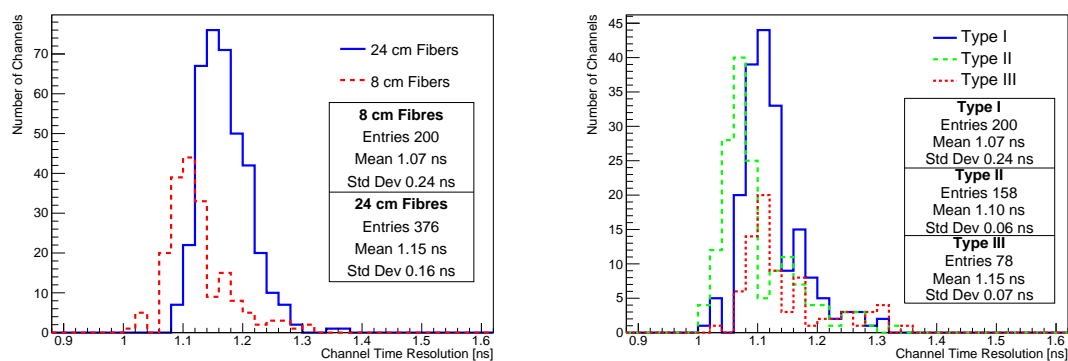


FIGURE 11.35: Histograms of the time resolution in different channels excluding those measured by FEB 18. The plot on the left show the distributions split by fiber axis. The plot on the right splits Y-fiber measurements by MPPC type. Figures from Ref. [6].

fact expected as the time resolution is affected by the random delays affecting the signal photons, e.g. during the scintillation process, the wavelength-shifting and the transport. The resolution is however determined by the time of arrival of the first photons which, for a large light yield, becomes asymptotically a deterministic process. Due to this, attempts were made to measure the time resolution at a higher light yield using protons. However, the small number of events limited this study which rendered inconclusive results. Due to this, a continuation of this studies was made two years later using neutron beam test data, as later presented in Sec. 11.5.

11.3.9 Particle identification

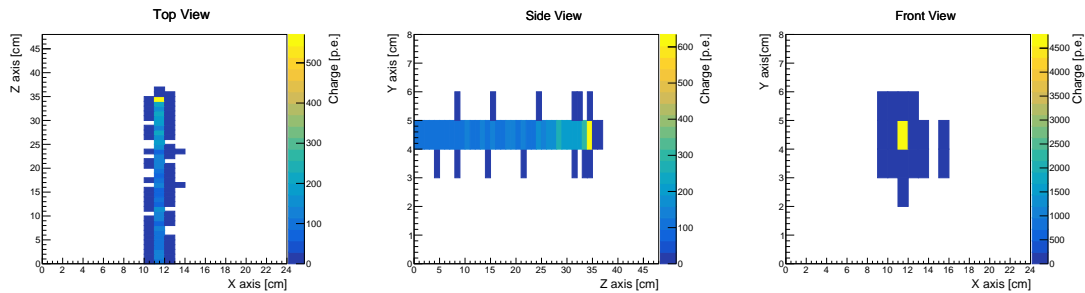


FIGURE 11.36: Event display of a stopping proton. Figure from Ref. [6].

When building particle identification (PID) criteria to identify different particle types it is crucial to understand the response of the detector to each of them. In SuperFGD a key PID variable will be the track ionization per unit length, i.e. the dE/dx . To study the dE/dx , a run of 800 MeV/c protons was studied. Remarkably, although for this energy protons are not expected to stop in the detector, the presence of the HARP TPC in front of SuperFGD reduced the protons momentum about 50 MeVs, making them to typically stop in the last layers of the detector. For protons, a very characteristic dE/dx pattern is expected. As protons stop, they become less relativistic and more ionizing such that their dE/dx abruptly rises creating a peak, known as the Bragg peak. This feature makes protons ideal candidates to treat oncological patients, as discussed in Appendix B. In neutrino experiments, the Bragg peak can be used to identify protons reliably. An event display for a stopping proton in the prototype is presented in Figure 11.36. The measured dE/dx results,

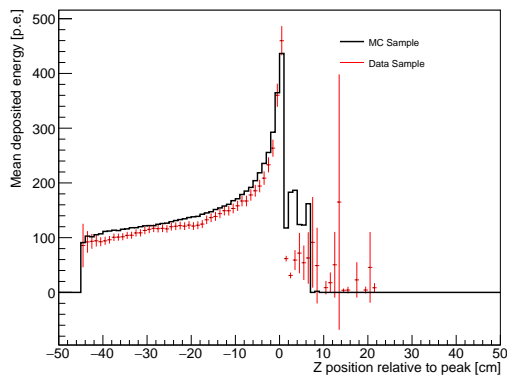


FIGURE 11.37: Measurement of the dE/dz at a given distance relative to the proton stopping layer compared to the simulated prediction. Figure from Ref. [6].

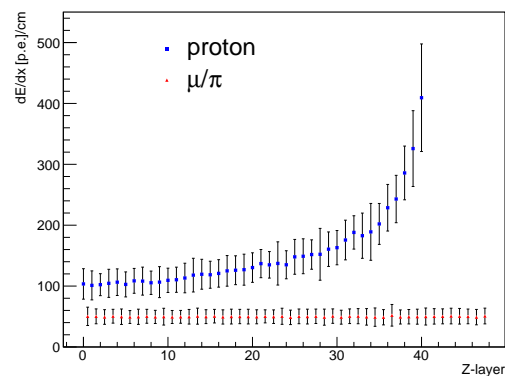


FIGURE 11.38: Measurement of the dE/dz at each layer for 0.8 GeV/c particles with either proton or μ/π trigger. Figure from Ref. [6].

in this context sometimes referred to as dE/dz , were compared to simulation predictions, as presented in Figure 11.37, showing overall a good agreement. Further details on the simulation are presented later in Sec. 11.4.3.

The light yield of low ionizing and high ionizing particles was compared by studying protons vs muons and pions all with the same momentum of 0.8 GeV/c. Selecting straight going tracks the light yield in each layer was used to fill independent distributions which were fitted with a Gaussian. The mean and sigma of those fits are presented in Figure 11.37. As it can be seen, even when using a single fiber (we expect to use three fibers) the measured ionization profile provides a strong particle identification tool.

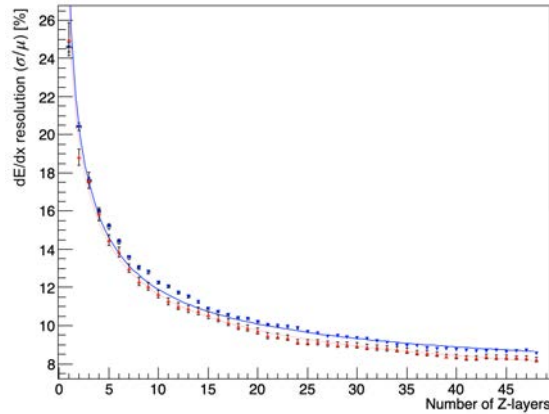


FIGURE 11.39: dE/dx resolution as a function of the number of Z-layers used to do the estimate, with (red) and without (blue) applying intercalibration corrections.

Interestingly, for MIP tracks the dE/dx is stable such that measurements in different layers can be used as independent estimators for its dE/dx . This situation is analogous to that in the TPCs. Consequently, it is possible to combine these measurements in order to obtain a single estimate of the dE/dx . To do this, N of the 48 possible layers for a straight going MIP were used to obtain a single estimate of the dE/dx . Interestingly, this measurement allows to study the impact it might have to perform a channel intercalibration, as better channel uniformity reduces the smearings in the independent estimates of the dE/dx . In order to test this, we used two different samples of MIPs. One has used to compute intercalibration factors, defined as multiplicative constants that shifted the mean of each channel to be equivalent to the average mean of all channels. The other was used to compute the dE/dx resolution with and without using the intercalibration factors. The results are presented in Figure 11.39. Two main conclusions can be drawn. First, the HATPC and SuperFGD performances in determining the ionization of MIPs is comparable, having both a dE/dx resolution similar to 8.5% for tracks of the same length (36 cm). In the second place the use of intercalibration factors improves the performance of the detector. As these factors were obtained directly from tracks, the method was proven to be effective, such that an analogous correction can be derived for the final installed SuperFGD using cosmic tracks. Finally, it is worth noting that in this study only a single projection has been used to estimate the dE/dx . If the information from the three projections is considered, potentially, the dE/dx resolution could improve by $\sqrt{3}$, reaching an outstanding resolution similar to 5% for 36 cm tracks.

11.3.10 Electron-gamma separation

Reducing the gamma background from π^0 decays in ν_e selection samples is a major interest for T2K. In SuperFGD, gamma events are expected to produce very distinct signatures by converting into an e^+e^- pair. Using the prototype some of these signatures were searched for using simple algorithms and leading to positive results. One candidate event is displayed in Figure 11.40.

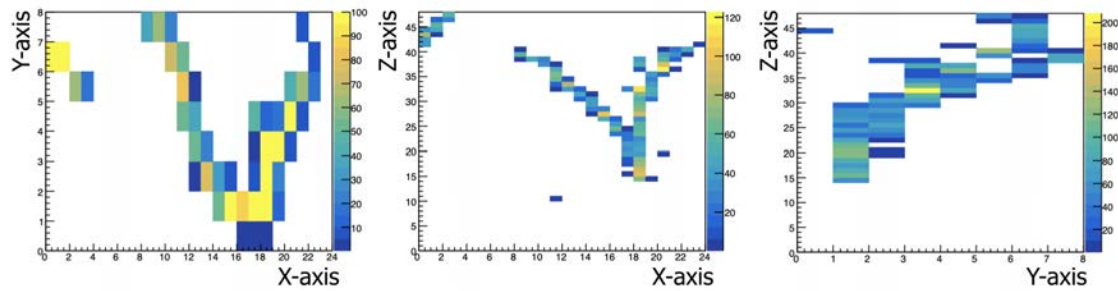


FIGURE 11.40: Event display of a gamma conversion candidate. Figure from Ref. [6].

11.4 Track reconstruction and signal classification

The novel design of SuperFGD will allow to have information at the 3D level by combining the hits in the three orthogonal 2D views. Once in 3D, the event will be reconstructed grouping the information into tracks and each track will be classified according to PID criteria.

For the 3D reconstruction, however, there is a prominent obstacle. The 3D matching of 2D hits introduces some unavoidable geometric ambiguities that need to be addressed in order to minimize their detrimental effect in the detector performances. Moreover, optical crosstalk hits thicken the 3D tracks and makes associating a reconstructed energy deposit to each of them a complex task. In order to deal with this problem a novel method to classify signals at the 3D level based on Graph Neural Network was studied, and the results are described in Ref. [7]. The most prominent findings of this study are summarized below.

11.4.1 2D to 3D matching

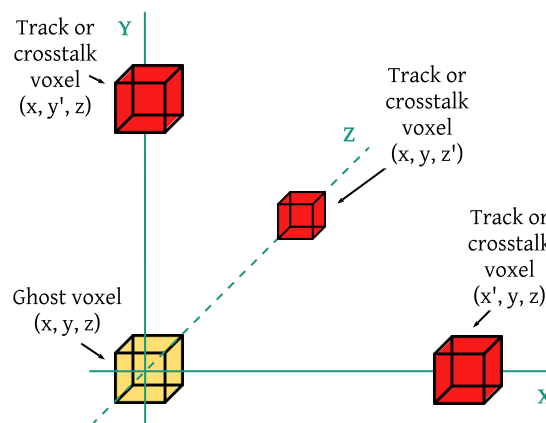


FIGURE 11.41: Example of a ghost voxel arising from a 2D to 3D matching ambiguity. A 2D hit from each of the three track or crosstalk voxels (red) intersect generating a ghost voxel (yellow). Figure from Ref. [7].

For a given physics event the signals output in SuperFGD consists of a list of 2D hits each consisting of well defined spatial coordinates in its plane, a time stamp and a light yield measurement. In order to map this hits into signals at the cube level, i.e. build 3D hits named hereafter as *voxels*, it is necessary to match this 2D hits. A simple strategy for this is to look for 3D coordinate combinations which can be formed independently combining 2D hits from two different pairs of planes. There are, however situations in which more than one possible matching combination is possible, see Figure 11.41. Due to this, we can differentiate between

three different types of voxels:

- **Track Voxel:** A reconstructed 3D hit with coordinates corresponding to a cube whose true energy deposit corresponds, partially or totally, to the scintillation light generated in that same cube.
- **Crosstalk Voxel:** A reconstructed 3D hit with coordinates corresponding to a cube whose true energy deposit corresponds exclusively to light-leakage from other cubes.
- **Ghost:** A reconstructed 3D hit with coordinates corresponding to a cube with no true energy deposit which arises from ambiguities in the 2D to 3D matching.

An illustrative example of a 3D reconstructed event showing the true labels of its voxels is presented in Figure 11.42. From the physics perspective ghost voxels correspond to a potential nuisance as they can mislead the event interpretation forging the existence of additional 3D tracks. Additionally, both ghost and crosstalk voxels thicken the tracks trajectories difficulting the 3D energy deposit reconstruction, and the range and vertex position estimates. Consequently, identifying each reconstructed voxel as track-, crosstalk- or ghost-like can very significantly enhance the final performance of the reconstruction chain algorithm.

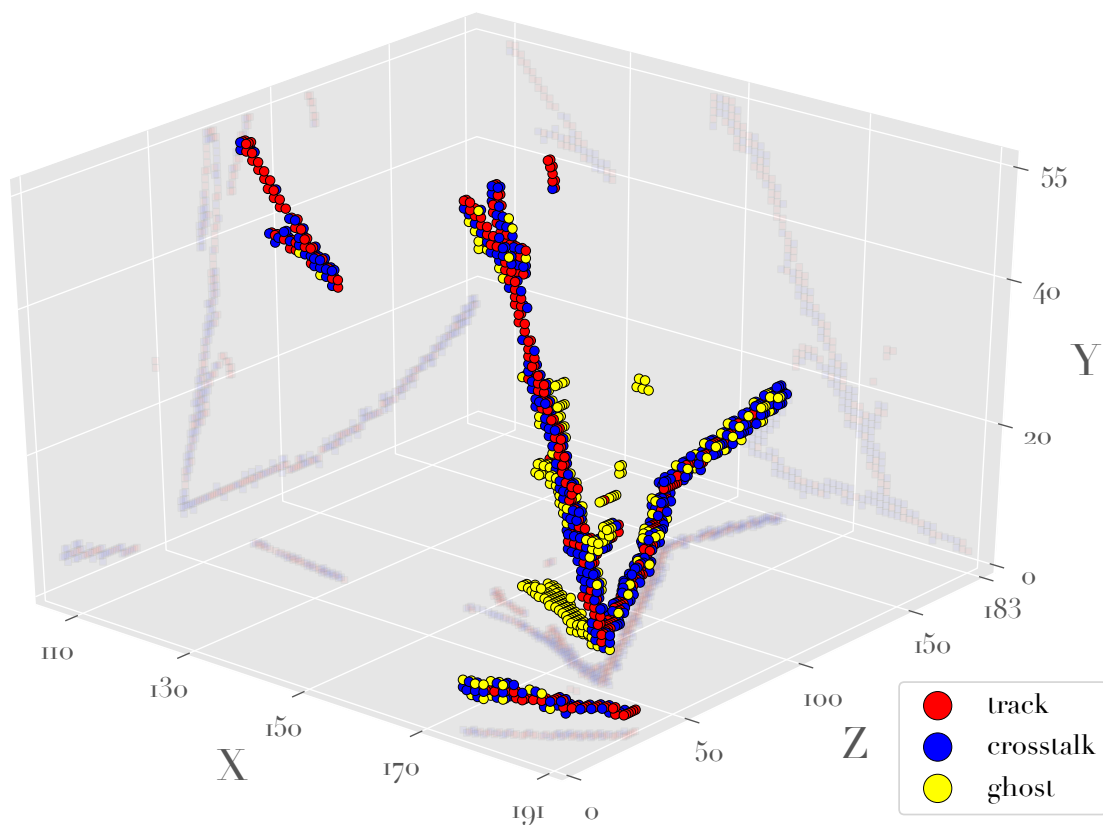


FIGURE 11.42: The event display in Figure 11.2 is colored according to its true voxel labels. Figure from Ref. [7].

11.4.2 GNN voxel classification

Given the former definitions of voxels as belonging to three mutually exclusive categories and provided a simulation able to generate realistic SuperFGD events it is possible to design an algorithm to classify the reconstructed voxels and to evaluate its performance.

Among the possible options for this task were Convolutional Neural Networks (CNNs) [535] which have been used for a multitude of tasks already in neutrino physics including the classification of events [536, 537, 12, 538, 539, 540, 541] and hits [542, 543]. As neutrino detectors often collect very sparse data submanifold sparse convolutional networks (SCCNs) [544], which have been used by the MicroBooNE [543, 545] and NEXT [546] collaborations, were other potential candidates for this task. An alternative solution is that of Graph Neural Networks (GNNs) [547, 548] which have recently started to be used in high energy physics [549, 550, 551, 552]. Graphs allow to define custom relations between nodes which contain an arbitrary ensemble of information. Due to this, GNNs were regarded as the best suiting solution to classify voxels in SuperFGD as they allowed for a custom definition of the graph connectivity and to embed a large set of features in each node. In particular, a GNN inspired by the GraphSAGE algorithm [553] was implemented and tested for this task.

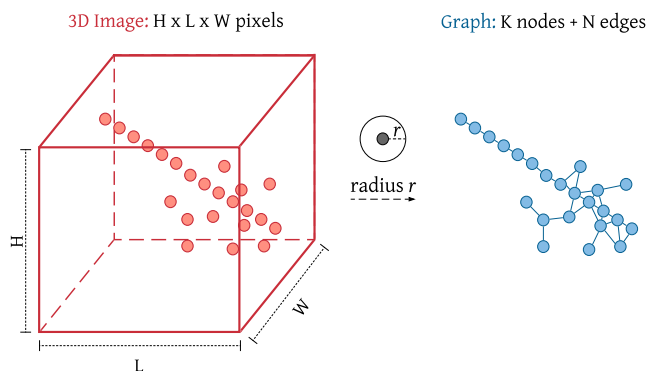


FIGURE 11.43: Drawing of the data reduction of a detector with $H \times L \times W$ pixels into a graph of K nodes and N edges. In our studies the graphs were built up connecting reconstructed voxels with centers closer than $r=1.75$ cm.

The algorithm consists on the following steps. First, every event is transformed into a graph by mapping each voxel into a node and connecting the nodes to form an undirected graph. The connectivity of the graph was defined upon the spatial closeness of the voxels under consideration, see Figure 11.43. In particular, all voxels with a center closer than 1.75 cm were connected to relate all voxels sharing either a side or a corner. Then, for each node a list of 25 features was built (the numbers at the beginning define the feature index):

- **0-2** The number of photons detected in each fiber (p_X, p_Y, p_Z) corrected for the expected attenuation.
- **3-5** The voxel multiplicity (m_X, m_Y, m_Z) defined as the number of reconstructed voxels intersected by the fiber.
- **6** The average number of detected photons weighted by the voxel multiplicity in each fiber (pW_{av}).
- **7-9** The asymmetries (a_X, a_Y, a_Z) between the light measured in two different 2D planes, defined as $a^i = \frac{p^j - p^k}{p^j + p^k}$.
- **10** The total uniformity of the hits light yield defined as the squared distance from each p_X, p_Y, p_Z to their average weighted by their average squared.

- **11** The total relative difference t_D of the light yield weighted by their voxel multiplicities defined as $t_D = \frac{d^x d^y + d^x d^z + d^y d^z}{pW_{av}}$ where $d^i = \left(\frac{p^j}{m^j - \frac{p^k}{m^k}} \right) / \left(\frac{p^j}{m^j} + \frac{p^k}{m^k} \right)$.
- **12** The ratio between the total voxel multiplicity $m_X + m_Y + m_Z$ and pW_{av} .
- **13-14** The number of reconstructed voxels in a sphere of 1 cm and 5 cm (r_1, r_5).
- **15-20** Boolean neighbor indicators $x^+, x^-, y^+, y^-, z^+, z^-$ representing the existence of a reconstructed voxel in each of the 6 sides of the cube.
- **21** A boolean variable which is 1 if any of $x^+, x^-, y^+, y^-, z^+, z^-$ is 1.
- **22** The ratio from close-to-far voxels r_r defined as $r_r = r_2 / (r_5 + 10^{-7})$.
- **24-23** The average Euclidian distance a_{Dis} to all voxels in a radius of 2.5 cm, and the ratio between a_{Dis} and pW_{av}

The algorithm then created embeddings for each node by aggregating the features of all of its neighbors and the neighbors of the neighbors, namely, a neighborhood depth of three was used. To combine the information a mean aggregator was used which averaged the neighbor features. The connectivity of each node at the depth of three defined a finite number of possible sub-graphs. For each, a Multi Layer Perceptron (MLP) consisting of two fully connected layers followed by a LeakyRELU activation function and a softmax layer was used. The output layer of the model had three neurons, one per each possible category (track, crosstalk or ghost). Since the sum of the value for the three output neurons is always one, each neuron value provides a fractional score that can be interpreted as a probability and can be used to classify the voxels. The architecture details of the network are presented in Table 11.2 and Figure 11.44 illustrates the overall procedure. The algorithm optimized the weights of the GNN layers by minimizing a categorical cross-entropy loss function, which is standard in machine learning for multi-class classification problems.

Parameter	value
Encoding size	128
Depth	3
Aggregator	mean
Fully Connected Layer 1	128 neurons
Fully Connected Layer 2	128 neurons
Fully Connected Layer 3 (output)	3 neurons

TABLE 11.2: GNN architectural parameters. Table from Ref. [7].

11.4.3 SuperFGD simulation

The SuperFGD detector geometry was simulated according to the ND280 upgrade TDR [3]. The physics simulation was based on a GEANT $v4-10.6.1$ [462] framework and customized from the code used in the sensitivity studies carried out in the context of the ND280 upgrade TDR. For an input set of particles with known kinematic properties, i.e. momentum and angle, the simulation generated a list of energy deposits in each of the SuperFGD cubes. For this study only those deposits in the first 100 ns were considered since, as earlier discussed in Sec. 11.3.3, signals separated by more than 100 ns can be identified in the same channel and therefore can be dealt with forming independent graphs. All energy deposits were corrected to account for Birks' quenching [412]. Crosstalk deposits were simulated by randomly sharing the initial energy deposits among neighbor cubes. The shared deposits were subtracted from the original cube. The sharing was made by sampling from a Poisson distribution, with $\mu = 2.7\%$, similar to prototype

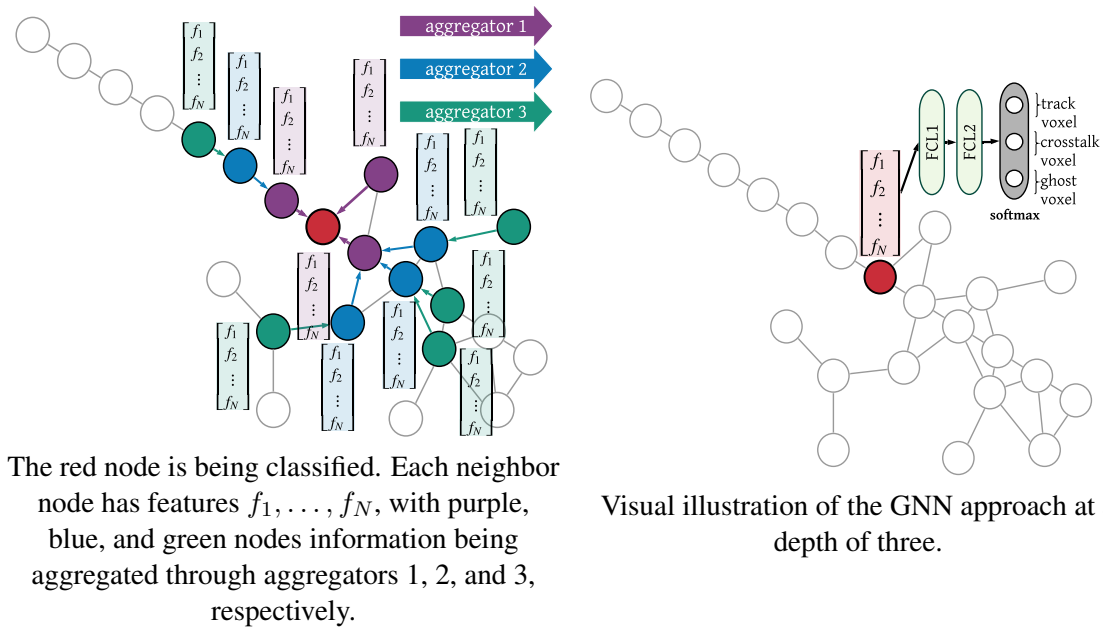


FIGURE 11.44: Illustrative sketches of the working concept for the GNN. Figures from Ref.[7].

measurements. The simulated cube energy deposits were projected to create a list of 2D hits. In this process the deposits were discretized into photons and weighted by distance dependent attenuation factors. To account for the quantum detection efficiency of the photosensors the photons were randomly accepted with 35% probability. A minimum threshold of 2 PE was applied. The 2D hits were matched to form a list of 3D reconstructed voxels following the method described in Sec 11.4. The final list of voxels was labeled as track, crosstalk or ghost. Finally, for each voxel the list of 25 features described above was calculated and each event was converted into a GNN input graph.

11.4.4 Datasets

Two different types of datasets were generated for the studies presented below. In one hand, GENIE datasets were created using the initial particle types and kinematics provided by the GENIE-G18.10b neutrino interaction software [258] when run on the SuperFGD geometry with T2K's flux [433]. On the other hand, Particle bomb (P-bomb) datasets were built as a complementary input not affected by the specific tunings of a neutrino event generator. Each P-bomb dataset was created adding equal number of events of the following particle gun combinations, each with flat solid angle and momentum [10-1000 MeV/c]: $1 \mu^-$; $1 \mu^-$ and 1 proton; $1 \mu^-$ and $1 \pi^-$; $1 \mu^-$ and $1 \pi^+$; $1 \mu^-$ and 2 protons; and $1 \mu^-$, $1 \pi^+$ and 3 protons. Table 11.3 shows a summary of the datasets. A comparison of the GENIE and P-Bomb dataset distributions is presented in Figure 11.45.

11.4.5 GNN training

As it is standard in machine learning each dataset that was used for training was split into three disjoint groups: the training set (to optimize the model's parameters); the validation set (to avoid overfitting) and the test set (to verify the performance of the model in new data). The network was trained for 50 epochs (passes to all training examples) using Python 3.6.9 and PyTorch 1.3.0 [554] and the Adam [555] optimizer. The mini-batch size was set to 32 and an initial learning rate of 0.001 divided by 10 when the error plateaus, as suggested in [556], were used. To validate the

GENIE dataset		Training	Validation	Testing
	# Events	6k	2k	11.5k
	# Voxels	1.83M	606.7k	3.58M
P-Bomb dataset		Training	Validation	Testing
	# Events	6k	2k	39.5k
	# Voxels	1.84M	618k	12.3M
		Track	Crosstalk	Ghost
Fraction		43%	37%	20%
		Track	Crosstalk	Ghost
Fraction		49%	38%	13%

TABLE 11.3: Summary of the GENIE and P-Bomb datasets including the number of events and number of voxels used to train, validate and test the models. Table from Ref.[7].

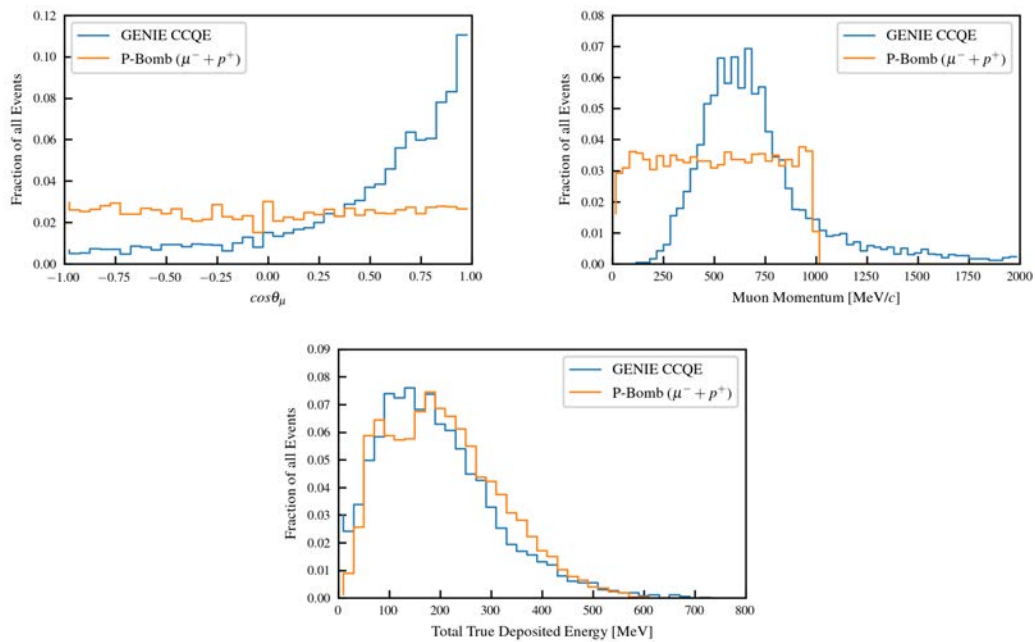


FIGURE 11.45: Distributions of CCQE GENIE interactions compared to $\mu^- + p^+$ interactions in P-Bomb. Figures from Ref.[7].

results during training the F_1 -score metric was used. In this way, the trained models used for inference correspond to the model state in the epoch with maximum F_1 -score.

11.4.6 Results

The performance of the algorithm was tested by comparing the true and predicted voxel labels. In this studies the predicted label was defined as the most likely voxel-type according to the GNN. However, in the future this criteria might be optimized or used in a different way. The efficiency and purity of the predictions were calculated per voxel and per event (as the average of the voxels in the event). The results are summarized in Table 11.4. An illustrative example of the GNN outcome is presented in Figure 11.46.

To evaluate the GNN classification performance the predictions were studied as a function of different sensitive variables, see Figure 11.47. Increasing the number of voxels and tracks slightly decreases the overall performance of the network. This is expected as denser events often produce a larger fraction of ghost voxels which are the hardest to classify. Despite of this, the network

		GENIE Training				P-Bomb Training			
GENIE Testing	Per Voxel	Track	Crosstalk	Ghost	Track	Crosstalk	Ghost		
		Efficiency	93%	90%	84%	Efficiency	93%	89%	80%
	Purity	93%	87%	91%	Purity	91%	86%	89%	
	Per Event	Track	Crosstalk	Ghost	Track	Crosstalk	Ghost		
Efficiency		94%	94%	88%	Efficiency	94%	93%	88%	
P-Bomb Testing	Per Voxel	Track	Crosstalk	Ghost	Track	Crosstalk	Ghost		
		Efficiency	94%	93%	87%	Efficiency	95%	93%	88%
	Purity	95%	90%	92%	Purity	95%	91%	92%	
	Per Event	Track	Crosstalk	Ghost	Track	Crosstalk	Ghost		
Efficiency		94%	94%	87%	Efficiency	95%	93%	88%	
Purity	96%	90%	92%	Purity	96%	91%	92%		

TABLE 11.4: Mean efficiencies and purities of voxel classification per voxel and per event. Table from Ref.[7].

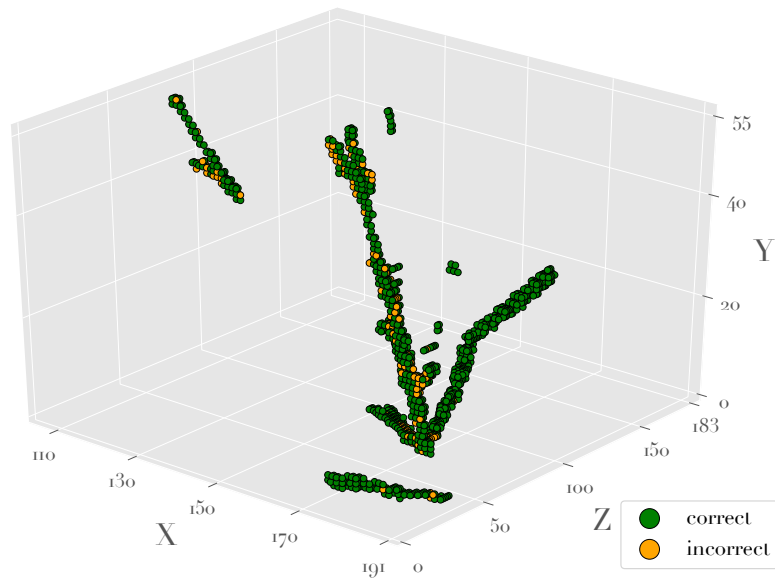


FIGURE 11.46: GNN prediction results for the interaction in Fig. 11.42. Figures from Ref.[7].

performance is generally very high with efficiencies and purities always above 85% across all voxel categories. This is also true close to the vertex position, a crucial feature for the reliable study of the neutrino events.

GNN			Charge Cut		
	Track	Other	Efficiency	Track	Other
Efficiency	94%	96%	93%	80%	
Purity	96%	95%	80%	91%	

TABLE 11.5: Mean efficiencies and purities for the voxel classification using the GNN and the charge cut. Table from Ref.[7].

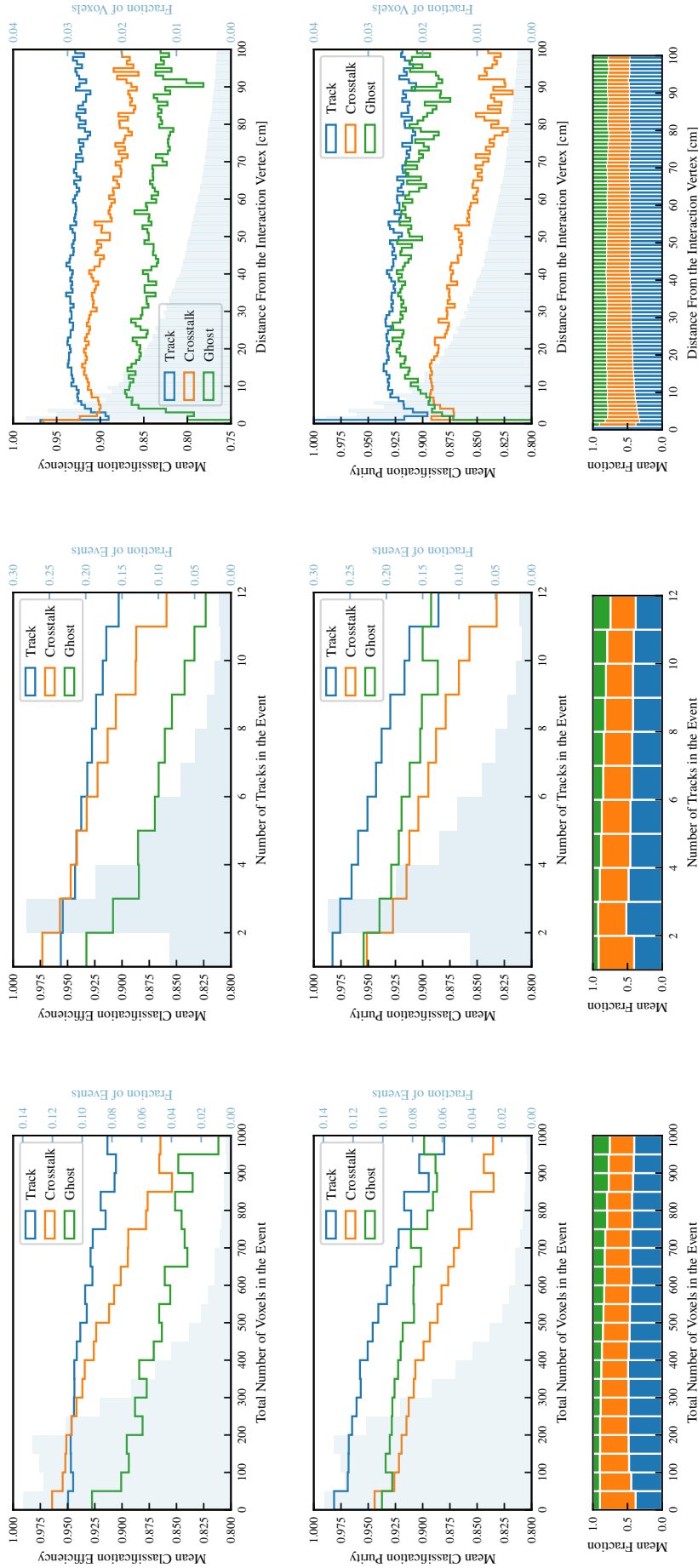


FIGURE 11.47: Efficiencies, purities, and fraction of voxels of each label (blue = track, orange = crosstalk, green = ghost) as a function the number of voxels (left), tracks (center) and distance from the vertex (right) for a sample trained and tested on GENIE simulated events. Figures from Ref.[7].

The GNN algorithm will be used to clean up the deleterious ghost voxels. Consequently, the algorithm must mispredict true track voxels as ghost voxels very rarely. For the GENIE dataset only 1.1% (3.3%) of true track (crosstalk) voxels were classified as ghost voxels. Moreover, 84.5% of all true ghost voxels were correctly labeled and only 4.3% of them were mislabeled as track voxels. To see the impact of this method cleaning up events we removed ghost voxels following two strategies. On one hand, the prediction of the GNN was used. On the other hand a simple light yield cut of 12 PE was applied to 2D, see Figure 11.48, prior to the 2D to 3D matching. The results, presented in Figure 11.49, show the superior performance of the GNN. Moreover, as presented in Table 11.5, if the classification is limited to two categories, i.e. Track and Other, the GNN widely outperforms the light yield cut. Additionally, fake ghost tracks, e.g. in Figure 11.42, appear from the shadows of high light yield real track hits and consequently a simple light yield cut is not expected to be able to eliminate them effectively.

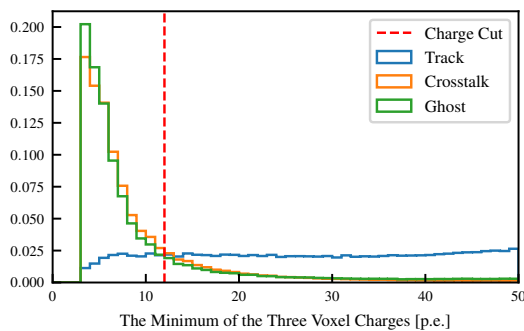


FIGURE 11.48: Distribution of the minimum charge among the three voxel 2D hits for the GENIE sample. Figure from Ref.[7].

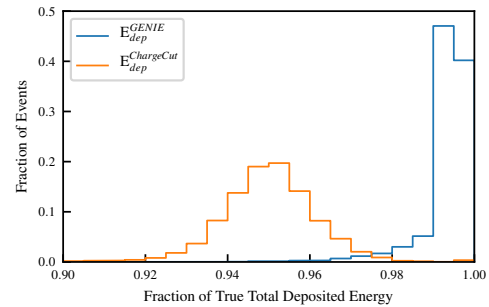


FIGURE 11.49: Fraction of the total deposited after rejected voxels predicted as ghost-like using the GNN or using the 2D charge cut. Figure from Ref.[7].

11.4.7 Systematic uncertainties associated to the GNN

For its integration in T2K's analysis pipeline the systematic uncertainties introduced by this method need to be accounted for. The GNN will be trained in simulated events and used in real data. Consequently, potential uncertainties can arise from the differences of the train and test datasets. Having this in mind, the GENIE and P-Bomb datasets were designed to have, by construction, much larger relative differences than GENIE has to real neutrino interactions. Then, we used these two datasets to characterize the relative variations in the total reconstructed energy when training in GENIE and in P-Bomb datasets. The results, presented in Figure 11.50, show very small uncertainties similar to 1% parametrized as a function of the true energy. Another possible source of discrepancy in the datasets is the imperfect modeling of the detector response in the simulation. To account for this, in addition to the nominal optical crosstalk of 2.7% two further test datasets were simulated using 2% and 5% crosstalk fractions. Once again, the results in Table 11.6 show the robustness of the GNN even for extreme mismodeling cases such as 5% crosstalk. In general, as many similar tests as necessary can be made in the future and, for each, the performance differences can be used to develop detector model systematic uncertainties. In particular, the assessment of the uncertainty associated to the inhomogeneous detector response will be studied once SuperFGD data is available.

11.5 Neutron detection in SuperFGD

The fine 3D segmentation of SuperFGD is expected to allow to identify signals related to neutrons. The detection concept is as follows. First, a neutron is ejected in the vertex as a direct or indirect

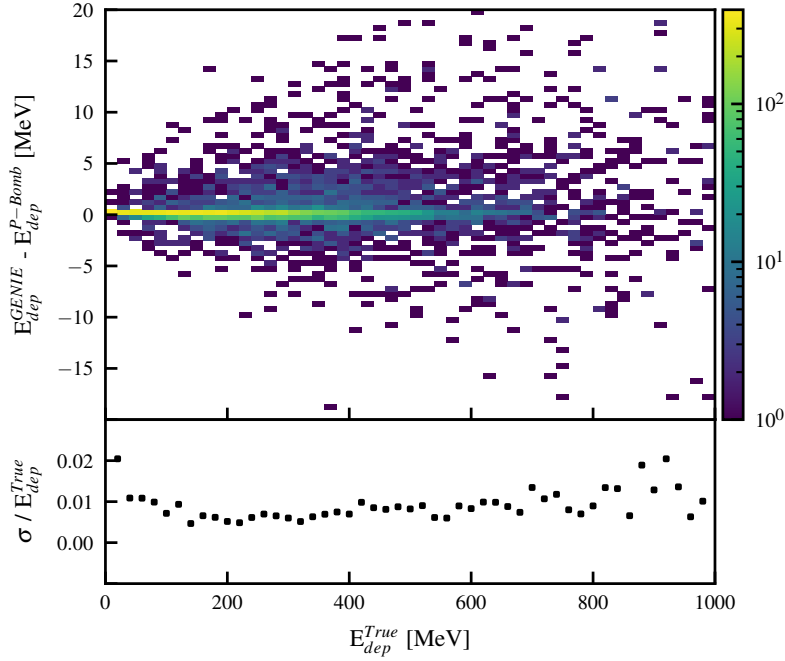


FIGURE 11.50: Difference in the total energy after removing the ghost voxels classified by GENIE- and P-Bomb-trained GNNs as a function of the total true energy deposit and its associated fractional standard deviation. Figure from Ref.[7].

Nominal		Track	Crosstalk	Ghost
Crosstalk	Efficiency	93%	90%	84%
2.7%	Purity	92%	87%	91%
Crosstalk		Track	Crosstalk	Ghost
2%	Efficiency	92%	89%	81%
	Purity	94%	83%	89%
Crosstalk		Track	Crosstalk	Ghost
5%	Efficiency	94%	89%	88%
	Purity	86%	91%	93%

TABLE 11.6: Mean classification efficiencies and purities per voxel for different crosstalk values. The GNN was trained with GENIE samples with nominal crosstalk and tested on samples with different crosstalk values. Table from Ref.[7].

(FSI) result of a neutrino interaction. The neutron’s energy is typically in the range from tens to few hundreds of MeV such that it is not relativistic. As neutrons are neutral particles they travel undetected through SuperFGD until they undergo a strong interaction, producing a measurable signal. The neutron signature appears then in the detector as a disconnected set of voxels, which might be as small as a single voxel, delayed in time with respect to the vertex. Tracing a line from vertex to the start of the neutron signal cluster allows to estimate the distance and the time delay can be used to compute the magnitude of the neutron momentum. This concept is illustrated in Figure 11.51.

The reconstruction of the neutron momentum is done by time-of-flight and therefore its resolution is directly related to time resolution of the detector. Figure 11.52 shows the expected neutron momentum resolution under the hypothesis of two possible time resolutions:

$$\sigma_t^{ly} = \left\{ 0.95 \text{ ns} / \sqrt{3} \right\} \cdot \sqrt{40 \text{ PE/LY}}, \quad \sigma_t^{ly} > 200 \text{ ps} \quad (11.3)$$

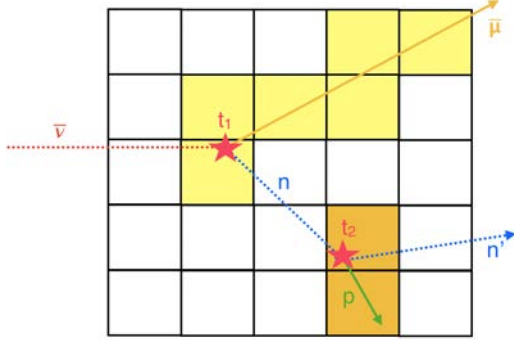


FIGURE 11.51: Sketch of the neutron identification in SuperFGD as a delayed and spatially disjoint cluster of signals. The time-of-flight ($t_2 - t_1$) together with the distance and direction from the vertex are used to reconstruct the neutron kinematics. Figure from Ref. [8].

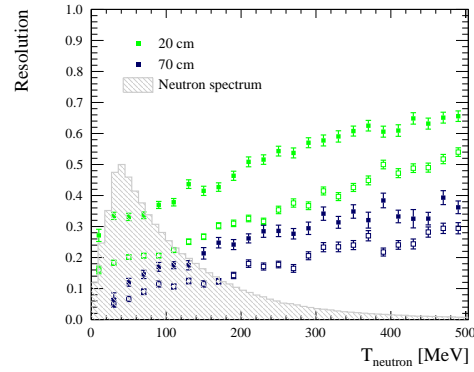


FIGURE 11.52: Simulated neutron momentum resolution for two minimum flight distances of 20 cm and 70 cm and for two time resolution expressions. Filled (empty) markers correspond to Eq. 11.3 (Eq. 11.4). The light gray shadow shows the momentum spectrum of neutrons emitted in neutrino interactions according to NEUT 5.4.0. Figure from Ref. [8].

$$\sigma_{ch}^{ly} = \left\{ 0.95 \text{ ns} / \sqrt{\#\text{channels}} \right\}, \quad \sigma_t^{ch} > 200 \text{ ps} \quad (11.4)$$

Which correspond respectively to the optimal (it improves with the light yield) and the conservative time resolutions.

The study of neutrons and their kinematics with SuperFGD is expected to lead to new analysis possibilities. One of this options, studied in Ref. [8], is to use the neutron kinematics in antineutrino $\text{CC}0\pi$ events to identify events with little nuclear effects. The idea consists in measuring the transverse kinematic imbalance, δ_{p_T} , from the known muon and neutron transverse kinematics (\vec{p}_T^μ and \vec{p}_T^n respectively), defined as:

$$\delta_{p_T} = |\vec{p}_T^\mu + \vec{p}_T^n|. \quad (11.5)$$

δ_{p_T} is informative of the amount of nuclear effects. Therefore, cutting on events with good neutron kinematics resolution and selecting events with low δ_{p_T} can allow for a better neutrino energy reconstruction, as presented in Figure 11.53, of great interest for the study of neutrino oscillations.

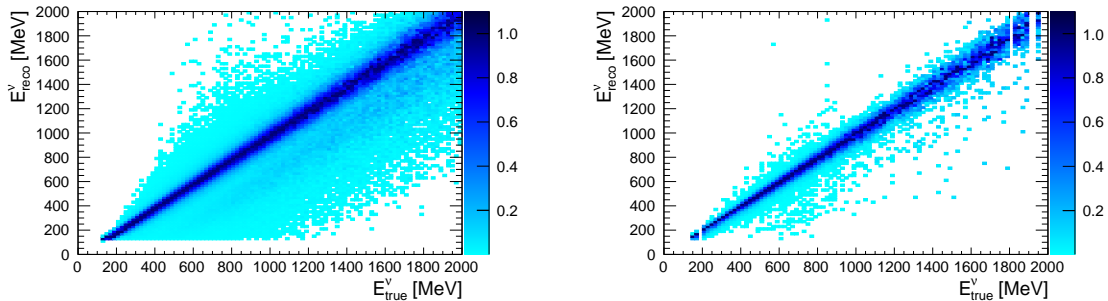


FIGURE 11.53: Correlation of the true and reconstructed energies without (left) and with (right) cuts. The cuts are $\delta_{p_T} < 40 \text{ MeV}/c$ and a minimum distance of 10 cm. Figure from Ref. [8].

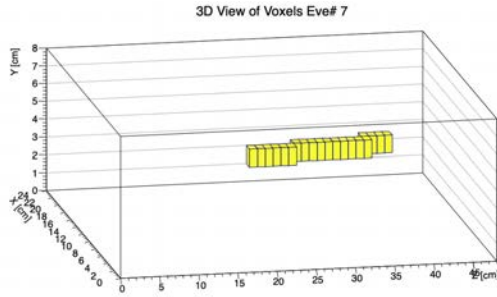


FIGURE 11.54: Event display of a neutron event candidate in the $24 \times 8 \times 48$ SuperFGD prototype using LANL neutron beam.

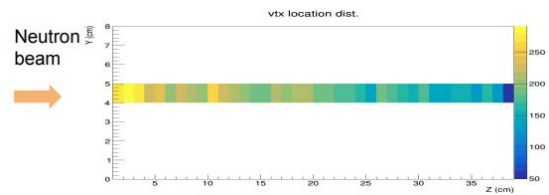


FIGURE 11.55: Observed number of interactions (colormap) as a function of the vertex position for the selected neutron events.

11.5.1 Neutron measurements with the $24 \times 8 \times 48$ SuperFGD prototype

In order to validate the neutron detection capabilities of SuperFGD the $24 \times 8 \times 48$ prototype was exposed in 2019 and in 2020 to a beam of neutron in LANL. A neutron candidate event display, ejecting a forward going track in the middle of the detector is presented in Figure 11.54. The neutron flux attenuates along the prototype as neutrons interact in the detector, see Figure 11.55. The reduction of this flux allows to study the neutron cross section by the so-called extinction method:

$$N(x, E) = N_0 \exp^{-\sigma(E)Tx} \quad (11.6)$$

where N_0 is the initial number of neutrons, T is the number of nuclear targets, σ is the cross-section and E and x are the neutron kinetic energy and interaction depth respectively. In LANL the energy of each detected neutron can be determined by the time-of-flight between a trigger signal at the emission point and the detection time in the SuperFGD prototype 90 m away. Using the extinction method a measurement of the neutron cross-section in plastic is about to be finished. Once completed, this measurement will characterize the neutron cross section in the most important energy interval for accelerator based neutrino oscillation experiments. In addition, this study validates the ability of SuperFGD to do precision measurements involving neutrons.

Lastly, it is worth noting that neutrons energy deposition in the detector is only loosely correlated with their kinetic energy. Accordingly, using neutron data it is possible to collect hits with very different light yields covering the whole dynamic range of interest for SuperFGD. This allowed to study the time resolution dependence with the light yield. The measurement was done selecting

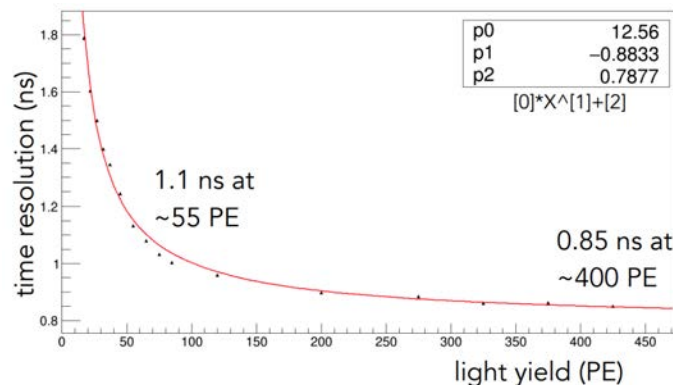


FIGURE 11.56: Light yield dependence of the time resolution.

neutron tracks and measuring the time resolution of type I MPPCs hits. The time reference was obtained as the width of a distribution filled with the time difference of hits in one plane and a hit reference in the perpendicular plane. The width was divided by $\sqrt{2}$ to obtain the time resolution

for a single channel. The analysis was made in bins of light yield to characterize its possible dependence. The results, presented Figure 11.56, reveals the important influence of the light yield in the time resolution of hits. The resolution for 55 PE was found to be similar to 1.1 ns, and hence the results from the CERN beam test were recovered. Interestingly, for hits with a low light yield similar to 10 PE the time resolution degrades to about 2 ns. For high light yields, such as those expected close to the vertex or in the endpoint of stopping particles, the resolution is as good as 0.85 ns. For infinite light yield, the fit predicts an asymptotic light yield of 0.78 ns, not far from the limit time resolution of the 400 MHz sampling of $2.5/\sqrt{12} \simeq 0.72$ ns.

Chapter 12

The Time-of-Flight panels

“Whenever technical progress opened a new window into the surrounding world, I felt the urge to look through this window.”

– BRUNO ROSSI

Six Time-Of-Flight (ToF) panels will be installed in ND280 as part of its upgrade. This Chapter reviews the development of this technology and the ongoing final characterization tests for the assembled detector prior to its installation in Japan. Additionally a novel method, inspired by the necessities and characteristics of the ToF waveform signals, to perform data-driven detector signal characterization with constrained bottleneck autoencoders, presented in Ref. [9], is discussed.

12.1 Overview and Motivations

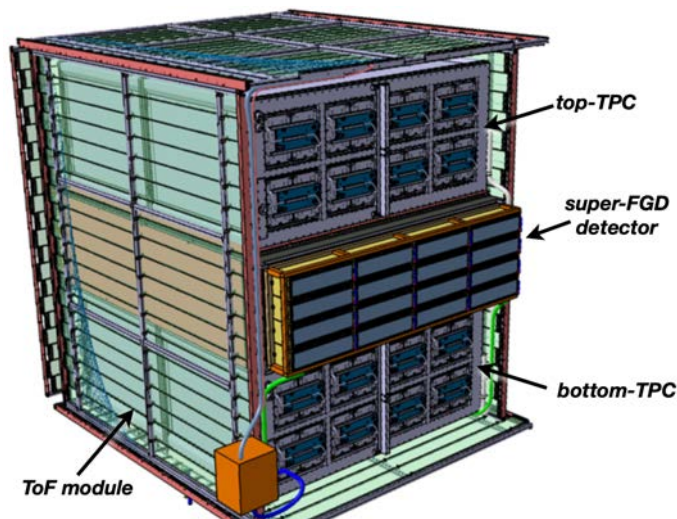


FIGURE 12.1: Computer drawing of the upstream most part of the ND280 basket where the ND280 upgrade new modules will be installed. Figure from [557].

Neutrino interactions happening out of the fiducial volume (OOFV) of the detector under study are an important source of background in ND280. OOFV events often arise from the incorrect reconstruction of the tracks sense of motion, which, in the absence of time-of-flight (ToF) information are assumed to be forward. Even for those tracks where ToF information exists the limited timing capabilities of the existing sub-detectors in ND280 lead to a non-negligible amount of

OOFV being selected. For CC samples, this is typically around 2-6%, but for some CC samples, e.g. those involving a single charged track or backward going tracks, this proportion can extend well beyond 10%, see for instance Refs. [355, 354] or Sec. 7.3 relative to the selection of $\text{NC1}\pi^+$ events.

To address this problem the ND280 upgrade includes six ToF panels forming a nearly hermetic box, hereafter named ToF-Cage (TFC). As presented in Figure 12.3, the TFC will be mounted around the HATPCs-SuperFGD sandwich and it is expected to provide excellent timing information for virtually all tracks entering to or outgoing from its inner volume. About 90% of the selected OOFV events in CC samples are generated by charged tracks. Therefore, the use of the TFC is expected to greatly reduce this background and help to develop much cleaner selection samples for SuperFGD and enhanced selection samples for backward going tracks starting in FGD1.

12.2 Development of the ToF technology

The ToF panels technology for the ND280 upgrade first appeared in 2017 in Ref. [558]. The development of large area SiPMs few years before [559, 560] allowed to replace the traditionally preferred option to read large areas of a plastic scintillator, PMTs, by arrays of large area SiPMs with a number of benefits: compactness, mechanical robustness, higher photon detection efficiency, low operation voltage, insensitivity to magnetic fields, low material budget and the possibility to omit light-guides [525]. Hence, the ToF panels were proposed as made up of plastic scintillator bars aligned in a single plane. Each of those bars would be measured by arrays of large area SiPMs coupled directly to the plastic scintillator bulk, on both ends of the bar and readout by fast electronics allowing to perform excellent time resolution measurements over large surface areas.

The first tests for this technology, presented in Ref. [558], reported an outstanding time resolution similar to 80 ns in scintillator bars of $150\times 6\times 1\text{ cm}^3$ and $120\times 11\times 2.5\text{ cm}^3$. These bars used arrays of eight $6\times 6\text{ mm}^2$ SiPMs, amplified and processed with a custom 8-channel board named eMUSIC based on the MUSIC ASIC [561]. After the prototype results from 2017, two experiments decided to incorporate the ToF panels technology with slightly different geometries and specifications to their design: The recently proposed Search of Hidden Particles (SHiP) experiment at CERN [562, 563] and the ND280 upgrade [3].

12.3 The ToF panels for the ND280 upgrade

The final ToF panels for the ND280 upgrade were built at CERN and the construction of the six planes was finished in 2020. Each module consists of a set of 20 plastic scintillator bars of $230\times 12\times 1\text{ cm}^3$ made of EJ-200 plastic scintillator. EJ-200 cast plastic scintillator was found to provide an optimal combination of high light output, low attenuation length, and fast timing (rise time of 0.9 ns, decay time of 2.1 ns and attenuation length of 380 cm). In addition, its scintillation light spectrum with a higher fraction of photons towards the green than other plastic options, e.g. EJ-204 and EJ-230, overlaps with the region of higher photon detection efficiency (PDE) of the S13360-6050PE SiPM by Hamamatsu ($6\times 6\text{ mm}^2$, 50 μm pitch). Eight of such SiPMs are placed on each bar end using custom amplifier boards attached to the bar bulk with 3D printed end-caps. The bars are arranged in a single plane covering a total area of 5.4 m^2 . Given the limited space inside the ND280 basket the bars are mounted in a single plane, without staggering, requiring a thin gap of about 1.5 mm between bars to include steel brackets that fix each bar to an outer aluminum frame responsible of the mechanical robustness of the panel. On the two sides of each frame, panels are installed to route one high-voltage (HV) and one signal cable to each SiPM amplifier board. The signal cables (20 per side) are guided towards a patch panel on the

top-center of the plane were all the 40 signal cables are grouped. The HV is distributed by two dedicated boards placed on the panel corners. This structure is identical for all planes except for the bottom module. On the bottom panel the to most external bars are not installed leaving 12 cm wide gaps necessary to install trays that will guide the SuperFGD and HATPCs service cables outside of the ND280 basket.

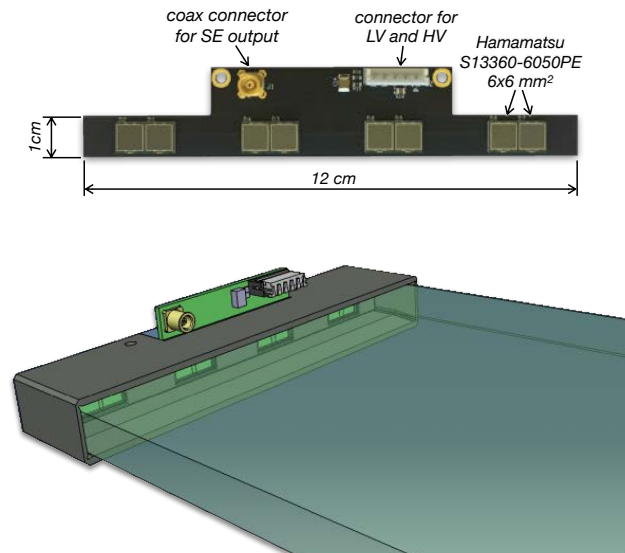


FIGURE 12.2: Picture of one amplifier PCB with 8 SiPMs (top) and a computer drawing of its positioning inside the end-cap when mounted on the bar (bottom). Figure from [557].



FIGURE 12.3: Picture of four of the final ToF planes. Figure from [557].

12.3.1 SiPMs amplifier board

The SiPMs are mounted in a custom board grouped in four pairs of two SiPMs as depicted in Figure 12.2. The time resolution degrades with the sensors capacitance as it increases the signal width and rise time. To reduce this effect each pair of SiPMs are connected in series and amplified and shaped independently prior to its aggregation in a summation node. The SiPMs are grouped in sets of eight with similar breakdown voltages allowing to operate each board with a single bias voltage and reducing the complexity and economic cost of each board. A shaper is used to reduce the time constant of the signal trailing edge decreasing the signal width by about 4 times fitting in a typical window of 10 ns. The amplifier dynamic range was adjusted to 1 V closely matching the range of the DAQ digitizer.

12.3.2 DAQ

The initial T2K ToF tests were done with a 64 channels WaveCatcher DAQ module [564]. The WaveCatcher acquires waveforms of 1024 samples at a maximum sampling rate of 3.2 GHz. The final DAQ system for the TFC is built around the SAMPIC ASIC [565]. It is a 16-channel chip which plays the role of both a time-to-digital-converted (TDC) and a waveform sampler. The SAMPIC chip acquires waveforms of 64 samples at a tunable sampling rate which can as high as 6.4 GHz. Four boards, each with 4 SAMPIC ASICs (reading up to 256 channels) will be used to measure all the 236 TFC channels. A picture of the final boards in its crate, together with a master board used for control and communication, are presented in Figure 12.4.



FIGURE 12.4: Picture of the final SAMPIC-based DAQ.

12.3.3 Performance tests with a single bar

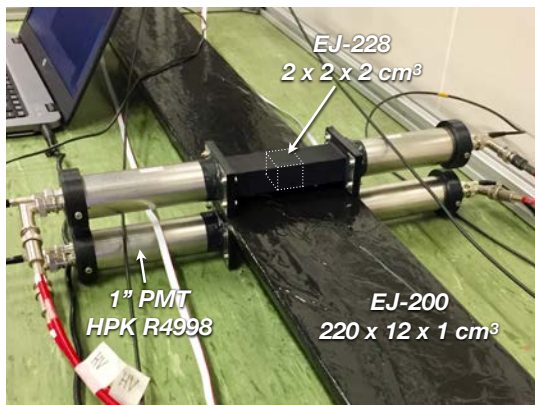


FIGURE 12.5: Single bar setup used in the studies reported in Ref. [557]. Figure from [557].

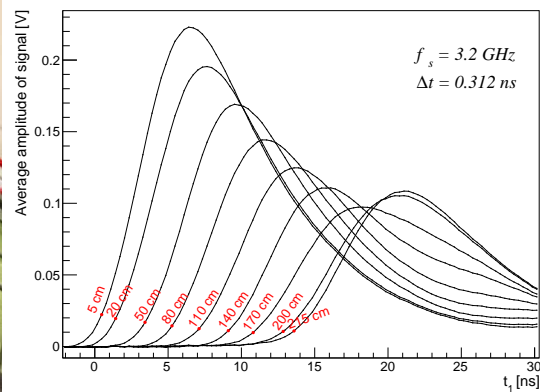


FIGURE 12.6: Average waveforms recorded at different trigger positions. Figure from [557].

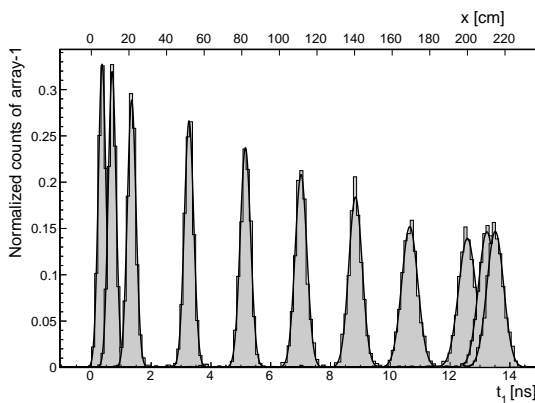


FIGURE 12.7: Time difference between the time recorded on one of the bar-end and the trigger signal for several trigger positions. Figure from [557].

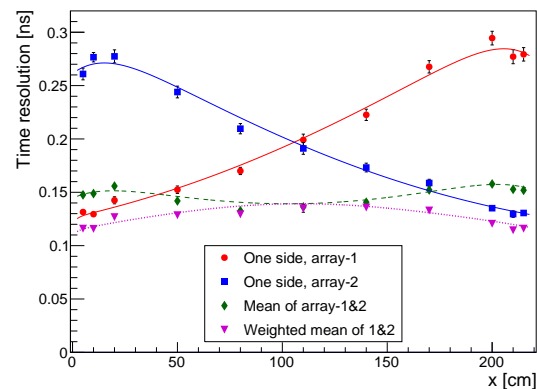


FIGURE 12.8: Time resolution for a single bar at different trigger positions. Figure from [557].

To characterize the detector response tests with a single bar were made in 2020 using the Wave-Catcher DAQ [564]. The setup, presented in a picture in Figure 12.5, consisted of a single TFC bar and a movable structure equipped 4 PMTs grouped in two pairs reading two plastic scintillator cubes placed above and below the bar. The signal of all PMTs in coincidence was used to record cosmic ray tracks crossing the bar at a well defined position. Typical waveforms at different positions are presented in Figure 12.6. To estimate the time associated to each cosmic crossing a constant discrimination fraction of 10% was used. The difference of this time relative to the PMT trigger signal is presented in Figure 12.7. For smaller time differences (trigger closer to the bar end being measured) the spread of the time difference is smaller and equivalently the time resolution, characterized by this spread, is better. The time resolution of the system for various trigger positions is presented in Figure 12.8. The resolution for a single end is always better than 0.3 ns. The weighted combination of both bar ends leads to an excellent time resolution equal or better than 130 ps for all bar positions.

Further test to characterize the detector using a single bar are ongoing, in particular, with the aim to better understand the optimal way to extract the time information from the signals, the waveform shape dependence with the position and to validate the performance of the system with the final SAMPIC-based DAQ.

12.4 Final tests at CERN

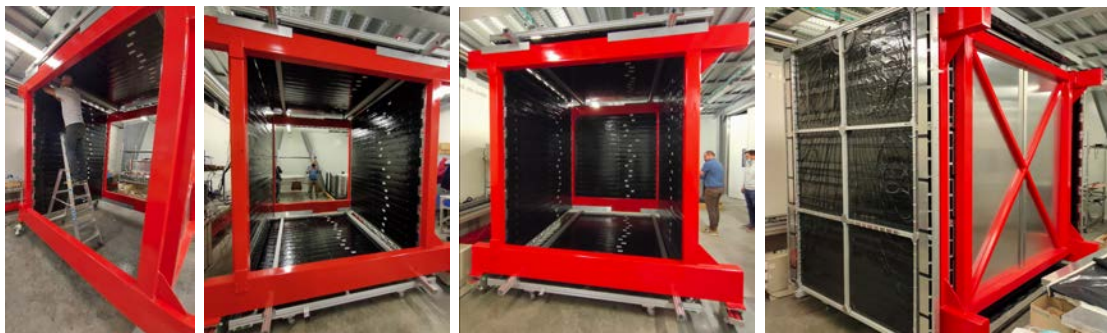


FIGURE 12.9: Pictures of different stages of the installation of the six ToF planes in the baby-basket.

To evaluate the adequate performance of the system under realistic installation and geometrical conditions a metal structure which mimics the upstream portion of the ND280 basket (so-called baby-basket) was assembled at CERN. The adequate operation of the TFC requires adequate synchronization and similar behavior for all its channels. To test the system prior to its shipment to Japan, all ToF planes were mounted in its final geometry in the baby-basket and cabling operations have started. Illustrative pictures of the procedure and result are presented in Figure 12.9. In the near future, the SAMPIC DAQ will be connected to all channels to perform final tests.

12.5 Data-driven detector signal characterization with constrained bottleneck autoencoders

The waveform's shape variation observed in Figure 12.6 has been recently revisited, see Figure 12.10 and Figure 12.11 and, in general terms, at least two effects seem to play an effect. The rising edge of the waveform is mainly the consequence of the direct light reaching the photosensors. The closer the track is to the bar-end the steeper is the rising of the signal. Light reflected on the opposite bar end reaches the photosensor with a predictable delay equivalent to two times the bar length (220 cm) divided by the effective velocity of the light in the bar, which is about

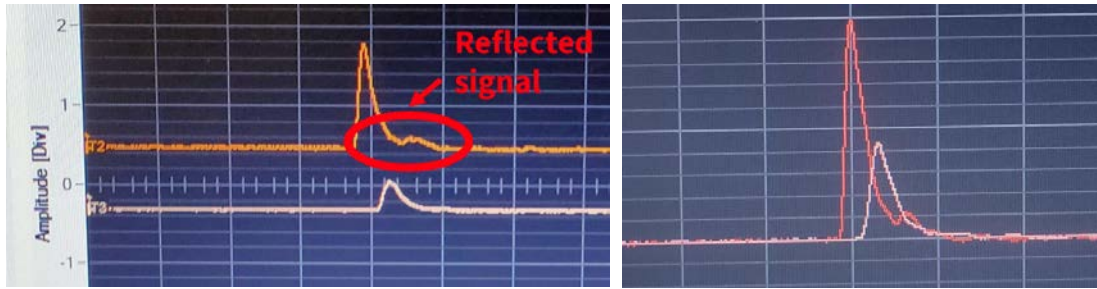


FIGURE 12.10: Pictures of recorded signals for a single ToF bar. Different waveforms correspond the two arrays of SiPMs in one bar. When the track crosses the bar off-center a secondary peak appears in the waveform shape due to the light reflected on the opposite end. If the waveforms are superposed, it is clear that one waveform is delayed with respect to the other due to the uneven distance to the arrays of SiPMs. Image Credit: Emanuele Vila.

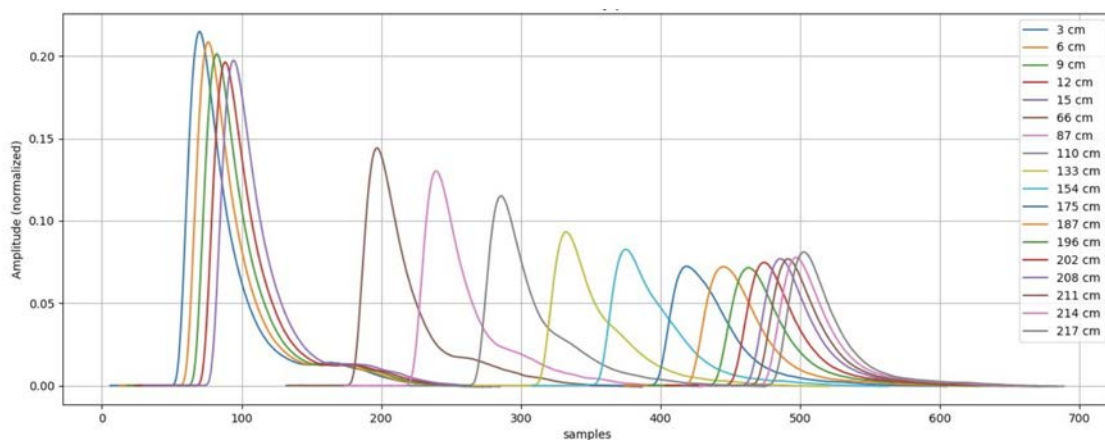


FIGURE 12.11: Average waveforms generated by cosmic rays crossing a single ToF bar at different distances of the SiPM array used to measure the signal. Image Credit: Emanuele Vila.

16 cm/ns.

The fall of the signal created by primary photons and the rise of the reflected photons create a signal waveform which changes quite significantly along the bar distance, see Figure 12.11. For some positions, the primary and secondary signals can even create a double peaked waveform. The modeling and prediction of this signal as a function of the track position is a difficult problem as no analytical description exists for the underlying mechanism ruling this behavior. Numerical simulations able to reproduce the complexity of the problem are difficult to build as several subtle effects play a role: The scintillation time in the plastic, the photon reflections in the bar, the attenuation experienced by each photon trajectory, the response of the electronics, etc. However, with the single bar setup waveform examples with labeled positions can be easily collected. The characterization of the ToF signals from labeled data examples corresponds to an instance of a common problem in HEP experiments, which is that to characterize detector signals directly from data when the underlying model is unknown but the physical parameters playing a role are understood and can be measured with the help of additional instruments.

Inspired by the particular necessities of the ToF, a generic solution involving constrained bottleneck autoencoders was presented in Ref. [9]. In the next subsections, the study is reviewed with minor additional comments.

Problem definition

Consider the deterministic response of a detector as a transformation f that maps a set of physics parameters, \vec{p} , (e.g. track position, angle, energy deposit, etc) into a set of detector signals \vec{s} , namely,

$$f(\vec{p}) \mapsto \vec{s}; \quad f^{-1}(\vec{s}) \mapsto \vec{p}. \quad (12.1)$$

Then, our aim was to learn transformations \hat{f} (and \hat{f}^{-1}) as similar as possible to f (and f^{-1}) directly from data with the only requirement of knowing the set of \vec{p} playing a role in the system and being able to collect data samples of \vec{s} for known \vec{p} configurations. It is worth noting that this situation is analogous to that of the ToF, where for each recorded waveform signal a the distance is known with the aid of the trigger system.

Toy problem

To mimic a functional shape similar to that earlier presented in Figure 12.6 and Figure 12.10 a toy transformation f was defined as:

$$\begin{aligned} \vec{s}(x) &= f(\vec{p} = \{\theta, \eta\})(x) \\ &= (1 + 0.5\theta)\mathcal{M}(-7|1 + 0.3\theta) + \mathcal{M}(7(\eta - 1)|1.2 + \theta) \end{aligned} \quad (12.2)$$

Where, the shorthand notation $\mathcal{M}(\mu|c)$ defines a Moyal distribution [566] with location parameter μ and scale c , which describes the energy loss of a charged relativistic particle due to ionization of the medium and approximates the Landau distribution with a systematically lower tail. The model takes two generic input physics parameters $\vec{p} = \{\theta, \eta\}$. In the case of the ToF, after normalizing the waveforms amplitude, the system might be well described by the use of a single physical parameter, the distance. However, to illustrate and discuss the method in a more generic fashion, potentially interesting to other experiments, a model with two physical parameters was used.

If x is interpreted as time, a signal $s(x)$ is measured in the detector at discrete consecutive instances of x such that a collection of signals \vec{s} constitutes a 1D waveform. Since for a given choice of \vec{p} the output waveform changes its shape, the this toy model was used to generate pairs of \vec{s} and \vec{p} reproducing what could be collected in the laboratory. Later, we pretended that f was unknown to face the problem of learning \hat{f} and \hat{f}^{-1} as close as possible to f and f^{-1} directly from the synthetic data examples.

12.5.1 Autoencoders

Over the last years deep learning methods have become crucial for modern data analysis and have started to play a important role in HEP. So far, most solutions have been reached through supervised algorithms, particularly applied to classification problems, with deep neural networks at the forefront. Recently, deep generative models have aroused as a novel unsupervised alternative, able to deal with both labeled and unlabeled datasets and to learn sophisticated transformation between spaces of very different dimensionality [567]. Autoencoders are a particular type of this novel algorithms. In autoencoders (AEs) a real input of arbitrary dimensionality \mathbb{R}^A is mapped into a real space output of the same dimensionality by following a set of transformations characterized by a bottleneck architecture. The bottleneck, often referred to as the latent space, has a reduced dimensionality \mathbb{R}^B , where typically $A \gg B$. As the algorithm is trained to minimize the difference between the input and the output distributions the autoencoder learns a compact representation of the data which is encoded into the latent space. Due to this, the transformation which maps the input into the latent space is named the encoder whereas the transformation which maps the latent space into the output is named the decoder.

Despite their recent appearance in the physics literature, AEs have already been studied for several interesting HEP applications. On one hand, AEs can be used to compress data by storing the much lighter latent space representation [568, 569, 570]. On the other hand, AEs average out the noise from different data examples during training and, therefore, they have great potential to denoise signals [571, 572, 573]. AE transformations are greatly interesting by themselves. If an AE is trained using non-anomalous signals, for instance produced with a well understood simulation, the AE reconstruction error can later be used to identify outliers and tag them as anomaly candidates. Thus, so far, anomaly detection has been among the most widely explored applications involving AEs in the HEP literature [574, 575, 576, 577, 578]. AEs can also be used to learn signal or background distributions directly from data. In this applications, AEs enable the generation of synthetic data by sampling in the latent space, an option explored in several studies [579, 580, 581]. However, if the latent space is unconstrained, no physical interpretation can be made of the latent space. Due to this, architectures in where the bottleneck is constrained have been studied in computer science, leading to the proposal of modified AEs, such as the Bounded-Information-Bottleneck AE (BIB-AE) [582]. The main difference with a standard AE is that in these modified algorithms additional information in the form of labels is used in the training phase in order to make the latent space interpretable. In HEP, this approach has been first explored recently via an algorithm dubbed the end-to-end Sinkhorn AE. Its use has been explored in the context of producing complex high fidelity simulation outputs for calorimeters by replacing simulators with AEs trained in simulated data [583, 584]. This has the main advantage of reducing the time and computational cost of generating simulated events. On this study, we further discussed the potential of latent space constrained autoencoders in HEP. In particular, we focused on a powerful and unexplored application: its use for data-driven detector signal characterization and, even more, how the same trained algorithm can be used not only to generate signals but also to do physical parameter estimations and signal denoising.

The constrained bottleneck autoencoder

A modified AE, similar to the BIB-AE, was used which, for generality, will be referred to as a constrained bottleneck autoencoder. A sketch of the algorithm is presented in Figure 12.12. Its main features are as follows: For training, events consisting of signals \vec{s} associated to physical configuration parameters \vec{p} are given as the input to the algorithm. The algorithm then performs a series of sequential transformations which generate an output signal \vec{s}' with equal dimensionality to \vec{s} . The bottleneck \vec{p}' corresponds to the centermost transformation layer and has the same dimensionality as \vec{p} . With the former settings, the network weights specifying the encoder and decoder transformations \hat{f}^{-1} and \hat{f} , corresponding to our target interest, are optimized by minimizing the loss over the set of input examples. Such loss consists of the sum of two terms. On one hand, the mean square error (MSE) between \vec{s} and \vec{s}' which accounts for the similarity of the input and output signals. On the other hand, the MSE between \vec{p} and \vec{p}' which accounts for the similarity between the latent space and the physical configuration parameters.

Architecture and implementation

The former architecture design has been driven by simple principles. In the first place, using convolutional transformation allows to identify patterns arising in the correlations among neighbor signal values. The number of iterations, filters, kernel size and stride were chosen after a set of dedicated architectural tests on the overall performance of the network. In the second place, the use of fully connected layers allows to combine the information from the different convolution filters and provides to the algorithm enough flexibility in the encoder and decoder transformations. Such flexibility is crucial, as our AE has a constrained bottleneck, and therefore, learning \hat{f} and \hat{f}^{-1} is significantly more challenging than in the unconstrained case. In this sense, stacking

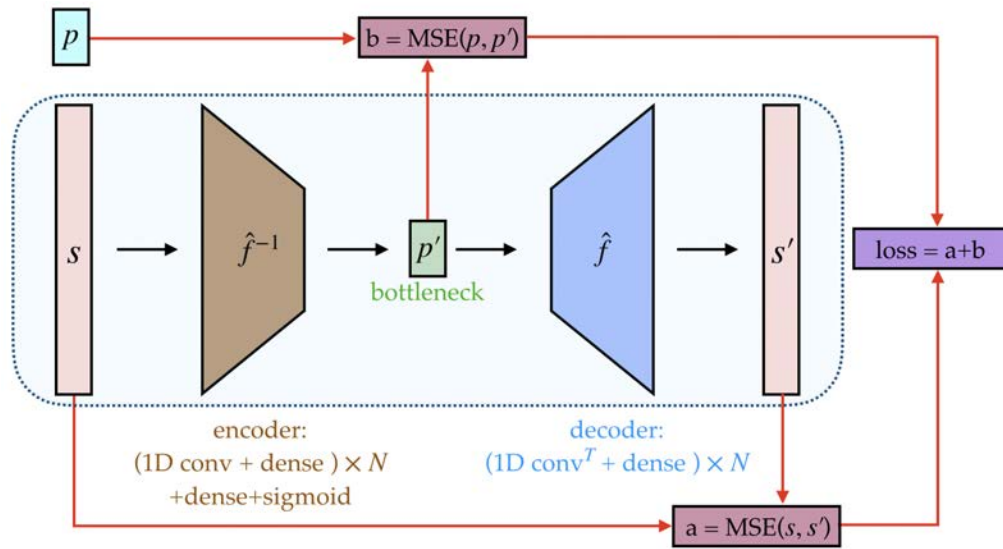


FIGURE 12.12: Sketch of the constrained bottleneck autoencoder under discussion.

N-times the former layers allows to organically increase the complexity of the network, either by increasing the number of filters, the number of repetitions, or both.

12.5.2 Methodology

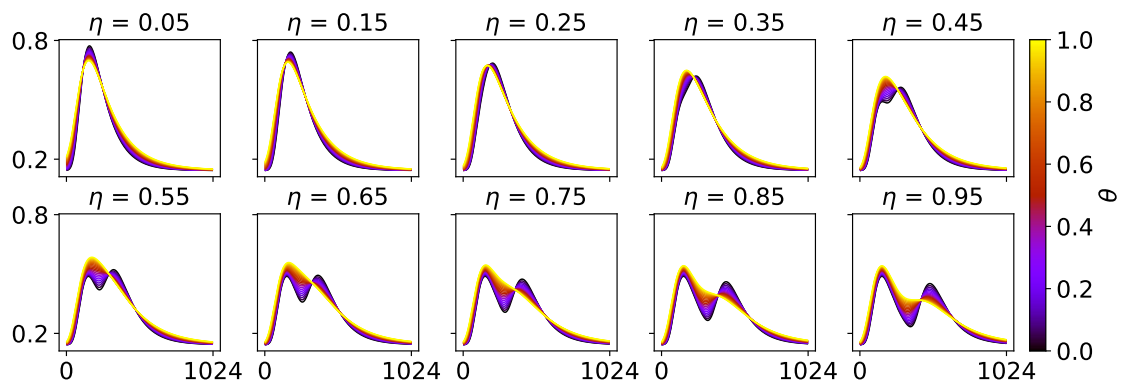


FIGURE 12.13: Functional normalized shape of $f(\vec{p})$ as described in Eq 12.2, evaluated in 1024 equidistant points along an interval of $x \in [-10, 10]$ to form waveforms. A colormap of θ for a series of slices of η is used to illustrate the dependency on both parameters.

In a realistic case, the waveforms would be affected by random fluctuations. To show the robustness of the method to random noise and to illustrate its denoising potential prior to the signal normalization each value of \vec{s} was varied independently, adding to it the result of random sampling from a Gaussian with the mean at the original signal value and a sigma of 0.05. At the normalization scale=0.8, this level of noise corresponds to 6.25% of the maximum possible signal amplitude. Example results of a set of 15 randomly chosen instances of \vec{s} compared to their associated $f(\vec{p})$ are presented in Figure 12.14.

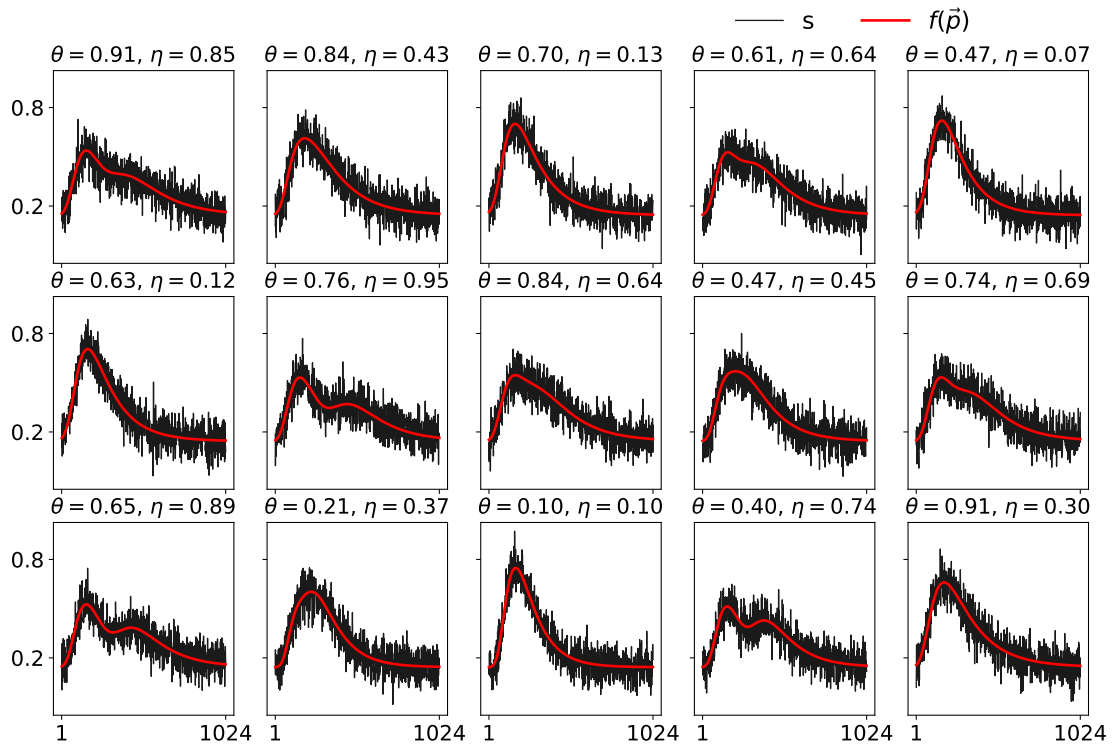


FIGURE 12.14: Examples of 15 random noisy waveforms in the test dataset compared to its original functional shape, specified by Eq. 12.2.

Training

For training and testing the system the dataset of 50k examples was split into two separate datasets: A training dataset with 40k signals and a test dataset with the remaining 10k events. The autoencoder was trained for 10 epochs (complete cycles to all the data), using the Adam optimizer with an initial learning rate of $5 \cdot 10^{-4}$ and a mini-batch size of 32 (which determines the amount of examples that are processed before updating the network parameters). During training the network weights are optimized by minimizing the loss function, which as earlier anticipated in Figure 12.12, consists on the addition of the minimum square error of the signal reconstruction accuracy and the latent space matching accuracy. The training for which the results are reported took about 50 min in a standard computer¹.

12.5.3 Results and discussion

The performance of the trained algorithm can be evaluated for different purposes. In the first hand, the quality of the learned $\hat{f}^{-1}(\vec{s}) \mapsto \vec{p}$ transformation is relevant to do estimates of the

¹2.3 GHz dual-core Intel Core i5.

physical parameters \vec{p} using signals as input. On the second hand the quality of the learned $\hat{f}(\vec{p}) \mapsto \vec{s}'$ is relevant to model the detector response and to produce realistic signals \vec{s} , e.g. if the algorithm is embedded in a Monte Carlo simulation. Notably, since the algorithm learns from multiple examples the random noise is averaged out, such that $\hat{f}(\vec{p})$ generates noiseless signals \vec{s}' , even if it learns from noisy examples \vec{s} . Due to this, the transformation $\hat{f}^{-1}(\hat{f}(\vec{s})) \mapsto \vec{s}'$ can be used to denoise signals. Each of these tasks were studied separately as presented in the following subsections.

Reconstruction of the physical parameters

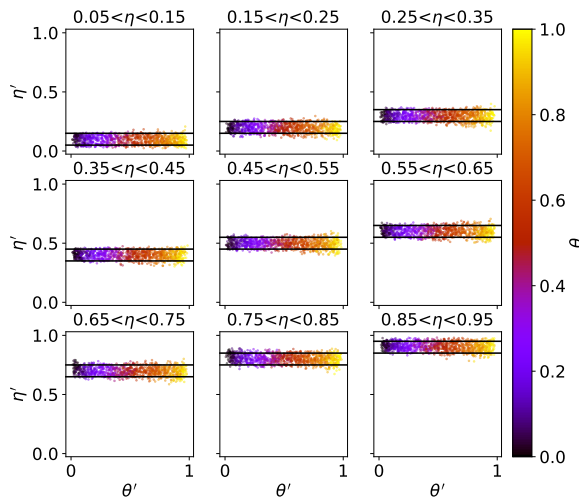


FIGURE 12.15: Distribution of the two reconstructed physical parameters (θ' and η') of the toy model for the whole test dataset. The reconstructed values are shown in slices of true η and colored with the true value of θ , allowing to visualize the latent space. The horizontal black lines show the constraints on the true values of η .

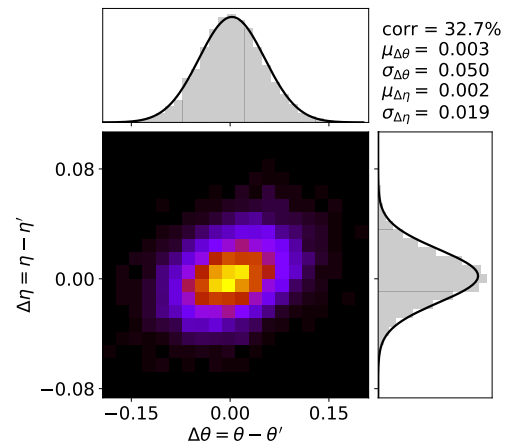


FIGURE 12.16: 2D distribution of the reconstruction error for θ and η and its 1D marginal error distributions including Gaussian fits. The correlation of the two errors is also presented.

The distribution of the reconstructed physical parameters, $\vec{p} = \{\theta, \eta\}$, associated to the signals for the whole test dataset of 10k events is presented in Figure 12.15. The results are presented in slices of true η and in a colormap of θ allowing to qualitatively understand the 2D latent space distributions in the whole phase-space. As expected, the encoder learns a transformation that maps signals \vec{s} associated to transformations determined by values of $\vec{p} = \{\theta, \eta\}$ to a latent space $\vec{p}' = \{\theta', \eta'\}$ where the typical distance between \vec{p} and \vec{p}' is small. This is explicitly shown in Figure 12.16 where the errors in each of the reconstructed physical parameters is presented as a 2D plot showing pairs of reconstructed $\{\theta', \eta'\}$ and their 1D marginal distributions. Notably, the errors are Gaussian distributed, and show negligible bias. The width of the distribution is different for the two parameters. This is expected, as the two parameters affect differently the waveform shape. In particular, looking into Figure 12.13 it is clear that a wide range of θ can render very similar waveforms, as for instance for small η values. From this results on the reconstructed latent space two major conclusions can be extracted. In the first place the algorithm is able to effectively learn the transformation $\hat{f}^{-1}(\vec{s}) \mapsto \vec{p}'$, allowing to do parameter estimations directly from detector signals. In the second place, no outliers are observed and the error distribution is Gaussian allowing to easily and reliably associate errors to the parameters estimated by means of this method.

Signal generation

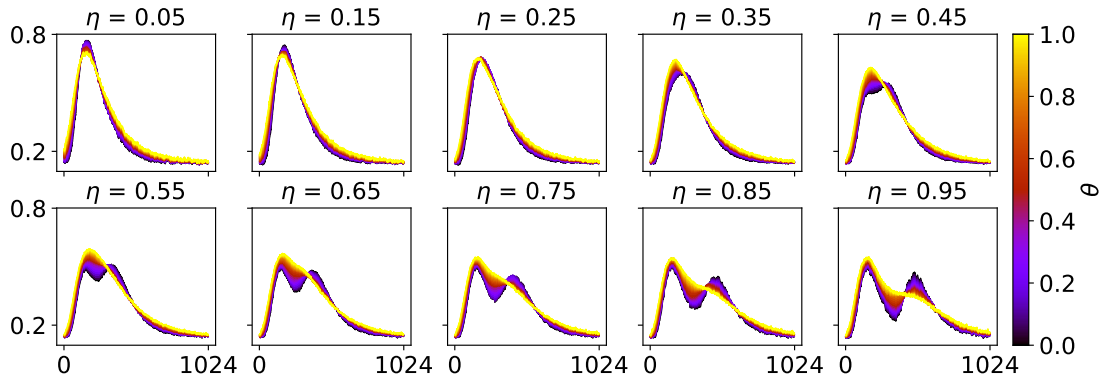


FIGURE 12.17: Functional shape of $\hat{f}(\vec{p})$ as learned by the algorithm. A colormap of θ for a series of slices of η is used to illustrate the dependency on both parameters.

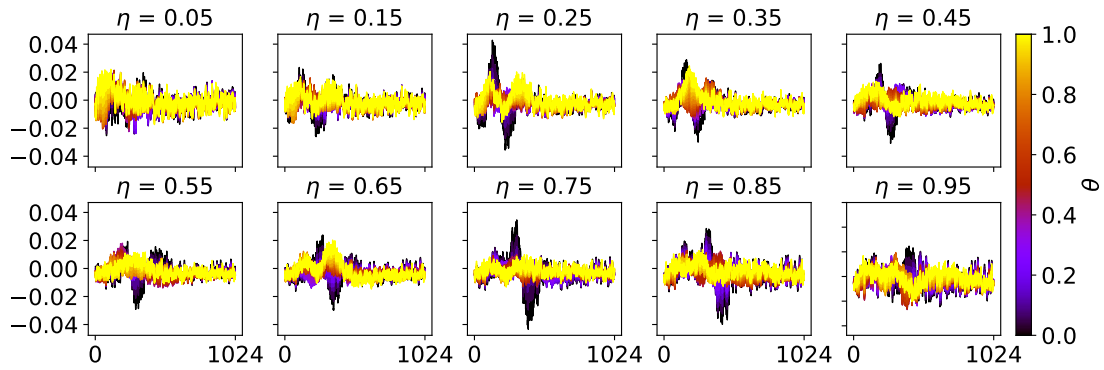


FIGURE 12.18: Subtraction of Figure 12.13 and Figure 12.17 to illustrate the difference of $f(\vec{p}) - \hat{f}(\vec{p})$.

The trained model can be used to characterize the transformation across the whole phase space, as presented in Figure 12.17. In the ideal case, this scan should be equivalent to that earlier presented in Figure 12.13. Eye inspection allows to draw qualitative conclusions. In the first place, overall, the algorithm has learned a transformation $\hat{f}(\vec{p})$ directly from data examples which generally resembles the true one, and the predicted signals do not show worrisome artifacts or instabilities. This is remarkable given that the transformation is learned from noisy data examples but the algorithm directly provides a denoised output. To draw quantitative conclusions, in Figure 12.18 we present a plot of the difference of the true and the learned model, namely a plot of $f(\vec{p}) - \hat{f}(\vec{p})$. For the majority of the phase-space the variations are very small, typically well contained within 2% of the maximum amplitude. The largest differences are below 4% of the maximum amplitude and are therefore sensibly smaller than the simulated noise level.

Signal denoising

Finally, as both $\hat{f}(\vec{s}) \mapsto \vec{p}'$ and $\hat{f}^{-1}(\vec{p}) \mapsto \vec{s}'$ were correctly learned we studied the reconstruction of $\hat{f}^{-1}(\hat{f}(\vec{s})) \mapsto \vec{s}'$. This has two main advantages. On one hand the results of the composite transformation map noisy signals to denoised signals. In the second hand, the errors in the reconstruction of physical parameters and in the generation of signals are correlated, and in consequence the composite transformation might have a superior performance than the two individual transformations.

To evaluate the quality of the reconstructed denoised signals \vec{s}' from noisy signals \vec{s} , the output

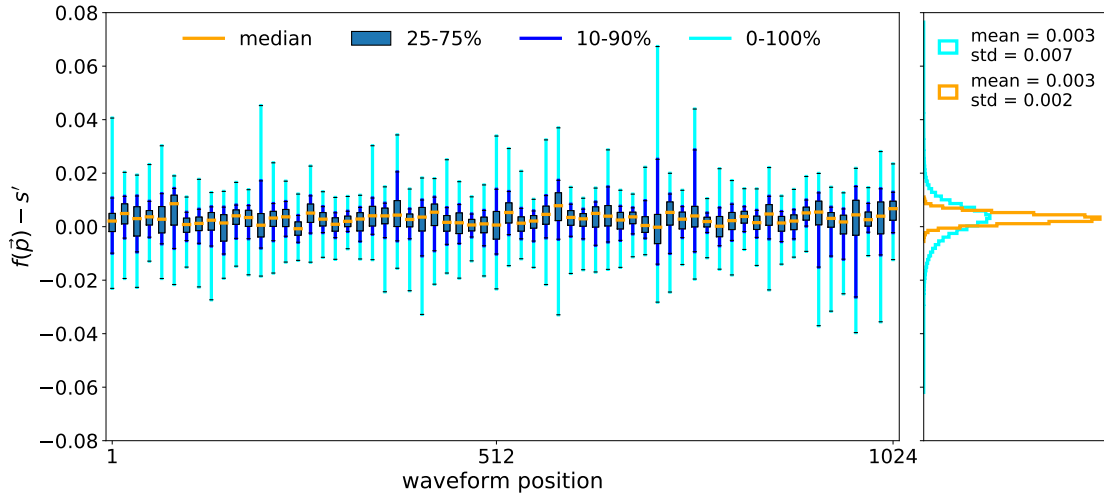


FIGURE 12.19: Left panel: Distributions of the signal reconstruction error including various quantiles for one every sixteen waveform positions for the whole test dataset of 10000 waveforms. Right panel: Aggregated distribution of all 1024×10000 signal reconstruction errors (cyan), and its 1024 medians (orange). The signal reconstruction error is defined as the difference between the normalized noiseless signals provided by Eq. 12.2 and the signals generated by the transformation $\hat{f}^{-1}(\hat{f}(\vec{s})) \mapsto \vec{s}$.

of $\hat{f}^{-1}(\hat{f}(\vec{s})) \mapsto \vec{s}$ were compared to $f(\vec{p})$ for the 10k events in the test dataset. The results are presented in Figure 12.19. In the left of the plot, the signal reconstruction error distributions for all waveform positions multiple of 16 are presented. The decision of showing only one in every 16 positions was driven by a clearer visualization, reducing the number of distributions from 1024 to 64. To show information for all the waveform positions, in the right part of the plot aggregated results for all the 1024 positions are shown. This aggregated results consists of a distribution of the 1024 median positions in each waveform position (orange) and the 1024×10^4 values reconstructed in any position for all events (cyan).

The results allow to draw numerous conclusions. In the first place, across all waveform positions the errors in the median are remarkably small, with a typical bias (standard deviation) similar to 0.3% (0.2%) of the maximum amplitude. The error in all reconstructed signals, is slightly wider but still of excellent quality with a typical bias of (standard deviation) 0.3% (0.7%). In the second place the reconstructed signals in all positions are densely packed around the median without any significant outliers. The maximum error for the 64 positions under consideration is comparable with noise fluctuations and a very smooth and well controlled signal prediction by the network across the whole test dataset is observed.

To illustrate the accuracy and signal fidelity of the results presented in Figure 12.19 all the 10k events in the test dataset were sorted by their mean squared signal reconstruction error. Waveforms at different error percentiles are presented in Figure 12.19, being the percentile 0 (percentile 100) the event with minimum (maximum) signal reconstruction error. The results show excellent prediction fidelity across all percentiles with very minor differences even for percentile 100.

12.6 ToF status and future plans

The ToF panels are expected to be transported to J-PARC in some months, i.e. before the end of the year 2022, and installed in ND280 between 2022 and 2023. Recently, data has been collected with a single bar and used to characterize the response of the detector. In this context, a novel method to perform data-driven signal characterization using constrained bottleneck autoencoders has been proposed [9], showing promising results. In the near future, testing the algorithm in ToF data is expected.

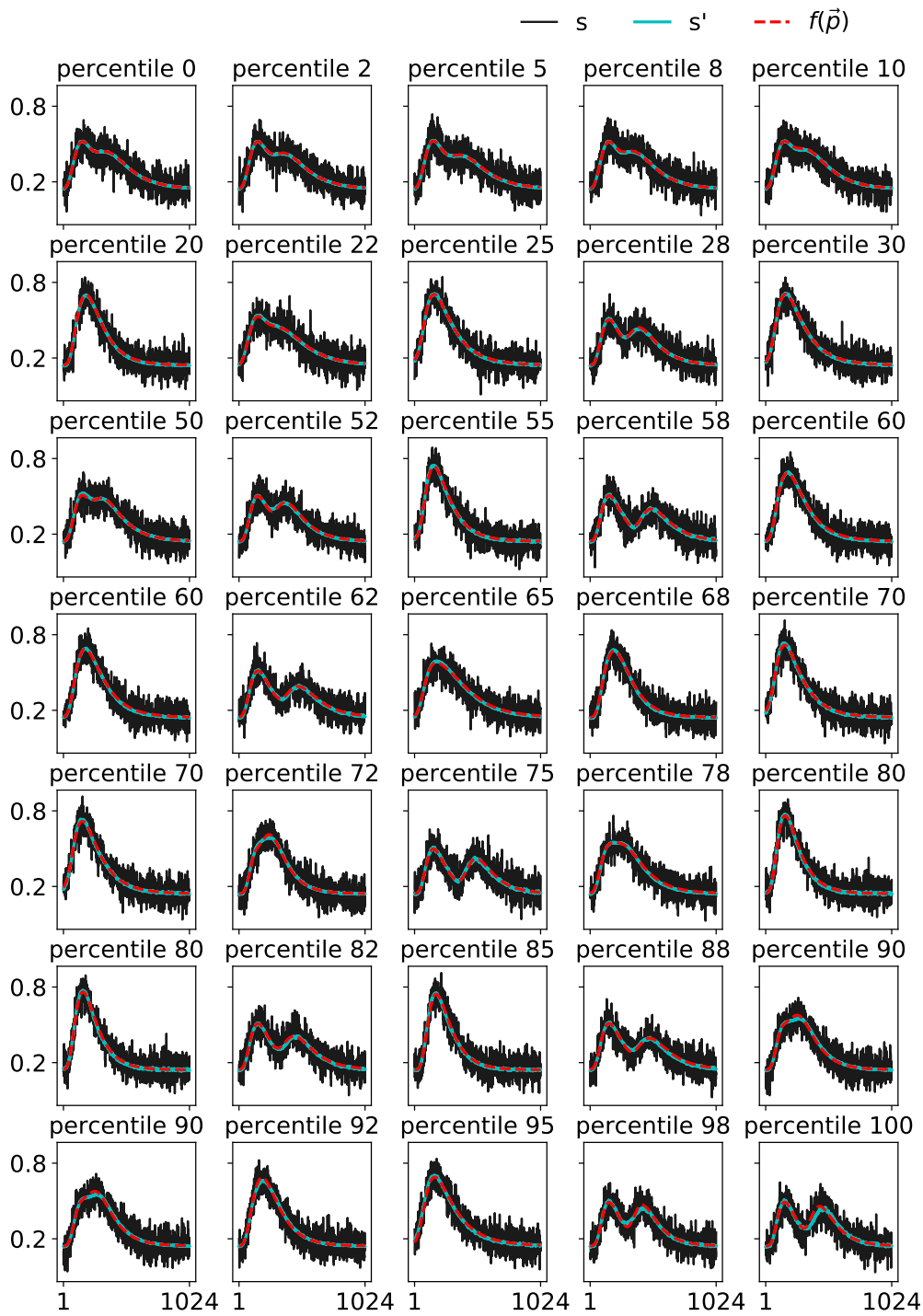


FIGURE 12.20: The input noisy signal \vec{s} is compared to the denoised generated signal \vec{s}' and to the true shape of the toy model $f(\vec{p})$ for a total of 35 examples in the test dataset. The examples are chosen by their mean squared reconstruction error percentile. Percentile 0 (100) corresponds to the best (worse) reconstructed signal in the whole test dataset of 10k waveforms.

As of now, most efforts are centered in developing a SAMPIC based DAQ. In this context, work is ongoing to validate the performance of the SAMPIC boards, to develop the DAQ software and to design the trigger logic and the calibration procedures. The integration of the ToF signals in the global ND280 upgrade reconstruction is also ongoing.

Part IV

Conclusions

Chapter 13

Conclusions

“The moon and the sun are travelers of eternity. So are the years that pass by. Either drifting life away on a boat or meeting age leading a horse, each day is a journey and the journey itself is home. [...] Some time ago, came a day when the clouds drifting along with the wind aroused a wanderlust in me, and I set off on a journey to roam along the seashores.”

– MATSUO BASHŌ

Neutrino physics is well immersed in the era of precision measurements. With the aim of finally solving questions that have been open for decades many experiments are ongoing and many others are planned to start its operation in the next years. Among them, T2K is a world-leading experiment in the study of neutrino interactions and neutrino oscillations. After 10 years of taking data T2K has made some of the most important discoveries in neutrino physics. A key element in this achievements has been the use of a pioneering near detector constrain that has reached an unprecedented degree of sophistication through the detailed control of the flux prediction, neutrino interaction and detector response models.

In recent years, the flux prediction has been notably improved with the use of T2K’s replica target data collected by the NA61/SHINE experiment. The neutrino interaction and detector response models are constantly revisited and expanded via dedicated studies, often leading to cross section measurements. After a decade of studying CC interactions, the level of error for these processes is now well controlled within the boundaries of what it is possible to understand with the existing amount of collected data and the capabilities of ND280. NC interactions, however, are much less understood. Due to this, neutrino neutral current interactions producing a single charged pion in the final state are an important source of uncertainty in T2K’s oscillation analysis.

To reduce this uncertainty and to extend T2K’s expertise on neutrino interactions to the domain of NC in this thesis the first detailed study of neutrino NC interactions producing a single positive pion ($\text{NC}1\pi^+$) has been carried out. These processes were only measured once before in history when event rates were reported by the Gargamelle bubble chamber experiment in 1978. The new selection criteria uses ND280 to identify the largest statistical sample ever studied for this process while retaining good purity in its most relevant kinematic phase space. In addition, three control regions have been developed to constrain the role of the most important backgrounds in the signal sample. The preliminary cross section measurement for protonless $\text{NC}1\pi^+$ events, limited to $\cos\theta > 0.3$ and $0.2 \text{ GeV}/c < p_\pi < 1 \text{ GeV}/c$, is in good statistical agreement with the prediction of both NEUT and GENIE. The uncertainty associated to this

measurement is of 21.5% and it has been estimated that reaching a level of error of about 15% could be possible in the future by simply increasing the amount of collected data. This result is a major step forward in the knowledge of this process. As of now, the best constrain for it in T2K is around 60%. The results are expected to lead to a publication and to a new constrain for future T2K's OAs.

In order to boost the current capabilities of T2K a set of upgrades are ongoing and planned for the near future, including a beam power increase and a major upgrade of the ND280 detector. In this Thesis, contributions to the assessment of the ND280 upgrade expected performance and to the development of the three new technologies to be installed in ND280 have been presented.

In the first place, simulation studies were done that support the ND280 upgrade project showing a significant increase in the collected data per POT, a widely improved angular acceptance and a dramatic reduction on the hadron detection thresholds.

In the second place, the novel HATPC readout technology based on the ERAM modules was validated and studied. The results show the excellent properties of the ERAMs that match or outperform all figures of merit in standard bulk Micromegas while reducing the readout channels by one third.

In the third place, numerous developments concerning the SuperFGD detector, which will play the role of the new neutrino target in ND280, have been presented. SuperFGD prototype data was used to do the most detailed studies so far about this technology that validate its novel concept and show excellent tracking and particle identification potential both for charged and neutral particles. Contributions to the final reconstruction methods of SuperFGD have been also presented, in particular, a novel solution to enhance the detector 3D tracking using graph neural networks was developed.

Lastly, the status of the ToF panels has been reviewed, including the ongoing activities to prepare this technology for installation and to better understand its waveform signals, crucial to extract optimal information from this detector. In that context, a novel method to perform data-driven signal characterization was developed that is rooted in constrained bottleneck autoencoders.

Overall, the activities related to the ND280 upgrade have contributed to push the novel detector concepts from the R&D stage to the state of readiness for installation. The installation is expected to start in the second half of 2022 and conclude in 2023.

Summing up, the work presented in this Thesis spans from analysis contributions to instrumentation developments for the T2K experiment. Independently, each of these studies provides value to the field of neutrino research advancing our knowledge on how neutrinos interact and how to improve the existing instruments to produce better measurements in the future. Combined, these projects aim to help the T2K experiment to continue its exciting line of research and to deepen our understanding of neutrino physics and of Nature at its most elementary level.

Appendix A

DUNE and the photon detection system of the protoDUNE-DP detector

“Most physicists like myself won’t believe the result until every possible caveat has been investigated and/or the result is confirmed elsewhere.”

– LISA RANDALL

This appendix overviews the DUNE experiment and the development of the LArTPC technology and presents the preparation, installation and preliminary performance of the photo-detection system (PDS) of the protoDUNE dual-phase (DP) detector.

A.1 Introduction

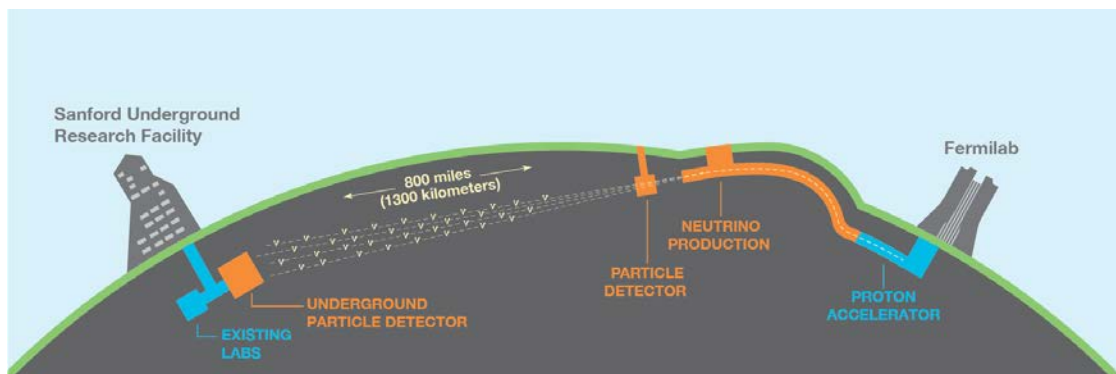


FIGURE A.1: Cartoon of the DUNE experiment showing LBNF beamline at Fermilab, in Illinois, and the DUNE detectors in Illinois and South Dakota, separated by 1300 km. Image Credit: <https://www.dunescience.org/>

The Deep Underground Neutrino Experiment (DUNE), illustrated in Figure A.1, is a future accelerator based neutrino oscillations experiment in the US which consists of three core components: A new high-intensity neutrino beamline, a composite near detector facility and a massive far detector complex consisting of several Liquid Argon (LAr) TPCs. The technical specifications and studies which back up this new experiment motivations and its design can be found in an extensive TDR consisting of four volumes [110, 12, 111, 112].

A.1.1 Working principle of LArTPCs

Liquid Argon TPCs, in general, work by the same principles of any other TPC and, accordingly, are excellent trackers and dE/dx sensitive instruments. The main disadvantage of gaseous TPCs for the study of neutrino interactions is their very low target mass. Replacing gas by liquid allows to increase very significantly the TPC target mass in the same volume. To keep the electron attachment at acceptable levels the liquid must be a noble gas and due to its abundance Argon is by far the most extended option for liquid TPCs. Nonetheless, to liquefy Argon and to maintain it in liquid state, cryogenic temperatures are necessary and, consequently, LArTPCs are enclosed in cryostats. Inside them, electrically isolated from the walls a set of rings forming a voltage divider are installed to provide a smooth electric field which guides the electrons towards the anode, located on one of the ends of the chamber. In the anode, the readout system is installed. Depending on its design we can distinguish between single- and dual-phase LArTPCs. For both solutions, a PDS is installed. In LAr the amount of primary scintillation light (s_1) is large enough to be detected. The time associated to the light detection gives a time reference which, paired with the known drift velocity, allows for a precise determination of the drift coordinate, making of LArTPCs excellent 3D trackers. Additionally, the light collection can be used to improve the calorimetry measurements and to trigger for non-beam events.

A.1.2 History and state-of-the-art of LArTPCs

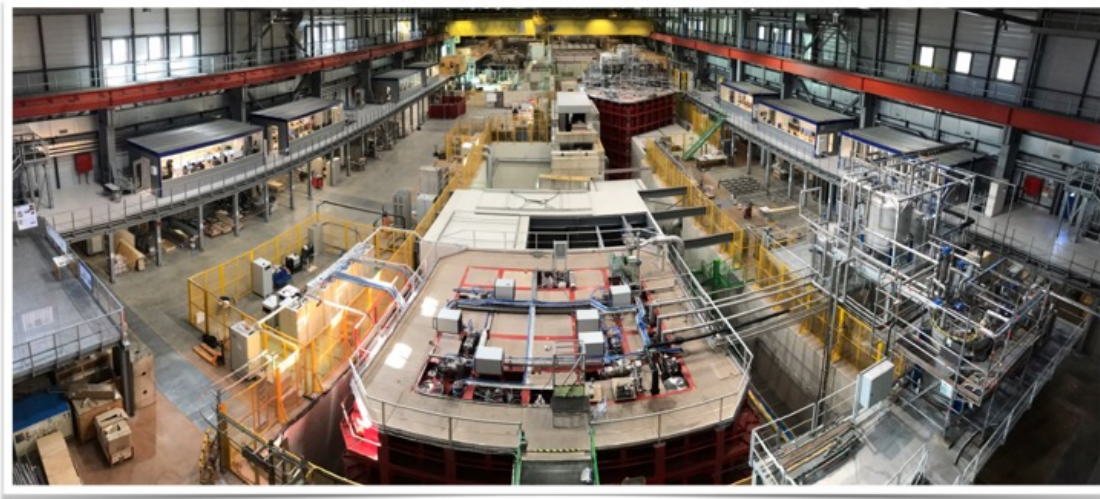


FIGURE A.2: ProtoDUNE-SP and ProtoDUNE-DP cryostats in the CERN Neutrino Platform at CERN. At front and center is the top of the ProtoDUNE-SP cryostat. The ProtoDUNE-DP cryostat with its painted red steel support frame visible is located at the rear of the photo on the right side of the hall. Figure from Ref. [12].

LArTPCs were first proposed in 1977 [585], and in the decades of the 1980s and 1990s several studies were made to prove the validity and potential of this technology [586, 587]. The most notable and largest of these experiments was the 3 ton LArTPC built for the ICARUS project [588, 589]. Building on this findings, in the 2000s the first proposals to build kileton scale LArTPC experiments started to arise [590]. Also in the 2000s the ICARUS T600 detector was built in Gran Sasso, with a large mass of 0.76 kT tons [591, 592]. In the 2010s, a LArTPC-based experimental neutrino program was ignited in the US with the aim to develop this technology, to exploit the Booster Neutrino Beam at Fermilab (BNB) [593] and to explore the LSND anomalous results [137]. In 2010, the 170 liters ArgoNeuT LArTPC was built in Fermilab, and used to measure for the first time differential neutrino cross sections in Argon [310]. In 2015, the

μ BooNE LArTPC with an Argon weight of 0.17 kT started tacking data [309] and a proposal was launched to build a three detector short-baseline neutrino oscillation facility at Fermilab [594]. It would consist of μ BooNE, a new (0.112 kT) LArTPC named Short Baseline Near Detector (SBND) [595] and the ICARUS T600 detector. In 2017, ICARUS T600 was moved to Farmilab, where it started tacking data in 2020 [596]. The DUNE experiment, with a CDR published in 2015 [597], it is expected to be the leading experiment for this type of technology in the future. For its far detector, two different types of LArTPCs are considered: A single-phase LArTPC, and a dual-phase LArTPC. To validate their designs and prove for the first time many technical challenges for this technologies two large prototypes were built an operated at CERN in the late 2010s and early 2020s: the protoDUNE single-phase (protoDUNE-SP) and the protoDUNE dual-phase (protoDUNE-DP) detectors, both with an approximate total Ar weight of 0.75 kT. A picture of the neutrino platform at CERN with this two prototypes is presented in Figure A.2.

A.2 The protoDUNE-DP detector

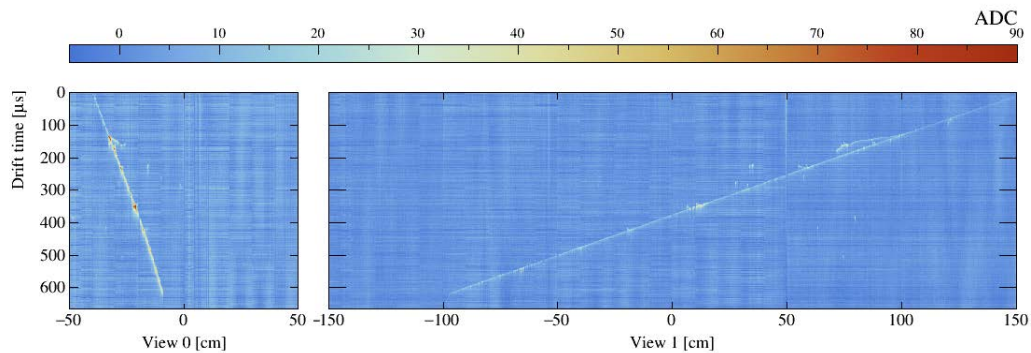


FIGURE A.3: Event display of a through going muon recorded in the WA105 detector. Figure from Ref. [598].

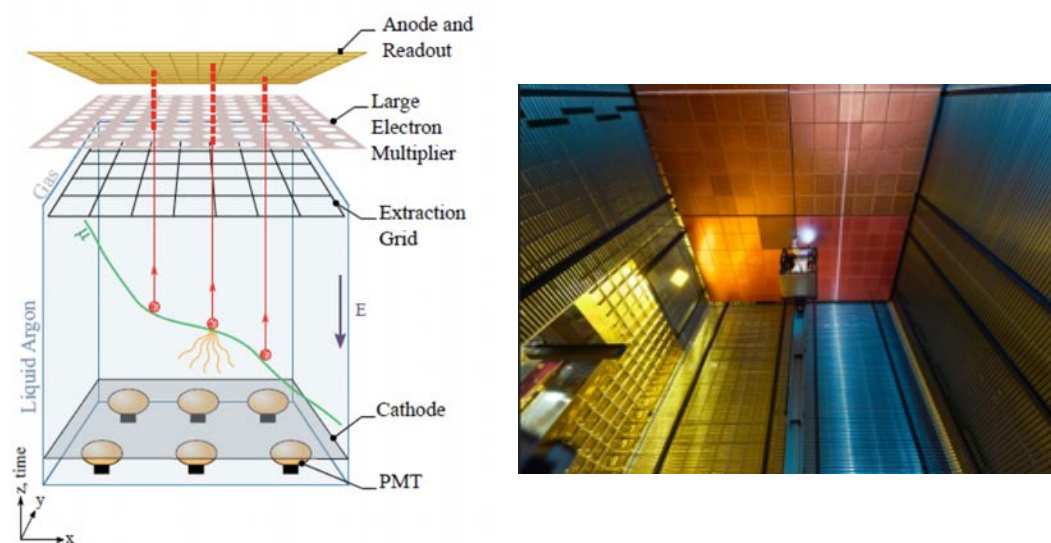


FIGURE A.4: Left: Sketch of protoDUNE-DP. Right: Picture of the protoDUNE-DP detector with the anode plane installed prior to the installation of the field cage structure. Figures from Ref. [12].

In dual-phase LArTPCs a vertical drift is used. This allows to fill the cryostat with LAr only up to a certain level, typically close to the anode plane, whilst the rest of the volume consists on gaseous Argon. Using an extraction grid at the liquid-gas interface the electrons are extracted from the liquid and inserted to the gas where a higher electric field is applied triggering an avalanche process that amplifies the primary ionization signal. During this avalanche process, electroluminescence secondary scintillation light (s_2) is produced.

The DP technology for DUNE was first tested at large scales using the WA105 detector at CERN [598, 599]. It was a $3 \times 1 \times 1$ m³ demonstrator, with an active target mass of 4 tons. An event display obtained with WA105 is presented in Figure A.3. The protoDUNE-DP, which started tacking data in 2020, is the largest of this detectors ever built. A sketch and a picture of the protoDUNE-DP detector are presented in Figure A.4.

A.3 The photo-detection system of the protoDUNE-DP detector

The light photo-detection system of the protoDUNE-DP detector consists of 36 PMTs (Hamamatsu R5912-02mod) with a diameter of 8 inches and a gain of up to 1×10^9 . All the PMTs were prepared (installed) in the summer of 2018 (2019) and used to collect data in 2019 and 2020. The results of the analysis of this data can be found in Ref. [13].

A.3.1 PMT preparation

Scintillation light in LAr is vacuum ultraviolet (VUV) with a wavelength similar to 127 nm. Due to this, the PMTs are usually coated with tetraphenyl-butadiene (TPB) that shifts the wavelength of VUV photons to about 430 nm, a wavelength to which the PMTs are directly sensitive to.

In 2018, a vacuum chamber developed to coat 360 PMTs with TPB for the ICARUS T600 experiment was used to prepare the 36 PMTs of the protoDUNE-DP detector. Figure A.5 shows a sketch and pictures of the instrument. A report on the coating procedure and most relevant results can be found in Ref. [11]. The overall methodology consisted in:

- Unpacking the PMT from its individual box.
- Test its signal response in a dark environment to check for good quality prior to the coating procedure.
- Dismount the metal frame housing each PMT and designed to install them in the protoDUNE-DP cryostat and to avoid them to float in the LAr.
- Clean the PMT with ethanol.
- Install the PMT in the vacuum chamber.
- Insert 0.8 g in a Knudsen cell.
- Close vacuum chamber and reach the necessary vacuum level (below 3×10^5 mbar).
- Warm up to Knudsen call to 220° C, opening a protecting shutter when reaching 190° C to evaporate and deposit the TPB on the PMT surface.
- Undo the vacuum, extract the coated PMT and perform a visual inspection check with a UV lamp.
- Reinstall the metal frame holder. Test the signal response of the PMT and store it ins original box.

In total 40 PMTs with polished surface were coated, including 4 spares. One of the spare PMTs was used to test the resistance of the TPB coating. The test consisted in placing the PMT in a small open dewar which was then filled with LAr from the bottom to avoid the LAr to flow directly across the PMT surface and was immersed completely in liquid argon before 1 hour.

Since neither the PMT nor the dewar were cooled down before the filling the LAr started to boil, leading to drops of LAr falling on the TPB coating, mainly from the side of the PMT close to the tube. The PMT was later examined for damage in the TPB coating and, as presented in Figure A.6, small spots with a near complete removal of the TPB were found. To explore this effect, further tests were performed in harsher conditions and were compared to that of sandblasted PMTs such as those used in the ICARUS T600 experiment. The results demonstrated that, whilst immersing a polished PMT in LAr in conditions similar to those expected in the detector cryostats no damage is observed, in harsher conditions sandblasted PMTs offer a superior performance in retaining their TPB coating. Additionally, the quantum detection efficiency for both polished and sandblasted PMTs was compared and found to be almost equivalent.

In light of the thermal shock tests results the decision was taken to remove the TPB coating in 30 of the PMTs by cleaning its surface with ethanol. To wavelength shift the photons a sheet of polyethylene naphthalate (PEN) was placed on top of each of the uncoated PMTs.

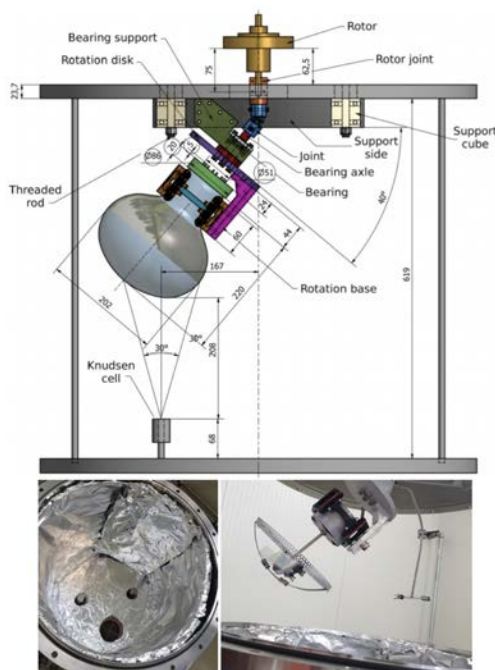


FIGURE A.5: Top: Sketch of the TPB coating instrument used to coat PMTs for the protoDUNE-DP detector Bottom: Images of the vacuum chamber and the PMT holder with a PMT mock up for calibration tests. Figure from Ref. [11].

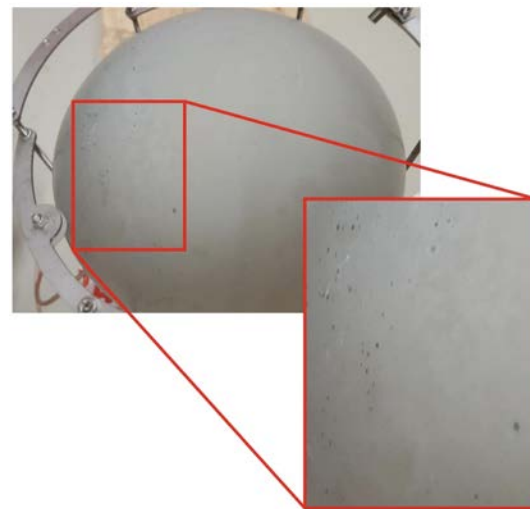


FIGURE A.6: Image of a polished PMT with TPB coating after immersion tests in LAr. The red box highlights the area with observable TPB coating imperfections. Figure from Ref. [11].

A.3.2 Installation

The protoDUNE-DP PDS system consists of a total of 36 PMTs, 30 with PEN foils and 6 coated with TPB, arranged in the configuration presented in Figure A.8. The installation consisted in placing the PMTs in its final location at the bottom of the cryostat and attach them to dedicated fixations using screws. Each PMT was connected to a single cable that is used to provide power and readout the signal. Additionally, a light calibration system (LCS) was installed, consisting of blue LED light distributed by a fiber system with a fiber-end pointing at each PMT. The necessary cables for the operation of the PDS were routed to the top of the 8 m high cryostat and guided outwards using feedthroughs. A picture of the installed PDS is presented in Figure A.8.

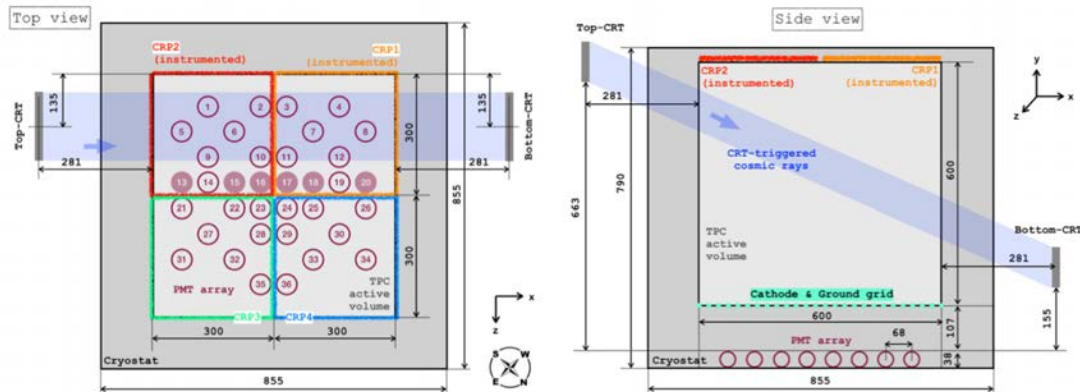


FIGURE A.7: Sketch of the protoDUNE-DP detector highlighting those elements relevant for its PDS. Filled (empty) circles correspond to PMTs with TPB coating (PEN foil). Figure from Ref. [13].

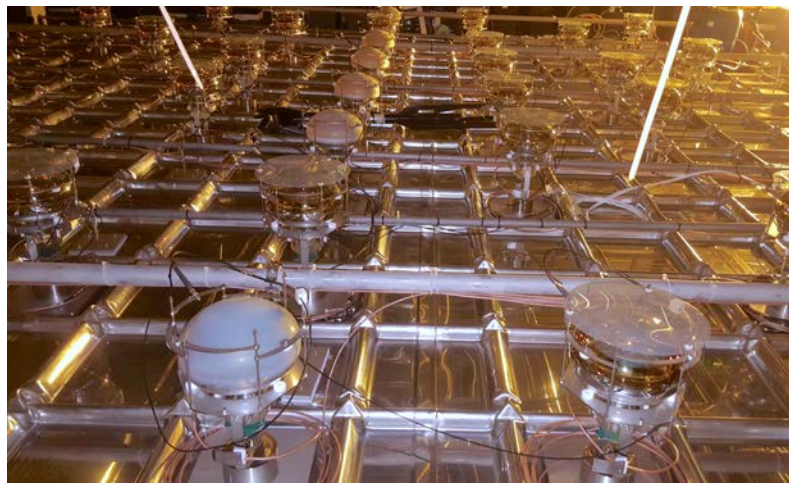


FIGURE A.8: Picture of the installed PDS in the protoDUNE-DP detector. Image from Ref [13].

A.3.3 Performance results

The analysis of the performance of the protoDUNE-DP PDS has been recently completed by collaborators using data and it is available in Ref. [13]. The main results are the following:

- Stable data collection conditions were achieved for all the 36 PMTs of operation along the 18 months of data tacking.
- PEN foils were used for the first time in a large scale LArTPC. The results show that the most widely extended option of coating the PMT surface with TPB is about three times more efficient than the PEN foil. In consequence, a PDS based exclusively in PMTs coated with TPB will be needed for DUNE in the future to achieve its low-energy physics program goals.
- Both s_1 and s_2 signals were recorded successfully and observed in all PMTs even at the maximum drift distance of 7 m.
- A significant ($\sim \times 2$) light detection increase was achieved by doping the LAr with Xenon (5.8 ppm).

Appendix B

ASTRA a novel range telescope for proton computerized tomography

“In the Radiation Laboratory we count it a privilege to do everything we can to assist our medical colleagues in the application of these new tools to the problems of human suffering.”

– ERNEST LAWRENCE

In the context of the development of new technologies for the ND280 upgrade presented in this thesis the possibility came up to combine multiple of those advancements to propose a novel range telescope for proton computerized tomography. This appendix reproduces the studies described in Ref. [14], where the proposed detector, named ASTRA, as well as the feasibility studies made to evaluate its potential performance are described.

B.1 Introduction

Cancer is the second most likely cause of death worldwide [600]. Consequently, developing novel methods and technologies to treat oncological patients is a very active field of research. From the high energy physics perspective multiple significant contributions have been made especially concerning diagnostic methods based on medical imaging and treatments consisting in attacking tumors by means of high energy particle beams. In this regard, among oncology treatments, X-ray radiotherapy is a well established technique, being used in about 30% of the patients [601]. However, a photon beam dose profile is exponentially decaying such that in order to treat the tumor a radiation dose is unavoidably delivered to the healthy tissue. Due to this, a better alternative is that of proton beam therapy [602]. As it has been earlier reviewed in this thesis, protons deposit more energy as they slow down delivering a very high and localized dose close to the stopping point. Because of this, if a beam of protons is prepared to stop in the tumorous tissue the patient can be treated effectively whilst reducing the damage to healthy tissue [603, 604]. There is however a major setback, as in order to plan the proton treatment a high quality 3D map of the proton stopping power (PSP) in the patient’s body is necessary. State-of-the art techniques consist in building this map with photons, however, the conversion from photon to proton stopping powers results in non-negligible uncertainties that hinder this method [605]. Therefore, in order to advance this treatment alternative it is urgently necessary to develop a substitute method which allows to reliably and safely generate accurate PSP maps. In this sense, proton computerized tomography (pCT) it is widely regarded as the best fitting candidate, however, devices able to meet

optimal performance are not yet available. In this sense, the ASTRA detector, which is presented below, is intended to fill this gap.

B.2 pCT design

In general, a pCT system requires:

- A *position tracker*, able to reconstruct the proton trajectory within the body.
- An *energy tagger*, able to reconstruct the proton energy.

Hence, in order to evaluate the potential performance of the proposed range telescope we proposed a full pCT system, which is sketched in Figure B.1. It consists on a position tracker made up of four Depleted Monolithic Active Pixel Sensors (DMAPS) placed in pairs either side of a phantom and A Super-Thin RANGE telescope (ASTRA) located downstream.

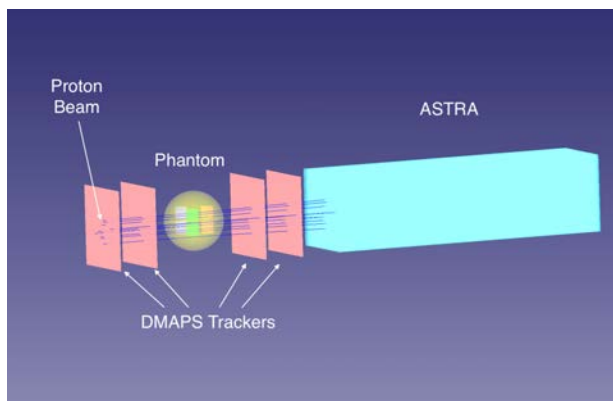


FIGURE B.1: 3D visualization of the pCT system with 4 DMAPS planes, a spherical phantom with 6 cylindrical inserts and the ASTRA range telescope. In the image, ten protons (dark blue lines) are shot into the system. Figure from Ref. [14].

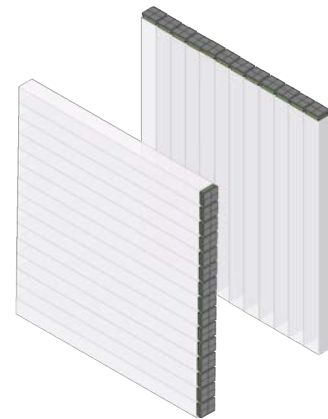


FIGURE B.2: Drawing of 2 layers of the ASTRA geometry. Each plane is made up of bars. The beam would enter in perpendicular to the planes surface. Image Credit: Dana Douqa.

B.2.1 The DMAPS-based tracker

DAMPS were developed in the context of the high-luminosity upgrade of the inner tracker of the ATLAS detector [606, 607]. They have a fast response and fine pixelization, making them excellent candidates to build a proton tracker. The DMAPS-based tracker would consist of four identical DMAPS organized in two sub-trackers, front and back, each formed by a pair of DMAPS separated by 50 mm. The distance between the first and last DMAPS would be of 150 mm. We simulated the DMAPS following the specifications in Ref. [608], with a Silicon thickness of 100 μm and a total area of $10 \times 10 \text{ cm}^2$ containing 2500×2500 pixels of $40 \times 40 \mu\text{m}^2$.

B.2.2 ASTRA

The ASTRA detector geometry was inspired by the Fine Grained Detector (FGD) modules in ND280 [452]. Its design combines technological advancements developed for the Time-of-Flight panels [558, 525] and the SuperFGD detector [533, 3], earlier reviewed in this thesis. In particular ASTRA was conceptualized as made of bars of $3 \times 3 \times 96 \text{ mm}^3$ arranged in layers oriented in alternate axis, see FigName B.2. We assumed the same plastic material as in SuperFGD, including an

etched surface of 50 μm to achieve good optical isolation between bars. MPPCs would be coupled to plastic bulk of each bar as in the bars of the ToF detector. For the electronics specifications we guided our studies assuming that CITIROC-based electronics, such as those in SuperFGD [6], could be used.

B.3 Methodology

A custom GEANT4-based simulation was implemented including all the relevant geometrical features of the detector earlier described. The detector response was simulated as follows. The energy deposits provided by GEANT4 in each DMAPS plane was discretized in a list of pixels following a structure analogous to that expected in the real output. This included a threshold of 850 electrons, based on preliminary laboratory tests, with the goal to minimize the noise generated by secondary electrons. For ASTRA, the energy deposits were converted in to a number of photoelectrons (PE) and discretized in a list of bars hits. This process included the random detection of the photoelectrons by the MPPCs, which generated a smearing of about 10%. Detection thresholds of 3 PE were included.

The performance of the detector was studied using protons in the relevant range of energies, i.e. from 40 to 240 MeV. The ability of the system to reconstruct events with multiple simultaneous protons was studied using datasets consisting of N simultaneous protons being shot simultaneously at the detector.

B.3.1 Tracking

Custom algorithms were developed in order to associate the former lists of DMAPS and ASTRA hits into tracks. Notably, this algorithms were made with the primary goal to provide a sufficient performance to characterize the potential of the system under discussion. In consequence, it is expected that dedicated reconstruction studies will reach a superior performance in the future. In this sense, it is worth noting that there are currently ongoing efforts to develop new versions of this algorithms based on Deep Learning methods. Because of this, the results presented below, and especially those concerning the multi-proton capabilities of the detector, might be interpreted as a lower bound of the expected performance of the final system with optimized reconstruction algorithms.

DMAPS tracking

The DMAPS tracking algorithm match a set of input hits into a set of reconstructed trajectories running the following steps:

- Define the number of tracks N as the lowest number of hits in a plane.
- Generate all the possible track combinations (N^4) and compute a fitness value (η) for each.
- Select the N tracks with best overall fitness not sharing any common point.

Two approaches were investigated to define the η parameter. First, it was defined as the χ^2 of a straight line fit to all four pixel positions. Second, it was considered as the minimum line-to-line distance using the two trajectories reconstructed with the two first and the two last planes. The latter was chosen as the final criteria as it was found to work better. Performance results can be seen in Figure B.3.

Two figures of merit were defined to study the performance of the algorithms, the purity (p) and the efficiency (ε), defined as:

$$\varepsilon = \frac{N_{\text{reconstructed}}}{N_{\text{total}}}, \quad p = \frac{N_{\text{good}}}{N_{\text{reconstructed}}} \quad (\text{B.1})$$

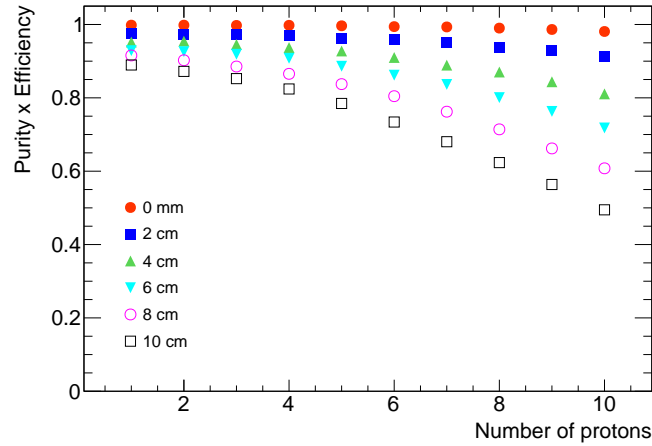


FIGURE B.3: Tracking performance of the DMAPS tracker as function of the number of protons per event for different thicknesses of the phantom in place. The studies are made using a Gaussian beam ($\sigma = 10$ mm) containing 180 MeV protons. Figure from Ref. [14].

where N_{total} , $N_{\text{reconstructed}}$ and N_{good} stand respectively for the total number of simulated tracks, the total number of reconstructed tracks, and the total number of reconstructed tracks with all hits belonging to the same true track.

ASTRA tracking

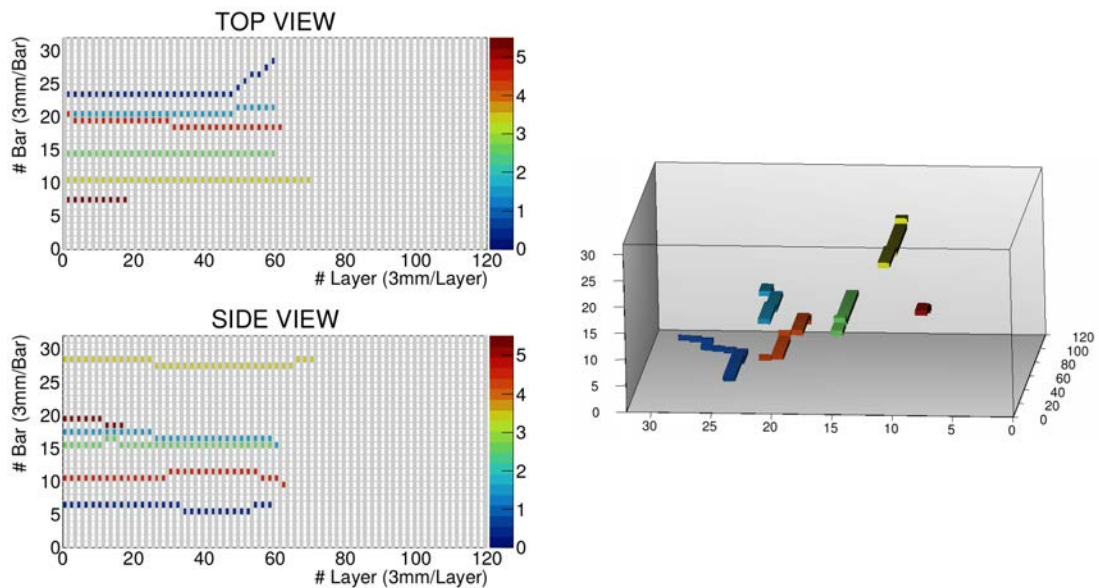


FIGURE B.4: Top and side view of the the ASTRA hits and the associated 3D reconstructed event. The colors represent the reconstructed track IDs. Figures from Ref. [14].

The ASTRA tracking algorithm found a set of reconstructed trajectories running the following steps:

- Make all possible 3D point combinations using the two first ASTRA layers.
- Set as track seeds all 3D points closer than a distance D to the trajectory defined by the last two DMAPS.

- For each seed iterate going upstream layer by layer. For each new layer 3D point candidates were formed from the available hits. If it found more than one 3D point closer than D only the one with higher light yield in the last layer was included.
- If no new 3D points were found closer than D in the following layer the tracking for the seed was completed, and a new reconstructed track was formed. The hits used on the track were set as not available and the algorithms continued with the next seed. The algorithm finished when all seeds had been considered.

An example of the tracking result of four simultaneous protons is presented in Figure B.4.

B.3.2 Performance tests

The performance of the system was studied doing a series of imaging tests on phantoms placed between the second and third DMAPS planes. In this tests a a 180 MeV monoenergetic proton beam with a Gaussian profile ($\sigma = 10$ mm) was used, matching the characteristics of the iThemba proton beam facility [609].

Energy reconstruction by range

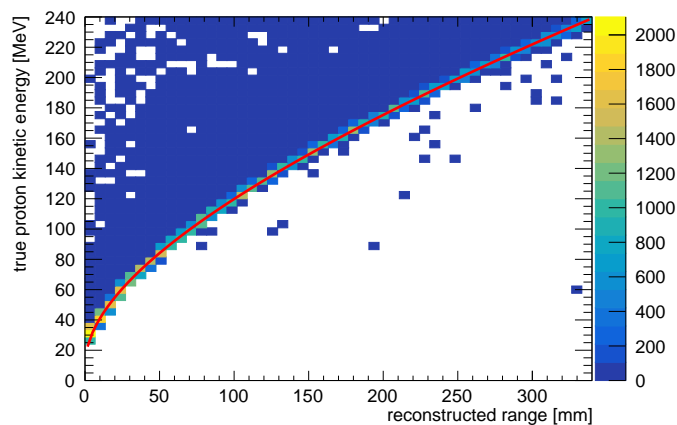


FIGURE B.5: True proton kinetic energy from GEANT4 compared to the reconstructed range in ASTRA. The map from the reconstructed range to the reconstructed energy corresponds to the fit in red. Figure from Ref. [14].

The protons kinetic energy was reconstructed in ASTRA by building a map, presented in Figure B.5 of the reconstructed range to the true kinetic energy of the protons specified by the simulation framework. The functional form of the conversion between the range and the expected energy was parametrized by fitting the most likely with an heuristic function. For the calculation of the energy resolution distributions of $1 - E_{\text{true}}/E_{\text{reco}}$ were filled, in intervals of 20 MeV. Then, this distributions were fitted using a Gaussian distribution and the width of the fit (σ) was used to define the energy resolution. For illustration, two example distributions are presented in Figure B.6.

Energy reconstruction including calorimetry

As the CITIROC chip provides calorimetric information by ToT and as it might be possible to develop custom electronics for this detector in the future, the usefulness of adding calorimetric information to the energy reconstruction was studied. The strategy consisted in embedding the reconstructed range and the light yield for all the hits in each reconstructed track in a vector of

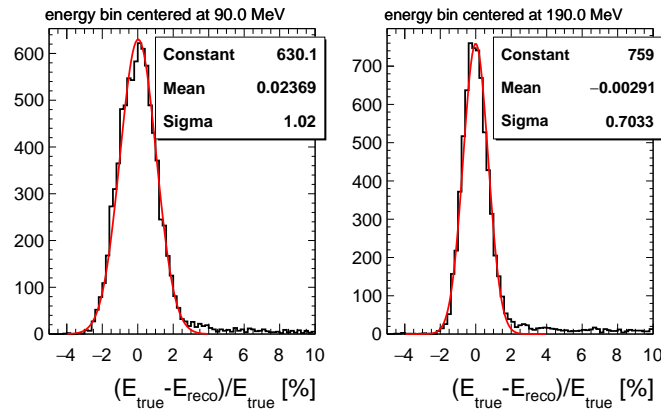


FIGURE B.6: Examples of two of the distributions for bars of 3 mm used in Figure B.7. The left (right) plot corresponds to a resolution of 1.02% (0.70%). Figure from Ref. [14].

features. This vector was then used to train a boost decision tree (BDT). In particular BDTG method from the TMVA libraries [610] was used. The training was made using half a million reconstructed protons. The performance of this method was later evaluated using the trained BDT to predict the reconstructed energy in previously unseen events.

Imaging

The phantoms used for imaging were composed by up to seven different materials defined in Table B.1.

Material	Density [g/cm^3]
Water	1.00
Adipose	0.92
Perspex	1.177
Lung	0.30
HC bone	1.84
Rib bone	1.40
Air	0.0013

TABLE B.1: Density values of the simulated materials used for imaging. Table adapted from Ref. [14].

Two different types of images were performed: A simple 2D radiography and a 3D pCT scan. For the 2D radiography the phantom was scanned with a proton beam moving the center of its Gaussian distribution through a grid over the phantom surface. The image was made by projecting the reconstructed tracks trajectory on an imaginary plane, perpendicular to the beam, located at the center of the phantom. The pixels of the radiography were defined setting up a 2D grid of 200×200 pixels, each with a size of $400 \times 400 \mu\text{m}^2$, for a total image area of $8 \times 8 \text{ cm}^2$. The color of each pixel was defined from the center of a 1D histogram distribution filled with the reconstructed energies of the protons passing through the area of the pixel. For the pCT scan a total of 360 radiographies were made, rotating for each the phantom by one degree. In the pCT only the energies of those protons reconstructed within 2σ around the most probable value of each pixel were used with the purpose of removing potentially deleterious tails. The end-product images were used as input to an algorithm developed by the PRaVDA collaboration [611]. Notably, for all imaging results calorimetric information was ignored such that the results correspond to do the energy reconstruction exclusively by range.

B.4 Results

The simulated energy resolution of ASTRA is presented in Figure B.7.

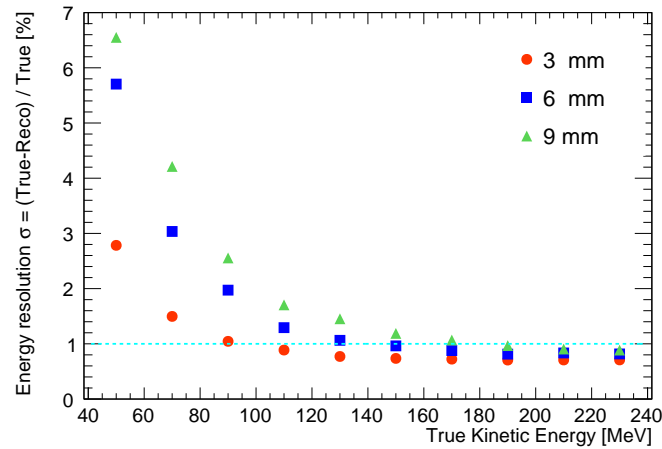


FIGURE B.7: Energy resolution of the ASTRA range telescope using range only information for three different squared-shaped bar sizes of 3, 6, and 9 mm. In all cases ASTRA is 360 mm long, and for each configuration 32, 16, and 11 bars are arranged in each layer respectively. The dashed line highlights the 1% threshold. Figure from Ref. [14].

In these studies bars of different sizes were considered, as using thicker bars would translate in reduced production costs for ASTRA. In general the results show an energy resolution better than 1% for the 3 mm bars for energies above 100 MeV. It has to be noted that this is the most relevant range of energies for pCT. The energy resolution asymptotically tends to an excellent performance of about $\sim 0.7\%$. Remarkably, coarser segmentation also achieves this high resolution in the high energy limit. Nonetheless, to investigate the potential multi-proton capabilities of the system the rest of the studies were centered in the 3 mm configuration. This is justified by the much better performance in multi-proton tracking for thinner bars presented in Figure B.8.

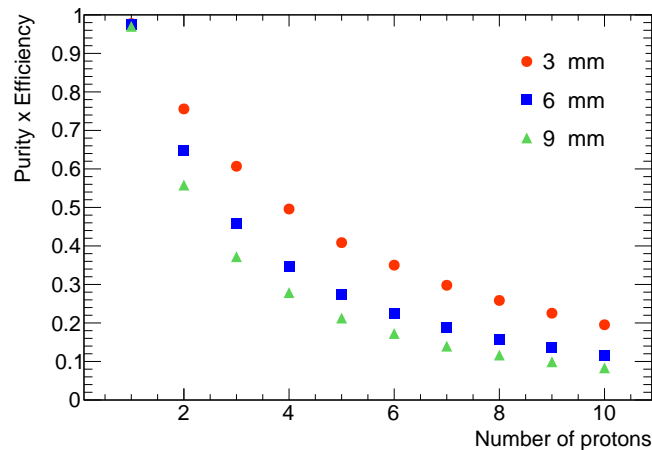


FIGURE B.8: Tracking performance for different number of simultaneous protons for the 3 mm, 6 mm and 9-mm ASTRA bar configurations. Figure from Ref. [14].

Since protons undergo inelastic interactions, when their energy is reconstructed solely by range some unavoidable energy reconstruction errors are made. This nuisance is accentuated when dealing with multiple simultaneous protons since tracking errors further smear the range estimates. Consequently, it is possible to identify typically two regimes in the energy reconstruction: A Gaussian one associated to the successful reconstruction of protons without inelastic interactions

and one conformed by long tails arising from tracking errors and inelastic protons. For events with only one proton tracking errors are expected to be close to zero, such that the performance results allow to investigate the role of inelastic interactions. In general, however, the most relevant metric to study is the fraction of protons which are considered good for imaging, i.e. those that are in the end used to generate the pCT images. To study this, the fraction of protons good for imaging was measured for two different beam profiles and several number of simultaneous protons by counting the fraction of events within 2σ of the typical energy reconstruction with respect to the total number of incident protons. The results are presented in Figure B.9. As expected, the more spaced the protons are in the beam the easier is to reconstruct them, reducing the number of tracking errors and increasing the fraction of protons good for imaging. Notably, even for the realistic Gaussian beam, about 1 proton per bunch is good for imaging regardless of whether there are one, two or simultaneous protons in the event.

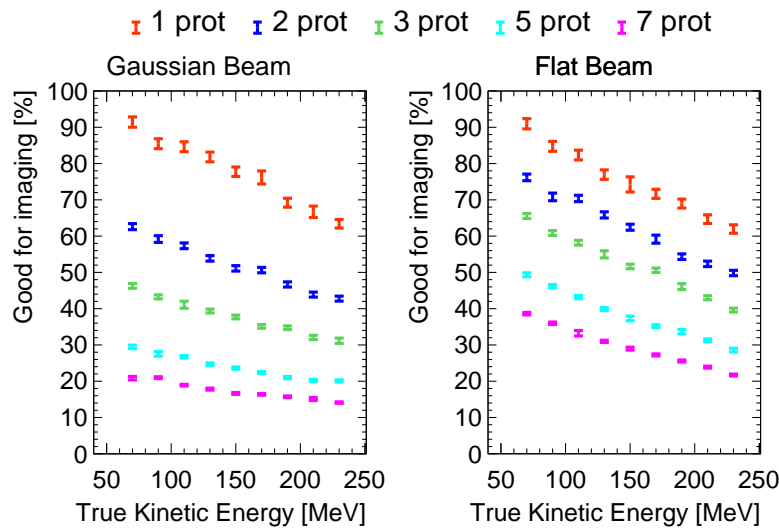


FIGURE B.9: Fraction of protons good for imaging as a function of the proton true kinetic energy using different number of simultaneous protons for a Gaussian beam ($\sigma = 10 \text{ mm}$) and for a flat $75 \times 75 \text{ mm}^2$ beam. Figure from Ref. [14].

Additionally, the energy resolution of the reconstructed protons in the Gaussian regime was studied as a function of the number of protons in the event. As presented in Figure B.10, the resolution of the system is kept constant showing the robustness of the method.

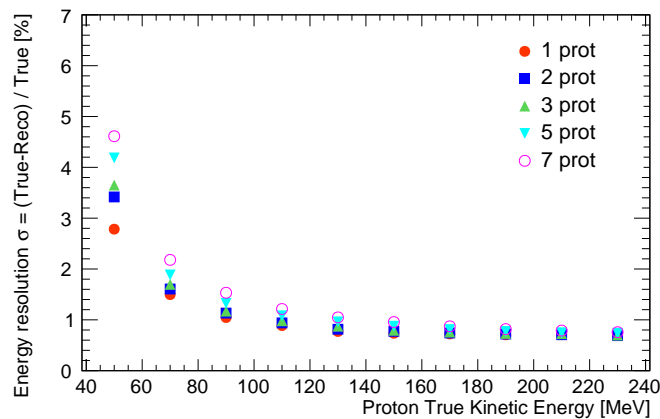


FIGURE B.10: Energy resolution for different number of simultaneous protons as a function of the proton initial kinetic energy.

The influence of using calorimetric information in ASTRA was studied comparing the range-only approach to the range and calorimetry method. In this studies, we kept in mind the demanding data rates that the envision pCT system would need to deal with in order to store the calorimetric information. Because of this we simulated the light in the bars as being digitized by a N-bits ADC by discretizing the bars output in 2^N values. In particular, we investigated the results for 4-bits and 12-bits ADCs, with associate light yield qualities compared qualitatively in Figure B.11.

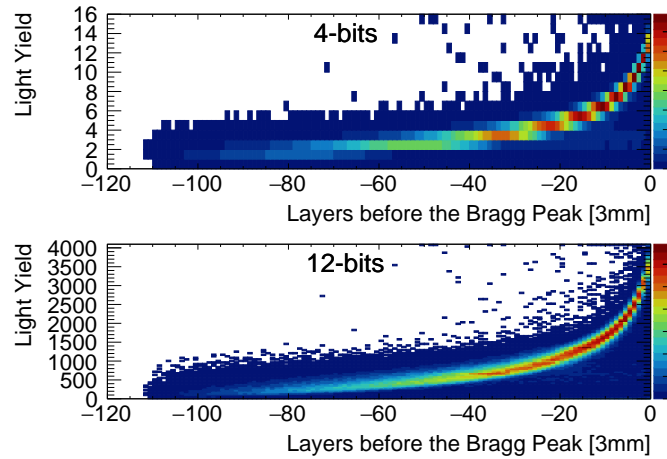


FIGURE B.11: Reconstructed protons light yield as a function of the distance to the layer with maximum recorded light yield for the 4-bits and 12-bits configurations. Figure from Ref. [14].

The energy resolution performance results are presented in Figure B.12. As it can be seen a significant improvement is achieved for low proton energies. For high energy protons the resolution is also improved reaching a resolution similar to $\sim 0.5\%$. Interestingly, this studies indicate that a 4-bit ADC might be sufficient to reach a significant improvement.

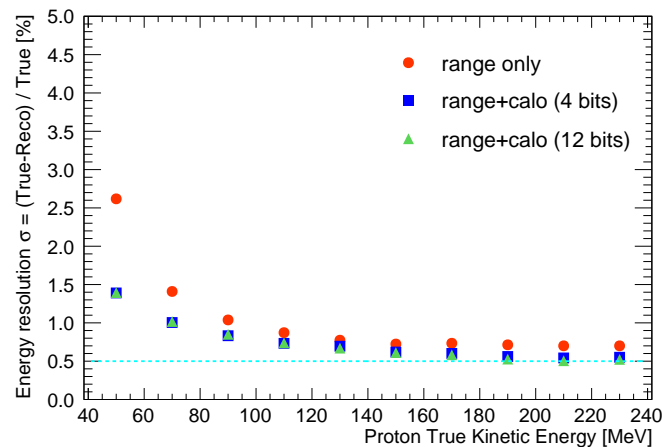


FIGURE B.12: Energy resolution for single proton events with and without using calorimetric information. The dashed line highlights the 0.5 % threshold. Figure from Ref. [14].

B.4.1 Radiography

The phantom under radiography consisted of a water equivalent material (WEM) squared frame of $50 \times 50 \text{ mm}^2$ and 30 mm pierced by four columns of cylindrical inserts of 30 mm length. Each column consisted of four cylinders of the same material organized in four rows, each with a different radius. From left to right the materials were simulated as equivalent to lung tissue, rib bone,

hard cortical bone, and adipose tissue. From the bottom to the top row the radius are 0.5, 1.0, 1.5 and 2 mm. The radiography was made using events with a single proton and with three simultaneous protons. The result images are presented in Figure B.13. A very high image resolution and

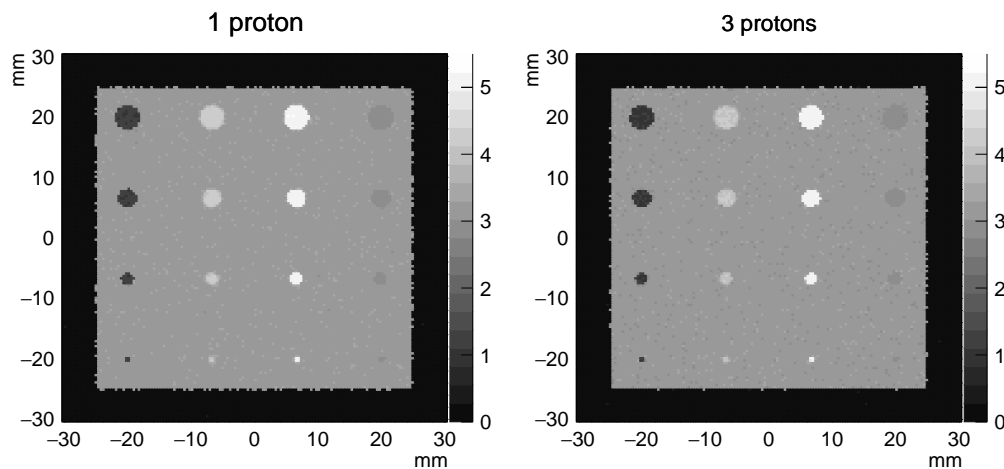


FIGURE B.13: Proton radiography of the squared phantom using 1 and 3 protons. From left to right the materials are simulated as equivalent to lung tissue, rib bone, hard cortical bone, and adipose tissue. From the bottom to the top row the radius are 0.5, 1.0, 1.5 and 2 mm. Each image used $5 \cdot 10^6$ protons. The Z-axis (color) corresponds to Water Equivalent Path Length (WEPL) in mm. Figure from Ref. [14].

high contrast is achieved and simple eye-inspection does not lead to appreciable differences in the results of the 1 proton and 3 protons results. A noise analysis revealed small differences in the color contrast for both. In particular, water equivalent path length (WEPL) fluctuations of 0.03 cm (0.06 cm) were measured for events made with 1 proton (3 proton) events. This corresponds to a significant relative degradation moving from 1% to about 2% WEPL fluctuations.

B.4.2 Proton CT scan

For the study of the 3D pCT imaging performances a spherical phantom was used consisting in a sphere of 75 mm in diameter made of Perspex (PMMA) with six different cylindrical inserts 15 mm high with 15mm diameter. The cylinders were placed in a three by three disposition forming two equilateral triangle in two different planes placed 9 mm above and below the center. The image results are presented in Figure B.14 in the form of two sliced sections of a pCT made with single proton events. The slices corresponds to the half height of the top (left image) and bottom (right image) sets of inserts. The RSP values for each material, computed from the average of several pCT pixels associated to the that material, are presented in Table B.2. Reference RSP values were computed using the true energy of the proton trajectories. The results show an excellent performance matching true and reconstructed RSP values within 0.5 %. For an analogous pCT image made exclusively with events with 3 protons some degradation is observed. Nonetheless, it is worth to have in mind that the 3 protons performance is comparable to the single proton events performance of other technologies [612]. Moreover, in a real life situation a beam could be tuned to consist mostly of 1 proton events and the multiproton capabilities of ASTRA used to deal with multi-proton eventualities, currently rejected in other technologies, hence increasing the system efficiency and the usefulness of the dose delivered to the patient.

The spatial resolution of the pCT was investigated by studying a RSP profile as presented in Figure B.15. The results show a stable RSP profile with an overall smooth trend and a flat plateau. The spatial resolution, see Figure B.15 was calculated by measuring the spread of the transition region between being inside and outside the insert, leading to a resolution similar to 1.1 mm.

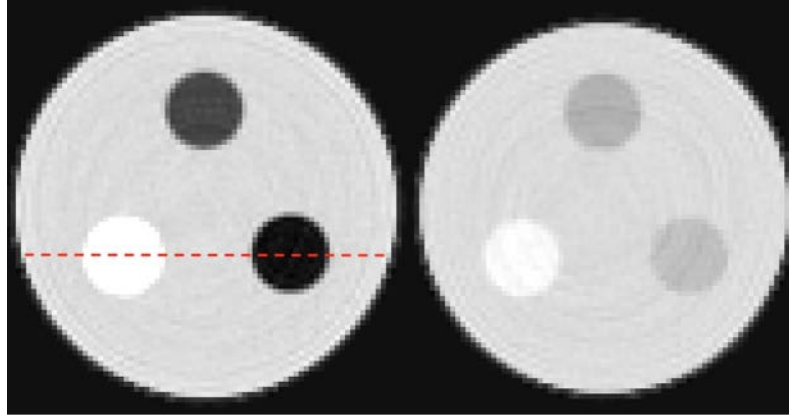


FIGURE B.14: Slices of a proton computed tomography using single proton events showing the contrast in RSP for the six inserts. The different insert materials have been simulated to be equivalent to (from left to right): rib bone, water and adipose tissue (left slice) and hard cortical bone, lung and air (right slice). The red dashed line highlights the data used in Figure B.15. Figure from Ref. [14].

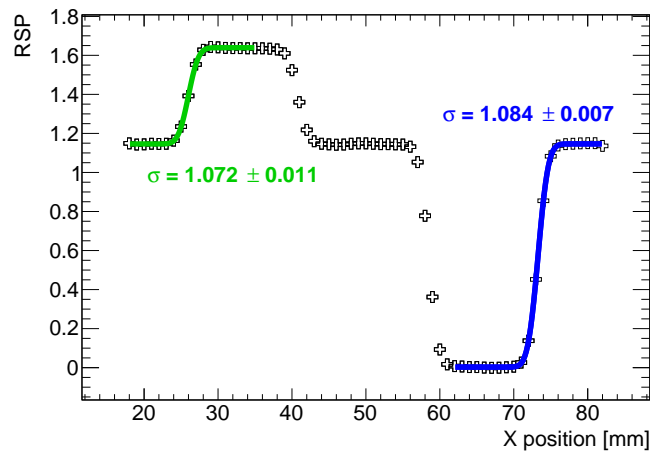


FIGURE B.15: Projection of the RSP along the line highlighted in Figure B.14. The rise in the RSP value has been fitted with an error function for the two inserts, hard cortical bone (green) and air (blue), characterized by a sigma detailed in the image.

Material	RSP (True)	RSP (Reco 1p)	RSP (Reco 3p)	%diff (1p)	%diff (3p)
Water	0.994 ± 0.002	0.992 ± 0.002	1.033 ± 0.002	0.201	3.924
Air	0.008 ± 0.002	0.009 ± 0.002	0.076 ± 0.006	-12.5	850.0
Adipose	0.917 ± 0.005	0.916 ± 0.006	0.96 ± 0.02	0.109	3.60
Rib bone	1.326 ± 0.001	1.325 ± 0.003	1.34 ± 0.04	0.075	1.06
HC bone	1.646 ± 0.002	1.641 ± 0.003	1.66 ± 0.02	0.304	0.85
Perspex	1.149 ± 0.002	1.144 ± 0.004	1.14 ± 0.01	0.455	-0.78
Lung	0.302 ± 0.003	0.302 ± 0.002	0.35 ± 0.02	0.000	15.89

TABLE B.2: Relative Stopping Power (RSP) values for seven different materials extracted from the pCT image of the spherical phantom. The labels *True* and *Reco* stand for the energy used to compute the RSP. Results are presented for both 1 proton and 3 simultaneous proton events. The differences (diff) compare the True and Reco values for the RSP. Table from Ref. [14].

B.5 Conclusions, status and plans

The feasibility studies of the novel proposed technology showed the potential of ASTRA. Overall, excellent performances were reached in terms of energy resolution, significantly outperforming existing technologies. The quality of the system was confirmed by imaging tests revealing both an excellent image contrast and spatial definition. Moreover, based on the current knowledge of the components of this technology we expect that ASTRA will be able to cope with up to 10^8 protons/s (100 MHz). This figure-of-merit is up to two orders of magnitude higher than that in existing technologies. Additionally, ASTRA allows to deal with events with multiple protons potentially allowing to decrease unavoidable inefficiencies in other existing solutions.

As a consequence of this studies, an international collaboration is emerging, including IFAE in Spain, University of Birmingham in UK and University of Geneva in Switzerland with the aim to build and test a first ASTRA prototype. In addition, a project is currently ongoing to improve the reconstruction performances of ASTRA using Deep Learning.

Bibliography

- [1] K. Abe et al. “Constraint on the matter–antimatter symmetry-violating phase in neutrino oscillations”. *Nature* 580.7803 (2020). [Erratum: *Nature* 583, E16 (2020)], pp. 339–344. DOI: [10 . 1038 / s41586 - 020 - 2177 - 0](https://doi.org/10.1038/s41586-020-2177-0). arXiv: [1910.03887](https://arxiv.org/abs/1910.03887) [hep-ex].
- [2] K. Abe et al. “Improved constraints on neutrino mixing from the T2K experiment with 3.13×10^{21} protons on target” (Jan. 2021). arXiv: [2101.03779](https://arxiv.org/abs/2101.03779) [hep-ex].
- [3] K. Abe et al. “T2K ND280 Upgrade - Technical Design Report” (Jan. 2019). arXiv: [1901 . 03750](https://arxiv.org/abs/1901.03750) [physics.ins-det].
- [4] D. Attié et al. “Performances of a resistive Micromegas module for the Time Projection Chambers of the T2K Near Detector upgrade”. *Nucl. Instrum. Meth. A* 957 (2020), p. 163286. DOI: [10 . 1016 / j . nima . 2019 . 163286](https://doi.org/10.1016/j.nima.2019.163286). arXiv: [1907.07060](https://arxiv.org/abs/1907.07060) [physics.ins-det].
- [5] D. Attié et al. “Characterization of resistive Micromegas detectors for the upgrade of the T2K Near Detector Time Projection Chambers”. *Nucl. Instrum. Meth. A* 1025 (2022), p. 166109. DOI: [10 . 1016 / j . nima . 2021 . 166109](https://doi.org/10.1016/j.nima.2021.166109). arXiv: [2106 . 12634](https://arxiv.org/abs/2106.12634) [physics.ins-det].
- [6] A. Blondel et al. “The SuperFGD Prototype Charged Particle Beam Tests”. *JINST* 15.12 (2020), P12003. DOI: [10 . 1088 / 1748 - 0221 / 15 / 12 / P12003](https://doi.org/10.1088/1748-0221/15/12/P12003). arXiv: [2008 . 08861](https://arxiv.org/abs/2008.08861) [physics.ins-det].
- [7] Saúl Alonso-Monsalve et al. “Graph neural network for 3D classification of ambiguities and optical crosstalk in scintillator-based neutrino detectors”. *Phys. Rev. D* 103.3 (2021), p. 032005. DOI: [10 . 1103 / PhysRevD . 103 . 032005](https://doi.org/10.1103/PhysRevD.103.032005). arXiv: [2009 . 00688](https://arxiv.org/abs/2009.00688) [physics.data-an].
- [8] L. Munteanu et al. “New method for an improved antineutrino energy reconstruction with charged-current interactions in next-generation detectors”. *Phys. Rev. D* 101.9 (2020), p. 092003. DOI: [10 . 1103 / PhysRevD . 101 . 092003](https://doi.org/10.1103/PhysRevD.101.092003). arXiv: [1912 . 01511](https://arxiv.org/abs/1912.01511) [physics.ins-det].
- [9] César Jesús-Valls, Thorsten Lux, and Federico Sánchez. “Data-driven detector signal characterization with constrained bottleneck autoencoders” (Mar. 2022). arXiv: [2203 . 04604](https://arxiv.org/abs/2203.04604) [physics.ins-det].
- [10] Joan Marc Cabot Canyelles et al. *Photonic System for Liquid Biopsy - PHIL*. Oct. 2021. DOI: [10 . 5281 / zenodo . 5608565](https://doi.org/10.5281/zenodo.5608565). URL: <https://doi.org/10.5281/zenodo.5608565>.
- [11] B. Burak et al. “Comparison between photon detection efficiency and tetraphenyl-butadiene coating stability of photomultiplier tubes immersed in liquid argon”. *JINST* 15.04 (2020), p. C04021. DOI: [10 . 1088 / 1748 - 0221 / 15 / 04 / C04021](https://doi.org/10.1088/1748-0221/15/04/C04021).
- [12] Babak Abi et al. “Deep Underground Neutrino Experiment (DUNE), Far Detector Technical Design Report, Volume II DUNE Physics” (Feb. 2020). arXiv: [2002.03005](https://arxiv.org/abs/2002.03005) [hep-ex].
- [13] Adam Abed Abud et al. “Scintillation light detection in the 6-m drift-length ProtoDUNE Dual Phase liquid argon TPC” (Mar. 2022). arXiv: [2203.16134](https://arxiv.org/abs/2203.16134) [physics.ins-det].
- [14] Marc Granado-González et al. “A novel range telescope concept for proton CT”. *Phys. Med. Biol.* 67.3 (2022), p. 035013. DOI: [10 . 1088 / 1361 - 6560 / ac4b39](https://doi.org/10.1088/1361-6560/ac4b39). arXiv: [2109.03452](https://arxiv.org/abs/2109.03452) [physics.med-ph].
- [15] James Chadwick. “Possible existence of a neutron”. *Nature* 129.3252 (1932), pp. 312–312.
- [16] Edoardo Amaldi. “From the discovery of the neutron to the discovery of nuclear fission”. *Physics Reports* 111.1-4 (1984), pp. 1–331.
- [17] Wolfgang Pauli. *Pauli letter collection: letter to Lise Meitner*. Tech. rep. 1930.
- [18] Enrico Fermi. “Versuch einer Theorie der β -Strahlen. I”. *Zeitschrift für Physik* 88.3 (1934), pp. 161–177.
- [19] Fred L Wilson. “Fermi’s theory of beta decay”. *American Journal of Physics* 36.12 (1968), pp. 1150–1160.
- [20] George Gamow and Edward Teller. “Selection Rules for the β -Disintegration”. *Physical Review* 49.12 (1936), p. 895.
- [21] Hans Bethe and Rudolph Peierls. “The neutrino”. *Nature* 133.3366 (1934), pp. 689–690.
- [22] Seth H Neddermeyer and Carl D Anderson. “Note on the nature of cosmic-ray particles”. *Physical Review* 51.10 (1937), p. 884.
- [23] Jabez C Street and EC Stevenson. “New evidence for the existence of a particle of mass intermediate between the proton and electron”. *Physical Review* 52.9 (1937), p. 1003.
- [24] Bruno Rossi and David B Hall. “Variation of the rate of decay of mesotrons with momentum”. *Physical Review* 59.3 (1941), p. 223.

- [25] Bruno Rossi. “The disintegration of mesotrons”. *Reviews of Modern Physics* 11.3-4 (1939), p. 296.
- [26] Enrico Fermi. “The ionization loss of energy in gases and in condensed materials”. *Physical Review* 57.6 (1940), p. 485.
- [27] Bruno Rossi and Kenneth Greisen. “Cosmic-ray theory”. *Reviews of Modern Physics* 13.4 (1941), p. 240.
- [28] Evan James Williams and GE Roberts. “Evidence for transformation of mesotrons into electrons”. *Nature* 145.3665 (1940), pp. 151–151.
- [29] Robert B Leighton, Carl D Anderson, and Aaron J Seriff. “The energy spectrum of the decay particles and the mass and spin of the mesotron”. *Physical Review* 75.9 (1949), p. 1432.
- [30] JM Robson. “The radioactive decay of the neutron”. *Physical Review* 83.2 (1951), p. 349.
- [31] Clyde L Cowan et al. “Detection of the free neutrino: a confirmation”. *Science* 124.3212 (1956), pp. 103–104.
- [32] Emil J Konopinski and Hormoz M Mahmoud. “The universal Fermi interaction”. *Physical Review* 92.4 (1953), p. 1045.
- [33] Frédéric Joliot and Irène Curie. *Artificial production of a new kind of radio-element*. 1934.
- [34] Harold Agnew and Warren Nyer. *Argonne Nuclear Pioneers: Chicago Pile 1*. Tech. rep. Argonne National Lab.(ANL), Argonne, IL (United States), 2012.
- [35] Raymond Davis. “Attempt to Detect the Antineutrinos from a Nuclear Reactor by the $\text{Cl}^{37}(\bar{\nu}, e^-)\text{A}^{37}$ Reaction”. *Phys. Rev.* 97 (3 Feb. 1955), pp. 766–769. DOI: [10.1103/PhysRev.97.766](https://doi.org/10.1103/PhysRev.97.766). URL: <https://link.aps.org/doi/10.1103/PhysRev.97.766>.
- [36] Gaillard Danby et al. “Observation of high-energy neutrino reactions and the existence of two kinds of neutrinos”. *Physical Review Letters* 9.1 (1962), p. 36.
- [37] V. Weisskopf and Eugene P. Wigner. “Calculation of the natural brightness of spectral lines on the basis of Dirac’s theory”. *Z. Phys.* 63 (1930), pp. 54–73. DOI: [10.1007/BF01336768](https://doi.org/10.1007/BF01336768).
- [38] Paul Adrien Maurice Dirac. “Quantised singularities in the electromagnetic field”. *Proc. Roy. Soc. Lond. A* 133.821 (1931), pp. 60–72. DOI: [10.1098/rspa.1931.0130](https://doi.org/10.1098/rspa.1931.0130).
- [39] W. Heisenberg and H. Euler. “Consequences of Dirac’s theory of positrons”. *Z. Phys.* 98.11-12 (1936), pp. 714–732. DOI: [10.1007/BF01343663](https://doi.org/10.1007/BF01343663). arXiv: [physics/0605038](https://arxiv.org/abs/physics/0605038).
- [40] Richard P Feynman. “The development of the space-time view of quantum electrodynamics”. *Science* 153.3737 (1966), pp. 699–708.
- [41] Freeman J Dyson. “The S matrix in quantum electrodynamics”. *Physical Review* 75.11 (1949), p. 1736.
- [42] Chen-Ning Yang and Robert L Mills. “Conservation of isotopic spin and isotopic gauge invariance”. *Physical review* 96.1 (1954), p. 191.
- [43] Paul AM Dirac. “Gauge-invariant formulation of quantum electrodynamics”. *Canadian Journal of Physics* 33.11 (1955), pp. 650–660.
- [44] T. D. Lee and Chen-Ning Yang. “Question of Parity Conservation in Weak Interactions”. *Phys. Rev.* 104 (1956), pp. 254–258. DOI: [10.1103/PhysRev.104.254](https://doi.org/10.1103/PhysRev.104.254).
- [45] Chien-Shiung Wu et al. “Experimental test of parity conservation in beta decay”. *Physical review* 105.4 (1957), p. 1413.
- [46] Richard P Feynman and Murray Gell-Mann. “Theory of the Fermi interaction”. *Physical Review* 109.1 (1958), p. 193.
- [47] S. L. Glashow. “Partial Symmetries of Weak Interactions”. *Nucl. Phys.* 22 (1961), pp. 579–588. DOI: [10.1016/0029-5582\(61\)90469-2](https://doi.org/10.1016/0029-5582(61)90469-2).
- [48] Yoichiro Nambu and Giovanni Jona-Lasinio. “Dynamical model of elementary particles based on an analogy with superconductivity. I”. *Physical review* 122.1 (1961), p. 345.
- [49] Jeffrey Goldstone. “Field theories with «Superconductor» solutions”. *Il Nuovo Cimento (1955-1965)* 19.1 (1961), pp. 154–164.
- [50] John Bardeen, Leon N Cooper, and John Robert Schrieffer. “Theory of superconductivity”. *Physical review* 108.5 (1957), p. 1175.
- [51] François Englert and Robert Brout. “Broken symmetry and the mass of gauge vector mesons”. *Physical Review Letters* 13.9 (1964), p. 321.
- [52] Peter W Higgs. “Broken symmetries and the masses of gauge bosons”. *Physical Review Letters* 13.16 (1964), p. 508.
- [53] Gerald S Guralnik, Carl R Hagen, and Thomas WB Kibble. “Global conservation laws and massless particles”. *Physical Review Letters* 13.20 (1964), p. 585.
- [54] Abdus Salam. “Weak and Electromagnetic Interactions”. *Conf. Proc. C* 680519 (1968), pp. 367–377. DOI: [10.1142/9789812795915_0034](https://doi.org/10.1142/9789812795915_0034).
- [55] Steven Weinberg. “A Model of Leptons”. *Phys. Rev. Lett.* 19 (1967), pp. 1264–1266. DOI: [10.1103/PhysRevLett.19.1264](https://doi.org/10.1103/PhysRevLett.19.1264).
- [56] F. J. Hasert et al. “Search for Elastic ν_μ Electron Scattering”. *Phys. Lett. B* 46 (1973), pp. 121–124. DOI: [10.1016/0370-2693\(73\)90494-2](https://doi.org/10.1016/0370-2693(73)90494-2).

- [57] Murray Gell-Mann. “A schematic model of baryons and mesons”. *Physics Letters* 8.3 (1964), pp. 214–215.
- [58] George Zweig. *An SU(3) model for strong interaction symmetry and its breaking*. Tech. rep. CM-P00042884, 1964.
- [59] O. W. Greenberg. “Spin and Unitary Spin Independence in a Paraquark Model of Baryons and Mesons”. *Phys. Rev. Lett.* 13 (1964), pp. 598–602. DOI: [10.1103/PhysRevLett.13.598](https://doi.org/10.1103/PhysRevLett.13.598).
- [60] Moo-Young Han and Yoichiro Nambu. “Triplet model with double SU (3) symmetry”. *Physical Review* 139.4B (1965), B1006.
- [61] James D Bjorken and Emmanuel A Paschos. “Inelastic electron-proton and γ -proton scattering and the structure of the nucleon”. *Physical Review* 185.5 (1969), p. 1975.
- [62] Richard P Feynman. “Very high-energy collisions of hadrons”. *Physical Review Letters* 23.24 (1969), p. 1415.
- [63] Sheldon L Glashow, Jean Iliopoulos, and Luciano Maiani. “Weak interactions with lepton-hadron symmetry”. *Physical review D* 2.7 (1970), p. 1285.
- [64] Makoto Kobayashi and Toshihide Maskawa. “CP-violation in the renormalizable theory of weak interaction”. *Progress of theoretical physics* 49.2 (1973), pp. 652–657.
- [65] Haim Harari. “A new quark model for hadrons”. *Physics Letters B* 57.3 (1975), pp. 265–269.
- [66] Jean-Jacques Aubert et al. “Experimental observation of a heavy particle J”. *Physical Review Letters* 33.23 (1974), p. 1404.
- [67] J-E Augustin et al. “Discovery of a Narrow Resonance in e^+e^- Annihilation”. *Physical Review Letters* 33.23 (1974), p. 1406.
- [68] Yung-Su Tsai. “Decay Correlations of Heavy Leptons in $e^{++}e^- \rightarrow l^{++}l^-$ ”. *Physical Review D* 4.9 (1971), p. 2821.
- [69] SW Herb et al. “Observation of a dimuon resonance at 9.5 GeV in 400-GeV proton-nucleus collisions”. *Physical Review Letters* 39.5 (1977), p. 252.
- [70] Haim Harari. “Three generations of quarks and leptons”. *Proceedings of the XII Rencontre de Moriond* (1977), p. 170.
- [71] Shahriar Abachi et al. “Observation of the top quark”. *Physical Review Letters* 74.14 (1995), p. 2632.
- [72] K Kodama et al. “Observation of tau neutrino interactions”. *Physics Letters B* 504.3 (2001), pp. 218–224.
- [73] Robert Oerter. *The theory of almost everything: The standard model, the unsung triumph of modern physics*. Penguin, 2006.
- [74] Serguei Chatrchyan et al. “Observation of a new boson at a mass of 125 GeV with the CMS experiment at the LHC”. *Physics Letters B* 716.1 (2012), pp. 30–61.
- [75] Georges Aad et al. “Observation of a new particle in the search for the Standard Model Higgs boson with the ATLAS detector at the LHC”. *Physics Letters B* 716.1 (2012), pp. 1–29.
- [76] Ettore Majorana. “Teoria simmetrica dell’elettrone e del positrone”. *Il Nuovo Cimento (1924-1942)* 14.4 (1937), pp. 171–184.
- [77] B. Pontecorvo. “Mesonium and anti-mesonium”. *Sov. Phys. JETP* 6 (1957), p. 429.
- [78] Ziro Maki, Masami Nakagawa, and Shoichi Sakata. “Remarks on the unified model of elementary particles”. *Progress of Theoretical Physics* 28.5 (1962), pp. 870–880.
- [79] B. Pontecorvo. “Neutrino Experiments and the Problem of Conservation of Leptonic Charge”. *Zh. Eksp. Teor. Fiz.* 53 (1967), pp. 1717–1725.
- [80] Hans Albrecht Bethe. “Energy production in stars”. *Physical Review* 55.5 (1939), p. 434.
- [81] B Pontecorvo. “On a method for detecting free neutrinos”. *National Research Council of Canada Report No. PD* 141 (1945), p. 21.
- [82] Raymond Davis Jr, Don S Harmer, and Kenneth C Hoffman. “Search for neutrinos from the sun”. *Physical Review Letters* 20.21 (1968), p. 1205.
- [83] J. N. Bahcall et al. “Solar neutrino flux”. *Astrophys. J.* 137 (1963), pp. 344–346. DOI: [10.1086/147513](https://doi.org/10.1086/147513).
- [84] M. Cribier. “Results of the whole GALLEX experiment”. *Nucl. Phys. B Proc. Suppl.* 70 (1999). Ed. by A. Bottino, Alessandra Di Credico, and Piero Monacelli, pp. 284–291. DOI: [10.1016/S0920-5632\(98\)00438-1](https://doi.org/10.1016/S0920-5632(98)00438-1).
- [85] M. Altmann et al. “Complete results for five years of GNO solar neutrino observations”. *Phys. Lett. B* 616 (2005), pp. 174–190. DOI: [10.1016/j.physletb.2005.04.068](https://doi.org/10.1016/j.physletb.2005.04.068). arXiv: [hep-ex/0504037](https://arxiv.org/abs/hep-ex/0504037).
- [86] J. N. Abdurashitov et al. “Solar neutrino flux measurements by the Soviet-American Gallium Experiment (SAGE) for half the 22 year solar cycle”. *J. Exp. Theor. Phys.* 95 (2002), pp. 181–193. DOI: [10.1134/1.1506424](https://doi.org/10.1134/1.1506424). arXiv: [astro-ph/0204245](https://arxiv.org/abs/astro-ph/0204245).
- [87] H Ikeda et al. “The Kamioka proton decay experiment”. *Third Workshop on Grand Unification*. Springer, 1982, pp. 56–71.
- [88] K. Hirata et al. “Observation of a Neutrino Burst from the Supernova SN 1987a”. *Phys. Rev. Lett.* 58 (1987). Ed. by K. C. Wali, pp. 1490–1493. DOI: [10.1103/PhysRevLett.58.1490](https://doi.org/10.1103/PhysRevLett.58.1490).
- [89] C. B. Bratton et al. “Angular Distribution of Events From Sn1987a”. *Phys. Rev. D* 37 (1988), p. 3361. DOI: [10.1103/PhysRevD.37.3361](https://doi.org/10.1103/PhysRevD.37.3361).

- [90] E. N. Alekseev et al. “Detection of the Neutrino Signal From SN1987A in the LMC Using the Inr Baksan Underground Scintillation Telescope”. *Phys. Lett. B* 205 (1988), pp. 209–214. DOI: [10.1016/0370-2693\(88\)91651-6](https://doi.org/10.1016/0370-2693(88)91651-6).
- [91] K. S. Hirata et al. “Observation of B-8 Solar Neutrinos in the Kamiokande-II Detector”. *Phys. Rev. Lett.* 63 (1989), p. 16. DOI: [10.1103/PhysRevLett.63.16](https://doi.org/10.1103/PhysRevLett.63.16).
- [92] Y. Fukuda et al. “Atmospheric muon-neutrino / electron-neutrino ratio in the multiGeV energy range”. *Phys. Lett. B* 335 (1994), pp. 237–245. DOI: [10.1016/0370-2693\(94\)91420-6](https://doi.org/10.1016/0370-2693(94)91420-6).
- [93] Kurt Riesselmann. *Neutrino oscillation*. URL: <https://www.symmetrymagazine.org/article/february-2010/neutrino-oscillation?language=en&page=3> (visited on 08/29/2021).
- [94] Y. Fukuda et al. “Evidence for oscillation of atmospheric neutrinos”. *Phys. Rev. Lett.* 81 (1998), pp. 1562–1567. DOI: [10.1103/PhysRevLett.81.1562](https://doi.org/10.1103/PhysRevLett.81.1562). arXiv: [hep-ex/9807003](https://arxiv.org/abs/hep-ex/9807003).
- [95] Claudio Giganti, Stéphane Lavignac, and Marco Zito. “Neutrino oscillations: The rise of the PMNS paradigm”. *Prog. Part. Nucl. Phys.* 98 (2018), pp. 1–54. DOI: [10.1016/j.pnpnp.2017.10.001](https://doi.org/10.1016/j.pnpnp.2017.10.001). arXiv: [1710.00715](https://arxiv.org/abs/1710.00715) [hep-ex].
- [96] Q. R. Ahmad et al. “Direct evidence for neutrino flavor transformation from neutral current interactions in the Sudbury Neutrino Observatory”. *Phys. Rev. Lett.* 89 (2002), p. 011301. DOI: [10.1103/PhysRevLett.89.011301](https://doi.org/10.1103/PhysRevLett.89.011301). arXiv: [nucl-ex/0204008](https://arxiv.org/abs/nucl-ex/0204008).
- [97] L. Wolfenstein. “Neutrino Oscillations in Matter”. *Phys. Rev. D* 17 (1978), pp. 2369–2374. DOI: [10.1103/PhysRevD.17.2369](https://doi.org/10.1103/PhysRevD.17.2369).
- [98] S. P. Mikheyev and A. Yu. Smirnov. “Resonance Amplification of Oscillations in Matter and Spectroscopy of Solar Neutrinos”. *Sov. J. Nucl. Phys.* 42 (1985), pp. 913–917.
- [99] A. D. Sakharov. “Violation of CP Invariance, C asymmetry, and baryon asymmetry of the universe”. *Pisma Zh. Eksp. Teor. Fiz.* 5 (1967), pp. 32–35. DOI: [10.1070/PU1991v034n05ABEH002497](https://doi.org/10.1070/PU1991v034n05ABEH002497).
- [100] M. Fukugita and T. Yanagida. “Baryogenesis Without Grand Unification”. *Phys. Lett. B* 174 (1986), pp. 45–47. DOI: [10.1016/0370-2693\(86\)91126-3](https://doi.org/10.1016/0370-2693(86)91126-3).
- [101] A. Osipowicz et al. “KATRIN: A Next generation tritium beta decay experiment with sub-eV sensitivity for the electron neutrino mass. Letter of intent” (Sept. 2001). arXiv: [hep-ex/0109033](https://arxiv.org/abs/hep-ex/0109033).
- [102] M. G. Aartsen et al. “IceCube-Gen2: A Vision for the Future of Neutrino Astronomy in Antarctica” (Dec. 2014). arXiv: [1412.5106](https://arxiv.org/abs/1412.5106) [astro-ph.HE].
- [103] S. Adrian-Martinez et al. “Letter of intent for KM3NeT 2.0”. *J. Phys. G* 43.8 (2016), p. 084001. DOI: [10.1088/0954-3899/43/8/084001](https://doi.org/10.1088/0954-3899/43/8/084001). arXiv: [1601.07459](https://arxiv.org/abs/1601.07459) [astro-ph.IM].
- [104] A. D. Avrorin et al. “Baikal-GVD: status and prospects”. *EPJ Web Conf.* 191 (2018). Ed. by V. E. Volkova et al., p. 01006. DOI: [10.1051/epjconf/201819101006](https://doi.org/10.1051/epjconf/201819101006). arXiv: [1808.10353](https://arxiv.org/abs/1808.10353) [astro-ph.IM].
- [105] K. Abe et al. “Hyper-Kamiokande Design Report” (May 2018). arXiv: [1805.04163](https://arxiv.org/abs/1805.04163) [physics.ins-det].
- [106] K. Abe et al. “Physics potential of a long-baseline neutrino oscillation experiment using a J-PARC neutrino beam and Hyper-Kamiokande”. *PTEP* 2015 (2015), p. 053C02. DOI: [10.1093/ptep/ptv061](https://doi.org/10.1093/ptep/ptv061). arXiv: [1502.05199](https://arxiv.org/abs/1502.05199) [hep-ex].
- [107] K. Abe et al. “Physics potentials with the second Hyper-Kamiokande detector in Korea”. *PTEP* 2018.6 (2018), p. 063C01. DOI: [10.1093/ptep/pty044](https://doi.org/10.1093/ptep/pty044). arXiv: [1611.06118](https://arxiv.org/abs/1611.06118) [hep-ex].
- [108] Zelimir Djurcic et al. “JUNO Conceptual Design Report” (Aug. 2015). arXiv: [1508.07166](https://arxiv.org/abs/1508.07166) [physics.ins-det].
- [109] Fengpeng An et al. “Neutrino Physics with JUNO”. *J. Phys. G* 43.3 (2016), p. 030401. DOI: [10.1088/0954-3899/43/3/030401](https://doi.org/10.1088/0954-3899/43/3/030401). arXiv: [1507.05613](https://arxiv.org/abs/1507.05613) [physics.ins-det].
- [110] Babak Abi et al. “Volume I. Introduction to DUNE”. *JINST* 15.08 (2020), T08008. DOI: [10.1088/1748-0221/15/08/T08008](https://doi.org/10.1088/1748-0221/15/08/T08008). arXiv: [2002.02967](https://arxiv.org/abs/2002.02967) [physics.ins-det].
- [111] Babak Abi et al. “Volume III. DUNE far detector technical coordination”. *JINST* 15.08 (2020), T08009. DOI: [10.1088/1748-0221/15/08/T08009](https://doi.org/10.1088/1748-0221/15/08/T08009). arXiv: [2002.03008](https://arxiv.org/abs/2002.03008) [physics.ins-det].
- [112] Babak Abi et al. “Volume IV. The DUNE far detector single-phase technology”. *JINST* 15.08 (2020), T08010. DOI: [10.1088/1748-0221/15/08/T08010](https://doi.org/10.1088/1748-0221/15/08/T08010). arXiv: [2002.03010](https://arxiv.org/abs/2002.03010) [physics.ins-det].
- [113] C. Giunti and C.W Kim. *Fundamentals of neutrino physics and astrophysics*. Oxford university press, 2007.
- [114] F. Halzen and Alan D. Martin. *QUARKS AND LEPTONS: AN INTRODUCTORY COURSE IN MODERN PARTICLE PHYSICS*. 1984. ISBN: 978-0-471-88741-6.

- [115] David Griffiths. *Introduction to elementary particles*. 2008. ISBN: 978-3-527-40601-2.
- [116] Steven Weinberg. *The quantum theory of fields*. Vol. 2. Cambridge university press, 1995.
- [117] Michael E Peskin. *An introduction to quantum field theory*. CRC press, 2018.
- [118] R. D. Peccei and Helen R. Quinn. “CP Conservation in the Presence of Instantons”. *Phys. Rev. Lett.* 38 (1977), pp. 1440–1443. DOI: [10.1103/PhysRevLett.38.1440](https://doi.org/10.1103/PhysRevLett.38.1440).
- [119] Particle Data Group et al. “Review of particle physics”. *Progress of Theoretical and Experimental Physics* 2020.8 (2020), p. 083C01.
- [120] Gian Luigi Fogli, E. Lisi, and A. Palazzo. “Quasi energy independent solar neutrino transitions”. *Phys. Rev. D* 65 (2002), p. 073019. DOI: [10.1103/PhysRevD.65.073019](https://doi.org/10.1103/PhysRevD.65.073019). arXiv: [hep-ph/0105080](https://arxiv.org/abs/hep-ph/0105080).
- [121] Stephen J. Parke. “Nonadiabatic Level Crossing in Resonant Neutrino Oscillations”. *Phys. Rev. Lett.* 57 (1986). Ed. by S. C. Loken, pp. 1275–1278. DOI: [10.1103/PhysRevLett.57.1275](https://doi.org/10.1103/PhysRevLett.57.1275).
- [122] D. D’Angelo et al. “Recent Borexino results and prospects for the near future”. *EPJ Web Conf.* 126 (2016). Ed. by Larisa Bravina, Yiota Foka, and Sonja Kabana, p. 02008. DOI: [10.1051/epjconf/201612602008](https://doi.org/10.1051/epjconf/201612602008). arXiv: [1405.7919](https://arxiv.org/abs/1405.7919) [hep-ex].
- [123] Mattias Blennow and Alexei Yu. Smirnov. “Neutrino propagation in matter”. *Adv. High Energy Phys.* 2013 (2013), p. 972485. DOI: [10.1155/2013/972485](https://doi.org/10.1155/2013/972485). arXiv: [1306.2903](https://arxiv.org/abs/1306.2903) [hep-ph].
- [124] Hisakazu Minakata. “An Effective Two-Flavor Approximation for Neutrino Survival Probabilities in Matter”. *JHEP* 05 (2017), p. 043. DOI: [10.1007/JHEP05\(2017\)043](https://doi.org/10.1007/JHEP05(2017)043). arXiv: [1702.03332](https://arxiv.org/abs/1702.03332) [hep-ph].
- [125] Petr Vogel, LJ Wen, and Chao Zhang. “Neutrino oscillation studies with reactors”. *Nature Communications* 6.1 (2015), pp. 1–12.
- [126] *NuFit webpage*. <http://www.nu-fit.org>.
- [127] P. F. De Salas et al. *Chi2 profiles from Valencia neutrino global fit*. 2021. DOI: [10.5281/zenodo.4726908](https://doi.org/10.5281/zenodo.4726908). URL: [%7Bhttps://doi.org/10.5281/zenodo.4726908%7D](https://doi.org/10.5281/zenodo.4726908%7D).
- [128] Anastasiia Kalitkina et al. “Simulation of long-baseline accelerator neutrino experiments with the global neutrino analysis package”. *AIP Conf. Proc.* 2163.1 (2019). Ed. by Alexey Aparin et al., p. 030005. DOI: [10.1063/1.5130091](https://doi.org/10.1063/1.5130091).
- [129] F. Capozzi et al. “Neutrino masses and mixings: Status of known and unknown 3ν parameters”. *Nucl. Phys. B* 908 (2016), pp. 218–234. DOI: [10.1016/j.nuclphysb.2016.02.016](https://doi.org/10.1016/j.nuclphysb.2016.02.016). arXiv: [1601.07777](https://arxiv.org/abs/1601.07777) [hep-ph].
- [130] P. F. de Salas et al. “Status of neutrino oscillations 2018: 3σ hint for normal mass ordering and improved CP sensitivity”. *Phys. Lett. B* 782 (2018), pp. 633–640. DOI: [10.1016/j.physletb.2018.06.019](https://doi.org/10.1016/j.physletb.2018.06.019). arXiv: [1708.01186](https://arxiv.org/abs/1708.01186) [hep-ph].
- [131] Ivan Esteban et al. “Updated fit to three neutrino mixing: exploring the accelerator-reactor complementarity”. *JHEP* 01 (2017), p. 087. DOI: [10.1007/JHEP01\(2017\)087](https://doi.org/10.1007/JHEP01(2017)087). arXiv: [1611.01514](https://arxiv.org/abs/1611.01514) [hep-ph].
- [132] Ivan Esteban et al. “Global analysis of three-flavour neutrino oscillations: synergies and tensions in the determination of θ_{23} , δ_{CP} , and the mass ordering”. *JHEP* 01 (2019), p. 106. DOI: [10.1007/JHEP01\(2019\)106](https://doi.org/10.1007/JHEP01(2019)106). arXiv: [1811.05487](https://arxiv.org/abs/1811.05487) [hep-ph].
- [133] Ivan Esteban et al. “The fate of hints: updated global analysis of three-flavor neutrino oscillations”. *JHEP* 09 (2020), p. 178. DOI: [10.1007/JHEP09\(2020\)178](https://doi.org/10.1007/JHEP09(2020)178). arXiv: [2007.14792](https://arxiv.org/abs/2007.14792) [hep-ph].
- [134] Y. Nakajima. “SuperKamiokande”. Talk given at the *XXIX International Conference on Neutrino Physics and Astrophysics*, Chicago, USA, June 22–July 2, 2020 (online conference).
- [135] Guido Fantini et al. “Introduction to the Formalism of Neutrino Oscillations”. *Adv. Ser. Direct. High Energy Phys.* 28 (2018), pp. 37–119. DOI: [10.1142/9789813226098_0002](https://doi.org/10.1142/9789813226098_0002). arXiv: [1802.05781](https://arxiv.org/abs/1802.05781) [hep-ph].
- [136] S. Schael et al. “Precision electroweak measurements on the Z resonance”. *Phys. Rept.* 427 (2006), pp. 257–454. DOI: [10.1016/j.physrep.2005.12.006](https://doi.org/10.1016/j.physrep.2005.12.006). arXiv: [hep-ex/0509008](https://arxiv.org/abs/hep-ex/0509008).
- [137] A. Aguilar-Arevalo et al. “Evidence for neutrino oscillations from the observation of $\bar{\nu}_e$ appearance in a $\bar{\nu}_\mu$ beam”. *Phys. Rev. D* 64 (2001), p. 112007. DOI: [10.1103/PhysRevD.64.112007](https://doi.org/10.1103/PhysRevD.64.112007). arXiv: [hep-ex/0104049](https://arxiv.org/abs/hep-ex/0104049).
- [138] A. A. Aguilar-Arevalo et al. “Significant Excess of ElectronLike Events in the MiniBooNE Short-Baseline Neutrino Experiment”. *Phys. Rev. Lett.* 121.22 (2018), p. 221801. DOI: [10.1103/PhysRevLett.121.221801](https://doi.org/10.1103/PhysRevLett.121.221801). arXiv: [1805.12028](https://arxiv.org/abs/1805.12028) [hep-ex].
- [139] A. A. Aguilar-Arevalo et al. “Updated MiniBooNE neutrino oscillation results with increased data and new background studies”. *Phys. Rev. D* 103.5 (2021), p. 052002. DOI: [10.1103/PhysRevD.103.052002](https://doi.org/10.1103/PhysRevD.103.052002). arXiv: [2006.16883](https://arxiv.org/abs/2006.16883) [hep-ex].
- [140] P. Abratenko et al. “Search for an anomalous excess of charged-current quasi-elastic ν_e interactions with the MicroBooNE experiment using Deep-Learning-based reconstruction” (Oct. 2021). arXiv: [2110.14080](https://arxiv.org/abs/2110.14080) [hep-ex].

- [141] P. Abratenko et al. “Search for an anomalous excess of charged-current ν_e interactions without pions in the final state with the MicroBooNE experiment” (Oct. 2021). arXiv: [2110.14065](https://arxiv.org/abs/2110.14065) [hep-ex].
- [142] P. Abratenko et al. “Search for Neutrino-Induced Neutral-Current Δ Radiative Decay in MicroBooNE and a First Test of the Mini-BooNE Low Energy Excess under a Single-Photon Hypothesis”. *Phys. Rev. Lett.* 128.11 (2022), p. 111801. DOI: [10.1103/PhysRevLett.128.111801](https://doi.org/10.1103/PhysRevLett.128.111801). arXiv: [2110.00409](https://arxiv.org/abs/2110.00409) [hep-ex].
- [143] Carlo Giunti and T. Lasserre. “eV-scale Sterile Neutrinos”. *Ann. Rev. Nucl. Part. Sci.* 69 (2019), pp. 163–190. DOI: [10.1146/annurev-nucl-101918-023755](https://doi.org/10.1146/annurev-nucl-101918-023755). arXiv: [1901.08330](https://arxiv.org/abs/1901.08330) [hep-ph].
- [144] Th. A. Mueller et al. “Improved Predictions of Reactor Antineutrino Spectra”. *Phys. Rev. C* 83 (2011), p. 054615. DOI: [10.1103/PhysRevC.83.054615](https://doi.org/10.1103/PhysRevC.83.054615). arXiv: [1101.2663](https://arxiv.org/abs/1101.2663) [hep-ex].
- [145] Patrick Huber. “On the determination of antineutrino spectra from nuclear reactors”. *Phys. Rev. C* 84 (2011). [Erratum: *Phys. Rev. C* 85, 029901 (2012)], p. 024617. DOI: [10.1103/PhysRevC.85.029901](https://doi.org/10.1103/PhysRevC.85.029901). arXiv: [1106.0687](https://arxiv.org/abs/1106.0687) [hep-ph].
- [146] Basudeb Dasgupta and Joachim Kopp. “Sterile Neutrinos”. *Phys. Rept.* 928 (2021), p. 63. DOI: [10.1016/j.physrep.2021.06.002](https://doi.org/10.1016/j.physrep.2021.06.002). arXiv: [2106.05913](https://arxiv.org/abs/2106.05913) [hep-ph].
- [147] F. P. An et al. “Antineutrino energy spectrum unfolding based on the Daya Bay measurement and its applications”. *Chin. Phys. C* 45.7 (2021), p. 073001. DOI: [10.1088/1674-1137/abfc38](https://doi.org/10.1088/1674-1137/abfc38). arXiv: [2102.04614](https://arxiv.org/abs/2102.04614) [hep-ex].
- [148] Y. J. Ko et al. “Sterile Neutrino Search at the NEOS Experiment”. *Phys. Rev. Lett.* 118.12 (2017), p. 121802. DOI: [10.1103/PhysRevLett.118.121802](https://doi.org/10.1103/PhysRevLett.118.121802). arXiv: [1610.05134](https://arxiv.org/abs/1610.05134) [hep-ex].
- [149] I Alekseev et al. “Search for sterile neutrinos at the DANSS experiment”. *Phys. Lett. B* 787 (2018), pp. 56–63. DOI: [10.1016/j.physletb.2018.10.038](https://doi.org/10.1016/j.physletb.2018.10.038). arXiv: [1804.04046](https://arxiv.org/abs/1804.04046) [hep-ex].
- [150] A. P. Serebrov et al. “First Observation of the Oscillation Effect in the Neutrino-4 Experiment on the Search for the Sterile Neutrino”. *Pisma Zh. Eksp. Teor. Fiz.* 109.4 (2019), pp. 209–218. DOI: [10.1134/S0021364019040040](https://doi.org/10.1134/S0021364019040040). arXiv: [1809.10561](https://arxiv.org/abs/1809.10561) [hep-ex].
- [151] M. Andriamirado et al. “Note on arXiv:2005.05301, ‘Preparation of the Neutrino-4 experiment on search for sterile neutrino and the obtained results of measurements’” (June 2020). arXiv: [2006.13147](https://arxiv.org/abs/2006.13147) [hep-ex].
- [152] Pilar Coloma, Patrick Huber, and Thomas Schwetz. “Statistical interpretation of sterile neutrino oscillation searches at reactors”. *Eur. Phys. J. C* 81.1 (2021), p. 2. DOI: [10.1140/epjc/s10052-020-08774-2](https://doi.org/10.1140/epjc/s10052-020-08774-2). arXiv: [2008.06083](https://arxiv.org/abs/2008.06083) [hep-ph].
- [153] H. Almazán et al. “Improved sterile neutrino constraints from the STEREO experiment with 179 days of reactor-on data”. *Phys. Rev. D* 102.5 (2020), p. 052002. DOI: [10.1103/PhysRevD.102.052002](https://doi.org/10.1103/PhysRevD.102.052002). arXiv: [1912.06582](https://arxiv.org/abs/1912.06582) [hep-ex].
- [154] M. Andriamirado et al. “Improved short-baseline neutrino oscillation search and energy spectrum measurement with the PROSPECT experiment at HFIR”. *Phys. Rev. D* 103.3 (2021), p. 032001. DOI: [10.1103/PhysRevD.103.032001](https://doi.org/10.1103/PhysRevD.103.032001). arXiv: [2006.11210](https://arxiv.org/abs/2006.11210) [hep-ex].
- [155] F. Dydak et al. “A Search for Muon-neutrino Oscillations in the Delta m^2 Range 0.3-eV 2 to 90-eV 2 ”. *Phys. Lett. B* 134 (1984), p. 281. DOI: [10.1016/0370-2693\(84\)90688-9](https://doi.org/10.1016/0370-2693(84)90688-9).
- [156] K. B. M. Mahn et al. “Dual baseline search for muon neutrino disappearance at $0.5\text{eV}^2 < \Delta m^2 < 40\text{eV}^2$ ”. *Phys. Rev. D* 85 (2012), p. 032007. DOI: [10.1103/PhysRevD.85.032007](https://doi.org/10.1103/PhysRevD.85.032007). arXiv: [1106.5685](https://arxiv.org/abs/1106.5685) [hep-ex].
- [157] G. Cheng et al. “Dual baseline search for muon antineutrino disappearance at $0.1\text{eV}^2 < \Delta m^2 < 100\text{eV}^2$ ”. *Phys. Rev. D* 86 (2012), p. 052009. DOI: [10.1103/PhysRevD.86.052009](https://doi.org/10.1103/PhysRevD.86.052009). arXiv: [1208.0322](https://arxiv.org/abs/1208.0322) [hep-ex].
- [158] M. G. Aartsen et al. “Searches for Sterile Neutrinos with the IceCube Detector”. *Phys. Rev. Lett.* 117.7 (2016), p. 071801. DOI: [10.1103/PhysRevLett.117.071801](https://doi.org/10.1103/PhysRevLett.117.071801). arXiv: [1605.01990](https://arxiv.org/abs/1605.01990) [hep-ex].
- [159] P. Adamson et al. “Search for sterile neutrinos in MINOS and MINOS+ using a two-detector fit”. *Phys. Rev. Lett.* 122.9 (2019), p. 091803. DOI: [10.1103/PhysRevLett.122.091803](https://doi.org/10.1103/PhysRevLett.122.091803). arXiv: [1710.06488](https://arxiv.org/abs/1710.06488) [hep-ex].
- [160] M. H. Moulai et al. “Combining Sterile Neutrino Fits to Short Baseline Data with IceCube Data”. *Phys. Rev. D* 101.5 (2020), p. 055020. DOI: [10.1103/PhysRevD.101.055020](https://doi.org/10.1103/PhysRevD.101.055020). arXiv: [1910.13456](https://arxiv.org/abs/1910.13456) [hep-ph].
- [161] Takehiko Asaka and Mikhail Shaposhnikov. “The ν MSM, dark matter and baryon asymmetry of the universe”. *Phys. Lett. B* 620 (2005), pp. 17–26. DOI: [10.1016/j.physletb.2005.06.020](https://doi.org/10.1016/j.physletb.2005.06.020). arXiv: [hep-ph/0505013](https://arxiv.org/abs/hep-ph/0505013).
- [162] Y. F. Li and Zhi-zhong Xing. “Possible Capture of keV Sterile Neutrino Dark Matter on Radioactive β -decaying Nuclei”. *Phys. Lett. B* 695 (2011), pp. 205–210. DOI: [10.1016/j.physletb.2010.11.015](https://doi.org/10.1016/j.physletb.2010.11.015). arXiv: [1009.5870](https://arxiv.org/abs/1009.5870) [hep-ph].

- [163] Frank T. Avignone III, Steven R. Elliott, and Jonathan Engel. “Double Beta Decay, Majorana Neutrinos, and Neutrino Mass”. *Rev. Mod. Phys.* 80 (2008), pp. 481–516. DOI: [10.1103/RevModPhys.80.481](https://doi.org/10.1103/RevModPhys.80.481). arXiv: [0708.1033](https://arxiv.org/abs/0708.1033) [nucl-ex].
- [164] Hiroshi Nunokawa, Stephen J. Parke, and Jose W. F. Valle. “CP Violation and Neutrino Oscillations”. *Prog. Part. Nucl. Phys.* 60 (2008), pp. 338–402. DOI: [10.1016/j.pnpnp.2007.10.001](https://doi.org/10.1016/j.pnpnp.2007.10.001). arXiv: [0710.0554](https://arxiv.org/abs/0710.0554) [hep-ph].
- [165] Rabindra N. Mohapatra and Goran Senjanovic. “Neutrino Mass and Spontaneous Parity Non-conservation”. *Phys. Rev. Lett.* 44 (1980), p. 912. DOI: [10.1103/PhysRevLett.44.912](https://doi.org/10.1103/PhysRevLett.44.912).
- [166] M. Zralek. “On the possibilities of distinguishing Dirac from Majorana neutrinos”. *Acta Phys. Polon. B* 28 (1997). Ed. by K. Kolodziej, pp. 2225–2257. arXiv: [hep-ph/9711506](https://arxiv.org/abs/hep-ph/9711506).
- [167] U. D. Jentschura and B. J. Wundt. “Neutrino helicity reversal and fundamental symmetries”. *J. Phys. G* 41 (2014), p. 075201. DOI: [10.1088/0954-3899/41/7/075201](https://doi.org/10.1088/0954-3899/41/7/075201). arXiv: [1206.6342](https://arxiv.org/abs/1206.6342) [hep-ph].
- [168] Boris Kayser, F. Gibrat-Debu, and F. Perrier. *The Physics of massive neutrinos*. Vol. 25. 1989.
- [169] Robert-Jan Hagebout. “Beyond the Standard Model with neutrino physics” (2014).
- [170] Wendell H Furry. “On transition probabilities in double beta-disintegration”. *Physical Review* 56.12 (1939), p. 1184.
- [171] Maria Goepfert-Mayer. “Double beta-disintegration”. *Physical Review* 48.6 (1935), p. 512.
- [172] Ruben Saakyan. “Two-neutrino double-beta decay”. *Annual Review of Nuclear and Particle Science* 63 (2013), pp. 503–529.
- [173] Matteo Agostini, Giovanni Benato, and Jason Detwiler. “Discovery probability of next-generation neutrinoless double- β decay experiments”. *Phys. Rev. D* 96.5 (2017), p. 053001. DOI: [10.1103/PhysRevD.96.053001](https://doi.org/10.1103/PhysRevD.96.053001). arXiv: [1705.02996](https://arxiv.org/abs/1705.02996) [hep-ex].
- [174] Matteo Agostini et al. “Toward the discovery of matter creation with neutrinoless double-beta decay” (Feb. 2022). arXiv: [2202.01787](https://arxiv.org/abs/2202.01787) [hep-ex].
- [175] F. Edzards. “The Future of Neutrinoless Double Beta Decay Searches with Germanium Detectors”. *J. Phys. Conf. Ser.* 1690.1 (2020). Ed. by Petr Teterin, p. 012180. DOI: [10.1088/1742-6596/1690/1/012180](https://doi.org/10.1088/1742-6596/1690/1/012180).
- [176] N. Abgrall et al. “The Large Enriched Germanium Experiment for Neutrinoless $\beta\beta$ Decay: LEGEND-1000 Preconceptual Design Report” (July 2021). arXiv: [2107.11462](https://arxiv.org/abs/2107.11462) [physics.ins-det].
- [177] Pavel P. Povinec. “Background constrains of the SuperNEMO experiment for neutrinoless double beta-decay searches”. *Nucl. Instrum. Meth. A* 845 (2017). Ed. by G. Badurek et al., pp. 398–403. DOI: [10.1016/j.nima.2016.06.104](https://doi.org/10.1016/j.nima.2016.06.104).
- [178] R. Arnold et al. “Probing New Physics Models of Neutrinoless Double Beta Decay with SuperNEMO”. *Eur. Phys. J. C* 70 (2010), pp. 927–943. DOI: [10.1140/epjc/s10052-010-1481-5](https://doi.org/10.1140/epjc/s10052-010-1481-5). arXiv: [1005.1241](https://arxiv.org/abs/1005.1241) [hep-ex].
- [179] G. Wang et al. “CUPID: CUORE (Cryogenic Underground Observatory for Rare Events) Upgrade with Particle Identification” (Apr. 2015). arXiv: [1504.03599](https://arxiv.org/abs/1504.03599) [physics.ins-det].
- [180] O. Azzolini et al. “First Result on the Neutrinoless Double- β Decay of ^{82}Se with CUPID-0”. *Phys. Rev. Lett.* 120.23 (2018), p. 232502. DOI: [10.1103/PhysRevLett.120.232502](https://doi.org/10.1103/PhysRevLett.120.232502). arXiv: [1802.07791](https://arxiv.org/abs/1802.07791) [nucl-ex].
- [181] C. Alduino et al. “First Results from CUORE: A Search for Lepton Number Violation via $0\nu\beta\beta$ Decay of ^{130}Te ”. *Phys. Rev. Lett.* 120.13 (2018), p. 132501. DOI: [10.1103/PhysRevLett.120.132501](https://doi.org/10.1103/PhysRevLett.120.132501). arXiv: [1710.07988](https://arxiv.org/abs/1710.07988) [nucl-ex].
- [182] K. Singh. “Neutrino Physics with SNO+ and Detector Status”. *14th ICATPP Conference on Astroparticle, Particle, Space Physics and Detectors for Physics Applications*. 2014, pp. 297–303. DOI: [10.1142/9789814603164_0046](https://doi.org/10.1142/9789814603164_0046).
- [183] V. Albanese et al. “The SNO+ experiment”. *JINST* 16.08 (2021), P08059. DOI: [10.1088/1748-0221/16/08/P08059](https://doi.org/10.1088/1748-0221/16/08/P08059). arXiv: [2104.11687](https://arxiv.org/abs/2104.11687) [physics.ins-det].
- [184] A. Gando et al. “Search for Majorana Neutrinos near the Inverted Mass Hierarchy Region with KamLAND-Zen”. *Phys. Rev. Lett.* 117.8 (2016). [Addendum: *Phys.Rev.Lett.* 117, 109903 (2016)], p. 082503. DOI: [10.1103/PhysRevLett.117.082503](https://doi.org/10.1103/PhysRevLett.117.082503). arXiv: [1605.02889](https://arxiv.org/abs/1605.02889) [hep-ex].
- [185] G. Adhikari et al. “nEXO: Neutrinoless double beta decay search beyond 10^{28} year half-life sensitivity” (June 2021). arXiv: [2106.16243](https://arxiv.org/abs/2106.16243) [nucl-ex].
- [186] V. Alvarez et al. “NEXT-100 Technical Design Report (TDR): Executive Summary”. *JINST* 7 (2012), T06001. DOI: [10.1088/1748-0221/7/06/T06001](https://doi.org/10.1088/1748-0221/7/06/T06001). arXiv: [1202.0721](https://arxiv.org/abs/1202.0721) [physics.ins-det].

- [187] J. Martín-Albo et al. “Sensitivity of NEXT-100 to Neutrinoless Double Beta Decay”. *JHEP* 05 (2016), p. 159. DOI: [10.1007/JHEP05\(2016\)159](https://doi.org/10.1007/JHEP05(2016)159). arXiv: [1511.09246](https://arxiv.org/abs/1511.09246) [physics.ins-det].
- [188] Ke Han. “PandaX-III: Searching for Neutrinoless Double Beta Decay with High Pressure Gaseous Time Projection Chambers”. *J. Phys. Conf. Ser.* 1342.1 (2020). Ed. by Ken Clark et al., p. 012095. DOI: [10.1088/1742-6596/1342/1/012095](https://doi.org/10.1088/1742-6596/1342/1/012095). arXiv: [1710.08908](https://arxiv.org/abs/1710.08908) [physics.ins-det].
- [189] Joseph A. Formaggio, André Luiz C. de Gouvêa, and R. G. Hamish Robertson. “Direct Measurements of Neutrino Mass” (Jan. 2021). arXiv: [2102.00594](https://arxiv.org/abs/2102.00594) [nucl-ex].
- [190] M. Aker et al. “First direct neutrino-mass measurement with sub-eV sensitivity” (May 2021). arXiv: [2105.08533](https://arxiv.org/abs/2105.08533) [hep-ex].
- [191] Benjamin Monreal and Joseph A. Formaggio. “Relativistic Cyclotron Radiation Detection of Tritium Decay Electrons as a New Technique for Measuring the Neutrino Mass”. *Phys. Rev. D* 80 (2009), p. 051301. DOI: [10.1103/PhysRevD.80.051301](https://doi.org/10.1103/PhysRevD.80.051301). arXiv: [0904.2860](https://arxiv.org/abs/0904.2860) [nucl-ex].
- [192] Ali Ashtari Esfahani et al. “Determining the neutrino mass with cyclotron radiation emission spectroscopy—Project 8”. *J. Phys. G* 44.5 (2017), p. 054004. DOI: [10.1088/1361-6471/aa5b4f](https://doi.org/10.1088/1361-6471/aa5b4f). arXiv: [1703.02037](https://arxiv.org/abs/1703.02037) [physics.ins-det].
- [193] Gary Steigman. “Neutrinos And Big Bang Nucleosynthesis”. *Adv. High Energy Phys.* 2012 (2012), p. 268321. DOI: [10.1155/2012/268321](https://doi.org/10.1155/2012/268321). arXiv: [1208.0032](https://arxiv.org/abs/1208.0032) [hep-ph].
- [194] Daniel D Baumann et al. “First constraint on the neutrino-induced phase shift in the spectrum of baryon acoustic oscillations”. *Nature Phys.* 15 (2019), pp. 465–469. DOI: [10.1038/s41567-019-0435-6](https://doi.org/10.1038/s41567-019-0435-6). arXiv: [1803.10741](https://arxiv.org/abs/1803.10741) [astro-ph.CO].
- [195] Daniel D Baumann et al. “First constraint on the neutrino-induced phase shift in the spectrum of baryon acoustic oscillations”. *Nature Phys.* 15 (2019), pp. 465–469. DOI: [10.1038/s41567-019-0435-6](https://doi.org/10.1038/s41567-019-0435-6). arXiv: [1803.10741](https://arxiv.org/abs/1803.10741) [astro-ph.CO].
- [196] P. A. R. Ade et al. “Planck 2015 results. XIII. Cosmological parameters”. *Astron. Astrophys.* 594 (2016), A13. DOI: [10.1051/0004-6361/201525830](https://doi.org/10.1051/0004-6361/201525830). arXiv: [1502.01589](https://arxiv.org/abs/1502.01589) [astro-ph.CO].
- [197] Romina Ahumada et al. “The 16th Data Release of the Sloan Digital Sky Surveys: First Release from the APOGEE-2 Southern Survey and Full Release of eBOSS Spectra”. *Astrophys. J. Suppl.* 249.1 (2020), p. 3. DOI: [10.3847/1538-4365/ab929e](https://doi.org/10.3847/1538-4365/ab929e). arXiv: [1912.02905](https://arxiv.org/abs/1912.02905) [astro-ph.GA].
- [198] Kevork N. Abazajian et al. “CMB-S4 Science Book, First Edition” (Oct. 2016). arXiv: [1610.02743](https://arxiv.org/abs/1610.02743) [astro-ph.CO].
- [199] Kendall Mahn, Chris Marshall, and Calcium Wilkinson. “Progress in Measurements of 0.1–10 GeV Neutrino–Nucleus Scattering and Anticipated Results from Future Experiments”. *Ann. Rev. Nucl. Part. Sci.* 68 (2018), pp. 105–129. DOI: [10.1146/annurev-nucl-101917-020930](https://doi.org/10.1146/annurev-nucl-101917-020930). arXiv: [1803.08848](https://arxiv.org/abs/1803.08848) [hep-ex].
- [200] C HL Smith. *NEUTRINO REACTIONS AT ACCELERATOR ENERGIES*. Tech. rep. Stanford Univ., Calif., 1972.
- [201] G. Hohler et al. “Analysis of Electromagnetic Nucleon Form-Factors”. *Nucl. Phys. B* 114 (1976), pp. 505–534. DOI: [10.1016/0550-3213\(76\)90449-1](https://doi.org/10.1016/0550-3213(76)90449-1).
- [202] R. G. Sachs. “High-Energy Behavior of Nucleon Electromagnetic Form Factors”. *Phys. Rev.* 126 (1962), pp. 2256–2260. DOI: [10.1103/PhysRev.126.2256](https://doi.org/10.1103/PhysRev.126.2256).
- [203] S. S. Gershtein and Ya. B. Zeldovich. “Meson corrections in the theory of beta decay”. *Zh. Eksp. Teor. Fiz.* 29 (1955). Ed. by Yu. A. Trutnev, pp. 698–699.
- [204] Zhihong Ye et al. “Proton and neutron electromagnetic form factors and uncertainties”. *Physics Letters B* 777 (2018), pp. 8–15.
- [205] T. Leitner et al. “Electron- and neutrino-nucleus scattering from the quasielastic to the resonance region”. *Phys. Rev. C* 79 (2009), p. 034601. DOI: [10.1103/PhysRevC.79.034601](https://doi.org/10.1103/PhysRevC.79.034601). arXiv: [0812.0587](https://arxiv.org/abs/0812.0587) [nucl-th].
- [206] Oleksandr Tomalak. “Axial and pseudoscalar form factors from charged current quasielastic neutrino-nucleon scattering”. *Physical Review D* 103.1 (2021), p. 013006.
- [207] MA-P Brown et al. “New result for the neutron β -asymmetry parameter A_0 from UCNA”. *Physical Review C* 97.3 (2018), p. 035505.
- [208] S. K. Singh and E. Oset. “Quasielastic neutrino (anti-neutrino) reactions in nuclei and the axial vector form-factor of the nucleon”. *Nucl. Phys. A* 542 (1992), pp. 587–615. DOI: [10.1016/0375-9474\(92\)90259-M](https://doi.org/10.1016/0375-9474(92)90259-M).
- [209] Konstantin S. Kuzmin, Vladimir V. Lyubushkin, and Vadim A. Naumov. “Quasielastic axial-vector mass from experiments on neutrino-nucleus scattering”. *Eur. Phys. J. C* 54 (2008), pp. 517–538. DOI: [10.1140/epjc/s10052-008-0582-x](https://doi.org/10.1140/epjc/s10052-008-0582-x). arXiv: [0712.4384](https://arxiv.org/abs/0712.4384) [hep-ph].

- [210] John R. Ellis. “Strangeness and hadron structure”. *Nucl. Phys. A* 684 (2001). Ed. by Chi-Yee Cheung et al., pp. 53–70. DOI: [10.1016/S0375-9474\(01\)00488-2](https://doi.org/10.1016/S0375-9474(01)00488-2). arXiv: [hep-ph/0005322](https://arxiv.org/abs/hep-ph/0005322).
- [211] Jeremy Green et al. “High-precision calculation of the strange nucleon electromagnetic form factors”. *Phys. Rev. D* 92.3 (2015), p. 031501. DOI: [10.1103/PhysRevD.92.031501](https://doi.org/10.1103/PhysRevD.92.031501). arXiv: [1505.01803](https://arxiv.org/abs/1505.01803) [hep-lat].
- [212] Raza Sabbir Sufian et al. “Strange quark magnetic moment of the nucleon at the physical point”. *Physical review letters* 118.4 (2017), p. 042001.
- [213] Raza Sabbir Sufian, Keh-Fei Liu, and David G. Richards. “Weak neutral current axial form factor using $(\bar{\nu})\nu$ -nucleon scattering and lattice QCD inputs”. *JHEP* 01 (2020), p. 136. DOI: [10.1007/JHEP01\(2020\)136](https://doi.org/10.1007/JHEP01(2020)136). arXiv: [1809.03509](https://arxiv.org/abs/1809.03509) [hep-ph].
- [214] R Ph Feynman, M Kislinger, and F Ravndal. “Current matrix elements from a relativistic quark model”. *Physical Review D* 3.11 (1971), p. 2706.
- [215] Dieter Rein and Lalit M Sehgal. “Neutrino-excitation of baryon resonances and single pion production”. *Annals of Physics* 133.1 (1981), pp. 79–153.
- [216] D Rein. “Angular distribution in neutrino-induced single pion production processes”. *Zeitschrift für Physik C Particles and Fields* 35.1 (1987), pp. 43–64.
- [217] Konstantin S. Kuzmin, Vladimir V. Lyubushkin, and Vadim A. Naumov. “Lepton polarization in neutrino nucleon interactions”. *Mod. Phys. Lett. A* 19 (2004). Ed. by A. V. Efremov and O. V. Teryaev, pp. 2815–2829. DOI: [10.1142/S0217732304016172](https://doi.org/10.1142/S0217732304016172). arXiv: [hep-ph/0312107](https://arxiv.org/abs/hep-ph/0312107).
- [218] Emmanuel A Paschos, Ji-Young Yu, and Makoto Sakuda. “Neutrino production of resonances”. *Physical Review D* 69.1 (2004), p. 014013.
- [219] Krzysztof M. Graczyk and Jan T. Sobczyk. “Form Factors in the Quark Resonance Model”. *Phys. Rev. D* 77 (2008). [Erratum: *Phys.Rev.D* 79, 079903 (2009)], p. 053001. DOI: [10.1103/PhysRevD.79.079903](https://doi.org/10.1103/PhysRevD.79.079903). arXiv: [0707.3561](https://arxiv.org/abs/0707.3561) [hep-ph].
- [220] Krzysztof M Graczyk and Jan T Sobczyk. “Lepton mass effects in weak charged current single pion production”. *Physical Review D* 77.5 (2008), p. 053003.
- [221] Ch Berger and LM Sehgal. “Lepton mass effects in single pion production by neutrinos”. *Physical Review D* 76.11 (2007), p. 113004.
- [222] E Hernandez, J Nieves, and M Valverde. “Weak pion production off the nucleon”. *Physical Review D* 76.3 (2007), p. 033005.
- [223] J. Nieves, I. Ruiz Simo, and M. J. Vicente Vacas. “Inclusive Charged-Current Neutrino-Nucleus Reactions”. *Phys. Rev. C* 83 (2011), p. 045501. DOI: [10.1103/PhysRevC.83.045501](https://doi.org/10.1103/PhysRevC.83.045501). arXiv: [1102.2777](https://arxiv.org/abs/1102.2777) [hep-ph].
- [224] Monireh Kabirnezhad. “Single pion production in neutrino-nucleon Interactions”. *Phys. Rev. D* 97.1 (2018), p. 013002. DOI: [10.1103/PhysRevD.97.013002](https://doi.org/10.1103/PhysRevD.97.013002). arXiv: [1711.02403](https://arxiv.org/abs/1711.02403) [hep-ph].
- [225] M. Kabirnezhad. “Single pion production in electron-nucleon interactions”. *Phys. Rev. D* 102.5 (2020), p. 053009. DOI: [10.1103/PhysRevD.102.053009](https://doi.org/10.1103/PhysRevD.102.053009). arXiv: [2006.13765](https://arxiv.org/abs/2006.13765) [hep-ph].
- [226] G. Breit and E. Wigner. “Capture of Slow Neutrons”. *Phys. Rev.* 49 (1936), pp. 519–531. DOI: [10.1103/PhysRev.49.519](https://doi.org/10.1103/PhysRev.49.519).
- [227] A. D. Martin et al. “Parton distributions for the LHC”. *Eur. Phys. J. C* 63 (2009), pp. 189–285. DOI: [10.1140/epjc/s10052-009-1072-5](https://doi.org/10.1140/epjc/s10052-009-1072-5). arXiv: [0901.0002](https://arxiv.org/abs/0901.0002) [hep-ph].
- [228] Samoil M. Bilenky. “Neutrinos” (Mar. 2001). arXiv: [physics/0103091](https://arxiv.org/abs/physics/0103091).
- [229] E. A. Paschos and L. Wolfenstein. “Tests for Neutral Currents in Neutrino Reactions”. *Phys. Rev. D* 7 (1973), pp. 91–95. DOI: [10.1103/PhysRevD.7.91](https://doi.org/10.1103/PhysRevD.7.91).
- [230] Omar Benhar et al. “Electron- and neutrino-nucleus scattering in the impulse approximation regime”. *Phys. Rev. D* 72 (2005), p. 053005. DOI: [10.1103/PhysRevD.72.053005](https://doi.org/10.1103/PhysRevD.72.053005). arXiv: [hep-ph/0506116](https://arxiv.org/abs/hep-ph/0506116).
- [231] Callum Wilkinson. “Overview of Neutrino-Nucleus Interaction Physics”. NNN Conference. 2017. URL: <https://indi.to/LRGT9>.
- [232] Ernest J Moniz et al. “Nuclear fermi momenta from quasielastic electron scattering”. *Physical Review Letters* 26.8 (1971), p. 445.
- [233] Golan Tomasz. “Modeling nuclear effects in NuWro Monte Carlo neutrino event generator”. PhD thesis. University of Wroclaw, 2014.
- [234] A. Bodek, M. E. Christy, and B. Coopersmith. “Effective Spectral Function for Quasielastic Scattering on Nuclei”. *Eur. Phys. J. C* 74.10 (2014), p. 3091. DOI: [10.1140/epjc/s10052-014-3091-0](https://doi.org/10.1140/epjc/s10052-014-3091-0). arXiv: [1405.0583](https://arxiv.org/abs/1405.0583) [hep-ph].
- [235] Luke Pickering. “Examining nuclear effects in neutrino interactions with transverse kinematic imbalance”. *JPS Conf. Proc.* 12 (2016), p. 010032. DOI: [10.7566/JPSCP.12.010032](https://doi.org/10.7566/JPSCP.12.010032). arXiv: [1602.06730](https://arxiv.org/abs/1602.06730) [hep-ex].
- [236] R. A. Smith and E. J. Moniz. “Neutrino reactions on nuclear targets”. *Nucl. Phys. B* 43 (1972). [Erratum: *Nucl.Phys.B* 101, 547 (1975)], p. 605. DOI: [10.1016/0550-3213\(75\)90612-4](https://doi.org/10.1016/0550-3213(75)90612-4).

- [237] S. K. Singh and E. Oset. “Inclusive quasielastic neutrino reactions in C-12 and O-16 at intermediate-energies”. *Phys. Rev. C* 48 (1993), pp. 1246–1258. DOI: [10.1103/PhysRevC.48.1246](https://doi.org/10.1103/PhysRevC.48.1246).
- [238] K. Gallmeister, U. Mosel, and J. Weil. “Neutrino-Induced Reactions on Nuclei”. *Phys. Rev. C* 94.3 (2016), p. 035502. DOI: [10.1103/PhysRevC.94.035502](https://doi.org/10.1103/PhysRevC.94.035502). arXiv: [1605.09391 \[nucl-th\]](https://arxiv.org/abs/1605.09391).
- [239] Omar Benhar and Adelchi Fabrocini. “Two-nucleon spectral function in infinite nuclear matter”. *Physical Review C* 62.3 (2000), p. 034304.
- [240] M. Leuschner et al. “Quasielastic proton knockout from O-16”. *Phys. Rev. C* 49 (1994), pp. 955–967. DOI: [10.1103/PhysRevC.49.955](https://doi.org/10.1103/PhysRevC.49.955).
- [241] Joanna Ewa Sobczyk. “Intercomparison of lepton-nucleus scattering models in the quasielastic region”. *Phys. Rev. C* 96.4 (2017), p. 045501. DOI: [10.1103/PhysRevC.96.045501](https://doi.org/10.1103/PhysRevC.96.045501). arXiv: [1706.06739 \[nucl-th\]](https://arxiv.org/abs/1706.06739).
- [242] A. Bodek, M. E. Christy, and B. Coopersmith. “Effective Spectral Function for Quasielastic Scattering on Nuclei”. *Nucl. Part. Phys. Proc.* 273-275 (2016). Ed. by M Aguilar-Benitez et al., pp. 1705–1710. DOI: [10.1016/j.nuclphysbps.2015.09.275](https://doi.org/10.1016/j.nuclphysbps.2015.09.275).
- [243] A. Bodek, M. E. Christy, and B. Cooper-smith. “Effective spectral function for quasielastic scattering on nuclei from ${}^2_1\text{H}$ to ${}^{208}_{82}\text{Pb}$ ”. *AIP Conf. Proc.* 1680.1 (2015). Ed. by Barbara Szczerbinska and Elizabeth Worcester, p. 020003. DOI: [10.1063/1.4931862](https://doi.org/10.1063/1.4931862). arXiv: [1409.8545 \[nucl-th\]](https://arxiv.org/abs/1409.8545).
- [244] C. Maieron et al. “Nuclear model effects in charged current neutrino nucleus quasielastic scattering”. *Phys. Rev. C* 68 (2003), p. 048501. DOI: [10.1103/PhysRevC.68.048501](https://doi.org/10.1103/PhysRevC.68.048501). arXiv: [nucl-th/0303075](https://arxiv.org/abs/nucl-th/0303075).
- [245] Andrea Meucci, Carlotta Giusti, and Franco Davide Pacati. “Relativistic Green’s function approach to charged current neutrino nucleus quasielastic scattering”. *Nucl. Phys. A* 739 (2004), pp. 277–290. DOI: [10.1016/j.nuclphysa.2004.04.108](https://doi.org/10.1016/j.nuclphysa.2004.04.108). arXiv: [nucl-th/0311081](https://arxiv.org/abs/nucl-th/0311081).
- [246] G. T. Garvey et al. “Recent Advances and Open Questions in Neutrino-induced Quasi-elastic Scattering and Single Photon Production”. *Phys. Rept.* 580 (2015), pp. 1–45. DOI: [10.1016/j.physrep.2015.04.001](https://doi.org/10.1016/j.physrep.2015.04.001). arXiv: [1412.4294 \[hep-ex\]](https://arxiv.org/abs/1412.4294).
- [247] AA Aguilar-Arevalo et al. “First measurement of the muon neutrino charged current quasielastic double differential cross section”. *Physical Review D* 81.9 (2010), p. 092005.
- [248] Veronique Bernard, Latifa Elouadrhiri, and Ulf-G. Meissner. “Axial structure of the nucleon: Topical Review”. *J. Phys. G* 28 (2002), R1–R35. DOI: [10.1088/0954-3899/28/1/201](https://doi.org/10.1088/0954-3899/28/1/201). arXiv: [hep-ph/0107088](https://arxiv.org/abs/hep-ph/0107088).
- [249] M. Martini et al. “A Unified approach for nucleon knock-out, coherent and incoherent pion production in neutrino interactions with nuclei”. *Phys. Rev. C* 80 (2009), p. 065501. DOI: [10.1103/PhysRevC.80.065501](https://doi.org/10.1103/PhysRevC.80.065501). arXiv: [0910.2622 \[nucl-th\]](https://arxiv.org/abs/0910.2622).
- [250] J. E. Sobczyk, J. Nieves, and F. Sánchez. “Exclusive-final-state hadron observables from neutrino-nucleus multinucleon knockout”. *Phys. Rev. C* 102.2 (2020), p. 024601. DOI: [10.1103/PhysRevC.102.024601](https://doi.org/10.1103/PhysRevC.102.024601). arXiv: [2002.08302 \[nucl-th\]](https://arxiv.org/abs/2002.08302).
- [251] L. Alvarez-Ruso, Y. Hayato, and J. Nieves. “Progress and open questions in the physics of neutrino cross sections at intermediate energies”. *New J. Phys.* 16 (2014), p. 075015. DOI: [10.1088/1367-2630/16/7/075015](https://doi.org/10.1088/1367-2630/16/7/075015). arXiv: [1403.2673 \[hep-ph\]](https://arxiv.org/abs/1403.2673).
- [252] L. Alvarez-Ruso et al. “NuSTEC White Paper: Status and challenges of neutrino–nucleus scattering”. *Prog. Part. Nucl. Phys.* 100 (2018), pp. 1–68. DOI: [10.1016/j.pnpnp.2018.01.006](https://doi.org/10.1016/j.pnpnp.2018.01.006). arXiv: [1706.03621 \[hep-ph\]](https://arxiv.org/abs/1706.03621).
- [253] Callum Wilkinson et al. “Reanalysis of bubble chamber measurements of muon-neutrino induced single pion production”. *Phys. Rev. D* 90.11 (2014), p. 112017. DOI: [10.1103/PhysRevD.90.112017](https://doi.org/10.1103/PhysRevD.90.112017). arXiv: [1411.4482 \[hep-ex\]](https://arxiv.org/abs/1411.4482).
- [254] G. D’Agostini. “A Multidimensional unfolding method based on Bayes’ theorem”. *Nucl. Instrum. Meth. A* 362 (1995), pp. 487–498. DOI: [10.1016/0168-9002\(95\)00274-X](https://doi.org/10.1016/0168-9002(95)00274-X).
- [255] Ko Abe et al. “Measurement of double-differential muon neutrino charged-current interactions on C₈H₈ without pions in the final state using the T2K off-axis beam”. *Phys. Rev. D* 93.11 (2016), p. 112012. DOI: [10.1103/PhysRevD.93.112012](https://doi.org/10.1103/PhysRevD.93.112012). arXiv: [1602.03652 \[hep-ex\]](https://arxiv.org/abs/1602.03652).
- [256] C. Andreopoulos et al. “Summary of the NuSTEC Workshop on Shallow- and Deep-Inelastic Scattering”. *NuSTEC Workshop on Shallow- and Deep-Inelastic Scattering*. July 2019. arXiv: [1907.13252 \[hep-ph\]](https://arxiv.org/abs/1907.13252).
- [257] L. Aliaga et al. “Summary of the NuSTEC Workshop on Neutrino-Nucleus Pion Production in the Resonance Region”. *NuSTEC Workshop on Neutrino-Nucleus Pion Production in the Resonance Region*. Nov. 2020. arXiv: [2011.07166 \[hep-ph\]](https://arxiv.org/abs/2011.07166).

- [258] C. Andreopoulos et al. “The GENIE Neutrino Monte Carlo Generator”. *Nucl. Instrum. Meth. A* 614 (2010), pp. 87–104. DOI: [10.1016/j.nima.2009.12.009](https://doi.org/10.1016/j.nima.2009.12.009). arXiv: [0905.2517](https://arxiv.org/abs/0905.2517) [hep-ph].
- [259] Y. Hayato. “NEUT”. *Nucl. Phys. B Proc. Suppl.* 112 (2002). Ed. by J. G. Morfin, M. Sakuda, and Y. Suzuki, pp. 171–176. DOI: [10.1016/S0920-5632\(02\)01759-0](https://doi.org/10.1016/S0920-5632(02)01759-0).
- [260] O. Buss et al. “Transport-theoretical Description of Nuclear Reactions”. *Phys. Rept.* 512 (2012), pp. 1–124. DOI: [10.1016/j.physrep.2011.12.001](https://doi.org/10.1016/j.physrep.2011.12.001). arXiv: [1106.1344](https://arxiv.org/abs/1106.1344) [hep-ph].
- [261] Cezary Juszczak, Jaroslaw A. Nowak, and Jan T. Sobczyk. “Simulations from a new neutrino event generator”. *Nucl. Phys. B Proc. Suppl.* 159 (2006). Ed. by F. Cavanna, J. G. Morfin, and T. Nakaya, pp. 211–216. DOI: [10.1016/j.nuclphysbps.2006.08.069](https://doi.org/10.1016/j.nuclphysbps.2006.08.069). arXiv: [hep-ph/0512365](https://arxiv.org/abs/hep-ph/0512365).
- [262] P. Stowell et al. “NUISANCE: a neutrino cross-section generator tuning and comparison framework”. *JINST* 12.01 (2017), P01016. DOI: [10.1088/1748-0221/12/01/P01016](https://doi.org/10.1088/1748-0221/12/01/P01016). arXiv: [1612.07393](https://arxiv.org/abs/1612.07393) [hep-ex].
- [263] Ciro Riccio. “Measurement of the antineutrino flux and cross section at the near detector of the T2K experiment”. PhD thesis. Naples U., 2017.
- [264] A. Bodek and J. L. Ritchie. “Fermi Motion Effects in Deep Inelastic Lepton Scattering from Nuclear Targets”. *Phys. Rev. D* 23 (1981), p. 1070. DOI: [10.1103/PhysRevD.23.1070](https://doi.org/10.1103/PhysRevD.23.1070).
- [265] R. Bradford et al. “A New parameterization of the nucleon elastic form-factors”. *Nucl. Phys. B Proc. Suppl.* 159 (2006). Ed. by F. Cavanna, J. G. Morfin, and T. Nakaya, pp. 127–132. DOI: [10.1016/j.nuclphysbps.2006.08.028](https://doi.org/10.1016/j.nuclphysbps.2006.08.028). arXiv: [hep-ex/0602017](https://arxiv.org/abs/hep-ex/0602017).
- [266] Luis Alvarez-Ruso et al. “Recent highlights from GENIE v3”. *Eur. Phys. J. ST* 230.24 (2021), pp. 4449–4467. DOI: [10.1140/epjs/s11734-021-00295-7](https://doi.org/10.1140/epjs/s11734-021-00295-7). arXiv: [2106.09381](https://arxiv.org/abs/2106.09381) [hep-ph].
- [267] Konstantin S. Kuzmin, Vladimir V. Lyubushkin, and Vadim A. Naumov. “Axial masses in quasielastic neutrino scattering and single-pion neutrino production on nucleons and nuclei”. *Acta Phys. Polon. B* 37 (2006). Ed. by K. M. Graczyk and J. T. Sobczyk, pp. 2337–2348. arXiv: [hep-ph/0606184](https://arxiv.org/abs/hep-ph/0606184).
- [268] M. Glück, E. Reya, and A. Vogt. “Dynamical parton distributions revisited”. *Eur. Phys. J. C* 5 (1998), pp. 461–470. DOI: [10.1007/s100520050289](https://doi.org/10.1007/s100520050289). arXiv: [hep-ph/9806404](https://arxiv.org/abs/hep-ph/9806404).
- [269] Z. Koba, Holger Bech Nielsen, and P. Olesen. “Scaling of multiplicity distributions in high-energy hadron collisions”. *Nucl. Phys. B* 40 (1972), pp. 317–334. DOI: [10.1016/0550-3213\(72\)90551-2](https://doi.org/10.1016/0550-3213(72)90551-2).
- [270] T. Yang et al. “A Hadronization Model for Few-GeV Neutrino Interactions”. *Eur. Phys. J. C* 63 (2009), pp. 1–10. DOI: [10.1140/epjc/s10052-009-1094-z](https://doi.org/10.1140/epjc/s10052-009-1094-z). arXiv: [0904.4043](https://arxiv.org/abs/0904.4043) [hep-ph].
- [271] Torbjorn Sjostrand, Stephen Mrenna, and Peter Z. Skands. “PYTHIA 6.4 Physics and Manual”. *JHEP* 05 (2006), p. 026. DOI: [10.1088/1126-6708/2006/05/026](https://doi.org/10.1088/1126-6708/2006/05/026). arXiv: [hep-ph/0603175](https://arxiv.org/abs/hep-ph/0603175).
- [272] Steve Dytman, Hugh Gallagher, and Michael Kordosky. “Hadronic Shower Energy Scale Uncertainty in the MINOS Experiment” (June 2008). arXiv: [0806.2119](https://arxiv.org/abs/0806.2119) [hep-ex].
- [273] Steven Dytman. “Final state interactions in neutrino-nucleus experiments”. *Acta Phys. Polon. B* 40 (2009). Ed. by Arthur Ankowski and Jan Sobczyk, pp. 2445–2460.
- [274] H. Faissner et al. “Measurement of Elastic Muon Neutrino Scattering Off Protons”. *Phys. Rev. D* 21 (1980), pp. 555–561. DOI: [10.1103/PhysRevD.21.555](https://doi.org/10.1103/PhysRevD.21.555).
- [275] H. Faissner et al. “Observation of Neutrino and Anti-neutrino Induced Coherent Neutral Pion Production Off ^{27}Al ”. *Phys. Lett. B* 125 (1983), pp. 230–236. DOI: [10.1016/0370-2693\(83\)91274-1](https://doi.org/10.1016/0370-2693(83)91274-1).
- [276] S. J. Barish et al. “Study of Neutrino Interactions in Hydrogen and Deuterium. 1. Description of the Experiment and Study of the Reaction Neutrino $d \rightarrow \mu^- p(s)$ ”. *Phys. Rev. D* 16 (1977), p. 3103. DOI: [10.1103/PhysRevD.16.3103](https://doi.org/10.1103/PhysRevD.16.3103).
- [277] L. A. Ahrens et al. “A Study of the Axial Vector Form-factor and Second Class Currents in Antineutrino Quasielastic Scattering”. *Phys. Lett. B* 202 (1988). Ed. by A. K. Mann et al., pp. 284–288. DOI: [10.1016/0370-2693\(88\)90026-3](https://doi.org/10.1016/0370-2693(88)90026-3).
- [278] A. Entenberg et al. “Measurement of the Elastic Scattering of Neutrinos and Anti-neutrinos by Protons”. *Phys. Rev. Lett.* 42 (1979), p. 1198. DOI: [10.1103/PhysRevLett.42.1198](https://doi.org/10.1103/PhysRevLett.42.1198).
- [279] J. Campbell et al. “Study of the reaction $\nu n \rightarrow \mu^- p$ ”. *Phys. Rev. Lett.* 30 (1973), pp. 335–339. DOI: [10.1103/PhysRevLett.30.335](https://doi.org/10.1103/PhysRevLett.30.335).
- [280] S. J. Barish et al. “Study of Neutrino Interactions in Hydrogen and Deuterium: Inelastic Charged Current Reactions”. *Phys. Rev. D* 19 (1979), p. 2521. DOI: [10.1103/PhysRevD.19.2521](https://doi.org/10.1103/PhysRevD.19.2521).

- [281] G. M. Radecky et al. “Study of Single Pion Production by Weak Charged Currents in Low-energy Neutrino d Interactions”. *Phys. Rev. D* 25 (1982). [Erratum: *Phys.Rev.D* 26, 3297 (1982)], pp. 1161–1173. DOI: [10.1103/PhysRevD.25.1161](https://doi.org/10.1103/PhysRevD.25.1161).
- [282] D. Day et al. “STUDY OF neutrino D CHARGED CURRENT TWO PION PRODUCTION IN THE THRESHOLD REGION”. *Phys. Rev. D* 28 (1983), pp. 2714–2720. DOI: [10.1103/PhysRevD.28.2714](https://doi.org/10.1103/PhysRevD.28.2714).
- [283] Gian Luigi Fogli and G. Nardulli. “Neutral Current Induced One Pion Production: A New Model and Its Comparison With the Experiment”. *Nucl. Phys. B* 165 (1980), pp. 162–184. DOI: [10.1016/0550-3213\(80\)90312-0](https://doi.org/10.1016/0550-3213(80)90312-0).
- [284] M. Derrick et al. “Study of the Reaction Neutrino $N \rightarrow$ Neutrino $p\pi^-$ ”. *Phys. Lett. B* 92 (1980). [Erratum: *Phys.Lett.B* 95, 461 (1980)], p. 363. DOI: [10.1016/0370-2693\(80\)90283-X](https://doi.org/10.1016/0370-2693(80)90283-X).
- [285] D. Allasia et al. “Investigation of exclusive channels in neutrino / anti-neutrino deuteron charged current interactions”. *Nucl. Phys. B* 343 (1990), pp. 285–309. DOI: [10.1016/0550-3213\(90\)90472-P](https://doi.org/10.1016/0550-3213(90)90472-P).
- [286] M. Aderholz et al. “Measurement of Total Cross-sections for Neutrino and Anti-neutrino Charged Current Interactions in Hydrogen and Neon”. *Phys. Lett. B* 173 (1986). Ed. by S. C. Loken, p. 211. DOI: [10.1016/0370-2693\(86\)90248-0](https://doi.org/10.1016/0370-2693(86)90248-0).
- [287] N. J. Baker et al. “Quasielastic Neutrino Scattering: A Measurement of the Weak Nucleon Axial Vector Form-Factor”. *Phys. Rev. D* 23 (1981), pp. 2499–2505. DOI: [10.1103/PhysRevD.23.2499](https://doi.org/10.1103/PhysRevD.23.2499).
- [288] P. Coteus et al. “Measurement of Elastic Muon-neutrino and Anti-muon-neutrino Scattering on Protons”. *Phys. Rev. D* 24 (1981), pp. 1420–1423. DOI: [10.1103/PhysRevD.24.1420](https://doi.org/10.1103/PhysRevD.24.1420).
- [289] G. Fanourakis et al. “Study of Low-energy Anti-neutrino Interactions on Protons”. *Phys. Rev. D* 21 (1980), p. 562. DOI: [10.1103/PhysRevD.21.562](https://doi.org/10.1103/PhysRevD.21.562).
- [290] T. Kitagaki et al. “Charged Current Exclusive Pion Production in Neutrino Deuterium Interactions”. *Phys. Rev. D* 34 (1986), pp. 2554–2565. DOI: [10.1103/PhysRevD.34.2554](https://doi.org/10.1103/PhysRevD.34.2554).
- [291] Won-Yong Lee et al. “Single Pion Production in Neutrino and anti-neutrino Reactions”. *Phys. Rev. Lett.* 38 (1977), p. 202. DOI: [10.1103/PhysRevLett.38.202](https://doi.org/10.1103/PhysRevLett.38.202).
- [292] T. Kitagaki et al. “High-Energy Quasielastic Muon-neutrino $n \rightarrow \mu^- p$ Scattering in Deuterium”. *Phys. Rev. D* 28 (1983), pp. 436–442. DOI: [10.1103/PhysRevD.28.436](https://doi.org/10.1103/PhysRevD.28.436).
- [293] J. Bell et al. “Cross-section Measurements for the Reactions Neutrino $p \rightarrow \mu^- \pi^+ p$ and Neutrino $p \rightarrow \mu^- K^+ p$ at High-energies”. *Phys. Rev. Lett.* 41 (1978), p. 1008. DOI: [10.1103/PhysRevLett.41.1008](https://doi.org/10.1103/PhysRevLett.41.1008).
- [294] S. J. Barish et al. “Study of the Reaction Anti-neutrino $p \rightarrow \mu^+ p\pi^-$ ”. *Phys. Lett. B* 91 (1980), p. 161. DOI: [10.1016/0370-2693\(80\)90684-X](https://doi.org/10.1016/0370-2693(80)90684-X).
- [295] S. Bonetti et al. “Study of Quasielastic Reactions of Neutrino and anti-neutrino in Gargamelle”. *Nuovo Cim. A* 38 (1977), pp. 260–270. DOI: [10.1007/BF02730023](https://doi.org/10.1007/BF02730023).
- [296] M. Pohl et al. “Study of Neutrino Proton Elastic Scattering in the GARGAMELLE Freon Experiment”. *Phys. Lett. B* 72 (1978), pp. 489–492. DOI: [10.1016/0370-2693\(78\)90741-4](https://doi.org/10.1016/0370-2693(78)90741-4).
- [297] N. Armenise et al. “CHARGED CURRENT ELASTIC ANTI-NEUTRINO INTERACTIONS IN PROPANE”. *Nucl. Phys. B* 152 (1979), pp. 365–375. DOI: [10.1016/0550-3213\(79\)90087-7](https://doi.org/10.1016/0550-3213(79)90087-7).
- [298] W. Krenz et al. “Experimental Study of Exclusive One Pion Production in All Neutrino Induced Neutral Current Channels”. *Nucl. Phys. B* 135 (1978), pp. 45–65. DOI: [10.1016/0550-3213\(78\)90213-4](https://doi.org/10.1016/0550-3213(78)90213-4).
- [299] T. Bolognese et al. “Single Pion Production in Anti-neutrino Induced Charged Current Interactions”. *Phys. Lett. B* 81 (1979), pp. 393–396. DOI: [10.1016/0370-2693\(79\)90361-7](https://doi.org/10.1016/0370-2693(79)90361-7).
- [300] J. Brunner et al. “Quasielastic Nucleon and Hyperon Production by Neutrinos and Anti-neutrinos With Energies Below 30-GeV”. *Z. Phys. C* 45 (1990), p. 551. DOI: [10.1007/BF01556267](https://doi.org/10.1007/BF01556267).
- [301] H. J. Grabosch et al. “Cross-section Measurements of Single Pion Production in Charged Current Neutrino and Anti-neutrino Interactions”. *Z. Phys. C* 41 (1989), p. 527. DOI: [10.1007/BF01564697](https://doi.org/10.1007/BF01564697).
- [302] S. V. Belikov et al. “Quasielastic Neutrino and Anti-neutrinos Scattering: Total Cross-sections, Axial Vector Form-factor”. *Z. Phys. A* 320 (1985), p. 625. DOI: [10.1007/BF01411863](https://doi.org/10.1007/BF01411863).
- [303] J. A. Formaggio and G. P. Zeller. “From eV to EeV: Neutrino Cross Sections Across Energy Scales”. *Rev. Mod. Phys.* 84 (2012), pp. 1307–1341. DOI: [10.1103/RevModPhys.84.1307](https://doi.org/10.1103/RevModPhys.84.1307). arXiv: [1305.7513 \[hep-ex\]](https://arxiv.org/abs/1305.7513).
- [304] P. A. Zyla et al. “Review of Particle Physics”. *PTEP* 2020.8 (2020), p. 083C01. DOI: [10.1093/ptep/ptaa104](https://doi.org/10.1093/ptep/ptaa104).
- [305] K. Abe et al. “J-PARC Neutrino Beamline Upgrade Technical Design Report” (Aug. 2019). arXiv: [1908.05141 \[physics.ins-det\]](https://arxiv.org/abs/1908.05141).

- [306] Pintaudi Giorgio. “T2K-WAGASCI: First physics run of the WAGASCI-BabyMIND detector with full setup”. *PoS LeptonPhoton2019* (2019), p. 142. DOI: [10 . 22323 / 1 . 367 . 0142](https://doi.org/10.22323/1.367.0142).
- [307] Takahiro Odagawa. “Prospect and status of the physics run of the NINJA experiment”. *PoS NuFact2019* (2020), p. 144. DOI: [10 . 22323 / 1 . 369 . 0144](https://doi.org/10.22323/1.369.0144).
- [308] Charlie Naseby. “Improving Hyper-Kamiokande sensitivity to CP violation with high precision near detector electron neutrino cross-section measurements”. *J. Phys. Conf. Ser.* 2156 (2021), p. 012121. DOI: [10 . 1088 / 1742-6596/2156/1/012121](https://doi.org/10.1088/1742-6596/2156/1/012121).
- [309] R. Acciarri et al. “Design and Construction of the MicroBooNE Detector”. *JINST* 12.02 (2017), P02017. DOI: [10 . 1088 / 1748 - 0221 / 12 / 02 / P02017](https://doi.org/10.1088/1748-0221/12/02/P02017). arXiv: 1612 . 05824 [physics.ins-det].
- [310] C. Anderson et al. “First Measurements of Inclusive Muon Neutrino Charged Current Differential Cross Sections on Argon”. *Phys. Rev. Lett.* 108 (2012), p. 161802. DOI: [10 . 1103 / PhysRevLett . 108 . 161802](https://doi.org/10.1103/PhysRevLett.108.161802). arXiv: 1111.0103 [hep-ex].
- [311] R. Acciarri et al. “Measurements of Inclusive Muon Neutrino and Antineutrino Charged Current Differential Cross Sections on Argon in the NuMI Antineutrino Beam”. *Phys. Rev. D* 89.11 (2014), p. 112003. DOI: [10 . 1103 / PhysRevD . 89 . 112003](https://doi.org/10.1103/PhysRevD.89.112003). arXiv: 1404 . 4809 [hep-ex].
- [312] P. Abratenko et al. “First Measurement of Inclusive Muon Neutrino Charged Current Differential Cross Sections on Argon at $E_\nu \sim 0.8$ GeV with the MicroBooNE Detector”. *Phys. Rev. Lett.* 123.13 (2019), p. 131801. DOI: [10 . 1103 / PhysRevLett . 123 . 131801](https://doi.org/10.1103/PhysRevLett.123.131801). arXiv: 1905.09694 [hep-ex].
- [313] P. Abratenko et al. “First Measurement of Energy-Dependent Inclusive Muon Neutrino Charged-Current Cross Sections on Argon with the MicroBooNE Detector”. *Phys. Rev. Lett.* 128.15 (2022), p. 151801. DOI: [10 . 1103 / PhysRevLett . 128 . 151801](https://doi.org/10.1103/PhysRevLett.128.151801). arXiv: 2110.14023 [hep-ex].
- [314] P. Abratenko et al. “Measurement of the flux-averaged inclusive charged-current electron neutrino and antineutrino cross section on argon using the NuMI beam and the MicroBooNE detector”. *Phys. Rev. D* 104.5 (2021), p. 052002. DOI: [10 . 1103 / PhysRevD . 104 . 052002](https://doi.org/10.1103/PhysRevD.104.052002). arXiv: 2101.04228 [hep-ex].
- [315] B. G. Tice et al. “Measurement of Ratios of ν_μ Charged-Current Cross Sections on C, Fe, and Pb to CH at Neutrino Energies 2-20 GeV”. *Phys. Rev. Lett.* 112.23 (2014), p. 231801. DOI: [10 . 1103 / PhysRevLett . 112 . 231801](https://doi.org/10.1103/PhysRevLett.112.231801). arXiv: 1403.2103 [hep-ex].
- [316] P. A. Rodrigues et al. “Identification of nuclear effects in neutrino-carbon interactions at low three-momentum transfer”. *Phys. Rev. Lett.* 116 (2016). [Addendum: *Phys.Rev.Lett.* 121, 209902 (2018)], p. 071802. DOI: [10 . 1103 / PhysRevLett . 116 . 071802](https://doi.org/10.1103/PhysRevLett.116.071802). arXiv: 1511.05944 [hep-ex].
- [317] J. Mousseau et al. “Measurement of Partonic Nuclear Effects in Deep-Inelastic Neutrino Scattering using MINERvA”. *Phys. Rev. D* 93.7 (2016), p. 071101. DOI: [10 . 1103 / PhysRevD . 93 . 071101](https://doi.org/10.1103/PhysRevD.93.071101). arXiv: 1601 . 06313 [hep-ex].
- [318] J. Devan et al. “Measurements of the Inclusive Neutrino and Antineutrino Charged Current Cross Sections in MINERvA Using the Low- ν Flux Method”. *Phys. Rev. D* 94.11 (2016), p. 112007. DOI: [10 . 1103 / PhysRevD . 94 . 112007](https://doi.org/10.1103/PhysRevD.94.112007). arXiv: 1610.04746 [hep-ex].
- [319] L. Ren et al. “Measurement of the antineutrino to neutrino charged-current interaction cross section ratio in MINERvA”. *Phys. Rev. D* 95.7 (2017). [Addendum: *Phys.Rev.D* 97, 019902 (2018)], p. 072009. DOI: [10 . 1103 / PhysRevD . 95 . 072009](https://doi.org/10.1103/PhysRevD.95.072009). arXiv: 1701 . 04857 [hep-ex].
- [320] P. Adamson et al. “Neutrino and Antineutrino Inclusive Charged-current Cross Section Measurements with the MINOS Near Detector”. *Phys. Rev. D* 81 (2010), p. 072002. DOI: [10 . 1103 / PhysRevD . 81 . 072002](https://doi.org/10.1103/PhysRevD.81.072002). arXiv: 0910.2201 [hep-ex].
- [321] Q. Wu et al. “A Precise measurement of the muon neutrino-nucleon inclusive charged current cross-section off an isoscalar target in the energy range $2.5 < E(\nu) < 40$ -GeV by NOMAD”. *Phys. Lett. B* 660 (2008), pp. 19–25. DOI: [10 . 1016 / j . physletb . 2007 . 12 . 027](https://doi.org/10.1016/j.physletb.2007.12.027). arXiv: 0711.1183 [hep-ex].
- [322] Y. Nakajima et al. “Measurement of Inclusive Charged Current Interactions on Carbon in a Few-GeV Neutrino Beam”. *Phys. Rev. D* 83 (2011), p. 012005. DOI: [10 . 1103 / PhysRevD . 83 . 012005](https://doi.org/10.1103/PhysRevD.83.012005). arXiv: 1011 . 2131 [hep-ex].
- [323] K. Abe et al. “Measurement of the inclusive charged current cross section on carbon in the near detector of the T2K experiment”. *Phys. Rev. D* 87.9 (2013), p. 092003. DOI: [10 . 1103 / PhysRevD . 87 . 092003](https://doi.org/10.1103/PhysRevD.87.092003). arXiv: 1302 . 4908 [hep-ex].
- [324] K. Abe et al. “Measurement of inclusive double-differential ν_μ charged-current cross section with improved acceptance in the T2K off-axis near detector”. *Phys. Rev. D* 98 (2018), p. 012004. DOI: [10 . 1103 / PhysRevD . 98 . 012004](https://doi.org/10.1103/PhysRevD.98.012004). arXiv: 1801.05148 [hep-ex].

- [325] K. Abe et al. “Measurement of the ν_μ charged-current cross sections on water, hydrocarbon, iron, and their ratios with the T2K on-axis detectors” (Apr. 2019). DOI: [10.1093/ptep/ptz070](https://doi.org/10.1093/ptep/ptz070). arXiv: [1904.09611](https://arxiv.org/abs/1904.09611) [hep-ex].
- [326] K. Abe et al. “Measurement of the inclusive ν_μ charged current cross section on iron and hydrocarbon in the T2K on-axis neutrino beam”. *Phys. Rev. D* 90.5 (2014), p. 052010. DOI: [10.1103/PhysRevD.90.052010](https://doi.org/10.1103/PhysRevD.90.052010). arXiv: [1407.4256](https://arxiv.org/abs/1407.4256) [hep-ex].
- [327] K. Abe et al. “Measurement of the muon neutrino inclusive charged-current cross section in the energy range of 1–3 GeV with the T2K INGRID detector”. *Phys. Rev. D* 93.7 (2016), p. 072002. DOI: [10.1103/PhysRevD.93.072002](https://doi.org/10.1103/PhysRevD.93.072002). arXiv: [1509.06940](https://arxiv.org/abs/1509.06940) [hep-ex].
- [328] K. Abe et al. “Measurement of the Inclusive Electron Neutrino Charged Current Cross Section on Carbon with the T2K Near Detector”. *Phys. Rev. Lett.* 113.24 (2014), p. 241803. DOI: [10.1103/PhysRevLett.113.241803](https://doi.org/10.1103/PhysRevLett.113.241803). arXiv: [1407.7389](https://arxiv.org/abs/1407.7389) [hep-ex].
- [329] K. Abe et al. “Measurement of the electron neutrino charged-current interaction rate on water with the T2K ND280 π^0 detector”. *Phys. Rev. D* 91 (2015), p. 112010. DOI: [10.1103/PhysRevD.91.112010](https://doi.org/10.1103/PhysRevD.91.112010). arXiv: [1503.08815](https://arxiv.org/abs/1503.08815) [hep-ex].
- [330] K. Abe et al. “Measurement of the charged-current electron (anti-)neutrino inclusive cross-sections at the T2K off-axis near detector ND280”. *JHEP* 10 (2020), p. 114. DOI: [10.1007/JHEP10\(2020\)114](https://doi.org/10.1007/JHEP10(2020)114). arXiv: [2002.11986](https://arxiv.org/abs/2002.11986) [hep-ex].
- [331] K. Abe et al. “Measurement of $\bar{\nu}_\mu$ and ν_μ charged current inclusive cross sections and their ratio with the T2K off-axis near detector”. *Phys. Rev. D* 96.5 (2017), p. 052001. DOI: [10.1103/PhysRevD.96.052001](https://doi.org/10.1103/PhysRevD.96.052001). arXiv: [1706.04257](https://arxiv.org/abs/1706.04257) [hep-ex].
- [332] R. Acciarri et al. “Detection of Back-to-Back Proton Pairs in Charged-Current Neutrino Interactions with the ArgoNeuT Detector in the NuMI Low Energy Beam Line”. *Phys. Rev. D* 90.1 (2014), p. 012008. DOI: [10.1103/PhysRevD.90.012008](https://doi.org/10.1103/PhysRevD.90.012008). arXiv: [1405.4261](https://arxiv.org/abs/1405.4261) [nucl-ex].
- [333] R. Gran et al. “Measurement of the quasi-elastic axial vector mass in neutrino-oxygen interactions”. *Phys. Rev. D* 74 (2006), p. 052002. DOI: [10.1103/PhysRevD.74.052002](https://doi.org/10.1103/PhysRevD.74.052002). arXiv: [hep-ex/0603034](https://arxiv.org/abs/hep-ex/0603034).
- [334] P. Abratenko et al. “First Measurement of Differential Charged Current Quasielastic-like ν_μ -Argon Scattering Cross Sections with the MicroBooNE Detector”. *Phys. Rev. Lett.* 125.20 (2020), p. 201803. DOI: [10.1103/PhysRevLett.125.201803](https://doi.org/10.1103/PhysRevLett.125.201803). arXiv: [2006.00108](https://arxiv.org/abs/2006.00108) [hep-ex].
- [335] G. A. Fiorentini et al. “Measurement of Muon Neutrino Quasielastic Scattering on a Hydrocarbon Target at $E_\nu \sim 3.5$ GeV”. *Phys. Rev. Lett.* 111 (2013), p. 022502. DOI: [10.1103/PhysRevLett.111.022502](https://doi.org/10.1103/PhysRevLett.111.022502). arXiv: [1305.2243](https://arxiv.org/abs/1305.2243) [hep-ex].
- [336] L. Fields et al. “Measurement of Muon Antineutrino Quasielastic Scattering on a Hydrocarbon Target at $E_\nu \sim 3.5$ GeV”. *Phys. Rev. Lett.* 111.2 (2013), p. 022501. DOI: [10.1103/PhysRevLett.111.022501](https://doi.org/10.1103/PhysRevLett.111.022501). arXiv: [1305.2234](https://arxiv.org/abs/1305.2234) [hep-ex].
- [337] M. Betancourt et al. “Direct Measurement of Nuclear Dependence of Charged Current Quasielasticlike Neutrino Interactions Using MINER ν A”. *Phys. Rev. Lett.* 119.8 (2017), p. 082001. DOI: [10.1103/PhysRevLett.119.082001](https://doi.org/10.1103/PhysRevLett.119.082001). arXiv: [1705.03791](https://arxiv.org/abs/1705.03791) [hep-ex].
- [338] T. Walton et al. “Measurement of muon plus proton final states in ν_μ interactions on hydrocarbon at $\langle E_\nu \rangle \geq 4.2$ GeV”. *Phys. Rev. D* 91.7 (2015), p. 071301. DOI: [10.1103/PhysRevD.91.071301](https://doi.org/10.1103/PhysRevD.91.071301). arXiv: [1409.4497](https://arxiv.org/abs/1409.4497) [hep-ex].
- [339] J. Wolcott et al. “Measurement of electron neutrino quasielastic and quasielasticlike scattering on hydrocarbon at $\langle E_\nu \rangle = 3.6$ GeV”. *Phys. Rev. Lett.* 116.8 (2016), p. 081802. DOI: [10.1103/PhysRevLett.116.081802](https://doi.org/10.1103/PhysRevLett.116.081802). arXiv: [1509.05729](https://arxiv.org/abs/1509.05729) [hep-ex].
- [340] D. Ruterbories et al. “Measurement of Quasielastic-Like Neutrino Scattering at $\langle E_\nu \rangle \sim 3.5$ GeV on a Hydrocarbon Target”. *Phys. Rev. D* 99.1 (2019), p. 012004. DOI: [10.1103/PhysRevD.99.012004](https://doi.org/10.1103/PhysRevD.99.012004). arXiv: [1811.02774](https://arxiv.org/abs/1811.02774) [hep-ex].
- [341] C. E. Patrick et al. “Measurement of the Muon Antineutrino Double-Differential Cross Section for Quasielastic-like Scattering on Hydrocarbon at $E_\nu \sim 3.5$ GeV”. *Phys. Rev. D* 97.5 (2018), p. 052002. DOI: [10.1103/PhysRevD.97.052002](https://doi.org/10.1103/PhysRevD.97.052002). arXiv: [1801.01197](https://arxiv.org/abs/1801.01197) [hep-ex].
- [342] X. G. Lu et al. “Measurement of final-state correlations in neutrino muon-proton mesonless production on hydrocarbon at $\langle E_\nu \rangle = 3$ GeV”. *Phys. Rev. Lett.* 121.2 (2018), p. 022504. DOI: [10.1103/PhysRevLett.121.022504](https://doi.org/10.1103/PhysRevLett.121.022504). arXiv: [1805.05486](https://arxiv.org/abs/1805.05486) [hep-ex].
- [343] R. Gran et al. “Antineutrino Charged-Current Reactions on Hydrocarbon with Low Momentum Transfer”. *Phys. Rev. Lett.* 120.22 (2018), p. 221805. DOI: [10.1103/PhysRevLett.120.221805](https://doi.org/10.1103/PhysRevLett.120.221805). arXiv: [1803.09377](https://arxiv.org/abs/1803.09377) [hep-ex].

- [344] A. A. Aguilar-Arevalo et al. “First Measurement of the Muon Neutrino Charged Current Quasielastic Double Differential Cross Section”. *Phys. Rev. D* 81 (2010), p. 092005. DOI: [10.1103/PhysRevD.81.092005](https://doi.org/10.1103/PhysRevD.81.092005). arXiv: [1002.2680](https://arxiv.org/abs/1002.2680) [hep-ex].
- [345] A. A. Aguilar-Arevalo et al. “First measurement of the muon antineutrino double-differential charged-current quasielastic cross section”. *Phys. Rev. D* 88.3 (2013), p. 032001. DOI: [10.1103/PhysRevD.88.032001](https://doi.org/10.1103/PhysRevD.88.032001). arXiv: [1301.7067](https://arxiv.org/abs/1301.7067) [hep-ex].
- [346] A. A. Aguilar-Arevalo et al. “Measurement of muon neutrino quasi-elastic scattering on carbon”. *Phys. Rev. Lett.* 100 (2008), p. 032301. DOI: [10.1103/PhysRevLett.100.032301](https://doi.org/10.1103/PhysRevLett.100.032301). arXiv: [0706.0926](https://arxiv.org/abs/0706.0926) [hep-ex].
- [347] A. A. Aguilar-Arevalo et al. “Measurement of the Neutrino Neutral-Current Elastic Differential Cross Section on Mineral Oil at $E_\nu \sim 1$ GeV”. *Phys. Rev. D* 82 (2010), p. 092005. DOI: [10.1103/PhysRevD.82.092005](https://doi.org/10.1103/PhysRevD.82.092005). arXiv: [1007.4730](https://arxiv.org/abs/1007.4730) [hep-ex].
- [348] A. A. Aguilar-Arevalo et al. “Measurement of the Antineutrino Neutral-Current Elastic Differential Cross Section”. *Phys. Rev. D* 91.1 (2015), p. 012004. DOI: [10.1103/PhysRevD.91.012004](https://doi.org/10.1103/PhysRevD.91.012004). arXiv: [1309.7257](https://arxiv.org/abs/1309.7257) [hep-ex].
- [349] P. Adamson et al. “Study of quasielastic scattering using charged-current $\nu\mu$ -iron interactions in the MINOS near detector”. *Phys. Rev. D* 91.1 (2015), p. 012005. DOI: [10.1103/PhysRevD.91.012005](https://doi.org/10.1103/PhysRevD.91.012005). arXiv: [1410.8613](https://arxiv.org/abs/1410.8613) [hep-ex].
- [350] V Lyubushkin et al. “A Study of quasi-elastic muon neutrino and antineutrino scattering in the NOMAD experiment”. *Eur. Phys. J. C* 63 (2009), pp. 355–381. DOI: [10.1140/epjc/s10052-009-1113-0](https://doi.org/10.1140/epjc/s10052-009-1113-0). arXiv: [0812.4543](https://arxiv.org/abs/0812.4543) [hep-ex].
- [351] L. Wan et al. “Measurement of the neutrino-oxygen neutral-current quasielastic cross section using atmospheric neutrinos at Super-Kamiokande”. *Phys. Rev. D* 99.3 (2019), p. 032005. DOI: [10.1103/PhysRevD.99.032005](https://doi.org/10.1103/PhysRevD.99.032005). arXiv: [1901.05281](https://arxiv.org/abs/1901.05281) [hep-ex].
- [352] K. Abe et al. “First measurement of the ν_μ charged-current cross section on a water target without pions in the final state”. *Phys. Rev. D* 97.1 (2018), p. 012001. DOI: [10.1103/PhysRevD.97.012001](https://doi.org/10.1103/PhysRevD.97.012001). arXiv: [1708.06771](https://arxiv.org/abs/1708.06771) [hep-ex].
- [353] K. Abe et al. “First measurement of the charged current $\bar{\nu}_\mu$ double differential cross section on a water target without pions in the final state”. *Phys. Rev. D* 102.1 (2020), p. 012007. DOI: [10.1103/PhysRevD.102.012007](https://doi.org/10.1103/PhysRevD.102.012007). arXiv: [1908.10249](https://arxiv.org/abs/1908.10249) [hep-ex].
- [354] K. Abe et al. “First combined measurement of the muon neutrino and antineutrino charged-current cross section without pions in the final state at T2K”. *Phys. Rev. D* 101.11 (2020), p. 112001. DOI: [10.1103/PhysRevD.101.112001](https://doi.org/10.1103/PhysRevD.101.112001). arXiv: [2002.09323](https://arxiv.org/abs/2002.09323) [hep-ex].
- [355] K. Abe et al. “Simultaneous measurement of the muon neutrino charged-current cross section on oxygen and carbon without pions in the final state at T2K”. *Phys. Rev. D* 101.11 (2020), p. 112004. DOI: [10.1103/PhysRevD.101.112004](https://doi.org/10.1103/PhysRevD.101.112004). arXiv: [2004.05434](https://arxiv.org/abs/2004.05434) [hep-ex].
- [356] K. Abe et al. “Measurement of the ν_μ charged current quasielastic cross section on carbon with the T2K on-axis neutrino beam”. *Phys. Rev. D* 91.11 (2015), p. 112002. DOI: [10.1103/PhysRevD.91.112002](https://doi.org/10.1103/PhysRevD.91.112002). arXiv: [1503.07452](https://arxiv.org/abs/1503.07452) [hep-ex].
- [357] K. Abe et al. “Measurement of the ν charged-current quasielastic cross section on carbon with the ND280 detector at T2K”. *Phys. Rev. D* 92.11 (2015), p. 112003. DOI: [10.1103/PhysRevD.92.112003](https://doi.org/10.1103/PhysRevD.92.112003). arXiv: [1411.6264](https://arxiv.org/abs/1411.6264) [hep-ex].
- [358] K. Abe et al. “Measurement of the neutrino-oxygen neutral-current interaction cross section by observing nuclear deexcitation γ rays”. *Phys. Rev. D* 90.7 (2014), p. 072012. DOI: [10.1103/PhysRevD.90.072012](https://doi.org/10.1103/PhysRevD.90.072012). arXiv: [1403.3140](https://arxiv.org/abs/1403.3140) [hep-ex].
- [359] K. Abe et al. “Measurement of neutrino and antineutrino neutral-current quasielasticlike interactions on oxygen by detecting nuclear deexcitation γ rays”. *Phys. Rev. D* 100.11 (2019), p. 112009. DOI: [10.1103/PhysRevD.100.112009](https://doi.org/10.1103/PhysRevD.100.112009). arXiv: [1910.09439](https://arxiv.org/abs/1910.09439) [hep-ex].
- [360] K. Abe et al. “Characterization of nuclear effects in muon-neutrino scattering on hydrocarbon with a measurement of final-state kinematics and correlations in charged-current pionless interactions at T2K”. *Phys. Rev. D* 98.3 (2018), p. 032003. DOI: [10.1103/PhysRevD.98.032003](https://doi.org/10.1103/PhysRevD.98.032003). arXiv: [1802.05078](https://arxiv.org/abs/1802.05078) [hep-ex].
- [361] R. Acciarri et al. “First Measurement of Neutrino and Antineutrino Coherent Charged Pion Production on Argon”. *Phys. Rev. Lett.* 113.26 (2014). [Erratum: *Phys.Rev.Lett.* 114, 039901 (2015)], p. 261801. DOI: [10.1103/PhysRevLett.113.261801](https://doi.org/10.1103/PhysRevLett.113.261801). arXiv: [1408.0598](https://arxiv.org/abs/1408.0598) [hep-ex].
- [362] R. Acciarri et al. “Measurement of ν_μ and $\bar{\nu}_\mu$ neutral current $\pi^0 \rightarrow \gamma\gamma$ production in the ArgoNeuT detector”. *Phys. Rev. D* 96.1 (2017), p. 012006. DOI: [10.1103/PhysRevD.96.012006](https://doi.org/10.1103/PhysRevD.96.012006). arXiv: [1511.00941](https://arxiv.org/abs/1511.00941) [hep-ex].

- [363] A. Rodriguez et al. “Measurement of single charged pion production in the charged-current interactions of neutrinos in a 1.3-GeV wide band beam”. *Phys. Rev. D* 78 (2008), p. 032003. DOI: [10.1103/PhysRevD.78.032003](https://doi.org/10.1103/PhysRevD.78.032003). arXiv: [0805.0186](https://arxiv.org/abs/0805.0186) [hep-ex].
- [364] M. Hasegawa et al. “Search for coherent charged pion production in neutrino-carbon interactions”. *Phys. Rev. Lett.* 95 (2005), p. 252301. DOI: [10.1103/PhysRevLett.95.252301](https://doi.org/10.1103/PhysRevLett.95.252301). arXiv: [hep-ex/0506008](https://arxiv.org/abs/hep-ex/0506008).
- [365] C. Mariani et al. “Measurement of inclusive π^0 production in the Charged-Current Interactions of Neutrinos in a 1.3-GeV wide band beam”. *Phys. Rev. D* 83 (2011), p. 054023. DOI: [10.1103/PhysRevD.83.054023](https://doi.org/10.1103/PhysRevD.83.054023). arXiv: [1012.1794](https://arxiv.org/abs/1012.1794) [hep-ex].
- [366] S. Nakayama et al. “Measurement of single π^0 production in neutral current neutrino interactions with water by a 1.3-GeV wide band muon neutrino beam”. *Phys. Lett. B* 619 (2005), pp. 255–262. DOI: [10.1016/j.physletb.2005.05.044](https://doi.org/10.1016/j.physletb.2005.05.044). arXiv: [hep-ex/0408134](https://arxiv.org/abs/hep-ex/0408134).
- [367] C. Adams et al. “First measurement of ν_μ charged-current π^0 production on argon with the MicroBooNE detector”. *Phys. Rev. D* 99.9 (2019), p. 091102. DOI: [10.1103/PhysRevD.99.091102](https://doi.org/10.1103/PhysRevD.99.091102). arXiv: [1811.02700](https://arxiv.org/abs/1811.02700) [hep-ex].
- [368] B. Eberly et al. “Charged Pion Production in ν_μ Interactions on Hydrocarbon at $\langle E_\nu \rangle = 4.0$ GeV”. *Phys. Rev. D* 92.9 (2015), p. 092008. DOI: [10.1103/PhysRevD.92.092008](https://doi.org/10.1103/PhysRevD.92.092008). arXiv: [1406.6415](https://arxiv.org/abs/1406.6415) [hep-ex].
- [369] C. L. McGivern et al. “Cross sections for ν_μ and $\bar{\nu}_\mu$ induced pion production on hydrocarbon in the few-GeV region using MINERvA”. *Phys. Rev. D* 94.5 (2016), p. 052005. DOI: [10.1103/PhysRevD.94.052005](https://doi.org/10.1103/PhysRevD.94.052005). arXiv: [1606.07127](https://arxiv.org/abs/1606.07127) [hep-ex].
- [370] A. Higuera et al. “Measurement of Coherent Production of π^\pm in Neutrino and Antineutrino Beams on Carbon from E_ν of 1.5 to 20 GeV”. *Phys. Rev. Lett.* 113.26 (2014), p. 261802. DOI: [10.1103/PhysRevLett.113.261802](https://doi.org/10.1103/PhysRevLett.113.261802). arXiv: [1409.3835](https://arxiv.org/abs/1409.3835) [hep-ex].
- [371] T. Le et al. “Measurement of $\bar{\nu}_\mu$ Charged-Current Single π^- Production on Hydrocarbon in the Few-GeV Region using MINERvA”. *Phys. Rev. D* 100.5 (2019), p. 052008. DOI: [10.1103/PhysRevD.100.052008](https://doi.org/10.1103/PhysRevD.100.052008). arXiv: [1906.08300](https://arxiv.org/abs/1906.08300) [hep-ex].
- [372] A. Mislivec et al. “Measurement of total and differential cross sections of neutrino and antineutrino coherent π^\pm production on carbon”. *Phys. Rev. D* 97.3 (2018), p. 032014. DOI: [10.1103/PhysRevD.97.032014](https://doi.org/10.1103/PhysRevD.97.032014). arXiv: [1711.01178](https://arxiv.org/abs/1711.01178) [hep-ex].
- [373] T. Le et al. “Single Neutral Pion Production by Charged-Current $\bar{\nu}_\mu$ Interactions on Hydrocarbon at $\langle E_\nu \rangle = 3.6$ GeV”. *Phys. Lett. B* 749 (2015), pp. 130–136. DOI: [10.1016/j.physletb.2015.07.039](https://doi.org/10.1016/j.physletb.2015.07.039). arXiv: [1503.02107](https://arxiv.org/abs/1503.02107) [hep-ex].
- [374] O. Altinok et al. “Measurement of ν_μ charged-current single π^0 production on hydrocarbon in the few-GeV region using MINERvA”. *Phys. Rev. D* 96.7 (2017), p. 072003. DOI: [10.1103/PhysRevD.96.072003](https://doi.org/10.1103/PhysRevD.96.072003). arXiv: [1708.03723](https://arxiv.org/abs/1708.03723) [hep-ex].
- [375] J. Wolcott et al. “Evidence for Neutral-Current Diffractive π^0 Production from Hydrogen in Neutrino Interactions on Hydrocarbon”. *Phys. Rev. Lett.* 117.11 (2016), p. 111801. DOI: [10.1103/PhysRevLett.117.111801](https://doi.org/10.1103/PhysRevLett.117.111801). arXiv: [1604.01728](https://arxiv.org/abs/1604.01728) [hep-ex].
- [376] A. A. Aguilar-Arevalo et al. “Measurement of Neutrino-Induced Charged-Current Charged Pion Production Cross Sections on Mineral Oil at $E_\nu \sim 1$ GeV”. *Phys. Rev. D* 83 (2011), p. 052007. DOI: [10.1103/PhysRevD.83.052007](https://doi.org/10.1103/PhysRevD.83.052007). arXiv: [1011.3572](https://arxiv.org/abs/1011.3572) [hep-ex].
- [377] A. A. Aguilar-Arevalo et al. “Measurement of the ν_μ charged current π^+ to quasi-elastic cross section ratio on mineral oil in a 0.8-GeV neutrino beam”. *Phys. Rev. Lett.* 103 (2009), p. 081801. DOI: [10.1103/PhysRevLett.103.081801](https://doi.org/10.1103/PhysRevLett.103.081801). arXiv: [0904.3159](https://arxiv.org/abs/0904.3159) [hep-ex].
- [378] A. A. Aguilar-Arevalo et al. “Measurement of ν_μ -induced charged-current neutral pion production cross sections on mineral oil at $E_\nu \in 0.5 - 2.0$ GeV”. *Phys. Rev. D* 83 (2011), p. 052009. DOI: [10.1103/PhysRevD.83.052009](https://doi.org/10.1103/PhysRevD.83.052009). arXiv: [1010.3264](https://arxiv.org/abs/1010.3264) [hep-ex].
- [379] Alexis A. Aguilar-Arevalo et al. “Measurement of ν_μ and $\bar{\nu}_\mu$ induced neutral current single π^0 production cross sections on mineral oil at $E_\nu \sim \mathcal{O}(1\text{GeV})$ ”. *Phys. Rev. D* 81 (2010), p. 013005. DOI: [10.1103/PhysRevD.81.013005](https://doi.org/10.1103/PhysRevD.81.013005). arXiv: [0911.2063](https://arxiv.org/abs/0911.2063) [hep-ex].
- [380] A. A. Aguilar-Arevalo et al. “First Observation of Coherent π^0 Production in Neutrino Nucleus Interactions with $E_\nu < 2$ GeV”. *Phys. Lett. B* 664 (2008), pp. 41–46. DOI: [10.1016/j.physletb.2008.05.006](https://doi.org/10.1016/j.physletb.2008.05.006). arXiv: [0803.3423](https://arxiv.org/abs/0803.3423) [hep-ex].
- [381] P. Adamson et al. “Measurement of single π^0 production by coherent neutral-current ν Fe interactions in the MINOS Near Detector”. *Phys. Rev. D* 94.7 (2016), p. 072006. DOI: [10.1103/PhysRevD.94.072006](https://doi.org/10.1103/PhysRevD.94.072006). arXiv: [1608.05702](https://arxiv.org/abs/1608.05702) [hep-ex].

- [382] C. T. Kullenberg et al. “A Measurement of Coherent Neutral Pion Production in Neutrino Neutral Current Interactions in NOMAD”. *Phys. Lett. B* 682 (2009), pp. 177–184. DOI: [10.1016/j.physletb.2009.10.083](https://doi.org/10.1016/j.physletb.2009.10.083). arXiv: [0910.0062](https://arxiv.org/abs/0910.0062) [hep-ex].
- [383] M. A. Acero et al. “Measurement of neutrino-induced neutral-current coherent π^0 production in the NOvA near detector”. *Phys. Rev. D* 102.1 (2020), p. 012004. DOI: [10.1103/PhysRevD.102.012004](https://doi.org/10.1103/PhysRevD.102.012004). arXiv: [1902.00558](https://arxiv.org/abs/1902.00558) [hep-ex].
- [384] K. Hiraide et al. “Search for Charged Current Coherent Pion Production on Carbon in a Few-GeV Neutrino Beam”. *Phys. Rev. D* 78 (2008), p. 112004. DOI: [10.1103/PhysRevD.78.112004](https://doi.org/10.1103/PhysRevD.78.112004). arXiv: [0811.0369](https://arxiv.org/abs/0811.0369) [hep-ex].
- [385] Y. Kurimoto et al. “Measurement of Inclusive Neutral Current Neutral π^0 Production on Carbon in a Few-GeV Neutrino Beam”. *Phys. Rev. D* 81 (2010), p. 033004. DOI: [10.1103/PhysRevD.81.033004](https://doi.org/10.1103/PhysRevD.81.033004). arXiv: [0910.5768](https://arxiv.org/abs/0910.5768) [hep-ex].
- [386] Y. Kurimoto et al. “Improved Measurement of Neutral Current Coherent π^0 Production on Carbon in a Few-GeV Neutrino Beam”. *Phys. Rev. D* 81 (2010), p. 111102. DOI: [10.1103/PhysRevD.81.111102](https://doi.org/10.1103/PhysRevD.81.111102). arXiv: [1005.0059](https://arxiv.org/abs/1005.0059) [hep-ex].
- [387] K. Abe et al. “First measurement of the muon neutrino charged current single pion production cross section on water with the T2K near detector”. *Phys. Rev. D* 95.1 (2017), p. 012010. DOI: [10.1103/PhysRevD.95.012010](https://doi.org/10.1103/PhysRevD.95.012010). arXiv: [1605.07964](https://arxiv.org/abs/1605.07964) [hep-ex].
- [388] K. Abe et al. “Measurement of Coherent π^+ Production in Low Energy Neutrino-Carbon Scattering”. *Phys. Rev. Lett.* 117.19 (2016), p. 192501. DOI: [10.1103/PhysRevLett.117.192501](https://doi.org/10.1103/PhysRevLett.117.192501). arXiv: [1604.04406](https://arxiv.org/abs/1604.04406) [hep-ex].
- [389] K. Abe et al. “Measurement of the muon neutrino charged-current single π^+ production on hydrocarbon using the T2K off-axis near detector ND280”. *Phys. Rev. D* 101.1 (2020), p. 012007. DOI: [10.1103/PhysRevD.101.012007](https://doi.org/10.1103/PhysRevD.101.012007). arXiv: [1909.03936](https://arxiv.org/abs/1909.03936) [hep-ex].
- [390] K. Abe et al. “Measurement of the single π^0 production rate in neutral current neutrino interactions on water”. *Phys. Rev. D* 97.3 (2018), p. 032002. DOI: [10.1103/PhysRevD.97.032002](https://doi.org/10.1103/PhysRevD.97.032002). arXiv: [1704.07467](https://arxiv.org/abs/1704.07467) [hep-ex].
- [391] D. Casper. “The Nuance neutrino physics simulation, and the future”. *Nucl. Phys. B Proc. Suppl.* 112 (2002). Ed. by J. G. Morfin, M. Sakuda, and Y. Suzuki, pp. 161–170. DOI: [10.1016/S0920-5632\(02\)01756-5](https://doi.org/10.1016/S0920-5632(02)01756-5). arXiv: [hep-ph/0208030](https://arxiv.org/abs/hep-ph/0208030).
- [392] W. R. Leo. *Techniques for Nuclear and Particle Physics Experiments: A How to Approach*. 1987. ISBN: 978-3-540-57280-0.
- [393] John David Jackson. *Classical electrodynamics*. 1999.
- [394] Peter Sigmund. “Particle penetration and radiation effects volume 2”. *Springer series in solid-state sciences*. Vol. 179. Springer, 2014.
- [395] M. Demarteau et al. “Particle and nuclear physics instrumentation and its broad connections”. *Rev. Mod. Phys.* 88.4 (2016), p. 045007. DOI: [10.1103/RevModPhys.88.045007](https://doi.org/10.1103/RevModPhys.88.045007).
- [396] Jerrold T Bushberg and John M Boone. *The essential physics of medical imaging*. Lippincott Williams & Wilkins, 2011.
- [397] Erika Garutti. “Lecture notes: The physics of particle detectors” (). URL: http://hep.fcfm.buap.mx/cursos/2017/FM/L2_Interaction_radiationMatter.pdf.
- [398] Konrad Kleinknecht. *Detectors for particle radiation*. Cambridge University Press, 1998.
- [399] R. M. Sternheimer and R. F. Peierls. “General expression for the density effect for the ionization loss of charged particles”. *Phys. Rev. B* 3 (1971), pp. 3681–3692. DOI: [10.1103/PhysRevB.3.3681](https://doi.org/10.1103/PhysRevB.3.3681).
- [400] I. Wingerter-Seez. “Particle Physics Instrumentation”. *2nd Asia-Europe-Pacific School of High-Energy Physics*. 2017, pp. 295–314. DOI: [10.23730/CYRSP-2017-002.295](https://doi.org/10.23730/CYRSP-2017-002.295). arXiv: [1804.11246](https://arxiv.org/abs/1804.11246) [physics.ins-det].
- [401] Shuji Miyamoto and Ken Horikawa. “NewSUB-ARU gamma-ray beam source and application research”. *Reza Kenkyu* 36.12 (2008), pp. 798–805.
- [402] *Interaction of Neutrons With Matter*. URL: <http://www0.mi.infn.it/~sleoni/TEACHING/Nuc-Phys-Det/PDF/Lezione-partI-3-neutrons.pdf>.
- [403] Georges Charpak et al. “The Use of Multiwire Proportional Counters to Select and Localize Charged Particles”. *Nucl. Instrum. Meth.* 62 (1968), pp. 262–268. DOI: [10.1016/0029-554X\(68\)90371-6](https://doi.org/10.1016/0029-554X(68)90371-6).
- [404] F. Sauli. “Principles of Operation of Multiwire Proportional and Drift Chambers” (May 1977). DOI: [10.5170/CERN-1977-009](https://doi.org/10.5170/CERN-1977-009).
- [405] Jay N. Marx and David R. Nygren. “The Time Projection Chamber”. *Phys. Today* 31N10 (1978), pp. 46–53. DOI: [10.1063/1.2994775](https://doi.org/10.1063/1.2994775).
- [406] Rlinehan. URL: <https://commons.wikimedia.org/w/index.php?curid=45798181>.

- [407] Stephen G Kukolich. “Demonstration of the ramsauer-townsend effect in a xenon thyratron”. *American Journal of Physics* 36.8 (1968), pp. 701–703.
- [408] Erika Garutti. “Vertex and Tracking detectors: position and momentum measurement” (). URL: https://www.desy.de/~garutti/LECTURES/ParticleDetectorSS12/L9_Tracking.pdf.
- [409] R. L. Gluckstern. “Uncertainties in track momentum and direction, due to multiple scattering and measurement errors”. *Nucl. Instrum. Meth.* 24 (1963), pp. 381–389. DOI: [10.1016/0029-554X\(63\)90347-1](https://doi.org/10.1016/0029-554X(63)90347-1).
- [410] Claudio Giganti. “Particle Identification in the T2K TPCs and study of the electron neutrino component in the T2K neutrino beam”. PhD thesis. IRFU, Saclay, 2010.
- [411] Werner Riegler. “Particle Physics Instrumentation”. *6th CERN-Latin-American School of High-Energy Physics*. 2013, pp. 393–404. DOI: [10.5170/CERN-2014-001.241](https://doi.org/10.5170/CERN-2014-001.241). arXiv: [1406.7745](https://arxiv.org/abs/1406.7745) [physics.ins-det].
- [412] J B Birks. “Scintillations from Organic Crystals: Specific Fluorescence and Relative Response to Different Radiations”. *Proceedings of the Physical Society. Section A* 64.10 (Oct. 1951), pp. 874–877. DOI: [10.1088/0370-1298/64/10/303](https://doi.org/10.1088/0370-1298/64/10/303). URL: <https://doi.org/10.1088%2F0370-1298%2F64%2F10%2F303>.
- [413] L. Michel. “Interaction between four half spin particles and the decay of the μ meson”. *Proc. Phys. Soc. A* 63 (1950). Ed. by Thibault Damour, Ivan Todorov, and Boris Zhilinskii, pp. 514–531. DOI: [10.1088/0370-1298/63/5/311](https://doi.org/10.1088/0370-1298/63/5/311).
- [414] Yasuhiro Nishimura. “New 50 cm Photo-Detectors for Hyper-Kamiokande”. *PoS ICHEP2016* (2017), p. 303. DOI: [10.22323/1.282.0303](https://doi.org/10.22323/1.282.0303).
- [415] P. Buzhan et al. “Silicon photomultiplier and its possible applications”. *Nucl. Instrum. Meth. A* 504 (2003). Ed. by P. Bourgeois et al., pp. 48–52. DOI: [10.1016/S0168-9002\(03\)00749-6](https://doi.org/10.1016/S0168-9002(03)00749-6).
- [416] D. Renker and E. Lorenz. “Advances in solid state photon detectors”. *JINST* 4 (2009), P04004. DOI: [10.1088/1748-0221/4/04/P04004](https://doi.org/10.1088/1748-0221/4/04/P04004).
- [417] M. Yokoyama et al. “Application of Hamamatsu MPPC to T2K Neutrino Detectors”. *Nucl. Instrum. Meth. A* 610 (2009). Ed. by Philippe Bourgeois et al., pp. 128–130. DOI: [10.1016/j.nima.2009.05.077](https://doi.org/10.1016/j.nima.2009.05.077). arXiv: [0807.3145](https://arxiv.org/abs/0807.3145) [physics.ins-det].
- [418] K. Abe et al. “The T2K experiment”. *Nuclear Instruments and Methods in Physics Research Section A: Accelerators, Spectrometers, Detectors and Associated Equipment* 659.1 (2011), pp. 106–135.
- [419] M. H. Ahn et al. “Indications of neutrino oscillation in a 250 km long baseline experiment”. *Phys. Rev. Lett.* 90 (2003), p. 041801. DOI: [10.1103/PhysRevLett.90.041801](https://doi.org/10.1103/PhysRevLett.90.041801). arXiv: [hep-ex/0212007](https://arxiv.org/abs/hep-ex/0212007).
- [420] M. H. Ahn et al. “Measurement of Neutrino Oscillation by the K2K Experiment”. *Phys. Rev. D* 74 (2006), p. 072003. DOI: [10.1103/PhysRevD.74.072003](https://doi.org/10.1103/PhysRevD.74.072003). arXiv: [hep-ex/0606032](https://arxiv.org/abs/hep-ex/0606032).
- [421] Y. Itow et al. “Letter of Intent: A Long Baseline Neutrino Oscillation Experiment using the JHF 50 GeV Proton-Synchrotron and the Super-Kamiokande Detector” (2000).
- [422] T2K Collaboration K. Nishikawa et al. “Letter of intent for a neutrino oscillation experiment at JHF”. *KEK Report* (2003).
- [423] Y Ajima et al. “Tokai-to-Kamioka (T2K) Long Baseline Neutrino Oscillation Experiment Proposal”. *Program Advisory Committee for Nuclear and Particle Physics Experiments, Proposal* 60611 (2006).
- [424] K. Abe et al. “Indication of Electron Neutrino Appearance from an Accelerator-produced Off-axis Muon Neutrino Beam”. *Phys. Rev. Lett.* 107 (2011), p. 041801. DOI: [10.1103/PhysRevLett.107.041801](https://doi.org/10.1103/PhysRevLett.107.041801). arXiv: [1106.2822](https://arxiv.org/abs/1106.2822) [hep-ex].
- [425] K. Abe et al. “Observation of Electron Neutrino Appearance in a Muon Neutrino Beam”. *Phys. Rev. Lett.* 112 (2014), p. 061802. DOI: [10.1103/PhysRevLett.112.061802](https://doi.org/10.1103/PhysRevLett.112.061802). arXiv: [1311.4750](https://arxiv.org/abs/1311.4750) [hep-ex].
- [426] K. Abe et al. “First Muon-Neutrino Disappearance Study with an Off-Axis Beam”. *Phys. Rev. D* 85 (2012), p. 031103. DOI: [10.1103/PhysRevD.85.031103](https://doi.org/10.1103/PhysRevD.85.031103). arXiv: [1201.1386](https://arxiv.org/abs/1201.1386) [hep-ex].
- [427] K. Abe et al. “Precise Measurement of the Neutrino Mixing Parameter θ_{23} from Muon Neutrino Disappearance in an Off-Axis Beam”. *Phys. Rev. Lett.* 112.18 (2014), p. 181801. DOI: [10.1103/PhysRevLett.112.181801](https://doi.org/10.1103/PhysRevLett.112.181801). arXiv: [1403.1532](https://arxiv.org/abs/1403.1532) [hep-ex].
- [428] K. Abe et al. “Measurements of neutrino oscillation in appearance and disappearance channels by the T2K experiment with $6.6 \cdot 10^{20}$ protons on target”. *Phys. Rev. D* 91.7 (2015), p. 072010. DOI: [10.1103/PhysRevD.91.072010](https://doi.org/10.1103/PhysRevD.91.072010). arXiv: [1502.01550](https://arxiv.org/abs/1502.01550) [hep-ex].
- [429] Breakthrough Prize. *Koichiro Nishikawa and the K2K and T2K Collaboration*. 2016. URL: <https://breakthroughprize.org/Laureates/1/L155>.

- [430] K. Abe et al. “Measurement of neutrino and antineutrino oscillations by the T2K experiment including a new additional sample of ν_e interactions at the far detector”. *Phys. Rev. D* 96.9 (2017). [Erratum: *Phys.Rev.D* 98, 019902 (2018)], p. 092006. DOI: [10.1103/PhysRevD.96.092006](https://doi.org/10.1103/PhysRevD.96.092006). arXiv: [1707.01048](https://arxiv.org/abs/1707.01048) [hep-ex].
- [431] K. Abe et al. “Search for CP Violation in Neutrino and Antineutrino Oscillations by the T2K Experiment with 2.2×10^{21} Protons on Target”. *Phys. Rev. Lett.* 121.17 (2018), p. 171802. DOI: [10.1103/PhysRevLett.121.171802](https://doi.org/10.1103/PhysRevLett.121.171802). arXiv: [1807.07891](https://arxiv.org/abs/1807.07891) [hep-ex].
- [432] Amanda Weltman and Anthony Walters. *Viruses, microscopy and fast radio bursts: 10 remarkable discoveries from 2020*. 2020.
- [433] K. Abe et al. “T2K neutrino flux prediction”. *Phys. Rev. D* 87.1 (2013). [Addendum: *Phys. Rev.D* 87,no.1,019902(2013)], p. 012001. DOI: [10.1103/PhysRevD.87.012001](https://doi.org/10.1103/PhysRevD.87.012001), [10.1103/PhysRevD.87.019902](https://doi.org/10.1103/PhysRevD.87.019902). arXiv: [1211.0469](https://arxiv.org/abs/1211.0469) [hep-ex].
- [434] T. Nakamoto et al. “Construction of Superconducting Magnet System for the J-PARC Neutrino Beam Line”. *IEEE Trans. Appl. Supercond.* 20.3 (2010), pp. 208–213. DOI: [10.1109/TASC.2009.2038800](https://doi.org/10.1109/TASC.2009.2038800).
- [435] T. Ogitsu et al. “Commissioning of superconducting combined function magnet system for J-PARC neutrino beam line” (2009).
- [436] K. Matsuoka et al. “Design and Performance of the Muon Monitor for the T2K Neutrino Oscillation Experiment”. *Nucl. Instrum. Meth. A* 624 (2010), pp. 591–600. DOI: [10.1016/j.nima.2010.09.074](https://doi.org/10.1016/j.nima.2010.09.074). arXiv: [1008.4077](https://arxiv.org/abs/1008.4077) [physics.ins-det].
- [437] A. Carroll D. Beavis and I. Chiang. *Long baseline neutrino oscillation experiment at the AGS. Physics design report*. Tech. rep. Brookhaven National Lab., 1995.
- [438] Tomislav Vladislavjevic. “Constraining the T2K Neutrino Flux Prediction with 2009 NA61/SHINE Replica-Target Data”. *Prospects in Neutrino Physics*. Apr. 2018. DOI: [10.5281/zenodo.1300546](https://doi.org/10.5281/zenodo.1300546). arXiv: [1804.00272](https://arxiv.org/abs/1804.00272) [physics.ins-det].
- [439] Alfredo Ferrari et al. “FLUKA: A multi-particle transport code (Program version 2005)” (Oct. 2005). DOI: [10.2172/877507](https://doi.org/10.2172/877507).
- [440] Giuseppe Battistoni et al. “Overview of the FLUKA code”. *Annals Nucl. Energy* 82 (2015), pp. 10–18. DOI: [10.1016/j.anucene.2014.11.007](https://doi.org/10.1016/j.anucene.2014.11.007).
- [441] René Brun et al. “GEANT Detector Description and Simulation Tool” (Oct. 1994). DOI: [10.17181/CERN.MUHF.DMJ1](https://doi.org/10.17181/CERN.MUHF.DMJ1).
- [442] C. Zeitnitz and T. A. Gabriel. “The GEANT-CALOR interface”. *3rd International Conference on Calorimetry in High-energy Physics (Note: dates changed from Oct 6-9)*. Sept. 1992.
- [443] N. Abgrall et al. “Measurements of π^\pm , K^\pm , K_S^0 , Λ and proton production in proton-carbon interactions at 31 GeV/c with the NA61/SHINE spectrometer at the CERN SPS”. *Eur. Phys. J. C* 76.2 (2016), p. 84. DOI: [10.1140/epjc/s10052-016-3898-y](https://doi.org/10.1140/epjc/s10052-016-3898-y). arXiv: [1510.02703](https://arxiv.org/abs/1510.02703) [hep-ex].
- [444] N. Abgrall et al. “Measurements of π^\pm , K^\pm and proton double differential yields from the surface of the T2K replica target for incoming 31 GeV/c protons with the NA61/SHINE spectrometer at the CERN SPS”. *Eur. Phys. J. C* 79.2 (2019), p. 100. DOI: [10.1140/epjc/s10052-019-6583-0](https://doi.org/10.1140/epjc/s10052-019-6583-0). arXiv: [1808.04927](https://arxiv.org/abs/1808.04927) [hep-ex].
- [445] T. Vladislavjevic et al. *T2K-TN354: Flux Prediction and Uncertainty with NA61/SHINE 2009 Replica-Target Data*. June 2020.
- [446] K. Abe et al. “Measurements of the T2K neutrino beam properties using the INGRID on-axis near detector”. *Nucl. Instrum. Meth. A* 694 (2012), pp. 211–223. DOI: [10.1016/j.nima.2012.03.023](https://doi.org/10.1016/j.nima.2012.03.023). arXiv: [1111.3119](https://arxiv.org/abs/1111.3119) [physics.ins-det].
- [447] J. Altegoer et al. “The NOMAD experiment at the CERN SPS”. *Nucl. Instrum. Meth. A* 404 (1998), pp. 96–128. DOI: [10.1016/S0168-9002\(97\)01079-6](https://doi.org/10.1016/S0168-9002(97)01079-6).
- [448] S. Aoki et al. “The T2K Side Muon Range Detector (SMRD)”. *Nucl. Instrum. Meth. A* 698 (2013), pp. 135–146. DOI: [10.1016/j.nima.2012.10.001](https://doi.org/10.1016/j.nima.2012.10.001). arXiv: [1206.3553](https://arxiv.org/abs/1206.3553) [physics.ins-det].
- [449] D. Allan et al. “The Electromagnetic Calorimeter for the T2K Near Detector ND280”. *JINST* 8 (2013), P10019. DOI: [10.1088/1748-0221/8/10/P10019](https://doi.org/10.1088/1748-0221/8/10/P10019). arXiv: [1308.3445](https://arxiv.org/abs/1308.3445) [physics.ins-det].
- [450] S. Assylbekov et al. “The T2K ND280 Off-Axis Pi-Zero Detector”. *Nucl. Instrum. Meth. A* 686 (2012), pp. 48–63. DOI: [10.1016/j.nima.2012.05.028](https://doi.org/10.1016/j.nima.2012.05.028). arXiv: [1111.5030](https://arxiv.org/abs/1111.5030) [physics.ins-det].
- [451] Melanie Day. “Electron Neutrinos in the Pi-Zero Detector of the T2K Experiment”. PhD thesis. Rochester U., 2012.
- [452] P. A. Amaudruz et al. “The T2K Fine-Grained Detectors”. *Nucl. Instrum. Meth. A* 696 (2012), pp. 1–31. DOI: [10.1016/j.nima.2012.08.020](https://doi.org/10.1016/j.nima.2012.08.020). arXiv: [1204.3666](https://arxiv.org/abs/1204.3666) [physics.ins-det].

- [453] Pascal Baron et al. “AFTER, an ASIC for the readout of the large T2K time projection chambers”. *IEEE Trans. Nucl. Sci.* 55 (2008), pp. 1744–1752. DOI: [10.1109/TNS.2008.924067](https://doi.org/10.1109/TNS.2008.924067).
- [454] K. Jiae et al. *T2K-TN-104. Michel Electron Tagging in the FGDs*. URL: https://www.t2k.org/docs/technotes/104/michel-electron-tagging-efficiency_v2.
- [455] Caio Augusto P. D. B. Licciardi. “Measurement of Single Positive Pion Production in Neutrino Neutral Current Interactions in the ND280 Detector and Particle Identification with the Fine Grained Detector at T2K”. PhD thesis. Regina U., 2012.
- [456] N. Abgrall et al. “Time Projection Chambers for the T2K Near Detectors”. *Nucl. Instrum. Meth. A* 637 (2011), pp. 25–46. DOI: [10.1016/j.nima.2011.02.036](https://doi.org/10.1016/j.nima.2011.02.036). arXiv: [1012.0865](https://arxiv.org/abs/1012.0865) [physics.ins-det].
- [457] I. Giomataris et al. “Micromegas in a bulk”. *Nucl. Instrum. Meth. A* 560 (2006), pp. 405–408. DOI: [10.1016/j.nima.2005.12.222](https://doi.org/10.1016/j.nima.2005.12.222). arXiv: [physics/0501003](https://arxiv.org/abs/physics/0501003).
- [458] Y. Giomataris et al. “MICROMEGAS: A High granularity position sensitive gaseous detector for high particle flux environments”. *Nucl. Instrum. Meth. A* 376 (1996), pp. 29–35. DOI: [10.1016/0168-9002\(96\)00175-1](https://doi.org/10.1016/0168-9002(96)00175-1).
- [459] A. Vacheret et al. “First results of the Trip-t based T2K front end electronics performance with GM-APD”. *PoS PD07* (2006), p. 027. DOI: [10.22323/1.051.0027](https://doi.org/10.22323/1.051.0027).
- [460] *Maximum Integration Data Acquisition System: MIDAS*. URL: https://midas.triumf.ca/MidasWiki/index.php/Main_Page (visited on 06/16/2021).
- [461] R. Brun and F. Rademakers. “ROOT: An object oriented data analysis framework”. *Nucl. Instrum. Meth. A* 389 (1997). Ed. by M. Werlen and D. Perret-Gallix, pp. 81–86. DOI: [10.1016/S0168-9002\(97\)00048-X](https://doi.org/10.1016/S0168-9002(97)00048-X).
- [462] S. Agostinelli et al. “GEANT4—a simulation toolkit”. *Nucl. Instrum. Meth. A* 506 (2003), pp. 250–303. DOI: [10.1016/S0168-9002\(03\)01368-8](https://doi.org/10.1016/S0168-9002(03)01368-8).
- [463] C. Arnault. “CMT: A software configuration management tool”. *11th International Conference on Computing in High-Energy and Nuclear Physics*. Feb. 2000.
- [464] Simon Yuill. “Concurrent versions system”. *Software Studies: A Lexicon* 64 (2008).
- [465] Radovan Bast and Roberto Di Remigio. *CMake Cookbook: Building, testing, and packaging modular software with modern CMake*. Packt Publishing Ltd, 2018.
- [466] Scott Chacon and Ben Straub. *Pro git*. Springer Nature, 2014.
- [467] T2K collaboration. *Publicly available T2K images*. URL: <http://t2k-experiment.org/wp-content/uploads/> (visited on 06/17/2021).
- [468] Adrian Cho. *The Unruly Neutrino*. 2013.
- [469] D. Barrow et al. *Super-Kamiokande Data Quality, MC, and Systematics in Run 10*. URL: <https://t2k.org/docs/technotes/399/v2r1>.
- [470] G. P. Zeller. “Low-energy neutrino cross-sections: Comparison of various Monte Carlo predictions to experimental data”. *2nd International Workshop on Neutrino-Nucleus Interactions in the Few GeV Region*. Dec. 2003. arXiv: [hep-ex/0312061](https://arxiv.org/abs/hep-ex/0312061).
- [471] X. Li and M. Wilking. *FitQun Event Selection Optimization*. URL: https://t2k.org/docs/technotes/319/tn-319_v1.1.
- [472] C. Licciardi and M. Barbi. *Measurement of Single π^+ Production Induced by ν_μ NC Interactions Using the ND280 Tracker*. URL: https://t2k.org/docs/technotes/129/ncspip_t2knote_v1.pdf.
- [473] Jun Kameda. *Updated study of the systematic error in ν_μ disappearance analyses from Super-Kamiokande*. URL: <https://t2k.org/docs/technotes/159/2nddraft>.
- [474] P. Bartet et al. *T2K-TN212: ν_μ CC events selection in the ND280 tracker using Run 2+3+4 data*. Oct. 2015.
- [475] G. Christodoulou et al. *Selection of ν_e and $\bar{\nu}_e$ in the ND280 tracker using anti-neutrino beam data from Run5 and Run6*. URL: https://t2k.org/docs/technotes/282/NuE_RHC_v5_19072016.pdf.
- [476] M. A. Thomson. *Fitting and Hypothesis testing*. 2015. URL: https://www.hep.phy.cam.ac.uk/~thomson/lectures/statistics/Fitting_Handout.pdf.
- [477] S. S. Wilks. “The Large-Sample Distribution of the Likelihood Ratio for Testing Composite Hypotheses”. *Annals Math. Statist.* 9.1 (1938), pp. 60–62. DOI: [10.1214/aoms/1177732360](https://doi.org/10.1214/aoms/1177732360).
- [478] S. Bolognesi et al. *T2K-TN214: Model independent $\text{numu CC0}\pi$ cross-section in ND280*. 2014.
- [479] S. Cao et al. *T2K-TN261: Measurement of the ν_μ charged-current coherent pion production cross-section with the Proton Module*. 2015.
- [480] F. Di Lodovico et al. *T2K-TN263: T2K cross section measurement best practice*. 2015.
- [481] S. Dolan et al. *T2K-TN287: Probing nuclear effects with a $\text{CC0}\pi + \text{Np}$ differential cross-section measurement*. 2016.
- [482] C. Riccio et al. *T2K-TN337: Measurement of NuMu and AntiNuMu $\text{CC-0}\pi$ cross-section on carbon*. 2017.

- [483] M. Buizza Avanzini et al. *T2K-TN338: Measurement of flux-integrated cross-section on Oxygen and Oxygen/Carbon ratio of CC0pi events in FGD1+FGD2*. 2017.
- [484] A. Cudd et al. *T2K-TN384: Measurement of flux-integrated joint on/off-axis numu CC0pi cross-section using FGD1 and the Proton Module*. 2019.
- [485] F. James and M. Roos. “Minit: A System for Function Minimization and Analysis of the Parameter Errors and Correlations”. *Comput. Phys. Commun.* 10 (1975), pp. 343–367. DOI: [10.1016/0010-4655\(75\)90039-9](https://doi.org/10.1016/0010-4655(75)90039-9).
- [486] M. Hatlo et al. “Developments of mathematical software libraries for the LHC experiments”. *IEEE Trans. Nucl. Sci.* 52 (2005), pp. 2818–2822. DOI: [10.1109/TNS.2005.860152](https://doi.org/10.1109/TNS.2005.860152).
- [487] William C Davidon. “Variable metric method for minimization”. *SIAM Journal on Optimization* 1.1 (1991), pp. 1–17.
- [488] L. Berns. “13av7.1 flux release with SK up to run10, ND up to run9” (2020). URL: <https://t2k.org/beam/NuFlux/FluxRelease/13areplica/13av7/13av7-1-flux-release-slides>.
- [489] Takaaki Mori. “Status of the Super-Kamiokande gadolinium project”. *Nucl. Instrum. Meth. A* 732 (2013). Ed. by T. Bergauer et al., pp. 316–319. DOI: [10.1016/j.nima.2013.06.074](https://doi.org/10.1016/j.nima.2013.06.074).
- [490] Hiroyuki Sekiya. “The Super-Kamiokande Gadolinium Project”. *PoS ICHEP2016* (2016), p. 982. DOI: [10.22323/1.282.0982](https://doi.org/10.22323/1.282.0982).
- [491] K. Abe et al. “Letter of Intent: The Hyper-Kamiokande Experiment — Detector Design and Physics Potential —” (Sept. 2011). arXiv: [1109.3262](https://arxiv.org/abs/1109.3262) [hep-ex].
- [492] E. Kearns et al. “Hyper-Kamiokande Physics Opportunities”. *Community Summer Study 2013: Snowmass on the Mississippi*. Sept. 2013. arXiv: [1309.0184](https://arxiv.org/abs/1309.0184) [hep-ex].
- [493] K. Abe et al. “A Long Baseline Neutrino Oscillation Experiment Using J-PARC Neutrino Beam and Hyper-Kamiokande”. Dec. 2014. arXiv: [1412.4673](https://arxiv.org/abs/1412.4673) [physics.ins-det].
- [494] Ko Abe et al. “Proposal for an Extended Run of T2K to 20×10^{21} POT” (Sept. 2016). arXiv: [1609.04111](https://arxiv.org/abs/1609.04111) [hep-ex].
- [495] Kenji Yasutome. “Development of New Muon Monitors for J-PARC Neutrino Experiment”. *PoS NuFact2019* (2020), p. 065. DOI: [10.22323/1.369.0065](https://doi.org/10.22323/1.369.0065).
- [496] Megan Friend, Christophe Bronner, and Mark Hartz. “Beam Induced Fluorescence Monitor R&D for the J-PARC Neutrino Beamline”. *5th International Beam Instrumentation Conference*. Feb. 2017. DOI: [10.18429/JACoW-IBIC2016-WEFG66](https://doi.org/10.18429/JACoW-IBIC2016-WEFG66).
- [497] Kenji Yasutome. “First physics run of the WAGASCI-BabyMIND detector with full setup”. *PoS NuFact2019* (2020), p. 119. DOI: [10.22323/1.369.0119](https://doi.org/10.22323/1.369.0119).
- [498] T. Koga et al. “Water/CH Neutrino Cross Section Measurement at J-PARC (WAGASCI Experiment)”. *JPS Conf. Proc.* 8 (2015), p. 023003. DOI: [10.7566/JPSCP.8.023003](https://doi.org/10.7566/JPSCP.8.023003).
- [499] A. Blondel et al. “The WAGASCI experiment at JPARC to measure neutrino cross-sections on water”. *PoS EPS-HEP2015* (2015), p. 292. DOI: [10.22323/1.234.0292](https://doi.org/10.22323/1.234.0292).
- [500] Benjamin Quilain and Akihiro Minamino. “The WAGASCI detector as an off-axis near detector of the T2K and Hyper-Kamiokande experiments”. *J. Phys. Conf. Ser.* 888.1 (2017), p. 012166. DOI: [10.1088/1742-6596/888/1/012166](https://doi.org/10.1088/1742-6596/888/1/012166). arXiv: [1610.06367](https://arxiv.org/abs/1610.06367) [physics.ins-det].
- [501] K. Abe et al. “Measurements of $\bar{\nu}_\mu$ and $\bar{\nu}_\mu + \nu_\mu$ charged-current cross-sections without detected pions or protons on water and hydrocarbon at a mean anti-neutrino energy of 0.86 GeV”. *PTEP* 2021.4 (2021), p. 043C01. DOI: [10.1093/ptep/ptab014](https://doi.org/10.1093/ptep/ptab014). arXiv: [2004.13989](https://arxiv.org/abs/2004.13989) [hep-ex].
- [502] Hitoshi Oshima et al. “First cross section measurement of neutrino charged current interactions in the iron ECC”. *PoS NuFact2019* (2020), p. 122. DOI: [10.22323/1.369.0122](https://doi.org/10.22323/1.369.0122).
- [503] Tsutomu Fukuda. “Neutrino research program with Nuclear Emulsion at J-PARC”. *PoS KMI2017* (2017), p. 012. DOI: [10.22323/1.294.0012](https://doi.org/10.22323/1.294.0012).
- [504] T. Fukuda et al. “Automatic scanning of nuclear emulsions with wide-angle acceptance for nuclear fragment detection”. *JINST* 8 (2013), P01023. DOI: [10.1088/1748-0221/8/01/P01023](https://doi.org/10.1088/1748-0221/8/01/P01023). arXiv: [1301.1768](https://arxiv.org/abs/1301.1768) [physics.ins-det].
- [505] T. Toshito et al. “Charge identification of highly ionizing particles in desensitized nuclear emulsion using high speed read-out system”. *Nucl. Instrum. Meth. A* 556 (2006), pp. 482–489. DOI: [10.1016/j.nima.2005.11.047](https://doi.org/10.1016/j.nima.2005.11.047).
- [506] K. Kodama et al. “Momentum measurement of secondary particle by multiple Coulomb scattering with emulsion cloud chamber in DONuT experiment”. *Nucl. Instrum. Meth. A* 574 (2007), pp. 192–198. DOI: [10.1016/j.nima.2007.01.162](https://doi.org/10.1016/j.nima.2007.01.162).
- [507] N. Agafonova et al. “Momentum measurement by the Multiple Coulomb Scattering method in the OPERA lead emulsion target”. *New J. Phys.* 14 (2012), p. 013026. DOI: [10.1088/1367-2630/14/1/013026](https://doi.org/10.1088/1367-2630/14/1/013026). arXiv: [1106.6211](https://arxiv.org/abs/1106.6211) [physics.ins-det].

- [508] K. Kodama et al. “Observation of tau neutrino interactions”. *Phys. Lett. B* 504 (2001), pp. 218–224. DOI: [10.1016/S0370-2693\(01\)00307-0](https://doi.org/10.1016/S0370-2693(01)00307-0). arXiv: [hep-ex/0012035](https://arxiv.org/abs/hep-ex/0012035).
- [509] N. Agafonova et al. “Observation of a first ν_τ candidate in the OPERA experiment in the CNGS beam”. *Phys. Lett. B* 691 (2010), pp. 138–145. DOI: [10.1016/j.physletb.2010.06.022](https://doi.org/10.1016/j.physletb.2010.06.022). arXiv: [1006.1623](https://arxiv.org/abs/1006.1623) [hep-ex].
- [510] H. Oshima et al. “First measurement using a nuclear emulsion detector of the ν_μ charged-current cross section on iron around the 1 GeV energy region”. *PTEP* 2021.3 (2021), p. 033C01. DOI: [10.1093/ptep/ptab027](https://doi.org/10.1093/ptep/ptab027). arXiv: [2012.05221](https://arxiv.org/abs/2012.05221) [hep-ex].
- [511] A. Hiramoto et al. “First measurement of $\bar{\nu}_\mu$ and ν_μ charged-current inclusive interactions on water using a nuclear emulsion detector”. *Phys. Rev. D* 102.7 (2020), p. 072006. DOI: [10.1103/PhysRevD.102.072006](https://doi.org/10.1103/PhysRevD.102.072006). arXiv: [2008.03895](https://arxiv.org/abs/2008.03895) [hep-ex].
- [512] J-PARC Program Advisory Committee. *NINJA-T2K Memorandum of Understanding at 26th J-PARC PAC meeting*. 2018. URL: http://j-parc.jp/researcher/Hadron/en/pac_1807/PAC26thMinutes_approved.pdf (visited on 06/29/2021).
- [513] Saba Parsa. “Novel Design features of the Baby MIND Detector for T59-WAGASCI experiment”. *PoS NuFact2017* (2017), p. 152. DOI: [10.22323/1.295.0152](https://doi.org/10.22323/1.295.0152).
- [514] R. Asfandiyarov et al. “Proposal for SPS beam time for the baby MIND and TASD neutrino detector prototypes” (May 2014). arXiv: [1405.6089](https://arxiv.org/abs/1405.6089) [physics.ins-det].
- [515] A. Stahl et al. “Expression of Interest for a very long baseline neutrino oscillation experiment (LBNO)” (June 2012).
- [516] Gabriella Rolando et al. “New and Optimized Magnetization Scheme for the Baby Magnetized Iron Neutrino Detector at J-PARC”. *IEEE Trans. Magnetics* 53.5 (2017), p. 8000706. DOI: [10.1109/TMAG.2017.2664053](https://doi.org/10.1109/TMAG.2017.2664053).
- [517] O. Basille et al. “Baby MIND Readout Electronics Architecture for Accelerator Neutrino Particle Physics Detectors Employing Silicon Photomultipliers”. *JPS Conf. Proc.* 27 (2019), p. 011011. DOI: [10.7566/JPSCP.27.011011](https://doi.org/10.7566/JPSCP.27.011011).
- [518] M. Antonova et al. “Baby MIND Experiment Construction Status”. *Prospects in Neutrino Physics*. Apr. 2017. arXiv: [1704.08917](https://arxiv.org/abs/1704.08917) [physics.ins-det].
- [519] A. Ajmi et al. “Baby MIND detector first physics run”. *Prospects in Neutrino Physics*. Apr. 2020. arXiv: [2004.05245](https://arxiv.org/abs/2004.05245) [physics.ins-det].
- [520] Hiroyuki Sekiya. “The Super Kamionade Gadolinium Project”. *J. Phys. Conf. Ser.* 1342.1 (2020). Ed. by Ken Clark et al., p. 012044. DOI: [10.1088/1742-6596/1342/1/012044](https://doi.org/10.1088/1742-6596/1342/1/012044).
- [521] John F. Beacom and Mark R. Vagins. “GAD-ZOOKS! Anti-neutrino spectroscopy with large water Cherenkov detectors”. *Phys. Rev. Lett.* 93 (2004), p. 171101. DOI: [10.1103/PhysRevLett.93.171101](https://doi.org/10.1103/PhysRevLett.93.171101). arXiv: [hep-ph/0309300](https://arxiv.org/abs/hep-ph/0309300).
- [522] Kavli IPMU. *Annual Report 2020*. 2020.
- [523] Chenyuan Xu. “Current status of SK-Gd project and EGADS”. *J. Phys. Conf. Ser.* 718.6 (2016), p. 062070. DOI: [10.1088/1742-6596/718/6/062070](https://doi.org/10.1088/1742-6596/718/6/062070).
- [524] Ll. Marti et al. “Evaluation of gadolinium’s action on water Cherenkov detector systems with EGADS”. *Nucl. Instrum. Meth. A* 959 (2020), p. 163549. DOI: [10.1016/j.nima.2020.163549](https://doi.org/10.1016/j.nima.2020.163549). arXiv: [1908.11532](https://arxiv.org/abs/1908.11532) [physics.ins-det].
- [525] A. Korzenev et al. “Plastic scintillator detector with the readout based on an array of large-area SiPMs for the ND280/T2K upgrade and SHiP experiments”. *JPS Conf. Proc.* 27 (2019), p. 011005. DOI: [10.7566/JPSCP.27.011005](https://doi.org/10.7566/JPSCP.27.011005). arXiv: [1901.07785](https://arxiv.org/abs/1901.07785) [physics.ins-det].
- [526] M. S. Dixit et al. “Position sensing from charge dispersion in micropattern gas detectors with a resistive anode”. *Nucl. Instrum. Meth. A* 518 (2004), pp. 721–727. DOI: [10.1016/j.nima.2003.09.051](https://doi.org/10.1016/j.nima.2003.09.051). arXiv: [physics/0307152](https://arxiv.org/abs/physics/0307152) [physics].
- [527] C. Jesús-Valls. “Performances of two resistive MicroMegas prototypes for the Time Projection Chambers of the T2K Near Detector upgrade”. *JINST* 15.08 (2020), p. C08016. DOI: [10.1088/1748-0221/15/08/C08016](https://doi.org/10.1088/1748-0221/15/08/C08016). arXiv: [2005.05695](https://arxiv.org/abs/2005.05695) [physics.ins-det].
- [528] G Prior, HARP collaboration, et al. “The HARP time projection chamber”. *Nuclear Physics B- Proceedings Supplements* 125 (2003), pp. 37–42.
- [529] Martin Ester et al. “A density-based algorithm for discovering clusters in large spatial databases with noise”. *Proceedings of the Second International Conference on Knowledge Discovery and Data Mining*. AAAI Press, 1996, pp. 226–231.
- [530] M. S. Dixit and A. Rankin. “Simulating the charge dispersion phenomena in micro pattern gas detectors with a resistive anode”. *Nucl. Instrum. Meth. A* 566 (2006), pp. 281–285. DOI: [10.1016/j.nima.2006.06.050](https://doi.org/10.1016/j.nima.2006.06.050). arXiv: [physics/0605121](https://arxiv.org/abs/physics/0605121) [physics].

- [531] K. Boudjemline et al. “Spatial resolution of a GEM readout TPC using the charge dispersion signal”. *Nucl. Instrum. Meth. A* 574 (2007), pp. 22–27. DOI: [10 . 1016 / j . nima . 2007.01.017](https://doi.org/10.1016/j.nima.2007.01.017). arXiv: [physics/0610232](https://arxiv.org/abs/physics/0610232) [physics].
- [532] R. Diener et al. “The DESY II Test Beam Facility”. *Nucl. Instrum. Meth. A* 922 (2019), pp. 265–286. DOI: [10 . 1016 / j . nima . 2018 . 11 . 133](https://doi.org/10.1016/j.nima.2018.11.133). arXiv: [1807 . 09328](https://arxiv.org/abs/1807.09328) [physics.ins-det].
- [533] A. Blondel et al. “A fully active fine grained detector with three readout views”. *JINST* 13.02 (2018), P02006. DOI: [10 . 1088 / 1748 - 0221 / 13 / 02 / P02006](https://doi.org/10.1088/1748-0221/13/02/P02006). arXiv: [1707 . 01785](https://arxiv.org/abs/1707.01785) [physics.ins-det].
- [534] O. Mineev et al. “Beam test results of 3D fine-grained scintillator detector prototype for a T2K ND280 neutrino active target”. *Nucl. Instrum. Meth. A* 923 (2019), pp. 134–138. DOI: [10 . 1016 / j . nima . 2019 . 01 . 080](https://doi.org/10.1016/j.nima.2019.01.080). arXiv: [1808.08829](https://arxiv.org/abs/1808.08829) [physics.ins-det].
- [535] Y. LeCun et al. “Backpropagation Applied to Handwritten Zip Code Recognition”. *Neural Computation* 1.4 (Dec. 1989), pp. 541–551. ISSN: 0899-7667. DOI: [10 . 1162 / neco . 1989.1.4.541](https://doi.org/10.1162/neco.1989.1.4.541).
- [536] A. Aurisano et al. “A convolutional neural network neutrino event classifier”. *Journal of Instrumentation* 11.09 (2016), P09001. URL: <http://stacks.iop.org/1748-0221/11/i=09/a=P09001>.
- [537] R. Acciarri et al. “Convolutional Neural Networks Applied to Neutrino Events in a Liquid Argon Time Projection Chamber”. *JINST* 12.03 (2017), P03011. DOI: [10.1088/1748-0221/12/03/P03011](https://doi.org/10.1088/1748-0221/12/03/P03011). arXiv: [1611 . 05531](https://arxiv.org/abs/1611.05531) [physics.ins-det].
- [538] B. Abi et al. “Neutrino interaction classification with a convolutional neural network in the DUNE far detector”. *Physical Review D* 102.9 (Nov. 2020). ISSN: 2470-0029. DOI: [10 . 1103 / physrevd . 102 . 092003](https://doi.org/10.1103/physrevd.102.092003). URL: <http://dx.doi.org/10.1103/PhysRevD.102.092003>.
- [539] C. Adams et al. “Sensitivity of a tonne-scale NEXT detector for neutrinoless double beta decay searches”. May 2020. arXiv: [2005.06467](https://arxiv.org/abs/2005.06467) [physics.ins-det].
- [540] Maximilian Kronmueller and Theo Glauch. “Application of Deep Neural Networks to Event Type Classification in IceCube”. *PoS ICRC2019* (2020), p. 937. DOI: [10 . 22323 / 1 . 358 . 0937](https://doi.org/10.22323/1.358.0937). arXiv: [1908 . 08763](https://arxiv.org/abs/1908.08763) [astro-ph.IM].
- [541] Z. Li et al. “Simulation of charge readout with segmented tiles in nEXO”. *JINST* 14.09 (2019), P09020. DOI: [10 . 1088 / 1748 - 0221 / 14 / 09 / P09020](https://doi.org/10.1088/1748-0221/14/09/P09020). arXiv: [1907 . 07512](https://arxiv.org/abs/1907.07512) [physics.ins-det].
- [542] B. Abi et al. “The Single-Phase ProtoDUNE Technical Design Report”. June 2017. arXiv: [1706.07081](https://arxiv.org/abs/1706.07081) [physics.ins-det].
- [543] C. Adams et al. “Deep neural network for pixel-level electromagnetic particle identification in the MicroBooNE liquid argon time projection chamber”. *Phys. Rev. D* 99 (9 May 2019), p. 092001. DOI: [10.1103/PhysRevD.99.092001](https://doi.org/10.1103/PhysRevD.99.092001). URL: <https://link.aps.org/doi/10.1103/PhysRevD.99.092001>.
- [544] Benjamin Graham and Laurens van der Maaten. *Submanifold Sparse Convolutional Networks*. 2017. arXiv: [1706.01307](https://arxiv.org/abs/1706.01307) [cs.NE].
- [545] MicroBooNE Collaboration. “Semantic Segmentation with Sparse Convolutional Neural Network for Event Reconstruction in MicroBooNE”. 2020.
- [546] M. Kekic et al. *Demonstration of background rejection using deep convolutional neural networks in the NEXT experiment*. 2020. arXiv: [2009.10783](https://arxiv.org/abs/2009.10783) [physics.ins-det].
- [547] A. Sperduti and A. Starita. “Supervised neural networks for the classification of structures”. *IEEE Transactions on Neural Networks* 3 (1997), pp. 714–735.
- [548] Jie Zhou et al. *Graph Neural Networks: A Review of Methods and Applications*. 2018. arXiv: [1812.08434](https://arxiv.org/abs/1812.08434) [cs.LG].
- [549] Steven Farrell et al. *Novel deep learning methods for track reconstruction*. 2018. arXiv: [1810.06111](https://arxiv.org/abs/1810.06111) [hep-ex].
- [550] Shah Rukh Qasim et al. “Learning representations of irregular particle-detector geometry with distance-weighted graph networks”. *The European Physical Journal C* 79.7 (July 2019). ISSN: 1434-6052. DOI: [10 . 1140 / epjc / s10052 - 019 - 7113 - 9](https://doi.org/10.1140/epjc/s10052-019-7113-9). URL: <http://dx.doi.org/10.1140/epjc/s10052-019-7113-9>.
- [551] Xiangyang Ju et al. *Graph Neural Networks for Particle Reconstruction in High Energy Physics detectors*. 2020. arXiv: [2003.11603](https://arxiv.org/abs/2003.11603) [physics.ins-det].
- [552] Francois Drielsma et al. *Clustering of Electromagnetic Showers and Particle Interactions with Graph Neural Networks in Liquid Argon Time Projection Chambers Data*. 2020. arXiv: [2007.01335](https://arxiv.org/abs/2007.01335) [physics.ins-det].
- [553] William L. Hamilton, Rex Ying, and Jure Leskovec. *Inductive Representation Learning on Large Graphs*. 2017. arXiv: [1706.02216](https://arxiv.org/abs/1706.02216) [cs.SI].

- [554] Adam Paszke et al. “Pytorch: An imperative style, high-performance deep learning library”. *Advances in neural information processing systems* 32 (2019).
- [555] Diederik P. Kingma and Jimmy Ba. “Adam: A Method for Stochastic Optimization”. *CoRR* abs/1412.6980 (2014). arXiv: 1412.6980. URL: <http://arxiv.org/abs/1412.6980>.
- [556] Kaiming He et al. “Deep Residual Learning for Image Recognition”. *CoRR* abs/1512.03385 (2015). arXiv: 1512.03385. URL: <http://arxiv.org/abs/1512.03385>.
- [557] A. Korzenev et al. “A 4π time-of-flight detector for the ND280/T2K upgrade”. *JINST* 17.01 (2022), P01016. DOI: 10.1088/1748-0221/17/01/P01016. arXiv: 2109.03078 [physics.ins-det].
- [558] C. Betancourt et al. “Application of large area SiPMs for the readout of a plastic scintillator based timing detector”. *JINST* 12.11 (2017), P11023. DOI: 10.1088/1748-0221/12/11/P11023. arXiv: 1709.08972 [physics.ins-det].
- [559] Paolo W. Cattaneo et al. “Development of High Precision Timing Counter Based on Plastic Scintillator with SiPM Readout”. *IEEE Trans. Nucl. Sci.* 61.5 (2014), pp. 2657–2666. DOI: 10.1109/TNS.2014.2347576. arXiv: 1402.1404 [physics.ins-det].
- [560] C. Betancourt et al. “SiPM readout for the SHiP timing detector”. *JINST* 12.02 (2017). Ed. by Pietro Govoni et al., p. C02058. DOI: 10.1088/1748-0221/12/02/C02058.
- [561] Sergio Gómez et al. “MUSIC: An 8 channel readout ASIC for SiPM arrays”. *Optical Sensing and Detection IV*. Vol. 9899. International Society for Optics and Photonics. 2016, 98990G.
- [562] M. Anelli et al. “A facility to Search for Hidden Particles (SHiP) at the CERN SPS” (Apr. 2015). arXiv: 1504.04956 [physics.ins-det].
- [563] C. Ahdida et al. “The experimental facility for the Search for Hidden Particles at the CERN SPS”. *JINST* 14.03 (2019), P03025. DOI: 10.1088/1748-0221/14/03/P03025. arXiv: 1810.06880 [physics.ins-det].
- [564] D. Breton et al. *The WaveCatcher Family of SCA-Based 12-Bit 3.2-GS/s Fast Digitizers*. RT2014 - 19th Real-Time Conference. Poster. May 2014. URL: <http://hal.in2p3.fr/in2p3-00995691>.
- [565] E Delagnes et al. “The sampic waveform and time to digital converter”. *2014 IEEE Nuclear Science Symposium and Medical Imaging Conference (NSS/MIC)*. IEEE. 2014, pp. 1–9.
- [566] J.E. Moyal. “XXX. Theory of ionization fluctuations”. *The London, Edinburgh, and Dublin Philosophical Magazine and Journal of Science* 46.374 (1955), pp. 263–280. DOI: 10.1080/14786440308521076. URL: <https://doi.org/10.1080/14786440308521076>.
- [567] Lars Ruthotto and Eldad Haber. “An introduction to deep generative modeling”. *GAMM-Mitteilungen* (2021), e202100008.
- [568] Giuseppe Di Guglielmo et al. “A reconfigurable neural network ASIC for detector front-end data compression at the HL-LHC”. *IEEE Trans. Nucl. Sci.* 68 (2021), p. 2179. DOI: 10.1109/TNS.2021.3087100. arXiv: 2105.01683 [physics.ins-det].
- [569] Yi Huang et al. *Efficient Data Compression for 3D Sparse TPC via Bicephalous Convolutional Autoencoder*. Nov. 2021. arXiv: 2111.05423 [cs.LG].
- [570] Boram Yoon et al. “Prediction and compression of lattice QCD data using machine learning algorithms on quantum annealer”. *PoS LAT-TICE2021* (2021), p. 143. arXiv: 2112.02120 [hep-lat].
- [571] Pengcheng Ai et al. “Timing and characterization of shaped pulses with MHz ADCs in a detector system: a comparative study and deep learning approach”. *JINST* 14.03 (2019), P03002. DOI: 10.1088/1748-0221/14/03/P03002. arXiv: 1901.07836 [physics.data-an].
- [572] *Denosing Gravitational Waves with Enhanced Deep Recurrent Denosing Auto-Encoders*. Mar. 2019. DOI: 10.1109/ICASSP.2019.8683061. arXiv: 1903.03105 [astro-ph.CO].
- [573] M. Erdmann, F. Schlüter, and R. Smida. “Classification and Recovery of Radio Signals from Cosmic Ray Induced Air Showers with Deep Learning”. *JINST* 14.04 (2019), P04005. DOI: 10.1088/1748-0221/14/04/P04005. arXiv: 1901.04079 [astro-ph.IM].
- [574] Marco Farina, Yuichiro Nakai, and David Shih. “Searching for New Physics with Deep Autoencoders”. *Phys. Rev. D* 101.7 (2020), p. 075021. DOI: 10.1103/PhysRevD.101.075021. arXiv: 1808.08992 [hep-ph].
- [575] Jan Hajer et al. “Novelty Detection Meets Collider Physics”. *Phys. Rev. D* 101.7 (2020), p. 076015. DOI: 10.1103/PhysRevD.101.076015. arXiv: 1807.10261 [hep-ph].
- [576] Andrew Blance, Michael Spannowsky, and Philip Waite. “Adversarially-trained autoencoders for robust unsupervised new physics searches”. *JHEP* 10 (2019), p. 047. DOI: 10.1007/JHEP10(2019)047. arXiv: 1905.10384 [hep-ph].

- [577] M. Crispim Romão, N. F. Castro, and R. Pedro. “Finding New Physics without learning about it: Anomaly Detection as a tool for Searches at Colliders”. *Eur. Phys. J. C* 81.1 (2021). [Erratum: *Eur.Phys.J.C* 81, 1020 (2021)], p. 27. DOI: [10.1140/epjc/s10052-021-09813-2](https://doi.org/10.1140/epjc/s10052-021-09813-2). arXiv: [2006.05432](https://arxiv.org/abs/2006.05432) [hep-ph].
- [578] Taoli Cheng et al. *Variational Autoencoders for Anomalous Jet Tagging*. July 2020. arXiv: [2007.01850](https://arxiv.org/abs/2007.01850) [hep-ph].
- [579] P. Holl et al. “Deep learning based pulse shape discrimination for germanium detectors”. *Eur. Phys. J. C* 79.6 (2019), p. 450. DOI: [10.1140/epjc/s10052-019-6869-2](https://doi.org/10.1140/epjc/s10052-019-6869-2). arXiv: [1903.01462](https://arxiv.org/abs/1903.01462) [physics.ins-det].
- [580] Chung-Hao Liao and Feng-Li Lin. “Deep generative models of gravitational waveforms via conditional autoencoder”. *Phys. Rev. D* 103.12 (2021), p. 124051. DOI: [10.1103/PhysRevD.103.124051](https://doi.org/10.1103/PhysRevD.103.124051). arXiv: [2101.06685](https://arxiv.org/abs/2101.06685) [astro-ph.IM].
- [581] J. W. Monk. “Deep Learning as a Parton Shower”. *JHEP* 12 (2018), p. 021. DOI: [10.1007/JHEP12\(2018\)021](https://doi.org/10.1007/JHEP12(2018)021). arXiv: [1807.03685](https://arxiv.org/abs/1807.03685) [hep-ph].
- [582] Slava Voloshynovskiy et al. “Information bottleneck through variational glasses”. *arXiv preprint arXiv:1912.00830* (2019).
- [583] Erik Buhmann et al. “Getting High: High Fidelity Simulation of High Granularity Calorimeters with High Speed”. *Comput. Softw. Big Sci.* 5.1 (2021), p. 13. DOI: [10.1007/s41781-021-00056-0](https://doi.org/10.1007/s41781-021-00056-0). arXiv: [2005.05334](https://arxiv.org/abs/2005.05334) [physics.ins-det].
- [584] Erik Buhmann et al. “Fast and Accurate Electromagnetic and Hadronic Showers from Generative Models”. *EPJ Web Conf.* 251 (2021), p. 03049. DOI: [10.1051/epjconf/202125103049](https://doi.org/10.1051/epjconf/202125103049).
- [585] C. Rubbia. “The Liquid Argon Time Projection Chamber: A New Concept for Neutrino Detectors” (May 1977).
- [586] E. Aprile, K. L. Giboni, and C. Rubbia. “A Study of Ionization Electrons Drifting Large Distances in Liquid and Solid Argon”. *Nucl. Instrum. Meth. A* 241 (1985), pp. 62–71. DOI: [10.1016/0168-9002\(85\)90516-9](https://doi.org/10.1016/0168-9002(85)90516-9).
- [587] F. Arneodo et al. “The ICARUS 50-l LAr TPC in the CERN neutrino beam”. *INFN Eloisatron Project: 36th Workshop: New Detectors*. Dec. 1998, pp. 3–12. arXiv: [hep-ex/9812006](https://arxiv.org/abs/hep-ex/9812006).
- [588] P. Benetti et al. “A 3-ton liquid argon time projection chamber”. *Nucl. Instrum. Meth. A* 332 (1993), pp. 395–412. DOI: [10.1016/0168-9002\(93\)90297-U](https://doi.org/10.1016/0168-9002(93)90297-U).
- [589] P. Cennini et al. “Performance of a 3-ton liquid argon time projection chamber”. *Nucl. Instrum. Meth. A* 345 (1994), pp. 230–243. DOI: [10.1016/0168-9002\(94\)90996-2](https://doi.org/10.1016/0168-9002(94)90996-2).
- [590] A. Rubbia. “Experiments for CP violation: A Giant liquid argon scintillation, Cerenkov and charge imaging experiment?” *2nd International Workshop on Neutrino Oscillations in Venice (NO-VE 2003)*. Feb. 2004, pp. 321–350. arXiv: [hep-ph/0402110](https://arxiv.org/abs/hep-ph/0402110).
- [591] S. Amerio et al. “Design, construction and tests of the ICARUS T600 detector”. *Nucl. Instrum. Meth. A* 527 (2004), pp. 329–410. DOI: [10.1016/j.nima.2004.02.044](https://doi.org/10.1016/j.nima.2004.02.044).
- [592] C. Rubbia et al. “Underground operation of the ICARUS T600 LAr-TPC: first results”. *JINST* 6 (2011), P07011. DOI: [10.1088/1748-0221/6/07/P07011](https://doi.org/10.1088/1748-0221/6/07/P07011). arXiv: [1106.0975](https://arxiv.org/abs/1106.0975) [hep-ex].
- [593] A. A. Aguilar-Arevalo et al. “The Neutrino Flux prediction at MiniBooNE”. *Phys. Rev. D* 79 (2009), p. 072002. DOI: [10.1103/PhysRevD.79.072002](https://doi.org/10.1103/PhysRevD.79.072002). arXiv: [0806.1449](https://arxiv.org/abs/0806.1449) [hep-ex].
- [594] M. Antonello et al. “A Proposal for a Three Detector Short-Baseline Neutrino Oscillation Program in the Fermilab Booster Neutrino Beam” (Mar. 2015). arXiv: [1503.01520](https://arxiv.org/abs/1503.01520) [physics.ins-det].
- [595] Nicola McConkey. “SBND: Status of the Fermilab Short-Baseline Near Detector”. *J. Phys. Conf. Ser.* 888.1 (2017), p. 012148. DOI: [10.1088/1742-6596/888/1/012148](https://doi.org/10.1088/1742-6596/888/1/012148).
- [596] Christian Farnese. “Short-Baseline neutrino oscillation searches with the ICARUS detector”. *J. Phys. Conf. Ser.* 2156 (2021), p. 012141. DOI: [10.1088/1742-6596/2156/1/012141](https://doi.org/10.1088/1742-6596/2156/1/012141).
- [597] R. Acciarri et al. “Long-Baseline Neutrino Facility (LBNF) and Deep Underground Neutrino Experiment (DUNE): Conceptual Design Report, Volume 2: The Physics Program for DUNE at LBNF” (Dec. 2015). arXiv: [1512.06148](https://arxiv.org/abs/1512.06148) [physics.ins-det].
- [598] B. Aimard et al. “A 4 tonne demonstrator for large-scale dual-phase liquid argon time projection chambers”. *JINST* 13.11 (2018), P11003. DOI: [10.1088/1748-0221/13/11/P11003](https://doi.org/10.1088/1748-0221/13/11/P11003). arXiv: [1806.03317](https://arxiv.org/abs/1806.03317) [physics.ins-det].
- [599] B. Aimard et al. “Performance study of a 3×1×1 m³ dual phase liquid Argon Time Projection Chamber exposed to cosmic rays”. *JINST* 16.08 (2021), P08063. DOI: [10.1088/1748-0221/16/08/P08063](https://doi.org/10.1088/1748-0221/16/08/P08063). arXiv: [2104.08227](https://arxiv.org/abs/2104.08227) [physics.ins-det].
- [600] Hannah Ritchie. *Causes of death. Our World in Data*. <https://ourworldindata.org/causes-of-death>. 2018.

- [601] Alex K. Bryant et al. “Trends in Radiation Therapy among Cancer Survivors in the United States, 2000–2030”. *Cancer Epidemiology and Prevention Biomarkers* 26.6 (2017), pp. 963–970. ISSN: 1055-9965. DOI: [10.1158/1055-9965.EPI-16-1023](https://doi.org/10.1158/1055-9965.EPI-16-1023). eprint: <https://cebp.aacrjournals.org/content/26/6/963.full.pdf>. URL: <https://cebp.aacrjournals.org/content/26/6/963>.
- [602] Robert R. Wilson. “Radiological Use of Fast Protons”. *Radiology* 47.5 (1946). PMID: 20274616, pp. 487–491. DOI: [10.1148/47.5.487](https://doi.org/10.1148/47.5.487). eprint: <https://doi.org/10.1148/47.5.487>. URL: <https://doi.org/10.1148/47.5.487>.
- [603] Prashant Gabani et al. “Clinical outcomes and toxicity of proton beam radiation therapy for re-irradiation of locally recurrent breast cancer”. *Clinical and Translational Radiation Oncology* 19 (2019), pp. 116–122. ISSN: 2405-6308. DOI: <https://doi.org/10.1016/j.ctro.2019.09.005>. URL: <https://www.sciencedirect.com/science/article/pii/S2405630819300990>.
- [604] “Acute toxicity of proton beam radiation for pediatric central nervous system malignancies. *Pediatr Blood Cancer*.” (2013 Apr 22.). DOI: [doi: 10.1002/pbc.24554](https://doi.org/10.1002/pbc.24554).
- [605] Ming Yang et al. “Comprehensive analysis of proton range uncertainties related to patient stopping-power-ratio estimation using the stoichiometric calibration”. *Physics in Medicine & Biology* 57.13 (2012), p. 4095.
- [606] Heinz Pernegger et al. “First tests of a novel radiation hard CMOS sensor process for Depleted Monolithic Active Pixel Sensors”. *JINST* 12.06 (2017), P06008. DOI: [10.1088/1748-0221/12/06/P06008](https://doi.org/10.1088/1748-0221/12/06/P06008).
- [607] T. Wang et al. “Development of a Depleted Monolithic CMOS Sensor in a 150 nm CMOS Technology for the ATLAS Inner Tracker Upgrade”. *JINST* 12.01 (2017), p. C01039. DOI: [10.1088/1748-0221/12/01/C01039](https://doi.org/10.1088/1748-0221/12/01/C01039). arXiv: [1611.01206](https://arxiv.org/abs/1611.01206) [physics.ins-det].
- [608] Coralie Neubüser et al. “Sensor design optimization of innovative low-power, large area MAPS for HEP and applied science” (Nov. 2020). arXiv: [2011.09723](https://arxiv.org/abs/2011.09723) [physics.ins-det].
- [609] Michela Esposito et al. “CMOS Active Pixel Sensors as energy-range detectors for proton Computed Tomography”. *Journal of Instrumentation* 10.06 (2015), p. C06001.
- [610] Jan Therhaag. “TMVA: Toolkit for multivariate data analysis”. *AIP Conf. Proc.* 1504.1 (2012). Ed. by Theodore E. Simons and George Maroulis, pp. 1013–1016. DOI: [10.1063/1.4771869](https://doi.org/10.1063/1.4771869).
- [611] Michela Esposito et al. “PRaVDA: The first solid-state system for proton computed tomography”. *Physica Medica* 55 (2018), pp. 149–154. ISSN: 1120-1797. DOI: <https://doi.org/10.1016/j.ejomp.2018.10.020>. URL: <https://www.sciencedirect.com/science/article/pii/S1120179718313073>.
- [612] Caesar E. Ordoñez et al. “A Real-time Image Reconstruction System for Particle Treatment Planning Using Proton Computed Tomography (pCT)”. *Physics Procedia* 90 (2017). Conference on the Application of Accelerators in Research and Industry, CAARI 2016, 30 October – 4 November 2016, Ft. Worth, TX, USA, pp. 193–199. ISSN: 1875-3892. DOI: <https://doi.org/10.1016/j.phpro.2017.09.058>. URL: <https://www.sciencedirect.com/science/article/pii/S1875389217302171>.